

# **Calcium carbonate biomineralisation in plant roots and the rhizosphere: processes, products and the fossil record**

**Adrijan Košir**

Submitted in partial fulfilment of the requirements for the degree of  
**Doctor of Philosophy**

February 2022



School of Earth and  
Environmental Sciences

---

Ysgol Gwyddorau'r  
Ddaear a'r Amgylchedd

## Summary

The primary aim of the thesis was to examine calcification processes in roots of terrestrial plants and to apply these mechanisms to the study of calcified roots in the fossil record. The central idea is a hypothesis that fine roots of vascular plants, i.e. the part of the root system responsible for water and nutrient uptake, play a central role in carbonate formation and diagenesis in near surface terrestrial vadose settings, particularly in certain types of calcretes.

Introductory literature review chapter, providing an overview of geobiology of calcium carbonate in the plant root–soil system, presents the concepts of fine roots, the rhizosphere and related biomineralisation processes in soils. Chapter Two re-examines root-related carbonate micromorphology of some classical Quaternary calcrete localities on the Bahamian islands and re-evaluates the rhizogenic calcrete model. Chapter Three documents immense carbonate biomineralisation products from modern soil environments, forming through intracellular calcification of root cortex, hypothetically linked with proton extrusion as an effective nutrient acquisition mechanism. Calcified roots have been studied in present-day calcareous soils of the Province of Alicante, SE Spain. Intracellular  $\text{CaCO}_3$  precipitation in plant roots is discussed in terms of biomineralisation processes, ecophysiology, and its geological significance. Chapter Four presents results of DNA identification of calcifying plants, based on DNA extracted from organic tissues preserved in modern intracellularly calcified roots. Chapter Five deals with *Microcodium*, a problematic biogenic calcite feature of calcretes and palaeosols. The major part is focused on morphological and ultrastructural analysis and stable isotope analysis of *Microcodium* material from Cretaceous and Palaeogene of south-central Europe and Quaternary of the Caribbean, its comparison with modern intracellularly calcified roots, and discusses the arguments opposing the rhizogenic interpretations, using recently published works as a discourse framework. Final section re-evaluates existing models of root calcification processes and products and propose directions of future research.



## *Acknowledgement*

Completion of this work has taken a long time, far too long. I would like to thank all of the many individuals who have provided research assistance, support and help over the years. Beyond any doubt, this thesis would not exist without the encouragement, patience and support of my supervisors at Cardiff, therefore, very special thanks go to (in order of appearance) Paul Wright, Lesley Cherns and Chris Berry.

## Contents

<b>Chapter 1</b>	<b>Geobiology of calcium carbonate in the plant root–soil system: Literature review</b>	1
1.1	Introduction: Plants and mineral weathering	1
1.2	Palaeosols and pedogenic carbonates	3
1.2.1	Calcretes	4
1.3	The plant root–soil system	5
1.3.1	Characteristics and functions of root systems	5
1.3.2	Fine roots	8
1.3.3	The rhizosphere concept	10
1.4	Rhizoliths and rhizogenic calcretes	11
1.4.1	Rhizosphere biomineralisation vs. inorganic CaCO <sub>3</sub> precipitation	15
1.4.2	Intracellular calcification in plant roots	17
1.5	The <i>Microcodium</i> controversy	18
1.6	Carbon and oxygen stable isotope signatures of root-related carbonates	19
<b>Chapter 2</b>	<b>Calcretes and fine-root systems: Quaternary rhizolites of the Bahamas</b>	21
2.1	Introduction	21
2.2	Geological setting	23
2.2.1	Climate and vegetation	24
2.3	Material and methods	26
2.4	Description and interpretation of rhizolite calcretes	28
2.4.1	Calcrete profiles and macromorphology	28
2.4.2	Mesoscale calcrete fabric	39
2.4.3	Microfabric	43
2.4.4	Mineralogy, elemental and stable isotope composition of rhizolites	55
2.5	Discussion	56
2.5.1	Laminar rhizolites: fine root-mat growth and carbonate mineralisation processes	56
2.5.2	Are macrorhizoliths mostly just coarse root-shaped rhizolite?	59

2.5.3	Calcrete-palaeokarst associations: geobiological processes, climatic factors and process rates	61
2.6	Conclusions	63
<b>Chapter 3</b>	<b>Intracellular calcification in plant roots</b>	<b>64</b>
3.1	Introduction	64
3.1.1	Terminological and conceptual compendium	66
3.2	Geological and environmental setting, soils and vegetation	68
3.2.1	Localities	71
3.3	Material and methods	80
3.3.1.	Field sample collection	80
3.3.2.	Laboratory sample preparation	81
3.3.3.	Thin section petrography	82
3.3.4.	Scanning electron microscopy	82
3.3.5.	SEM and EPMA elemental analysis	83
3.3.6.	Microsampling and stable isotope analysis of carbonate $\delta^{13}\text{C}$ and $\delta^{18}\text{O}$ and organic $\delta^{13}\text{C}$	83
3.3.7.	X-ray diffraction and FTIR mineralogical analysis	84
3.4	Results	86
3.4.1	Field occurrence and macroscopic appearance of iCRs	86
3.4.2	Morphology and architecture of iCR systems	88
3.4.2.1	Live iCRs and partly calcified fine roots	93
3.4.2.2	iCR-substrate relationships	95
3.4.3	Anatomy of iCRs	100
3.4.4	Shape, ultrastructure and crystal morphology of calcified cells	105
3.4.4.1	Non-vacuolar, small-scale mineral precipitates	112
3.4.4.2	Internal filamentous microfabric of calcified cells and weathered iCR aggregates	114
3.4.5	Mineralogy and elemental composition of iCRs and rhizosphere clays	120
3.4.6	$\delta^{13}\text{C}$ and $\delta^{18}\text{O}$ stable isotope composition of iCRs	120
3.5	Discussion	123
3.5.1	Root intracellular $\text{CaCO}_3$ biomineralisation processes and features	123
3.5.2	Functional traits of iCRs	128
3.5.2.1	Architecture and morphology of iCRs	129
3.5.2.2	Physiology of $\text{CaCO}_3$ biomineralisation in plant roots	131
3.5.3	Carbon and oxygen stable isotope signatures of iCRs	136
3.6	Summary and conclusions	141

<b>Chapter 4</b>	<b>Identification of the calcifying plants using DNA barcoding</b>	143
4.1	Introduction	143
4.2	Material and methods	146
4.3	Results and discussion	149
4.4	Conclusions	157
<b>Chapter 5</b>	<b>The <i>Microcodium</i> controversy</b>	158
5.1	Introduction	159
5.2	Material and methods	163
5.2.1	Thin section preparation and petrography	164
5.2.2	Scanning electron microscopy	165
5.2.3	Elemental analysis	166
5.2.4	Sampling and stable isotope analysis of carbonate $\delta^{13}\text{C}$ and $\delta^{18}\text{O}$	167
5.3	Morphology and architecture of <i>Microcodium</i>	168
5.3.1	Fine root rhizoliths, incipient <i>Microcodium</i> and intermediate morphologies	179
5.4	<i>Microcodium</i> -substrate relationships	181
5.5	Ultrastructure and crystal morphology of <i>Microcodium</i> grains	183
5.6	Internal filamentous microfabric of <i>Microcodium</i> grains	192
5.7	Stable isotope analysis of $\delta^{13}\text{C}$ and $\delta^{18}\text{O}$	199
5.8	Discussion: Ancient <i>Microcodium</i> and modern intracellularly calcified roots: similarities and differences	200
5.8.1	Architectural and morphological traits	200
5.8.2	Ultrastructure and crystal growth	204
5.8.3	Filamentous features: Evidence of mycorrhizae or nothing but microendolithic borings?	206
5.8.4	The $\delta^{13}\text{C}$ and $\delta^{18}\text{O}$ stable isotope signatures	208
5.8.5	Can <i>Microcodium</i> be related to special root organs?	216
5.9	Summary and conclusions	217
<b>Chapter 6</b>	<b>General conclusions and prospects</b>	219
	 <b>References</b>	 222

	<b>Appendices</b>	<b>276</b>
A1-1	Carbonate $\delta^{13}\text{C}$ and $\delta^{18}\text{O}$ stable isotope analysis data	277
A2-1	Rhizolites of the Bahamas: Climatic setting, location maps and complementary field photographs	289
A2-2	Holocene/Recent composite rhizoliths from Doukkala, Morocco	292
A2-3	Potential analogues of fine root mineralisation and taphonomy from modern soils	294
A2-4	Examples of live or non-decayed fine root mats in present-day soils	297
A2-5	$\delta^{13}\text{C}$ and $\delta^{18}\text{O}$ stable isotope data of the Bahamian laminar rhizolites and comparative material	298
A3-1	Localities in the Alicante Region	300
A3-2	Geological and climatic setting of the studied localities	302
A3-3	Sample preparation methods for intracellularly calcified roots	303
A3-4	Intracellularly calcified roots: complementary figures	305
A3-5	XRD and FTIR analysis of iCRs	325
A3-6	EPMA analysis of iCRs	328
A3-7	$\delta^{13}\text{C}$ and $\delta^{18}\text{O}$ stable isotope analysis of iCRs	331
A4-1	DNA Barcoding results: Bare sequences	333
A4.2	DNA Barcoding results: Significant BLASTN alignment results 1	337
A4.3	DNA Barcoding results: Significant BLASTN alignment results 2	345
A4-4	rbcLa sequences of selected species of Mediterranean Fabaceae	348
A4-5	Phylogenetic tree of selected species of Mediterranean Fabaceae	351
A5-1	Papers citing <i>Microcodium</i>	352
A5-2	<i>Microcodium</i> revisited: root calcification products of terrestrial plants on carbonate-rich substrates	356
A5-3	Localities of material described and illustrated in Chapter 5	381
A5-4	Petrography of <i>Microcodium</i> : Complementary material	388
A5-5	EPMA elemental analysis of <i>Microcodium</i> and permineralised fine roots/rhizoliths	409
A5-6	Stable isotope analysis of <i>Microcodium</i>	413
A5-7	Published C and O stable isotope data of <i>Microcodium</i> and calcified roots	415

## *Preface*

The primary aim of this thesis is to examine calcification processes in roots of terrestrial plants and to apply these mechanisms to the study of calcified roots in the fossil record. The central idea and a guiding concept of the thesis is a hypothesis that fine roots of vascular plants, i.e. the part of the root system responsible for water and nutrient uptake, play a central role in carbonate formation and diagenesis in soils/sediments in near surface vadose settings, particularly in certain types of calcretes. Rhizoliths – in a broad sense defined as traces and remains of plant roots preserved in mineral matter, particularly calcium carbonate – have been a central topic in palaeosol studies as one of the most prominent and recognisable soil-diagnostic features in sedimentary successions. An overall motivation of the thesis is to make a contribution to the understanding of rhizoliths – from their morphology and classification to metabolic processes responsible for calcium carbonate precipitation in and around plant roots.

Chapter One is a literature review, framed by specific objectives of the thesis and scope of the individual chapters. It provides a focused introductory review, integrating concepts of geobiology of the soil system, (palaeo)biology, (palaeo)ecology of plant roots, sedimentary and diagenetic processes in soil carbonates (calcretes), and principles of calcium carbonate biomineralisation. An attempt is made to bridge the gap between earth and life science disciplines by drawing attention to the concepts of fine roots, the rhizosphere and related biomineralisation processes in soils, which have been largely overlooked, or at least underemphasised, in the modern sedimentological literature.

The central part comprises four case-study chapters. Many of the fundamental concepts on calcrete formation mechanisms are based on well-exposed and thoroughly documented Quaternary shallow-marine and aeolian deposits in the Caribbean islands. Chapter Two re-examines root-related carbonate features in some classical localities on the Bahamian Islands (North Andros, San Salvador and New Providence) and is aimed at re-evaluation of the rhizogenic calcrete model.

The purpose of Chapter Three is to document impressive carbonate biomineralisation products from modern soil environments, forming through intracellular calcification of the root cortex, hypothetically linked with proton extrusion as an effective nutrient acquisition mechanism. Calcified roots have been studied in present-day calcareous soils from xerophyte-dominated semiarid Mediterranean environments of the Province of Alicante, SE Spain. Intracellular  $\text{CaCO}_3$  precipitation in plant roots is discussed in terms of biomineralisation processes, ecophysiology, and its geological significance.

In order to identify the plants producing intracellularly calcified roots, DNA extracted from very small amounts of organic tissue preserved in some of the sampled calcified fine roots has been analysed using DNA barcoding taxonomic identification tools. Because of the methodological specifics, results of DNA analysis of intracellularly calcified roots are presented as a separate Chapter Four.

Chapter Five is aimed at providing answers to the enduring controversy about the origin of *Microcodium*, a problematic biogenic calcitic feature of calcretes and palaeosols. The chapter is based on previous research (Košir 2004) which presented morphological evidence for the root origin of *Microcodium*, based on exquisitely preserved calcified fine roots and transitional forms from Paleocene calcretes of SW Slovenia, which showed that the typical *Microcodium* cellular structures could have formed through progressive radial growth of root cortical cells. The major part of the chapter is focused on morphological and ultrastructural analysis and stable isotope geochemical analysis of *Microcodium* material from Slovenia, Croatia, Spain, France, the Bahamas and Caicos, and discusses the arguments opposing the rhizogenic interpretations, using these counter-arguments from recently published works as a discourse framework.

The final Chapter Six provides a brief overview of root-related biomineralisation processes and carbonate rhizolith formation mechanisms, based on conclusions of the previous chapters. The concepts of rhizolith formation have not been significantly updated since the review of Klappa (1980b) who described general morphology, diagnostic criteria and classification of rhizoliths. The aim of Chapter Six is to set a basis for a critical re-evaluation of carbonate precipitation in plant root systems with a strong emphasis on biologically controlled and induced processes of fine roots and the rhizosphere.

# Chapter 1: Geobiology of calcium carbonate in the plant root–soil system: Literature review

## 1.1 Introduction: Plants and mineral weathering

By a simple and broad definition, soil is the biogeochemically altered material that lies between the lithosphere and the atmosphere (Amundson 2005), the biologically excited layer of the Earth's crust (Richter and Markewitz 1995). For the largest part of soil sciences the term “soil” stands for the medium for plant growth, typically consisting of vertical sequence of layers (soil horizons) of generally unconsolidated mineral and organic material (Birkeland 1999). However, taking into account a considerable maximum rooting depth of certain vegetation types, extending down for several tens of metres and often tapping into permanent or temporarily reliable water sources at depth (Canadell et al. 1996; Jackson et al. 1996; Schenk and Jackson 2002, 2005; Kirkham 2014; Dawson et al. 2020; Schwinning 2010, 2013, 2020; McCormick et al. 2021), such a broader perception of the soil zone largely corresponds to regolith or the unsaturated (vadose) belowground part of the Critical Zone – a system defined from the outer extent of vegetation down to the lower limits of groundwater (Brantley et al. 2006; Hasenmueller et al. 2017). The ‘criticality’ accentuates the essential role of this zone in natural and managed ecosystems because it represents the system of coupled chemical, biological, physical, and geological processes operating together to support life at the Earth's surface (Brantley et al. 2007, Banwart et al. 2019). Although this zone has been studied since the onset of science, the term itself is relatively new (US National Research Council Committee on Basic Research Opportunities in the Earth Sciences, 2001; Brantley et al. 2011; Amundson et al. 2007). The concept of Critical Zone provides a suitable interdisciplinary framework for the study of calcium carbonate biomineralisation in plant roots and the rhizosphere. Perhaps the term *Critical Zone* is not the most practical, relevant, and explicative, yet the concept puts an important (critical) stress on its interdisciplinarity.

Although vegetation has long been recognised as one of the five major factors of soil formation, together with climate, parent material, topography and time (Jenny 1941), the role of vegetation has been largely correlated with climate and climatic constraints for



plant ecology and biogeography. Geological studies have traditionally regarded weathering as a relatively simple set of inorganic (chemical and physical) rock-water interactions, however, during the last decades substantial attention has been paid to the function of rooted vascular plants and their associated microbiota in mineral weathering processes (van Breemen et al. 2000; Landeweert et al 2001; Finlay et al. 2020).

Berner et al. (2005) provided a thorough review of the effects of higher plants on weathering based on studies of plant-induced biogeochemical processes in present-day soils as well as the geological history of plants, weathering and evolution of the atmospheric CO<sub>2</sub>. Following Lucas (2001), Berner et al. (2005) outlined main types of element cycling by plants and their involvement in biogenic secondary mineral production. Among the chemical processes involving plants in weathering and soil formation, the most important part corresponds to biological pumping, that is, the recycling of inorganic constituents (Lucas 2001; Kelly et al. 1998). Plants act as biogeochemical pumps that take up life-essential elements from the soil solution, use them in metabolic processes, temporarily store them in their tissues, and return them to the soil through litterfall, root turnover, and whole plant decomposition after death (Tinker and Nye 2000; Lucas 2001; Amundson et al. 2007). These cycling processes include all major mineral nutrients (nitrogen, phosphorous, sulphur, potassium, magnesium and calcium), minor nutrients (iron, manganese, zinc etc.), as well as silicon and aluminium, i.e. elements that are not essential or in general highly beneficial for plants but are major lithospheric constituents (Marschner 1995; Epstein and Bloom 2005; Broadley et al. 2012a; Broadley et al. 2012b; Hawkesford et al. 2012). Importantly, precipitation of secondary minerals is a crucial component in the chemical evolution of the soil/weathering zone (Brantley et al. 2011) and largely results from biologically induced or biologically influenced mineralisation processes (Lucas 2001), or, in the case of intracellularly calcified roots (Chapter 3), from a complex plant-controlled biomineralisation process driven by plant metabolism (Hinsinger 2013).

Plants operate as geobiological agents on short (minutes to year) and very long (millions of years) timescales (Beerling and Butterfield 2012), the latter particularly by their vital function in global organic and inorganic carbon cycle. By enhancing weathering rates of silicate minerals, plants have played the key role in global climates of the past 400 million years in Earth's history (Beerling and Berner 2005; DiMichele and Gastaldo 2008; de Tombeur et al. 2021).

Over 80% of all land plants form some type of symbiotic association with mycorrhizal fungi (Brundrett 1991, 2004). By colonizing plant roots, mycorrhizal fungi absorb nutrients

and water from the bulk soil and obtain plant photosynthates in return (Landeweert et al. 2001). Mycorrhizal fungi appear to have coevolved with terrestrial plants from the dawn of their evolutionary history in the early Devonian (Brundrett 2002; Smith and Read 2008; Field et al. 2015), moreover, the key weathering processes since the colonization of land by plants have actually been driven by the combined activities of roots and mycorrhizal fungi (Taylor et al. 2009).

## 1.2 Palaeosols and pedogenic carbonates

Palaeosols are ancient soils that have been incorporated into the geological record. Since soils form in response to interactions of the lithosphere, hydrosphere, biosphere, and atmosphere, palaeosols potentially record physical, biological, and chemical information about past conditions near the Earth's surface. Palaeosol research has received an expanding attention over the last several decades. The importance of recognition and interpretation of palaeosols in marine and continental sedimentary systems (Mack et al. 1993; Wright 1994; Kraus 1999; Retallack 2001) has significantly broadened by qualitative and quantitative application of palaeosol indicators in reconstruction of terrestrial environments and climate in the past, reviewed by Sheldon and Tabor (2009) and recently by Tabor and Myers (2015).

One of the most utilized and the most studied palaeoecological and palaeoclimatic indicator in palaeosols is the isotopic composition of pedogenic (soil-formed or secondary) carbonates (Cerling 1984, 1999a, b; Cerling et al. 1989; Cerling and Quade 1993; Ekart et al. 1999; Nordt et al. 2000; Berner and Kothvala 2001; West et al. 2006). Pedogenic carbonates have been used as a tool for the reconstruction of palaeo- $p\text{CO}_2$  levels of the atmosphere using a diffusion-reaction model for the carbon isotopic composition the soil carbonate, assumedly precipitated in equilibrium with soil respired and atmospheric  $\text{CO}_2$  (Cerling 1984). Another application of carbon isotopes of pedogenic carbonates is an estimation of  $\text{C}_4$  vs.  $\text{C}_3$  vegetation biomass in (Neogene and younger) palaeosols (Cerling et al. 1989, 1993; Cerling 1999b).

Wright and Vanstone (1991) exposed theoretical and empirical constraints for the uncritical application of the Cerling model in certain types of soil carbonate, particularly those formed by biologically induced processes of carbonate precipitation, e.g. rhizogenic calcretes (see below).

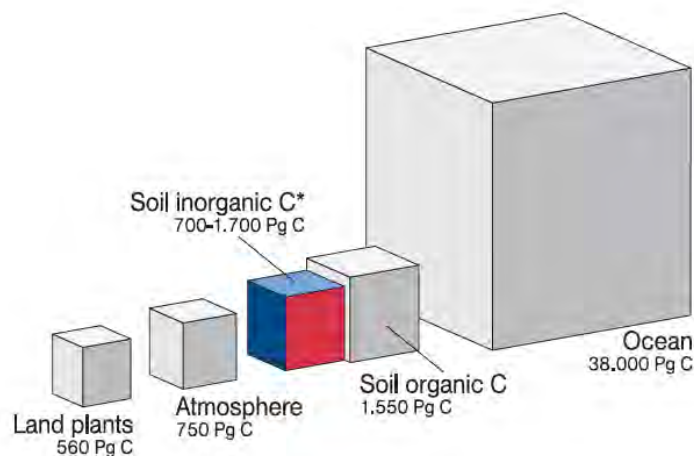


**Fig. 1.1.** Comparison of relative sizes of the principal carbon pools on Earth, based on Eswaran et al. (2000), Lal (2004) and Mackenzie & Lerman (2006). \*The discrepancy between the published estimates of the global soil inorganic carbon is largely due to inability to differentiate between the presence of primary (lithogenic) carbonates and soil carbonates of secondary origin (Lal & Kimble, 2000).  
1 Pg =  $10^{15}$  g = 1 Gt.

Another important aspect of soil carbonates is their role in the global carbon cycle and the fact that the soil inorganic carbon (SIC), predominantly bonded in secondary soil carbonate minerals, represents one of the principal large carbon pools on Earth (Fig. 1.1). Climate change is one of the major issues in the past few decades, hence most of the dealings with the global attributes of soil carbonates implicitly or explicitly tackle their relationship with atmospheric  $\text{CO}_2$  change and the potential mechanisms of using soil-formed carbonate in longer-term carbon sequestration (Lal et al. 2000; Nordt et al. 2000; Lal 2003, 2004; Monger 2014; Monger et al. 2015). In the context of investigation of global SIC stocks and their dynamics on a global and regional scale, Zamanian et al. (2016) discuss the formation mechanisms of pedogenic carbonate, including biogenic processes.

### 1.2.1 Calcretes

Calcretes are near surface, terrestrial accumulations of predominantly calcium carbonate, which occur in a variety of forms from powdery to nodular, highly indurated, massive and laminar, and result from cementation and replacive and displacive introduction of  $\text{CaCO}_3$  into soil profiles, sediments and bedrock, in areas where vadose and shallow phreatic waters are saturated with respect to calcium carbonate (Wright and Tucker 1991). The term calcrete is effectively synonymous with *caliche*, which is more widely used in North American literature (Wright 2007), but only partly with *pedogenic carbonate* since a broad definition of calcrete includes extensive authigenic carbonate bodies formed in the shallow phreatic zone (i.e. groundwater or phreatic calcretes), generally detached from the soil zone.

Comprehensive general reviews on calcretes have been given by Esteban and Klappa (1983), Wright and Tucker (1991), Alonso-Zarza (2003), Wright (2007), and Alonso-Zarza and Wright (2010a, b). Specific aspects of calcretes have been covered in numerous papers: contributions dealing with geobiology of calcretes include Braithwaite (1983), McLaren (1995), McLaren and Gardner (2004), Zhou and Chafetz (2009), Durand et al. (2010, 2018), and Li and Jones (2014), amongst others. Papers focused on root-related features and rhizogenic calcretes are discussed below (section 1.4).

### **1.3 The plant root–soil system**

As expressed by a series of comprehensive monographs on all aspects of plant root studies entitled “Plant Roots: The Hidden Half” (Waisel et al. 1991, 1996, 2002; Eshel and Beeckman 2013), the research on plant roots is a specific and separate discipline of plant sciences. If the root research somehow lags behind the immense progress in the study of the aboveground parts of the plant and biosciences in general (Eshel and Beeckman 2013), the perception of plant roots in sedimentary geology appears to be rather superficial and is mostly rooted in relatively basic textbook concepts. Therefore, important aspects of plant root systems and root-soil processes that are of key relevance for sedimentology, especially near-surface vadose diagenesis in carbonate settings, are briefly reviewed below.

#### ***1.3.1 Characteristics and functions of root systems***

Plant roots vary enormously in the morphology and physiology (Lauenroth and Gill 2003; Lynch 2005). Root systems differ significantly between the groups of “higher” vascular plants and seedless vascular plants (e.g. Kutschera et al. 1992, 1997; Kutschera and Lichtenegger 2013). By a general size and functional division of plant roots (Fitter 1996, 2002; Waisel and Eshel 2002), the root systems consist of coarse (secondary, woody) roots and fine roots (Fig. 1.2; see Section 1.3.2 below). Coarse roots form a “distributive” root system comprised of lower order roots (Fig. 1.2C), responsible for mechanical support (anchorage in soil) and the transport of substances between fine roots and the shoot (Gregory 2006; Danjon et al. 2013). Coarse roots develop a periderm and additional vascular tissue due to secondary growth, are characterised by cortex loss, normally have much longer lifespan than fine roots, and do not contain mycorrhizae (Pregitzer 2002, 2003; Freschet et al. 2021a, b).

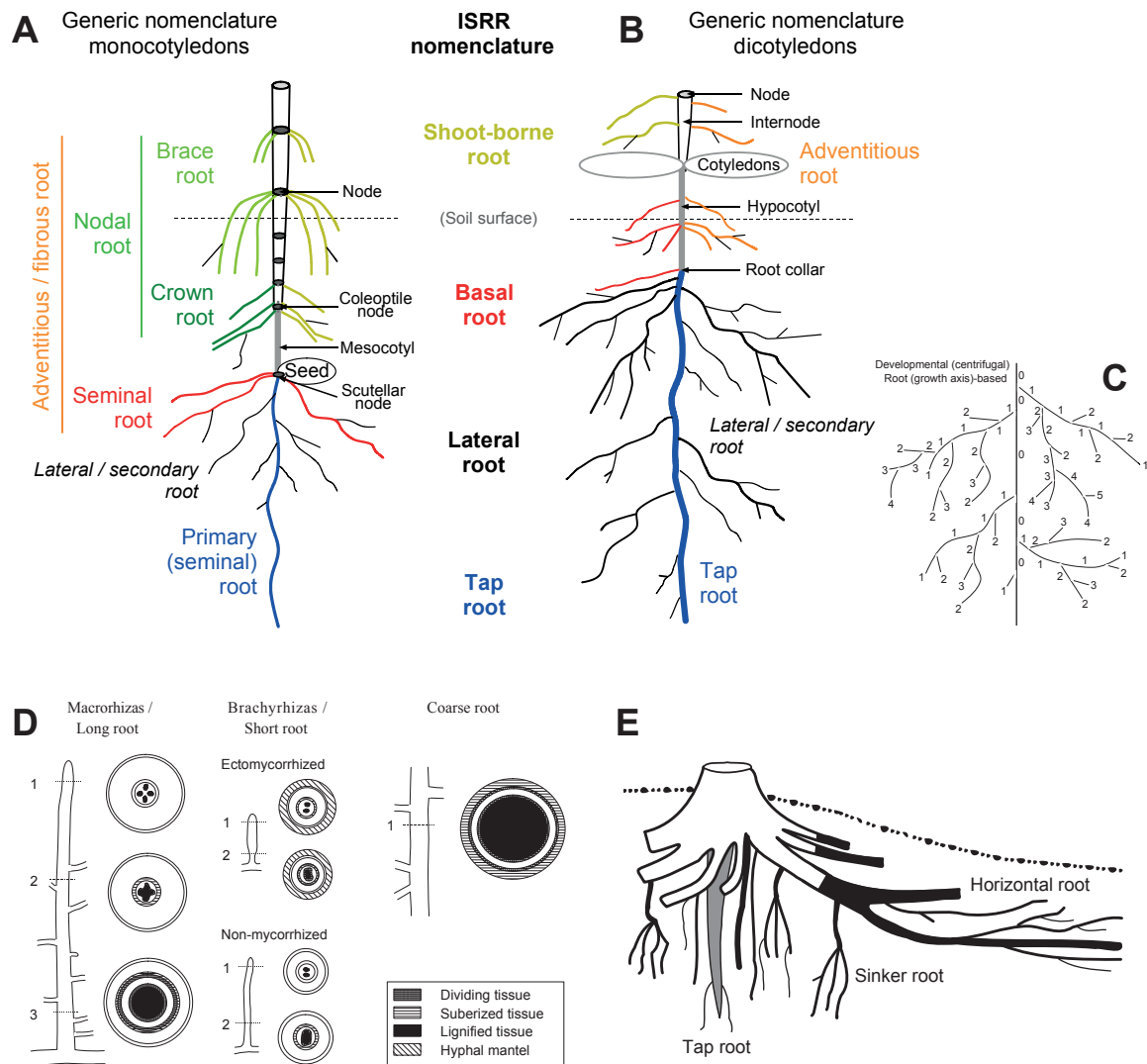


**Fig. 1.2.** Schematic presentations of generic root nomenclature in monocotyledonous (A) and dicotyledonous (B) plants and the corresponding nomenclature proposed by the International Society of Root Research (ISRR). (C) Developmental root branching classification approach. (D) Schematic illustrations of common root nomenclatures related to specific root morphological and anatomical traits. Macrorrhiza and brachyrhiza (fine roots) and woody coarse roots. (E) Taproot, sinker and horizontal roots in a schematic tree root system. From Freschet et al. (2021a).

Root architecture has developed complexity over the course of evolution of terrestrial plants (Brundrett 2002; Lynch 2005; Kenrick and Strullu-Derrien 2014). Bryophytes have rhizoids, which are relatively shallow, unbranched, and architecturally simple. Horsetails (Equisetales) have a more complex root architecture with branching nodes, homologous with their shoot architecture, whereas ferns, although including large and even arborescent species, still exhibit relatively simple root architecture (Kutschera et al. 1997; Lynch 2005).

In phanerogams (seed plants), a simplified diversity of root system types concurs with a division into woody and herbaceous plant types and further subdividing the herbaceous plants into those in which the root system of the established individual is organized around the primary root and those in which that is not the case (Lauenroth and Gill 2003). This leads to a division of vascular plants into three groups: (1) conifers and woody dicots, (2) herbaceous dicots, and (3) monocots. The first two groups share the unifying characteristic that the primary root or taproot commonly directs the branching and the whole root system of the plant (Fig. 1.2B), whereas the root systems of most monocots, particularly grasses (Poaceae) and grass-like plants (Cyperaceae and Juncaceae), consist entirely of stem-borne adventitious roots (Fig. 1.2A; Lauenroth and Gill 2003; Evert 2006).

The key attributes of the three groups are summarised in Lauenroth and Gill (2003, p. 63-64). The first group (conifers and woody dicots) differentiates from the others in secondary growth of elements of the root system. All conifers and woody dicots exhibit secondary growth (production of secondary tissue) in their taproot and main branch roots. Fine roots are a dynamic (short-lived) component of the root systems of conifers and woody dicots and are the only portion of the root system that is considered in evaluation of turnover.

In herbaceous dicots, root systems are characterised by the presence of a taproot and limited or no secondary tissue. Despite the lack of secondary growth, the relatively large diameter taproots of herbaceous dicots enable them to penetrate deeply into the soil. The group is characterised by enormous architectural diversity of root systems (Kutschera et al. 1997, 2013; Lynch 2005).

The third group, monocots, are characterised by stem-borne adventitious root systems. In contrast to the herbaceous dicots and their taproots, the adventitious fibrous root system consists of many main laterals, none of which is very large in diameter.

In woody plants, another classification of root system distinguishes fibrous roots (i.e. feeder, short or absorptive roots) and pioneer roots (i.e. long, framework or skeletal roots). The former correspond to fine roots (see below), principally responsible for water and nutrient absorption, whereas the latter are the main exploratory roots that eventually develop the framework of the whole root system. Pioneer roots typically undergo radial expansion into woody structural roots, whereas fibrous roots may not branch at all and do not develop secondary thickening (Zadworny and Eissesnstat 2011).



### 1.3.2 Fine roots

Fine roots, traditionally defined as those with diameter  $\leq 2$ mm, are higher order lateral roots responsible for most nutrient and water uptake, as well as for mycorrhizae formation (Eissenstat and Yanai 1997; Fig. 1.3). In both annual and perennial plants, roots  $<1$ - $2$  mm in diameter form a structurally and functionally complex population which is the dominant component of the root system. As a below ground analogue of leaves for resource uptake, fine roots are responsible for water and nearly all essential soil nutrient uptake by plants (Wells and Eissenstat 2002). Fine roots have short lifespans (days-months), but are replaced by the plant in a continuous process of root 'turnover': 33-50% of total plant tissue turnover may be represented by fine roots, accordingly, decomposition of fine root organic matter is a major factor in soil formation (Eissenstat et al. 2000; Freschet et al. 2017). Fine roots typically (but not necessarily) form mycorrhizal symbiosis, grow rapidly when soil is favourable, and shed quickly when soil conditions become unfavourable. Growth and maintenance of fine roots can consume up to 50% of daily photosynthate, while as much as 2/3 of annual net primary production can be allocated to fine roots in some ecosystems (Eissenstat 1992). A simple functional classification of McCormack et al. (2015; Fig. 1.3) distinguishes (1) *absorptive fine roots*, characterised by high surface area-to-volume ratio, high degree of mycorrhizal colonization, high root hair density, little to no secondary development, intact cortex, lower suberization, and absence of cork periderm, and (2) *transport fine roots* with high stele-to-diameter ratio, well-developed xylem conduits, and pronounced secondary development (loss of cortex and development of cork periderm, high suberization, increasing lignification).

In addition to primary and secondary root systems (Zobel 2005a), which consist of four classes (ISRR nomenclature in Fig. 1.2; Zobel and Waissel 2010), Zobel (2005b) defined tertiary root systems, made up of two or more classes of genetically and functionally distinct roots, smaller than 0.6 mm in diameter, that condition the observed functionality of mature root systems. Very fine absorptive roots may be  $<0.05$  mm in diameter in some grasses (Poaceae or Graminae) and ericaceous species roots (Fitter 1996; Eissenstat et al. 2015). These finest roots typically have very short lifespan and are replaced by new roots at roughly the same site (Zobel 2005b). Very fine roots are cheaper to construct and may be able to penetrate finer soil pores, however, they are generally more vulnerable to biotic

attack (Robinson et al. 2003). Importantly, tubular fabric in many published examples of laminar rhizolite crusts appears to correspond to such tertiary roots of very small diameter (discussed in Chapter 2).

Absorptive fine roots of most perennial plants form symbiotic associations with mycorrhizal fungi. Particularly ectomycorrhizal plants display high morphological diversity

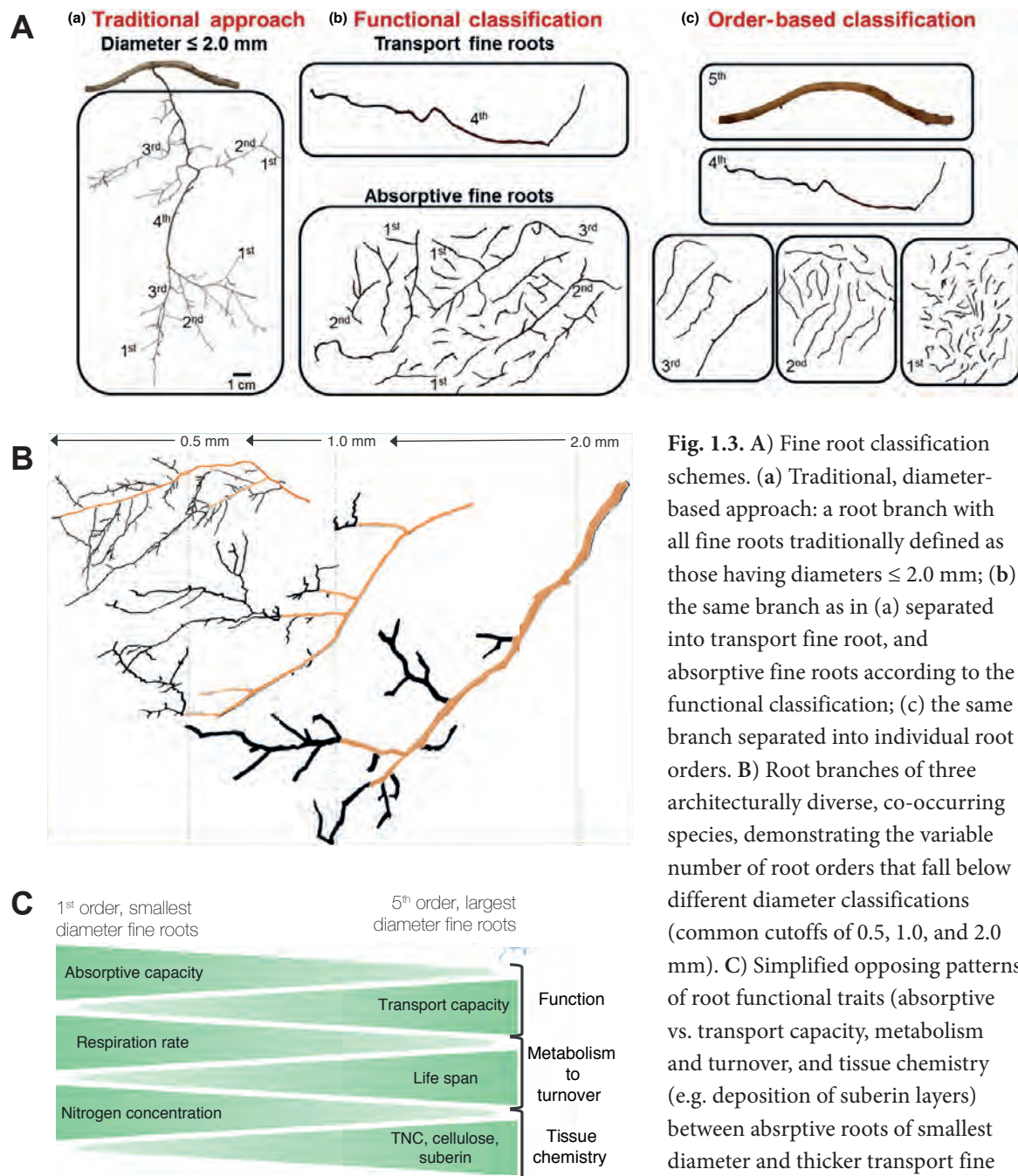


**Fig. 1.3.** A) Fine root classification schemes. (a) Traditional, diameter-based approach: a root branch with all fine roots traditionally defined as those having diameters  $\leq 2.0$  mm; (b) the same branch as in (a) separated into transport fine root, and absorptive fine roots according to the functional classification; (c) the same branch separated into individual root orders. B) Root branches of three architecturally diverse, co-occurring species, demonstrating the variable number of root orders that fall below different diameter classifications (common cutoffs of 0.5, 1.0, and 2.0 mm). C) Simplified opposing patterns of root functional traits (absorptive vs. transport capacity, metabolism and turnover, and tissue chemistry (e.g. deposition of suberin layers) between absorptive roots of smallest diameter and thicker transport fine roots. From McCormack et al. (2015).



of roots with ectomycorrhizae forming on short, determinate roots, displaying a range of forms from unbranched to highly branched structures (Smith and Read 2008). The degree of branching is determined by both plants and fungi, however, McCormack et al. (2015) suggest to exclude mycorrhizal short root structures from fine-root order classification since branching within the ectomycorrhizal cluster appears to be largely under fungal control.

### 1.3.3 The rhizosphere concept

The rhizosphere is defined in simplest terms as the volume of soil around living roots, which is influenced by root activity (Hinsinger et al. 2009). This means that, depending on the activity that one considers (exudation of reactive compounds, respiration, uptake of nutrients and water), the radial extension of the rhizosphere can range from sub-micron to supra-cm scales (Marschner 2012; Marschner and Rengel 2012; York et al. 2016; Kuzyakov and Razavi 2019; van Elsas 2019).

Changes in biochemical, chemical and physical properties of soil surrounding the root, compared with the bulk soil, arise either from processes for which roots are directly responsible, and /or activities of microorganisms that are stimulated in the vicinity of the roots as a consequence of the release of rhizodeposits by roots (Fig. 1.4; Hinsinger et al. 2005). Rhizodeposits consist of a mixture of sloughed cells, mucilage, small-

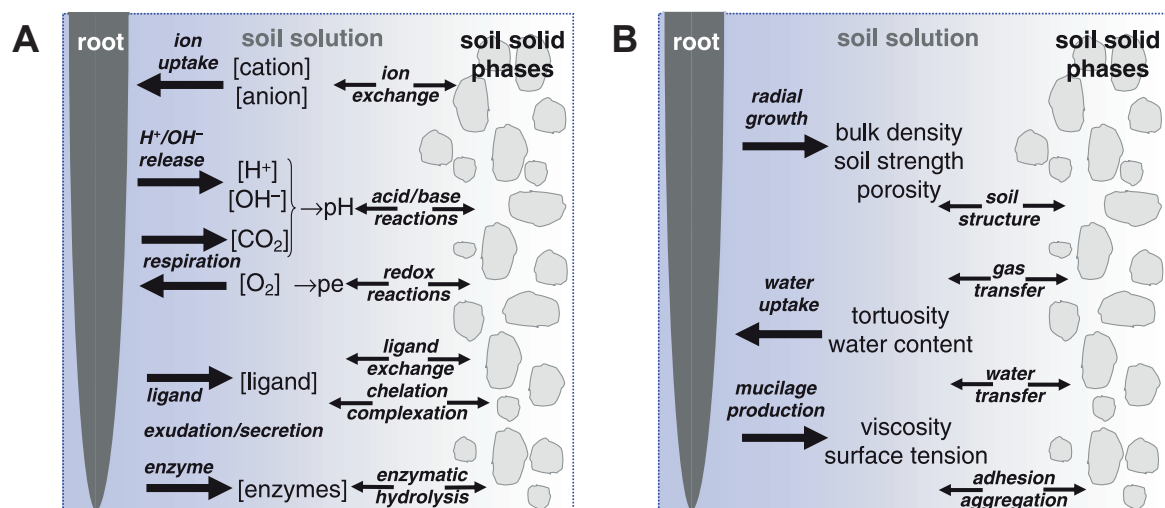


**Fig. 1.4.** Schematic representation of A) root functions involved in changes in physical properties and B) of root functions involved in changes of biochemical and chemical properties occurring in the rhizosphere. From Hinsinger et al. (2005).

molecular-weight sugars, amino acids, and other compounds leaked from root cells, which are deposited in the soil adjacent to the surface of fine roots (Ehrenfeld 2001, 2013). Importantly, this stimulation of microorganisms may be either beneficial or deleterious for plant roots, e.g. by attracting pathogenic microorganisms (Hinsinger et al. 2005). Because the roots of most terrestrial plants are colonised by mycorrhizae-forming symbiotic fungi, the rhizosphere can be logically extended to the mycorrhizosphere (Smith et al. 2003; Timonen and Marschner 2006; Finlay and Thorn 2019) to include the vast volume of soil influenced by networks of fungal hyphae (i.e. mycorrhizal hyphosphere of Finlay 2005). The concept of the mycorrhizosphere significantly expands the functional space and capabilities of the rhizosphere.

Apart from rhizodeposition, there are five key mechanisms of root-soil interaction induced directly by plants and their mycorrhizal fungi (Taylor et al. 2009; Hinsinger 2013): (1) root exudation (release of reactive species such as  $H^+$  and low molecular weight organic chelators), (2) respiration, increasing the  $pCO_2$  in soils, (3) decomposition of plant litter (increasing the concentration of high molecular weight organic acids and low molecular weight organic chelators in the soil solution, fuelling respiration by heterotrophs, and returning base cations from the biota to the soil solution), (4) evapotranspiration (increasing the flow of water-bearing base cations and other nutrients to plants, and affecting soil water residence times and the amount of rainfall on a regional scale), and (5) physical stabilisation of soils by root systems (soil aggregation and compression), e.g. binding of soil particles by roots and mycorrhizal hyphae.

#### 1.4 Rhizoliths and rhizogenic calcretes

Rhizoliths – in the simplest terms defined as traces and remains of plant roots preserved in mineral matter, particularly calcium carbonate – are among the most prominent features in many soils and palaeosols and may constitute the dominant fabrics in some forms of calcrete. Although widely introduced by Klappa (1980b), the term rhizolith (rhizolithus) dates back to at least Linné's *Systema Naturae* (Linnaeus 1770) and Wallerius' *Systema Mineralogicum* (Wallerius 1772, 1778; Fig. 1.5). Mineralised root traces have been described under different names such as rhizomorphs, rhizocretions, rhizoconcretions, ichnorhizomorphs/rhizo-ichnomorphs, etc. (Northrop 1890; Kindle 1923, 1925; Glennie and Evamy 1968; Ziehen 1980, 1981; Curran and White 2001; also see overviews in

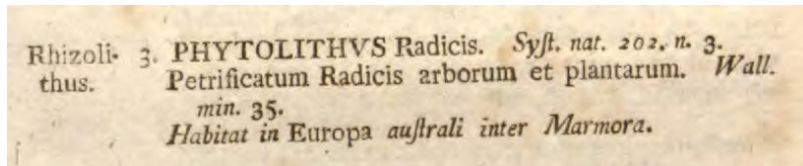


Fig. 1.5. Facsimiles of pages from Linnaeus (1770) *Systema Naturae* (Vol. 3, above) and Wallerius' (1778) *Systema Mineralogicum* (Vol. 2; below); both used the term *rhizolith* (rhizolithus, rhizolithi) for 'petrified plant (tree) roots'.

**3. PETRIFICATA VEGETABILIA, radicum arborum.  
RHIZOLITHI. Spec. 430.**

*Phytolithus radices arborum.* v. LINNÉ. 171. 3.

Sveth. STENWANDLAD ROTH

Gall. RIZOLITHE OU RACINE PETRIFIÉE

Germ. VERSTEINTE WURZELN

Sunt radices arborum vel plantarum petrificatæ, plerumque in achatinam duritiem mutatæ, quæ vero, quum ut plurimum æquali fere sint structura, nonnullæ & æquali cum ipso ligno, difficulter ab invicem vel

Sarjeant 1975, Klappa 1980b and Gregory et al. 2004). Rhizoliths exhibit fabrics reflecting various degrees of biological activity responsible for their formation. Except for their gross morphology, some forms may show no biologically influenced fabrics (for example, simple root moulds left after roots have decayed and subsequently filled with a cement), whereas others are characterized by biologically induced or controlled precipitation of (predominantly) calcium carbonate in, on, or around roots (Wright and Tucker 1991; two end-members are shown in Fig. 1.6).

Despite a widespread spatial and stratigraphic occurrence of rhizoliths, the basic concepts in the understanding their formation have not fundamentally changed since the classical review of Klappa (1980b) who defined genetic types of rhizoliths, their morphology and petrography, mechanisms of their formation and distribution in terrestrial carbonates, mostly based on Quaternary examples of the western Mediterranean. Pfefferkorn and Fuchs (1991) provided a morphological classification of fossil plant features formed through root-soil interactions, and numerous papers during the last four decades significantly improved the understanding of rhizoliths and root-related fabric at subaerial exposure surfaces in sedimentary successions (e.g. Semeniuk and Meagher 1981; Bown 1982; Cohen 1982; Esteban and Klappa 1983; Mount and Cohen 1984; Jones and Ng 1988; Loope 1988; Bockelie 1994; Dickson and Saller 1995; White and Curran 1997; Froede 2002; Liutkus et al. 2005; Alonso-Zarza et al. 2008; Alonso-Zarza 1999, 2018; Owen et al. 2008; Liutkus 2009; Cramer and Hawkins 2009; Semeniuk 2010; Genise et al. 2010; Gocke et al. 2010, 2011, 2014; Huguet et al. 2012, 2020, do Nascimento et al. 2019, amongst many others, cited in the following chapters).

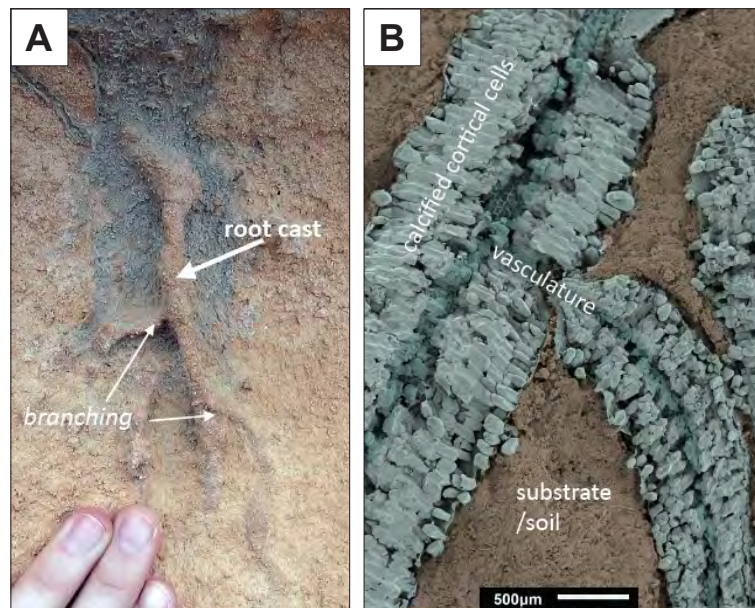


**Fig. 1.6.** Two end-members of the rhizolith family showing low and high degree of biological influence in their formation: A) almost trivial example of a root void in poorly-cemented carbonate aeolianite filled with same, only slightly more cemented sediment. Preservation potential or potential to recognise such feature in palaeosol is very small. Holocene aeolianite, Island of Mallorca. B) branched intracellularly calcified root formed wholly through biologically controlled calcite precipitation in cortical cells. Modern calcareous soil, Sella, Alicante region, Spain. False colours BSE SEM image.

Modern concepts of rhizosphere and fine plant roots, described above (Sections 1.3.2 and 1.3.3), hold important implications for the interpretation of biogeochemical processes in calcretes and rhizoliths. These concepts have largely developed after publication of Klappa's (1980b) paper, therefore, an updated review on rhizoliths would be more than needed. For example, a simple analysis of more than 750 publications listed in Google Scholar and Web of Science (retrieved on April 15, 2021), which cite Klappa (1980b), showed that none of the works mentioned "fine roots" in their title and/or abstract. However, it is important to note that although behaviour and functions of finest roots have intrigued many generations of plant biologists (Darwin and Darwin 1880; Weaver 1919; Epstein 1973), it was not until the seminal publications in the late 1900s and early 2000s which established the concept of fine root architecture, anatomy, physiology and ecology (Eissenstat 1992; Eissenstat and Yanai 1997, 2002; McCully 1995, 1999; Pregitzer 2002, 2003; Zobel 2003; McCormack et al. 2015 and references therein; Freschet et al. 2021a).

A special type of root-related terrestrial carbonate accumulations are rhizogenic calcretes, composed largely or wholly of textures related to calcification in or around roots (Wright et al. 1995). One of the subtypes of rhizogenic calcretes are accumulations of intracellularly calcified roots and *Microcodium* (see below; Chapters 3 and 5), whereas

the other group (termed *rhizolite* by Klappa 1980b) include laminar root-mat calcretes (Chapter 2) and calcretes dominated by calcareous pisoids and peloids and associated rhizoliths (Wright et al. 1988, 1995; Wright 1989, 2007). Although not always explicitly demonstrating the root-related origin, similar kinds of crudely laminar soil carbonate accumulations have been described by Multer and Hoffmeister (1968), James (1972), Read (1974, 1976) and Harrison (1977), sometimes under different names such as soilstone crusts (Robbin and Stipp 1979; Shinn and Lidz 1988; Lidz et al. 2008), root rocks (Perkins 1977), rootcretes (Jones 1992) or root calcretes (Alonso-Zarza and Jones 2007).

Perhaps it is worth noting that in plant biology the term rhizogenic pertains to (1) root-producing, (2) arising from root endodermis (as opposed to originating from pericycle), or (3) stimulating/promoting formation of roots. Rhizogenesis in the broad sense denotes differentiation and development of roots (Lawrence 2005) or, in restricted sense, a specific set of root growth and morphological adaptations, for example to soil drought (i.e., drought rhizogenesis; Vartanian 1996). Related to soil carbonates and calcrete formation, the term ‘rhizogenic’ has been used as ‘root-formed’ (i.e., carbonate generated by plant roots) and ‘root related’ (Wright et al. 1995) or caused/generated by roots (e.g., soil redox processes; Fimmen et al. 2008).

Such a broad terminological use is in agreement with, for example, OED which defines ‘-genic’ as a suffix [to form] for “adjectives with both the sense of *generating, producing (the thing or effect specified by the first element)*’ and ‘*of or relating to origin or development (of the thing or a kind specified by the first element)*’”. It may be useful, however, to re-evaluate terminology for root-related soil carbonate features. Intracellularly calcified roots (Chapter 3), for example, are an obvious and representative case of rhizogenic carbonate, directly produced by biomineralisation in plant root cells, whereas in many or most of the beta-type calcretes it cannot be easily perceived if the carbonate has formed by the influence of living roots (i.e. in the rhizosphere of functional fine roots) or after their senescence and decay. However, the presence of unambiguously preserved anatomic details of fine roots in many beta calcretes (Chapter 2) is a very good indicator of plant roots as a major (f)actor in soil carbonate accumulation even though the precipitated carbonate cannot be directly attributed to roots or is not necessarily connected with the rhizosphere processes (see e.g. distinction between active and relic rhizosphere in York et al. 2016).



### 1.4.1 Rhizosphere biomineralisation vs. inorganic $\text{CaCO}_3$ precipitation

As illustrated above, soil biogeochemical processes are most intensive in the area immediately surrounding live and metabolically active fine roots. Presumably, microbially driven precipitation of secondary soil minerals largely correspond to the rhizosphere and those parts of soil influenced by mycorrhizal and saprophytic fungi. Fungi significantly contribute to the accumulation of microcrystalline soil carbonates (Wright 1986; Phillips et al. 1987; Verrecchia 2000; Caldwell 2000; Gorbushina et al. 2002; Burford et al. 2003, 2006; Gadd et al. 2007; Fomina et al. 2010, amongst others), either directly by involvement in precipitation of fibrous microcrystalline calcite forms (needle-fibre calcite (NFC) and calcite nanofibres; Phillips and Self 1987; Jones and Kahle 1993; Verrecchia and Verrecchia 1994; Loisy et al. 1999; Cailleau et al. 2009a, b; Milliere et al. 2011a, b; Bindschedler et al. 2009, 2012, 2014, 2016) or through transformation of calcium oxalate, deposited on fungal hyphae and in plant tissues, to calcite by soil oxalotrophic bacteria (Verrecchia et al. 1993; Arnott 1995; Garvie 2003, 2006; Braissant et al. 2004; Kolo et al. 2005, 2007; Cailleau et al. 2011; Martin et al. 2012; Rowley et al. 2017, 2018; Uren 2018; Herve et al. 2018, 2021).

Fibrous microcrystalline forms of calcite (FMC) are probably the most ubiquitous form of calcium carbonate in subsurface terrestrial environments and are intimately related to rhizolith formation (Alonso-Zarza 1999, 2018). Although there is considerable evidence that deposits of NFC and calcite nanofibres (micro rods) make specific microbial ecosystems in the vadose zone, controversy remains regarding the role of microorganisms and the mechanism(s) of calcite precipitation. The prevailing biogenic hypotheses are largely based on common co-occurrence of fibrous calcite and microbial features, and the similarity in dimensions and morphology of calcite fibres and fungal hyphae and filamentous bacteria (Verrecchia and Verrecchia 1994; Bindchedler et al. 2016 and references therein). Morphological arguments for biogenicity have been supported by geochemical and petrographic data, considered as biosignatures preserved in certain forms of fibrous calcite. In contrast, purely physicochemical interpretations have linked the occurrence of NFC in vadose environments with highly evaporative conditions in such settings, leading to supersaturation and rapid crystal growth from pore waters (James 1972; Jones and Peng 2014 and references therein).

The biogenicity of NFC and calcite nanofibres has been a subject of the ongoing research (Martín-Pérez and Košir 2017a, b; Martín-Pérez et al. 2019a, b; Košir and Martín-Pérez 2018) using *in-situ* and laboratory investigation of moonmilk-type speleothems. The

studied fibrous microcrystalline carbonates show strikingly similar micromorphological features to calcite crystals produced *in vitro* by non-classical pathways of crystallisation (Olszta et al. 2004; Gower 2008). Results of this research indicate fundamentally different precipitation mechanism to interpretations in recent studies of Bindschedler et al. (2012, 2014), Cailleau et al. (2009a, b) and Milliere et al. (2011a), all explaining FMC as calcite pseudomorphs of fungal hyphae and cell-wall cellulose fibers.

Modern carbonate sedimentology, including its interdisciplinary research area dealing with biomineralisation, has only marginally integrated the ideas of one of the hottest topics in modern materials science, i.e. the concept of nonclassical mineral nucleation and crystal growth (DiMasi and Gower 2014; van Driessche et al. 2017). Calcium carbonate has been widely used as a model mineral, particularly in crystal growth experiments on oriented attachment, amorphous and mesocrystalline calcium carbonates, and polymer-induced liquid-precursor (PILP) processes (Wolf and Gower 2017). These ‘non-standard’ concepts are progressively entering other scientific disciplines and gaining relevance in ‘realistic’ systems such as biomineralisation processes. Precipitation of calcite in these experiments can be compared to natural processes of organomineralisation (= microbially-influenced mineralization of Dupraz et al. 2009) where the organic matrix (mostly microbial exopolymeric substances - EPS) influences crystal morphology and composition - with no living organism and no metabolic processes required. Striking similarity between the natural fibrous microcrystalline calcite and calcite morphologies produced *in vitro*, using e.g. polymer-induced liquid-precursor and solution-precursor-solid mechanisms (Gower 2008), supports further research into crystallization of NFC and calcite nanofibres under extrinsic influence of organic matter (Meldrum and Cölfen 2008).

Organic exudates, such as root and fungal mucilage deposits, critically influence water dynamics in the rhizosphere, particularly in soils affected by intense wetting and drying cycles (Czarnes et al. 2000; Chenu and Cosentino 2011; Carminati et al. 2016, 2017; Benard et al. 2018, 2019). Mucilage, along with root hairs, fungal hyphae and other microorganisms, is largely responsible for the agglutination of soil particles, forming so called rhizosheaths around fine roots (Watt et al. 1994, 2006; McCully 1995, 1999). Mucilage in the rhizosheath help this domain to hold more water than the bulk soil (Lynch et al. 2014), even during drought. Rhizosheaths form on young, active parts of roots where the epidermis is still intact (McCully 1995) but are lost from more mature portions of roots. Mucilage is a gel that can absorb large volumes of water and act as a hydraulic

bridge between roots and the soil (Carminati et al. 2016). It is tempting to presume that mucilaginous hydrogel matrix may critically influence crystallisation patterns of secondary carbonates around fine roots, either during their life (i.e. in the active rhizosphere) or during their decay. For example, Alonso-Zarza (1999) documented presence of mucilaginous films around roots and stressed their importance in early stages of calcrete formation.

#### *1.4.2 Intracellular calcification in plant roots*

Intracellularly calcified roots can be regarded as a special type of rhizoliths, which form entirely through plant-controlled  $\text{CaCO}_3$  (calcite) biomineralisation of the cortex of live fine roots. Micromorphology of intracellularly calcified roots has been exhaustively presented in the pioneering work of Jaillard (1987a) and co-authors (Callot et al. 1985; Jaillard et al. 1991). Calcified roots of Jaillard et al. (1991) have been widely cited as an example of biogenic precipitation of soil carbonate, resulting in extensive accumulations (Hinsinger 1998; Lambers et al. 2009). According to Jaillard (1987a, b) and Hinsinger (2013) the process of intracellular  $\text{CaCO}_3$  precipitation occurs as a result of intensive root activity which can dissolve large amounts of calcium carbonate in the rhizosphere as a consequence of respiration and proton release with calcium ultimately precipitating as calcite in the vacuoles of root cortical cells. Accumulation of  $\text{CaCO}_3$  in the root tissues thus reflects protection of the plant from excessive calcium concentrations entering the roots from soil solutions.

McConnaughey and Wheelan (1997) presented a model of root calcification as a potentially effective nutrient acquisition mechanism. Proton (acid) secretion in itself enables plants to mobilize sparingly soluble nutrients from the rhizosphere. Intracellular carbonate precipitation may, however, additionally increase production of protons, which are potentially useful for nutrient assimilation in nutrient-poor calcareous soils.

Although the intracellularly calcified root has been identified in many Quaternary palaeosols and recent soils, particularly in loess successions and calcretes (e.g. Khoklova et al. 2001a, b; Khormali et al. 2006; Barta 2011, 2014; and references therein), they have not been reported from generally well-studied calcareous soils in the Mediterranean coastal region of Spain. Chapter Three is largely based on examples from the extensive deposits of calcified roots in the Alicante region where they locally represent more than a half of the soil mass.



Intracellular carbonate precipitation in fine roots has been reported from *in vitro* experiments on model plants (Ross and Delaney 1977; Jaillard 1987a), whereas apparently no calcifying plants have been identified in their natural settings. Plant roots growing in a mixed below-ground community are difficult to identify at any taxonomic level, especially morphologically simple fine roots that acquire nutrients and take up water. Furthermore, it is hardly possible to trace the individual plant root system from a single calcified root fragment, excavated deep in a soil profile, to its coarse primary root and to the determinable aboveground part of a plant.

Therefore, a test study of DNA identification of intracellularly calcified roots from SE Spain has been performed; results are presented in Chapter Four. DNA barcoding is a molecular taxonomic identification tool, which uses a standard short genomic region, universally present in target biological material and has sufficient sequence variation to discriminate among taxa. DNA extracted from very small amounts of plant tissue (mostly vascular cylinders) preserved in calcified roots from Spain, has been analysed following procedures used for plant roots, described in Jackson et al. (1999), Linder et al. (2000), Kress and Erickson (2007), Erickson et al. (2008), Hollingsworth et al. (2009) and Burgess et al. (2011). This preliminary study provides the first attempt to identify plants, responsible for accumulations of  $\text{CaCO}_3$  in modern soils, formed through intracellular biomineralisation in fine roots.

### 1.5 The *Microcodium* controversy

Substantial part of the thesis is devoted to *Microcodium* – a problematic biogenic carbonate feature with a very distinctive cellular aggregate structure, composed of individual polyhedral, elongate crystalline elements of calcite, arranged in a radial pattern. *Microcodium* has a discontinuous stratigraphic distribution spanning from the late Palaeozoic to Quaternary, with a peak occurrence during the late Cretaceous and the early Palaeogene. Fundamental structural similarity with modern calcified roots has led some of the early researchers to interpret *Microcodium* as a product of root calcification.

Following an earlier publication in support of root origin of *Microcodium* (Košir 2004; Appendix A5-2), suggested by previous authors (Esteban 1974; Klappa 1978a, b; Wright et al. 1995), Kabanov et al. (2008) extensively reviewed occurrences of *Microcodium* from

Palaeozoic to the Recent and presented arguments against the root origin, reinterpreting its typical aggregate structure as a mineralised microbial (actinobacterial) feature.

*Microcodium* continuously generates a considerable interest in published studies, however, it is mostly used as a valuable diagnostic feature for subaerial exposure and soil formation in sedimentary successions. As a further contribution to morphological comparison of *Microcodium* with intracellularly calcified roots (Košir 2004), Chapters 3 and 5 include C and O stable isotope analysis of both features as well as comparative analysis with, as a matter of fact, very limited published isotope data.

Some examples of rhizoliths, showing well preserved structural details of plant root cellular tissues, have been linked to *Microcodium* as possible incipient forms representing early stages of root intracellular calcification without expanded cellular growth, typical for *Microcodium* elements (Esteban 1972, 1974; Alonso-Zarza et al. 1998; Košir 2004). Košir (2004) interpreted roots exhibiting selective (incomplete) calcification seen in some sections, in which only some of the cortical cells but not the intercellular spaces are calcified, as a unambiguous evidence for intracellular biomineralisation in the root cortex. However, cathodoluminescence and SEM petrographic analysis performed in this study (Chapter 5), which has not been applied in previous investigations of *Microcodium* ultrastructure, has been aimed at distinguishing between biomineralised *Microcodium* elements and intracellularly calcified roots on one side, and the textures, formed largely inorganically through permineralisation of fine root tissues on the other. Early diagenetic mineralisation and exceptional preservation of fine root tissues in calcretes, not related to biologically controlled intracellular calcification, are also discussed in Chapter 2.

## 1.6 Carbon and oxygen stable isotope signatures of root-related carbonates

As noted in Section 1.2, secondary soil carbonates have been widely used as a palaeoclimatic and palaeoecological indicator, especially as an estimate for palaeo-atmospheric  $p\text{CO}_2$  and as a geochemical proxy for the reconstruction of past terrestrial ecosystems and vegetation changes (e.g. Cerling 1991; Cerling et al. 1989, 1997; Ehleringer et al. 1997; Ekart et al. 1999). Models of C and O stable isotope composition of soil carbonates are based on many different assumptions, which are hard to verify particularly when secondary carbonates evidently form under strong biological influence (e.g.

discussion of Wright and Vanstone 1991, and Cerling 1992 and Wright and Vanstone 1992), associated with pronounced non-equilibrium isotope partitioning such as in intracellular  $\text{CaCO}_3$  biomineralisation in plant roots (discussed in Chapter 3) and *Microcodium* (Chapter 5), as well as in rapidly formed and thermodynamically unstable microcrystalline carbonate features, typical of rhizosphere microenvironments (Chapter 2) and usually related to microbial metabolism. Data of stable isotope analysis, performed in the framework of this thesis, are listed in Appendix A1-1.

## **Chapter 2: Calcretes and fine-root systems: Quaternary rhizolites of the Bahamas**

### **2.1 Introduction**

The root systems of terrestrial plants perform two primary functions: the acquisition and transport of soil based resources (water and ions) and anchorage (Fitter 2002; Waisel and Eshel 2002). As outlined in Section 1.3.1, in a general size and functional division of plant roots, the root systems consist of coarse (secondary, woody) roots and fine roots. Although root system morphologies are extremely variable, particularly in different groups of vascular plants (an extreme example can be represented by comparing root systems of a several thousand years old coniferous tree with those of annual herbaceous dicots or grasses), every single root system is composed of various constituents and displays a certain level of functional diversity (Waisel and Eshel 2002).

Immense plant science literature on root research is intrinsically aimed at fine root systems, that are structurally and functionally complex underground part of plants responsible for water and nearly all essential soil nutrient uptake by plants. The global ecological importance of fine roots is illustrated by that the growth and maintenance of fine roots can consume up to 50% of daily photosynthate, while as much as 2/3 of annual net primary production can be allocated to fine roots in some ecosystems (Section 1.3.2; Eissenstat 1992).

Geological research of plant roots, which mostly deals with rhizoliths, in the simplest terms defined as traces and remains of plant roots preserved in mineral matter, particularly calcium carbonate, seems to be strongly biased towards macroscopic, coarse root systems. As noted in Section 1.4, virtually none of the papers dealing with rhizoliths in soils and palaeosols, published after the seminal review of Klappa (1980b), clearly distinguishes root size and functional classes neither explicitly mentions fine roots as a particular part of the plant, performing specific vital functions. General geological perception of plant roots and their environments appears to be almost exclusively, although not explicitly, based on macroscopic roots, their shape and size, orientation and branching patterns, observable in the field and evaluated in comparison with animal burrow systems (Klappa

1980b). Moreover, disproportionately large part of published rhizolith-related research is concentrated on aeolian systems. Aeolian deposits represent a particular ecosystem – and a specific type of substrate and (ichno)facies that is physically relatively uniform and isotropic (i.e. homogeneous in all directions; Peng 2011). Nevertheless, many early works on rhizoliths have emphasised morphological complexity of root systems and their traces, as well as their relations with substrates (e.g. Cohen 1982; Mount and Cohen 1984). Although not definitely regarded as root-related, Reeves (1970), James (1972) and Harrison (1977) described irregular (wavy) calcrete stringers, predominantly parallel to subparallel to the outcrop surface, up to several millimetres thick, which commonly exhibit the same microstructure as the thicker laminar calcretes (Harrison 1977; Wright 1994; see below).

Functional distinction between coarse roots, mostly consisting of dead tissues and being responsible for water transport and plant structural support, and short lived, ephemeral fine roots, which are critically involved in water and nutrient uptake, is of vital importance for the understanding of carbonate precipitation in soils, particularly in large-scale carbonate accumulations which have been considered as products of biogenic, root-related processes. As emphasised by Klappa (1980b), rhizoliths can exhibit a range of textures, which reflect various degrees of biological activity responsible for their formation. Except for their gross morphology, some forms may show no biologically influenced fabrics (for example, simple root moulds left after roots have decayed and subsequently filled with a cement), whereas others are characterised by biologically controlled precipitation of calcium carbonate in the living cortical cells of fine roots. The latter type, i.e. intracellularly calcified roots, is presented and discussed in Chapter Three. This chapter is focused on root-related calcretes where calcium carbonate precipitates in the soil around the fine root system, but the mineralisation itself is not necessarily directly driven by roots.

The primary aim of this chapter is to show that the basic morphological and functional differentiation of plant roots into coarse roots and fine roots can be applied in description and interpretation of rhizoliths and rhizogenic calcretes (rhizolites). The study is based on examples of Pleistocene and Holocene root-related calcretes from the Bahamas, which include remains of fine roots with exquisitely preserved anatomical details and enable further insights into processes of (bio)mineralisation and taphonomy of fine root tissues in calcretes. One of the objectives is to re-evaluate the concept of rhizosphere applied to the processes of calcium carbonate precipitation around roots and to discuss a continuing

**Fig. 2.1.**

An ocean topography map of the Bahamian archipelago showing position of the studied locations. A - North Andros Island (Nicholls Town area); NP - New Providence Island; SS - San Salvador Island. Basemap compiled from data of ESRI Oceans Basemap (<https://www.ncei.noaa.gov/maps/bathymetry/>). Also see maps of individual islands in Appendix A2-1.

and recurring question if calcium carbonate accumulation occurs around living fine roots or during their turnover and decay (Klappa 1980b; Alonso-Zarza 2018; Huguet et al. 2020). These processes are further assessed as a mechanism of accretionary growth of laminar calcretes as related to formation and turnover of fine-root mats and progressive accumulation of rhizolites, and the possible link of episodic growth in relation to terrestrial ecosystem functioning and recurrent events like drought, floods and fire. Calcrete material from the Bahamas is supplemented by material of fine root-associated carbonate accumulations from modern soils in Spain and rhizoliths from modern aeolianites in Morocco.

## 2.2 Geological setting

The Bahamian archipelago (Fig. 2.1) consists of a series of shallow water carbonate banks less than 20 m deep, separated by deeper basins. The carbonate platform system has been separated from North American landmass and siliciclastic input throughout the Tertiary and has been used as one of the globally most important areas for the development of carbonate geoscience (Melim and Masferro 1997). Fundamental concepts of sedimentology of modern marine carbonate environments, depositional and diagenetic models, and subsurface geology of the Bahama banks, to a large part pioneered and developed by Robert Ginsburg, his students and associates (Swart et al. 2009a, b; Shinn 2019), resulted in an immense body of literature published during the past decades (e.g. Schlager 2005). Only ~5.5% of the total carbonate platform area is represented by

emergent islands (Sealey 1994). Terrestrial geology of the Bahamian archipelago has been comparatively less explored, however, together with South Florida and other areas of the Caribbean, carbonate islands of the Bahamas have provided numerous model examples such as for the meteoric carbonate diagenetic realm (e.g. James and Choquette 1984), carbonate aeolianites (Abegg et al. 2001), and karst development on carbonate islands (Myroie and Carew 1995).

The Bahamian islands largely exhibit a constructional landscape, i.e. the landforms that have been created by accumulation of carbonate sediments deposited by currents, waves, and winds (Carew and Myroie 1997). All major islands in the Bahamas are dominated by two landforms: eolianite ridges that commonly rise up to 30 m above sea level, and lowlands composed of marine and terrestrial deposits. Dissolution of the carbonates of the islands has produced a karst landscape that is superimposed on the overall constructional topography (Myroie et al. 1995; Myroie and Carew 1995). Most Bahamian islands are dominated by Pleistocene rocks, with a lesser amount of Holocene deposits, generally distributed along island fringes (Carew and Myroie 1997; Kindler and Hearty 1997). The Bahamian islands are mostly located close to the platform margins but they differ by their extension on the platforms, the width of the outer shelf, and their exposure to open-ocean energy (Kindler and Hearty 1997).

The physical stratigraphic scheme of the Bahamian islands is largely derived from studies on San Salvador, but has been also supported from and applied to other islands (Carew and Myroie 1995). The general stratigraphic division of late Quaternary deposits is tripartite (Appendix A2-1, Fig. A2-1.03B; Carew and Myroie 1995; see also detailed stratigraphic scheme of Hearty and Kindler 1993 and Kindler and Hearty 1997) and comprises the Owl's Hole Formation (mid-Pleistocene aeolianites), the Grotto Beach Formation, composed of a package of marine and aeolian units, deposited during the Marine Isotope Stage (MIS) substage-5e sea-level highstand (~132–119 ka; Chen et al. 1991) and well-exposed throughout the Bahamian islands, and the Rice Bay Formation (Holocene aeolianites). The units are mostly bounded by distinctive palaeosols, including prominent calcretes, which are among the most impressive features of the islands' landscapes and stratigraphic architecture. Throughout the Bahamian islands, rocks of the Grotto Beach Formation are capped by a hard, red terra-rossa palaeosol, or a beige to red-brown calcrete, except where it has been removed by later erosion (Carew and Myroie 1995; Boardman et al. 1995). The crests of eolianite ridges typically have a calcrete layer



a few centimetres thick, but in the swales and on regressive-phase aeolianites, complex palaeosols are commonly found. The complex palaeosol overlaying the Grotto Beach Formation developed during the MIS substage-5d to stage 1 (~118–6 ka; Hladil et al. 2004) lowstand. These palaeosol/calcrete caps are the youngest Pleistocene rocks in the Bahamas and are only locally covered with relatively thin Holocene aeolian deposits of the North Point and the Hanna Bay Member, respectively.

### 2.2.1 Climate and vegetation

Climatically, the Bahamas range from subtropical temperate in the north to semiarid regime in the south. Winters are mostly dry, with occasional cold fronts that cause increased rainfall especially in the northern part (Sealey 1994). There is a marked climatic gradient from wetter and cooler north-northwest (MAP >1.500 mm, average temperatures 18°C in January and 28°C in July) to the drier and warmer climate, typical for the southernmost Bahamian islands of Inagua, and the neighbouring Turks and Caicos (MAP ~700 mm; average temperatures 23.5°C in January and 28.5°C in July; Sealey 1994; Fig. A2-1.01). Estimates of potential evapotranspiration (PET) range from 1.300-1.400 mm/y for the northernmost part to >1.600 mm/y, thus characterised with a pronounced moisture deficit (Whitaker and Smart 1997).

Plant communities generally correspond to climate and to the major landscape types of the Bahamian islands, i.e. the ridgeland, the rockland, the coastland, and the wetland (Correll 1979; Sealey 1994; Smith and Vankat 1992). The vegetation of the northern islands consists largely of forests of the endemic Caribbean Pine (*Pinus caribaea* var. *bahamensis*; Farjon and Styles 1997). The pines grow on eroded limestone rock with pockets of lateritic soil, usually inland, on larger islands where there are relatively stable water lenses and reduced salt spray (Sanchez et al. 2019; Whitaker and Smart 1997). The pines are forming pure, open stands, usually with scattered or dense undergrowth of shrubs (often dominated by *Sabal palmetto* and mixed broad-leaf coppice), and also invading open scrubland forming secondary forest (Farjon and Styles 1997). Mangrove swamps are developed along low-lying coastal areas in almost all islands. Much of the island vegetation has been affected by human activities and is largely secondary.

Particularly on larger islands, such as North Andros, Caribbean pine is a keystone species as the only native tree in the pine forest ecosystem of the Bahaman archipelago (Sanchez et al. 2019). The pines make fire-climax forests where the pine seeds need light to



germinate, benefiting from natural fires, which clear the broadleaf undergrowth. In cases where fire is suppressed or absent, species in the undergrowth tend to take over, changing the vegetation from pine forest to coppice over time (Myers et al. 2004). The natural fire intervals for different islands have been estimated from 3 to 10 years (Myers et al. 2004; Sanchez et al. 2019). In comparison to Mediterranean climates with pronounced seasonal moisture regime (see Section 3.2), the low-altitude terrestrial ecosystems of the Bahamian islands, including soils and soil processes, are and have been critically influenced by lower-frequency but high-magnitude events, such as hurricane-related devastation and flooding, and also recurrent widespread fires.

### 2.3 Material and methods

Calcrete geometry and macrofabrics were studied in coastal outcrops at Nicholls Town, North Andros (coordinates: 25.14243° N, 78.00089° W), and six localities on San Salvador Island (North Point: 24.12445° N, 74.45735° W; a coast between Barker's Point and area S of Rocky Point: 24.09842° N, 74.52099° W; Cockburn Town: 24.05249° N, 74.53504° W; Fernandez Bay: 24.02621° N, 74.52418° W; E part of the French Bay: 23.94891° N, 74.52096° W; and The Gulf: 23.94739° N, 74.50878° W). Outcrops from New Providence Island at the Lyford Cay roadcut (25.02336° N, 77.53156° W) and Clifton Pier (25.00539° N, 77.54623° W) were not examined in detail but are used as a remarkable example of root-related calcretes.

Calcrete samples were cut into 1-2 cm thick slabs, which were examined under a stereomicroscope for microfabric details. Standard thin-section size slices were selected and cut from the slabs. Since most of the material had been sampled in coastal outcrops, all the slices were washed overnight in slowly running tap water, followed by several successive baths in deionized water to remove any remains of salts. Slices were then dried for 8h at 45°C and embedded in transparent low-viscosity epoxy resin (EpoTek® 301-1, Epoxy Technology Inc.) in a Struers Epovac vacuum chamber and cured in an oven for 48 h at 30°C. Forty standard petrographic thin sections were prepared from resin-embedded samples, supplemented by twelve ultra-thin, double-polished sections (10-15 µm thick), finished with 1µm diamond paste. Furthermore, selected complementary slices, remaining from thin-section preparation, were polished to enable combined observation of samples in

transmitted and reflected light. Certain type of rhizolith microfeatures appeared to be much more clearly visible in polished surfaces than in standard or even ultrathin sections.

Thin sections and polished slices were examined and photographed with a polarizing microscope Olympus BX51 TRF-6 with SC-50 digital camera in transmitted light, with a Wild M420/Leica DFC-450 photomicroscope in reflected light, and with a Leica DML microscope with reflected blue-wavelength fluorescent light, equipped with a Leica DFC-420 digital camera.

Selected polished thin sections and slices were observed uncoated under a JEOL JSM-IT100 Scanning Electron Microscope equipped with an integrated Energy Dispersive X-ray analysis (EDS) and backscattered electron (BSE) detector, operating in low vacuum mode (at 20–40 Pa) at an accelerating voltage of 15 and 20 kV, and a working distance from 9 to 11 mm. Images were taken in shadow BES imaging mode. Semi-quantitative EDS elemental analysis was performed at the same low-vacuum conditions. Elemental spectra were obtained from uncoated specimens using small area analysis with 100 seconds pre-set (live) time and automatic or manual element identification mode.

Mineralogical composition of six crushed and powdered calcrete slices was obtained with X-ray powder diffraction (XRD) using a Bruker AXS Endeavour diffractometer at the Department of Materials Synthesis, Jožef Stefan Institute in Ljubljana, operating at 40 kV and 30 mA, at 0.040°/sec, with monochromatic CuK $\alpha$  radiation. XRD analysis was complemented with Fourier Transform Infrared Spectroscopy (FTIR) performed at on several mm-sized fragments using the KBr pellet technique. For this, 1.5 mg of sample were mixed with 200 mg of KBr and subjected to a pressure of 10 ton cm<sup>-2</sup> during 10 min. Spectra were recorded in the 4000 to 400 cm<sup>-1</sup> range on a NICOLET NEXUS 670–680 spectrometer equipped with a DTGS detector.

Selected samples of laminar rhizolite calcretes were analysed for C and O stable isotope composition. Due to microstructural heterogeneity of laminar calcrete material observed in thin section, only test analysis has been performed on 'bulk' material, drilled from multiple laminae of rhizolites from North Andros and San Salvador, and compared with stable isotope composition of unpublished analyses of Quaternary root-related calcretes from SE and E Spain and Morocco, and Paleocene and Eocene rhizogenic laminar calcretes from the Liburnian Formation, Slovenia (Appendix A2-5, Table A2-5.1). Sample details, laboratories, and analytical procedures are listed in Appendix A1-1.

## 2.4 Description and interpretation of rhizolite calcretes

Calcretes, associated with major stratigraphic discontinuities in the Bahamian Quaternary successions, display a wide variety of forms and developmental stages, typical of palaeosols developed on consolidated and unconsolidated pure carbonate substrates, from massive to laminar hardpans and subsurface stringers, brecciated horizons, re-cemented in multiple stages etc. (e.g. James 1972; Harrison 1977; Perkins 1977; Wright and Tucker 1991; Boardman et al. 1995; Alonso-Zarza and Wright 2010a). This chapter deals exclusively with forms, macroscopically attributable to rhizolites (see section 1.4) or (laminar) rhizogenic calcretes (in the sense of Wright et al. 1988, 1995).

### 2.4.1 Calcrete profiles and macromorphology

Studied calcretes from North Andros, New Providence and San Salvador all correspond to the disconformity between the Pleistocene (MIS 5e) marine and aeolian deposits of the Grotto Beach Formation and locally deposited Holocene aeolianite deposits of the Rice Bay Formation (Fig. A2-1.03). Topographic relationships of substrate and laminar calcretes types are summarised in Figure 2.2. Two groups have been distinguished on the basis of the substrate: calcretes on well-lithified (mostly marine) limestone, and calcretes on less cohesive, mostly weakly and patchily cemented fine-grained aeolianite sand bodies.

At the Nicholls Town locality (Fig. 2.3, Fig. A2-1.02), laminar calcretes infill decimetre- to metre-scale subvertical dissolutional cavities in coral framestone, correlative with the fossil coral reef outcrops of the Cockburn Town Member on San Salvador (Fig. A2-1.03; Mylroie and Carew 2010). These deposits, exposed up to several metres above the present sea level, correspond to the Pleistocene MIS 5e maximum highstand. In limited, partly artificially enlarged coastal outcrops, palaeokarstic cavities, including possible solution pipes, are almost entirely filled by prominently laminar, yellowish brown coloured calcrete. From most of the cavities, laminar calcrete extends onto the adjacent surfaces; the topmost parts are ferruginous, dark red- to brown stained, indicating that the calcrete crusts had been covered by non-carbonate soil material (Foos and Bain 1995; Boardman et al. 1995).

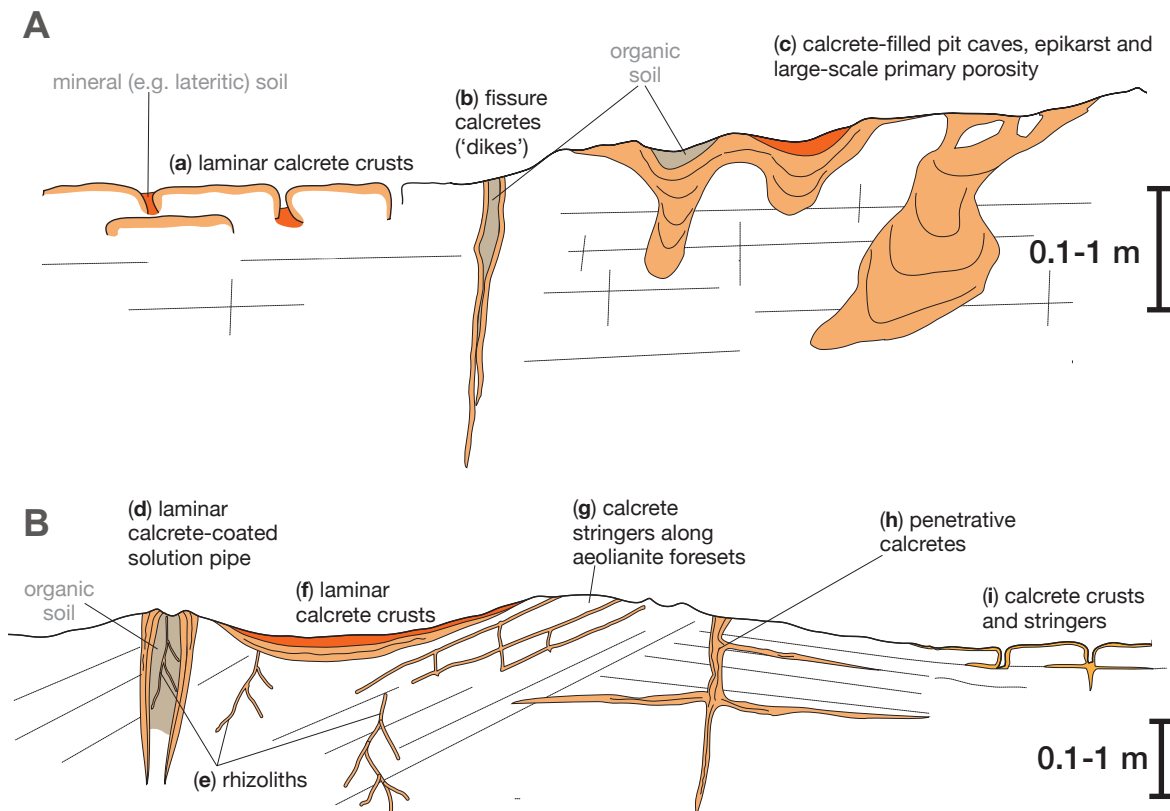


**Fig. 2.2.** Schematic summary of macroscopic root-related laminar calcrete forms in young Bahamian carbonates. **A**) Calcrete features in strongly cemented carbonate sediments/limestone: (a) Crudely to finely laminar calcretes coating horizontal and vertical (lateral) surfaces of well-cemented limestone beds/blocks and protruding along joints and bedding plane partings (Fig. 2.4). Laminar calcrete crusts are often red-brown pigmented by inclusions fine-grained mineral soils (Fe-rich laterite), concentrated especially in their top layer. (b) Vertical to subvertical fissures of different origin, metres to several 10s of metres long and centimetre to several decimetres wide. Large fissures are mostly related to extensional fractures adjacent to carbonate platform (bank) margins (Daugherty et al. 1987) and are filled (lined) by crudely laminar calcretes (Fig. 2.5). Calcretes in fissures commonly exhibit symmetric accretionary growth from both sides/fissure walls towards the centre; open fissures can be partly filled by loose sediment or organic soil. (c) Decimetre to metre scale topographic depressions, mostly karstic dissolution pits, coated or fully filled by crudely laminar calcrete, often interlayered with red clayey soil material and macrorhizoliths (Figs. 2.3, 2.6, and 2.7 and Figs. A2-1.04E and F). Incompletely calcrete-filled pits contain organic topsoil or mineral soils. Laminar calcrete crusts often continue from cavities and spread over adjacent surfaces (Fig. 2.3A, B, Fig. A2-1.04E, F). **B**) Calcrete forms on and in unlithified and poorly lithified carbonate sands. (d) Cross section through a solution pipe, coated with centripetally-accreted laminar calcrete (see Fig. 2.10 and Fig. A2-2.01G). (e) Unconsolidated aeolianites typically contain abundant macrorhizoliths (mm to cm-size in diameter, dm-m in length). See Figs. 2.8B, 2.9C, D, E. (f) Surficial laminar calcrete crusts, mm- to several cm thick, often covered by organic topsoil or mineral soil, typically thicker in depressions (Fig. 2.9A, Fig. A2-1.04H). (g) Millimetre to centimetre thick planar calcrete stringers occur along aeolianite layers (foresets) and along joints/fractures between layers (Figs. 2.8A, B, D, E), often forming boxwork structures, emphasised in weathered outcrops by resistant calcrete-cemented layers (Figs. 2.8A, B). (h) Penetrative calcretes are complex 3D structures, composed of crudely laminar calcrete layers, protruding metres deep from the surface and laterally spreading for several metres in several discrete levels (Rossinsky et al. 1992). (i) Thin surficial calcrete crusts and subsurface stringers are smaller-scale equivalent of penetrative calcretes. (Figs. 2.4C, D, 2.8C). Scale bars demonstrate a large variability in size of calcrete phenomena.



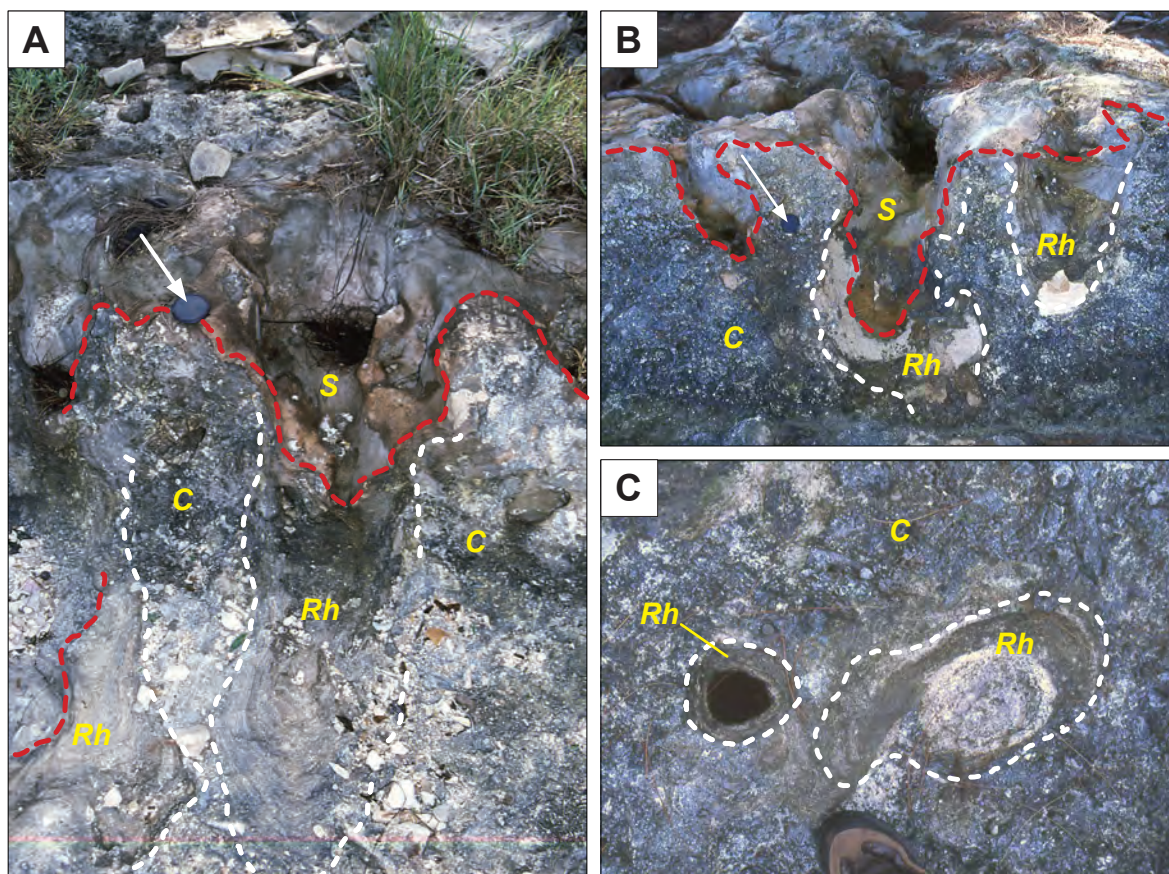


**Fig. 2.3.** Laminar rhizolites from coastal outcrops at Nicholls Town, North Andros. **A, B)** Subvertical/oblique section through a system of calcrete-filled karstic cavities (*Rh*) in Pleistocene coral framestone (*C*) of the Cockburn Town Member. White dashed lines outline the cavities, red dashed line marks the surface of the laminar calcrete, extending from the cavities and lining the whole surface (*S*). Lens cap for scale (white arrow). **C)** Artificially cut horizontal surface of the coral limestone (*C*) cross-cutting two cavities (?solution pipes, outlined with white dashed line), lined with laminar calcrete (*Rh*). Mesoscale features and microfabric of laminar calcrete samples from Fig. A are shown in Figs. 2.11A, B, C, 2.13A and 2.14-2.19.

North-western coastal outcrops of the San Salvador Island (Fig. A2-1.03A) are composed of massive to bedded marine limestone of the Cockburn Town Member, capped by a calcrete, typically having a red top layer (Fig. 2.4A, B). In many outcrops between the Fernandez Bay and the Barkers Point (Fig. A2-1.03A), the so-called “terra-rossa” palaeosol of Mylroie and Carew (2010 and references therein) is actually a laminar calcrete with minor amount of non-carbonate material (clays and Fe oxides), which is mostly concentrated in a millimetre thick surficial encrustation (Fig. 2.4B). Laminar calcretes make few millimetres to several centimetres thick crusts over the limestone beds and

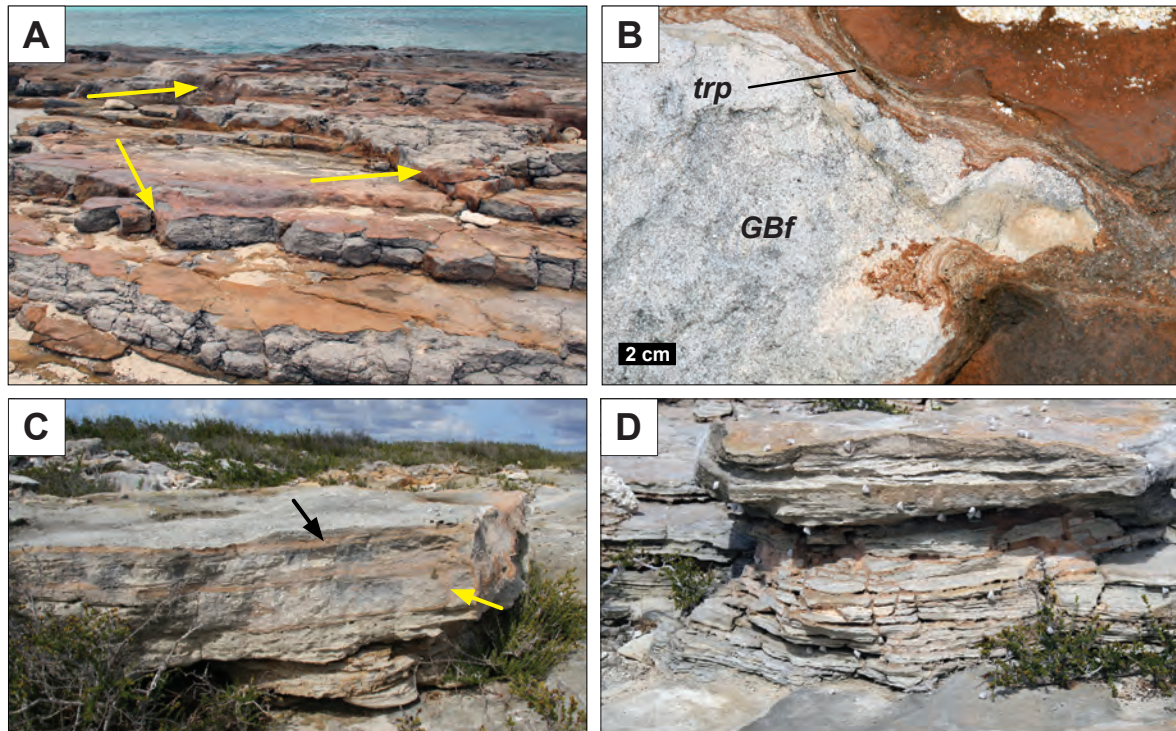


**Fig. 2.4.** A) Red crudely to finely laminar crust, mm to cm thick, coating bedding planes of well-bedded Pleistocene limestone (Cockburn Town Member) and vertical walls of dissolutional voids developed along joints, cutting across the beds. Thin red top layer indicates that the calcrete was overlain by Fe-rich (lateritic) soil (Foos and Bain 1995). Fernandez Bay, San Salvador. B) Close-up view of a finely laminar calcrete (*trp*) coating irregular surface of bioclastic limestone (*GBf* - Grotto Beach Formation, Pleistocene); *trp* stands for "terra rossa palaeosol" in the stratigraphic nomenclature of Mylroie and Carew (2010), although the laminar crust, except for the top mm, contains only minor amount of non-carbonate matter (Fe oxides and hydroxyoxides and clay material). Micromorphology of this laminar calcrete is shown Figs. 2.11E and 2.13C-G. Barker's Point, San Salvador. C, D) Well-cemented limestone bed showing boxwork-like structure made of brownish horizontal calcrete layers (black arrow), connected with vertical fissures (yellow arrow). Such brick wall-like brecciation structures (Rossinsky and Wanless 1992) are mostly caused by penetrative growth of coarse plant roots along bedding plane partings and vertical fissures (cf. Figs. A2-1.04A-D)

along the solution-enlarged joints, cross-cutting the bedding (Fig. 2.4A). Laminar calcretes also protrude into the bedding plane partings, producing characteristic brick wall-like patterns (Fig. 2.2A, type a). Similar features are frequently observed also on a smaller scale, e.g. in well lithified thin-bedded aeolianites (Fig. 2.4C, D), as a result of plant root-induced brecciation (James 1972; Rossinsky and Wanless 1992) and infill of the network of horizontal and vertical fissures by calcrete carbonate (also see Figs. A2-1.04A-D).



Fissure calcretes, also called ‘calcrete or caliche dikes’ (see White et al. 1984; White 1988; White and Curran 1988) are a prominent feature of coastal outcrops of the Cockburn Town fossil reef locality (Fig. 2.5, Fig. A2-1.03A). Large-scale fissures, which are widespread on Bahamian islands particularly adjacent to carbonate platform (bank) margins, are mostly related to extensional fractures (Daugherty et al. 1987) and are typically filled (lined) by crudely laminar calcretes. In the outcrops of the Cockburn Town fossil reef, fissures, 5-15 cm wide, typically display accretionary laminar growth of calcretes from both sides, i.e. from opposite walls of the fissure, progressively filling up the fissure (Fig. 2.5B). Larger fissures are associated with mm to cm wide and up to several metres long stringers, often cross-cutting (and post-dating) the large calcrete-filled fissures (Fig. 2.5C). Open, not fully calcrete-filled fissures, may contain loose soil or carbonate sediment.

Figure 2.6 shows an impressive example of rhizolite, filling up a large, metre scale dissolutional cave in marine beach and shallow foreshore cross-bedded sequence of the Cockburn Town Member at Clifton Pier, New Providence (Fig. A2-1.02). In comparison to similar karst/calcrete association from Nicholls Town (see above), the rhizolite fabric at Clifton pier is coarser, less cemented, composed of macroscopically visible rhizoliths (Figs. 2.5B, C). Roughly laminar stratigraphy of the cave infill indicates accretion of rhizolite laminae, progressively filling up the cave. Carbonate rhizolite is mixed with red-brown clayey soil material; remaining pockets of soil contain coarse macro-rhizoliths, few mm to cm in diameter, composed of fine root rhizoliths (Fig. 2.7). Subvertical tubular dissolutional voids (Fig. 2.7A, B) are coated by dense laminar calcrete layer, several cm thick, analogous to other laminar calcrete forms (Fig. 2.2).

Thin, generally only few mm thick calcrete layers, associated with aeolianite deposits (Fig. 2.2A), have been generally simply described as micrite crusts or ‘caliche dikes’ (White and Curran 1988; White 1988; technically, most of these are sills not dikes). Figure 2.8 shows typical examples from Pleistocene aeolian dune succession at Lyford Cay, New Providence Island (Figs. 2.8A-C), and Holocene aeolianites from North Point, San Salvador (Figs. 2.8D, E). Thin, planar calcrete layers, spreading along aeolianite cross bedding and joints, cross-cutting the bedding, show identical fabric as laminar rhizolites (see description of microfabric below). In strongly bioturbated aeolianites, lacking depositional lamination, rhizolites predominantly appear as irregular, anastomosing, mm-thick subhorizontal stringers, associated with vertical branching rhizoliths, mm to cm in diameter (Fig. 2.8C).



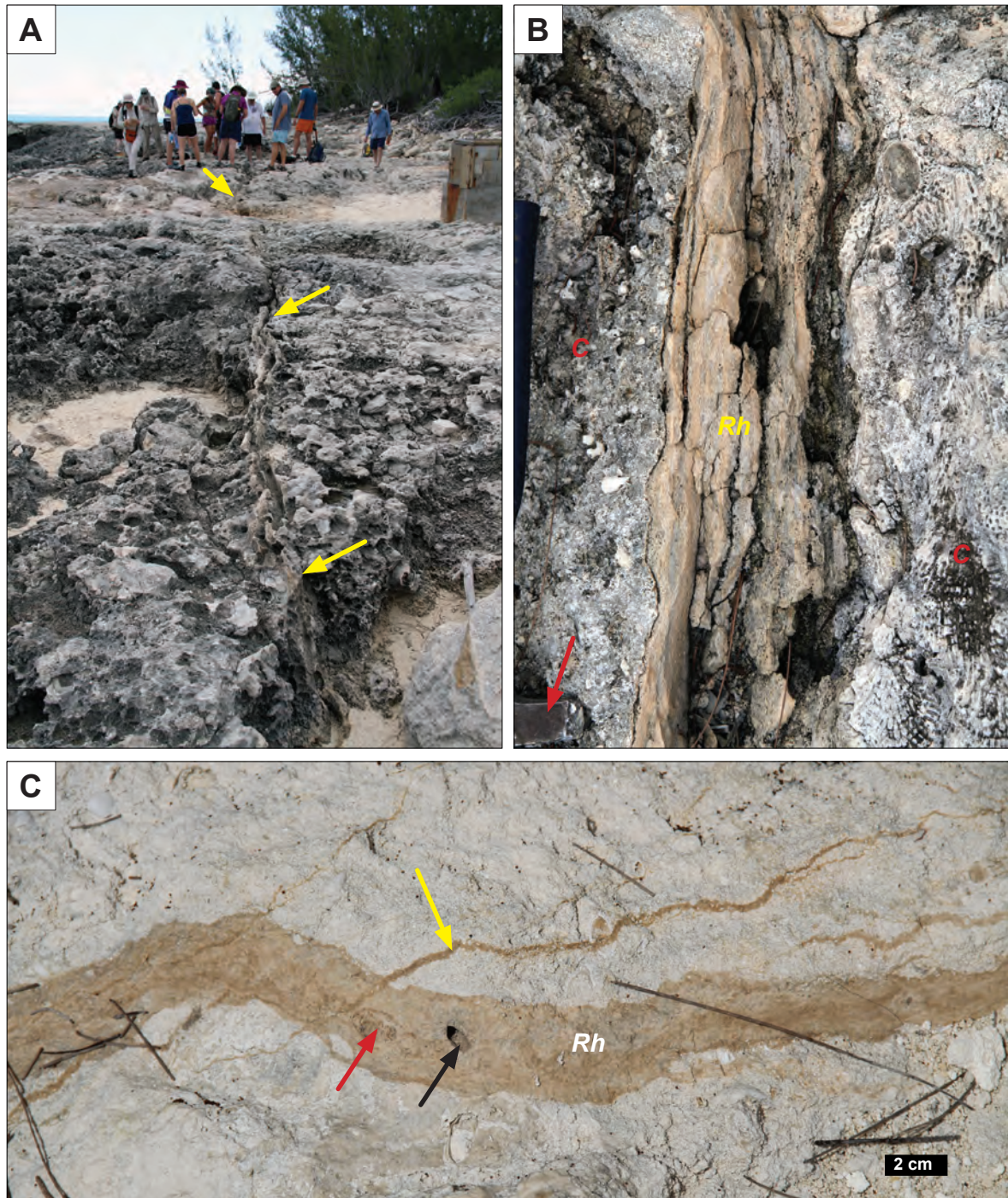


**Fig. 2.5.** Fissure calcretes in Pleistocene reef limestone (Cockburn Town Member), Cockburn Town fossil coral reef locality (Myroie and Carew 2010, Thompson et al. 2011). A) Sinuous, 5-15 cm wide calcrete-lined fissure which can be followed several 10s of meters, runs roughly parallel to the coastline. B) Close-up view of the calcrete-filled fissure (*Rh*) in coral limestone (*c*) showing crudely layered fabric, composed of dense beige layers and porous interlayers. Hammer face for scale (red arrow). C) Horizontal surface of bioclastic limestone cross-cutting 2-4 cm wide calcrete-filled fissure (*Rh*) cross-cut by thinner calcrete stringer (yellow arrow). Black arrow marks a tubule, probably left after a decayed coarse root. Red arrow points to an oval-shaped cross section of a composite rhizolith.



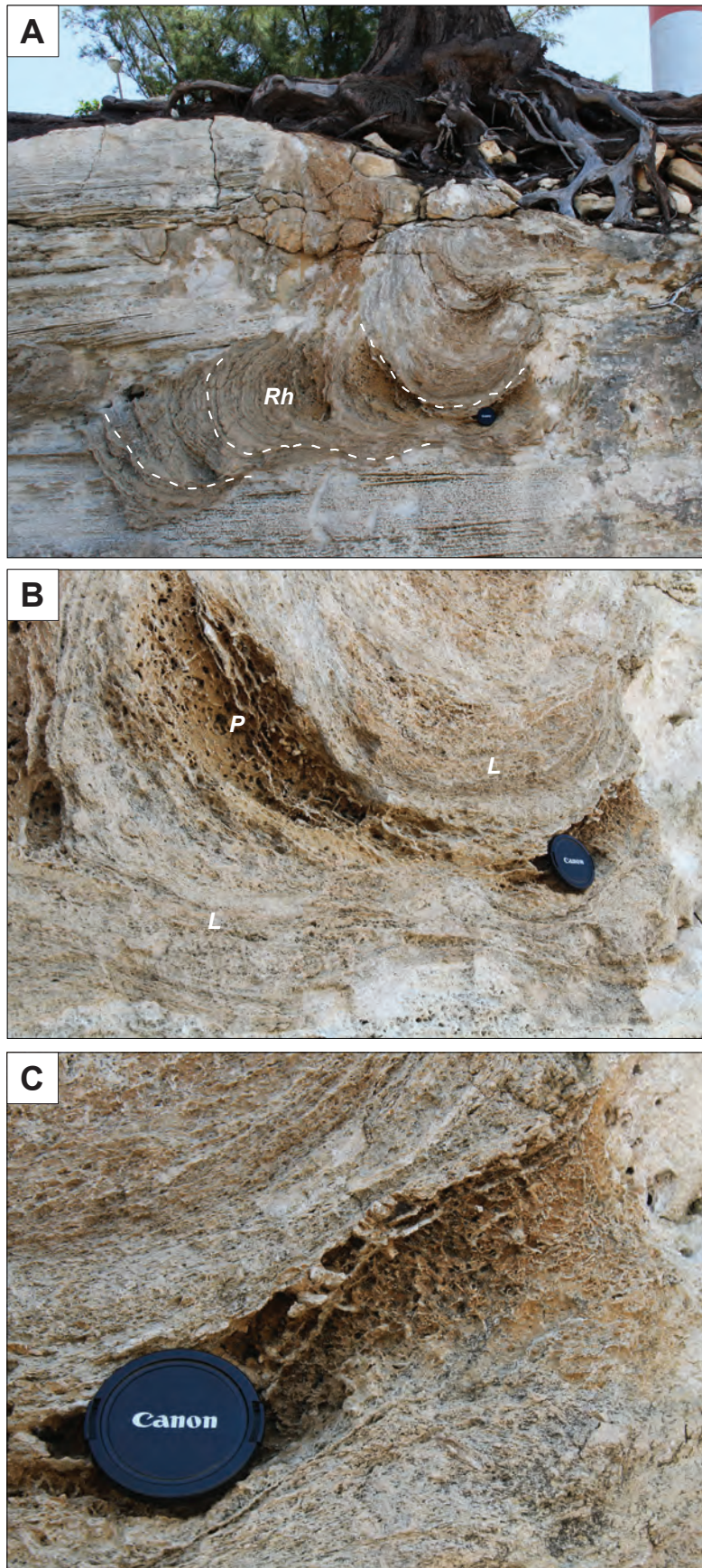


**Fig. 2.6.** Large rhizolite-filled dissolutional cave formed in Pleistocene marine beach and shallow foreshore cross-bedded sequence of the Cockburn Town Member at Clifton Pier, New Providence Island (Aurell et al. 1995; Mylroie et al. 2012, p. 36-37; Fig. 32).

A) Light brown rhizolite calcrete (*Rh*) infills the cavity and shows roughly layered structure (dashed lines). B) Close-up view showing a cavity (*P*), probably corresponding to a former pocket of red-brown soil containing cm-sized composite rhizoliths (cf. Fig. 2.7C) between the layered units (*L*). C) Detail of B. Camera objective cap is ~7 cm in diameter.



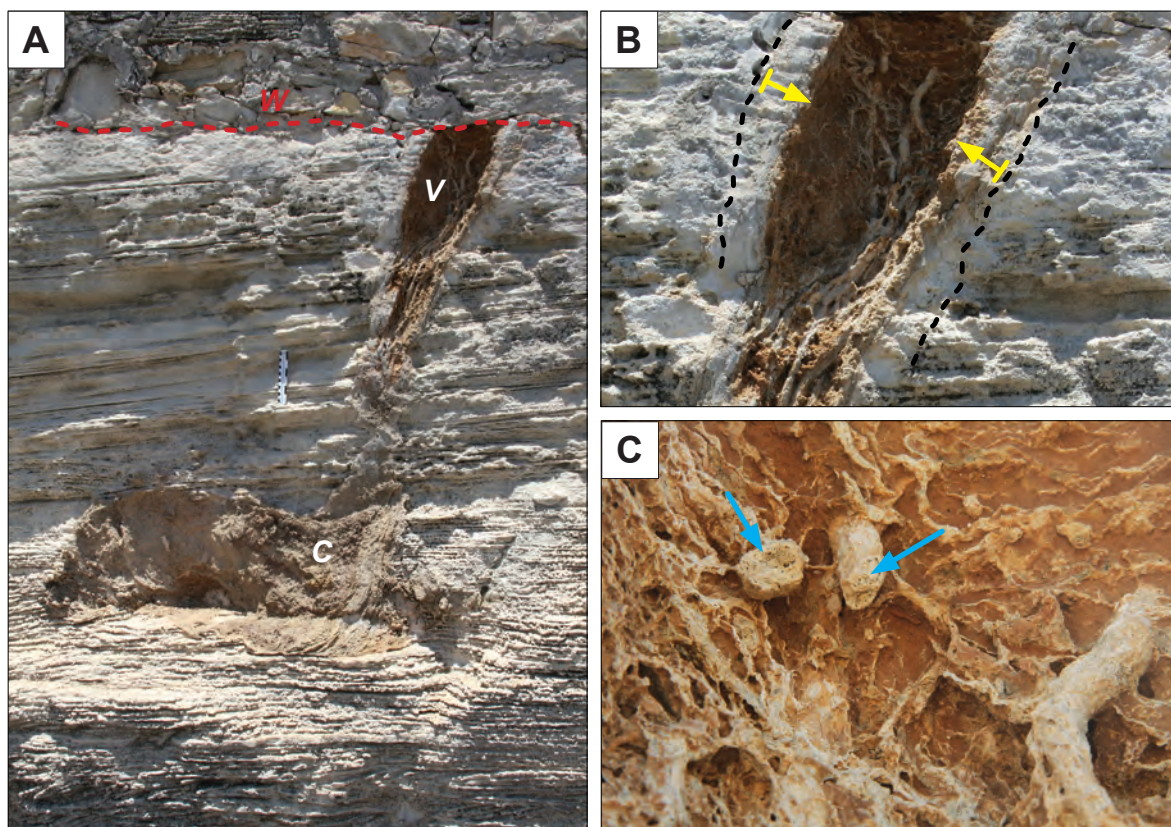


**Fig. 2.7.** Same outcrop as in Fig. 2.6. A) Smaller (remain of a) cavity infilled by crudely laminar rhizolite fabric. Red dashed line marks a wall (*w*) built on top of the outcrop. V - vertical dissolutional tubular void (cf. Mylroie et al. 2012, p. 36, Fig. 32) filled with remains of red soil material and cm-sized composite rhizolites. B, C) Details of the void showing several cm lining of laminar to massive calcrete (B; dotted black line and yellow arrows) and close-up view of composite macrorhizolites (C; blue arrows), composed of numerous millimetric tubes, corresponding to fine roots.

Coarse, macroscopic root structures, observed along the foresets in Holocene aeolianite at North Point (Fig. 2.8D, E), are mostly formed by composite rhizolites, composed of sub-millimetric, fine root microfeatures. White and Curran and (1997) and Curran and White (2001) deduced that some of the supposed rhizolites are not root traces and introduced the term thallo-ichnomorphs for tubular traces associated with micritic crusts. They interpreted them as traces of runners or stolons, i.e. stems of plants that that grow horizontally along the ground and extend for several metres across the surfaces of modern sand dunes, commonly seen on San Salvador. Thallo-ichnomorphs supposedly indicate that they developed contemporaneously with the accumulation of sand in the ancient dunal environment (Curran and White 2001). Although some of the rhizolites, associated with aeolian cross-lamination, may correspond to such surficial stems, most of the traces exposed on weathered coastal aeolian outcrops exhibit hierarchic branching patterns, more



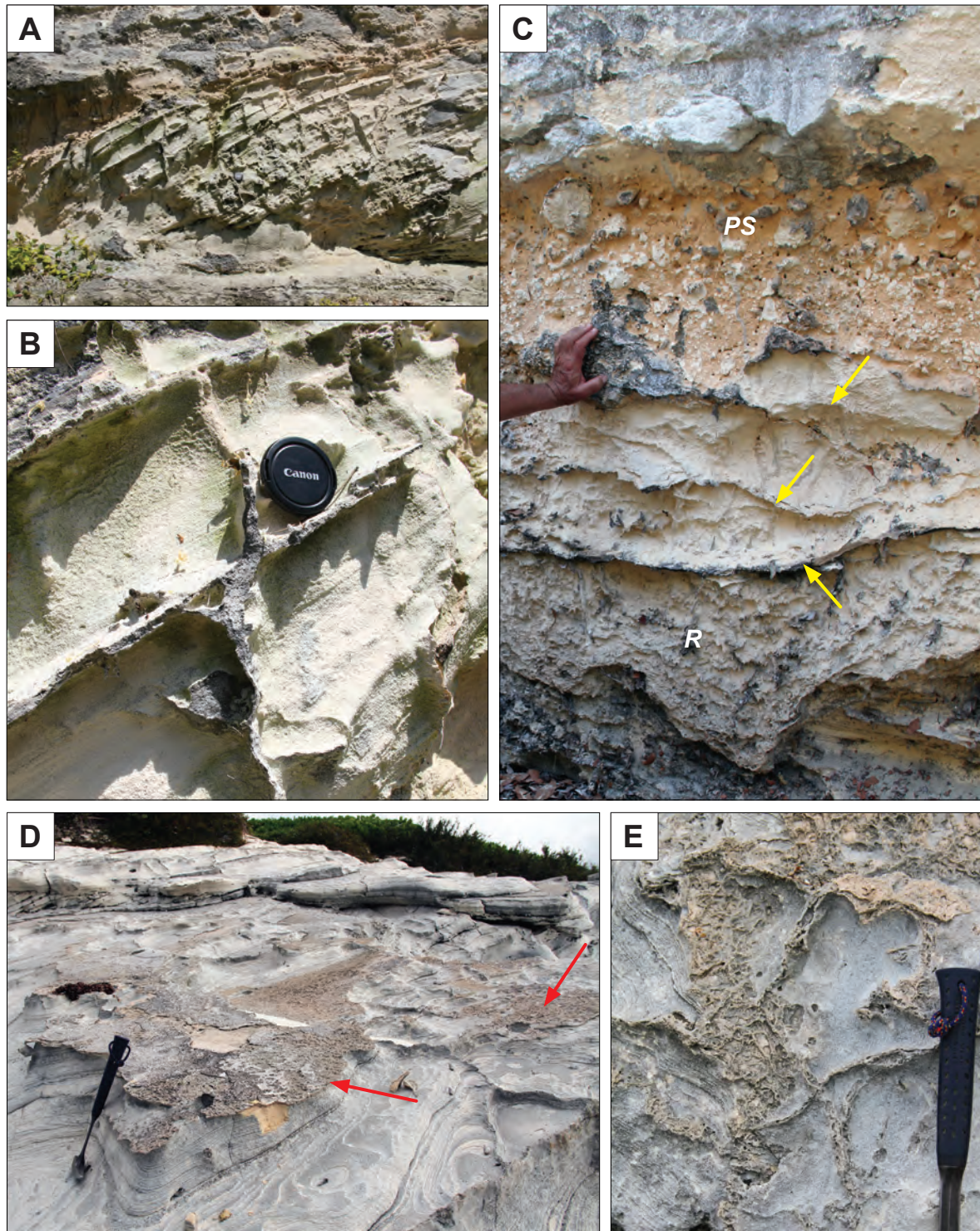


**Fig. 2.8.** Thin calcrete layers in aeolian dunes, Pleistocene of Lyford Cay, New Providence (A-C), and in Holocene dunes (North Point Member) at Rice Bay, San Salvador (D-E). **A, B**) Boxwork-like structures of mm-thick, cemented laminar calcrete layers, extending along parallel aeolianite foreset/backset laminae, connected with joints, cross-cutting the bedding. In thin sections, such thin cemented layers are made of one or several laminae, composed of millimetric tubular fabric, corresponding to fine roots. **C**) Palaeosol (*PS*) within a stacked sequence of aeolianite dunes, underlain by a meshwork of rhizolites (*R*) and irregular thin calcrete stringers (arrows) within weakly cemented carbonate sand. **D, E**) Weathered out, several mm thick rhizolite layers from Holocene aeolianite cross bedding showing clearly preserved macroscopic root structures (cf. White and Curran 1988).

compatible with root systems (Fig. A2-1.04E). Furthermore, as noted above, the internal structure of these traces typically shows composite fabric, composed of fine root rhizoliths (see discussion in Section 2.5.3).

Aeolianites with thin calcrete layers often display selectively weathered, boxwork structures (Fig. 2.8A, B), indicating preferential growth of plant root systems along particular laminae and connective joints, and corresponding precipitation of secondary carbonate, causing enhanced cementation of these layers.

Figure 2.9 shows root-related calcrete features from the well-known locality at The Gulf, San Salvador (e.g. Carew and Mylroie 1995; Hladil 2004). There, the upper part of the Cockburn Town Member is composed of regressive aeolian dunes, capped by a laminar calcrete (Fig. 2.9A), associated with several penetrative, laterally pinching out rhizolite layers (Fig. 2.9B). The locality is best known for impressive macrorhizoliths, protruding from selectively weathered bioturbated aeolianite (Figs. 2.9C, D). Importantly, the rhizoliths are almost indistinguishable from the matrix in freshly broken surfaces, indicating that such root traces may become largely unrecognisable by progressive diagenesis (cementation) of aeolianite sand.

Another common feature, mostly observed in weakly cemented aeolianite sand deposits, are circular structures, corresponding to laminar calcrete-coated vertical solution pipes and irregular dissolutional cavities, typically several dm in diameter (Fig. 2.10). The crusts in weathered pipes are several centimetres thick and associated with cm-scale rhizoliths in the sediment around the pipes (Fig. A2-1.04G), however, rhizoliths does not seem to be related or connected with the laminar rhizolite crust.



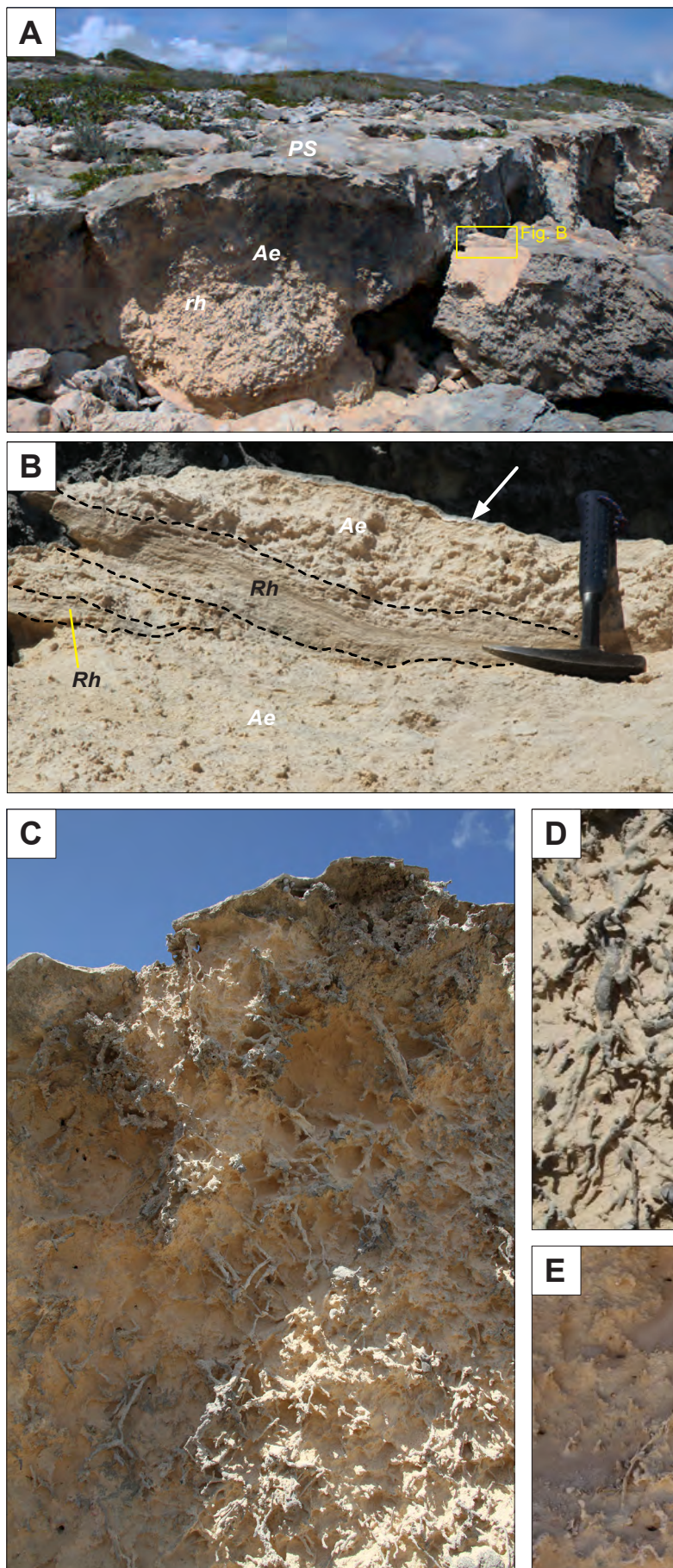


**Fig. 2.9.** The renowned locality with rhizolites at The Gulf, San Salvador (e.g. Carew and Mylroie 2001). A) Regressive aeolianite (*Ae*) of the Cockburn Town Member, capped by thin laminar calcrete (*PS* = complex palaeosol of Carew and Mylroie 1995); *rh* - macrorhizolites. B) Close up view of a freshly broken surface of a fallen block in Fig. A, showing thin surficial crust (calcrete or case-hardening; white arrow), 10-15 cm thick bioturbated layer of aeolianite sand (*Ae*), two pinching-out layers of laminar rhizolite (*Rh*), and the lower aeolianite layer. C-E) Typical appearance of macrorhizolites, pronounced by selective weathering in coastal outcrops of weakly cemented sand, while on the unweathered surface in lower part of the block in Fig. B, rhizolites are virtually indistinguishable from the matrix.



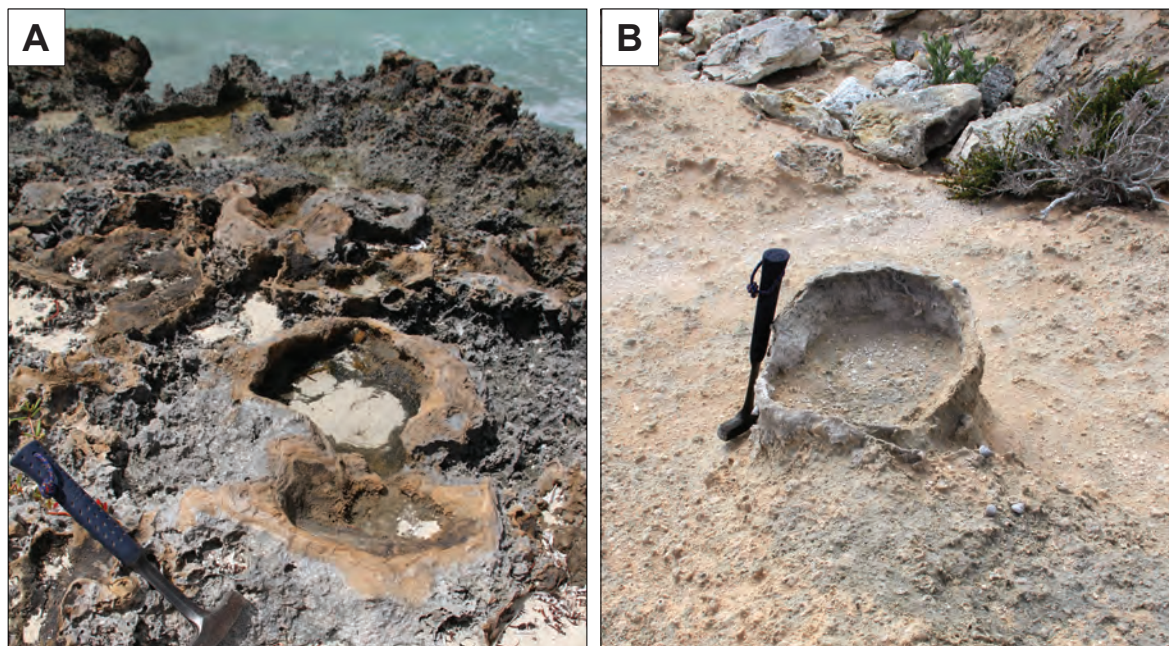


**Fig. 2.10.** Solutional cavities (pipes) coated with laminar rhizolite calcrete. A) Strongly weathered coastal outcrops at Rocky Point, San Salvador, and B) erosional remnant of a calcrete-lined solution pipe from partly deflated, weakly-cemented aeolian sand. Coast E of French Bay, San Salvador.

#### 2.4.2 Mesoscale calcrete fabric

Mesoscale fabric in cut calcrete slabs are typically beige to brown and red in colour, and display distinctive millimetric to sub-millimetric, gently undulating lamination or indistinctively layered texture (Figs. 2.11A, D, E, 2.13A, B, C). Particularly thicker laminar forms, from several to more than 10 cm thick, are commonly composed of interchanging porous layers with numerous tubular pores (Figs. 2.11A, 2.13A) and stronger cemented layers (Figs. 2.11A, 2.13A). Laminar fabric can contain discontinuity surfaces (micro-unconformities), typically emphasised by thin red or black laminae, mineralised by Fe and Mn oxides (Fig. 2.11B, 2.13A).

Lamination is mostly due to variation in microstructure (e.g. open or filled pores, Fig. 2.13A) and the degree of staining by occluded organic matter and non-carbonate mineral component (clay minerals, Fe and Mn oxides and hydroxyoxides). In spite of intensive red-brown colouration (e.g. sample in Fig. 2.13C), such laminar forms contain only trace amounts of Fe and negligible fraction of clay minerals (see Section 2.4.4).

Some laminar rhizolite samples contained distinctive purple-coloured cylindrical features, 0.2 to 0.5 mm in diameter, arranged in anastomosing laminae (Figs. 2.11E and



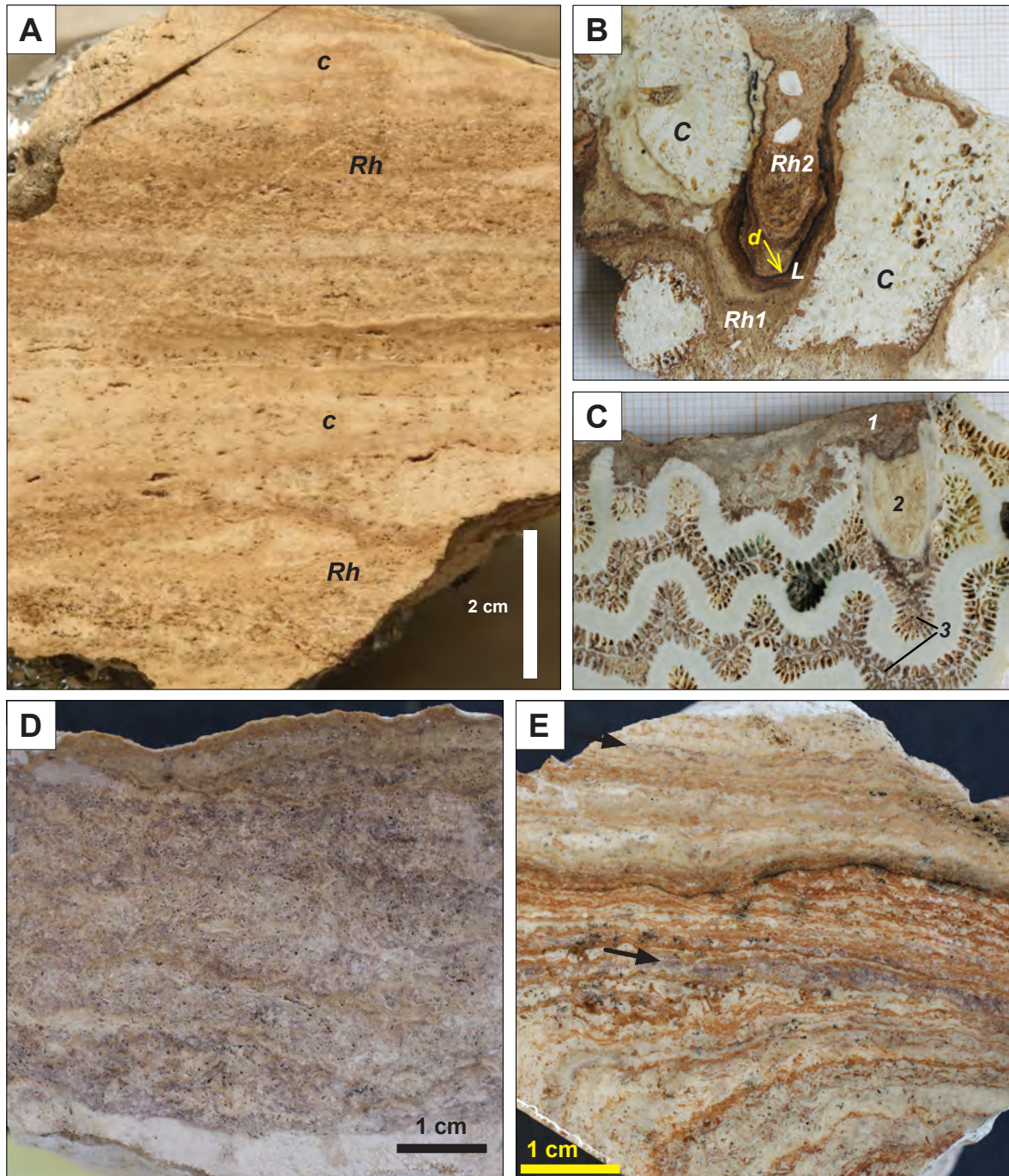


**Fig. 2.11.** Mesoscale calcrete fabric in slabs. A) Crudely laminar rhizolite composed of generally slightly darker porous microtubular layers (*Rh*) and denser cemented layers (*c*). B and C) Rhizolite in cm-sized cavities in coral rubble, composed of several phases of calcrete growth: *Rh1* - lower porous rhizolite layer; *L* - finely laminar layer, capped by Mn-oxide coated discontinuity surface (*d*), overlain by upper, crudely laminar rhizolite (*Rh2*). C) A slab of a coral with a rhizolite-filled boring bivalve (2), overlain by darker colour calcrete layer (1). Note fine tubular rhizolith features within the coral septa (3). Samples A-C: Nicholls Town, North Andros (see Fig. 2.3A). D) Indistinctly layered rhizolite crust composed of microtubules, corresponding to fine roots, mostly less than 1mm in diameter. Cf. Fig. 2.13B. Cockburn Town, San Salvador. E) Well-cemented, dense laminar rhizolite with layers composed of distinctive, purplish coloured fine root structures (black arrow) and beige and red-brown laminae with less pronounced tubular fabric. Also see Figs. 2.13C-G. Barker's Point, San Salvador.

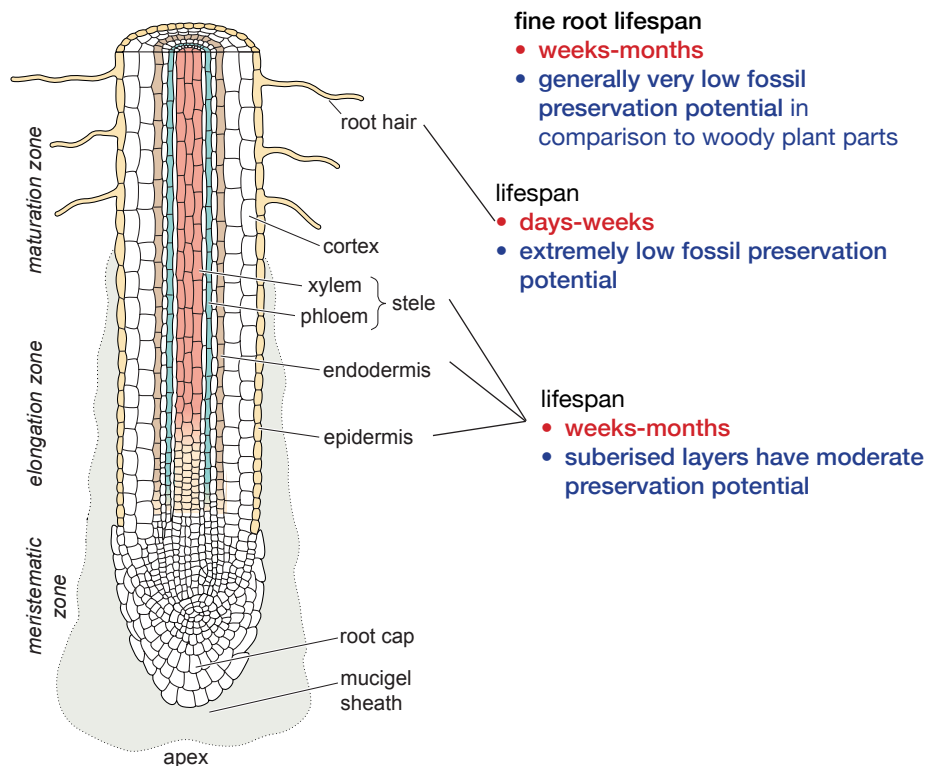


**Fig. 2.12.** Fine root anatomy, life-span of different tissues, and their fossil preservation potential. Diagram of a primary root with simplified cellular structure showing the root cap, the apical meristem, the elongation zone and the maturation zone at increasing distance from the root tip, modified from Taiz et al. (2015).

2.13C, D) or appearing as discrete points (2.11A). Microscopic analysis revealed that these purplish-stained microfeatures represent exquisitely preserved anatomical details of fine roots, described below (diagram in Fig. 2.12 and photomicrographs in Figs. 2.13D-G, 2.15-2.17).

The type and scale of layering in laminar calcretes is commonly used to distinguish laminar crusts (Read 1976; Verrecchia 1994, 1996; Verrecchia et al. 1995), which would include most of the published examples of Quaternary soilstone crusts (e.g. Kornicker 1958; Perkins 1977; Coniglio and Harrison 1983a, b; Swart 2015), from root-related calcrete forms (Wright et al. 1988; Wright 1989; Alonso-Zarza and Jones 2007 amongst others). Many of the examples described here (e.g. finely-laminar portions of calcrete in Fig. 2.11E) are identical to the archetypal, supposedly exclusively surficial (subaerially exposed) and phototrophic microbially-induced laminar forms, however, the presence of exceptionally preserved very fine root traces (<0.3 mm in diameter) within the sub-millimetric laminae (Fig. 2.13C), and the accretionary laminar fabric in calcretes coating deep cavities and



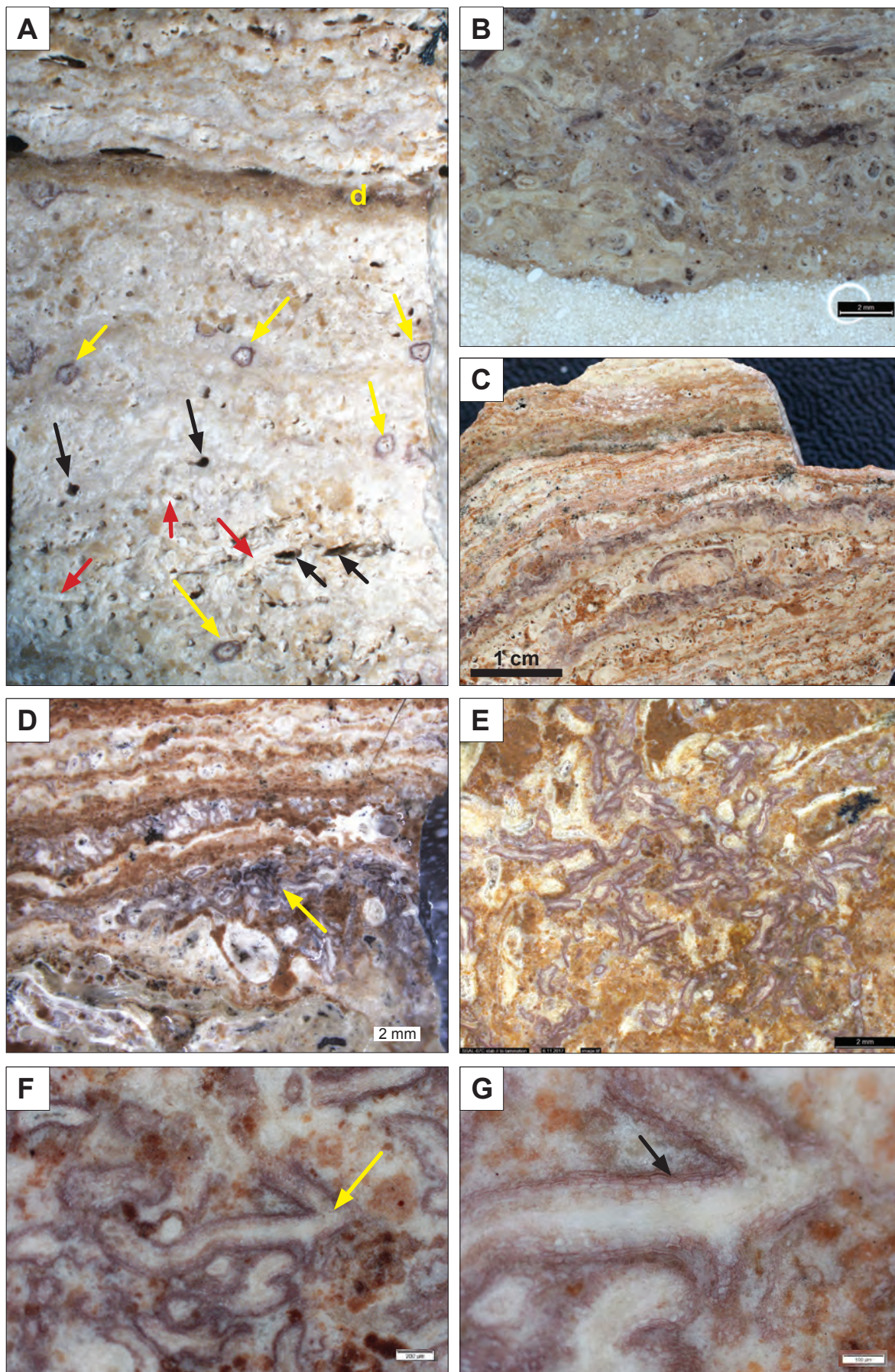


Fig. 2.13. (see caption on the following page)

**Fig. 2.13.** (previous page) A) Cut (unpolished) slab of the rhizolite from Nicholls Town, North Andros (cf. sample in Fig. 2.11A) showing different preservation modes of fine roots. Black arrows: tubular pores, corresponding to decayed roots without any preserved anatomical features; red arrows: white circular features corresponding to roots mineralised by microcrystalline carbonate; yellow arrows - fine root cross sections with exceptionally well preserved epidermis with root hairs and outer cortex layers (exodermis), shown in Figs. 2.15 and 2.16. *d* - darker layer marking a discontinuity surface. B) Thin section slice of a rhizolite crust on peloidal grainstone/packstone, composed of different cylindrical features, generally less than 1 mm in diameter, with indistinctive internal structure, consisting of central (vascular) cylinder and outer cortical layer. Cockburn Town, San Salvador. C) Polished slab of calcrete in Figs. 2.8B and 2.11C. Root anatomical details are best seen in purplish layers, composed of very fine roots, less than 0.5 mm in diameter. D) Cluster of well-preserved fine roots (arrow), polished remaining slice of a thin section. E-G) Same laminar calcrete sample as in Figs. C and D, cut parallel to lamination. Some of very fine roots in longitudinal sections exhibit branching (yellow arrow in F). Higher magnification images G and F (taken on polished slabs under petrographic microscope in reflected light) show distinctive cellular structure, particularly in epidermis and outer cortical layers (black arrow in G). Purple pigmentation probably corresponds to deposits of condensed tannin in roots that were undergoing browning (maturation) process. C-G: Barker's Point, San Salvador.

fissure walls (Figs. 2.3, 2.11C), contradict the model which puts subaerial exposure as a prerequisite for formation of laminar calcretes (crusts) and confirm the opposite, i.e. that they can 'form in a variety of settings and have a variety of origins' (see discussion in Wright et al. 1996 and Verrecchia et al. 1996).

### 2.4.3 Microfabric

In general, microfabric of laminar rhizolites is relatively poorly discernible in thin sections of standard thickness. Lamination is mostly expressed by interchange of dense micrite and more porous layers, containing 0.1 mm to 1 mm large tubular pores, and irregular reddish-brown-stained patches due to Fe oxide and clayey material. Furthermore, even in ultrathin, double polished thin sections (10-15  $\mu\text{m}$  thick), predominantly micritic composition generally enables to distinguish only gross features like tubular fenestrae and peloids (Fig. 2.14), and only exceptionally clear root cellular tissues and (Figs. 2.14B-C and 2.18).

Fine root microstructure appeared to be more visible in reflected light under a stereomicroscope or polarising microscope, in polished, resin-impregnated slices and even in rough, unpolished calcrete slabs. Figure 2.15 shows fine root sections in thin section (Fig. 2.15A, B) and slabs. Most of the roots, generally <0.5 mm in diameter, exhibit well-preserved cellular structure of epidermis and exodermis (i.e. the outer layer or two the cortex), including delicate root hair features (Figs. 2.15A-D, F, 2.16F). Clearly preserved cellular fabric appears to be due to organic pigmentation of the cell walls in the outer cortex



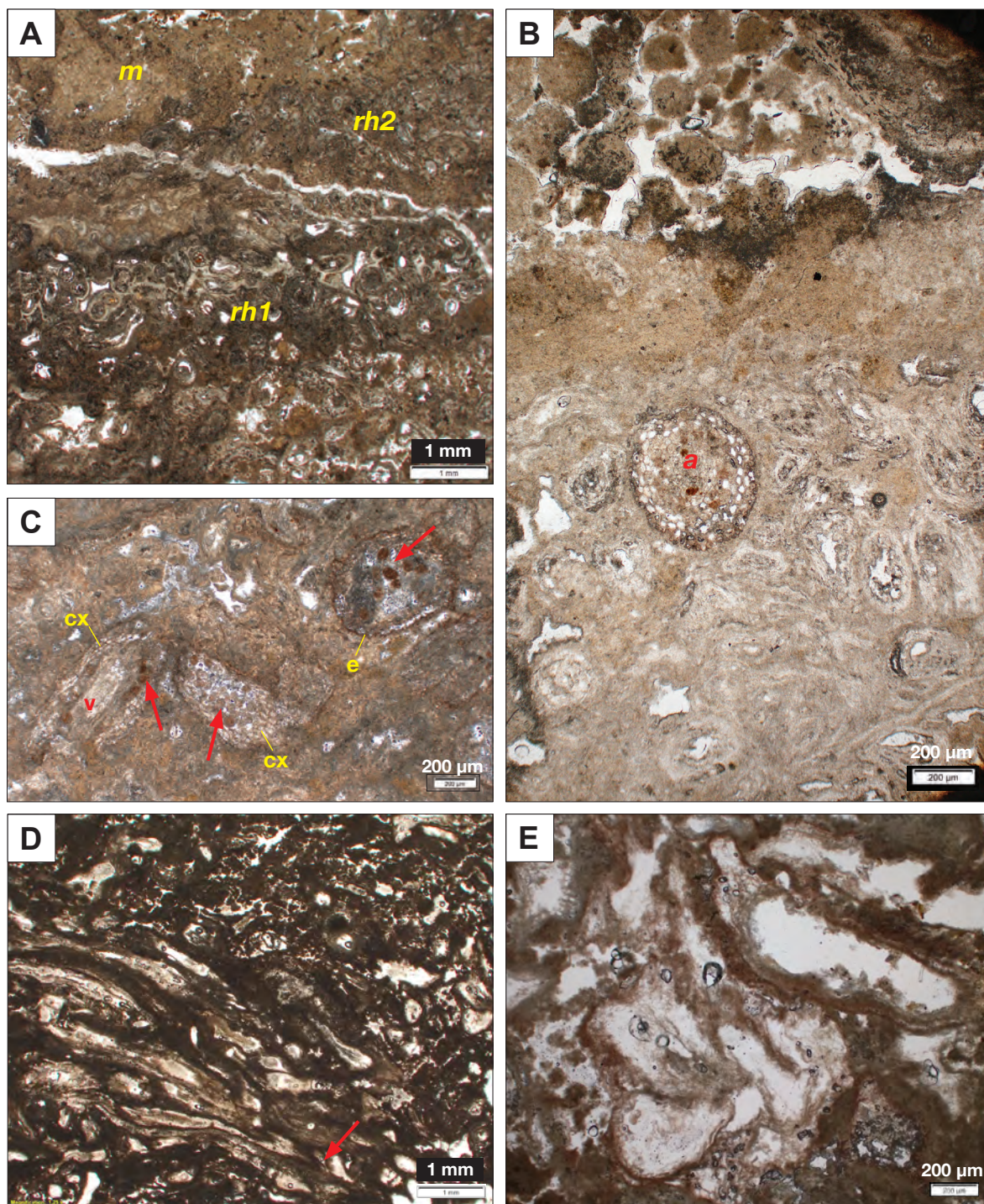


**Fig. 2.14.** A) Roughly layered structure composed of dense micrite (*m*) and closely packed very fine root rhizoliths (*rh1*), <0.5 mm in diameter, with relatively well discernible ultrastructure, while in layer *rh2*, root anatomical structures are almost unrecognisable. B) A cross section of a fine root (*a*) with relatively well-preserved cellular structure, particularly in comparison with adjacent traces of roots which exhibit only hardly distinguishable concentric fabric. C) Root sections showing partly preserved cortex (*cx*), pigmented epidermis (*e*), vascular cylinder (*v*) and spherical red-brown coprolites (red arrows). Also see Fig. 2.17. A-C: PPL thin section photomicrographs of the laminar rhizolite from Nichols Town. Subsample of the specimen in Fig. 2.13A. D, E) Microfabric of a crudely laminar calcrete from a karstic pit at Clifton Pier, New Providence. Cylindrical fenestrae surrounded by microlaminar micrite; note faint cellular fabric (red arrow). All images are PPL photomicrographs of polished ultrathin sections.



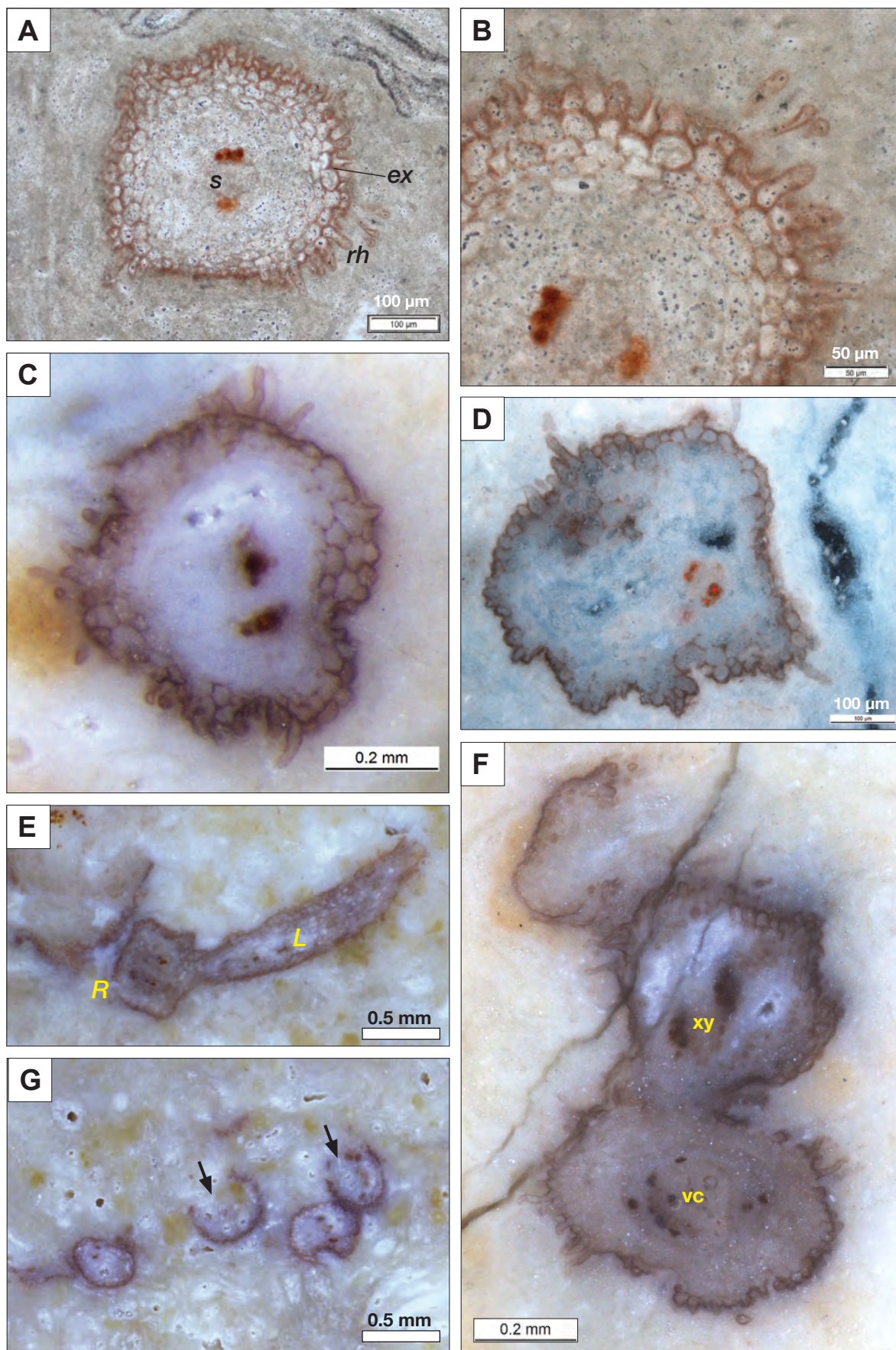


Fig. 2.15. See caption on the following page.

**Fig. 2.15.** (previous page) Exceptionally preserved fine roots in laminar rhizolite samples from Nicholls Town, North Andros. **A, B**) PPL thin section photomicrographs of a transverse section of a fine root with perfectly preserved epidermis with emerging root hairs (*rh*), exodermis (*ex*), and pigmented tissues (?diarch xylem) of the vascular cylinder (*s*). **C**) A root similar to A and B with slightly displaced dark-coloured elements of the vascular tissue. Stereomicroscope reflected light photomicrograph of polished, resin-embedded slab. **D**) Transverse root section with deformed (non circular) outer shape and without any trace of vascular tissues. Polished thin section photomicrograph, taken under blue luminescence reflected light. **E**) Fragment of a fine root (**R**) with a lateral root (**L**). Stereomicroscope reflected light photomicrograph of polished, resin-embedded slab. **F**) Three root sections showing different stages of decay process; arrows indicate roots with ruptured epidermal layer. The root in the middle shows two patches of pigmented cells (*xy* - ?xylem), whereas the lower root section shows partly preserved structure of the vascular cylinder (*vc*) with several pigmented cells. Note also exquisitely preserved root hairs in the lower specimen. Same specimen as E. **G**) Four fine roots transverse sections; arrows indicate disrupted epidermal/exodermal layer. Stereomicroscope photomicrograph, taken on a wet, non-polished slice with rough surface.

and epidermis, most probably deposits of condensed tannin. Similar staining is observable in internal parts of the roots, in transverse sections appearing in two distinctive spots, probably corresponding to (diarch) xylem tissues (Figs. 2.15A, C, 2.16B, C), or several pigment-filled discrete cells of the vascular cylinder tissues (Figs. 2.15F, 2.16D). Aligned, pigmented cells of the vascular cylinder are also visible in some longitudinal sections (Figs. 2.16A, E). In slices, cut approximately parallel to the lamination, pigmented roots show distinctive branching patterns (Figs. 2.13E, F, G).

Cellular structure of the internal part of the cortex has not been observed in any of the examined fine roots. Significantly, in many roots, pigmented parts of the vascular cylinder tissues (probably xylem parenchyma) are displaced from its anatomically normal central position (Figs. 2.15C, 2.16C). In many root sections, pigmented epidermis and rhizodermis exhibit strongly deformed (normally cylindrical) shape of the root (Figs. 2.15D, F, 2.16E) and disrupted parts (Fig. 2.15G, 2.16E). Many roots contain spherical, stained peloids, identical in colour to pigmented parts of root tissues (Fig. 2.17A-D). These peloids probably represent coprolites of small soil arthropods (mites) feeding on tannin containing root tissues and excreting coprolites inside decaying root tubules (cf. Wright 1983; Jones and Squair 1989; Strullu-Derrien et al. 2012). Figure 2.17E-H shows similar, tannin-pigmented plant tissue containing coprolites of comparable size from modern soil carbonate accumulations, associated with extensive root systems of *Pinus halepensis* in the Alicante Province (see Chapter 3).

Although many roots exhibit well-preserved cellular structure, they do not show evidence of intracellular biomineralisation of the cortex (see Chapter 3). In exceptional cases, outer cortical cell layers and epidermal cells display variability of cell preservation



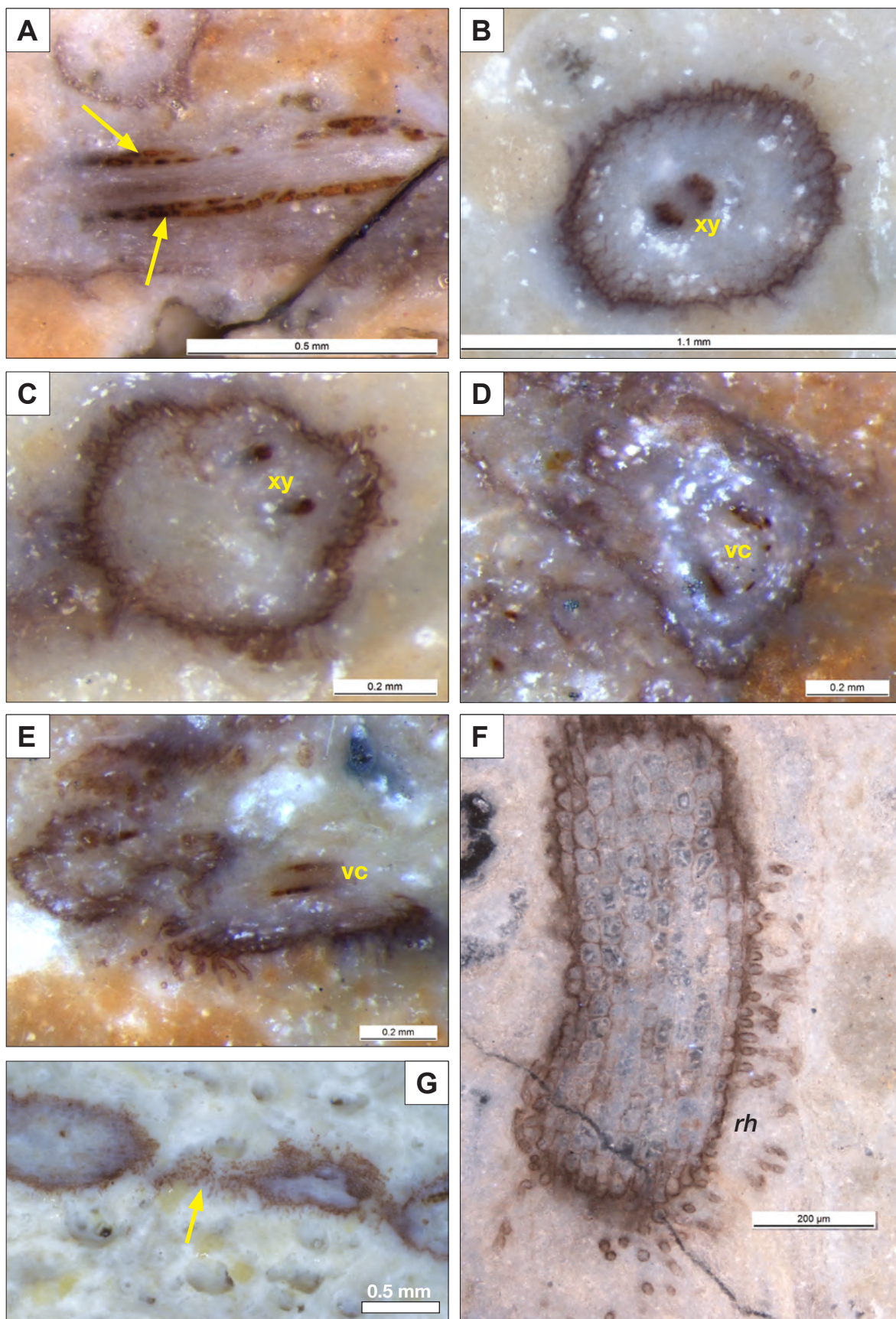


Fig. 2.16. See caption on the following page.

**Fig. 2.16.** (previous page) Same sample as in Fig. 2.15. Reflected light photomicrographs of polished slabs (A-F) or non-polished slices with rough surface (G), showing sections of fine roots with relatively well preserved epidedermal/exodermal tissues and remains of vascular tissues. A) Longitudinal section through the axial part of a root including the vascular cylinder, showing two lines of elongate cells, filled with yellow-brown organic matter (probably condensed tannin). B, C) Transverse sections of well-preserved pigmented cell walls of the epidermis/exodermis and two clusters of pigmented (condensed tannin-filled) cells of xylem tissues, displaced towards the margin of the root in C. D, E) Considerably decayed root remains with preserved pigmented cells of the vascular system (vc). F) Tangential section of a fine root showing well-preserved cellular structure, pigmented cell walls of the epidermis/exodermis, and root hairs (rh). G) Unpolished, wet surface of a calcrete slab showing isolated remains of root hairs or tiny sloughed-off cells (arrow).

in ultrathin sections (Fig. 2.18) where some of the cells are empty and other filled with microcrystalline carbonate of variable density, probably fibrous forms such as needle fibre calcite and calcite nanofibres. Polished, resin-impregnated thin sections, observed under SEM in BES mode, shows that the cell walls of the outer layers, showing pigmentation under optical microscope, are mostly mineralised with carbonate, forming irregular, 1-2  $\mu\text{m}$  thick walls (Fig. 2.19B). Cell lumina are either empty (Fig. 2.19A, B) or filled with spherical, probably bacterial features, encased in a meshwork of nanofibrous carbonate (Figs. 2.19B, C, D), or micro- or nanocrystalline material of different density (Figs. 2.19F-H), infilling the whole cell space or forming irregular coatings on the cell walls. Some mineralised cell walls display anastomosing tubular fabric (Figs. 2.19G, H).

Fine root features without preserved cellular structure typically consist of microlaminar micrite, forming cylindrical structures, 0.2 to 1 mm in diameter (Fig. 2.14D, E). In the studied laminar rhizolites from the Bahamas, microfabric of fine root cylindrical features is typically badly preserved for detailed SEM observation, however, it has likely formed through initial precipitation of needle fibre calcite (NFC) and calcite nanofibres (Figs. 2.19I-L; 2.21E, F). Potential modern analogues of  $\text{CaCO}_3$  precipitation around fine roots and their taphonomy are represented by active root systems from calcareous soils in SE Spain and rhizoliths from modern aeolianite deposits in Morocco, shown in Appendix A2-3.

**Fig. 2.17.** (following page) A-D) Fine roots in different stages of decay, mostly with well preserved pigmented epidermal layer only. Internal parts of roots contain abundant spherical red-brown coprolites, 30-60  $\mu\text{m}$  in diameter. Reflected light photomicrographs of polished slab, same calcrete sample as in Figs. 2.15 and 2.16; Pleistocene, Nicholls Town, North Andros. E, F) PPL and XPL thin section photomicrographs of peloids/coprolites from recent chalky calcrete deposits associated with root system of *Pinus halepensis* (Sella-Finestrat locality, Alicante Province, Spain; see Chapter 3 and Appendix A3-1). Peloids contain abundant red-brown particles of tannin-containing plant tissues, consumed and excreted by soil animals, probably mites. G, H) SEM photomicrographs of peloids (calcified coprolites) from the same locality, composed predominantly of nanoscopic forms of calcite (nanofibres) and  $\mu\text{m}$ -size nest-like microbial (?bacterial) features.



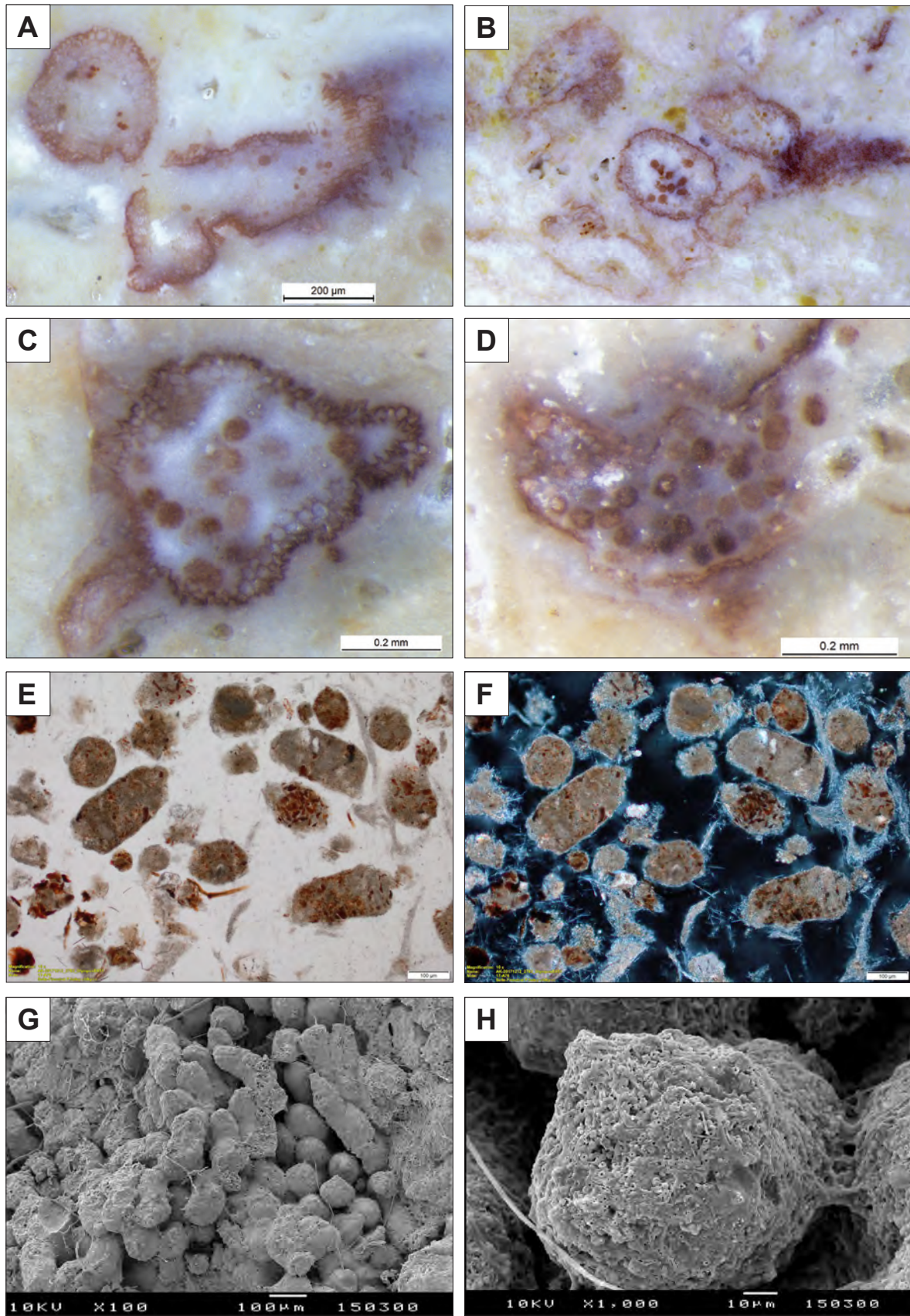
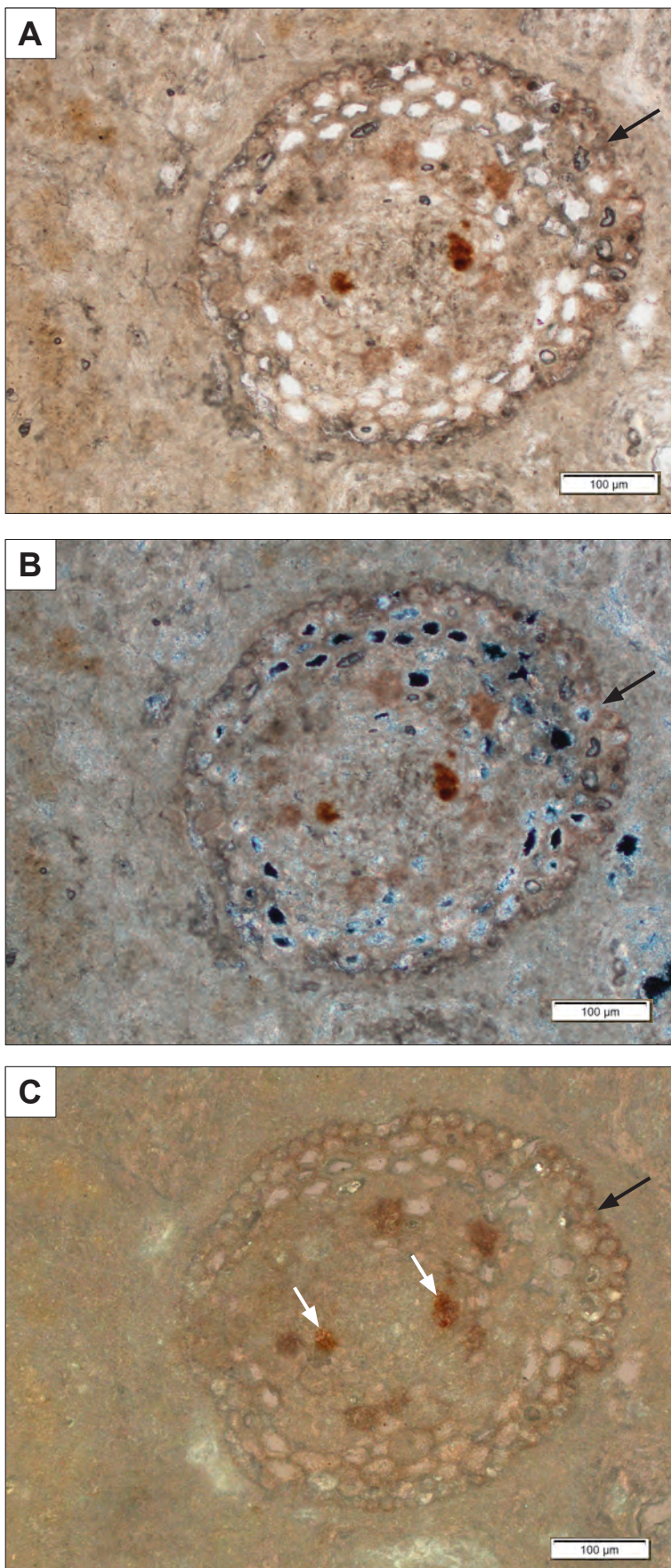


Fig. 2.17. See caption on the previous page.





**Fig. 2.18.** Ultra-thin (~10 μm), double polished thin section photomicrographs of a root in cross section, taken in A) transmitted PPL, B) XPL, and C) long-exposure reflected XPL light. Relatively well preserved cellular structure of the cortex is composed of empty cells (white in A and black in B) and cells, partly or fully infilled by microcrystalline carbonate. Red-brown patches in the center are remains of (probably) tannin-pigmented xylem tissues without discernible cellular structure but marked by dispersed organic matter, best seen in Fig. C (white arrows). Slightly pigmented cell walls are also visible in the epidermal layer and parts of the outer cortex (exodermis; black arrows) Also see SEM photomicrographs in Fig. 2.19. Nicholls Town, North Andros, sample NTW-E.



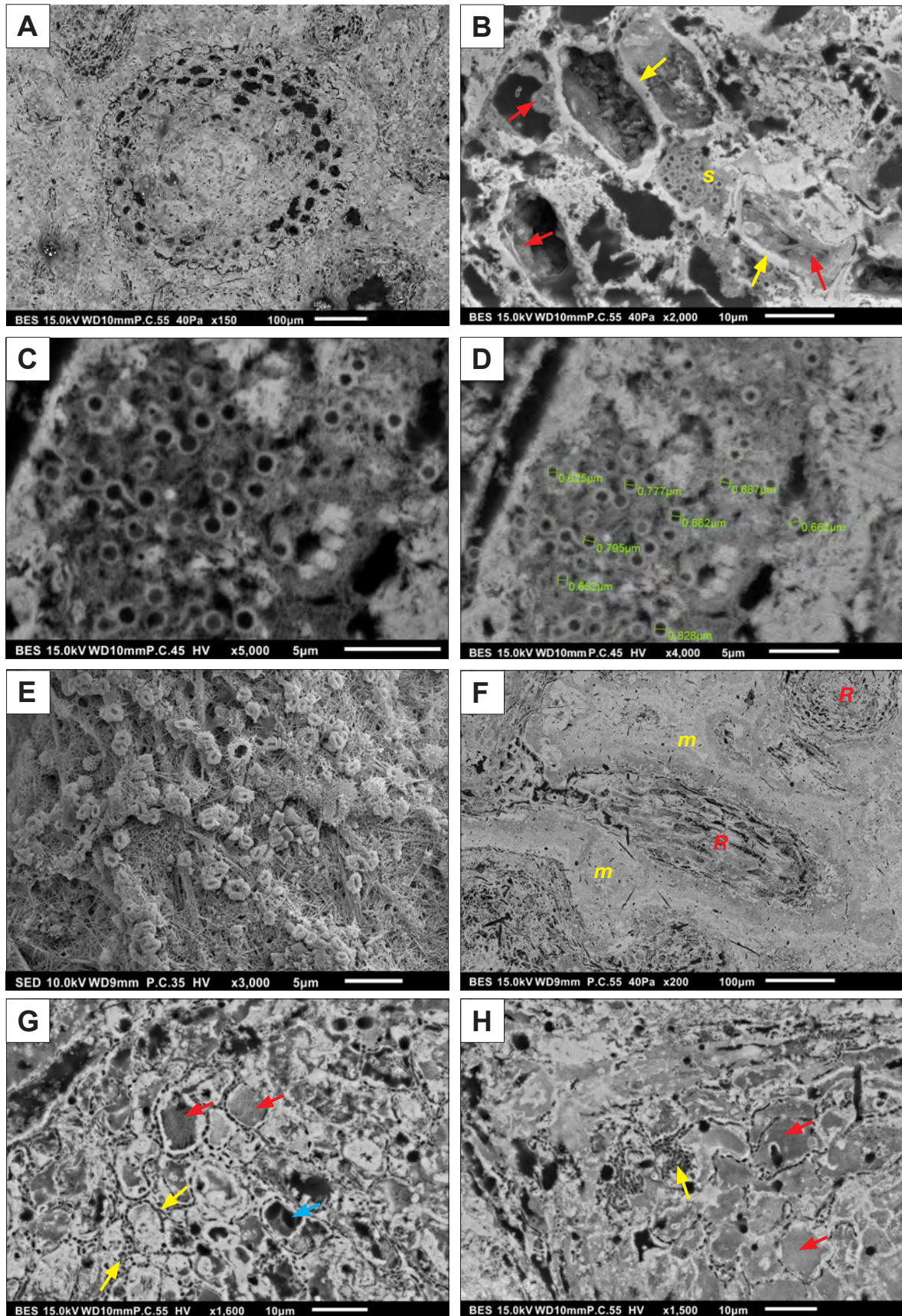
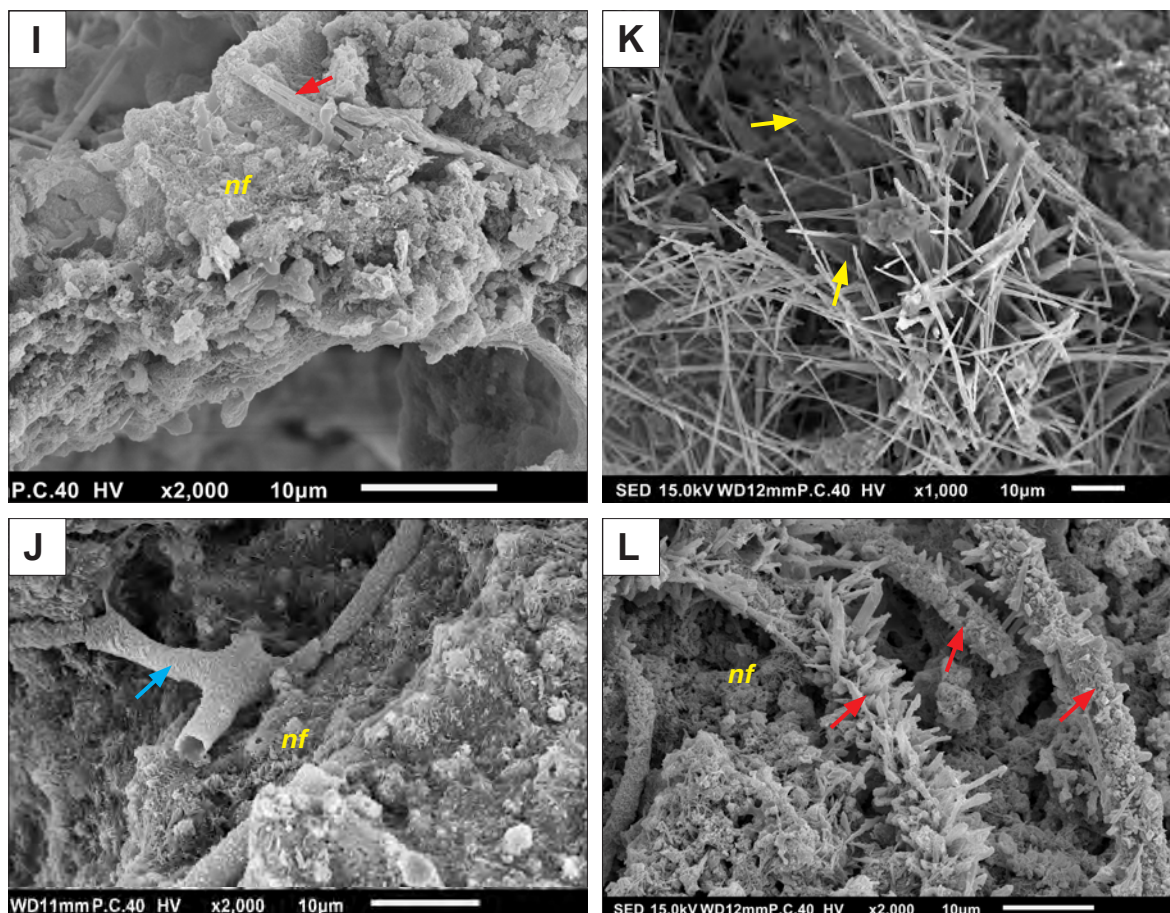


Fig. 2.19. See continuation on the following page.





**Fig. 2.19.** A-H (previous page): SEM photomicrographs of fine root ultrastructure in laminar rhizolites, Pleistocene, Nicholls Town, North Andros. All figures are backscattered electron (BES) images of polished, resin-impregnated thin sections, taken in low or high vacuum (see labels), except Fig. E which is a SED image of NFC/nanofibrous calcite in a freshly broken surface. A) Transverse section of the root in Fig. 2.18 showing empty cortical cells (black = resin) and cells displaying different fine textures and shades of grey, corresponding to microcrystalline infill of different density (darker grey = higher microporosity and correspondingly higher amount of resin). B) Partially preserved cellular structure of fine root cortex, composed of calcified cell walls (yellow arrows). Some cells contain nanocrystalline (probably nonfibrous) deposits (red arrows), or are infilled by spherical features (S). C, D) Detailed view of the texture, composed of closely packed spheres of uniform size, 0.6 to 0.8  $\mu\text{m}$  in diameter with 0.1-0.2  $\mu\text{m}$  thick walls, enclosed in a nanofibrous (?calcite) meshwork. E) Texture, possibly analogous to C and D, showing nanofibrous calcite fabric and bacterial 'nest-like' features; Recent soil from the Sella-Finestrat locality (see caption of Figs. 2.17G, H). F) Mineralised fine roots (R) in micritic matrix (m). G, H) Cellular structure of fine root cortex showing a variety of microfabric: yellow arrows: anastomosing microtubular fabric, apparently occurring along the cell walls and intercellular spaces; red arrows: cells infilled with nanocrystalline material (probably calcite nanofibres) of different density, showing indistinct fibrous texture in Fig. G; blue arrow: micro-scale alveolar septal structure, composed of nanofibres. I) SEM photomicrographs of Au-coated broken surface of a laminar rhizolite from Holocene aeolianite at North Point, San Salvador, showing a wall of a root tubule, 0.5 mm in diameter, composed of micrite - predominantly nanofibres (nf) and rare incorporated NFC rods (red arrow). J) Same sample as I, showing the wall of a millimetric tubular pore, coated by calcite nanofibres (nf) and ?calcite-mineralised fungal hyphae (cyan arrow). K, L) Internal fabric of submillimetric fine root tubules (cf. Fig. 2.14D,E) composed of NFC and possibly oxalate crystals (triangular needles marked with yellow arrows in K, nanofibrous micrite (nf), and mineralised fungal hyphae (?oxalate transformed to calcite). Clifton Pier, New Providence.



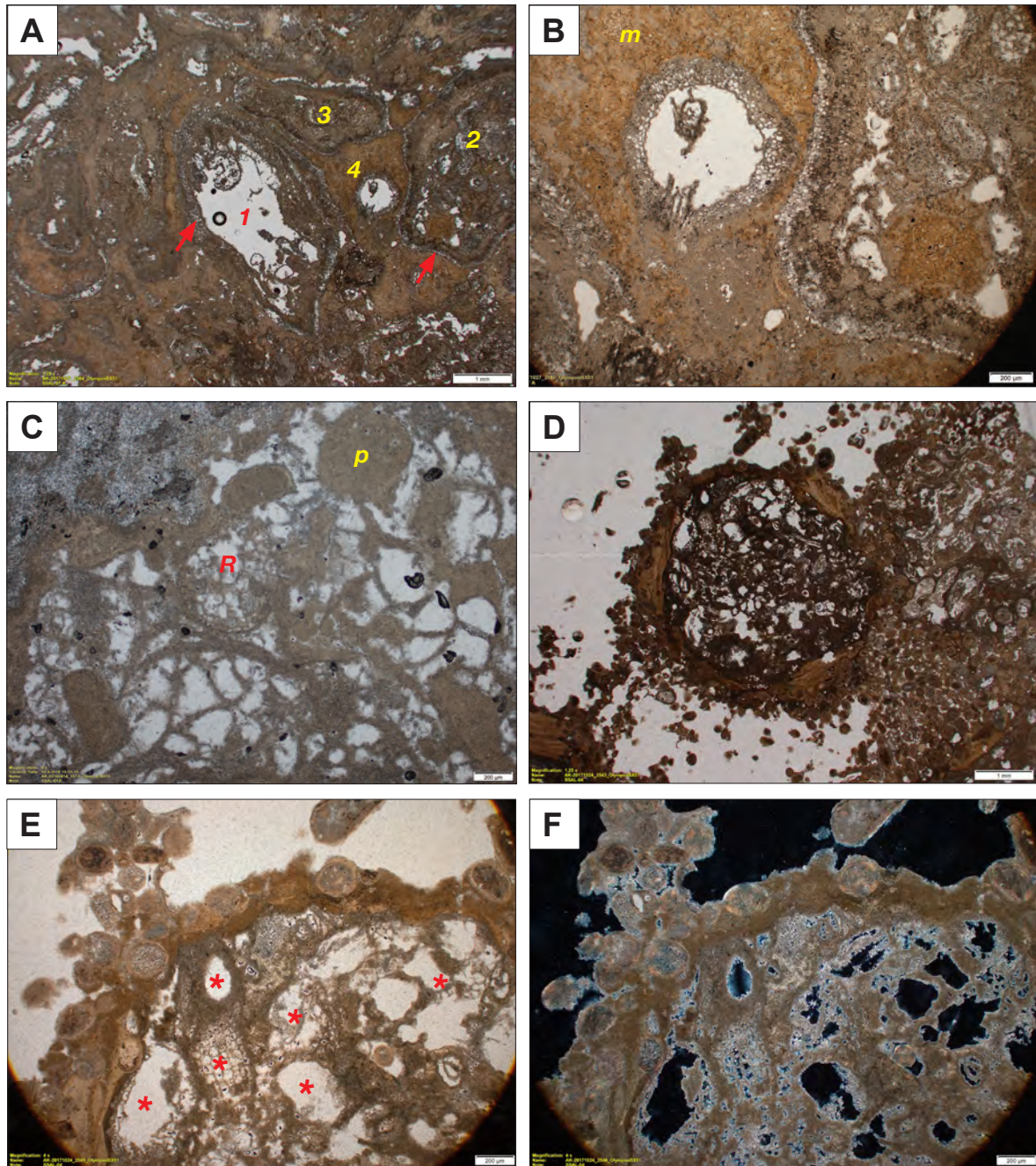


**Fig. 2.20.** Microfabric of composite macrorhizolites from San Salvador. Thin section photomicrographs. A) Coarser root rhizolites (numbered 1, 2, 3), 3-5 mm in diameter, and a smaller rhizolith (4), all showing indistinctive cellular fabric in their marginal parts (red arrows). B) Detail of A showing rhizolith #4 in micrite matrix. C) Cross section of a macrorhizolith, ~1 cm in diameter, composed of alveolar septal structure, peloids (*p*) and a fine root rhizolith (*R*) with poorly preserved cellular structure. D) Rhizolith, ~5 mm in diameter, composed of dense outer micrite wall. E, F) Detail of D showing internal structure of the rhizolith made of several distinguishable root tubules (marked with \*). PPL /XPL pair.



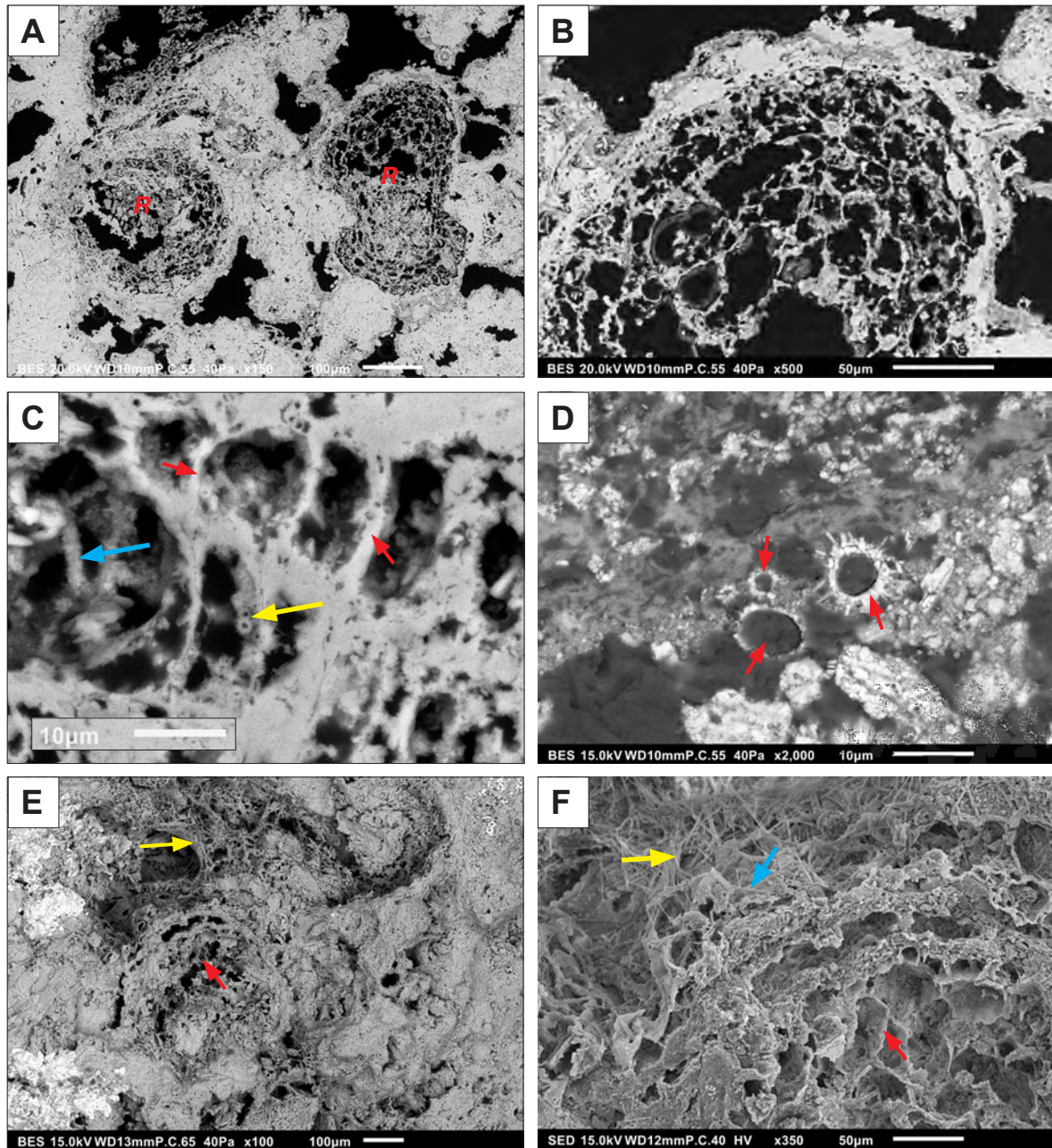


**Fig. 2.21.** BES SEM low-vacuum photomicrographs of a polished thin section of a composite rhizolith from San Salvador (A-D) and SED photomicrographs of a broken surface of fine root rhizolith (E-F). A) Irregular, disrupted cellular structure of fine root rhizolites (*R*); cell walls are coated or replaced by a thin layer of carbonate. B) Detail of A showing thin, disrupted cell walls, associated with tubular features (calcified filaments, i.e. probably mineralised fungal hyphae). C) Calcified cell walls (red arrows) and spherical features (yellow arrows; cf. Fig. 2.19C, D) or calcified fungal hyphae (blue arrow) in cross section (yellow arrows). D) Calcified fungal hyphae of different sizes in cross section (arrows). E, F) SED SEM photomicrographs of a fine root rhizolith with mineralised cell walls (red arrows). Outer surface is covered by calcite nanofibres (cyan arrow) and networks of needle fibre calcite (yellow arrows). San Salvador, Cockburn Town.

Classical macrorhizoliths, which are one of the most impressive geomorphic features in the Bahamian aeolianites, have not been investigated in detail in this study. Several samples, however, indicated that most of the larger rhizoliths, several mm to 1-2 cm in diameter, are displaying a compound fabric, composed of fine root micrite tubules (Figs. 2.20 and 2.21). The internal structure of composite rhizoliths is analogous to the fabric of crudely laminar rhizolites and indicates the same formation mechanism (Section 2.5.2).

#### *2.4.4 Mineralogy, elemental and stable isotope composition of laminar rhizolites*

XRD and FTIR analyses have been focused on the detection of possible Ca oxalate minerals, associated with tubular pores, observed in thin sections of rhizolite samples from Nicholls town and San Salvador. The XRD patterns have not revealed clear oxalate peaks but only predominantly calcite and minor amounts of aragonite (i.e. traces of host rock sediments), and trace amounts of hematite and smectitic clays. FTIR analyses of fine root rhizoliths confirmed only (low-Mg) calcite.

SEM EDS elemental analysis, performed on selected polished thin sections and slices, showed generally uniform, low-Mg carbonate composition of laminar rhizolites (<1.0 wt% Mg). Even intensively red-stained laminar samples (Fig. 2.13C) showed very low amounts of Si (<1.5 wt%) and Al (<1.2 wt%), whereas automatic detection EDS, obtained in approximately 1 mm<sup>2</sup> large areas, did not identify Fe and Mn or detected amounts close to detection limits (~0.1 wt%).

Stable isotope analysis was performed only on seven samples of laminar rhizolites from Nicholls Town locality and two samples from San Salvador (Appendix A2-5, Table A2-5.1). Results are plotted in Figure 2.22, together with data of comparative recent root-related carbonate accumulations from modern soils in SE Spain (Sella-Finestrat), Pleistocene calcretes from La Mora (E Spain), Quaternary rhizoliths of Morocco, and Paleogene rhizolites from Kras, Slovenia. Bahamian rhizolites from Nicholls Town show very uniform composition of  $\delta^{13}\text{C}$  (-10.0 to -9.4‰) and  $\delta^{18}\text{O}$  ranging from -3.6 to -2.3‰. The  $\delta^{13}\text{C}$  values of laminar rhizolites would correlate with carbonate precipitated in the predominance of C<sub>3</sub> plant-respired CO<sub>2</sub> or corresponding soil organic matter (see Chapter 3, section 3.5.3); the test analysis presented here, however, is too limited for any elaborate interpretation.

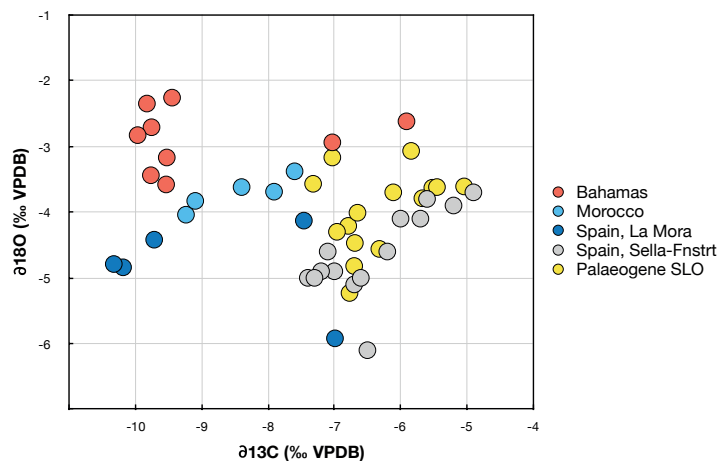


**Fig. 2.22.** Cross plot of  $\delta^{13}\text{C}$  and  $\delta^{18}\text{O}$  stable isotope results of selected Bahamian laminar rhizolites (red points) and comparative recent root-related carbonate accumulations from modern soils in SE Spain (Sella-Finestrat), Pleistocene calcretes from La Mora (E Spain), Quaternary of Morocco, and Paleogene rhizolites from Kras, Slovenia. See text for discussion.

## 2.5 Discussion

### 2.5.1 Laminar rhizolites: fine root-mat growth and carbonate mineralisation processes

The rhizogenic calcrete model of Wright et al. (1988, 1995) implies progressive  $\text{CaCO}_3$  mineralisation of laterally extensive, horizontal (surface-parallel) root mats within the soil profiles (also see comparison of laminar calcrete models in Wright 2007). Although not specifically highlighted, the mesoscale fabric and microfeatures of most published examples of laminar rhizogenic calcretes clearly show that they correspond to fine roots, mostly the finest root orders (i.e. secondary and tertiary root system of Zobel 2005), made up of roots <0.5 mm in diameter (Wright et al. 1988; Rossinsky and Wanless 1992; Fedoroff et al. 1994; Alonso-Zarza 1999; Alonso-Zarza and Jones 2007; Zhou and Chafetz 2009, 2012; Brlek et al. 2014; Li and Jones 2014; Liang and Jones 2015). In the model of root-mat calcrete growth (e.g. Fig. 1 of Wright et al. 1995), dense systems of (fine) roots spread along surfaces within the substrate, for example over weakly permeable massive calcrete (petrocalcic horizons) layers below the organic/mineral soil, and increase in thickness by progressive calcification of multiple, aggraded calcified root mats, few millimetres in thickness, producing beds (or domal buildups) of rhizolite, several 10s of centimetres thick. Another growth mechanism suggests that thicker rhizolite calcretes develop by progressive amalgamation of thin, millimetre- to centimetre-sized sheets or stringers, which may have used pre-existing fractures or discontinuities in the substrate (Wright et al. 1995, their Fig. 4). Identical

accretionary growth mechanism applies for laminar rhizolite forming in centimetre- to metre-sized cavities and voids, for example epikarst pits and solution pipes (Figs. 2.3, 2.6, 2.7, 2.10, 2.11B), and (sub)vertical fissures (Fig. 2.5).

Rot mats, i.e. dense systems of intertwined fine roots, develop as a consequence of limited space for root growth and proliferation, such as fractures, or along boundaries between materials of contrasting hydraulic properties, such as rock substrate and loose sediment/organic soil (Schwinning 2010, 2013; see examples of non-calcified modern root mats in Fig. Appendix A2-4). Hard rock substrate is of contradicting value to plant roots because it severely limits their spatial expansion, but on the other hand, the water stored in or on rock layers is protected from strong evaporative loss and can allow prolonged uptake by root systems. In both very narrow fissures in weathered bedrock and shallow soil-covered rock surfaces, such as topographies of karstic landscapes of carbonate islands, root systems tend to develop into nearly two-dimensional root fans or mats (Zwieniecki and Newton 1994, 1995, 1996; Poot et al. 2012; Hasenmueller et al. 2017). Formation of fine root systems in fissures and along soil-rock interfaces has been shown to represent a mechanism for the uptake of water stored in rocks. Schwinning (2020) has presented several different pathways of water transport between rock and root where rock-bound fine roots bypass the soil pathway but potentially increase the driving force for rock water release. The efficiency of the uptake of root water is supposedly further intensified via mycorrhizal hyphae, which are capable to penetrate in microfissures and extract water from microporosity, inaccessible to roots. However, root crowding on the surface of rocks might significantly reduce effective soil-to-root conductance. Schwinning (2020) has also noted a potential trade-off in the function of 'free' roots, embedded in soil, and rock-bound fine root mats. Development of free versus rock-bounded roots may represent a root allocation strategy, depending on climate and plant functional type.

Cemented carbonate rock surfaces, including calcrete hardpans or petrocalcic horizons at certain depth in the soil profile, appear to be highly restricting for both root growth (penetration) and water percolation. However, it has been shown that apparently highly cemented calcrete (plugged) horizons can exhibit very high water-holding capacity (Duniway et al 2007, 2010). It is thus tempting to correlate fine root mats as an ecohydrological strategy for the effective uptake of rock-stored water with accumulation of carbonate around fine roots, i.e. in their rhizosphere, as a mechanism for enhanced water-retention capacity in the critical interface between the rock surface and soil.



Rhizolites in karst cavities and fissures, shown in Section 2.4.1, indicate accretionary growth by aggrading laminae, resulting in progressive filling-up the space available for input of recyclable organic and mineral matter and for the root growth. If precipitation of calcium carbonate in fine-root mats may represent a short-term beneficial water-retention mechanism, precipitation and cementation creates irreversible long-term disadvantage due to reduction and final obliteration of the growth habitat, e.g. a karst soil pocket. However, progressive, episodic  $\text{CaCO}_3$  mineralisation of fine root mats may represent a trade-off strategy linked to specific vegetation types and probably to specific moisture-driven response of root systems.

Calcium carbonate cementation of the rhizosphere has been frequently reported as one of the fundamental mechanisms of biogenic calcrete formation (Jaillard 1982; Wright et al. 1988; Alonso-Zarza 1999; Košir 2004; Lambers et al. 2009), where “coalescence of calcite crystals around neighbouring roots result in continuous calcrete formation” (Hinsinger 2013). However, cementation of the active rhizosphere with  $\text{CaCO}_3$  appears to be at least undesirable for the efficient nutrient and water uptake by absorptive fine roots if not largely detrimental for functioning of the part of the root system involved in resource acquisition. Therefore, a fundamental question arises if the precipitation of  $\text{CaCO}_3$  around fine roots corresponds to plant-induced biomineralisation in the active rhizosphere (around live roots) or to processes of (mostly microbially-induced) mineralisation related to turnover and decay of fine roots, i.e. the relic rhizosphere – the part of soil left altered after the death of roots that modified it (York et al. 2016).

Exquisitely preserved anatomical features of fine roots, such as an undeformed epidermis and root hairs, shown in Figures 2.15 and 2.16, indisputably correspond to parts of absorptive fine roots, which are most active in nutrient and water acquisition. Consequently, these features could be simply taken as an evidence of a direct involvement of fine roots in calcrete formation, especially when considering a short life span of these fine root tissues (Fig. 2.12). However, although the root-hair covered (maturation) zone on a root is short because of their short life, the root hair walls can remain for quite long time after the root hair cell has ceased to function (Tinker and Nye 2000). Furthermore, it is often not readily apparent in fine roots whether an epidermal cell is dead or alive because the walls are thickened (suberised) and the outer walls are arched, mechanically strong, and they typically do not collapse when they die (Meyer and Peterson 2013).

Many examples of fine roots shown in Section 2.4 (Figs. 2.15-2.17) actually clearly indicate that the roots with well-preserved epidermis, exodermis and root hairs were largely

dead and undergoing decomposition. This is evidenced by partly collapsed and deformed overall cylindrical shape, apparently fully decayed cortex and displaced elements of vascular cylinder, and particularly by numerous faecal pellets (coprolites) inside the decaying roots (Fig. 2.17). Exceptional preservation of fine root tissues in the studied rhizolite calcretes was probably enhanced due to impregnation of tissues by tannin. Deposits of condensed tannin are the main cause of root browning, a process characteristic particularly of fine roots of trees, which become brown as the age (McKenzie and Peterson 1995a, b; Peterson et al. 1999; Enstone et al. 2001; Wells and Eissenstat 2002; Kumar et al. 2007). Although still preserving external morphology, brown roots largely lose their absorptive functions and are characterised by progressive senescence and death of cortical cell and the epidermis.

Although there are many published reports of rhizoliths (calcified roots) with (partially) preserved organic root tissues (e.g. Perkins 1977; McLaren 1995; Semeniuk 2010; Alonso-Zarza 2018), clear evidence of  $\text{CaCO}_3$  precipitation in the active rhizosphere around probably live roots or roots in early stages of decay is lacking. Appendix 2-3 shows fine roots from modern soils in SE Spain and W Morocco in various stages of decay. None of the fine roots with preserved epidermis and root hairs, but collapsed cortex and vascular system, show any considerable deposits of carbonate on their surface (Fig. A2-3.01). Some of the fine roots with intact root hairs are partly covered with open meshwork of needle fibre calcite (NFC) (Fig. A2-3.03.C-F). Decayed roots and their surrounding soil area are composed of highly porous network of NFC, calcite nanofibres and calcified filaments (i.e. Ca oxalate-mineralised fungal hyphae). The microfabric, dominated by NFC, nanofibres and Ca-oxalates, probably rapidly transformed into Ca carbonate, is usually considered representative of microenvironments influenced by fungi. Presumably, most of the microcrystalline  $\text{CaCO}_3$  and primary Ca oxalate around fine roots corresponds to fungal exoenzymatic metabolic processes, probably largely linked to oxalic acid excretion, particularly in decomposition of complex substrates such as root cellulose and lignin (Dutton and Evans 1996; Verrecchia 2000; Finlay 2006) in highly alkaline and Ca-rich microenvironments.

### 2.5.2 Are macrorrhizoliths mostly just coarse root-shaped rhizolite?

Klappa (1980b) defined the term *rhizolite* for “a rock showing structural, textural and fabric details determined largely by the activity, or former activity, of plant roots.” He did not,



however, define the size and shape of rhizolite. If a several millimetres thick laminar crust can be regarded a rhizolite, why would not the same apply for a coarse macrorhizolith, centimetres in diameter, which is largely or entirely composed of textures, clearly attributable to carbonate precipitation around fine root systems?

Although 'classical' rhizoliths have not been investigated in detail in this study, a majority of examined samples showed a complex fabric of macrorhizolith structures (Figs. 2.20, 2.21, Fig. A2-2.01), composed largely of mineralised fine roots. Formation of composite rhizoliths is in accord with well-known strategy of (fine) root proliferation in decaying roots and old root channels (Dell et al. 1983; McKee 2001). Such 'secondary' root exploitation is associated with nutrient poor substrates and probably represents a nutrient conservation and recycling mechanism in oligotrophic soil settings.

Rhizoliths, formed in tubular voids of larger diameter, left for example after decay of coarse tap roots, can exhibit more or less distinctive concentric lamination, indicating centripetal accretionary growth (see comparative material from W Morocco shown in Figs. A2-2.01A-L). Concentric lamination and accretionary deposition mechanism in larger root tubules is thus analogous to laminar growth on surfaces and particularly along the walls of larger dissolutional cavities such as solution pipes (Fig. 2.3; see also Figs. A2-4.01D, E as an example of fine roots, preferentially extending along the wall of a soil-filled karstic void). Developing composite rhizoliths also show patterns, observed in (non-mineralised) decaying roots with successive generations of fine roots growing inside increasingly smaller root channels (Fig. A2-2.01D; McKee 2001).

It has to be emphasised that not all macrorhizoliths are necessarily produced by carbonate precipitation around fine root systems, proliferating secondarily in coarse root pores. Classical rhizolith (root traces) types like root moulds, tubules, casts and certain forms of rhizcretions (Klappa 1980b) definitely provide unambiguous morphological evidence for former plant root systems, however, formation or preservation of such coarse rhizoliths typically do not imply any biological activity of plants, except their existence (see e.g. Gregory et al. 2004). Correspondingly, speaking of rhizosphere in association with formation of coarse root rhizoliths is to a large extent inconsequential, since the zone of soil around coarse roots – with their distributive and mechanical support functions – is not substantially influenced by plant-driven biochemical processes.

### *2.5.3 Calcrete-palaeokarst associations: geobiological processes, climatic factors and process rates*

Calcretes and palaeokarst phenomena are two groups of major macroscopic products of meteoric carbonate diagenesis. Although generally considered to represent contrasting styles of diagenetic processes in the vadose zone (e.g. James and Choquette 1984; Esteban and Klappa 1983; McKee and Ward 1983; Wright 1988; James and Jones 2016), ancient (epi)karst features and calcretes are often associated in carbonate depositional successions (Wright 1988; Vanstone 1991, 1998; Otoničar 2007, 2021). Modern surface and shallow subsurface karst on carbonate rocks as well as the buried ancient karst systems are characterised by dissolutional features generally developed under prevailing humid climatic conditions and predominance of dissolutional weathering. In contrast, calcretes are typically considered as an indicator of 'arid' (semiarid to subhumid) climate, characterised by precipitation of secondary calcium carbonate in soils or within shallow, near surface vadose diagenetic environment. This palaeoclimatic generalisation has been often used in the interpretation of palaeoexposure surfaces in stratigraphic sequences. However, as shown in the previous sections and published work, many calcretes form by predominance of biologically induced processes, particularly precipitation of calcium carbonate within the root systems of higher plants and associated microorganisms in soils. In its broadest definition, the depth of soil is defined by the rooting depth of plants (Richter and Markewitz 1995), and this zone generally overlaps with the epikarst. Most of calcretes, associated with karst, reflect specific biological processes involved in the precipitation of secondary carbonates rather than specific climatic conditions. Furthermore, occurrence of calcretes within a zone of prevailing dissolutional regime perhaps seem less contradictory when we compare the rates of carbonate dissolution in karst and estimated precipitation rates for biogenic calcretes. Solutional denudation of carbonate terrains has been relatively well assessed both on global and local scales (Ford and Williams 2007; Palmer 1991, 2007) whereas calcrete accretion is rather poorly understood and is based on few studies of (finely) laminar forms (e.g. Robbin and Stipp 1979) and unpublished reports of age determinations of root-related calcretes (root-rock) in South Florida (Perkins 1997).

Figure 2.23 shows comparison of published estimates of karst denudation rates (Ford and Williams 2007; Palmer 1991) and estimated accumulation rates of laminar calcretes, including a rough estimate of short-term accretionary potential of rhizolites, formed by

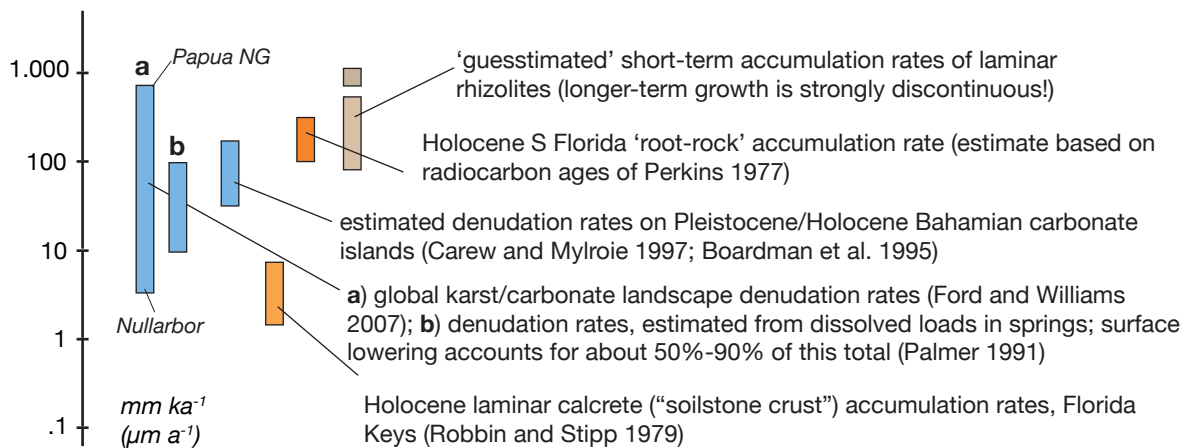


**Fig. 2.23.** Comparison of published estimates of karst denudation rates and estimated accumulation rates of laminar calcretes, including rough estimate of short-term accretionary potential of rhizolites, formed by progressive mineralisation of short-lived fine root systems (i.e. growth, turnover, and decay of fine-root mats).

progressive mineralisation of short-lived fine root systems (i.e. growth, turnover, and decay of fine-root mats). The figure shows that accumulation of  $\text{CaCO}_3$  in calcretes can be a relatively rapid process, and, operating across a wide climatic range, it can overlap with typical karst geomorphic settings and karst denudation rates.

In a considerable simplification, co-occurrence of karst dissolutional topography and calcretes in carbonate successions can be considered analogous to palaeokarst clastic and chemical sediments (speleothems), deposited in subsurface cavities and depressions. Despite formed in an overall erosional climatic regime and landscape setting, in which large portions of the rock record are removed, such sediments can preserve portions of the stratigraphic record that might have been removed by subsequent surface erosion (Plotnick et al. 2015).

Presented examples of rhizolite calcretes from the Bahamas have not been dated and might have formed during periods of considerably different climate within a considerably long time span between MIS 5e (~115 ka) and present. However, smaller-scale carbonate accumulations, associated with live fine root systems observed e.g. in aeolian carbonate dunes on San Salvador, indicate that root-related calcretes actively form under the current, relatively humid climate which is evidently suitable for the ongoing karst denudation (e.g. Boardman et al. 1995). In general, the climatic condition in the Bahamian archipelago during late Pleistocene glacial periods was probably characterised by higher rainfall rates and intensive events (and lower temperatures), and thus prone to intensive carbonate dissolution (Boardman et al. 1995).



## 2.6 Conclusions

The case study presented in Chapter 2 has been based on examples of Pleistocene and Holocene root-related calcretes from the Bahamas. Rhizolite calcretes from the islands of North Andros, San Salvador and New Providence have shown a variety of microfabric, attributable to fine root systems, including remains of with exquisitely preserved anatomical details of fine roots tissues.

Laminar rhizolites of young carbonates of the Bahamas appear as archetypal laminar calcrete crusts and are associated with karstic dissolutional topography and rock fissures. All rhizolite forms are characterised by similar fabric, composed of fine root cylindrical features (pores) and massive and laminar micrite. Laminated structure consists of sub-millimetric- to several millimetres thick, discrete, usually laterally discontinuous layers, commonly exhibiting discontinuities in accretion and truncated laminae, marking erosional micro-unconformities.

Petrographic observation of rhizolites has shown that fine root anatomical details are commonly better discernible in resin-impregnated, polished slabs than in standard or even ultrathin thin sections. Similarly, best SEM results were obtained in polished thin sections, observed in backscattered electron detection mode.

Microstructural examination has not shown any evidence of intracellular calcification in fine roots (see Chapter 3). Anatomical details of fine roots in laminar rhizolites were probably preserved due to organic pigmentation, most probably by condensed tannin.

Studied rhizolite calcretes can be regarded as typical examples of rhizogenic calcretes, formed by progressive mineralisation of thin, aggraded fine root mats. Calcification processes, however, do not seem to be controlled by roots as suggested by existing models. Disrupted fine root epidermal tissues, displaced vascular cylinders and faecal pellets (coprolites) within the roots indicate that carbonate did not precipitate in active rhizosphere but probably largely formed by microbially induced processes during decay of fine root remains.

## Chapter 3: Intracellular calcification in plant roots

### 3.1 Introduction

Intracellular calcium carbonate biomineralisation in fine roots has been well known for more than 30 years, since the classic studies of Jaillard et al. (1991) of modern calcareous soils in France. Although the process represents one of the most impressive examples of biomineralisation in present and past terrestrial ecosystems, intracellular calcium carbonate formation in roots has received disproportionately less attention than the well-documented precipitation of calcium oxalate in plant tissues (Franceschi and Horner 1980; Smith 1982; Arnott 1982; Franceschi and Loewus 1995; Horner and Wagner 1995; Webb 1999; Monje and Baran 2002; Nakata 2003; Franceschi and Nakata 2005; Raven and Giordano 2009; Raven and Knoll 2010; Bauer et al. 2011; He et al. 2012, 2014; Pylro et al 2013; Karabourniotis et al. 2020).

Most of the knowledge about the intracellular  $\text{CaCO}_3$  biomineralisation in plant roots is the result of the pioneering work of Jaillard and co-authors in the 1980s and their research in the early 1990s (Jaillard 1982, 1983, 1984, 1985, 1987a, 1987b, 1992; Jaillard and Callot 1987; Jaillard et al. 1991; Jaillard and Hinsinger 1993). Surprisingly, although repeatedly presented in highly-cited reviews (e.g. Lucas 2001; Lambers et al. 2009) as “one of the most dramatic cases of biogenic mineral formation in terrestrial ecosystems”, intracellularly calcified roots have received relatively limited scientific interest. Following publications of Jaillard, calcified roots have been identified as such and reported from soils and palaeosols in different environmental and geological settings, however, most of the papers largely regarded them as one of the diagnostic soil features or an example of (biogenic) soil carbonate, potentially useful for palaeoenvironmental or palaeoclimatic analysis (Kaemmerer and Revel 1991, 1996; Kaemmerer et al. 1991; Alonso-Zarza et al. 1998; Khoklova et al. 2001; 2016; Boguckij et al. 2006; Khormali et al. 2006; Wang & Greenberg 2007; Łacka et al. 2009; Bradák et al. 2014; Barta 2014; Luo et al. 2020, amongst others). Most of the mentioned case studies have neither investigated nor thoroughly discussed the mechanisms of carbonate biomineralisation in plant roots and their implications. Interestingly, even in modern soil micromorphology textbooks and handbooks,

intracellularly calcified roots are only marginally mentioned and merely interpreted as “petrification or impregnation of root cells by calcite” (Durand et al. 2010, 2018), “calcite crystals, pseudomorphic after root tissues” (Stoops 2021), or a micromorphological example of a root preservation mode, e.g. where “[calcite crystal] replaces the entire cell, fossilizing the root tissue” (Verrecchia and Trombino 2021).

The most stimulating input came from the work of McConnaughey and co-authors (McConnaughey and Whelan 1997, Cohen and McConnaughey 2003) who explored calcification in plant roots as a nutrient acquiring mechanism in comparison to carbonate biomineralisation in reef corals, that has been regarded as their adaptation to thrive in some of the most nutrient deficient regions of the planet. Physiology of  $\text{CaCO}_3$  biomineralisation in plant roots has been invoked by Košir (2004) as a possible explanation for the origin of *Microcodium* (Chapter 5).

A broad analogy can be drawn between carbonate production modes in the marine ecosystems and depositional environments and the terrestrial soil carbonates. The concept of marine carbonate factories (James 1979; Schlager 2000, 2005; Pomar 2020; Reijmer 2021, amongst others) has been based on three basic modes of carbonate precipitation, i.e. abiotic, biologically induced and/or influenced (generally microbial), and biologically controlled (generally skeletal) (Schlager 2000; also see Dupraz et al. 2009). Similarly, soil carbonates can form almost entirely through inorganic processes, in processes induced by soil microbial activity and associated organic matter, or through biologically controlled mineralisation processes (e.g. Lal et al. 2000; Alonso-Zarza and Wright 2010a). In comparison to coral reefs, which are probably the most impressive biomineralisation product on Earth and one of the biosphere’s largest carbon reservoirs (Cohen and McConnaughey 2003), soil carbonates represent much smaller carbon pool, although containing about double as much carbon as the atmosphere and a similar amount as soil organic carbon pool (Fig. 1.2 in Chapter 1; Eswaran et al. 2000, Lal 2004; Mackenzie and Lerman 2006). In this context, biomineralisation of corals and plant roots, both closely associated with nutrient deficient environments, may reflect an analogous adaptation strategy of massive and rapid accumulation of calcium carbonate as a mechanism and a ‘collateral product’ of acquisition of essential elements of limited availability, such as phosphorous and iron (McConnaughey and Whelan 1997; Pomar 2020).

The aim of this chapter is to investigate processes and products of intracellular calcium carbonate mineralisation in plant roots, including their ecophysiology and geological



significance. The research has been performed on original and previously unexplored material from the Mediterranean environments of southeastern Spain and has included detailed petrographic and micromorphological analysis of intracellularly calcified roots, integrated with mineralogical, elemental and stable isotope analysis of carbon and oxygen. Formation of intracellularly calcified roots is discussed in the framework of plant functional traits. The complementary chapter (Chapter 4) presents novel results of DNA molecular identification of calcifying plants from natural environments. A comparative analysis of intracellularly calcified roots from modern soils and ancient *Microcodium* structures is given and discussed in Chapter 5.

### 3.1.1. Terminological and conceptual compendium

Jaillard (1987a) and Jaillard et al. (1991) demonstrated that older soil science literature contained reports on features that were almost certainly calcified roots. Wieder and Yaalon (1974) presented analogous forms and referred to them as “calcans in voids”, whereas other authors mentioned “pseudomycéliums en forme de vermicelles”, “pseudomorphoses de racines”, “calcites intercalaires” (Jaillard et al. 1991). Disintegrated calcified roots have been termed cytomorphic calcite (Durand et al. 2018). A specific and complex, but not widely used terminology has been proposed for calcified roots by Herrero and co-authors (Herrero and Porta 1987, 2000; Porta and Herrero 1988; Herrero et al. 1992; Artieda and Herrero 2003). In their concept, a calcified root as a whole is called ‘*quera*’, while derivations of the term denote associated features (*quesparite* for equigranular sparitic crystals; *quedecal* for calcite-depleted hypocoating and quasioating, and *quevoids* for soil microchannels, left after calcified roots; for a recent example see e.g. Plata et al. 2021).

In their classification of rhizogenic calcretes, Wright et al. (1995) discriminated intracellular calcification as a specific type of carbonate formation in soils, which is markedly distinguishable from root-related processes operating in the rhizosphere *sensu stricto*, that is outside and not including the root itself (in extracellular or, better, extrarhizal soil environment). The present work follows this concept, and the adjective ‘intracellular’ is attempted to be used as consistently as possible to emphasise and differentiate calcium carbonate biomineralisation within the living root cells from other processes and environments. For simplification, an acronym *iCR*, standing for intracellularly calcified root(s), is used throughout the text.

It is perhaps also worth noting the wide and rather inconsistent use of the term *calcification*. In ocean sciences (Tyrell and Young 2009), calcification includes the synthesis of solid calcium carbonate from dissolved substances, whether passively by spontaneous formation of crystals in a supersaturated solution (inorganic calcification) or actively through the intervention of organisms (biocalcification). Calcification, as related to soil, soil processes, and palaeosols (e.g. Retallack 2021), generally pertains to the accumulation of calcium and magnesium carbonates in the subsurface horizons of soils. In life sciences and biological systems, until the early 1980s, calcification has been considered as a broad synonym of biomineralisation (Lowenstam 1981; Lowenstam and Weiner 1989; Sigel et al. 2008), reflecting the predominance of biologically formed calcium-containing minerals and the fact that calcium is the ‘cation of choice’ for most organisms (Weiner and Dove 2003) because it fulfils many fundamental functions in cell metabolism and regulation (Simkiss and Wilbur 1989; Berridge et al. 1998; Skinner and Jahren 2005; Skinner and Ehrlich 2014; Carafoli and Krebs 2016; Thor 2019). Importantly, the term calcification is not limited to carbonates but also refers to calcium-containing phosphate, oxalate and other mineral types!

Biom mineralisation processes are traditionally divided into two fundamentally different groups based upon degree of biological involvement in mineral formation (Lowenstam and Weiner 1989; Mann 2001; Weiner and Dove 2003; Berman 2008). In *biologically induced mineralisation*, precipitation of minerals occurs as a result of interactions between biological activity and the environment. In *biologically controlled mineralisation*, the organisms use cellular activities to direct the nucleation, growth, morphology and final location of the deposited minerals (Weiner and Dove 2003). Biologically controlled mineralisation occurs extra-, inter- or intracellularly. In the latter process, which includes intracellularly calcified roots, mineralisation takes place within specialised vesicles or vacuoles that direct the nucleation and growth of minerals within the cells. Accordingly, intracellular calcification of roots, in exact terms, refers to biologically controlled intracellular  $\text{CaCO}_3$  mineralisation.

### 3.2 Geological and environmental setting, soils and vegetation

Research on intracellularly calcified roots presented in this study was carried out on material from the area located in the north of the Province of Alicante (Alacant) on the eastern-southeastern Mediterranean coastal region of Spain (Fig. 3.1A). Impressive remains of intracellularly calcified roots have been initially discovered in fresh road-cut exposures E of the town of Sella (Fig. 3.1B) in a pilot exploration performed in the summer of 2002: the following field campaigns confirmed almost ubiquitous presence of iCRs in soils and weathered calcareous substrates throughout the study area. Fieldwork was performed in a broader mountainous terrain of the Serra d'Aitana (Sierra Aitana) mountain range and its surroundings between Villajoyosa and Benidorm (Costa Blanca) on the Mediterranean coast, and the area between Alcoy and Castalla (Fig. 3.1B and Fig. A3-1.1).

The study area is a part of the External Betics tectonic unit (Cordillera Bética), specifically, its external Prebetic Zone (Prebético), composed of Triassic to Miocene sedimentary units, deformed by the Alpine Orogeny (Gibbons & Moreno 2002; Vera 2004). The main part of the study area around Serra d'Aitana is characterised by series of folds and thrusts (Marco Molina et al. 2004), composed predominantly of Upper Cretaceous and Palaeogene carbonate and siliciclastic sequences (Fig. A3-2.01; Colodrón et al. 1981; Hernández Samaniego et al. 1993; Leret Verdú and Lendínez González 1978). Mesozoic and Cainozoic sedimentary units are in a relatively minor extent covered with Quaternary alluvial and colluvial sediments. In the western part of the study area (Ibi locality; Fig. 3.1B), Quaternary deposits (gravels, sands and muddy sediments) are widely distributed, especially in covering the depressions of Neogene sediments (Martínez del Olmo et al. 1978). Larger part of the study area corresponds to the drainage basin of the Amadorio River (Riu Amadorio; Fig. A3-1.02).

The area shows typical physical aspects of the Mediterranean mountain landscapes (Melis and Loddo 2012). The landscape and vegetation of the valleys of Serra d'Aitana (Marina Baixa) have been strongly influenced by agricultural expansion during the Modern times, most remarkably by reshaping of the natural terrain by 'terraced landscaping', forestry, followed by cessation of farming activities and re-colonisation of abandoned crop fields, extensive forest fires – particularly during the last several decades, and systematic reforestation (Giménez-Font 2013; Giménez-Font and Marco Molina 2017).



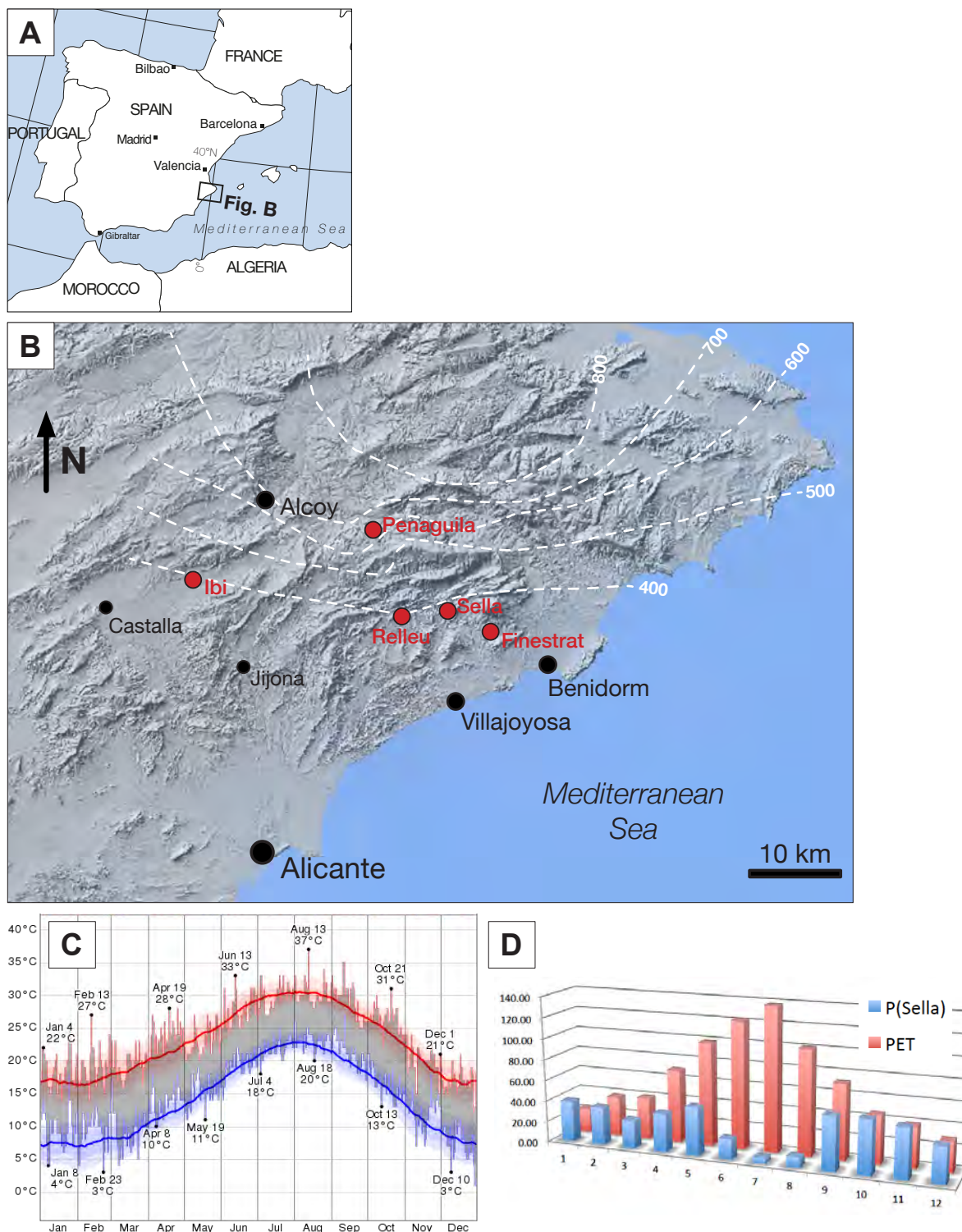


**Figure 3.1.** A) Map of the Iberian Peninsula with position of the map in Fig. B. B) Relief map of a part of the Alicante region showing main localities and mean annual rainfall lines. Precipitation data (average P in mm/yr) adapted from Calvo-Cases et al. (2003). All the studied localities (red) belong to the Marina Baja and Alcoià districts (Comarca de la Marina Baja and Comarca de l’Alcoià) in the Province of Alicante (Alacant) of the Valencian Community (Comunitat/Comunidad Valenciana). C) Daily temperature ranges and average minimum (blue) and maximum (red) values, Benidorm (AEMET, 2015). D) Average monthly precipitation (P) and potential evapotranspiration (PET) data (in mm) for the Sella weather station (data from Hornero Díaz et al. 2009 and AEMET, 2015). Also see Appendix A3-2.

All the studied sites were located on calcareous bedrock or loose carbonate parent materials, characterised by soil types of leptosols, lithic leptosols (rendzinas) and regosols (Boix-Fayos et al. 2001; Calvo-Cases et al. 2003), locally with substantial accumulation of secondary carbonates forming calcisols, petric calcisols, and calcic luvisols (IUSS Working Group WRB 2015).

Climate of the region is typically Mediterranean, characterised by mild wet winters and warm dry summers. The territory between the Costa Blanca coastal zone and the Valley of Guadalest on the northern side of the study area (Fig. A3-1.01), roughly corresponding to Marina Baixa, is represented by a steep gradient from semiarid to sub-humid Mediterranean and, partly, continental Mediterranean climate conditions (Calvo-Cases et al. 2003; Ortega et al. 2016). Figure 3.1 shows mean annual precipitation (MAP) lines of the region (Calvo-Cases et al. 2003) with marked study sites located within <400 and ~600 mm MAP range (Fig. 3.1B), as well as the temperature variation in Benidorm (AEMET 2015; Fig. 3.1C), and average monthly precipitation (P) and potential evaporation (PET) data for the Sella weather station (Hornero Díaz et al. 2009). This weather station can be considered as representative for the most of the studied localities. The P-PET plot (Fig. 3.1D) indicates a pronounced seasonal moisture regime with a strong moisture deficit from late spring to early autumn, and generally more humid conditions from October to February. It is important to note considerable rainfall and drought anomalies (Appendix A3-2, AEMET maps; Cerdà 1997) representing deviations from general climate patterns in the region, which critically affect the vegetation through (changes in) soil infiltration rates, evaporation and soil moisture distribution, and, consequentially, root growth and soil biogeochemical functioning (Austin et al. 2004; Collins and Bras 2007; Bao et al. 2014; Robbins and Dinneney 2015, 2018).

Predominantly calcareous lithologies, topographic relief and the climate critically determine terrestrial ecosystems of the studied area. Principal ecosystems are maquis – vegetation biomes dominated by evergreen sclerophyllous shrubs and trees, and garrigue – low growing secondary evergreen shrublands (Rundel and Cowling 2013; Soriano and Costa 2017; Alcaraz 2017).

One of the principal constituents of the vegetation in the study area is the Aleppo pine (*Pinus halepensis* Mill.), one of the most important and widely distributed conifers in the Mediterranean basin because of its ability to adapt to a wide range of environmental conditions (Quézel 2000). The surface area covered by this species has substantially increased as a consequence of spontaneous colonisation of abandoned lands as well as its

widespread use in plantation. As a pioneer drought-resistant species it has been extensively planted throughout the Western Mediterranean (Barbéro et al. 1998; Quézel 2000); in the Iberian Peninsula alone, almost a half of the current *P. halepensis* forests derives from afforestations (Maestre et al. 2003), whereas in the semiarid sector of the province of Alicante, *P. halepensis* is an absolutely predominant species in forests and as individual trees in open areas (Maestre and Cortina 2004), otherwise dominated by sclerophyllous woody shrubs, herbaceous perennials and grasses. Wild shrub ecosystems occur on soils with a low degree of mineral nutrients due to the low weathering regime of calcareous parent rocks, where in the topsoil the most significant sources of nutrients are litter decomposition and external inputs (Martínez et al. 1998). As a result of low-nutrient substrate and low and seasonally limited water availability, both herbaceous and woody perennials tend to have highly developed root systems (Martinez et al. 2002), often disproportionally large in comparison with the aboveground plant parts (Fig. 4.7 in Chapter 4). The predominant plant community type in the study area corresponds to *Quercus cocciferae-lentiscetum* and *Rosmarino-Ericion* associations (Crespo and Serra 1993; Boix-Fayos et al. 2001), characterised by *Quercus coccifera*, *Salvia rosmarinus* (= *Rosmarinus officinalis*), *Thymus vulgaris*, *Erica multiflora*, *Brachypodium retusum*, *Stipa* spp., *Festuca* spp., and different genera of Fabaceae (Leguminosae), i.e. *Hedysarum*, *Onobrychis*, *Ononis*, *Astragalus* etc. (HVMO 2021; Crespo and Serra 1993, p. 44; also see Chapter 4).

### 3.2.1 Localities

The main study locations, named after the nearest towns, are shown in Figures 3.1 and A3-1.01, whereas the sampling site coordinates are listed in Table A3-1.1.

#### *Sella*

The locality includes several outcrops and sampling points located along forest roads in the Barranc de l'Arc ravine, ENE of the Town of Sella, and along local roads S of the town (Figs. 3.2 and 3.3). Excavation and sampling sites were situated on NNW slopes in relatively fresh road cuts with exposed 1-3 m thick surficial layer of generally strongly weathered zone of Oligocene marl, marly limestone and calcarenite (Colodrón et al. 1981; Fig. A3-2.01B), locally overlain by Quaternary gravelly colluvial sediments. The locality yielded some of the best-preserved root systems of iCRs, formed along vertical and horizontal fissures in calcareous loamy substrate, and living roots in freshly excavated pits. Wild vegetation of



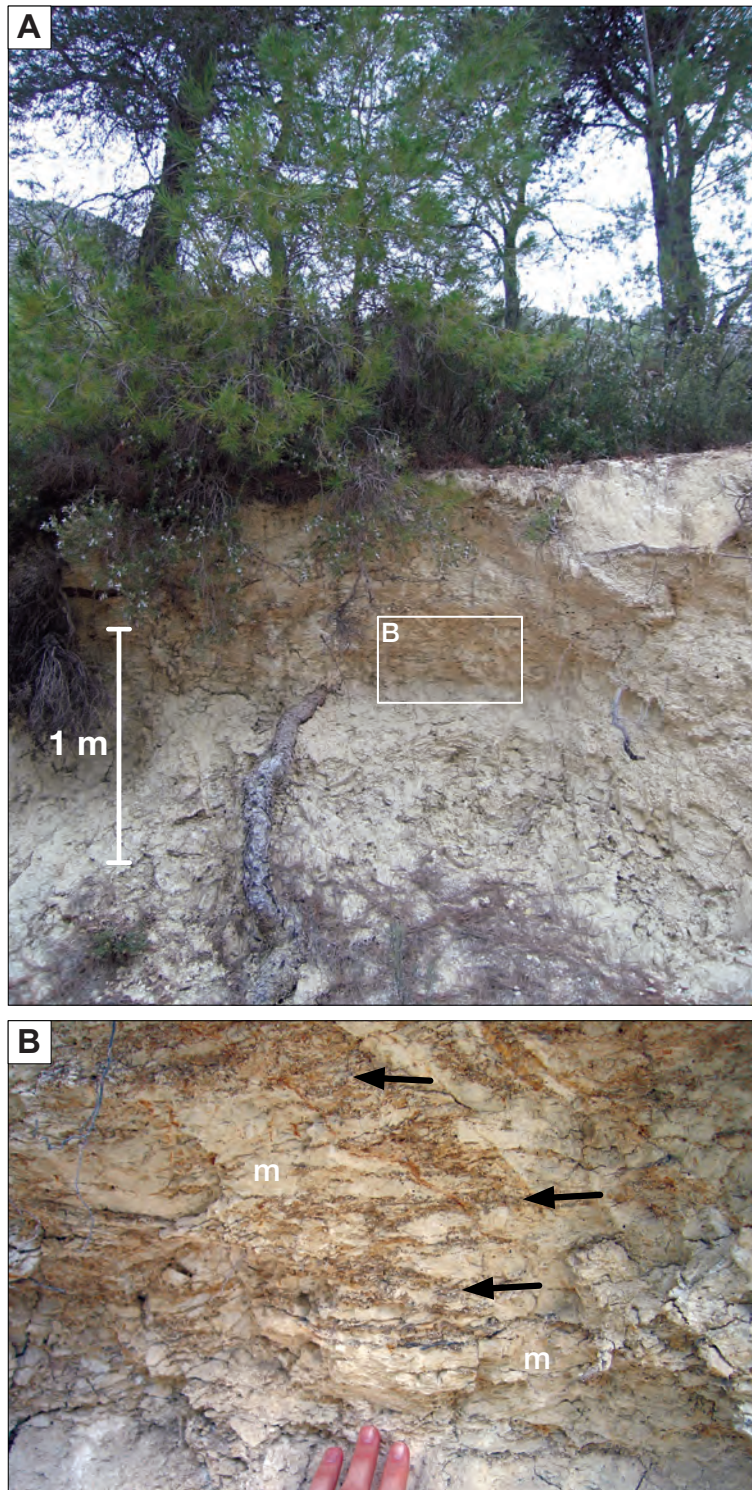


**Figure 3.2.** Soil profile with iCRs, locality Sella (site T14-463, Barranc de l'Arc ravine). See Table A3-1.1 and maps in Figs. A3-1.1 and A3-1.2. A) Weathered marl with a mixed vegetation, typical of 'pine wood and shrubland with rosemary and thyme garrigue' habitats (HVMO 2021). B) Close-up view of an area approx. 0.5-1 m below the surface showing marl (m) with horizontally-oriented layers (arrows) composed of iCR in brown clayey matrix.

the Sella sites is dominated by sparse *P. halepensis* canopy and an understorey, composed of patches of shrubs of *Salvia rosmarinus*, multiple representatives of Hedysareae, *Thymus* spp., and *Stipa* grasses (Fig. 3.3C). Abandoned terraced fields in the area also contain relicts of former cultivated species, e.g. almond (*Prunus amygdalus*) and olive trees (*Olea europaea*). Aggregates of iCRs have been observed from depth of 20-25 cm down to >7 m



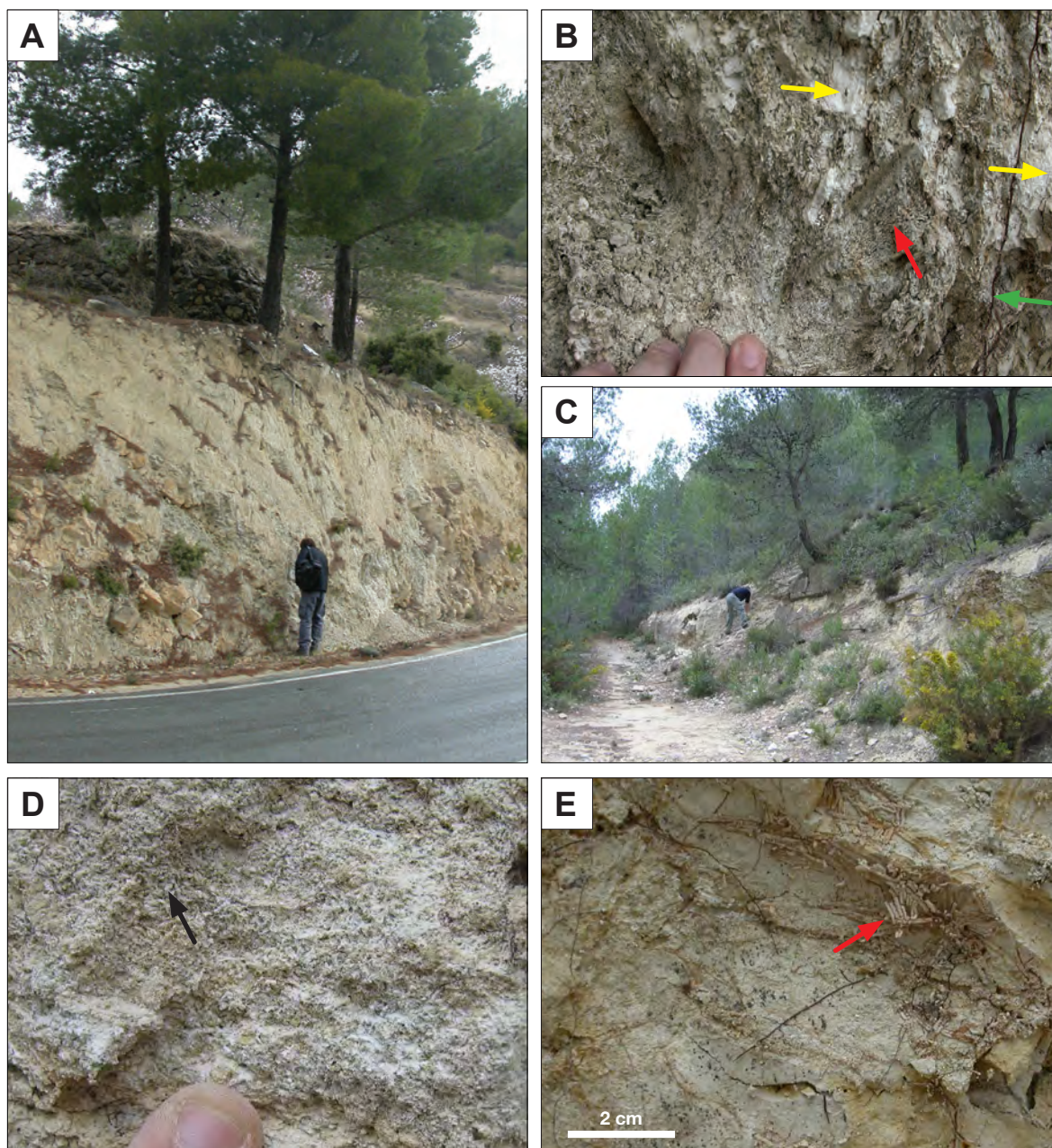


**Figure 3.3.** Sella locality. See maps in Figs. A3-1.1 and A3-1.2.

A) Road-cut in weathered marl with sandstone beds, S of the Sella village. The area is planted with *Pinus halepensis* and almonds (*Prunus amygdalus*). Recent coarse woody roots and iCRs occur throughout the profile to a depth of >7 m below the surface. B) Close up view, approx. 5 m below the surface: relicts of marl (yellow arrows) in a soil mass dominated by iCRs in clayey matrix. Red arrow indicates 'zebra' pattern layered structure, composed of iCRs and clayey interlayers. Green arrow points to a coarse active root. C) Site T14-463 (Barranc de l'Arc ravine; see Table A3-1.1): characteristic vegetation on a slope of ?Oligocene marls, sandstones and limestones, composed of *Pinus halepensis*, xerophyte shrubs and grasses. D) Soil, approx. 20 cm below the surface, composed entirely of interlaced iCR aggregates (arrow). See also Fig. A3-4.01B. E) Branching calcified root (arrow) from a vertical fissure in marl with partly preserved organic parts (vascular cylinders) which keep the root branches together. The root is embedded in a thin clayey layer (i.e. decalcified cylinder). Cf. Figs. 3.8C and 3.11.

below the surface (Fig. 3.3A), i.e. throughout the observed rooting depth range of present vegetation.

### *Finestrat*

Smaller outcrops are located along a paved road, cutting across Quaternary colluvial deposits on SW slopes of the Puig Campana Mountain (Fig. 3.4; Fig. A3-2.01B; Colodrón et al. 1981). The sediments are mostly composed of blocks and cobbles of limestone, embedded in finer grained matrix. Locally, centimetres to multi-decimetre sized pockets of matrix are composed almost exclusively of iCRs, forming layered masses between the larger limestone clasts (Figs. 3.4B, C, D, F). Accumulations of iCRs in the studied outcrops appeared to be relic: no iCRs have been observed associated with living (active) root systems. Sparse present vegetation consists of low shrubs, herbaceous species, grasses, and solitary trees of *P. halepensis* and *Quercus* spp.

### *Finestrat-Sella*

Several sites have been studied along an unpaved forest road between the Barranc de l'Arc ravine and NNW foot slope of the Puig Campana Mountain (Fig. 3.5). Old and largely overgrown road cuts in the area (Figs. 3.5A, 4.1B) were dug in Cretaceous and Palaeogene carbonate and clastic successions (Colodrón et al. 1981), predominantly marls (Fig. A3-2.01B). The area is partly covered by *P. halepensis* forest and mostly with dense mixed understorey of *Erica* sp., *Salvia rosmarinus*, grasses and diverse vegetation of herbaceous legume species. Smaller excavation pits at sites along the road(s) between Finestrat and Sella have yielded numerous fresh, living calcified roots, which have been applied for the DNA barcoding (Chapter 4).

### *Relleu*

Several sites were located in relatively fresh roadside outcrops of Upper Cretaceous (Coniacian to Maastrichtian) thin-bedded (platy) limestone, marly limestone and marl with globotruncanids (Colodrón et al. 1981). Intracellularly calcified roots were found along bedding plane partings from approximately 25 cm below the surface to the bottom of observable, 1-2 m high outcrops (Fig. 3.6A-C). No larger excavations were carried out at this locality. Sampled remains of iCRs from the Relleu locality have not been associated with well-preserved organic root tissues, except for smaller fragments of degraded vascular cylinders.



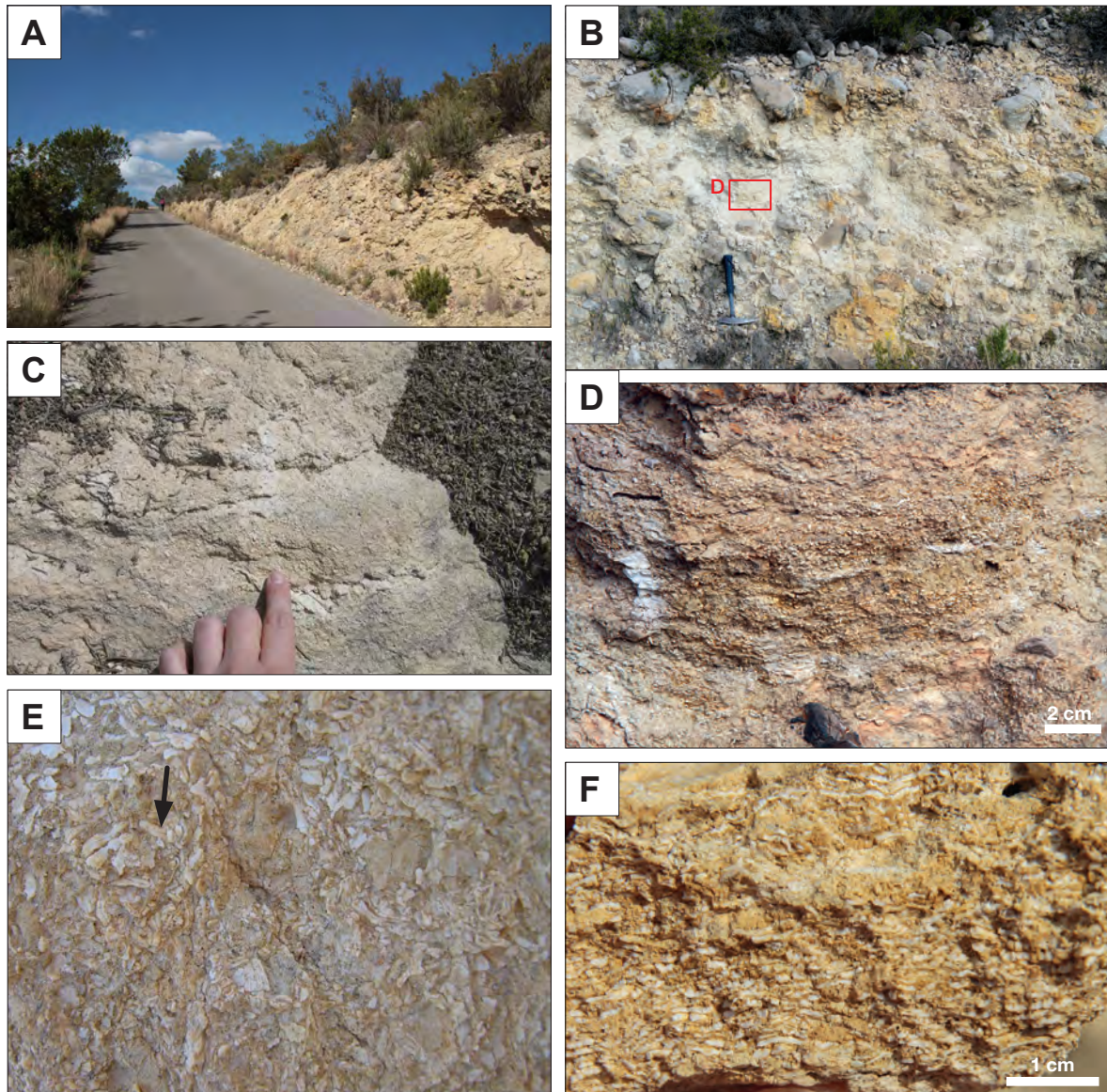


**Figure 3.4.** Finestrat, E of the Puig Campana Mountain. See maps in Figs. A3-1.1 and A3-1.2.

A) Road-cut outcrops of partly cemented Quaternary carbonate talus deposits, covered predominantly with xerophyte shrub vegetation and rare trees of *P. halepensis*. B) Weakly cemented blocky gravel. C) Finer-grained 'matrix' between larger clasts is composed almost exclusively of iCR aggregates. D) Detail of Fig. B showing indistinctly layered mass of iCRs and brown-red clayey matrix. E) Detail of Fig. C showing flat iCR aggregates, some with noticeable longitudinal linear and branching grooves (arrow), corresponding to former (non-calcified) vascular cylinders. Cf. Figs. 3.10A, C, D, E, 3.17 and 3.19. F) Freshly broken surface of the material in Fig. D showing layered asymmetric iCRs. Figs. B-F: site T15-820 (see Table A3-1.1).



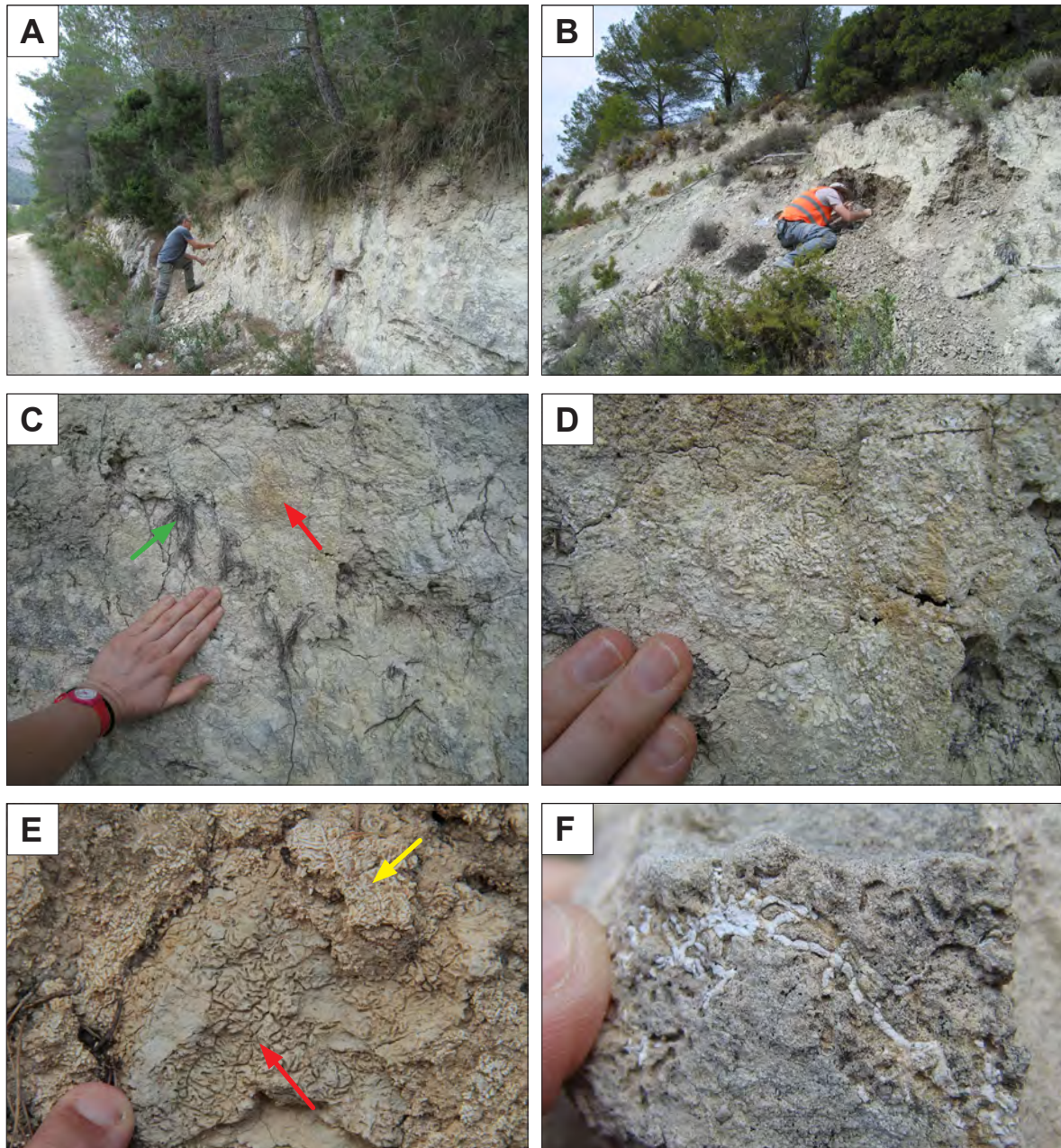


**Figure 3.5.** Finestrat-Sella, unpaved forest road N of Puig Campana. See maps in Figs. A3-1.1 and A3-1.2. A) Site T14-462: soil/weathered Cretaceous marl and marly limestones covered with *P. halepensis* and xerophyte shrubs. B) Site T14-461: relatively fresh road-cut exposures of Eocene marl with sparse shrubby vegetation. C) Same outcrops as in Fig. A: roots protruding from subvertical fissures (green arrow) in marl with abundant iCRs (red arrow). D) Detail of Fig. C showing aggregates of iCRs. E) Limestone bed with branched clusters of iCRs (yellow arrow) and corrosive channels (red arrow) produced by roots. See also Figs. 3.8D, 3.10H and A3-4.01C. F) Surface of calcarenite with iCRs preserved in corrosive channels. Site T15-823 (see Table A3-1.1).



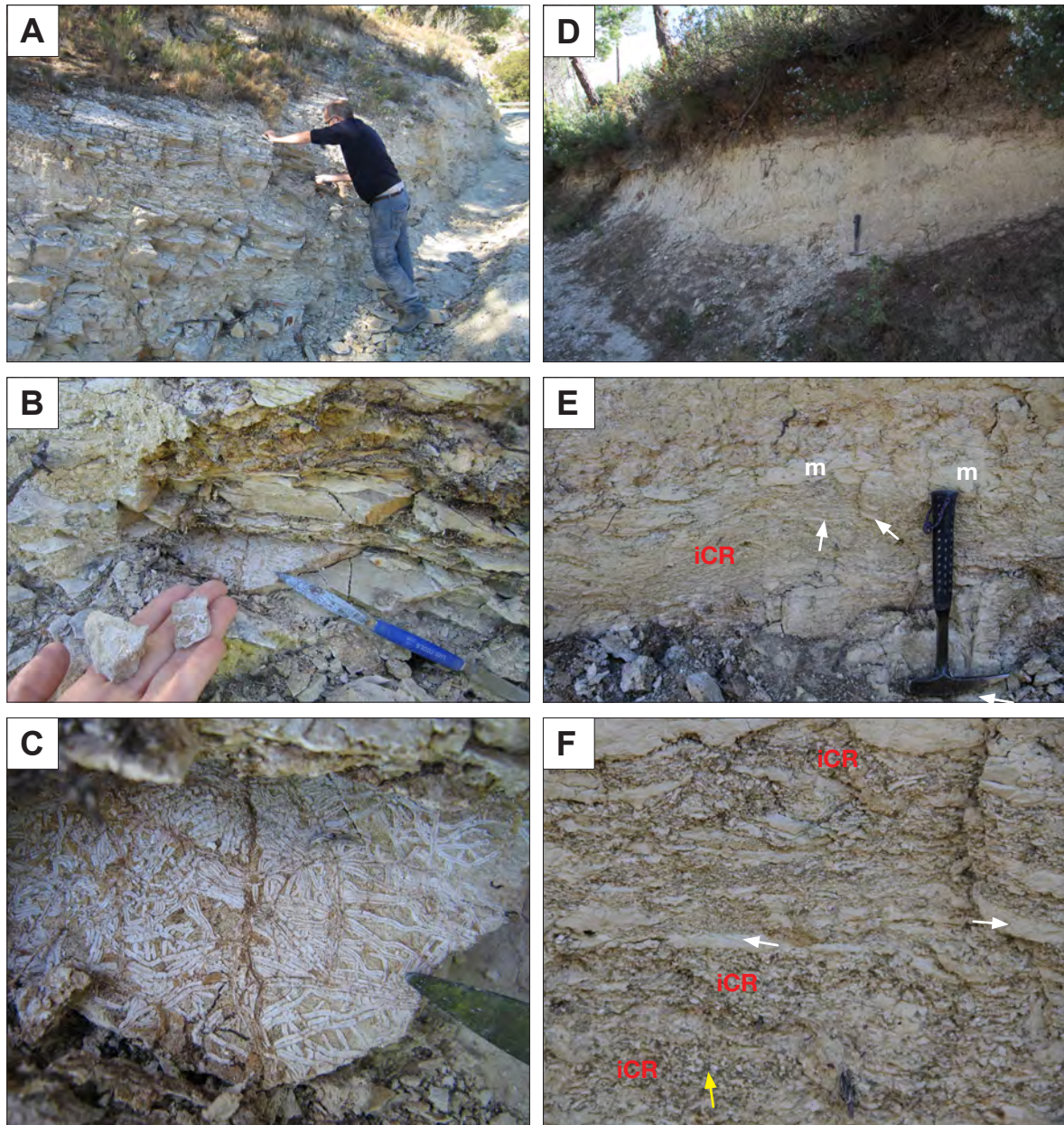


**Figure 3.6.** A) Rellu locality (Site T14-454, Table A3-1-1; Figs. A3-2.1 and A3-2.2): road-cut outcrops of Cretaceous thin-bedded marly limestones and marls. Root systems proliferate along bedding-plane partings and fractures. B) Branched systems of iCRs developed along a bedding plane (within a bedding plane fissure). C) Detail of Fig. B: calcified roots have been longitudinally split into identical, symmetric halves - the other half has been removed with the overlying limestone bed. See also Figs. 3.9, 3.13, and A3-4.01A. D) Penàguila locality (T14-457, Table A3-1-1; Figs. A3-2.1 and A3-2.2). Weathered beige marl below a humic topsoil layer is largely replaced by iCRs. E and F) Details of Fig. D: patches (layers) of marl (m and white arrows) within indistinctly layered mass of asymmetric, flat aggregates of intracellularly calcified roots (iCRs) associated with grey clay (yellow arrow). Also see Fig. A3-4.01D.



### *Penàguila*

Relatively fresh outcrops of Oligocene marl (Colodrón et al. 1981) along smaller forest roads (Fig. 3.6D-F), off the regional road between Sella and Penàguila, are characterised by several centimetres to decimetres thick layered structures, composed of flat iCR aggregates and relics of host rock (Figs. 3.6E, F). Accumulations of iCR occur throughout the weathered marl profile below humic topsoil layer but are most concentrated 1-2 m below the surface. Trees of *P. halepensis* and a dense thicket of *Erica* sp. and *Salvia rosmarinus* bushes dominated the vegetation of the sampled sites. No living calcified roots have been observed in Penàguila iCR material.

### *Ibi*

The locality comprises two sites near the town of Ibi. The area is covered by up to several 10s of metres thick succession of Quaternary alluvial deposits (Martínez del Olmo et al. 1978; Fig. A3-2.01A). Relatively fresh roadside outcrops revealed soil horizons, rich in iCRs, associated with thick calcretes under old *P. halepensis* trees (Figs. 3.7A, B). Stratigraphic relationships in the profiles and apparent lack of any active (fine) roots in the horizon with iCRs indicate that their formation probably predated formation of calcrete horizons of the upper part of the profile (Fig. 3.7B). Red-brown clayey soil with 30-60% of iCRs remains (Figs. 3.7D, E, 3.8A) contained prismatic and spherical chalky nodules, locally clearly incorporating iCRs. Larger part of sampled iCR material is strongly weathered. No samples of iCRs associated with organic root remains have been found that would provide evidence for recent or active intercellular calcification in roots in the studied profiles.

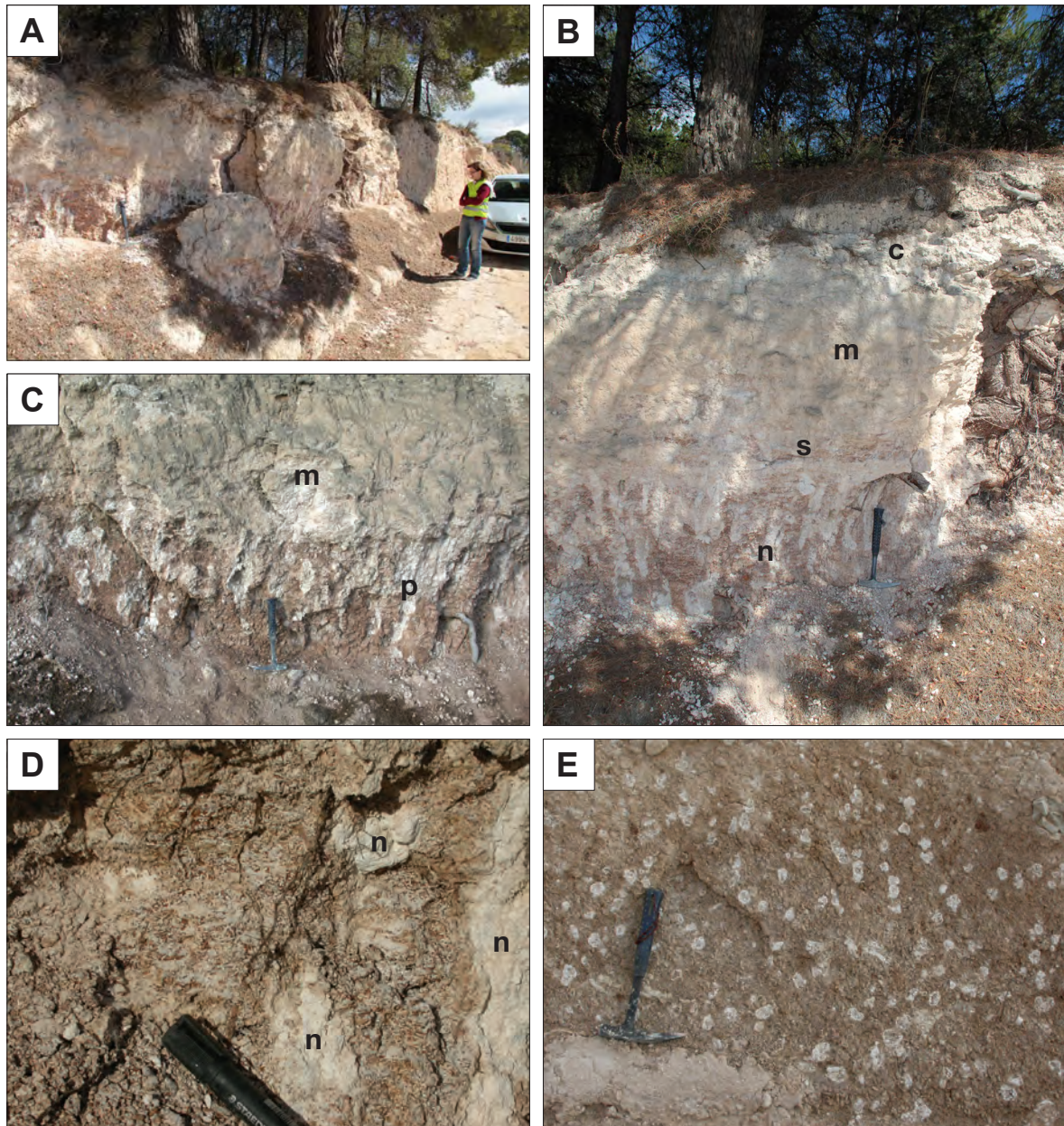


**Figure 3.7.** Ibi locality (see maps in Fig. 3.1 and Figs. A3-2.1 and A3-2.2).

A) Site T14-464 (Table A3-1.1): calcrete profile below old *P. halepensis* trees. B) The upper layer is chalky (c), strongly brecciated along the laterally spreading coarse pine roots; m - massive powdery to peloidal horizon; s - weakly cemented layer with harder sheet-like textures and anastomosing stringers; n - red-brown soil with iCRs and prismatic chalky glaebulae. C) m - massive horizon; p - horizon with vertically-elongate irregular chalky glaebulae. D) Red-brown clayey mass with white aggregates of iCRs. See close-up in Fig. 3.8A. n - weakly-cemented, chalky nodules. E) Site T14-464-1 (Table A3-1.1): massive brown soil, composed predominantly of iCRS in clayey matrix, with scattered chalky to concentrically cemented nodules, 1-4 cm in diameter.

### 3.3 Material and methods

#### 3.3.1. Field sample collection

Intracellularly calcified roots in soils are commonly extremely fragile; therefore, special care has been taken in sampling to prevent destruction of carbonate features as well as potential contamination of delicate microstructures with the soil material. Dry samples of a hand specimen size were wrapped *in situ* in aluminium foil and bubble wrap bags. Moist samples were temporarily wrapped in kitchen paper, placed in paper bags (envelopes), and then partly dried at the room temperature already during the field campaign. Sufficiently dry soil and rock samples with attached calcified roots with preserved organic parts were placed in transparent plastic boxes of appropriate size (from 12.5 to ~200 cm<sup>3</sup> volume; Krantz Rheinisches Mineralien-Kontor GmbH & Co.), prevented from moving with pieces of bubble wrap and enclosed with silica gel bags. Moist specimens, containing parts of partly calcified and apparently live fine roots (i.e., fresh, translucent roots, 0.5-2 mm in diameter, exhibiting normal turgidity of cell tissues) were sampled with an ample amount of moist soil material, loosely wrapped in cuts of filter paper and aluminium foil, and stored in the field in a cooler box with pre-cooled ice packs (keeping temperature at 4 – 8 °C) and transferred to a refrigerator.

#### 3.3.2. Laboratory sample preparation

In the laboratory, samples were further dried by being kept at room temperature and low humidity for several days and finally desiccated in an oven at 30 °C for 48 hours. Dry samples have been kept in plastic boxes and petri dishes along with silica gel.

Fragments of live fine roots, mm to cm sized, were picked from damp soil/rock samples under a stereomicroscope and observed immersed in cold water in glass petri dishes. Partly calcified roots were dissected with a scalpel; several mm long sections for SEM observation were dehydrated in successive steps of increased concentration from 35% to 95% and absolute ethanol, following a protocol described by Fratesi et al. (2004). Selected samples of fresh fine roots were observed without prior chemical fixation and dehydration under low-vacuum SEM (see below) using an adapted freeze-dry cryogenic technique of Suzuki (2005) and JEOL USA (2009), described in Appendix A3-3. Sub-millimetric sections of live roots



were produced from fine root fragments, sandwiched between pieces of Parafilm, following the procedure of Frohlich (1984). Fresh iCRs, obtained by preliminary experiments of biomineralisation of *Hedysarum coronarium*, grown in pots (Appendix A3-4, Figs. A3-4.03-04), were prepared by the same methodology.

Fully dried soil samples, several cm<sup>3</sup> large, with clusters of intracellularly calcified roots were placed into flexible silicon rubber mounting cups (FlexiForm, Struers GmbH, Germany), set in a vacuum chamber (Struers EpoVac) and kept at high vacuum for 30 minutes. Specimens were then impregnated and embedded with a transparent EpoTek 301-1 low-viscosity epoxy resin, successively introduced to the bottom of the mounting cups to enable thorough infusion into micropores. Individual dry calcified root fragments and smaller, cm-size chips of rock with attached calcified roots were placed onto a several mm thick bases, cut from remains of hardened epoxy resin, and placed in rubber mounting cups. As above, samples were kept under vacuum and then slowly covered and embedded with epoxy resin to make approximately 1.5 cm thick blocks. Resin-embedded samples in mounting cups were let hardened at room temperature for one week.

Twenty-two thin sections were prepared in the laboratory at the Institute of Palaeontology ZRC SAZU in Ljubljana. Resin-embedded blocks were cut into slices, 5-10 mm thick, using a precise Buehler Iso-Met low-speed diamond saw with propylene glycol as a cooling liquid to prevent mechanical damage of crystal ultrastructure. Slices were machine lapped on one side with silicon carbide (SiC) abrasive powder (600F/mean grit size 25 µm) and then manually polished using a succession of SiC-impregnated pads (Kemet, UK) of P1200 (15 µm grit size), P2500 (8 µm) and P4000 (5 µm). Polished faces were mounted at room temperature on glass slides using EpoTek 301-1 epoxy resin and a Logitech bonding jig, and left fixed for 48 hours to allow the resin to fully cure. Mounted slices were trimmed and machine lapped at slow rotation to approximately 40 µm thickness, followed by manual polishing using a succession of same SiC pads, producing thin sections, 20-30 µm thick. Selected thin sections were additionally machine-polished for 10–20 minutes using 1 µm diamond paste (SPI Diamond Compound, Structure Probe, Inc., West Chester, USA), dispersed on a polishing cloth mounted on an aluminium plate, on a Logitech PM5 machine. Eight thin sections for SEM EDS and EPMA analysis were finalised and highly polished at the Thin Section Laboratory UCM (Departamento de Mineralogía y Petrología, Facultad de Ciencias Geológicas, Universidad Complutense Madrid, Spain).

### 3.3.3. *Thin section petrography*

Thin sections were observed and photographed in transmitted light under conventional polarising microscopes and stereomicroscopes (an Olympus BX51 equipped with a digital camera Olympus SC180 and cellSens™ software; a Leitz Orhoplan and a Wild M420 equipped with a Leica DFC450 and LAS (Leica Application Suite) imaging software). Selected polished thin sections were examined with fluorescence microscopy in the Microscopy Lab (SEES, Cardiff) using a Leica DML microscope in reflected light with filters for blue and green wavelength fluorescent light, fitted with Leica LAS imaging software.

### 3.3.4. *Scanning electron microscopy*

Macro samples were photographed with a digital camera with a macro objective and observed under a stereomicroscope. Fragments of dry intracellularly calcified roots, mm to cm in size, were collected and mounted onto SEM stubs (aluminium cylinders and discs ø10, 30 and 51 mm) with carbon tape and conductive paste.

Scanning electron microscopy (SEM) was carried on a JEOL JSM 330A and a JEOL JSM IT100 LV microscope at the Microscopy Laboratory ZRC SAZU in Ljubljana. Uncoated specimens were observed and photographed in low-vacuum (LV) mode (20-40 Pa) with an accelerating voltage of 15 kV and 20 kV at a working distance from 9 to 11 mm. Photomicrographs were taken in topographic, compositional and shadow backscattered electron imaging (BET, BEC and BES) modes. Selected samples were Au-coated for 100-300 seconds using a Baltec SCD-50 Sputter Coater and observed in high vacuum (HV) SED mode. Several impregnated slices, remaining from thin section preparation, were manually polished on polishing pads (procedure described above), decalcified with diluted (8 %) formic acid for 3 minutes, washed three baths of distilled water and air-dried. Slices were fixed on aluminium discs (ø 51 mm) with conductive carbon tape, and Au-coated for SEM analysis.

SEM images of polished thin sections were collected either in LV on uncoated surfaces in BEI mode or coated with carbon (for several seconds, using a JEOL JEC-530 Carbon Coater) and observed in high vacuum with an accelerating voltage of 15 kV and 20 kV. Conventional backscattered electron imaging of uncoated thin sections was supplemented

by Charge Contrast Images (CCI) performed in LV conditions (40-60 Pa) with a powerful beam (maximum accelerating voltage and high probe current) using a low-vacuum Secondary Electron Detector (LV SED) or a backscattered detector.

### *3.3.5. SEM and EPMA elemental analysis*

Qualitative and semi-quantitative Energy Dispersive X-ray Spectroscopy elemental analysis (EDS) was performed at the same LV conditions. Elemental spectra were obtained on uncoated thin sections using point or small area analysis with 100 seconds pre-set (live) time and automatic or manual element identification mode. Elemental mapping was performed for manually selected elements in 10-50 mapping steps ('sweeps') of 100 seconds live time, and probe current adjusted for count rates from 15 to 25 kCPS.

Elemental analyses of three thin sections were performed on highly polished thin sections on a JEOL JXA-8900M WD/ED Electron Microprobe at the National Electronic Microscopy Centre (CNME) at the University Complutense Madrid. Microprobe was operating at 15 kV and 20 nA and employing an electron beam diameter of 5  $\mu\text{m}$  (for further analytical details see Appendix A3.5).

### *3.3.6. Microsampling and stable isotope analysis of carbonate $\delta^{13}\text{C}$ and $\delta^{18}\text{O}$ and organic $\delta^{13}\text{C}$*

Samples for C and O stable isotope analysis were collected under a stereomicroscope. Disaggregated calcified cells, devoid of matrix and organic material, were sampled with a scalpel with a sharp point blade and collected in a 3 ml glass vial. Vials with 0.5 to 5  $\text{mm}^3$  of calcified cells were filled with distilled water, closed and shaken; muddy water was decanted and remaining sediment collected using a disposable 1 ml Pasteur pipette with fine tip, transferred to a hour glass, and covered with several drops of 70% ethanol. Sediment was roughly separated by gently agitating watch glass; clean, translucent calcified cells were carefully pipetted from the watch glass under a stereomicroscope using a combination of transmitted and reflected light, and collected in plastic conical-bottom vials. Approximately 0.2 to 1  $\text{mm}^3$  of calcified roots cells were collected per sample.

In intracellularly calcified roots with preserved organic parts, a root fragment, 1-2 cm long, was cleaned of matrix, sandwiched between two pieces of adhesive tape and cut



lengthways into halves over a watch glass; calcified cells were scraped out of the root half-sections with a scalpel, collected on a watch glass and transferred into a vial.

Fragments of slightly cemented intracellularly calcified roots were picked from hand samples with a precise tweezers under a stereomicroscope and collected into a glass petri dish. Collected sediment was rinsed in several batches of distilled water. Clean iCR aggregates, 0.5-2 mm<sup>3</sup> large, were air dried and collected into plastic vials.

Carbon and oxygen stable isotope analyses of calcified roots were performed at the Stable Isotope Laboratory of the School of Earth and Environmental Sciences, Cardiff University, with additional analyses carried out at the University of Graz, Austria, GeoForschungsZentrum (GFZ) in Potsdam, Germany (see Appendix A1-1).

At Cardiff, isotopic determinations were performed on samples of calcified cells, crushed with a clean stirring rod in the vial, using a ThermoFinnigan MAT 252 mass spectrometer with a Kiel IV carbonate preparation device. For an individual sample, repeated measurements (typically quadruplicates) were done on sets of separated sub-samples, approximately 20-100 µg each. Isotope values are reported relative to Vienna Pee Dee Belemnite (VPDB) using the standard NBS-19. The average analytical precision of the standard analyses over the period of the investigation was ±0.05‰ for <sup>18</sup>O and ±0.03‰ for <sup>13</sup>C. Analytical details for laboratories at Graz and Potsdam are given in Appendix A1.1.

Three samples of iCRs with preserved organic tissues (see Table 3.1) were used for analysis of δ<sup>13</sup>C<sub>organic</sub> performed at the Department of Environmental Sciences, Jožef Stefan Institute (IJS), Ljubljana.

### 3.3.7. X-ray diffraction and FTIR mineralogical analysis

Mineralogical characterisation of calcified cells was done by X-ray diffraction (XRD) analysis. Samples of calcified cells were collected under stereomicroscope as described above. Approximately 0.5 cm<sup>3</sup> of sediment per sample was collected into a 100 ml glass beaker, soaked with deionised water, and agitated in an ultrasonic bath for 1 minute. Water with suspended fines (clay and organic material) was decanted and replaced with clean deionised water. The step was repeated 3 to 5 times. Collected material was dried at 40°C in an oven, crushed in an agate mortar, and sieved through 50 µm nylon sieve. Ten samples were analysed with XRD at the Department of Materials Synthesis, Jožef Stefan Institute in Ljubljana, using a Bruker AXS endeavour diffractometer operating at 40 kV and 30 mA, at

0.040°/sec, with monochromatic CuK $\alpha$  radiation. XRD spectra were obtained from 10° to 90° 2 $\theta$  range.

X-ray diffraction analysis was also performed on four samples of clayey matrix of the iCRs (Sella and Ibi localities; see Figs. 3.3B, 3.7D and 3.8A) at the Universität für Bodenkultur (BOKU), Vienna, Austria, by Marta Mileusnic. Approximately 50 g of sample was mixed with 500 ml of deionised water, processed for 5 minutes in an ultrasonic bath, and wet-sieved through 63  $\mu$ m sieve. Collected sediment was air dried, crushed in an agate mortar, and sieved through 50  $\mu$ m nylon sieve. Obtained samples were analysed using a Philips PW1710 diffractometer, operating at 40 kV and 30 mA, at 0.040°/sec, with monochromatic CuK $\alpha$  radiation. The XRD diagrams were obtained for 2 to 66° 2 $\theta$  range. Same samples were reused for slides prepared from separated of <2  $\mu$ m fraction, and analysed using the same analytical parameters as above.

### 3.4 Results

#### 3.4.1 *Field occurrence and macroscopic appearance of iCRs*

Appearance of intracellularly calcified roots in the field largely depends on their preservation state. Macroscopically, when not associated with active or partly decayed fine roots, iCRs appear as fine white or semitransparent cylindrical, vermiform structures, typically from 0.5 to 2.5 mm in diameter (Figs. 3.3B, D, Fig. A3-4.01G). Intracellularly calcified roots typically do not occur in organic topsoil horizons, whereas in shallow, biologically active subsoil layers, strongly affected by rhizoturbation and animal bioturbation, they rarely form any larger branching fragments but rather occur as disaggregated individual calcified cells and smaller aggregates, dispersed in the soil volume (Figs. 3.3D, 3.7D, 3.8A, Fig. A3-4.01B).

In most of the studied localities, where active soil was generally limited to a thin A horizon over an incipient B horizon or directly over more or less unaltered calcareous rock material, accumulations of iCRs were typically observed in association with active coarse root systems, exploring rock fissures (Figs. 3.3B, E; 3.5C, 3.6A, B, C) – from several 10s of centimetres below the surface to depths of more than 7 metres (Fig. 3.3A). Aggregates of iCRs are often concentrated in mm to cm thick horizontal layers (Fig. 3.2B), composed of iCRs, organic remains and active roots, and non-carbonate (clayey) matrix. Associated with deep root systems in strongly weathered marl, iCR structures locally form zebra-like layered fabrics (Fig. 3.3B). Similar, but larger scale and well-structured layered accumulations of iCRs occur between carbonate blocks in slope deposits (Fig. 3.4) and in layers, tens of centimetres thick, occurring 1-3 metres below the soil surface, laterally spreading in relatively soft weathered marl (Figs. 3.6D, E, F). Such layered masses are composed almost exclusively of iCR aggregates, associated with thin clayey layers (see Section 3.4.2 below, Figs. 3.12 and 3.17).

In thin fissures in limestone and marly limestone, iCRs formed highly ordered structures, representing larger portions of fully calcified, branched root systems. In outcrops of thin-bedded limestone, such as at the Relleu locality (Figs. 3.6A, B, C), millimetric or sub-millimetric bedding-plane partings in platy limestone often reveal perfectly preserved iCR systems, forming identical (mirror) halves of longitudinally split iCRs, attached on limestone plates from both sides of a fissure. In wider, several mm to several cm wide voids,



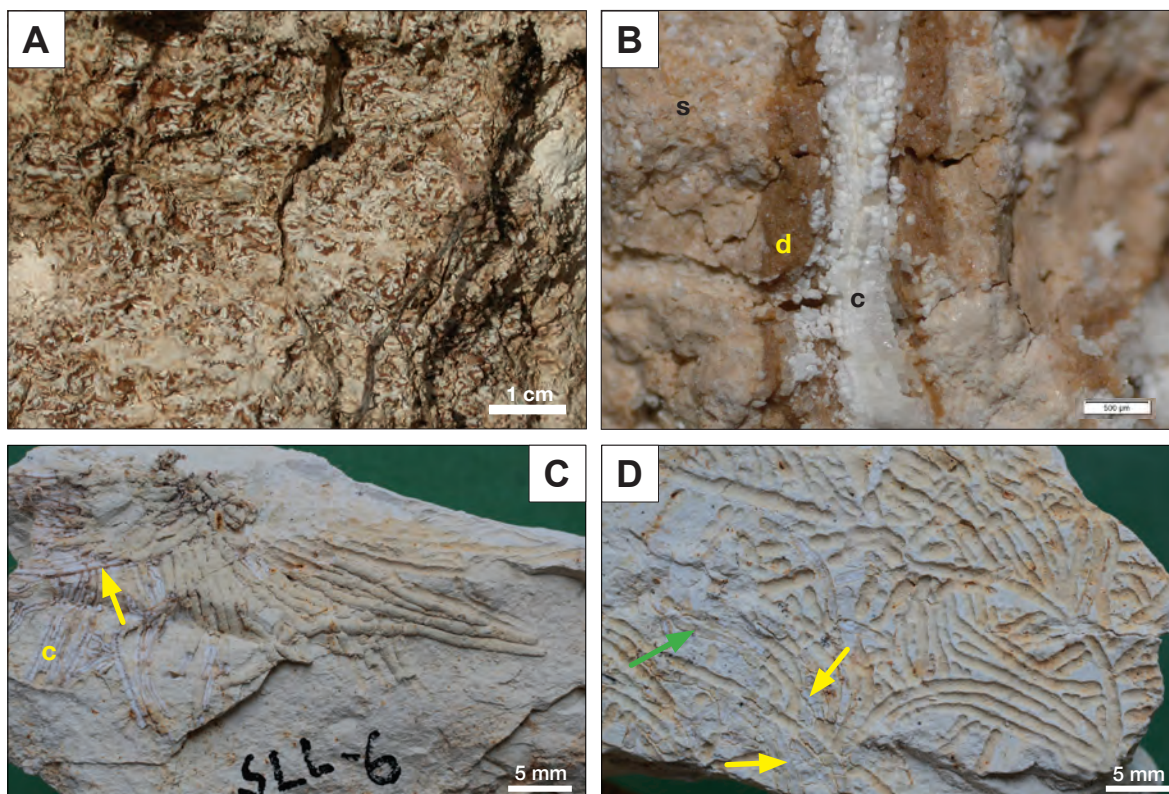


**Figure 3.8.** A) Detail of Fig. 3.7D: iCR aggregates (white) in brown clayey matrix. B) Very fine calcified root (c), <0.5 mm in diameter, in calcareous matrix/substrate (s), with carbonate-depleted zone (d), several 100s of  $\mu\text{m}$  thick, surrounding the root (i.e. rhizosphere). See also corresponding EDS elemental maps in Figs. 3.15B-E. Sella, site T14-463. C) Densely branched, fully intracellularly calcified root from a vertical joint in marl. Roots are enclosed in a film of clayey material (i.e. carbonate depleted zone). Roots on the left (c) are longitudinally bisected, showing fully calcified cortex and partly preserved organic vascular cylinders (arrow). Cf. Figs. 3.11, 3.12C, 3.14 and 3.15. Sella, site T14-463. D) Corrosion trace of a densely branched root system: bedding plane of marly limestone with channels, formed by root-induced dissolution. Some root 'casts' contain remains of iCRs (yellow arrows) and clayey films (green arrow) resulting from total carbonate dissolution in the immediate rhizosphere. Relleu, site T14-456.

occupied by roots and partly filled with soil material, iCRs appear to be present solely along the contact with the rock substrate, whereas organic (soil) material within the void does not contain calcified root remains.

Marls and loamy soils in exposures between Sella and Finestrat, freshly broken along fissures and exfoliation joints, exhibited excellently preserved iCR root systems (Figs. 3.3E and 3.5D, Figs. A3-4.01A-K), forming distinctive herringbone branching patterns (described below) and frequently associated with organic remains of terminal orders of live, wholly or partly calcified roots (Fig. 3.13), or dead iCRs in various stages of decay (Figs. 3.10, 3.11, 3.12).

Rock surfaces may display distinctively branched corrosive features (grooves), formed by root-induced dissolution. Such grooves, one to several mm wide, apparently correspond to weathered-out iCR systems (Figs. 3.5E, 3.8C, D, 3.11H), clearly indicated by remains of calcified cells and clayey films in channels (Figs. 3.5F, 3.8D, Fig. A3-4.01C).

### 3.4.2 Morphology and architecture of iCR systems

Somehow counter-intuitive to a common depiction of fine roots as cylindrical, radially symmetrical organs (e.g. Fig. 2.9), most intracellularly calcified roots do not exhibit such geometry. Figure 3.9 illustrates different morphological types of iCRs in cross sections. Common to all iCR morphologies is presence of a more or less clearly manifested zone, surrounding the root, characterised by apparent carbonate depletion of the substrate/growth medium. This zone is generally equivalent to the rhizosphere and roughly corresponds to the extent of the soil surrounding the roots, permeated by root hairs (Figs. 3.9B; also see Figs. 3.8B, 3.15C, D and 3.16).

Two morphological groups of iCR have been distinguished. Type I (iCR-I) comprise symmetrical morphologies (Figs. 3.9A, C, D) with centrally placed vascular cylinder. The most regular, radially symmetrical calcified roots (Fig. 3.9A) evidently reflect growth of iCRs in homogeneous, compositionally isotropic substrate. Compressed but symmetrical iCRs (i.e. having two perpendicular planes of symmetry), exhibiting rounded rectangle to elliptical shape in cross section and carbonate depletion zones on both sides (Fig. 3.9C), are typical of iCRs growing in relatively wide fissures, e.g. bedding plane partings of width similar to 'normal' fine root diameter (Figs. 3.15, 3.16). The third subtype of iCR-I comprises bilaterally symmetrical (in two axes), but pronouncedly flattened calcified roots, lens-shaped in cross section (Fig. 3.9D), associated with iCRs found in narrow fissures. This form is characteristic of iCR systems showing conspicuous herringbone branching patterns (Figs. 3.6C, 3.8C, 3.10, 3.14, and Figs. A3-4.01H-K). Accompanying carbonate-depleted zones on both sides of iCR-I type roots (Figs. 3.9C, D) are associated with remains of root hairs or microtubules in clayey material, left after their decay (Figs. 3.15C, D, E).

Type II intracellularly calcified roots are characterised by 'aberrant' asymmetrical (or bilaterally symmetrical) structure and are typically distinguished by wide, compressed shapes (Figs. 3.9E, F), 2-4 mm wide. A very common subtype of iCR-II roots includes forms with eccentric (ectopic), peripherally placed vascular cylinder (Fig. 3.9E) and a

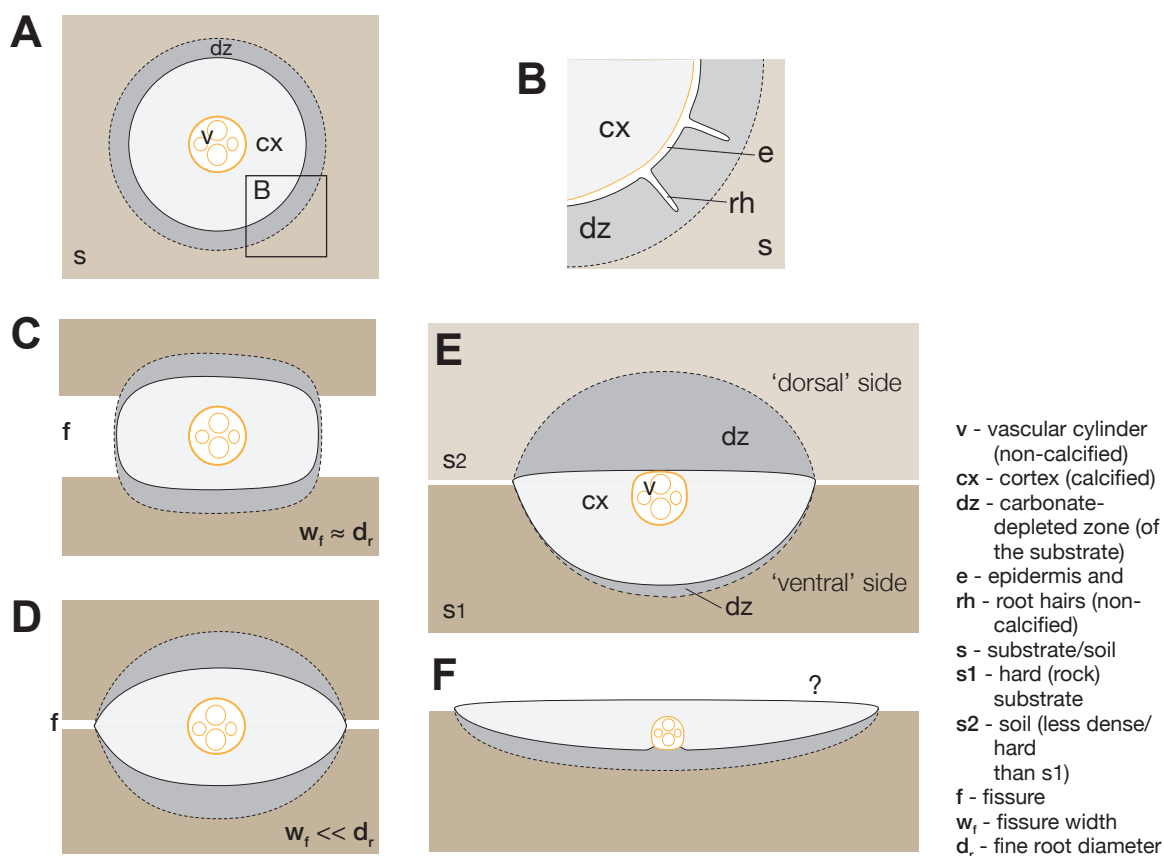


**Figure 3.9.** Scheme of calcified root morphologies in cross section. **A**) Fine roots, growing in homogeneous (isotropic) substrate normally exhibit circular and radially symmetrical iCR shape in cross section with the vascular cylinder placed centrally. **B**) Detail of **A** showing calcified cortex, epidermis (normally not calcified) and root hairs. Width of the carbonate-depleted zone around iCRs generally corresponds to the extent (length) of root hairs. Cf. Figs. 3.8B, 3.15C, D and 3.16. **C**) Bilaterally symmetrical iCR growing in a relatively wide fissure (e.g., bedding plane parting of width ( $w_f$ ) similar to 'normal' fine root diameter ( $d_r$ )) showing rounded rectangle to elliptical cross-section with carbonate-depleted zones of dissolutional grooves in contacts with substrate. Cf. Figs. 3.15D, E. **D**) Characteristic elliptical to biconvex arc shape of iCRs penetrating and dissolving narrow fissures ( $w_f \ll d_r$ ). **A**, **C** and **D** are subvarieties of type one (iCR-I) intracellularly calcified roots. **E**) Morphology of asymmetrical calcified roots (type two (iCR-II) or 'shovel' root type) growing along a contact between hard (calcareous) substrate ( $s_1$ ) surface and softer (less dense) soil ( $s_2$ ). A ventral side typically shows a relatively thin veneer of clayey material and a thicker dome-shaped carbonate-depleted zone on the dorsal side. The carbonate-depleted zone is interspersed with root hairs or tubules left after their decay (Figs. 3.19A, B and 3.20). Root hairs appear to be limited on the dorsal side. Note the vascular cylinder in ectopic, marginal position. Cf. Figs. 3.19, 3.20, 3.21 and Figs. A3-4.02. **F**) Extremely wide and flat variety of iCR-II (examples in Figs. 3.11 and 3.18D). No examples of this form have been found with preserved organic parts, therefore, the presence and position of root hairs in this type of iCRs is unknown. Cf. Fig. 3.11F.



general shape of an elliptic semicylinder. Relatively levelled to slightly convex side of iCRs, in contact with the vascular cylinder (the 'dorsal' side), is typically capped with a convex layer of clayey material (i.e. carbonate-depleted zone; Figs. 3.12), interspersed with root hairs tubules (Figs. 3.19A, B and 3.20). The ventral side is typically semi-elliptical to semi-circular in cross section and appears moulded into the substrate (Figs. 3.9E, 3.20B, E). Alive specimens and some of the exceptionally preserved dry iCRs of this type have shown that root hairs are present only on one, i.e. dorsal side of a root (Fig. 3.20), whereas the ventral side displays epidermis which is apparently totally devoid of root hairs (Figs. 3.20B, D, 3.21A-E, Figs. A3-4.02C-F). However, some roots exhibit an epidermal layer, composed of protuberant, non-calcified cells (Figs. 3.21C, D, E) with ruptures, approximately 20  $\mu\text{m}$  wide, comparable with typical root hair diameters (e.g. Fig. 3.20G).

An extreme variety of Type II iCRs (Figs. 3.9F) is represented by wide, thin, strongly compressed forms, associated with a sparse, a few 10s of  $\mu\text{m}$  thick clayey film on the dorsal side, that is the side in contact with the vascular cylinder (Figs. 3.11F, 3.18D). Since no examples of this form have been found with preserved organic parts or thicker clayey coatings, the presence and position of root hairs in this type of iCRs is unknown, however, their morphology can be derived from short, flattened lateral iCRs, shown in Figure 3.21F and Figures A3-4.02E, F.

Many *in situ* iCR root systems, i.e. wholly calcified terminal parts of fine root branches, preserved along fissures in substrate, exhibit strikingly regular, often highly ordered branching patterns (Figs. 3.10A-D, F, Fig. A3-4.01). Regular herringbone patterns are particularly well developed and well seen in iCR-I type root systems, when symmetrically split in half and thus exposing the median part, often emphasised by preserved vascular cylinders, darkened by fungal rotting (Figs. 3.10A, B, C, Figs. A3-4.01H, I). Herringbone patterns consist of a main root segment (axis) and lateral roots, emerging from it in more or less ordered manner, generally at relatively consistent intervals in alternating way on both sides (reconstruction in Figs. 3.14B and D). These patterns often constitute very dense network of fully calcified roots, virtually covering all available substrate surface and filling up whole fissure space, respectively (Figs. 3.10C, D, 3.14B; Fig. A3-4.01). Branching patterns indicate efficient 'navigation' of new root branches, growing in parallel bundles, exploring empty spaces/surfaces, and approaching but not crossing spaces/surfaces, occupied with previously grown lateral calcified roots (Fig. 3.10A, Figs. A3-4.01A, H-K).

Herringbone patterns occur also in asymmetrical, type II iCRs. In single layer root systems (Fig. 3.12D) they often form dense and straight, mutually parallel outgrowths from

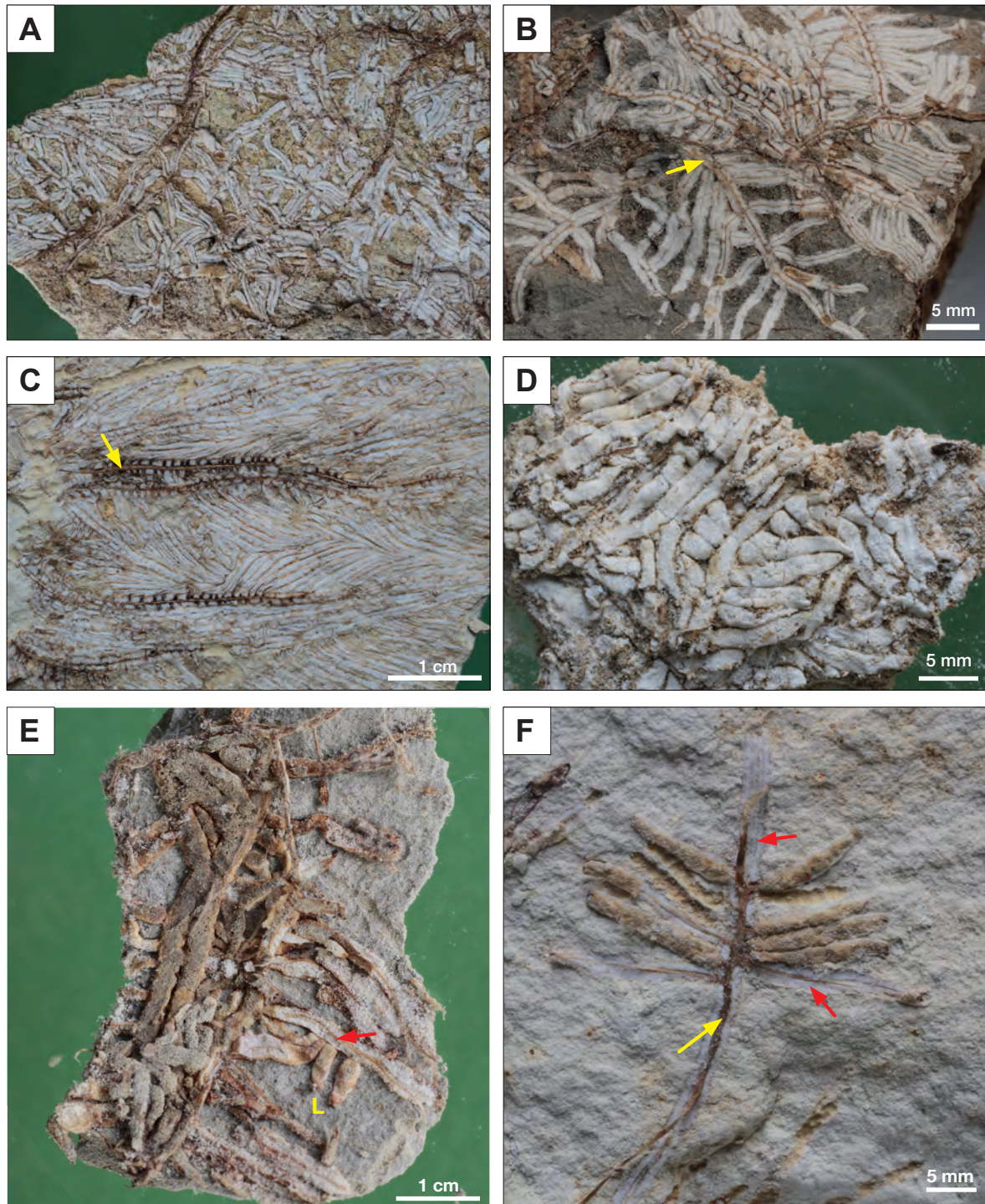


**Figure 3.10.** Bilaterally symmetrical iCRs (type I) in hand-specimens. A) Sample of a clayey limestone with iCRs growing on a surface. The sample and, correspondingly, iCRs, was split along a bedding plane parting; identical half of the calcified root system with irregular herringbone branching was preserved on the other bed/side of the fissure. Rellu, site T14-454. B) Similar to Fig. A; arrow indicates preserved non-calcified vascular cylinders. Finestrat-Sella, site T14-461. C) Similar to A and B: extremely dense architecture of a herringbone branching, fully calcified root system. Cf. SEM photomicrographs in Fig. 3.14. Sella, site T15-816. D) External side of a similarly densely branching, fully calcified root system. Penàguila, site T14-458. E) Portion of iCR root system with largely preserved organic parts: vascular cylinders (red arrow) and epidermis (e.g. in short laterals labelled with L). F) Small branching fragment of iCR-I; red arrows: calcified cortex; yellow arrow: preserved vascular cylinder. Sella, site T14-463.



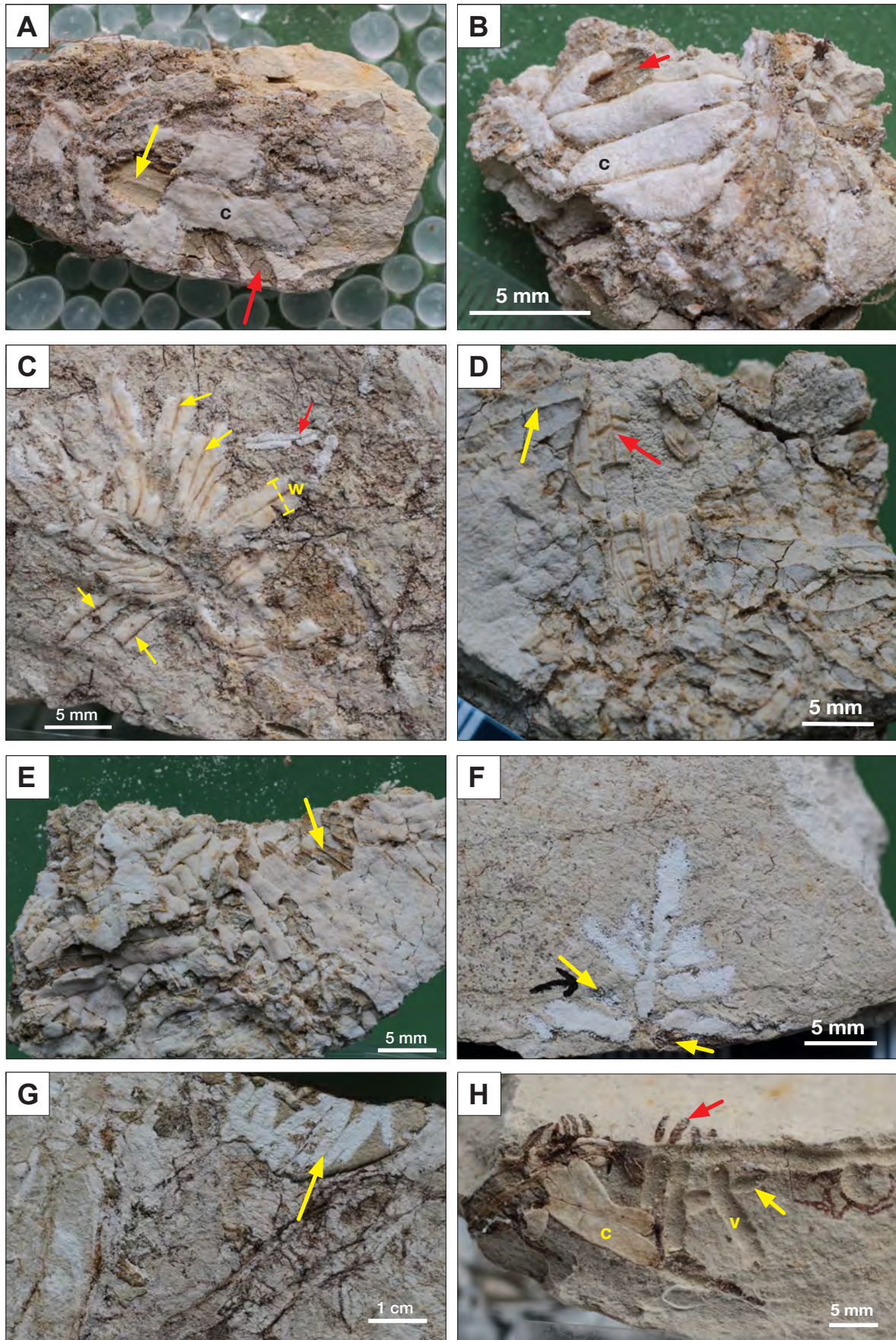


Figure 3.11. See caption on the following page.



**Figure 3.11.** (previous page). Asymmetrical iCRs (type II) in hand-specimens. **A)** Fragment of marl with extremely flat and wide asymmetric iCRs (label c indicates their ventral side). Yellow arrow shows a ridge-like cast corresponding to non-calcified, marginally placed vascular cylinder (cf. Figs. 3.9E, F). Red arrow: clayey, carbonate-depleted substrate. Silica gell beads (2-4 mm) for scale. Finestrat-Sella, site T14-462. **B)** Fragment of layered iCR-II aggregates: c - parallel branches of wide, flat iCRs (ventral sides); red arrow: exposed part of a clayey layer (carbonate-depleted zone) on the dorsal side of iCR. Finestrat-Sella, site T14-462. **C)** A structure of very wide (w = up to 4 mm), flat iCR-II branches (dorsal sides) showing vascular cylinder grooves (yellow arrows). Brown colouration indicates partly preserved organic material within the grooves. Red arrow: a short fragment of a symmetrical (type I) iCR. Finestrat-Sella, site T14-462. **D and E)** Layered structures composed of densely packed, flat iCR-II aggregates. See field appearance in Figs. 3.4D, F, and 3.6E, F. Yellow arrows: vascular cylinder imprints on dorsal sides. Red arrow: longitudinal grooves with lateral branches corresponding to branched vascular cylinders. Cf. iCRs in Fig. 3.4E. Samples: D - Relleu, site T14-454; E - Penàguila, site T14-459. **F)** Relatively poorly preserved iCR-II of a subvariety F in Fig. 3.9. Arrows: clayey layers on sides towards the substrate. Platy limestone, Relleu, site T14-456. **G)** Same as F: arrow indicates iCR-II aggregates forming thin, approximately 50-100  $\mu\text{m}$  thick layers. **H)** Asymmetric iCR-II aggregates (c) and their corresponding dissolutional grooves (v) on the edge of a marl fragment; yellow arrow indicates a groove corresponding to a short lateral root, red arrow point to non-calcified, organic remains of short laterals. Finestrat-Sella, site T14-462.

a main (parent) root axis. In iCR-II root systems, assembled in several layers, the branching geometry is less pronounced: asymmetric iCRs with associated decalcified semicylindrical clayey caps form intertwined, crudely layered structures (Fig. 3.12). Extremely flat varieties of iCR-II roots often form almost continuous layers, composed of wide, fully calcified iCRs, arranged in dense network with neighbouring roots in contact with each other (Figs. 3.11A, B, D, E, F). Such layered structures, made entirely of flattened iCRs and interlayered with clayey laminae, compose centimetre to decimetre thick laminar deposits (Figs. 3.4B, D, E, 3.6D, E, F). In such laminar accumulations, it is virtually impossible to recognise any root-like branching pattern, particularly in cross sections, whereas individual iCR fragments often show longitudinal linear and branching grooves, corresponding to former vascular cylinders (Figs. 3.4E, 3.11C).

#### 3.4.2.1 Live iCRs and partly calcified fine roots

Fragments of fine roots systems, partly or totally calcified and apparently live, i.e. exhibiting normal turgidity of cell tissues and typically having fresh, white epidermis, partly covered with a thin carbonate-depleted clayey layer and root hairs (Figs. 3.13C, D), have been sampled in individual excavation pits along the forest roads between Sella and Finestrat (Figs. 3.3E, 3.5B, 4.1). Apical parts (root tips) of live iCRs were fresh, transparent and non-calcified (Figs. 3.13A, B, 4.2E, F).

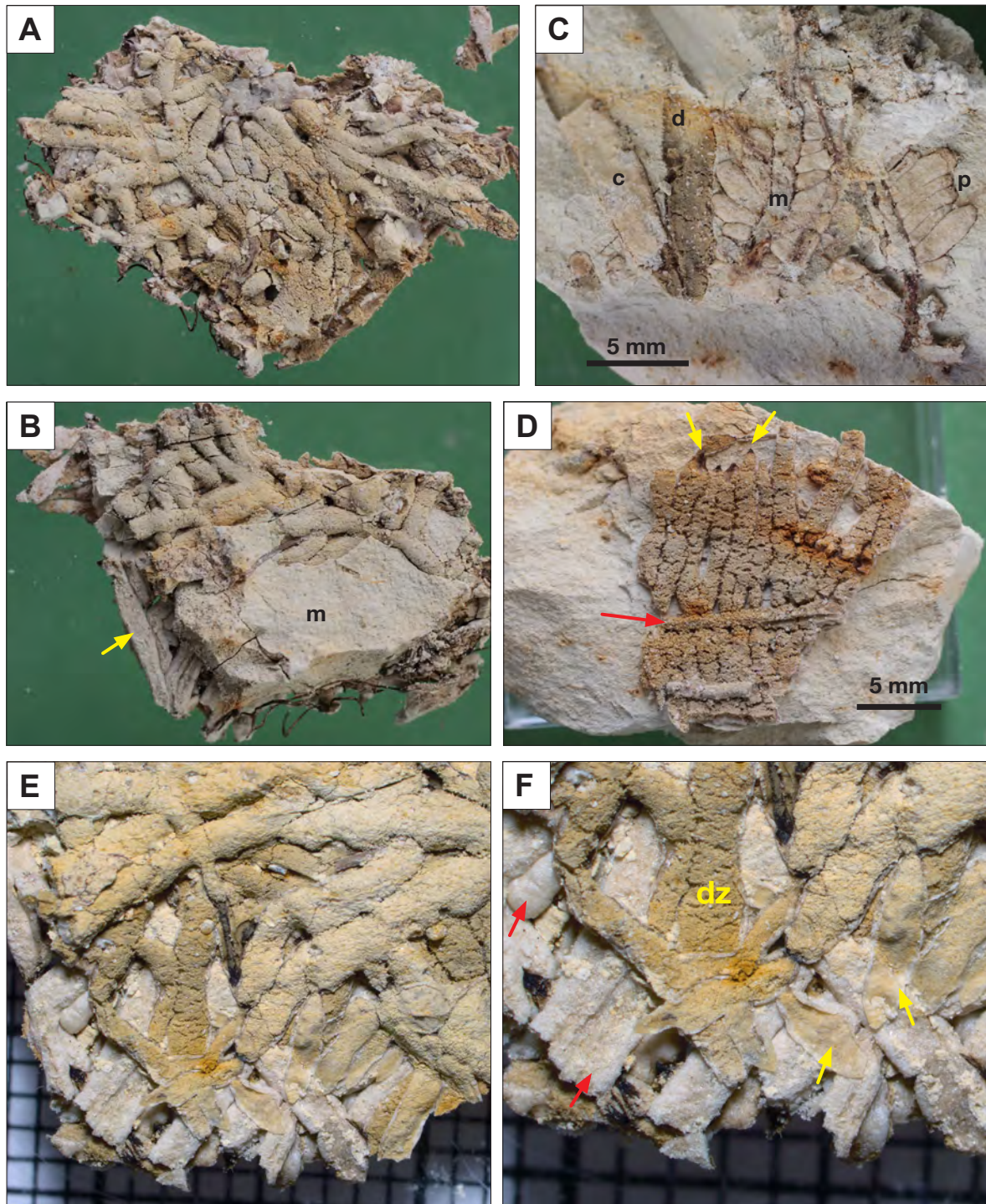


**Figure 3.12.** Asymmetrical iCRs (type II) with pronounced clayey coatings, corresponding to carbonate-depleted zone at the contact of iCRs with the substrate. A and B) Densely branched, interwoven system of iCR-II roots, embedde in clayey coatings, a same specimen seen from opposite sides. Yellow arrow: exposed iCRs without clayey coating; **m** - relict of a marl substrate. C) Type II iCRs on a fragment of marl; **c** - wide, flat iCR aggregate (ventral side); **d** - dissolutional groove with remain of clayey film (carbonate-depleted layer); **m** - fragment of an iCR branch composed of a 'primary' root (**m**) with closely packed short ('secondary') laterals; **p** - closely packed terminal order iCRs. D) A fragment of iCR-II system with perfect herringbone branching pattern. Red arrow: primary root; yellow arrows: partly preserved epidermis of non-calcified root tips. E, F) Intertwined type II iCRs with carbonate-depleted coatings (**dz**). Red arrows: exposed ventral sides of calcified cortex; Yellow arrows: preserved epidermis of 'deflated' non-calcified terminal roots. All samples from Finestrat-Sella locality, site T14-462.

Cross sections of fresh and translucent incipiently calcified fine roots, 0.5-2 mm in diameter, revealed individual calcified cortical cells, which are predominantly located in the internal part of the cortex close to vascular cylinder (Figs. 3.13F, G).

Calcified fine roots apparently die and start to decompose immediately after the calcification process in the cortex has completed (Jaillard 1983, 1987a). However, fully calcified iCRs, which were sampled and desiccated before the microbial degradation would strongly affect the organic tissues, may show exquisite anatomical details with well-preserved cell walls of the cortex (Fig. 3.18C; Section 3.4.3).

Significantly, none of the investigated samples of live iCRs or partly calcified dead fine root material have shown evidence of mycorrhizal association, neither external ectomycorrhizal structures (i.e. presence of a mantle of fungal hyphae) nor vesicular-arbuscular mycorrhizal structures within the root cells.

Comparative live iCR material, obtained in preliminary experimental growth of *Hedysarum coronarium*, has shown typical flattened, asymmetrical ('shovel') root morphologies (Tola et al. 2009) with partly calcified cortex (Figs. A3-4.03, A3-4.04). Some of the calcified terminal roots have shown a thin layer of non-carbonate material on the dorsal side of a root (Figs. A3-4.03D, E, G). Semi-cylindrical caps, analogous to carbonate-depleted zones along the root-hair covered parts of calcified roots, have not developed on iCRs of pot-grown *H. coronarium*, probably due to a homogeneous, fine-grained organic-mineral substrate, used in the experiment.

#### 3.4.2.2 iCR-substrate relationships

Imprints of root systems on carbonate rock surfaces, some of them associated with traces of calcified cortex (Figs. 3.5E, F, 3.8D, Fig. A3-4.01C), observed throughout the studied localities, provide an indisputable evidence of plant-driven corrosive activity, generated by root-induced pH changes in the rhizosphere (e.g. Hinsinger 2013 and references therein). Fitted geometrical relationships between iCRs and the corresponding corrosive grooves in the substrate (Figs. 3.14E, F, 3.15A, B, C, 3.20C, E) indicate that dissolution of the substrate obviously occurred simultaneously with carbonate precipitation in cortical cells. Furthermore, iCR-induced pH changes in the rhizosphere are demonstrated by carbonate-depleted, and correspondingly relatively Si- and Al-enriched zones around iCRs (Fig. 3.8B and corresponding SEM images and EDS elemental maps in Fig. 3.16). Flattened, strongly asymmetrical iCR-II forms are particularly indicative of a tendency of roots to maximise their surface in contact with the substrate.



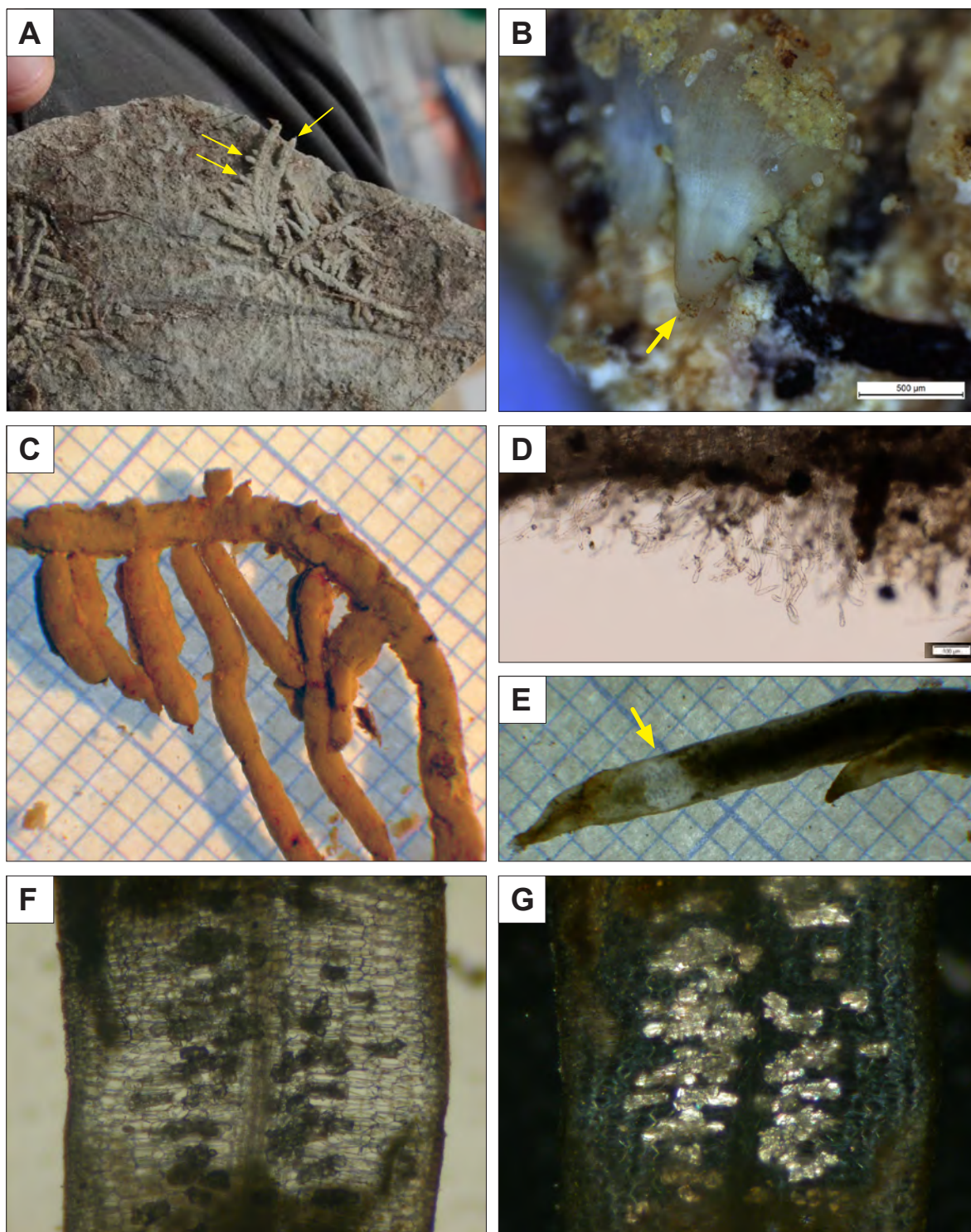


**Figure 3.13.** Living intracellularly calcified roots. A) Branched cluster of iCR on a surface of a piece of marl, showing clayey coating throughout the root surface except in terminal outgrowths (arrows), i.e., fresh, non-calcified root tips. Finestrat-Sella, site T15-823. B) Detail of sample in Fig. A: transparent, noncalcified root tip (arrow). Image of water-immersed root, taken under a stereomicroscope. C) Larger branched fragment of fully-calcified root with a thin non-carbonate coating. Sample immersed in water, millimetric paper for scale. Sella, site T14-463. D) Twisted root hairs of a subsample of root in Fig. C. PPL transmitted light photomicrograph. E) Fragment of partly calcified fine root with dissected part (arrow), cut through the cortex close to the vascular cylinder. Sella, site T14-463. F) PPL and G) XPL photomicrographs of the dissected part of the root in Fig. E showing discrete, calcite-filled cells, predominantly occurring in the central part, close to the vascular cylinder. See millimetric paper in fig. E for scale.



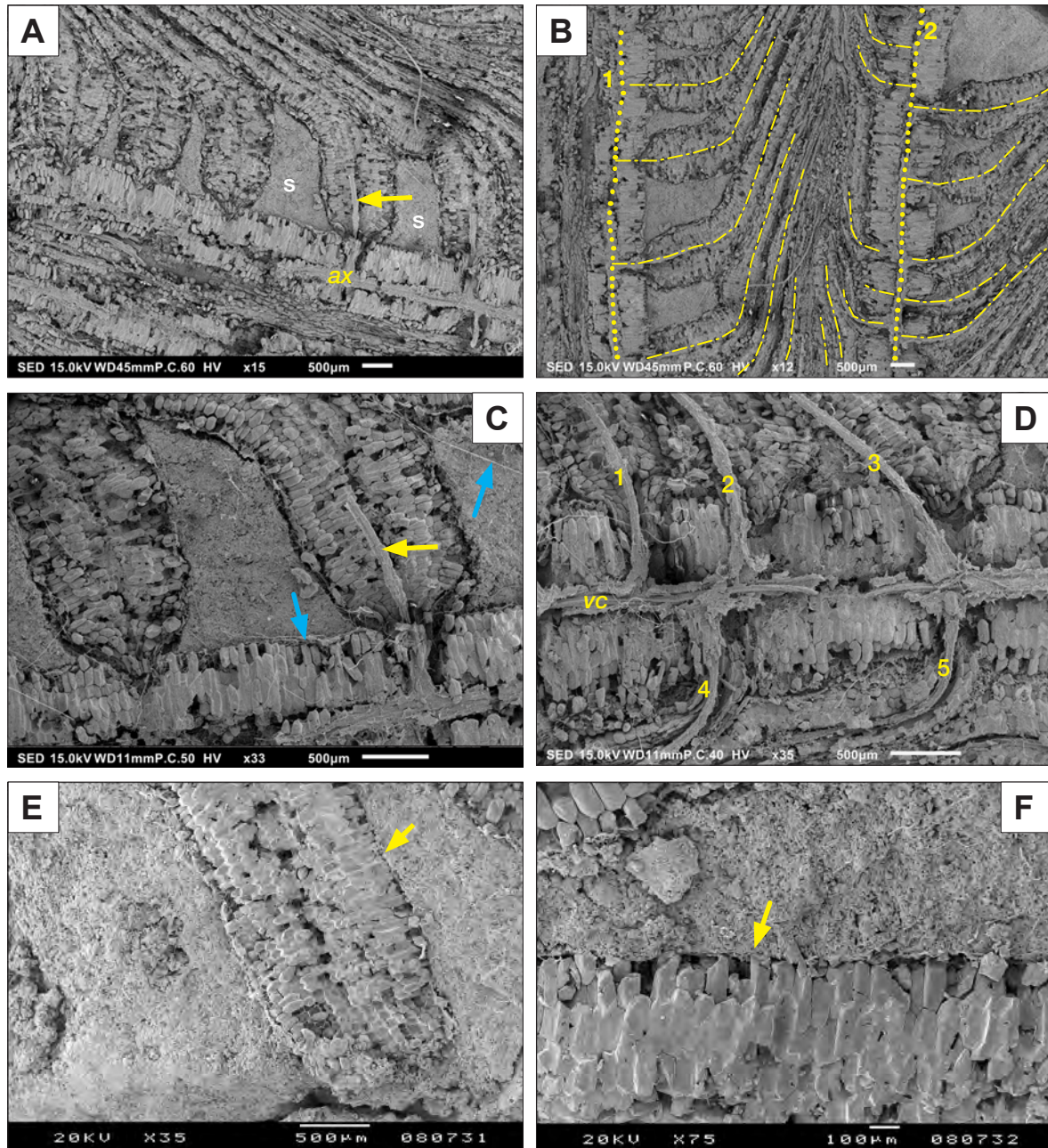


**Figure 3.14.** SEM photomicrographs of densely distributed type I iCR system. All images are from subsamples of iCRs in Fig. 3.11C (Sella locality, site T15-816). A) Distinctly regular 'herringbone'-type root system with a main root axis (ax) and lateral branches, mainly confined to one side of the main axis. Arrow: preserved organic tissue of the (non-calcified) vascular cylinder; s - marly substrate between fully calcified lateral iCR branches. B) Same sample as in Fig. A showing two main iCR axes (dotted lines 1 and 2) with their laterals, marked with thinner dash-dotted lines corresponding to the vascular system. Note difference in density and geometry of branching patterns between 1 and 2, and their 'mutually' arranged, parallel-aligned lateral iCRs. C) Detail of iCR in Fig. A: yellow arrow: organic tissue of a vascular cylinder; blue arrows: fungal hyphae. D) iCR fragment with preserved vascular tissues showing a typical herringbone-type branching pattern composed of a main root axis (vc) and lateral branches (numbered 1 to 5). E and F) iCR with fully calcified cortex. Arrows indicate direct contact of calcified cortical cells with the substrate without a gap which would correspond to (non-calcified) epidermis. Cf. *Microcodium* in Fig.5.12 and Fig. A5-4.10.



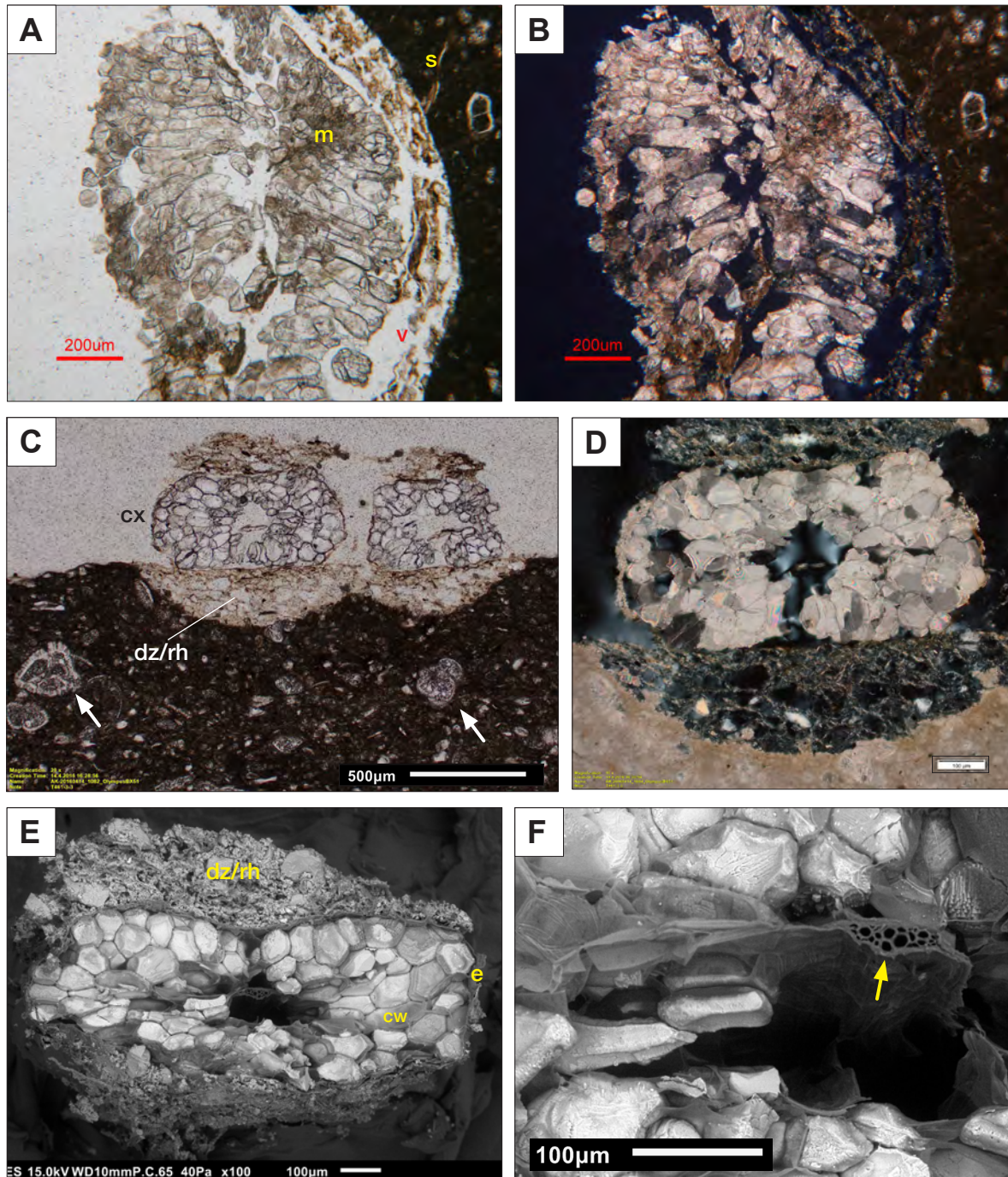


**Figure 3.15.** Bilaterally symmetrical type I iCRs. A) PPL and B) XPL thin section photomicrographs of an iCR aggregate, without preserved organic parts, in cross section; partly micritised (**m**) and in some parts slightly displaced fully calcified cortical cells; void (**v**) between iCR and the substrate on the right-hand side (**s**) is partly filled by clayey material. C) PPL thin section photomicrograph of two iCR-I in cross section; **cx** - calcified cortex, **dz/rh** - carbonate-depleted/root hair zone filling up a dissolution/corrosion channel in marly limestone with planktic forams (white arrows). D) Detail of Fig. C in XPL. E, F) Flat but laterally symmetrical iCR with centrally located vascular cylinder (cf. schematic drawing in Fig. 3.9C); **dz/rh** - carbonate-depleted/root hair zone; organic tissues are partly preserved: **e** - epidermis, **cw** - cell walls, yellow arrow (in F): collapsed xylem vessels. SEM BES (backscattered ('shadow') imaging mode).

All samples: Finestrat-Sella locality, site T14-461.



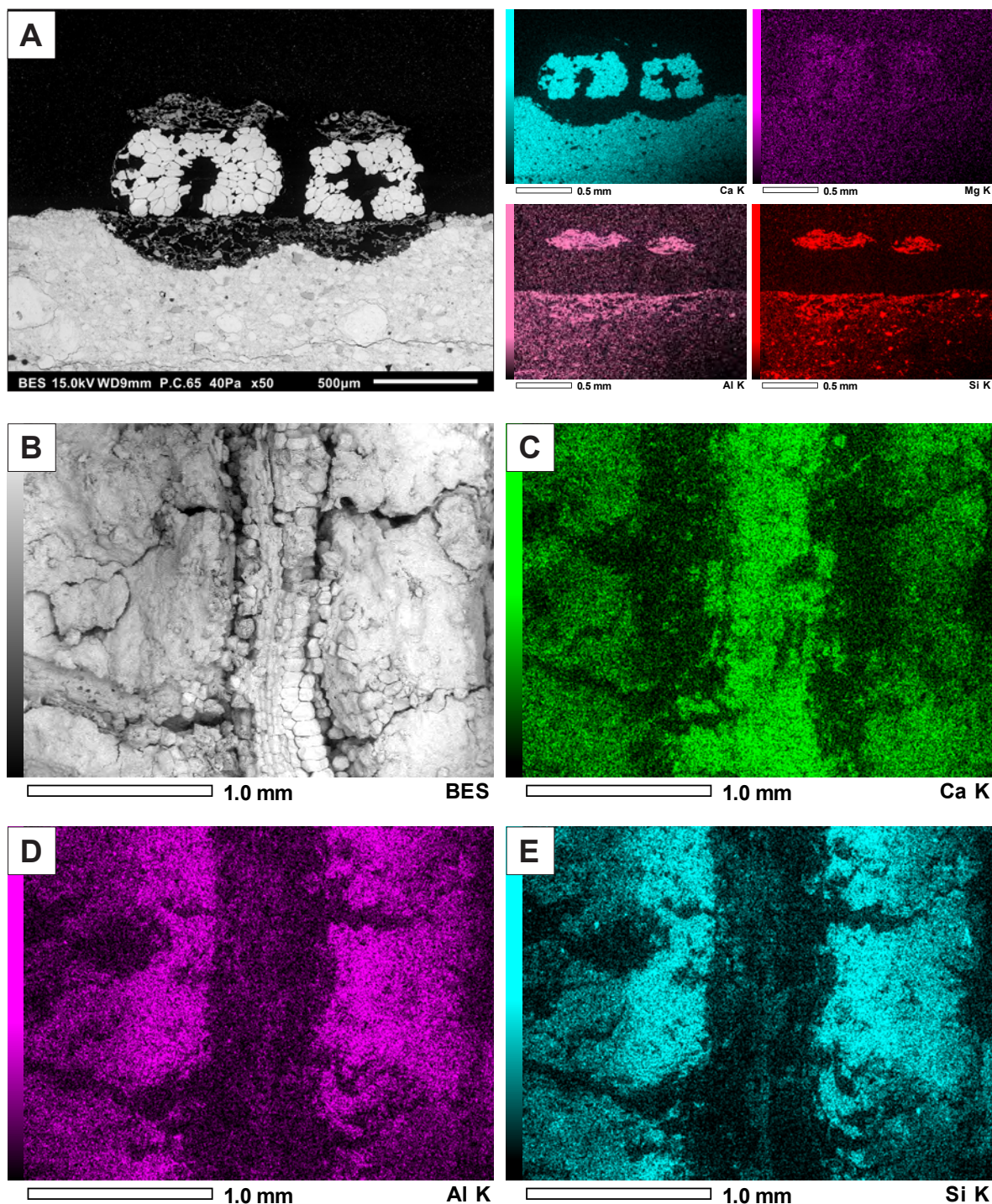


**Figure 3.16.** Backscattered electron SEM images and EDS elemental maps of type I iCRs. A) Left: BES image of two iCRs (cf. thin section photomicrograph in Fig. 3.15C); right: elemental maps for Ca, Mg, Al and Si. Note depletion of Ca corresponding to the extent of root hairs and the corresponding concentration/enrichment of Al and Si. B) BES image of a longitudinal section of iCR in Fig. 3.8B, split approximately through the center of the root. C-E) Elemental maps of Ca, Al and Si showing Ca depletion (C) in approximately 0.5 mm wide zone on both sides of iCR and corresponding concentration of Al (D) and Si (E), all representing the extent of the rhizosphere. Images B-E: sample A561\_IBI-08, Ibi locality, site T14-464. EDS mapping performed in quick mode (12 sweeps).

### 3.4.3 Anatomy of iCRs

Normal cellular tissues of fine roots (see diagram in Fig. 2.12) can be considerably modified by the intracellular crystal growth. Calcified parts of fine roots, in general 0.5 to 2 mm in diameter, are generally thicker than non-calcified fine roots and are often composed of radially elongate calcified cortical cells, indicating radial cell expansion which gives rise to a 'fat root' appearance (Figs. 3.3E, 3.8C, 3.13C). This makes a substantial deviation of iCRs from a normal cellular anatomy of fine roots, where the zones behind the growing tip (apical meristem) show longitudinal elongation of cells (Fig. 2.12). Precipitation of  $\text{CaCO}_3$  is limited to the cells of the cortical parenchyma, while the cells of the apical meristem, vascular cylinder and the epidermis are typically not calcified.

Anatomy of calcified cortex is primarily controlled by the overall morphology of iCRs. Fully calcified, symmetrical iCRs are generally composed of isodiametric to moderately elongate cells (Fig. 3.15C-F), 25 to 200  $\mu\text{m}$ , most often between 50 and 100  $\mu\text{m}$  in diameter (Fig. A3-4.05). In flattened morphologies of both symmetrical and asymmetrical iCR types, calcified cortical cells attain pronouncedly elongate shapes (Figs. 3.14, 3.17, 3.19), reaching lengths of 250 to 400  $\mu\text{m}$  and length:width ratio up to 8:1 (Fig. 3.22A-D). In bilaterally symmetrical iCR-I type roots, cortical cells are often aligned in parallel radial rows (Fig. 3.14D - F), arranged perpendicularly or at certain angle to the vascular cylinder (cf. Jaillard et al. 1991). In asymmetrical iCR-II morphologies, elongate cells generally appear aligned normal (i.e. with their long axes perpendicular) to the curve of the ventral side of iCR in contact with the substrate (Figs. 3.17, 3.19C, 3.20A, B, E, 3.22A). Cell elongation appears to be more pronounced in cortical layers on the dorsal side (Figs. 3.20A, B, 3.22A, B). In longitudinal cross sections, iCR-II forms consist of series of parallel-aligned elongate cells (Figs. 3.17A, B, C, E, F), a cellular palisade texture analogous to the arrangement of cells in lamellar *Microcodium* colonies (Section 5.3, Fig. 5.10, Fig. A5-4.06A, B).

Cortex of symmetrical iCR-I forms is typically composed of 3-6 cell layers (Fig. 3.15), whereas extremely compressed forms of iCR-II may consist of more than 10 cortical layers on each side of the vascular cylinder (Fig. 3.18).

Live intracellularly calcified roots and dead iCR aggregates, which are not yet fully decayed, incorporate remains of organic tissues. Calcified cortex may contain cell walls in different preservation states (Figs. 3.15E, F, 3.18C, 3.23A, E, 3.24B, C, Fig. A3-4.06A-D). Vascular cylinders, particularly xylem vessels, are often preserved (Figs. 3.10, 3.14) although



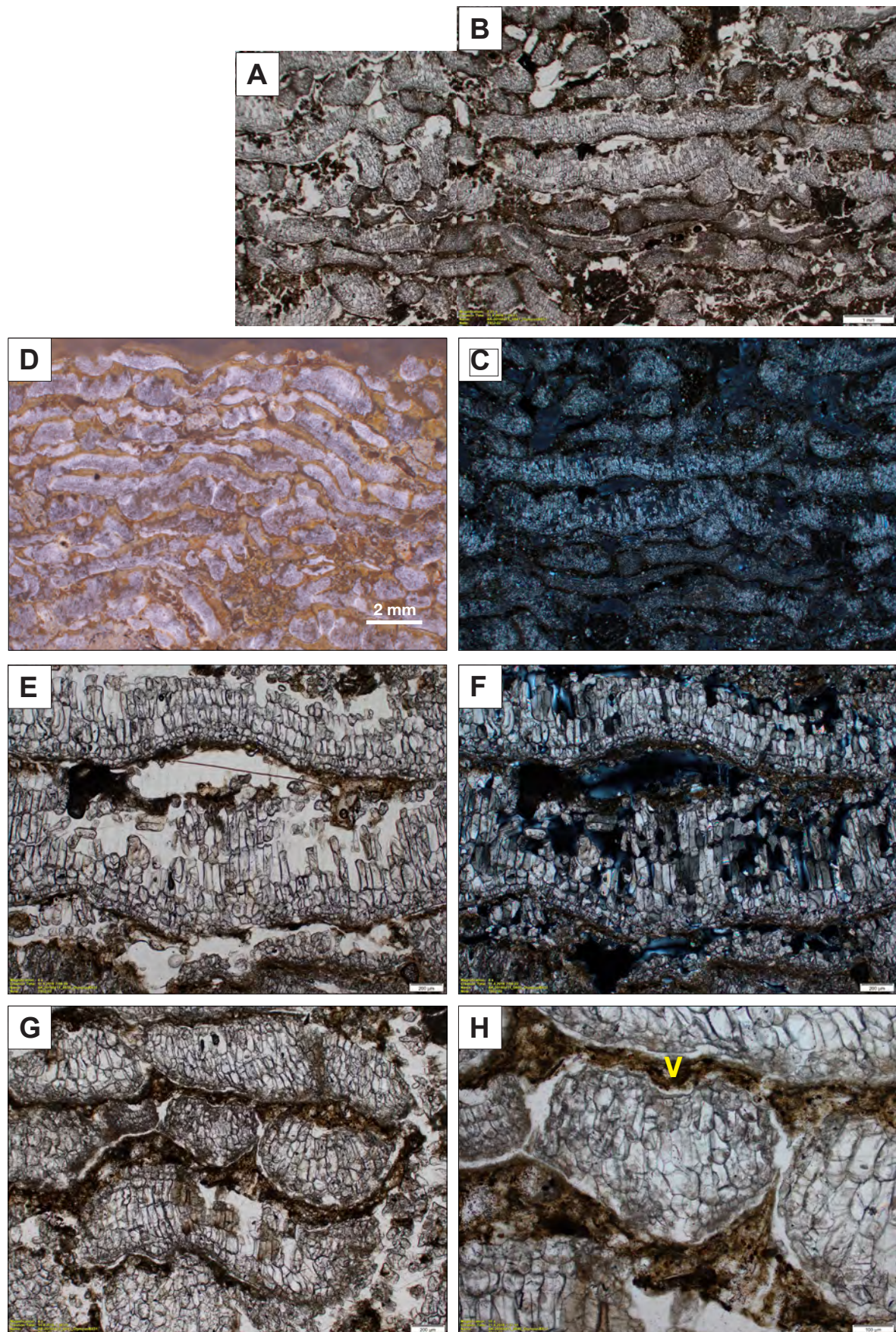
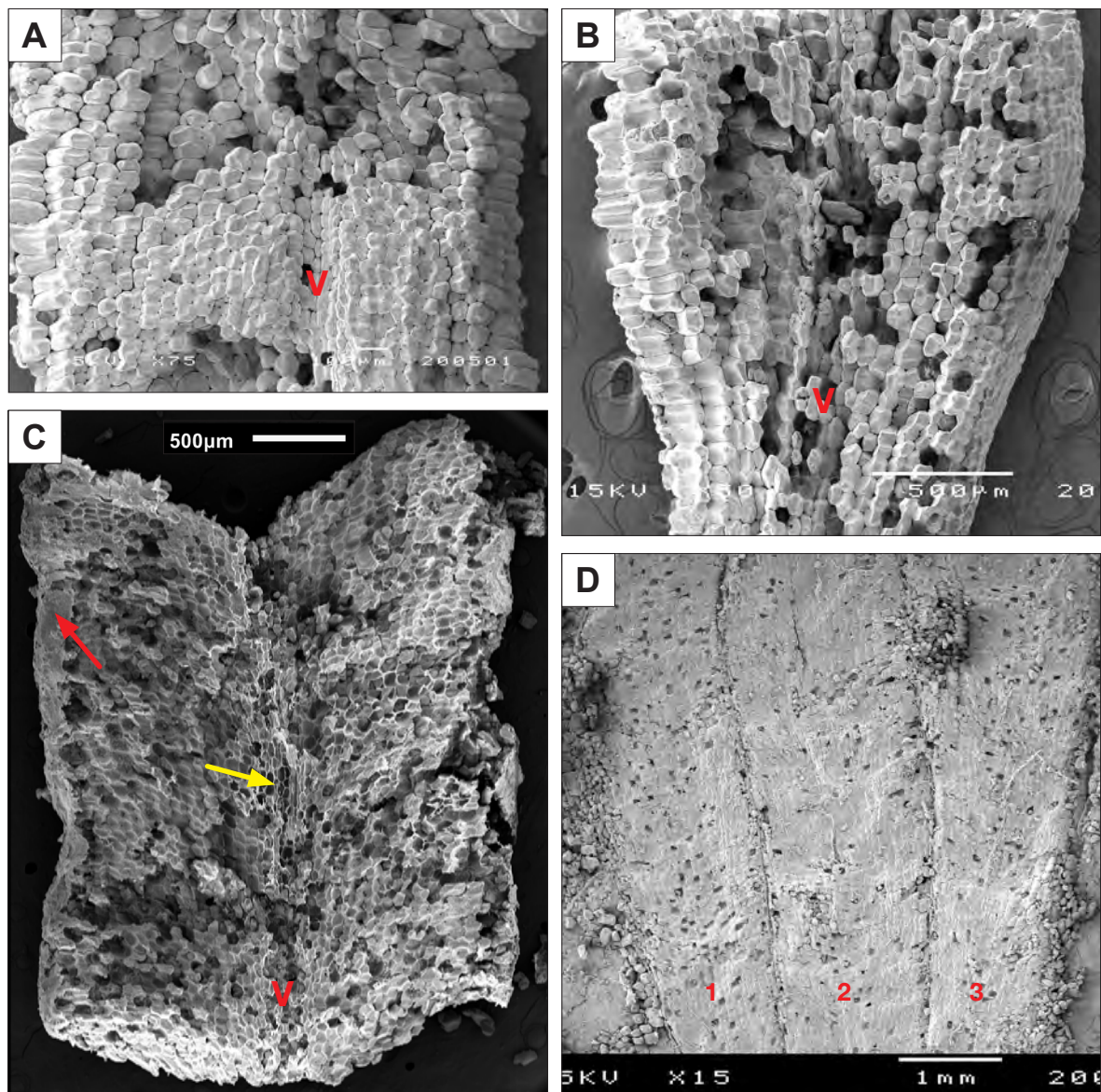


Figure 3.17. See caption on the following page.



**Figure 3.17.** (previous page). Asymmetric (type II) iCRs in thin sections, all samples from Penàguila, site T14-458. A and B) Collage of PPL photomicrographs of crudely layered (laminar) structure composed almost entirely of fully-calcified asymmetric iCRs in longitudinal and cross sections. C) XPL counterpart of Fig. B. D) A slab of resin-embeds iCRs remaining from thin section preparation. Note patches of non-carbonate (clayey) brownish material between iCRs and the resin. E) PPL and F) XPL photomicrographs (detail of Fig. B): longitudinal sections of iCRs composed of 4-5 layers of calcified cortical cells. Note strongly elongate cells in the lower iCR. G, H) Type II iCR in cross- and diagonal sections; v -groove corresponding to vascular cylinder. Cf. lamellar *Microcodium* structures in Chapter 5, Fig. 5.10, and Appendix A5-4, Figs. A5-4.06A, B.



**Figure 3.18.** SEM photomicrographs of type II iCRs, all in longitudinal orientation. A, B) Flat iCRs, dorsal side; Labels v indicate position of marginally placed vascular cylinder (not preserved). Penàguila, site T14-459. C) Flat iCR-II, dorsal view, with partly preserved cell walls (yellow arrow) and epidermis (red arrow); v - position of the vascular cylinder. Finestrat-Sella, site T14-462. D) Ventral side of three flat iCRs (labelled 1-3); note individual non-calcified (empty) cellular spaces. Cf. specimens in Fig. 3.11. Rellu, site T14-455.

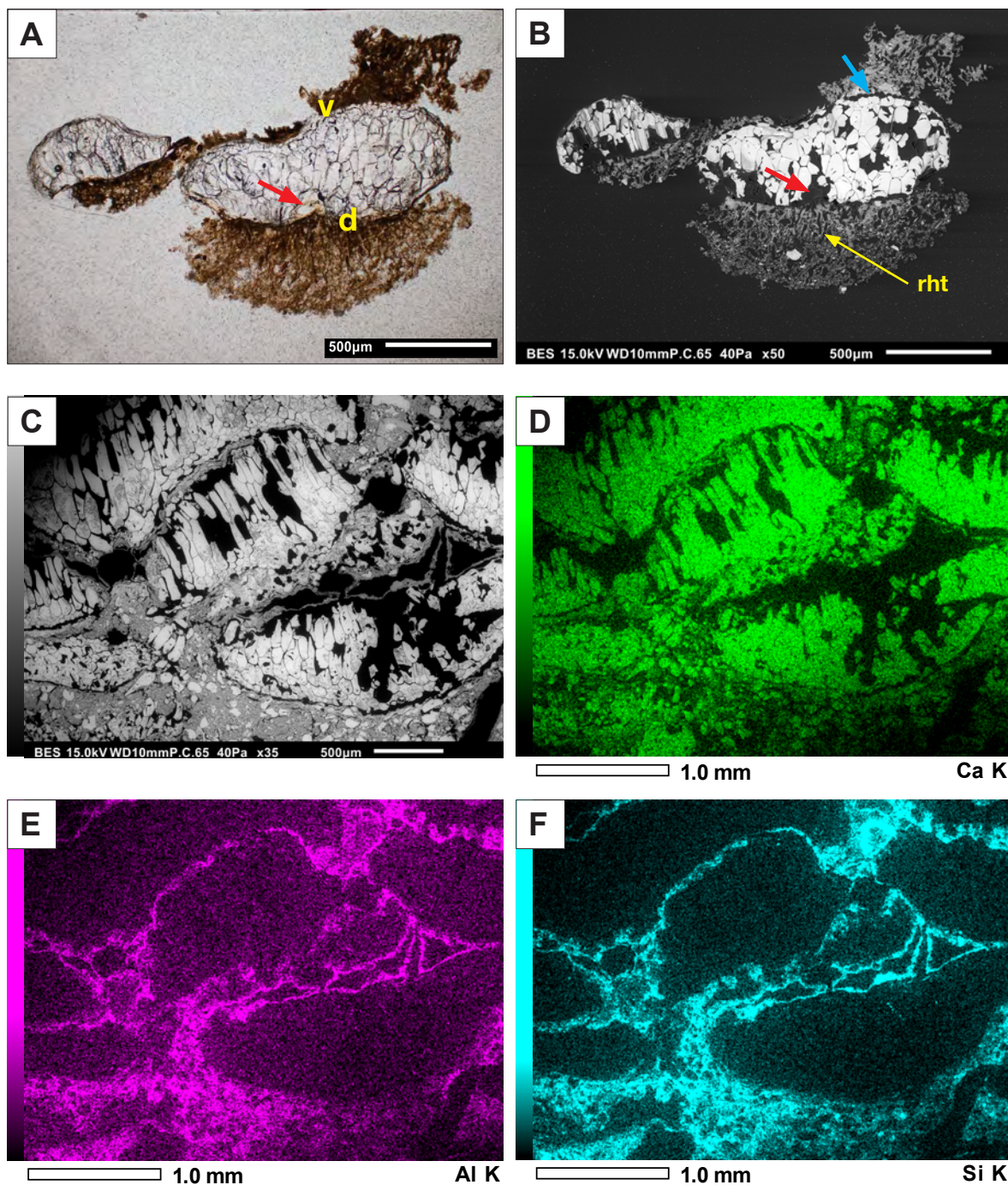


**Figure 3.19.** Asymmetric iCR-II aggregates under PPL and SEM.

A) PPL thin section photomicrograph of an isolated, dried and resin-embedded live iCR-II; v - ventral, d - dorsal side; red arrow: vascular cylinder with partly preserved xylem tissues (brown material). B) BES SEM counterpart of Fig. A with clearly visible root hair tubules (rht) in clayey cap (i.e., carbonate-depleted zone). Cyan arrow points to a thin layer of non-calcified cells of the epidermis; their rounded, swollen shapes and protrusive contacts with calcified cortical cells indicate normal cell turgor of the epidermis during the calcification of the cortex. See detailed view in Fig. A3-4.02A. Finestrat-Sella, site T14-462. C) BES photomicrograph of a polished, resin-impregnated thin section of asymmetric iCRs and corresponding EDS elemental maps of Ca (D), Al (E) and Si (F), respectively. Matrix between iCRs is composed of non-carbonate calyey material and individual calcified cells. C-F: Penáguila, site T14-458.



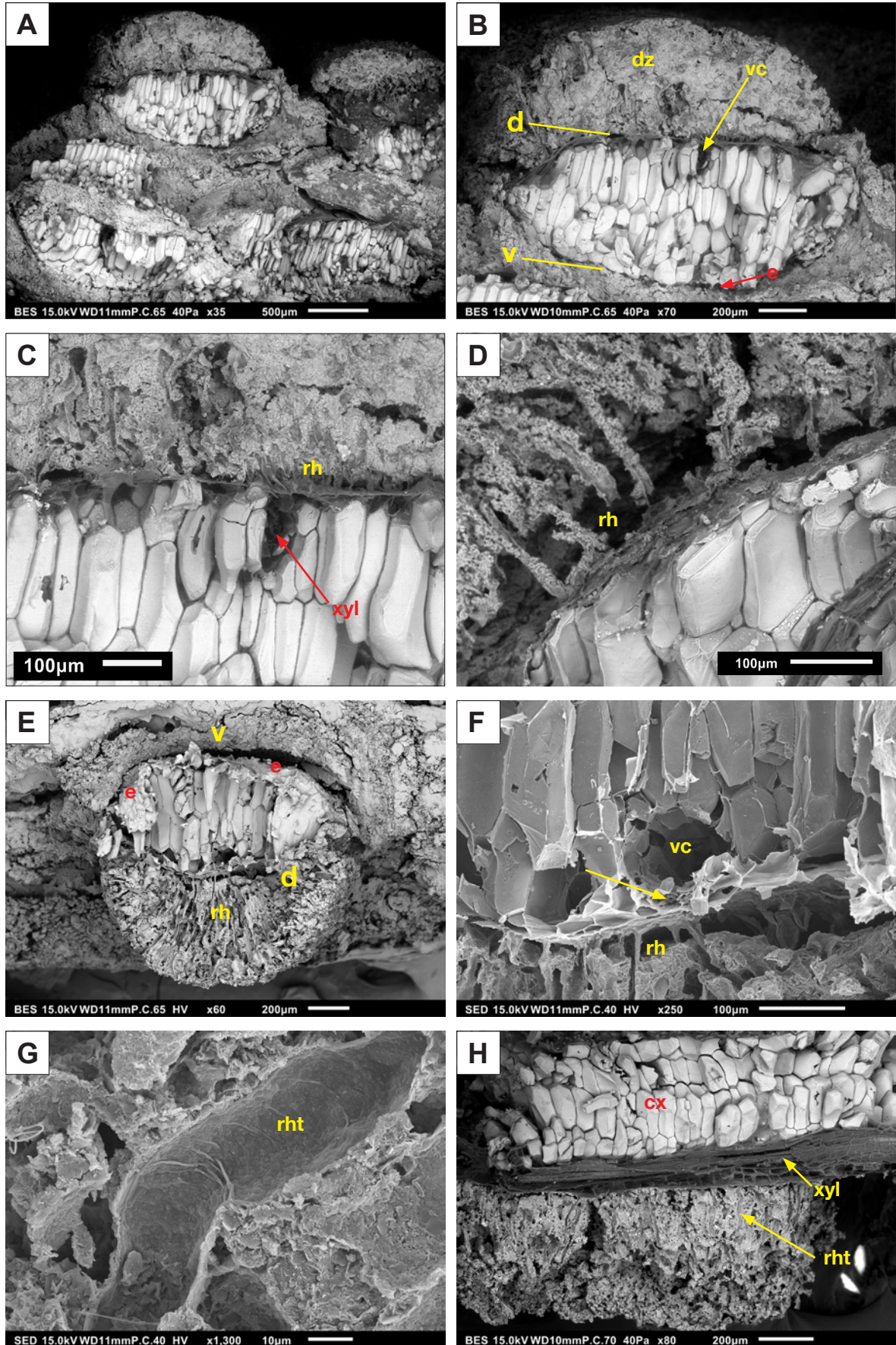


Figure 3.20. See caption on the following page.



**Figure 3.20.** (previous page). SEM photomicrographs of asymmetric iCR-II aggregates. **A)** Low magnification image of freshly broken surface of a cluster of intertwined iCR structures (sample in Figs. 3.12E, F). **B)** iCR-II in cross section showing thick dome-shaped accumulation of non-carbonate material (**dz**) on the upper (dorsal) side (**d**); **v** - ventral side, **vc** - vascular cylinder, **e** - epidermis. Note pronouncedly elongate calcified cells of the dorsal part. **C)** Close-up of Fig. B: **rh** - preserved root hairs emerging from a thin layer of epidermis on the dorsal side of iCR; **xyl** - relicts of xylem vessels. **D)** Well-preserved root hairs (**rh**) with thin veneers of clayey material. **E)** Perfect cross section of iCR-II with well-preserved epidermis (**e**) and root hairs (**rh**) in clayey matrix, forming a domed structure on the ventral side (**v**). Note apparent absence of root hairs on the dorsal side (**d**). Also see Figs. 3.21A, B and a diagram E in Fig. 3.9. **F)** iCR with collapsed xylem (arrow) in a hollow corresponding to the vascular cylinder. **G)** Internal part of a root hair tubule (**rht**). **H)** Longitudinal section of asymmetric iCR-II: **cx** - calcified cortex, **xyl** - xylem, **rht** - root hair tubules. All samples from Finestrat-Sella locality, site T14-462. Figures A-E and H: low-vacuum BES images of uncoated specimens; figures F and G: high-vacuum SED images of Au coated material.

typically with reduced size, contracted shape and collapsed cellular structure (Figs. 3.15E, F, 3.19B, 3.20B, C, F, H, 3.21A, F). Non-decayed dry iCR remains often show well-preserved epidermis (Figs. 3.15E, 3.20C, D, F, 3.21, Fig. A3-4.13C, D, E), in exceptional cases with root hairs, typically embedded in a clayey matrix of carbonate-depleted zone around roots (Figs. 3.15C-E, 3.19A, B, 3.20C-H, 3.21E, F, Fig. A3-4.02D-F). Non-calcified cells of the epidermis, which exhibit rounded, swollen shapes and protrusive contacts with calcified cortical cells (Fig. 3.19B and Fig. A3-4.02A), indicate normal cell turgor of the epidermis during the calcification of the cortex.

#### *3.4.4 Shape, ultrastructure and crystal morphology of calcified cells*

Even without preserved organic tissues, completely calcified roots accurately replicate the cellular structure of the cortex in which the entirely mineralised cells often retain the shape and topological details resulting from the arrangement and geometry of cell interfaces. In general, fully calcified cells exhibit various shapes of convex to concave polyhedra with curved faces (Figs. 3.15 E, 3.18A, B, 2.20, Fig. A3-4.05). Mosaics of fully calcified cortex show fitted cellular fabric with thin gaps, several  $\mu\text{m}$  wide, between the calcified cells corresponding to former organic cell walls (Figs. 3.16A, 3.19B). Larger non-calcified gaps (in triple or multiple cell junctions) correspond to intercellular spaces (Figs. 3.23F, 3.24B). Traces of intercellular spaces can be imprinted as facets along the edges of calcified cells (Figs. A3-4.05C, A3-4.06D). Discernable, overall cell shape can be preserved even in incompletely calcified cells (Figs. 3.24F, A3-4.05E).

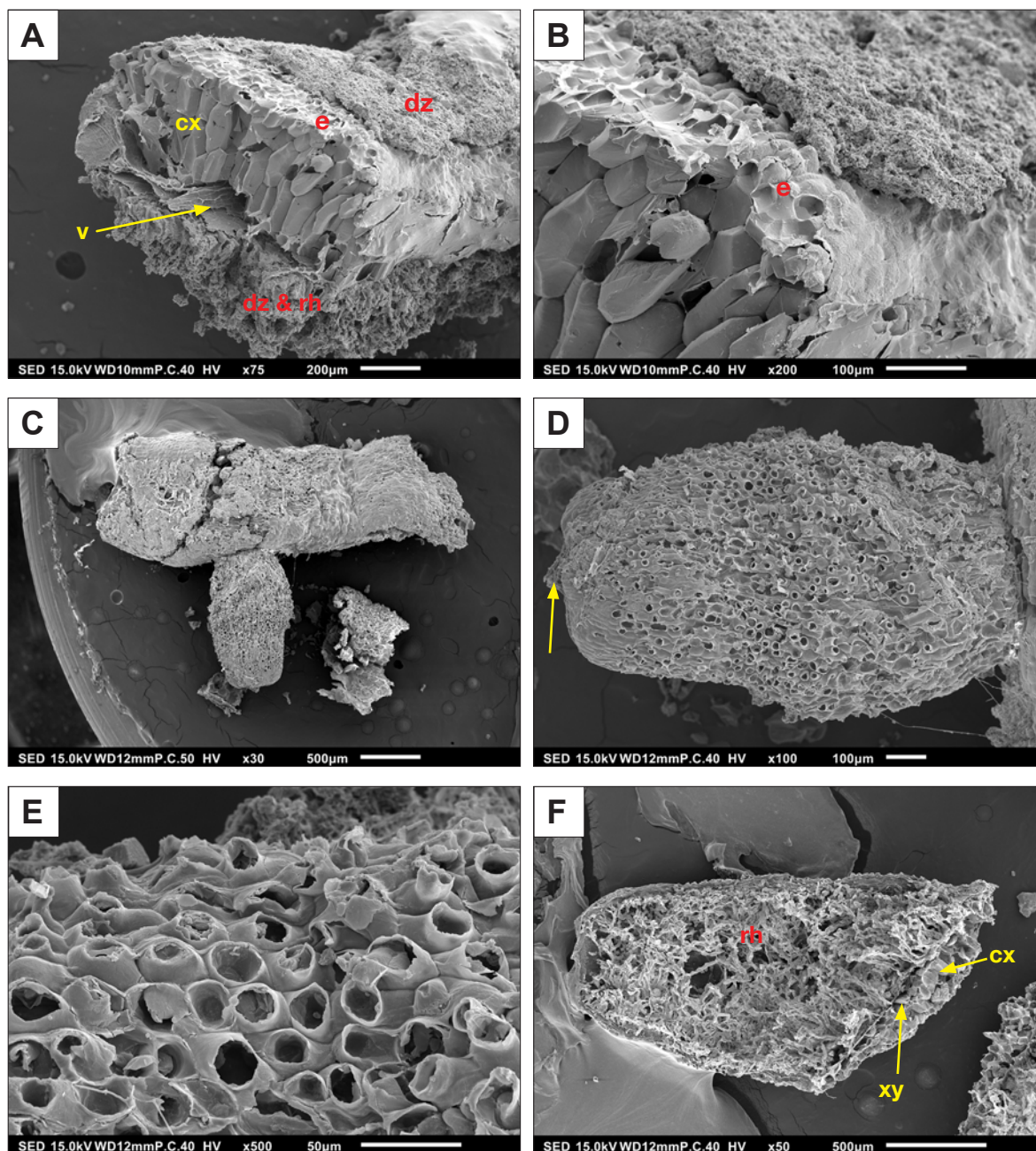


**Figure 3.21.** SEM photomicrographs of iCR-II specimen, Finestrat-Sella locality, site T14-462. All images in HV SED mode of Au-coated samples. A) Oblique view of iCR-II with preserved organic tissues; cx - calcified cortical cells, v - vascular cylinder cavity with relicts of cellular fabric; dz & rh - decalcified (carbonate-depleted) zone with root hairs, e - epidermis, dz - thin clayey layer covering epidermis on the ventral side. Cf. diagram E in Fig. 3.9. B) Close up of Fig. A: e - empty (non-calcified) epidermal cells, some having collapsed cell walls. C) Thicker fragment of iCR with a short lateral branch on the lower side. Ventral view. D) Detailed view of the short lateral root in Fig. C (arrow indicates the root tip), showing numerous ruptured (collapsed, blister-like epidermal cells), possibly representing short, root-hair like protuberances on the ventral side of iCR. E) Detail of Fig. D showing blister-like epidermal cells with ruptured (collapsed) outer walls. F) Fragment of flat iCR of the same root as in previous images, showing ventral side, covered with a dense mat of strongly twisted root hairs (rh); cx - thin calcified cortex; xy - remains of xylem.

Isolated, fully calcified individual cortical cells can replicate exquisite details of the cell wall texture such as folds (wrinkles; Fig. 3.22E) and fibrous fabric, possibly corresponding to cellulose fibril bundles (Fig. 3.22F), as well as micron-scale depressions and protuberances (Figs. 3.25E, A3-4.05F, G), probably representing traces of structures, connecting adjacent cells (e.g. plasmodesmata).

In standard thin sections, individual fully calcified cells show monocrystalline calcite or polycrystalline aggregate structure, commonly composed of two or more parts with different crystal orientation and uniform or undulose extinction patterns in cross-polarised light (Figs. 3.15A-D, 3.17B, C, E, F). Fragments of iCR, containing incompletely calcified cells, and particularly live and un-decomposed partly calcified roots, enable observation of different stages of intracellular mineralisation. Under SEM in backscattered electron imaging (BES) mode, cell walls may appear transparent under low vacuum (Fig. 3.23A) and exhibit very variable crystal ultrastructure and external morphology of intracellular (intravacuolar) carbonate precipitates. Figures 3.23A and B show high variability within a single iCR fragment, with individual cells composed either of calcite with rhombohedral, mesocrystalline or microlamellar ultrastructure. Secondary electron SEM images of parallel and interlaced microlamellar fabric (Fig. 3.23C-E, Fig. A3-4.07D) show highly porous crystal ultrastructure. In fully mineralised cells, porosity of primarily microlamellar structured calcite bodies appears to be occluded with second generation of calcite, yet showing well-distinguishable lamellar pattern in BES charge contrast images (CCI) in polished thin sections (Fig. 3.23F, Figs. A3-4.07A-F). Similarly, rhombohedral crystalline forms in incompletely calcified cells (Fig. 3.24A, B) are evident in BES CCI images (Fig. 3.24D), showing crystal growth lines.

Detailed SEM examination of calcified cells indicates that fully calcified cells with curved surfaces of calcite, reflecting the shape of the cell lumen (membrane), evidently form in a two-step process. A thin, several  $\mu\text{m}$  thick external layer, replicating the cell shape, is typically composed of mesocrystalline overgrowths (coatings) of the underlying coarser rhombohedral and lamellar crystal framework (Figs. 3.24E, F, 3.25, Figs. A3-4.08 to 4.10). The external layer often exhibit mesocrystalline structures formed through oriented (surficial parallel/epitaxial growth) assembly of nanosized globular particles or nano-scale polyhedral crystal blocks (Fig. 3.25C-H, Fig. A3-4-09C-E).



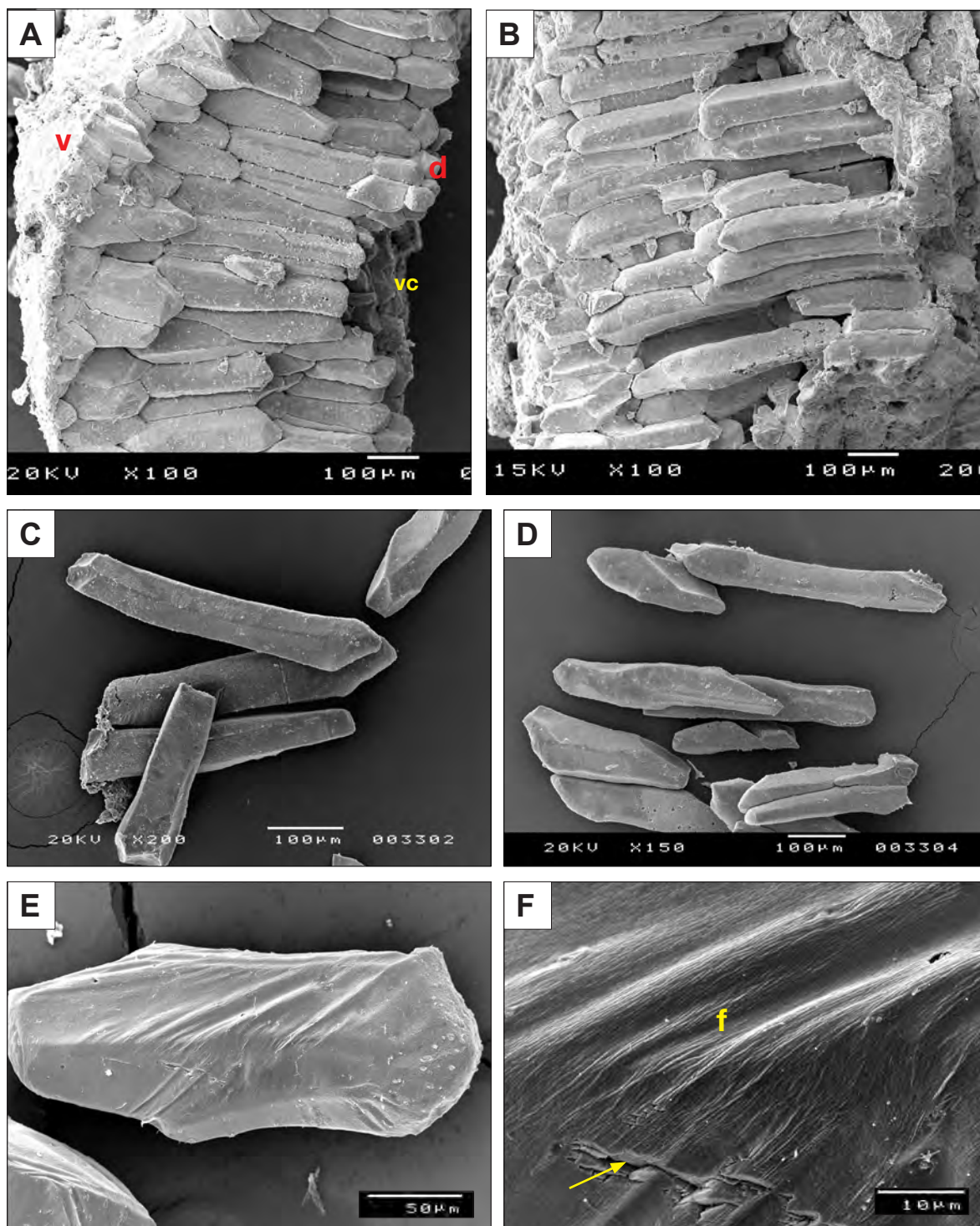


**Figure 3.22.** SEM images of strongly radially elongate cells in ‘shovel-type’, flat asymmetric iCRs. Penàguila locality (see Fig. 3.1 and Appendices A3-1 and A3-2). A) iCR aggregate in cross section; calcified cortex is composed of 3-4 layers of cells; v, d - ventral and dorsal side, respectively; vc - cavity/groove corresponding to a (non-calcified) vascular cylinder. B) iCR aggregate composed of prominently elongate calcified cells. Cross section of the iCR sample in Fig. 3.18B. C, D) Isolated elongate calcified cells. E) External morphology of a calcified cell renders an exact cast of a folded (wrinkled) cell-wall. F) Close-up of E showing detailed surficial morphology marked by a fibrous texture (f), probably representing cellulose fibril bundles, comprising the cell wall. Arrow indicates a step/irregularity in the crystal structure, corresponding to incomplete mineralisation of the external layer of calcite. Cf. Figs. 3.24C, D, 3.25B, C and Fig. A3-4.05G.

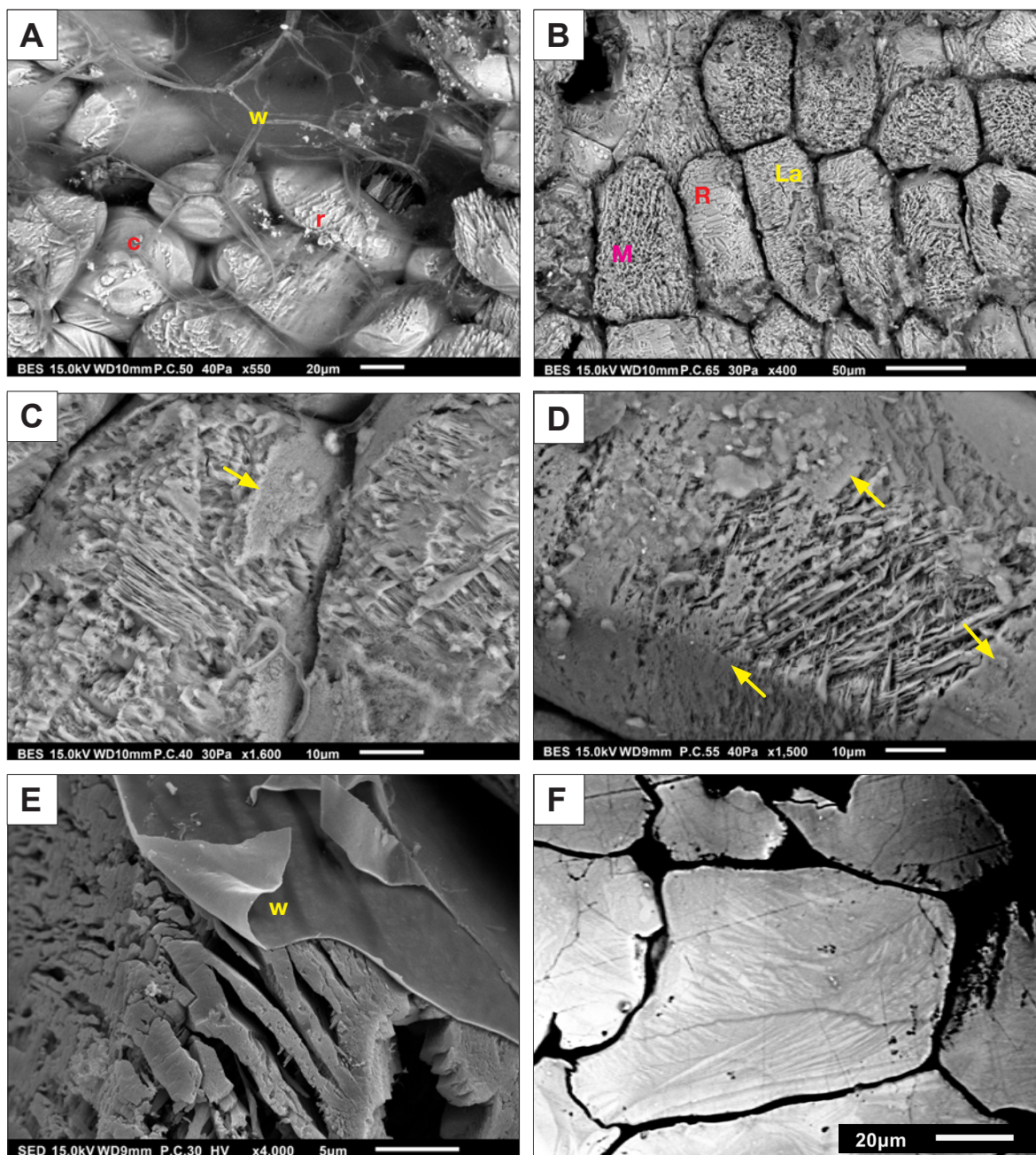


**Figure 3.23.** Ultrastructure of calcified cells under SEM. A) Fragment of partly calcified root with preserved cell walls (w) which appear transparent under low vacuum BES imaging mode. Some cells are apparently completely calcified (c), i.e., cell lumina are entirely filled up by calcite, rendering cell morphology, including minute details as  $\mu\text{m}$ -size plies of cell walls, whereas other cells show calcite bodies with irregular external morphology, with rhombohedral mesocrystalline shapes. B) Cortical cells filled with calcite exhibiting very variable crystal ultrastructure from rhombohedral (R), mesocrystalline (M) to lamellar (La). C and D) Calcified cells exhibiting parallel microlamellar and crossed (interlaced) lamellar ultrastructure. Arrows indicate thin, nanocrystalline overgrowth layers of calcite, resulting in perfect cast of cell lumen. E) Porous, incompletely calcified cell composed of microlamellar calcite; w - preserved organic cell wall. F) Charge contrast image of a polished thin section. Ultrastructure of fully-calcified cells characterised by cross-lamellar microstructure, analogous to cells in Figs. C-E. Image taken low-vacuum BES mode. Sella, site T14-463. Also see Fig. A3-4.07.

Figures A-D: uncoated material, LV BES images; figure E: HV SED image of Au-coated sample.



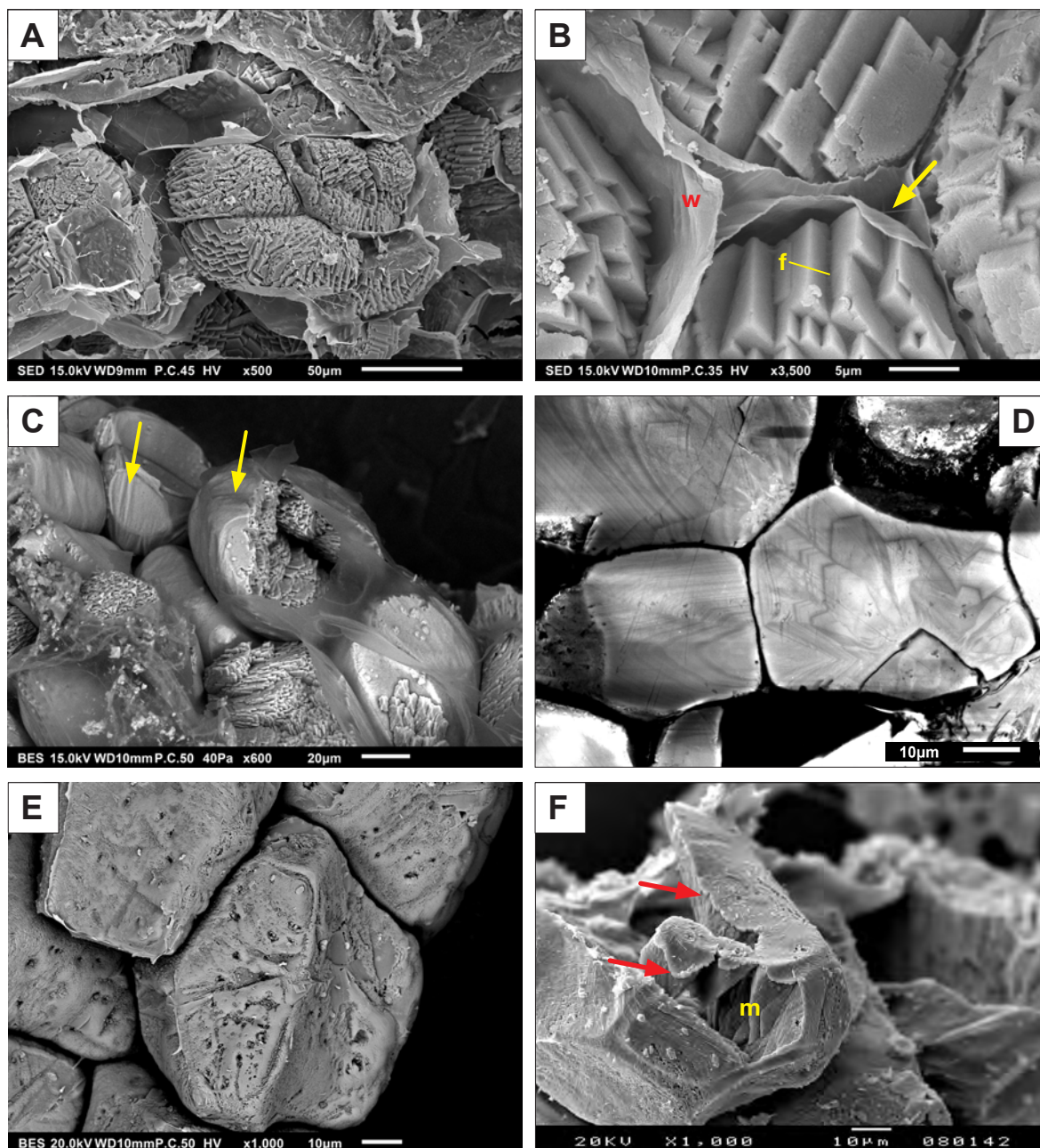


**Figure 3.24.** Ultrastructure of calcified cells under SEM. A) iCR cortical cells with rhombohedral (stepped polyhedral) calcite filling up most of the cell space. B) Detail of iCR in Fig. A showing well-preserved cell walls (w); rhombohedral calcite bodies are covered with a thin organic film (f) possibly representing contracted vacuolar membrane (tonoplast). Arrow indicates empty, non-calcified intercellular space. HV SED image. Finestrat-Sella, site T14-461. C) Partially calcified cortical cells of a pot-grown *H. coronarium* plant. Rhombohedral crystal bodies with partial overgrowths forming smooth calcite surfaces, replicating internal cell shape (arrows). LV BES image. D) Charge contrast BSE image of polished thin section. Calcified cells with crystal growth lines corresponding to rhombohedral shapes in 3D (cf. Fig. B). E) Calcified cells with thin external layer composed of globular, nanocrystalline particles, forming aligned textures. LH BES image. Finestrat-Sella, site T14-461. F) Incompletely calcified cell composed of calcite mesocrystals (m) and partly overgrown with several  $\mu\text{m}$  thick calcite layer, replicating the cell shape. HV SED image. Sella, site T14-463.



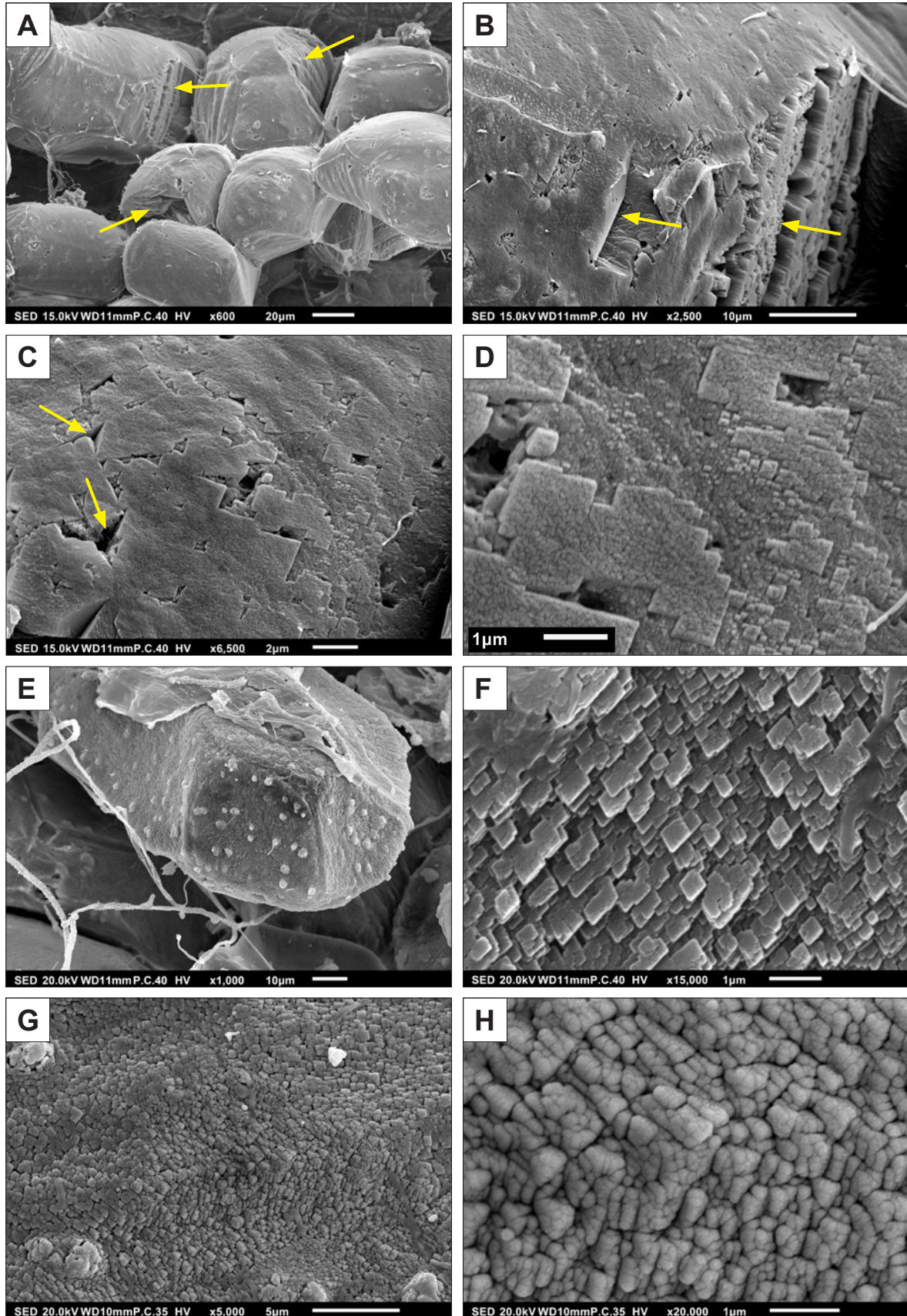


Figure 3.25. See caption on the following page.

**Figure 3.25.** (Previous page) Vacuolar crystal maturation and microstructure of external layer of iCR cells. All images taken in HV SED mode of Au-coated samples. Also see Figs. A3-4.08 to 4.10. A) Calcified cortex composed of almost completely calcified cell volumes and perfectly replicating textural details of flexible cell walls. Arrows indicate large irregularities in primary calcite crystal not covered with external layer. B) Detail of A showing smooth surface of the external layer and exposed crystal faces of the underlying, primary calcite crystal (arrows). C, D) Sub-micron thick mesostructured layer, formed through oriented (surficial parallel/ epitaxial growth) assembly of nanosized globular-to-polyhedral crystal blocks. Arrows indicate hollows - irregularities in the basal crystal, not (yet) overlain by the external, nanocrystalline layer. Also see Figs. A3-4.8C, D, E. Sella, site T14-462. E) Fully calcified cell exhibiting rough, nano-textured surface. Bulges, 2-3  $\mu\text{m}$  in diameter, possibly correspond to plasmodesmata - pores that span the adjoining walls of plant cells. F) Detail of E: mesostructured calcite crystals forming the surficial layer: rhombohedral crystallites formed through epitaxial growth on a larger basal crystal. G, H) Higher magnification images of E: external calcite layer apparently formed by aggregation of globular (possibly amorphous or poorly crystalline) nanosized particles (cf. measurements in Figs. A3-4.09E and 4.10F). High magnification image (H) shows mineral fabric consistent with aggregation structures of metastable particles, such as liquid, amorphous, or poorly crystalline particles, or of oriented (and nearly oriented) attachment of metastable nanocrystals, described by De Yoreo et al (2015).

Sample SLL-38, Sella locality, site T14-463.

#### 3.4.4.1 Non-vacuolar, small-scale mineral precipitates

In iCRs with preserved organic cell walls, empty cells commonly contain small-scale crystal forms, which are not related to intravacuolar calcification but most probably formed independently after the intracellular calcification process has completed (post-mortem). These forms include small, several 10s  $\mu\text{m}$  large calcite crystals with regular crystal surfaces (Fig. 3.26C), disc-shaped crystal bodies, 5-10  $\mu\text{m}$  in diameter (Fig. 3.26D and Figs. A3-4.11D, 4.12A), and druses of similar dimension (Fig. A3-4.11C), appearing on the surface of cell walls. Bulbous forms (Fig. A3-4.12C, D) and submicron-sized precipitates, concentrated at discrete points along the cell wall (Fig. 3.26F), possibly precipitate on spots of the cell wall corresponding to plasmodesmata (Fig. 3-4.12E, F). Calcite mineralogy of these forms has not been confirmed.

Another feature, unrelated to precipitation within the cell vacuoles, are calcite bodies, which replicate the shape of intercellular spaces. These forms can be occasionally observed between the fully calcified cells (3.26A) or within collapsed organic cell tissues (Fig. 3.26B). Rarely, individual cells of the outermost cortical layers in incompletely calcified iCR aggregates exhibit 1-10  $\mu\text{m}$  thick irregular layers of calcite, coating the cell wall (Fig. A3-4.11E, F). Presumably, these calcification forms are not related to intracellular calcification but correspond to post-mortem precipitation on decomposing cell wall material (cf. fine root rhizoliths in Chapter 2).



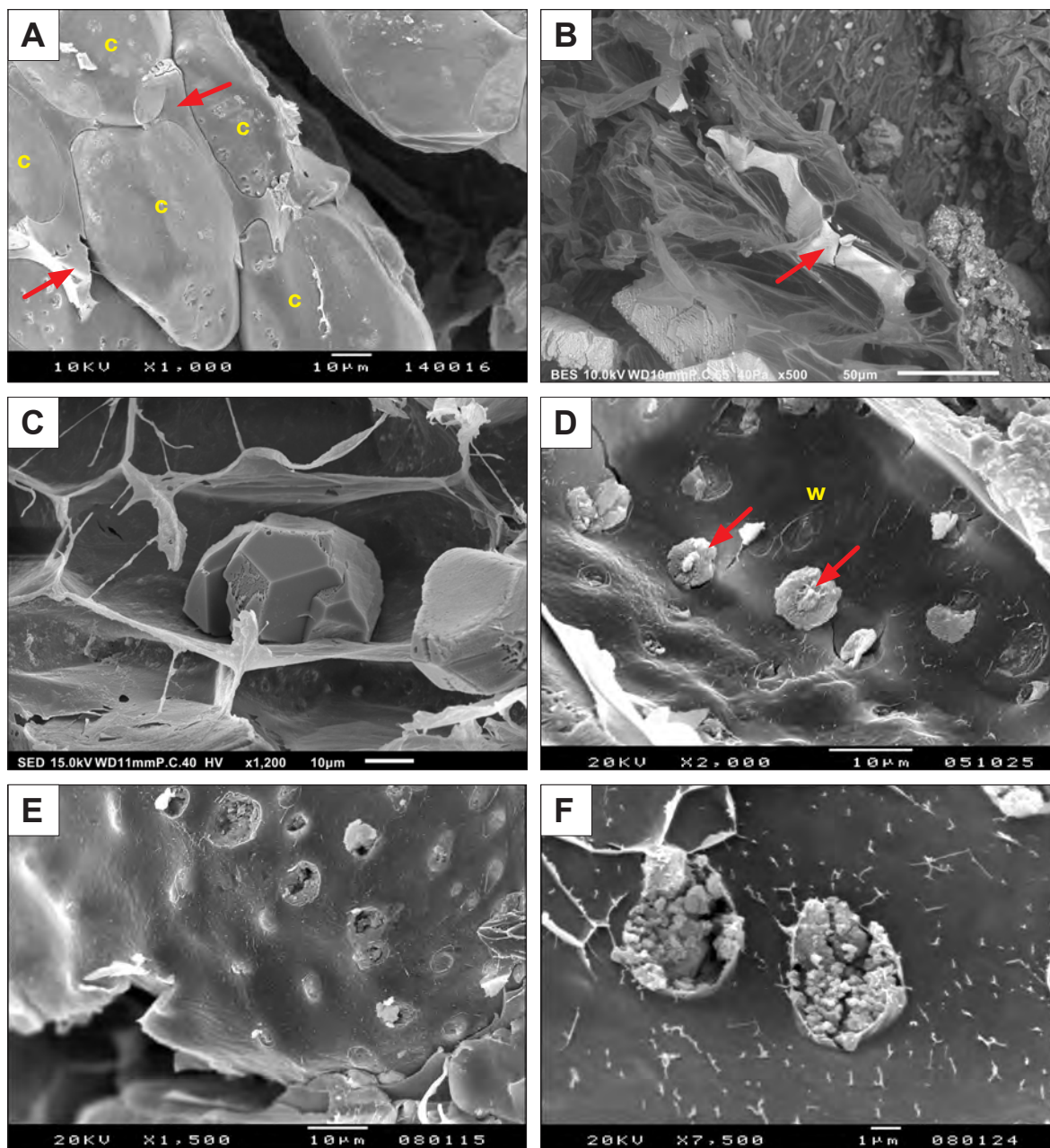


**Figure 3.26.** SEM photomicrographs of non-vacuolar, small-scale crystal forms. A) Calcite bodies (arrows) formed by entirely mineralised intercellular space (between full calcified cells (c)). B) Isolated intercellular calcification form (red arrow) enclosed in collapsed, semitransparent cell walls. Lab-grown *Hedysarum coronarium* iCRs. C) Calcite crystal with regular crystal faces grown on a cell wall. Finestrat-Sella, site T14-462. D) Interior of a cell with disc-shaped crystal bodies, 5-10  $\mu\text{m}$  in diameter, formed on the surface of the cell wall. Sella, site T14-463. Cf. forms illustrated by Jaillard (1987), their Figs. 5-11c-f. E) Fully calcified iCR cell, coated with relicts of a cell membrane. Protuberances and perforations probably correspond to plasmodesmata. Sella, site T14-463. F) Cell interior: fine grained ?calcite precipitates in hollows in the cell wall. Sella, site T15-816.

Images A and C-F taken in HV SED mode on Au-coated material; image E taken on uncoated sample in LV BES mode.

Also see Figs. A3-4.11 and A3-4.12.



#### 3.4.4.2 *Internal filamentous microfabric of calcified cells and weathered iCR aggregates*

Unaltered iCR calcite aggregates in thin sections and individual cells in transmitted light under a stereomicroscope are limpid. However, iCR aggregates often appear white and non-transparent. In thin sections, calcite of such weathered iCR aggregates displays opaque patches within otherwise limpid calcite of individual cells or whole cells, apparently unselectively affected by micritisation (Figs. 3.27A, B) or showing layered alteration patterns, following growth lines and intercrystalline boundaries in calcite crystals (Figs. 3.27C-F). Backscattered electron SEM images of polished thin sections (Fig. 3.28) clearly show that the micritisation is due to microendolithic modification of calcite. Microborings are of uniform tubular shape, approximately 0.5  $\mu\text{m}$  in diameter, and clearly follow intercrystalline layers in calcite, reflecting different composition (charge contrast image in Fig. 3.28C and EPMA backscattered electron image in Fig. 3.28F), most probably with endolithic borings following layers with higher amount of incorporated organic matter (fluorescence image in Fig. A3-4.14J; also see Section 5.6). Microborings are most probably produced by fungi which possess enzymes capable of digesting organic matter, incorporated in calcite (Glaub et al. 2007; Golubic et al. 1975, 2005; Golubic and Schneider 2001; Wisshak 2012; Taylor et al. 2015). Figure 3.29 shows 3D geometry of microborings and a drastic extent of microendolithic alteration of calcite, seen in resin-casted samples. In addition to layered structures, endolithic microborings can form small arbuscular structures, 20-40  $\mu\text{m}$  in diameter, apparently emerging from/through the surface of a calcified cell (Fig. 3.30 and Figs. A3-4.14I-L).

Microbial endolithic alteration probably starts almost instantly after the completed calcification of cortex as evidenced by preserved organic part of roots containing calcified cells infested by microendoliths. In addition to apparently rapid modification of original calcite by microbial endoliths, once released into the soil media, calcified cells can get intensively transformed by microbial weathering. Incompletely disintegrated iCR aggregates may still show recognisable cellular structure, although strongly obliterated by dissolution of original calcite and re-precipitation of carbonate in the form of needle fibre calcite and calcite nanofibres (Fig. 3.31A). Degraded cells often show dissolutional features (Fig. 3.31C) and are associated with Ca-oxalate encrusted fungal hyphae (Fig. 3.31B). With progressive, predominantly microbially induced alteration and partial replacement by fibrous microcrystalline carbonates (Fig. 3.31D), cell-shaped calcite grains lose their characteristic form and can finally transform into peloids (Figs. 3.31E, F). Progressive weathering stages can be well observed in larger, differentially preserved iCRs fragments (Figs. A3-4.15 to A3-4.18).

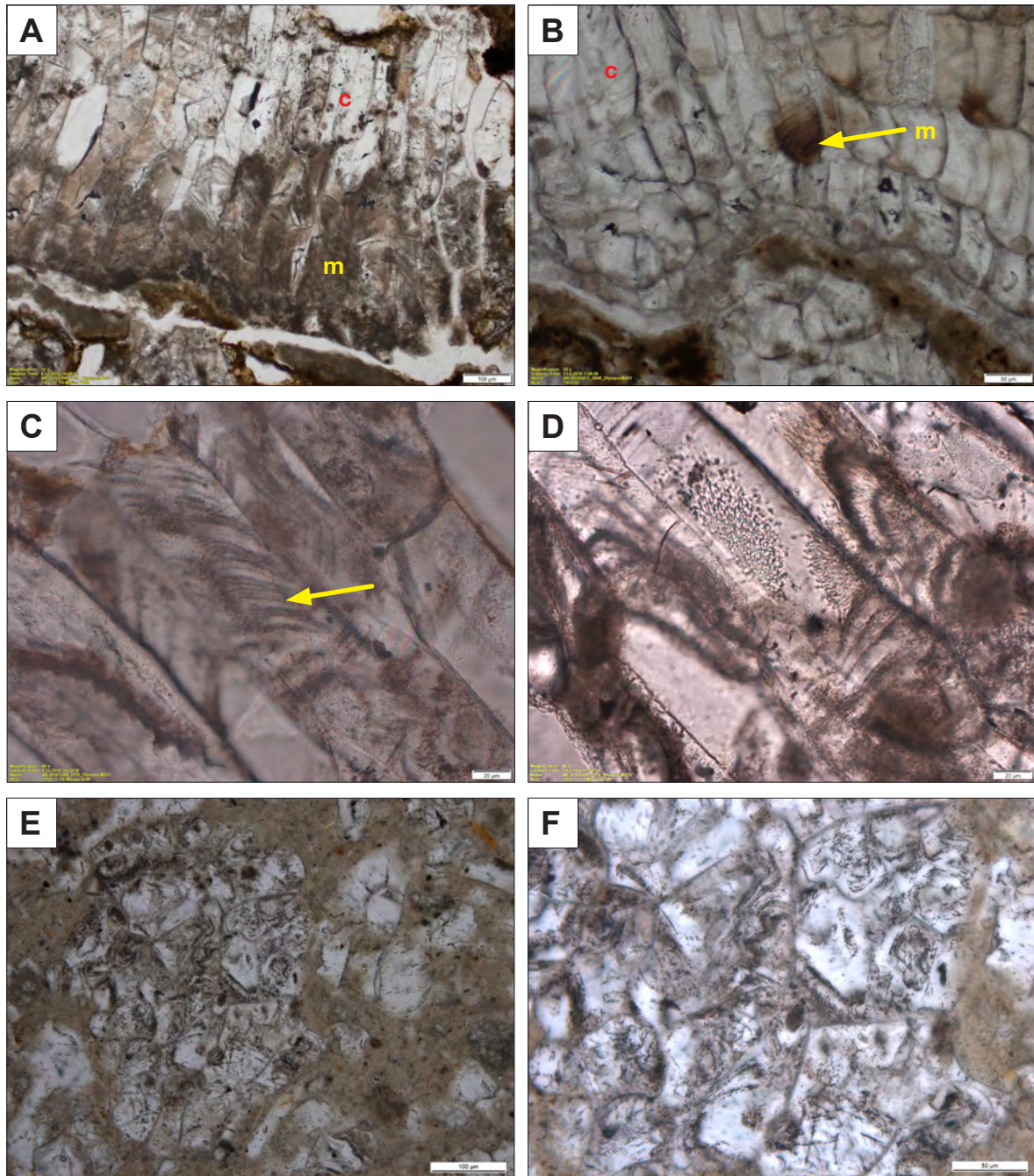


**Figure 3.27.** Micritisation of iCR calcite by microendoliths. Thin section photomicrographs in PPL. A and B) Type II iCR composed of elongate calcified cells. *c* - limpid, non-modified calcite, *m* - brownish, cloudy calcite. C) Strongly elongate calcified cell with layered structure enhanced by endolithic microborings following crystal growth lines (arrow), possibly corresponding to intracrystalline lamellae with incorporated (occluded) organic matter. Cf. SEM images in Figs. 3.28 and 3.29 and strongly similar textures in *Microcodium* shown in Figs. 5.21F and 5.22C. D) Dendroid pattern of endolithic microborings. E, F) Partly disaggregated iCR in fine grained matrix. Endolithic borings largely aligned along intracrystalline layers. Cf. CC image in 3.24D, BSE images in Fig. 3.28 in resin casts in Fig. 3.29. Samples in A-D: Penàguila, site T14-457; E, F: Finestrat-Sella, T15-823.



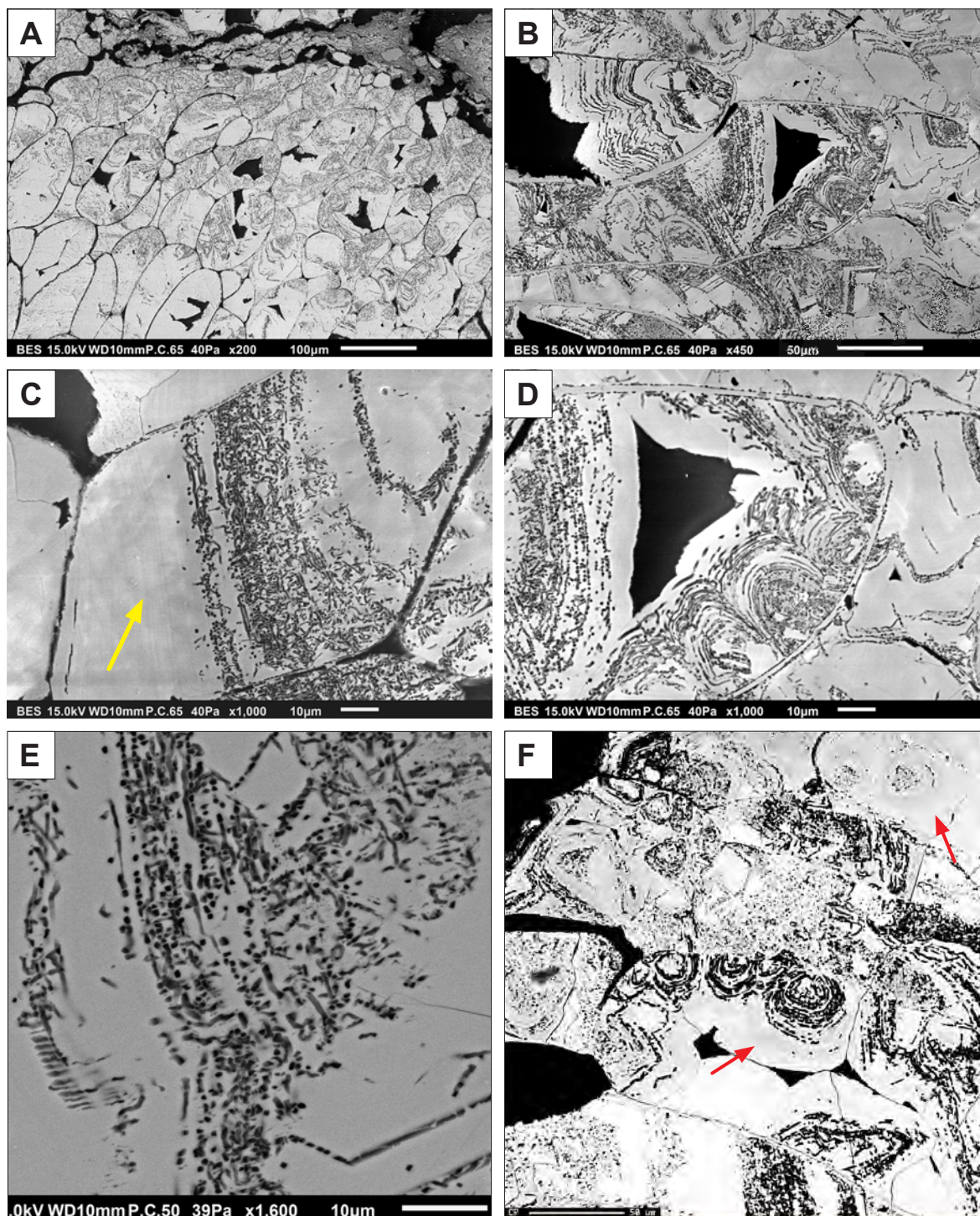


**Figure 3.28.** Endolithic microborings in iCR calcite: backscattered electron images of polished thin sections of resin-impregnated iCR samples. A) Roughly polished thin section. Endolithic microborings are more abundant and closely packed in calcified cell in the upper part, corresponding to outer cortical cells. Penàguila, site T14-458. B) Close-up view of A showing resin-filled microendoliths (black) aligned along crystal growth lines/intracrystalline layers. C) Charge-contrast enhanced BES image showing indistinct layering (arrow) and parallel to anastomosing microborings of uniform,  $\sim 0.5 \mu\text{m}$  diameter. Sella, site T14-463. D) Incompletely calcified cell (triangular resin-filled cavity in the center) with endolithic borings following growth lines in dome-shaped crystal structures. Cf. crystal shapes in Fig. A3-4.07G, H. E) Higher magnification of microborings in sample in Fig. C. F) EPMA backscattered image of microendoliths. Arrows indicate layering corresponding to difference in composition of calcite, apparently controlling distribution of microborings.



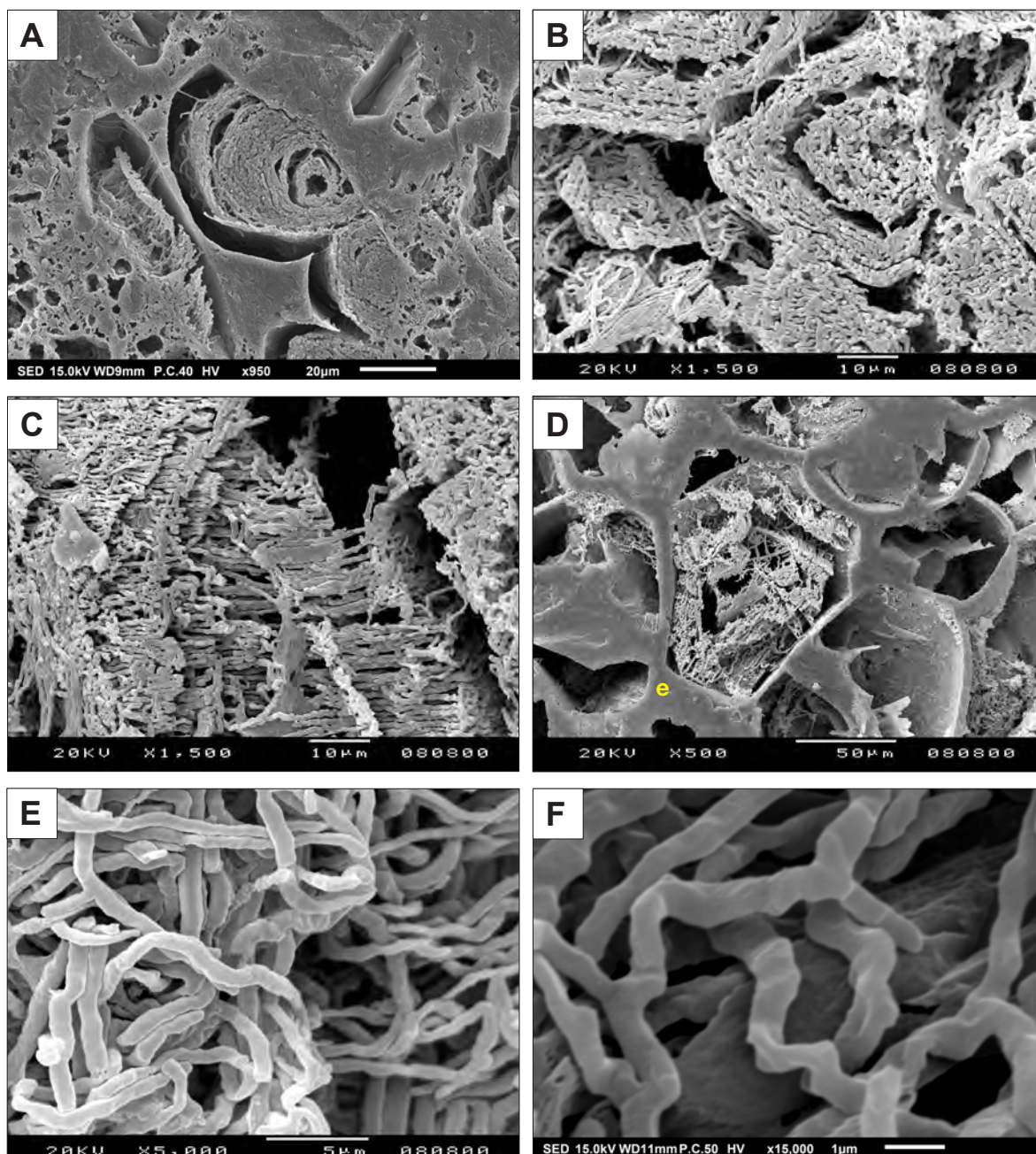


**Figure 3.29.** SEM photomicrographs of 3D resin casted microborings in iCR calcite. A, B) Densely-layered dome-shaped structure corresponding to structures in Figs. 3.28D and F. C) Roughly parallel microborings, correlative of textures in Fig. 3.28C. D) Microboring pattern following intercrystalline layers; cf. thin section photomicrographs in Figs. 3.27E, F. Spaces between (dissolved) iCR cells are filled with resin (e). E, F) Microboring casts at higher magnifications.

Material in all images is from Penàguila, site T14-458. All images taken on Au-coated material in HV SED imaging mode.

Also see Fig. A3-4.14.

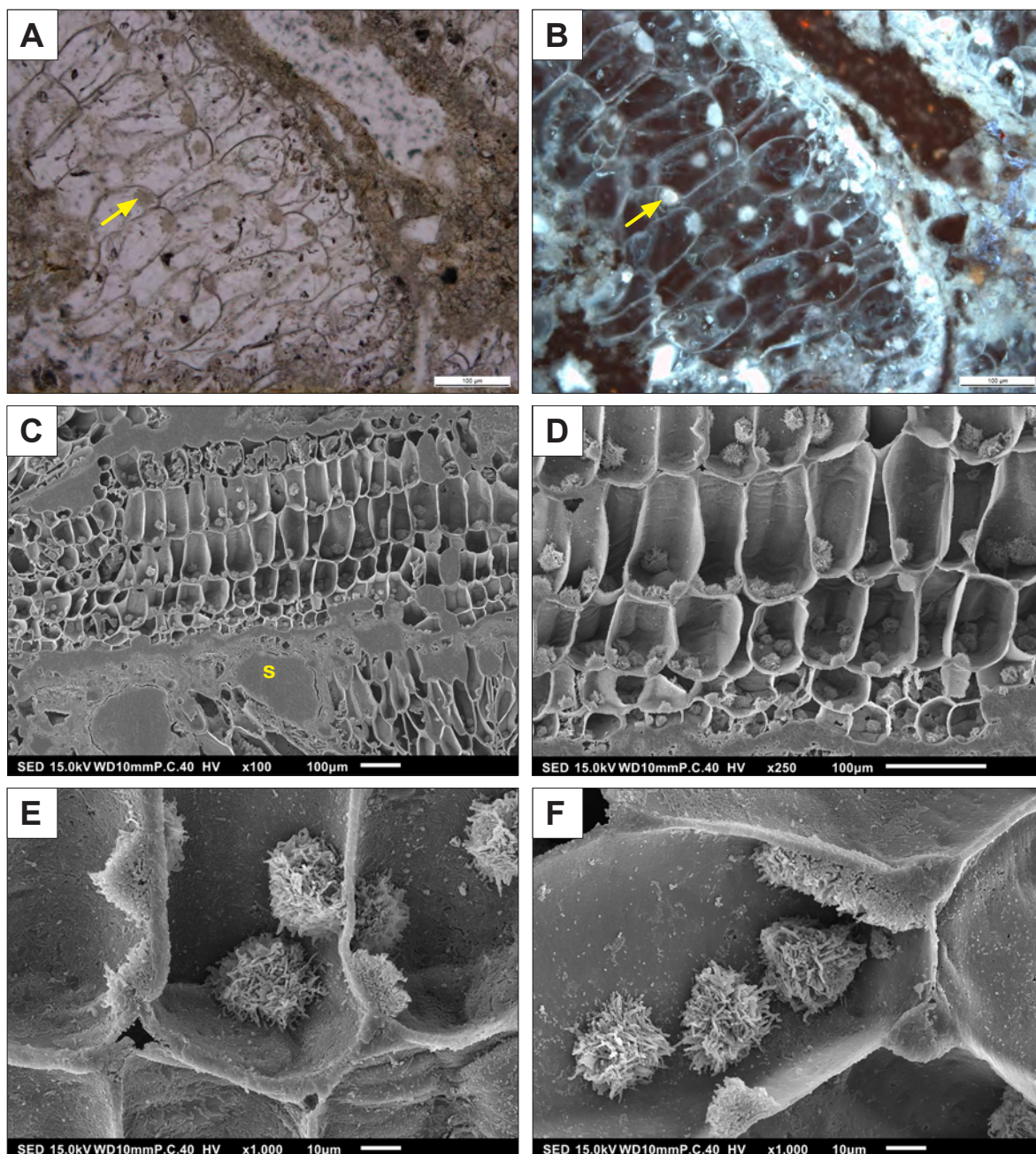


**Figure 3.30.** Arbuscular structures in iCR calcite produced by endolithic microorganisms. A and B) PPL and blue-fluorescence thin section photomicrographs showing lump-like structures; arrows indicate the same point in both images. Also see Figs. A3-4-14I, J. Finestrat-Sella, site T15-822. C, D) Resin casts of dissolved aggregate of asymmetric, type II iCR, showing arbuscular endolithic features, 20-40 µm in diameter, occurring predominantly in the lower parts of (dissolved) cell lumina, corresponding to the side of the root in contact with substrate (s). E, F) Higher magnification view of arbuscular endolithic structures, 'emerging' from cell walls. Cf. endolithic cavities on iCR cell surfaces in Figs. A3-4-14K, L. Figs. C-F: Penàguila, site T14-458.



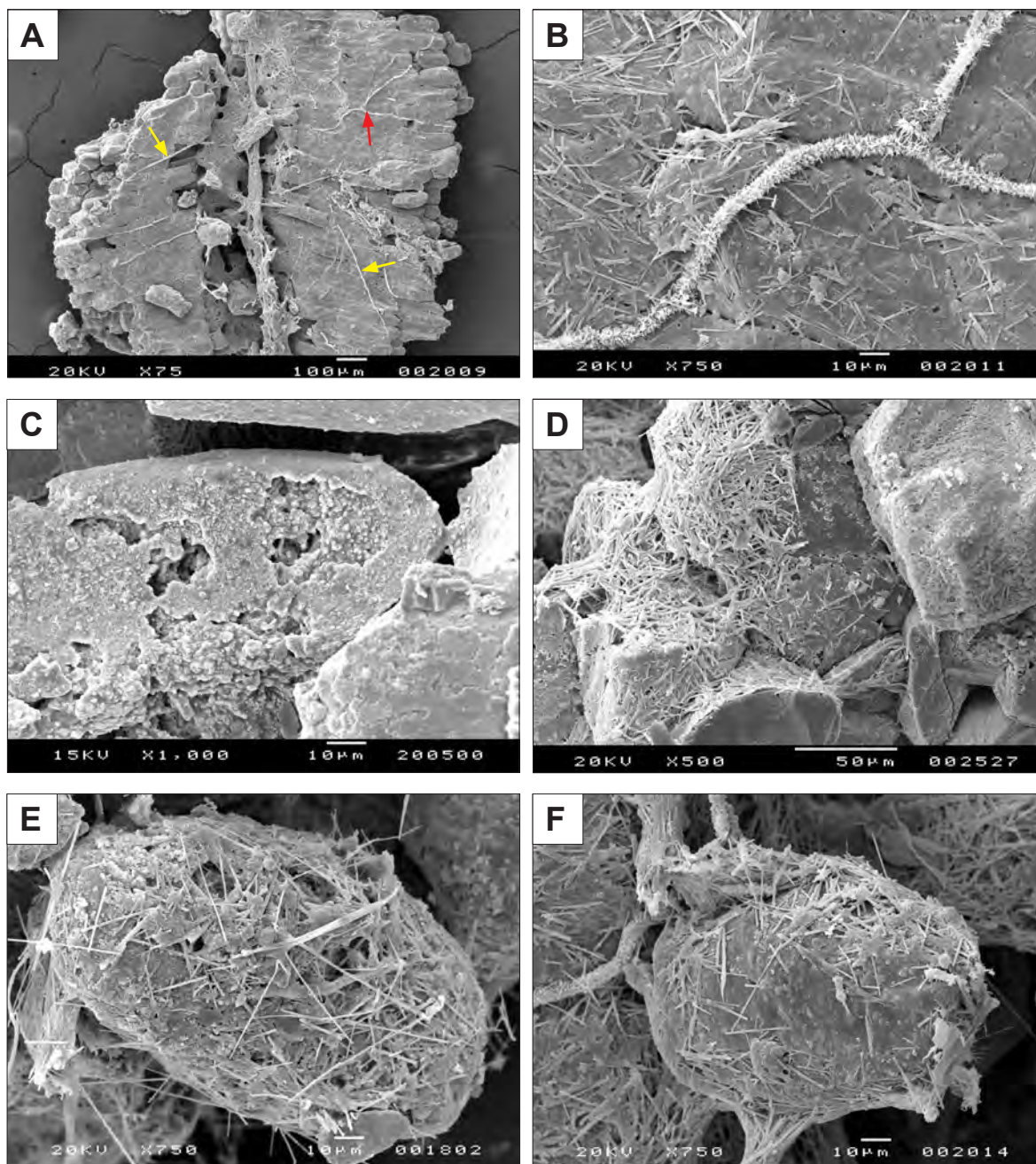


**Figure 3.31.** SEM photomicrographs of weathered (degraded) iCRs. A) Longitudinally split fragment of a type I iCR showing enlarged, probably dissolved central groove, corresponding to vascular cylinder, filled and coated with needle fiber calcite (NFC), forming alveolar-septal structures. Note also numerous mineralised fungal hyphae (arrows). B) Close-up view the area in Fig. A, marked with red arrow, showing bifurcate fungal hypha, fully covered by needle-shaped crystals of (originally) Ca oxalate, now probably transformed to calcite. Although strongly degraded, cellular structure of iCR is noticeable but covered by a film of NFC and calcite nanofibres. Sella, site T15-816. C) Weathered iCR cell with, probably microbially formed, dissolutional cavities. Penàguila, site T14-458. D) iCR fragment with cells partly ‘replaced’ by NFC crystals. E, F) Extremely weathered, internally probably intensively microbored calcified cells, covered by a film of NFC, nanofibres, mineralised bacteria and fungal hyphae. Figs. D-F: Sella, site T15-816.

All images taken on Au-coated material in HV SED mode.

Also see Figs. A3-4.15 to A3-4.18.



### ***3.4.5 Mineralogy and elemental composition of iCRs and rhizosphere clays***

Ten samples of isolated and powdered iCR aggregates, analysed by XRD, all showed same diffractogram patterns, corresponding to low-Mg calcite. Figure A3-5-01 (Appendix 3-5) shows spectra for five representative samples. None of the analysed iCR samples have shown presence of Ca oxalates.

Fourier Transform Infrared Spectroscopy (FTIR) examination of two samples of iCRs has confirmed XRD results, showing IR spectra, characteristic of low Mg calcite (Appendix A3-5, Fig. A3-5.02).

XRD analyses of four samples of clayey fraction, collected from carbonate-depleted zones associated with iCR aggregates from Sella and Ibi localities, have shown similar diffractograms. All samples were predominantly composed of smectite clays, small amounts of kaolinite, and minor amounts of illite.

Electron probe microanalysis (EPMA) of major and selected trace elements (Ca, Mg, Fe, Mn, Sr, P, S) of intracellularly calcified roots, corroding marine marly limestone, performed on polished thin sections (Appendix A3-6) confirmed low-Mg calcite composition of calcified cells with 0.1 to 0.6 wt% Mg and trace amounts of Fe (< 0.1 wt%), Mn (< 600 ppm), Sr (0.1 to 0.4 wt%), P (< 250 ppm), whereas values of S were below detection limits (Tables A3-6.2 and A3-6.3).

Low-vacuum backscattered electron SEM observations and EDS elemental mapping of uncoated thin sections and broken surfaces of iCRs with their matrix display discernible carbonate-depletion and Al-Si enrichment zones, respectively, in exceptional cases evidenced also by the extent of preserved root hairs or their tubular traces (Figs. 3.16, 3.19C-F).

### ***3.4.6 $\delta^{13}\text{C}$ and $\delta^{18}\text{O}$ stable isotope composition of iCRs***

The analysis of carbon and oxygen stable isotopes has been focused on pure iCR fragments, devoid of matrix, and calcified cells, separated from organic remains. The  $\delta^{13}\text{C}$  and  $\delta^{18}\text{O}$  results of a total of 116 measurements of iCR calcite are shown in Appendix A3-7. Four different groups of iCR samples were distinguished according to morphological types and preservation state (Table A3-7.1): iCR-I, iCR-II, morphologically unspecified iCR, and

apparently weathered (degraded) aggregates (iCR-D), characterised by predominantly opaque calcite cells. Overall  $\delta^{13}\text{C}$  values (VPDB) range from  $-20.3\text{‰}$  to  $-6.3\text{‰}$  with an average of  $-11.5\text{‰}$  ( $\sigma \pm 2.96\text{‰}$ ), whereas  $\delta^{18}\text{O}$  values range from  $-10.4$  to  $-0.1\text{‰}$  and average at  $-6.1\text{‰}$  ( $\sigma \pm 2.11\text{‰}$ ). Average values, excluding data for weathered iCRs, are  $-13.0\text{‰}$  for  $\delta^{13}\text{C}$ , and  $-6.2\text{‰}$  for  $\delta^{18}\text{O}$ , respectively. The  $\delta^{13}\text{C}$  and  $\delta^{18}\text{O}$  values are cross-plotted in Figure 3.32A. The  $\delta^{13}\text{C}$  shows considerable differences between iCR types (Fig. 3.32B); values for individual categories are:

iCR(unspec.) :  $n = 41$ , mean:  $-14.3\text{‰}$ ,  $\sigma \pm 1.9\text{‰}$ ; min:  $-20.3\text{‰}$ , max:  $-10.1\text{‰}$ ;

iCR-I:  $n = 18$ , mean:  $-12.8\text{‰}$ ,  $\sigma \pm 1.4\text{‰}$ , min:  $-15.3\text{‰}$ , max:  $-10.0\text{‰}$ ;

iCR-II:  $n = 22$ , mean:  $-10.4\text{‰}$ ,  $\sigma \pm 0.96\text{‰}$ , min:  $-12.7\text{‰}$ , max:  $-9.0\text{‰}$ ;

iCR-D:  $n = 35$ , mean:  $-8.2\text{‰}$ ,  $\sigma \pm 0.9\text{‰}$ , min:  $-10.9\text{‰}$ , max:  $-6.31\text{‰}$ .

The  $\delta^{18}\text{O}$  ranges and average values do not vary significantly except for the iCR-I category, which contains a subgroup of anomalously positive  $\delta^{18}\text{O}$  values (Fig. 3.32C).

Results for iCRs of pot-grown plants of *Hedysarum coronarium* (Appendix A3-8) are included in the iCR(unspec.) group (Table A3-7.1). *H. coronarium* calcite samples exhibit negative and relatively invariable  $\delta^{13}\text{C}$  values ( $n = 10$ , mean:  $-16.2\text{‰}$ ,  $\sigma \pm 0.41\text{‰}$ , min:  $-16.8\text{‰}$ , max:  $-15.5\text{‰}$ ), and consistent  $\delta^{18}\text{O}$  values (mean:  $-7.2\text{‰}$ ,  $\sigma \pm 0.33\text{‰}$ , min:  $-7.6\text{‰}$ , max:  $-6.8\text{‰}$ ), close to an overall average for iCRs ( $-6.1\text{‰}$ ,  $\sigma \pm 2.1\text{‰}$ ).

Comparison of the  $\delta^{13}\text{C}$  and  $\delta^{18}\text{O}$  values of iCR calcite with selected published data is shown in Figure 3.35. The group of morphologically unspecified iCRs includes unpublished data of four samples of iCR from weathered flysch soil from Beka near Kozina, SW Slovenia. Values of iCRs are compared with isotope composition of *Microcodium* in Figures 5.27 to 5.28 (Chapter 5) and further discussed in Section 5.8.4. Data of iCRs are also included in a cross plot of calcite  $\delta^{13}\text{C}$  vs.  $\delta^{13}\text{C}$  of the corresponding matrix (substrate) in Figure 5.26. Available data does not exhibit any correlation between  $\delta^{13}\text{C}$  stable isotope composition of substrate and  $\delta^{13}\text{C}$  of iCRs.

Results of  $\delta^{13}\text{C}_{\text{(organic)}}$  measurements are shown in Table 3.1. All three samples of organic tissues associated with iCRs yielded typical average values of C3 plants (Fig. 3.36) ranging between  $-25.5$  and  $-26.4\text{‰}$  VPDB.

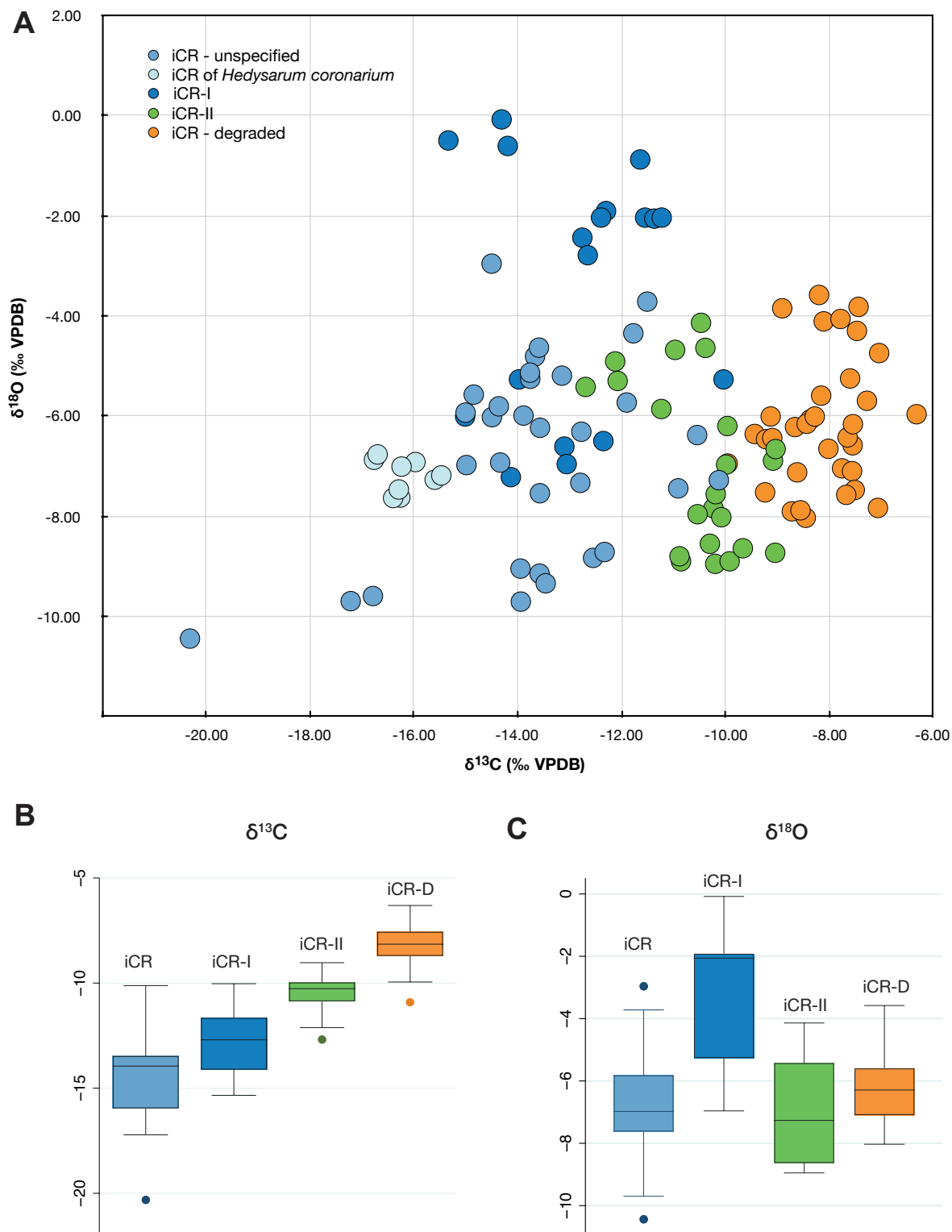


**Figure 3.32.** Stable isotope analysis of iCRs. A) Cross-plot of  $\delta^{13}\text{C}$  and  $\delta^{18}\text{O}$  values of intracellularly calcified roots, analysed in this study. Different colours represent groups based on morphological types (iCR-I, iCR-II and unspecified), lab-grown iCRs of *Hedysarum coronarium*, and weathered (degraded) iCRs (legend in upper left corner). B, C) Box and whisker plots for  $\delta^{13}\text{C}$  (B) and  $\delta^{18}\text{O}$  (C) for individual groups.



### 3.5 Discussion

#### 3.5.1 Root intracellular $\text{CaCO}_3$ biomineralisation processes and features

Fully calcified iCR aggregates, observed either in thin sections or under SEM, offer very limited petrographic information about the crystal growth processes forming iCRs. However, partly mineralised cells, particularly those in live or not significantly decayed roots, provide invaluable insight into the complexity of crystal forms and their evolution, as well as the crystallisation pathways potentially involved in intracellular mineralisation.

The most commonly reported and studied mineral precipitate in higher plants is calcium oxalate (Franceschi and Horner 1980; Nakata 2003; Franceschi and Nakata 2005). Calcium oxalate crystals typically develop in the vacuole within an organic matrix, which creates and controls the crystallisation microenvironment (Webb et al. 1995; Webb 1999). Higher plants produce Ca oxalate crystals in characteristic, species-specific morphologies, commonly in the shape of acicular crystals called raphides, or well-developed prismatic crystal shapes, crystal sand or druses (Franceschi and Nakata 2005). Calcium oxalate crystals are present in fruits, leaves stems and roots; their formation is generally regarded as a mechanism for regulating bulk-free calcium levels in tissues and organs, but also used as a physical protection strategy, such as defence against herbivores. Calcium oxalate typically form in highly specialised cells generally referred to as crystal idioblasts, in which crystal forms occurs exclusively inside the plant cell vacuole and is controlled by intravacuolar organic matrix (Webb et al. 1995; Nakata 2003). The most important in oxalate biosynthesis are matrix proteins, which are supposed to play a major role in nucleation and regulation of Ca oxalate crystal growth, and become included in the mature crystals (Franceschi and Nakata 2005).

Calcium carbonate biomineralisation in terrestrial higher plants has been generally treated as a relatively insignificant phenomenon, mostly referring to plant cystoliths as an archetypal and predominant  $\text{CaCO}_3$  form (Arnott 1982; Smith 1982; Setoguchi et al. 1989; Bauer et al. 2011; He et al 2014, 2015; Karabourniotis et al. 2020). This has been emphasised particularly in comparison with evolutionary and geologically important carbonate biomineralisation in aquatic photosynthetic organisms, such as cyanobacteria, benthic calcareous algae and marine phytoplankton (Leadbeater and Riding 1986; Skinner

and Ehrlich 2014). Furthermore, Raven and Giordano (2009) concluded that the most quantitatively important biogeochemical role of land plants today in biomineralisation is silica deposition in vascular plants, especially grasses, and that for terrestrial plants there is no significant fossil evidence on which to base the environment–evolution interactions of the production of calcium carbonate.

Although there is a general lack of micromorphological data about the intercellular calcium carbonate precipitation in plant roots, especially the early stages of biomineralisation in experimentally grown plants, calcite in iCRs does not appear to form specific crystal shapes, comparable to raphides and other highly-structured forms of plant Ca oxalate biominerals. Furthermore, completely calcified cortices of large fine iCR segments indicate that  $\text{CaCO}_3$  biomineralisation is not limited to specialised idioblast cells but unselectively involves whole fine root parenchyma. However, it is beyond doubt that nucleation and growth of  $\text{CaCO}_3$  in iCRs take place inside cell vacuoles and that crystallisation processes are critically controlled and regulated by the intravacuolar macromolecular organic matrix (Weiner and Dove 2003). Vacuoles are lytic compartments, which function as reservoirs for ions and metabolites (Marty 1999; Rea 2018; Cui et al. 2020). As membrane-bounded crystallisation environments, they maintain the ion transport and govern the resulting biomineral composition and morphology.

Ultrastructural SEM analysis iCR calcite, presented in the previous sections (Figs. 3.23 to 3.25 and Figs. A3-4.07 to A3-4.10), demonstrated different complex crystal forms, which presumably reflect progressive evolution and maturation of intracellular  $\text{CaCO}_3$  deposits (Fig. 3.33). Crystal forms of early mineralisation stages of iCRs considerably differ from archetypal, coarse rhombohedral forms of calcite, which can be observed in dead and potentially diagenetically modified iCR cells (e.g. rhombohedral geometry of calcite in broken cells shown by Jaillard et al. 1991). Many calcified cells display lamellar crystal ultrastructure, composed of planar crystal elements (lamellae), assembled in parallel structures or 3D interlaced structures, similar to dendritic crystals (e.g. Turner and Jones 2005; Imai 2007; Jones and Renaut 2008; Imai 2016) with lamellae oriented in multiple (three?), probably crystallographically-controlled directions (Fig. 3.23D, Fig. A3-4.07A-D). Other cells exhibit mesocrystalline structures, that is macroscopically structured crystal forms (Fig. 3.23B, Fig. A3-4.10A-C), which are ordered superstructures, composed of crystal elements of mesoscopic size, generally 1 nm to 1  $\mu\text{m}$  (Cölfen and Antonietti 2008; Song and Cölfen 2010; Cölfen 2010). External layer of fully calcified cells is typically composed of mesostructured calcite (Figs. 3.25C, D, F, Figs. A3-4.09, A3-4.10B-F),

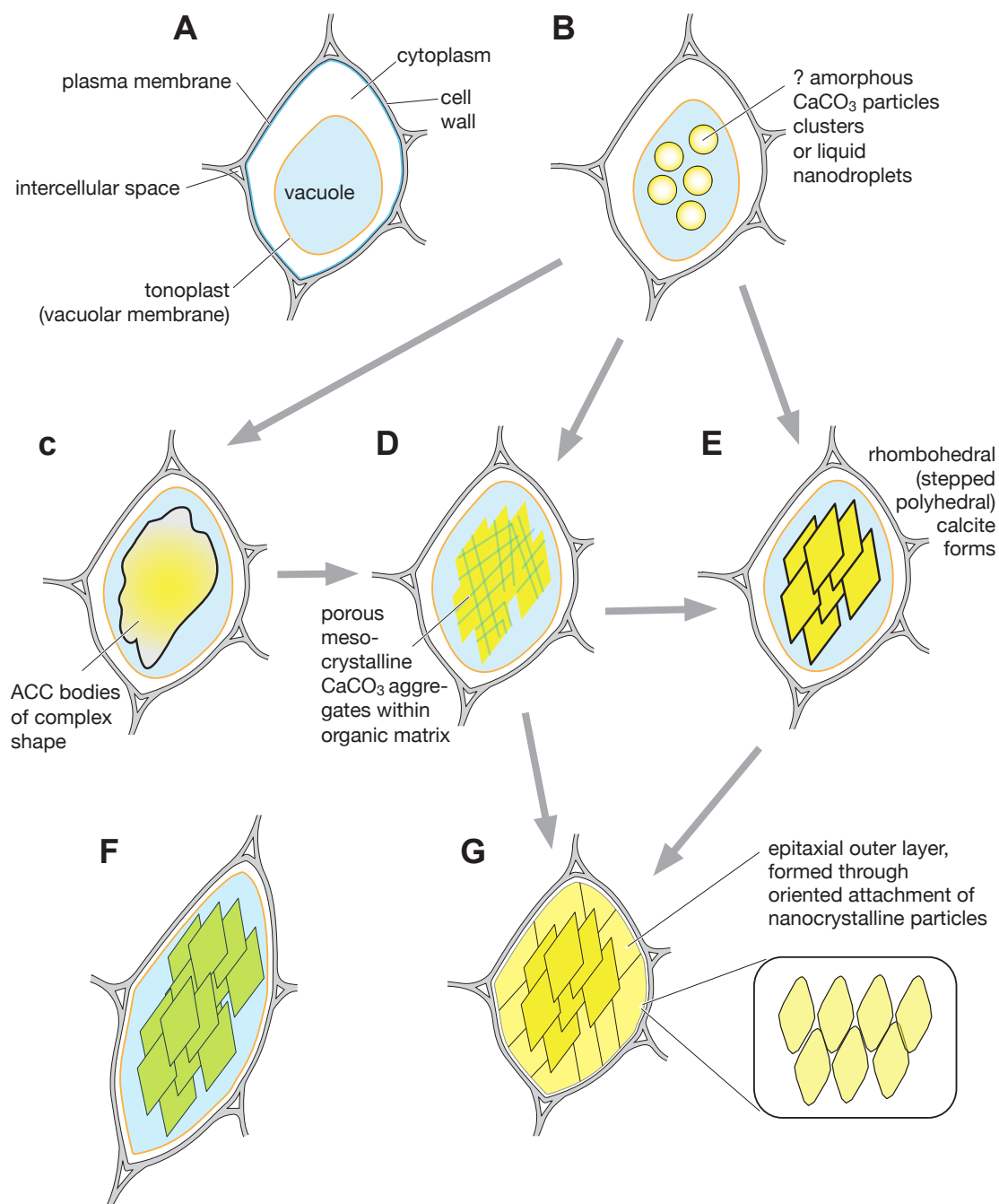


**Figure 3.33.** A) Diagrammatic representation of a plant cell of a fine root cortical parenchyma. B) Incipient precipitation of calcium carbonate within a vacuole possibly starts through non-classical crystal growth pathways in presence of polymers, likely in the form of amorphous  $\text{CaCO}_3$  particles or liquid precursor phases. C) Aggregation of amorphous nanoparticles or droplets possibly results in transient solid bodies of hydrated amorphous calcium carbonate (ACC). D) Lamellar mesostructured calcite forms can develop through transformation of ACC. E) Crystal maturation results in rhombohedral (stepped polyhedral) calcite morphologies. F) Extensive precipitation of  $\text{CaCO}_3$  in a vacuole can be associated with pronounced cell expansion and results in strongly elongate cells. G) Maturation of porous lamellar (D) and rhombohedral calcite forms (E) into fully calcified cells with curved surfaces by precipitation of an outer layer, replicating the cell shape, often showing epitaxial growth by oriented attachment of nanoparticles (see Fig. 3.25 and Figs. A3-4.08-4.10). The outer layer is strongly exaggerated here; commonly it represents less than 5% of the total calcified cell volume.



indicating growth by aggregation and oriented assembly of metastable nano-sized, possibly amorphous or poorly crystalline particles (Fig. 3.25G, H, Figs. A3-4.09C, E, F, A3-4.10E, F). All these ultrastructural features are strongly indicative of non-classical crystal growth pathways in presence of polymers (Gower 2008; DeYoreo et al. 2015; Van Driessche et al. 2017; Wolf and Gower 2017). These pathways include different crystallisation mechanisms, characterised by oriented attachment of solid, mostly poorly crystalline or amorphous particles, or liquid precursor phases (Gower 2008; De Yoreo 2015).

There is growing evidence that biologically produced amorphous calcium carbonate (ACC), as a precursor of crystalline carbonate phases (Addadi et al 2003), is widely distributed but often overlooked in mineralised tissues. Two forms, anhydrous transient ACC and a hydrated ACC containing about 1 mol of water that persists for longer time periods, exist as biominerals. Radha et al. (2010) substantiated preference for an amorphous structure during the early stages of crystal growth and stated that the initial binding of calcium to carbonate and subsequent growth of amorphous clusters in water is not only energetically favourable, but also virtually free from thermodynamic barriers. The transformation sequence observed in biomineralisation appears to be mainly energetically driven; the first phase deposited is hydrated ACC, which then converts to anhydrous ACC, and finally crystallizes to calcite (Weiner and Addadi 2011; Radha et al. 2010; Rodríguez-Blanco et al. 2011; Gal et al. 2015). Mesostructured calcite forms can develop through transformation of amorphous calcium carbonate (Rodríguez-Navarro et al. 2015).

Morphological variation in observed iCR calcite crystals, representing incipient intracellular calcification phase (Figs. 3.23, 3.24A-D), corresponds to a continuum of crystal forms in the model of morphological evolution as a function of driving force (supersaturation) and organic matrix (gel) density (Oaki and Imai 2003, Imai 2007, 2016). Classical faceted single crystals reflect near-equilibrium growth in low-density matrix (or without matrix), largely determined by kinetic-limited increase in crystal size at low supersaturation. On the other side, polycrystalline forms of increasing complexity (disorder) form with increased supersaturation, growth rate (largely limited by diffusion) and density of the matrix. Resulting mesocrystalline branched, dendritic and spherulitic morphologies reflect growth mode far from equilibrium (Imai 2016).

Mesostructured crystalline carbonate forms are characterised by very high surface area to volume ratios and are intrinsically prone to overgrowth and maturation. Maturation of porous lamellar forms into fully calcified cells with curved surfaces, replicating the

cell shape, is clearly perceivable under SEM by comparison of 3D structures with charge contrast images (Fig. 3.23C-F, Fig. A3-4.07A-F). Charge contrast photomicrographs suggest difference in composition between the early, interlaced lamellar fabric and the subsequent mineral precipitate, occluding the pores and 'sintering' the crystal into a cell-shaped body with curved surfaces.

Importantly, the final stages of crystal growth in fully calcified iCR cells (Fig. 3.33G) are probably independent from intravacuolar calcification. As noted in Section 3.4.4, several  $\mu\text{m}$  thick external layer, rendering the cell shape, appears to form by epitaxial overgrowths coating the underlying coarser rhombohedral and lamellar crystal framework (Figs. 3.24F, 3.35, Figs. A3-4.07B, A3-4.08, 4.09). A two-stage calcite crystal growth model of iCR has already been elucidated by Jaillard (1983). According to his interpretation, the first stage comprises nucleation and growth of a calcite crystal within the vacuole; the biogeochemical process of ion exchange and carbonate accumulation continues and produces 'endovacuolar' mineral deposits, occupying nearly 95% of the total cell volume. The second stage of crystal growth supposedly occurs after the cell death (Jaillard 1983, p. 295) and comprises massive entry of ions (high  $\text{CaCO}_3$  supersaturation), plasmolysis and rapid crystallisation within the remaining (~5%) cell volume. Jaillard (1983) concluded that calcification of the cells is completed before the lysis of the cytoplasm, which occurs less than a few tens of minutes after the death of the cell. Ultrastructural details of the studied iCR material generally comply well with Jaillard's mechanism of two-stage intracellular calcification.

Another important characteristic of intracellularly calcified roots is a common pronouncedly elongate shape of the calcified cells, including cases of extremely expanded forms (Figs. 3.22A-D; 3.33F). Cell expansion in fine roots, that is the increase in cell volume brought about by the increase in vacuolar volume and the concomitant increase in the cell's surface area (Dolan and Davies 2004), is most pronounced in the root elongation zone where cells expand (elongate) in one, i.e. longitudinal direction. However, in intracellularly calcified roots, cells appear to extend radially, giving iCR a characteristic 'fat-root' appearance (Fig 3.34). Intricate details of the internal cell wall surfaces in calcified cells indicate that, concomitant with cell expansion, there has been production of new wall and membrane along the surface of growing cells. Intravacuolar calcification, driven by ion transport during vacuolar growth, presumably critically mediates the increase in cell size and production of new cell wall and membranes. During expansion, the cell walls must

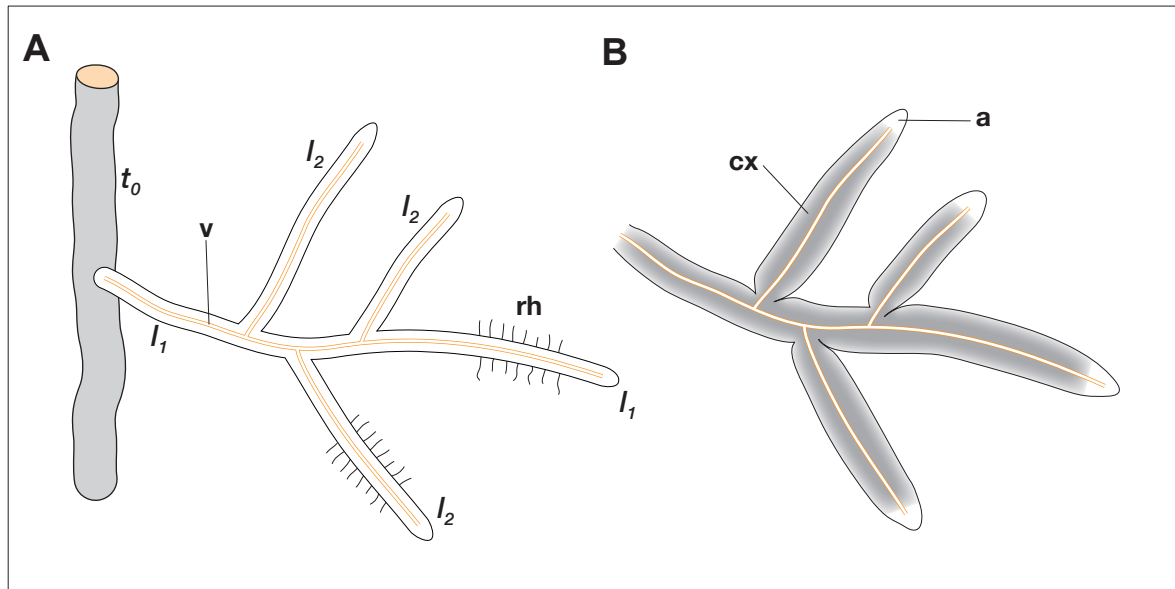


**Figure 3.34.** Diagram of a non-calcified root system (A) composed of a vertical (primary) coarse (woody) tap root ( $t_0$ ) and a lateral (secondary) fine root branch, composed of a 1<sup>st</sup> order main axis root ( $l_1$ ) and 2<sup>nd</sup> order laterals ( $l_2$ ).  $v$  - vascular system,  $rh$  - root hairs. **B**) Calcified root, corresponding to fine root in A, is characterised by considerably thickened, expanded cortex ( $cx$ ) as a result of intracellular mineralisation, giving rise to a characteristic 'fat-root' appearance.  $a$  - non-calcified apices of fine roots. Root hairs, not shown in Fig. B, can occur throughout the epidermal layer of calcified roots or are mainly limited to one side of flat, asymmetrically-modified roots (a.k.a. shovel roots).

have been strong enough to withstand the internal pressure of the growing protoplast but flexible enough to grow (Dolan and Davies 2004). Despite apparent formation of the outer, cell shape-replicating calcite layer during cell senescence or after death (Jaillard 1983), perfectly preserved textural details of calcified cells indicate that calcification process likely completes under relatively normal cell turgor and before breakdown of cell walls. Compelling evidence for normal cell turgor pressure during calcification is also given by empty, non-calcified cells, which have apparently kept their shape and have not deformed (shrunken) at expense of calcification in the neighbouring cells (Figs. 3.18B, 3.19C, D, Fig. A3-4.02A).

### 3.5.2 Functional traits of *iCRs*

Plant functional traits comprise morphological, physiological and phenological characteristics of plants that represent ecological life history strategies and are hypothesised



to determine the response of a plant to environmental factors (Bardgett et al. 2014). As discussed in Chapter 1, in addition to providing anchorage, the primary function of roots is to acquire nutrients and water from soil. Plants have evolved a wide range of belowground strategies to capture soil resources, and to respond to changes in their availability in space and time (Lambers et al. 2008). These strategies include *architectural root traits*, which determine the spatial configuration of the root system and its components; *morphological traits* of individual roots or root size classes, such as root diameter and specific root length; *physiological root traits*, such as root respiration and nutrient uptake kinetics as well as the release of root exudates; and, finally, *biotic root traits* that involve the ability of roots to interact with soil biota and form symbiotic associations (mycorrhizae, rhizobial symbiosis, actinorhizae) which play a major role in enhanced nutrient capture from soil (Bardgett et al. 2014; Faucon et al. 2017; Freschet et al. 2021b).

Attributes of intracellularly calcified roots, illustrated in Section 3.4, can be examined in a framework of fine root functional aspects, from soil exploration and exploitation geometries to nutrient acquisition strategies. Alleged plant functional strategies, underlying intracellular calcification in fine roots, include iCR architectural patterns, morphological modifications, and CaCO<sub>3</sub> biomineralisation processes.

### 3.5.2.1 Architecture and morphology of iCRs

Root branching architecture can display a wide range of topologies between two extreme growth patterns (Fitter 1996, 2002; Robinson et al. 2003). If branching is confined to the main axis, the root develops a *herringbone* structure. In the other extreme topology, i.e. *dichotomous* system, branching generation is equally probable in all exterior links. Dichotomous branching systems are generally considered as exploitative and develop in fertile soils or microsites within soil (Osmont et al. 2007; Ehrenfeld 2013). Herringbone branching topology is characterised by the highest exploitation efficiency (Fitter and Stickland 1991). Herringbone patterns are more common in roots growing in infertile soils as the lower amount of branching allows the root system to explore a larger volume of soil (Ehrenfeld 2013), which is a beneficial strategy particularly for resources such as phosphate that are relatively immobile in soil (Robinson et al. 2003).

Branching patterns of iCRs shown in Figures 3.10B-D and 3.11A-E illustrate almost paradigmatic herringbone topologies. Flattened iCRs in these examples are densely

arranged along the substrate surface (fissures), showing a tendency of the root system to maximise the area of the substrate in direct contact with (calcifying) roots (a common strategy of root clumping in cracks; de Willigen et al. 2017). Extremely flat asymmetrical iCR-II aggregates are often arranged in layers where branching topology and lateral extent of calcified aggregates occupy virtually total possible space/surface of the rock fissure/substrate (Figs. 3.11A, B, E, 3.12D). Geometry of iCRs in Figure 3.14 shows highly ordered and coordinated pattern of iCRs, composed of series of parallel main root axes and lateral iCR segments, emerging from main axes and growing in aligned, fitted patterns of maximum exploitation topology (Fig. 3.14B).

Conformable geometrical relationships between iCRs and calcareous substrates (Figs. 3.14E, F, 3.15A, B, C, 3.20C, E) provide an interactive link between intracellular calcification in the root cortex and simultaneous dissolution of the substrate in the rhizosphere. This phenomenon is particularly evident in flattened iCR forms with considerably increased surface-to-volume ratio. Assuming a regular cylindrical shape of calcified roots with a constant volume but variable, either circular cross section (with a diameter  $D$ ) or elliptical cross sections (with a longest axis  $A$ ), there is an increase of surface in elliptical shapes of ~35% for  $A = 2D$ , and ~100% for even more flattened shape with  $A = 3D$ . In the studied material, flat iCRs forms with roughly elliptical or semi-elliptical shape in cross section and an aspect ratio (thickness to width)  $> 1:3$  are common, especially in asymmetrical iCR-II examples (Figs. 3.11, 3.15E and 3.18).

In other words, the apparently increased root surface in flattened iCR varieties, potentially available for  $2H^+ / Ca^{2+}$  exchange between the root and the substrate (Section 3.5.2.2 below), presumably reflects additionally increased proton extrusion area/space in the framework of a plant strategy to utilise nutrients of limited mobility, largely bound to/ embedded in carbonate minerals, especially phosphorous and metal micronutrients like iron and zinc (Raven et al. 1990; Raven 1991; Jaillard and Hinsinger 1993; Marschner 1995; Hinsinger 2013; Ehrenfeld 2013).

In summary, both architectural patterns and morphological modifications of iCRs indicate highly controlled strategy for enhanced exploration of rock fissures and maximised exploitation of rock surfaces, associated with dissolution of the substrate.

### 3.5.2.2 Physiology of $\text{CaCO}_3$ biomineralisation in plant roots

Pedogenic carbonate forms in soils when the solution becomes supersaturated with calcite (Cerling 1999b). Equation:



and

$$K_{\text{Calcite}} = [a(\text{Ca}^{2+})] [a(\text{HCO}_3^-)]^2 / P(\text{CO}_2) \quad [2]$$

(where  $K_{\text{Calcite}}$ ,  $a(\text{Ca}^{2+})$ ,  $a(\text{HCO}_3^-)$  and  $p(\text{CO}_2)$  are the solubility product of calcite, the activity of the  $\text{Ca}^{2+}$  ion, the activity of the  $\text{HCO}_3^-$  ion, and  $p(\text{CO}_2)$  partial pressure of  $\text{CO}_2$ , respectively) shows that a calcite-saturated solution can become supersaturated in several ways, including a decrease in  $p(\text{CO}_2)$  in the soil, or an increase in the concentrations and activities of dissolved calcium and bicarbonate due to water loss by (evapo)transpiration or by direct evaporation (Cerling and Quade 1993). With the realization that the biological component of  $\text{CO}_2$  in soils is much larger than the amount of detrital carbonate dissolved on soil-formation time-scales ( $\text{CO}_2(\text{biological}) \gg \text{CaCO}_3(\text{detrital})$ , in the order of  $10^2$  to  $10^3$  times), Cerling (1984) introduced a general diffusion model of soil isotopic species of  $\text{CO}_2$ - $\text{H}_2\text{O}$ - $\text{CaO}$  system (see Section 5.8.4)

The general model of biologically induced precipitation of  $\text{CaCO}_3$  around fine roots (in the rhizosphere; Section 2.5) is based on an assumption that the process is mainly driven by plant transpiration. In Ca-rich soils, calcification may occur during the build-up of carbonate as a result of large amount of  $\text{Ca}^{2+}$  transferred towards the root surface as a consequence of mass flow of water and solutes (Cramer and Hawkins 2009; Hinsinger 2013; Kuzyakov and Razavi 2019). In simple terms, calcification in the rhizosphere may take place when a transpiring plant draws soil water into the roots, but excludes  $\text{Ca}^{2+}$  (McConnaughey and Whelan 1997).

However, intracellular root calcification certainly involves more than transpiration-driven ion accumulation around a root. In their pioneering studies, Jaillard and co-authors (Jaillard 1987a, Jaillard et al. 1991) interpreted intracellular accumulation of carbonate in root cortical cells with adaptation strategies of plants to cope with excessive calcium and bicarbonate concentrations in the soil solutions (Jaillard et al. 1991). Plant species that preferentially grow on calcareous soils (calcicoles) possess adaptive mechanisms for coping

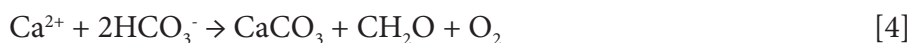


with constraints on growth and mineral nutrition such as low iron and zinc availability and often high calcium and bicarbonate concentrations (Marschner 1995). In this case, intracellular  $\text{CaCO}_3$  mineralisation can be largely regarded as a sequestration mechanism for excessive Ca, i.e. a result of root activity, which can dissolve abundant amounts of calcium carbonate in the rhizosphere as a consequence of respiration and proton release, with the Ca ultimately precipitating in the vacuoles of root cortical cells (Hinsinger 2013). Such a mechanism may simultaneously provide protection of the shoot tissue from excessive calcium concentrations by precipitation of  $\text{CaCO}_3$  in the root tissue (Marschner 1995).

Considerable proton effluxes from roots, often encountered in the rhizosphere, represent one of the modes of rhizosphere acidification as a profitable strategy for acquiring mineral nutrients (Jaillard et al. 2003). Rhizosphere acidification strategies are particularly evident in plants that grow preferentially on carbonate-rich alkaline soils of high acid-neutralizing capacity (Marschner 1995; Neumann and Römheld 2012). Furthermore,  $\text{CaCO}_3$  mineralisation within root cortical cells, coupled with extrusion of protons, probably represents an effective mechanism for the nutrient acquisition (McConnaughey and Whelan 1997; Cohen and McConnaughey 2003; McConnaughey 2012). The model of McConnaughey and Whelan (1997) links calcification with enhanced production of protons. Root proton (acid) secretion in itself enables plants to mobilise sparingly soluble nutrients in the rhizosphere (Marschner 1995), whereas carbonate precipitation in the vacuoles of cortical cells may additionally increase production of protons, which are potentially useful for nutrient assimilation. In the model (Fig. 3.35), intracellular calcification acts as a proton generator, i.e., calcification creates two types of products, minerals and protons (McConnaughey and Whelan 1997):



The biomineralisation mechanism implies enhanced production of protons through exchange of  $\text{Ca}^{2+}$  and  $2\text{H}^+$  using plant-respired  $\text{CO}_2$  (Fig. 3.35). Reaction [4] links calcification with photosynthesis:



Calcium is an essential structural, metabolic and signalling element in plants (Marschner 1995; White and Broadley 2003; Broadley et al. 2012a, b; Thor 2019). The physiological functions of  $\text{Ca}^{2+}$  are controlled by its transport across cell membranes,

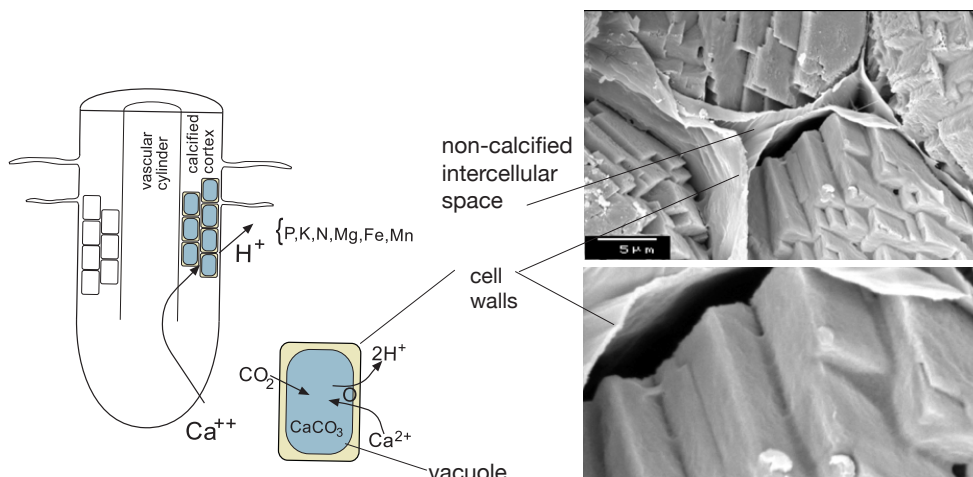


**Figure 3.35.** Diagrammatic longitudinal section of the apical region of a fine root, illustrating calcification physiology. Calcification within the vacuoles of root cortical cells act as a proton generator, allowing the plant to acidify the rhizosphere and thus acquire mineral nutrients from the soil. Production of protons is enhanced through exchange of  $\text{Ca}^{2+}$  and  $2\text{H}^+$  using plant-respired  $\text{CO}_2$ . (modified from Košir 2004 after McConnaughey and Whelan 1997).

regulated by  $\text{Ca}^{2+}$ -permeable ion channels,  $\text{Ca}^{2+}$ -ATPase enzymes and  $\text{Ca}^{2+}/\text{nH}^+$  antiporters (exchangers; Demidchik et al. 2018). Biochemical properties of  $\text{Ca}^{2+}$  transporters suggest that  $\text{Ca}^{2+}$  efflux from the cytosol occurs through the action of ATPases, localised at the cytoplasmic membrane and the tonoplast (vacuolar membrane). Tonoplast  $\text{Ca}^{2+}/\text{H}^+$  antiporters play a major role in  $\text{Ca}^{2+}$  sequestration in the vacuole, which act as the major plant calcium store (Bush 1995; Lee 1998; Garciadeblas et al. 2001).

The  $\text{Ca}^{2+}$ -ATPase-based mechanism is fundamental in most of biological calcification. The mechanism permits high  $\text{CaCO}_3$  supersaturation states and rapid mineral precipitation. The model of McConnaughey and Whelan (1997) integrates  $\text{Ca}^{2+}$ -ATPase mechanism in calcification by directional  $\text{Ca}^{2+}$  pumping, which creates  $\text{Ca}^{2+}$ -rich alkaline solution within a membrane-bound vesicle (vacuole).  $\text{CO}_2$  diffuses across the membrane into this fluid, ionises and induces precipitation of carbonate:



This model can be equally applied in extracellular biomineralisation (e.g. in corals and molluscs) and intracellular biomineralisation (e.g. precipitation of Ca oxalate and carbonate in plant cell vacuoles and specialised vesicles).

Calcification in the fine root cells of modern plants has been shown to be a rapid process. Jaillard (1987a, 1992) showed in *in vitro* experiments under controlled conditions that living roots of oilseed rape plantlets were able to precipitate calcite in the cortical cells within only a few hours, and that fully calcified cells were developed in a few days. Tola et al. (2009) showed in controlled growth of *Hedysarum coronarium* that four week-old plants developed multiple shovel roots with intracellular granular carbonate deposits.

Lambers et al. (2009) and Hinsinger (2013) emphasised the impact of intracellular calcification in plant roots on soil composition and properties but concluded that the understanding to what extent such processes feedback onto plant growth remains to be studied. Lambers et al (2009) summarised intracellular root calcification as processes “promoted by root activity, which can dissolve abundant amounts of Ca carbonates in the outer rhizosphere as a consequence of respiration and proton release, and alleviate Ca toxicity by precipitating it as calcite in the vacuoles of root cortical cells (Jaillard 1987a, b)”. However, the motivations for intravacuolar calcite precipitation in roots seem to be much stronger than merely a Ca-detox strategy. As suggested by the model of McConnaughey and Whelan (1997), intracellular calcification may represent a physiological fine-root trait with its specific nutrient uptake kinetics, biomineralisation mechanism and the concurrent release of exudates. Such physiological mechanism is in accord with architectural and morphological attributes of iCRs, described in the previous section (3.5.2.1).

As noted above, extrusion of protons is presumably utilised for absorption of specific elements (Fig. 3.35). McConnaughey and Whelan (1997, p. 106) listed illustrative acid-leaching reactions for some nutrients (P, N, K, Mg, Fe, and Mn). Among these essential elements of often limited availability, intracellular calcification and associated rhizosphere acidification maintained by H<sup>+</sup> excretion seem to be beneficial strategy particularly for the acquisition of phosphorous and iron (Vance et al. 2003; Lambers et al. 2006; Hodge 2015), especially on alkaline substrates such as calcareous soils of the Mediterranean basin (Hinsinger 2013).

Information about the distribution of intracellular carbonate mineralisation strategy among roots of different plant families is extremely limited. Except for the experimental calcification, performed by Jaillard (1987a) in culture solution-grown rapeseed plantlets (*Brassica napus*), natural occurrence of intracellularly CaCO<sub>3</sub>-biomineralised roots has observed in different species of the legume (Fabaceae or Leguminosae) family (Mottareale 1898; Severini 1908a, b; Ross and Delaney 1977, Tola 2009; Sablok et al. 2017; and Chapter 4). Legumes are the third largest group among the angiosperms and second only to the



grasses (Gramineae or Poaceae) in their importance to humans (Graham and Vance 2003). Ecologically, legumes owe much of their importance to their ability (confirmed in ~88% of species) to fix atmospheric nitrogen in symbiosis with various soil bacteria ('rhizobia'), forming special root organs called nodules (Doyle 1994; Hirsch et al. 2001; Oldroyd et al. 2011). It is important to note that intracellular calcification observed in legume species does not occur in rhizobial nodules but has been found in anatomically 'normal' terminal, higher order fine roots of (Ross and Delaney 1977) or in specialised shovel-shaped roots (Tola et al. 2009; Watt and Weston 2009). In addition to rhizobium symbiosis, certain species of legumes thus evidently possess an additional effective physiological pathway, which enable them to simultaneously uptake nitrogen and phosphorous - two of the most important nutrients and primary constituents of proteins and nucleic acid, and iron - one of the essential plant micronutrients (Marschner 1995; Watt and Weston 2009).

As noted in Section 3.2, xeric moisture regime of soils in the studied area is characterised by pronounced summer dryness when secondary carbonate might be expected to form on calcareous parent materials, and late autumn to early spring rainfall in excess of evapotranspiration (Fig. 3.1D), which would normally trigger carbonate dissolution and leaching even at relatively low rainfall intensity. Vegetation of the Mediterranean type ecosystems is equipped with adaptations (or exaptations) to tolerate low soil nutrient availability and restricted water availability (Rundel and Cowling 2013). Soil water availability is probably the main factor influencing fine root growth (Kramer et al. 1983; López et al. 1998). Consequently, seasonal patterns of fine-root growth reflect plant's activity in capturing water and nutrients (Davies and Bacon 2003). This happens during periods when the soil moisture meets the requirements for both plant nutrient acquisition and favours high levels of soil microbial activity. Presumably, as evidenced by common occurrence of live iCRs in the study area during the months of relatively high soil moisture (October to March), growth of ephemeral, short-lived fine roots, which perform intracellular calcification, corresponds to periods with sufficient soil moisture. Nutrient acquisition and concomitant production of iCRs is thus most probably most intensive during the wet season.

### 3.5.3 Carbon and oxygen stable isotope signatures of iCRs

In the general model of precipitation of soil carbonates, root respired  $\text{CO}_2$ , which approximates to the  $\delta^{13}\text{C}$  composition of plant organic carbon (soil organic matter SOM), undergoes several predictable steps of isotope fractionation, primarily involving  $\text{CO}_2$  diffusion-controlled  $^{13}\text{C}$  enrichment of  $\sim 4.4\text{‰}$ , and a temperature dependent fractionation in equilibrium carbonate (calcite) precipitation resulting in an average  $^{13}\text{C}$  enrichment of  $\sim 10.5\text{‰}$  (Cerling 1984; Romanek et al. 1992, Koch 1998), or, in terms of equilibrium carbonate-SOM pairs, characterised by  $\Delta^{13}\text{C}_{\text{carb-SOM}}$  from 13.5 to 16.5‰ with a mean effective fractionation of  $\sim 15\text{‰}$  (Cerling 1999; Rovira and Vallejo 2008; Montañez 2013).

The  $\text{Ca}^{2+}$ -ATPase-based mechanism of intracellular calcification, put forward in the previous section (McConnaughey and Whelan 1997), implies that plant respired  $\text{CO}_2$  diffuses across the vacuolar membrane, ionises in the vacuolar fluid, and induces precipitation of carbonate from the  $\text{Ca}^{2+}$ -rich solution (McConnaughey and Whelan 1997; equation [5] above). Such  $\text{CO}_2$ -based calcification model assumes that (vacuolar) membranes provide molecular filters that allow  $\text{CO}_2$  to reach the calcification site much faster than  $\text{HCO}_3^-$  and  $\text{CO}_3^{2-}$ , although after crossing the membrane,  $\text{CO}_2$  rapidly converts to  $\text{HCO}_3^-$ , making it hard to tell which molecules actually crossed the membrane (McConnaughey 2003).

Results of  $\delta^{13}\text{C}$  analysis of iCR calcite (Fig. 3.36) show considerably negative  $\delta^{13}\text{C}$  values (mean  $-13.0\text{‰}$ ,  $\sigma \pm 1.96\text{‰}$ , for iCRs of all types; Fig. 3.32), on average  $12.8\text{‰}$  higher than those of the corresponding plant organic matter ( $\sim -25.8\text{‰}$ ; Table 3.1; Fig. 3.37). The average values are within the range of estimated equilibrium  $^{13}\text{C}$  fractionations for calcite relative to  $\text{HCO}_3^-$  (+ 1.0) and relative to  $\text{CO}_2$  (+11.98 – 0.12 ( $T^\circ\text{C}$ )), respectively (Romanek et al. 1992). Considering rapid calcification in iCR, more negative  $\delta^{13}\text{C}$  values could exhibit stronger kinetic disequilibrium behaviour. In contrast, more positive  $\delta^{13}\text{C}$  values may reflect incorporation of soil inorganic carbon (DIC) resulting from dissolution of carbonate substrate, predominantly marine limestone and marl with  $\delta^{13}\text{C}$  composition between  $\sim -1.5$  and  $+1.0\text{‰}$  (see Table A1-1). Namely,  $\text{CO}_2$ -based calcification model does not preclude the entry of soil water containing DIC ( $\text{HCO}_3^-$ ) through the vacuole membrane to reach the calcification site (McConnaughey 2003).

Oxygen isotopic composition of iCRs supposedly primarily reflects isotopic

composition of meteoric (soil) water and its fractionation, which is strongly temperature dependent (Cerling 1984). Furthermore,  $\delta^{18}\text{O}$  composition of soil water can be significantly different than (average) local meteoric water, mostly due to differential infiltration and modification of meteoric water by evaporation (Cerling and Quade 1993). Large part of iCR calcite  $\delta^{18}\text{O}$  measurements ranges between  $-8.0$  and  $-6.0\text{‰}$  (VPDB; Fig. 3.32A, C), what correlates well with the isotopic composition of meteoric water in the area (see correlation data in Cerling and Quade 1993), varying between  $-10$  and  $-5\text{‰}$  (SMOW), with more negative values occurring in the winter periods (IAEA 2015).

Positively anomalous  $\delta^{18}\text{O}$  values for a group of iCR data in Figure 3.36B can be explained with presumably high evaporation during the precipitation of iCR calcite. Namely, all the data points with  $\delta^{18}\text{O}$  values between  $\sim -3.0\text{‰}$  and  $0.0\text{‰}$  belong to iCR samples from the same site (T14-461; Fig. 3.5B) on a barren marly area on the south facing slope with a direct solar exposure. Living iCRs and iCRs with partly preserved root tissues were sampled at the end of March 2014, following 6 months characterised by above average climatic conditions with very dry or dry and warm to extremely warm months (relative to long term average, based on measurements from 1951; AEMET 2015). The anomalous  $^{18}\text{O}$  values are compatible with commonly observed  $^{18}\text{O}$  enrichment of soil carbonate by  $2\text{--}10\text{‰}$  relative to calcite in equilibrium with meteoric water, owing to strong evaporative effects (Cerling and Quade 1993; Koch 1998). On the other side, a large dataset of published iCR isotope data from the Chinese Loess Plateau of Luo et al. (2020; and supplementary material therein) exhibit very negative  $^{18}\text{O}$  signatures (Fig. 3.36A). These authors have concluded that the climate information contained in the isotope composition of their analysed calcified roots is only limited to seasonality or even single event based signals, but have not explicated exceptionally negative  $\delta^{18}\text{O}$  signal of their calcified root material.

Other published data of  $\delta^{13}\text{C}$  and  $\delta^{18}\text{O}$  isotope composition of iCRs mostly come from palaeosols (see e.g. Barta 2014 and Luo et al. 2020 and references therein) and generally fit within the general range of values presented in this study, however, isotope results in the examined papers do not provide significant insights into the root intracellular calcification processes.

Due to a limited number of samples analysed in this study, the available stable isotope data do not allow rigorous or robust statistical testing of differences between individual iCR groups. Furthermore, the largest group of morphologically unspecified iCRs has been analysed before establishing a clear distinction between iCR-I and iCR-II types and



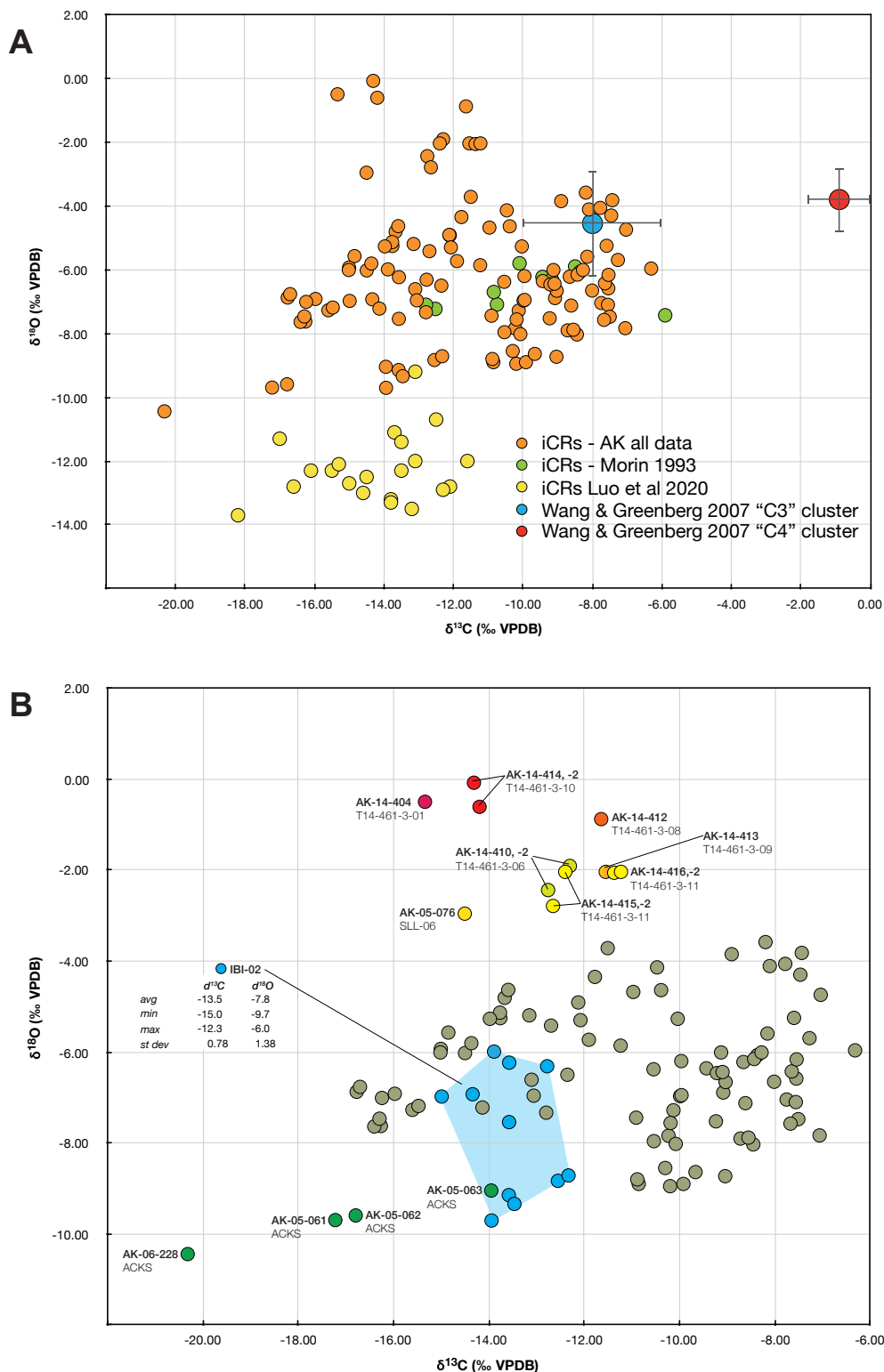


**Figure 3.36.** A) Cumulative cross-plot of  $\delta^{13}\text{C}$  and  $\delta^{18}\text{O}$  values of iCR analysed in this work (AK all data) together with data of iCR isotope analyses of Morin (1993), Luo et al. (2020) and Wang & Greenberg (2007). The later authors did not provide datasets, therefore their data are represented by average value points and range bars. B) Cross-plot of  $\delta^{13}\text{C}$  and  $\delta^{18}\text{O}$  values of iCR of this study showing the main data cloud (green-grey circles), outlier groups and an examples of large intrasample variability in  $\delta^{13}\text{C}$  and  $\delta^{18}\text{O}$  values. See text for explanation. Also see comparative analysis of iCR and *Microcodium* isotope composition in Figs. 5.27 and 5.28.

**Table 3.1.** Stable isotope analyses of  $\delta^{13}\text{C}_{\text{org}}$  of organic tissues of calcified roots and organic matter in chalky calcrete associated with *Pinus halepensis* root systems.

sample	$\delta^{13}\text{C}_{\text{org}}$ (‰ VPDB)	Lab	material	pretreatment
A_SLL-04 (T14-463, Sella)	-26.4 (1 measurement)	IJS, Ljubljana	vascular cylinder fragments, extracted from fully calcified roots	$\text{CaCO}_3$ removed with 10% HCl, OM washed and dried at 60°C
B_SLL-A (T14-463, Sella)	-25.5 ± 0.04	IJS, Ljubljana	coarse root fragment of ?Hedysareae plant with attached lateral iCR	carbonate mechanically removed
C_SLL-23 (T14-463, Sella)	-25.6 ± 0.07	IJS, Ljubljana	fragments of iCR with well preserved epidermis and vascular parts	$\text{CaCO}_3$ removed with 10% HCl, OM washed and dried at 60°C
T15-826-1B (Sella-Finestrat)	-26.4	Beta Analytic Inc., Miami	organic matter of powdery calcrete associated with <i>P. halepensis</i> root systems	acid washes (@Beta)

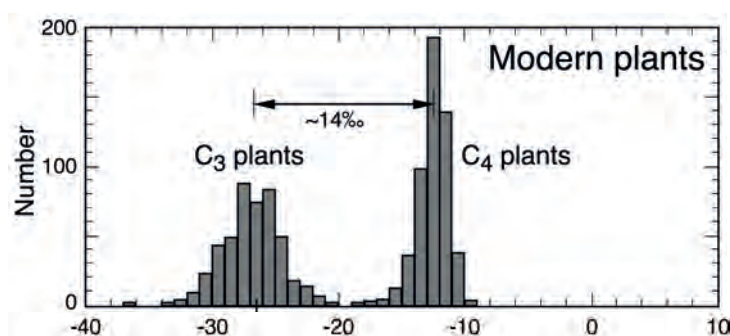


**Figure 3.37.** Histogram of  $\delta^{13}\text{C}_{\text{org}}$  composition of modern plants. From Kohn & Cerling (2002) based on data of O'Leary (1989) and Farquhar et al. (1989). C3 plants have an average isotope composition of  $\sim -26$  to  $-27$ ‰ (Ehrelinger and Cerling 2002a, b; Marshall et al. 2007).

discovery of the extreme flat morphologies of the latter group. The values of unspecified samples largely overlap with the two sub-groups.

In addition to very probable strong kinetic fractionation effects and possible incorporation of DIC from soil solutions, highly variable  $\delta^{13}\text{C}$  and  $\delta^{18}\text{O}$  results of the isotopic composition of iCRs may be strongly influenced by carbonate crystallisation pathways. Morphological variability of intracellular carbonate deposits and particularly multiple stages of crystal growth (shown in Section 3.4.3) can potentially bring additional variation in stable isotope composition, deviating from biologically controlled biomineralisation.

Although a special care has been taken in microsampling of iCRs material for stable isotope analysis, reliable interpretation of stable isotope composition of iCRs its relationship with calcification environments and physiological pathways would definitely require root calcification experiments in controlled conditions. Consistent preliminary stable isotope results obtained in intracellular  $\text{CaCO}_3$  calcification in pot-grown plants of *H. coronarium* (Fig. 3.32A) indicate a great potential in experimental calcification of plant roots. Plants were grown in a mixture of organic soil and crushed marl of known carbonate isotope composition ( $\delta^{13}\text{C} \sim 0.8\text{‰}$ ,  $\delta^{18}\text{O} \sim -2.9\text{‰}$ ) and shown relatively invariable composition of their iCRs ( $\delta^{13}\text{C} -16.2 \pm 0.6\text{‰}$ ;  $\delta^{18}\text{O} -7.2 \pm 0.4\text{‰}$ ). Assuming  $\delta^{13}\text{C}_{(\text{organic})}$  composition of *H. coronarium* equal to the sample of wild-grown Hedysareae ( $-25.5\text{‰}$ ; Table 3.1), analysed iCRs show an average  $^{13}\text{C}$  enrichment of 9.3 with respect to plant organic carbon.

Furthermore, as any other form of soil carbonate, iCR calcite can be strongly modified by weathering, especially microbially driven (Section 3.4.4.2). Admixtures of microbially influenced microcrystalline carbonate forms such as needle fibre calcite (NFC) and calcite nanofibres, commonly associated with dead iCRs (Fig. 3.31), may considerably affect resulting 'bulk'  $\delta^{13}\text{C}$  and  $\delta^{18}\text{O}$  results.

Interestingly, the subgroup of degraded iCR aggregates (type iCR-D in Fig. 3.32 and Table A3-7.1) apparently shows significantly higher  $\delta^{13}\text{C}$  values than unaltered iCR varieties, whereas  $\delta^{18}\text{O}$  of degraded iCRs does not show difference. In general, under a stereomicroscope inspection these degraded iCR samples did not contain visible coatings or traces of NFC and nanofibres but were largely modified by microbial endoliths, as illustrated in Figures 3.27 to 3.30, corresponding to sparmicritisation of Kahle (1977). Since endolithic microborings do not seem to incorporate any secondary, newly formed carbonate, a possible, although purely speculative explanation can be that parts of iCR calcite, 'digested' by endolithic microorganisms, correspond to portions of calcite, relatively depleted in  $^{13}\text{C}$ . Consequently, degraded iCRs thus show enrichment in  $^{13}\text{C}$  relative to unaltered calcite. Namely, geometry of endolithic structures clearly reflects preferential proliferation of microendolithic organisms along particular layers in calcite, likely corresponding to lamellae with incorporated (occluded) organic matter (see also discussion in Section 5.8.3).



### 3.6 Summary and conclusions

The research, performed on original and previously unexplored material from the Mediterranean environments of the Alicante Province in southeastern Spain has included detailed petrographic and micromorphological analysis of intracellularly calcified roots, integrated with mineralogical, elemental and stable isotope analysis of carbon and oxygen.

The study area is dominated by xerophyte shrub and herbaceous vegetation and is characterized by a seasonal moisture regime. Soils, developed over marl and limestone bedrock, are typically associated with accumulations of secondary soil carbonate. In the studied profiles, aggregates of calcified fine roots may locally represent more than a half of the soil mass.

Architectural and morphological analysis of intracellularly calcified root (iCR) systems revealed two morphological groups: symmetrical iCR aggregates and asymmetrical, extremely flattened iCR forms with peripherally placed vascular cylinders. Such aberrant morphologies of calcified roots have not been previously reported in the literature.

Branching architecture of iCR growing in rock fractures have shown extremely ordered, densely spaced herringbone morphologies, which have been interpreted as a root strategy to explore as maximum as possible space and contact surface with the substrate. Intracellularly calcified roots have been found associated with intensively dissolved (corroded) limestone substrates, clearly indicating the link between intracellular carbonate biomineralisation and extrusion of protons (rhizosphere acidification).

Anatomy of calcified root cortex includes highly elongate crystal form, corresponding to radial expansion of cell during the vacuolar biomineralisation. These forms are fully comparable to typical elongate elements of *Microcodium* structures (Chapter 5). SEM investigation of iCR ultrastructure has shown a high diversity of intracellular crystal forms of calcite. It has been suggested that intracellular biomineralisation involves non-classical crystallisation pathways, likely influenced by intravacuolar organic polymers. Final shape of fully calcified cells, replicating intracellular structures to the submicron-size details, apparently forms in two steps, with nanocrystalline carbonate overgrowths deposited on primary mesocrystalline calcite aggregates, formed inside plant vacuoles.

Petrography of apparently micritised calcified cells have confirmed intensive post-mortem alteration of intracellular calcite by microendolithic borings. The phenomenon is analogous to pervasive endolithic modification of *Microcodium* elements (Chapter 5).

Stable isotope analysis of intracellularly calcified roots has shown relatively negative  $\delta^{13}\text{C}$  values, probably largely reflecting plant-respired  $\text{CO}_2$ -based calcification mechanism. Variability of  $\delta^{18}\text{O}$  of iCR calcite most probably reflects variations in O isotopic composition of soil (meteoric) water, likely induced by evaporation.

Architectural, morphological and physiological traits, inferred from iCR-substrate relationship and their geochemical signatures, are in agreement with hypothesis that intracellular  $\text{CaCO}_3$  biomineralisation, coupled with proton extrusion, represents an efficient nutrient-acquiring mechanism and adaptational strategy to nutrient-poor, highly calcareous soils.

## Chapter 4: Identification of the calcifying plants using DNA barcoding

### 4.1 Introduction

As noted in the previous chapter, calcium carbonate formation in plants has gained much less interest than calcium oxalate biomineralisation, what is understandable, considering almost ubiquitous occurrence of Ca oxalates in more than 215 families of angiosperms and gymnosperms (Horner and Wagner 1995; Franceschi and Nakata 2005). On the other hand, almost a total lack of taxonomic information about the distribution of intracellular carbonate mineralisation in plant roots is highly surprising, especially taking into account the immense amounts of iCR produced in modern soils of France that have been well known for almost four decades (Jaillard et al. 1991; Hinsinger 2013). Research on intracellularly calcified roots (iCR) from SE Spain, presented in Chapter 3, has shown extremely widespread occurrence of iCRs, forming massive deposits throughout the study area, and confirmed the influence of intracellular calcification in plant roots on soil functioning and probably functioning of a Mediterranean terrestrial ecosystem on calcareous substrate as a whole. However, a fairly large body of literature about land ecosystems and soils of the Mediterranean Basin and Mediterranean coastal part of Spain in particular (Yaalon 1997; Vogiatzakis 2012; Doblás-Miranda et al. 2015; Ortega et al. 2016 and references therein) does not pay any attention to a specific but apparently widespread and extensive soil biomineralisation activity in terrestrial ecosystems (Lambers et al. 2009). Correspondingly, except for isolated attempts to determine the plants, associated with formation of iCRs from natural or cultivated habitats, there has been no systematic research on the taxonomy of calcifying plants. Jaillard (1983) hypothetically attributed their studied iCRs to grasses (Gramineae or Poaceae), but solely according to the morphology and cell size of the calcified cortex. In several sites in southern France, Jaillard et al. (1991) observed iCRs in soils planted with fruit trees (cherry, peach), which showed evidence of chlorosis (i.e. iron deficiency); unfortunately, the authors did not identify calcifying plants. Experimental root calcification work of Jaillard (1987a) was done on rapeseed crop plants (*Brassica napus*), a plant medium providing limited relevance for the natural



habitats. Two other known systematic studies of intracellular  $\text{CaCO}_3$  biomineralisation in roots were carried on forage legume species. Ross and Delaney (1977) observed massive accumulation of  $\text{CaCO}_3$  in roots of sainfoin (*Onobrychis viciifolia*), a major forage crop in the Rocky Mountain Region of the United States, whereas Tola et al. (2009) experimentally investigated shovel roots of *Hedysarum coronarium*, a perennial legume species, native of the Mediterranean basin and widely distributed from Morocco, Algeria, and Tunisia to mainland Spain and Balearic Islands, Corsica and central to southern Italy. Similarly to *O. viciifolia*, *H. coronarium*, known also as Spanish sainfoin, is widely exploited as a forage crop due to its pronounced drought resistance, strong tolerance to alkaline soils, and good agronomical yield (Tola et al. 2009). Interestingly, calcification in special shovel roots of *H. coronarium* has already been observed more than hundred years ago by Mottareale (1898) and Severini (1908a, b), however, these early discoveries have largely remained unnoticed (Tola et al. 2009).

Plant roots growing in a mixed belowground community are usually difficult to identify at any taxonomic level, especially morphologically simple fine roots (Cutler 1987; Jackson et al. 2000; Cutler et al. 2008). Without extensive and often necessarily invasive digging (fascinating reconstructions of root systems based on extensive excavations are presented in the work of Kutschera, Lichtenegger and Sobotik (Kutschera et al. 1997, 2013)), it is virtually impossible to trace an individual root system from a calcified fragment, excavated deep in the soil or weathered rock profile, to its coarse parent root and further to the determinable aboveground part of a plant.

The study area in the Alicante Region (Fig. 3.1 in the previous chapter) is largely situated in the areas in Serra d'Aitana under partial natural protection regime (Giménez-Font and Marco Molina 2017, Fig. 2), preventing extensive excavations in the natural habitats. Given the inconspicuousness of fine roots and the fact that deep roots are generally indistinguishable from one another without the use of molecular tools (Jackson et al. 1999, 2000; Linder et al. 2000; Brunner et al. 2001; Maeght et al. 2013), utilisation of DNA barcoding seems to provide a promising identification method for calcified roots

The principal aim of this pilot study has been to test the applicability of methods of root identification based on DNA sequences to intracellularly calcified roots with relatively small amount of preserved organic tissues, typically existing in iCR samples. Applied DNA barcoding method uses a standard short genomic region that is universally present in



**Figure 4.1.** Field sampling of iCR material for DNA analysis. Terrain map (captured from Google Maps, april 2021) of the area E of the Village of Sella, showing sampling locations of roots used in DNA barcoding (red pointers). B) Sampling in one of the excavation pits at the site T14-462. C) Dense network of intertwined root systems penetrating into weathered marl. Pit excavated in an old forest road-cut, approximately 1.5 m belowground, site T14-461.

target biological material and has sufficient sequence variation to discriminate among taxa (Hollingsworth et al. 2009; Fazekas et al. 2012; de Vere et al. 2015). One of the objectives of the study was to produce a methodological framework for a subsequent systematic sampling campaign(s), based on comparative DNA analysis of calcified roots and ideally including aboveground plant parts, identified by both classical taxonomic methods and DNA barcoding. Although limited in number, the first results of identification of calcifying plants based on successfully extracted, amplified and sequenced DNA provide good basis for the selection of species and genera for future experimental setup of iCR biomineralisation physiology and biogeochemistry.

## 4.2 Material and methods

Field sampling of live iCRs was performed in March 2014 and complemented in late May 2015 with collecting prospective calcifying plants for morphological determination based on fresh leaves, flowers and seed pods. The latter material has been included in the herbarium collection at the Institute of Biology ZRC SAZU, for potential use in future comparative DNA barcoding studies.

Material was sampled at two localities along the unpaved road in the Barranc de l'Arc ravine, E of the Town of Sella (Figs. 4.1A, 3.1; Table A3-1). At each site, several shallow, approximately 0.5 m deep pits were excavated in the marly substrate exposed in roadcuts, corresponding to depths 1 to 1.5 m below the surface. The pits were excavated deep enough to encounter fresh iCR material (Fig. 4.1B, C). Hand-specimen size pieces of marl with iCR structures with preserved organic tissues (Figs. 4.2A, B, 4.3C-F) were carefully wrapped in filter paper and aluminium foil. Fresh live fine roots (Fig. 4.2E, F) and portions of thicker fine roots with attached iCR fragments (Figs. 4.2C, 4.3A, B) were extracted with clean tweezers, inserted between two sheets of filter paper and placed into paper bags together with an ample amount of fresh silica gel. During the field sampling campaign, samples were kept at room temperature and dry conditions. In the laboratory, samples were further dried by being kept at room temperature and low humidity for several days and finally desiccated in an oven at 30°C for 48 hours. Dry samples have been kept in plastic boxes and petri dishes along with silica gel.

Organic root tissues were collected from samples under a stereomicroscope using sterile tweezers. Twenty-one samples were taken for DNA extraction, consisting of preserved vascular cylinders, coarse root fragments with attached fine iCR, and fully calcified iCRs with preserved epidermis, parts of cortex and vascular system (Fig. 4.2; also see details in Table 4.1). From 0.5 to 2.5 mg of dehydrated organic material was obtained per sample; prior to analysis, samples were stored in plastic containers filled with silica gel desiccant.

DNA isolation was performed at the Evolutionary Zoology Lab of the Institute of Biology ZRC SAZU in Ljubljana, following general protocols of the Plant DNA Barcode Project (Department of Botany NMHN, Smithsonian Institution, Washington, D.C.).

DNA was isolated from organic parts of iCR samples using the DNeasy Plant Mini Kit (QIAGEN, <https://www.qiagen.com/>) following the protocol, and adding the pre-step of homogenization of dry tissue with a pestle in 1.5ml Eppendorf tube.



**Table 4.1.** Samples of calcified roots with preserved organic remains, selected for DNA extraction and barcoding. Only samples with codes, listed in the first column (EZL = Evolutionary Zoology Lab at the Institute of Biology ZRC SAZU) yielded enough extracted DNA material for sequencing. Samples of above-ground plant material, marked with \*, yielded enough extracted DNA but have not been sequenced yet. For sample locations (T14-461, -462, and -458) see map in Fig. 4.1 and Table A3-1.1 in Appendix A3-1).

EZL sample code	sample #	material	remarks (pre-preparation etc.)	dry mass [mg]
<b>A01</b>	T14-461-01-01	coarse (tap) root of "Astragalus-type" plant with attached, partly calcified fine root (iCR)	peeled, mm stripes of coarse root fragment (cortex/xylem/phloem); bark peeled away	1.3
*	T14-461-02-01	same plant specimen as above; above ground part of "Astragalus-type" plant	bark peeled off, 3 mm-long stripes cut from cortex and phloem/xylem	>5
*	T14-462-20-A	<i>S. rosmarinus</i> - aboveground part: woody stem and leaves	peeled, mm stripes of stem; bark peeled off	>5
<b>A05</b>	T14-462-20-B	supposedly same plant as above - coarse (woody) root, ~3mm diam., with fine roots associated with largely disarticulated iCRs	peels of coarser woody root, bark peeled off; not clear if coarser woody root is related to calcified cortices	2.4
<b>A08</b>	T14-462-08-1	fine root vascular parts, extracted from a lump of iCR	not clearly associated/related to calcified root cortices/aggregates	2.0
	T14-462-02-1	small iCR, shovel roots = type II	preserved vascular cylinder and fragments of epidermis	1.0
<b>A07</b>	T14-462-18-1	iCR with organic parts (type II)	4 pieces of fine root tips; well preserved epidermis, vascular cylinders and root cap part; organic parts cleared of calcified cortex	1.3
	T14-462-18-2	iCR with organic parts	epidermis, vascular cylinders, clay ('decalcified cylinder') present; organic parts cleared of calcified cortex	0.9
<b>A06</b>	T14-462-16-1	iCR (type II) with organic parts	pieces of fine root tips; well preserved epidermis, root hairs, vascular cylinders and root cap part; organic parts cleared of calcified cortex	1.4
	T14-462-03-1	iCR (type II) with organic parts	pieces of fine root tips; preserved epidermis, vascular cylinders and root cap part; organic parts cleared of calcified cortex; small amount of organic material	0.8
<b>A03</b>	T14-461-03-06	iCR (type I) with preserved vascular cylinder	dry vascular cylinders associated with calcified cortex; organic parts cleared of calcified cells	1.8
<b>A04</b>	T14-461-03-08	iCR (?type II) with preserved vascular cylinder	dry vascular cylinders associated with calcified cortex; fungal spores abundant	1.8
	T14-461-03-08/D	same as above	same as above	1.5

Table 4.1 (continued)

EZL sample code	sample #	material	remarks (pre-preparation etc.)	dry mass [mg]
	T14-461-03-10	small portion of live (fresh) roots, fully calcified cortex	tips (root cap part), epidermis and vascular part; very small amount of organic material	0.8
	T14-461-03-10/A	same as above	epidermis and vascular part; very small amount of organic material	0.6
	T14-461-03-09A	fragment of coarse (secondary-thickened) root with attached iCR part	redish-coloured epidermis	1.1
<b>A02</b>	T14-461-03-01	small portion of fresh fine root, fully calcified cortex (iCR type I)	vascular cylinder and epidermis; fungal spores present	1.4
	T14-461-03-11	dry vascular cylinders associated with fully calcified cortices	relatively well preserved mm-size parts of vascular cylinders; fungal spores present	1.6
	T14-461-03-11A	same as above	same as above	1.6
	T14-458-31	fine root, attached to a coarse root of ? <i>S. rosmarinus</i> , associated with clusters of iCRs (type I)	not clear if calcified or not	0.9

Amplifications were performed for fragments of three plastid loci (*rbcL* and *matK* and *trnH-psbA*) and one nuclear (ITS) gene region, which have become the standard barcode of choice in most investigations for plant phylogenetics (Hollingsworth 2011; Hollingsworth et al. 2009, 2011; Fazekas et al. 2012, De Vere et al. 2015, Kress et al. 2005, 2015, 2107).

PCR reactions had a total volume of 30  $\mu$ l, consisting of 14.0  $\mu$ l of dd H<sub>2</sub>O, 5.0  $\mu$ l of PCR buffer GoTaq® Flexi (Promega Corporation), 3.0  $\mu$ l of MgCl<sub>2</sub> (25 mM, Promega), 3.0  $\mu$ l of dNTP Mix (2  $\mu$ M each, Biotools B&M Labs, S.A., Madrid), 1.5  $\mu$ l of each forward and reverse 10  $\mu$ M primer, 0.6  $\mu$ l of bovine serum albumin (Promega, 10 mg/ml), 0.4  $\mu$ l of 5 U GoTaqFlexi Polymerase and 1.0 - 2.0  $\mu$ l of DNA. Amplification was performed on a Veriti® 96-Well Fast Thermal Cycler (Applied Biosystems).

For each gene fragment different protocols were used with varying annealing temperatures and PCR cycles. The majority of samples was processed using a touch up protocol or a post-PCR protocol.

PCR products were subjected to electrophoresis on agarose gel (1%) and photographed under UV light, then purified using a Wizard® SV Gel and PCR Clean-Up System

(Promega). Products were sequenced by Macrogen Europe Inc. service (Amsterdam, Netherlands). Chromatograms were combined and manually edited using Geneious Pro 5.6.6 software package (Biomatters, Auckland, NewZealand; <https://www.geneious.com>).

Edited sequences were compared with sequence databases using NCBI BLAST (Basic Local Alignment Search Tool; Altschul et al. 1990). FASTA format or bare sequences were copied into the query input ('Search' text area). Individual sequences and combined data from all 3 markers were determined using the BLASTN (standard nucleotide BLAST) sequence matching (Appendix A4-2) using different options (Agostino 2013). In the "Program Selection" box, 'highly similar sequences (megablast)' mode was chosen as a BLAST algorithm.

### 4.3 Results and discussion

Of the 21 processed samples (Table 4.1), gene fragments were obtained for 8 samples (8 *rbcLa*, 3 *matK*, and 4 ITS, respectively). Experiments with *trnH-psbA* loci have not yielded positive results. Edited sequences for samples A01 to A08 are presented in Appendix A4-1. Comparison of sequences with published sequence databases using BLAST tool was performed applying different search criteria. Significant BLAST alignment (matching) results for individual samples are presented for two gene regions (*rbcLa* and ITS) in Appendix A4-2 and A4-3, respectively. BLAST sequence identification results for individual samples are listed and commented below.

#### Sample A01 (Fig. 4.3B)

Material of this sample consisted of clean, several mm large stripes peeled from the central part of a coarse tap root with clearly attached lateral fine roots with a fragment of calcified cortex. The sample yielded sequences for all gene loci. Sequence matching with BLAST showed very good match with different species of the genus *Onobrychis*. The best match, showing 99% identity with *Onobrychis viciifolia*, was gained for all gene regions as well as for using combinations, e.g. of *rbcLa* and *matK* sequences.

#### Sample A02 (Fig. 4.3C)

Material consisted of fully calcified iCRs with preserved epidermis, parts of cortex and vascular system. Sequencing results were gained for *rbcLa* locus only. BLAST showed best



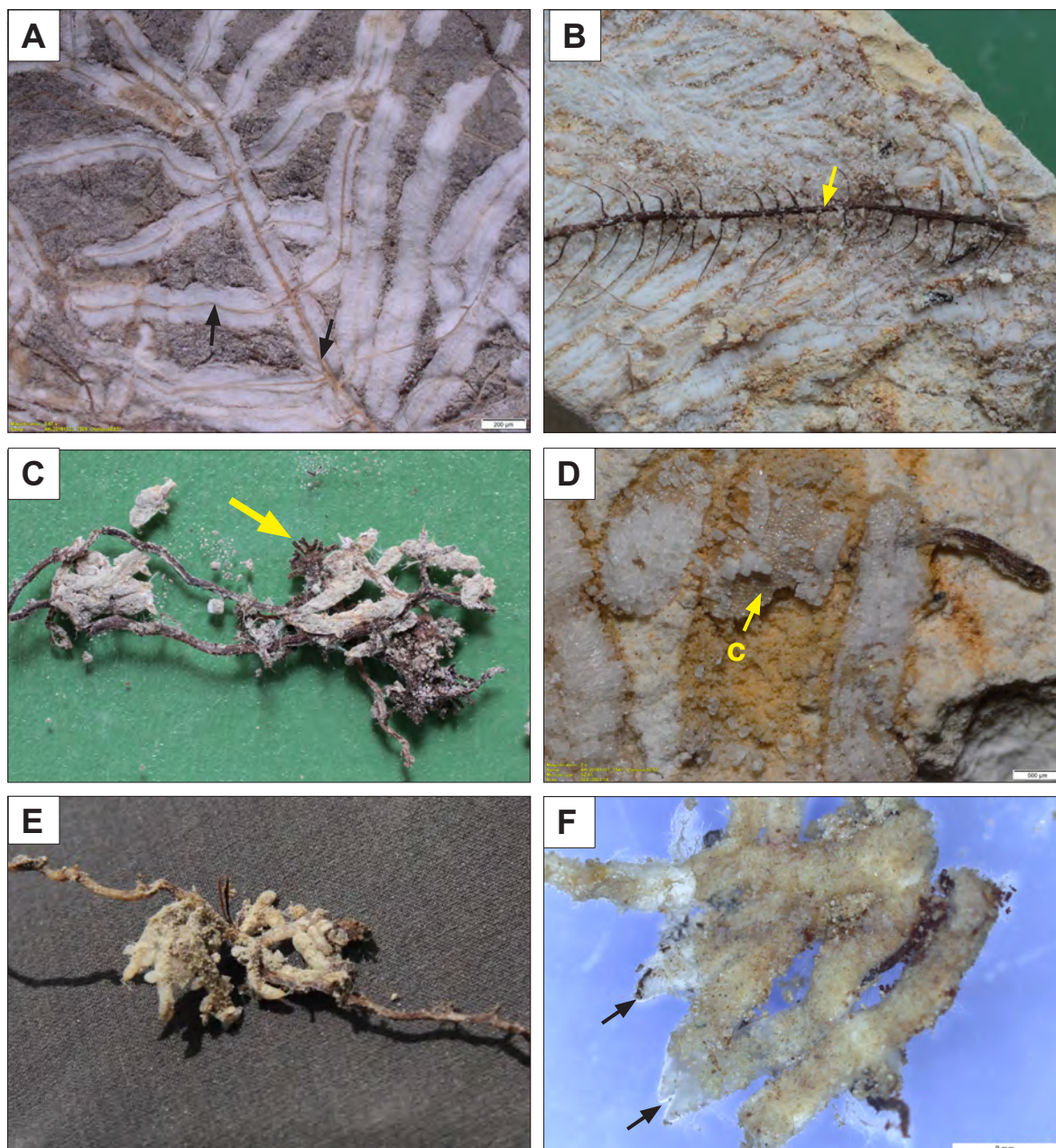


**Figure 4.2.** Different types of sampled calcified fine-root material with preserved organic material, potentially suitable for DNA extraction. A) Fully calcified 'herringbone' branching root system from a bedding plane fissure with well-preserved vascular system (black arrows). Sample T14-461-3-13. B) Herringbone branching iCR system similar to A, with preserved thicker, non-calcified main root axis with emerging lateral branches of vascular tissues. Sample . C) Clusters of iCRs (white) attached to interwoven coarser roots of different plants. Arrow indicates dry typical, dark brown short pine roots, probably ectomycorrhizal. Sample T14-461-3-02 (not used in DNA extraction). D) iCR with small part of preserved epidermis (arrow). E) Clusters of live iCRs attached to a coarse root. F) Detail of E: cluster of partly calcified roots with non-calcified root apices (black arrows). Water-immersed sample, image taken under stereomicroscope with combined transmitted and reflected light. Finestrat-Sella, site T15-823.



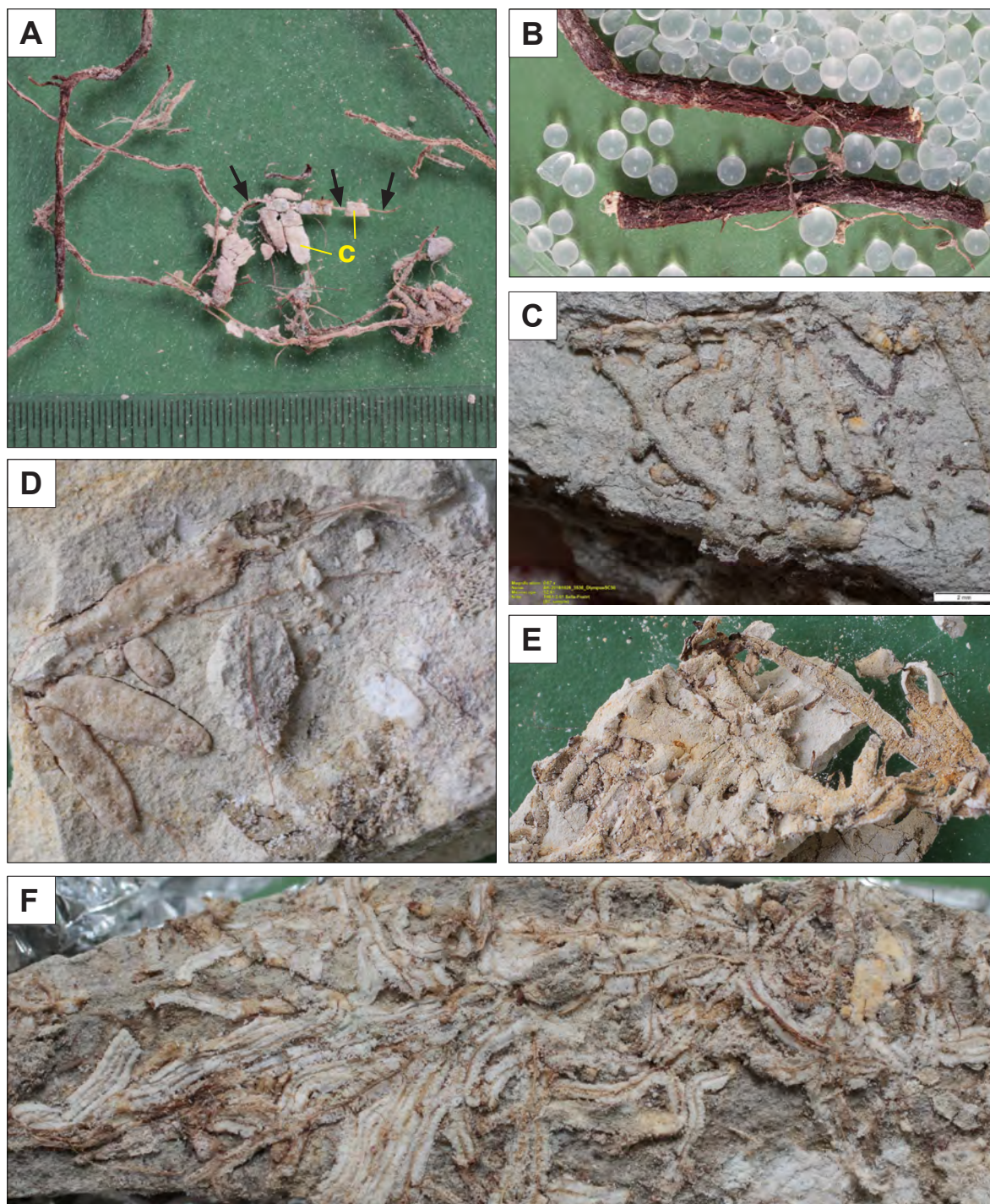


**Figure 4.3.** Selected root material used for DNA extraction. A) Type II iCRs with calcified fragments of cortex (c) and preserved vascular cylinders (arrows). Sample T14-461-3-09. B) Coarse root pieces with connected fine roots, partly calcified. Sample T14-461-1-01 (A01). C) Fully-calcified iCRs with preserved epidermis, parts of cortex and vascular system. Sample T14-461-3-01 (A02). D) Type-II iCRs, fully calcified. Sample T14-462-08. E) Type-II iCRs, fully calcified. Sample T14-462-18 (A07). F) Intertwined calcified roots with well-preserved vascular system and epidermal tissues. Sample 14-461-3-08 (A04).

similarity results for different genera of the IRLC legume group (inverted repeat-lacking clade) showing e.g. 93% identity with *Melilotus* sp. and 92% identity with *Trifolium* sp.

### **Sample A03**

Material included well-preserved dry vascular cylinders associated with calcified cortex. Sequences were obtained for all three gene regions. Sequence matching using BLAST showed excellent match with *Onobrychis viciifolia* (98% identity for *rbcLa* and 99% identity for ITS sequence, respectively). Perfect match between samples A01 and A03 is also evident on phylogenetic trees in Figures 4.4 and 4.5.

### **Sample A04 (Fig. 4.3F)**

Material comprised fragments of dry vascular cylinders and epidermis. Sequencing results were gained for *rbcLa* locus only. BLAST search showed best match results for different groups of the IRL clade (cf. sample A02), including Hedysareae (>93% identity).

### **Sample A05**

Material consisted of extracted peels of coarse (woody) root, ~3mm in diameter, with attached fine root branches, associated with abundant disaggregated iCRs clusters. However, it was impossible to confirm if organic remains of fine roots were calcified. Sequences were obtained for all three gene regions. BLAST search showed 100% match with multiple published sequences of *Salvia rosmarinus*. The result is ambiguous and indicates that the analysed material is very probably not related to iCRs.

### **Sample A06**

Material consisted of several pieces of fine root apical parts with well preserved epidermis, root hairs, vascular cylinders and root cap parts. Sequencing results were gained for *rbcLa* locus only. BLAST search showed best match results for different groups of the IRL clade (see sample A02), e.g. Trifolieae (>93% identity). Figure 4.4 shows close relationship with sample A04.

### **Sample A07 (Fig. 4.3E)**

Material comprised several fragments of terminal portions of a partly calcified fine root with well-preserved epidermis, vascular cylinders and dried root caps. Sequencing results



were gained for *rbcLa* and ITS loci. BLAST search showed excellent matches with different species of genus *Ononis*, a large genus of the legume tribe Trifolieae. Identity of 98% with *O. tridentata* was shown for ITS sequence and 98% identity with *O. reclinata* for *rbcLa* sequence.

### Sample A08

Material consisted of fine root vascular parts, extracted from a lump of iCRs. Organic material was not clearly associated/related to iCR aggregates. Sequencing results were obtained for *rbcLa* only. BLAST search returned very good match with different species of the genus *Erica*, showing 98% identity with *Erica tetralix*. Because of the unclear correspondence of organic parts with iCR aggregates, the results are considered highly questionable.

Phylogenetic relationship of samples, based on *rbcLa* gene sequences, successfully acquired for all samples, is shown in Figure 4.4. The neighbour-joining tree diagram in Figure 4.5 is based exclusively on six sequences of the members of the legume family, whereas the sequences of two ambiguous samples (A05 = *Salvia rosmarinus* (Lamiaceae), and A08 = *Erica* sp. (Ericaceae)) were excluded from the analysis. All six samples apparently belong to the IRLC group (inverted repeat-lacking clade, a monophyletic group of Fabaceae; Wojciehowski et al. 2004), which includes tribes Hedysareae (including two closely related genera *Hedysarum* and *Onobrychis*), Trifolieae (with important genera *Medicago*, *Melilotus*, *Ononis* and *Trifolium*), and Astragaleae (genus *Astragalus*). Representatives of the listed genera are extremely widespread and highly adapted to calcareous soils of the study area and the Western Mediterranean region in general (HVMO 2021, Crespo and Serra 1993). Furthermore, these genera and groups of legumes include several well-studied model plants, which can be particularly suitable for future experimental setup.

Of the two genera, identified with DNA barcoding with highest similarity with published data (*Onobrychis* in samples A01 and A03, and *Ononis* in sample A07), morphological identification of plant material collected during the flowering season (in May 2015), including flowers and diagnostic seed pods, confirmed only presence of *Onobrychis* sp. The other species, morphologically determined on a subspecies level, is *Hedysarum boveanum* ssp. *europaum* (Figs. 4.6 and 4.7; B. Surina, personal communication). Importantly, at the time of performing the BLAST matching (April 2021), GenBank database did not include *rbcLa*, *matK* and ITS sequence data for *Hedysarum*

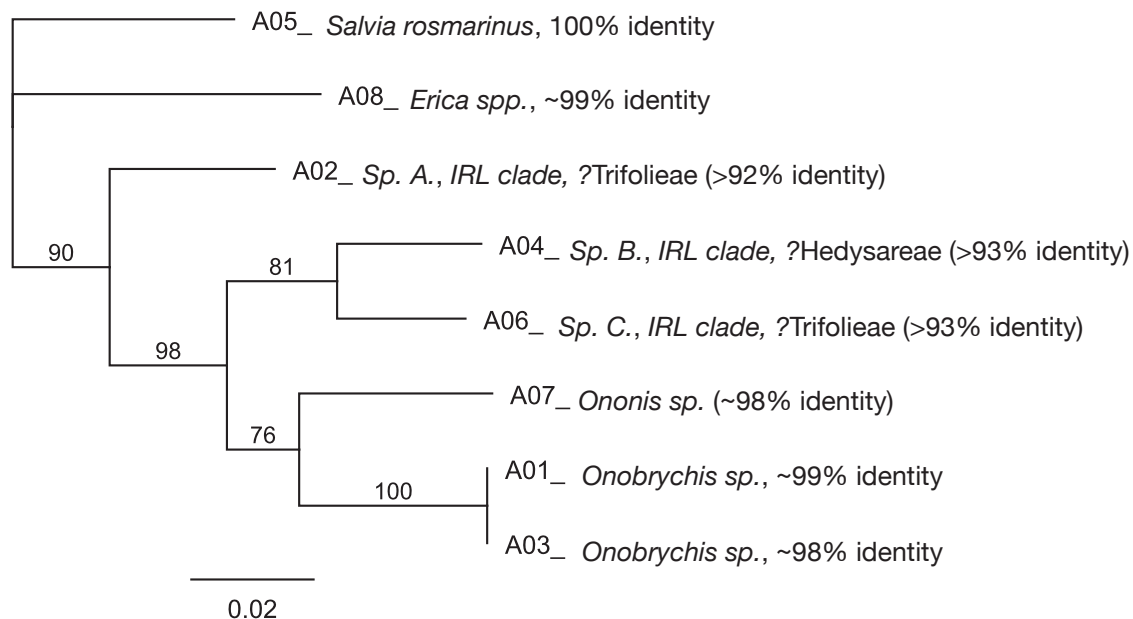


**Figure 4.4.** Phylogenetic neighbour-joining tree diagram showing relationship of DNA barcoding samples A01 to A08, based on *rbcLa* gene sequences, obtained for all eight samples, with tentative species/genus identification of samples based on queries producing significant BLASTN alignment results.

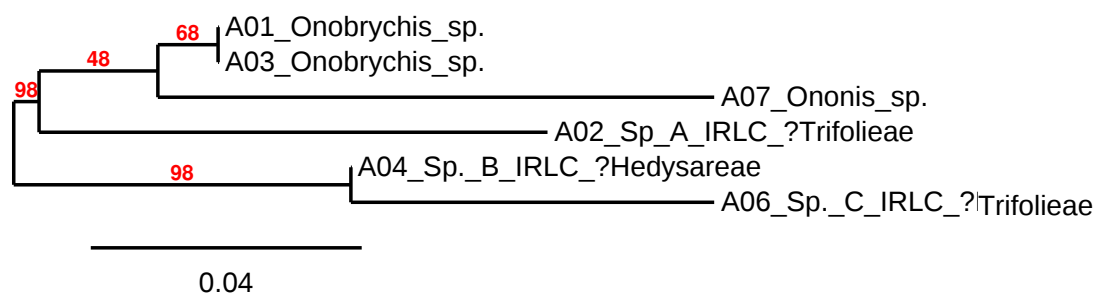


**Figure 4.5.** Phylogenetic neighbour-joining tree diagram showing relationship of 6 Leguminosae (Fabaceae) *rbcLa* sequences (excluding data of A5 and A8). IRLC = inverted repeat-lacking clade, a monophyletic clade of a subfamily Faboideae. Tree constructed using PhyML software tool, Online Phlogeny Analysis programme (<https://www.phylogeny.fr>). Also see Appendix A4-5 with a phylogenetic tree of selected species of Mediterranean Fabaceae, based on published BLAST *rbcLa* sequences listed in Appendix A4-4.

*boveanum*. FASTA format *rbcLa* sequences from NCBI GenBank® (<https://www.ncbi.nlm.nih.gov/>) of selected representative species of common Mediterranean legumes, listed in Appendix A4-4. Their relationships are shown in Appendix A4-5 in a phylogenetic tree constructed on the basis of listed *rbcLa* sequences. Sequences of *Hedysarum alpinum*, *H. boreale* and *H. coronarium* were used instead of *H. boveanum*.

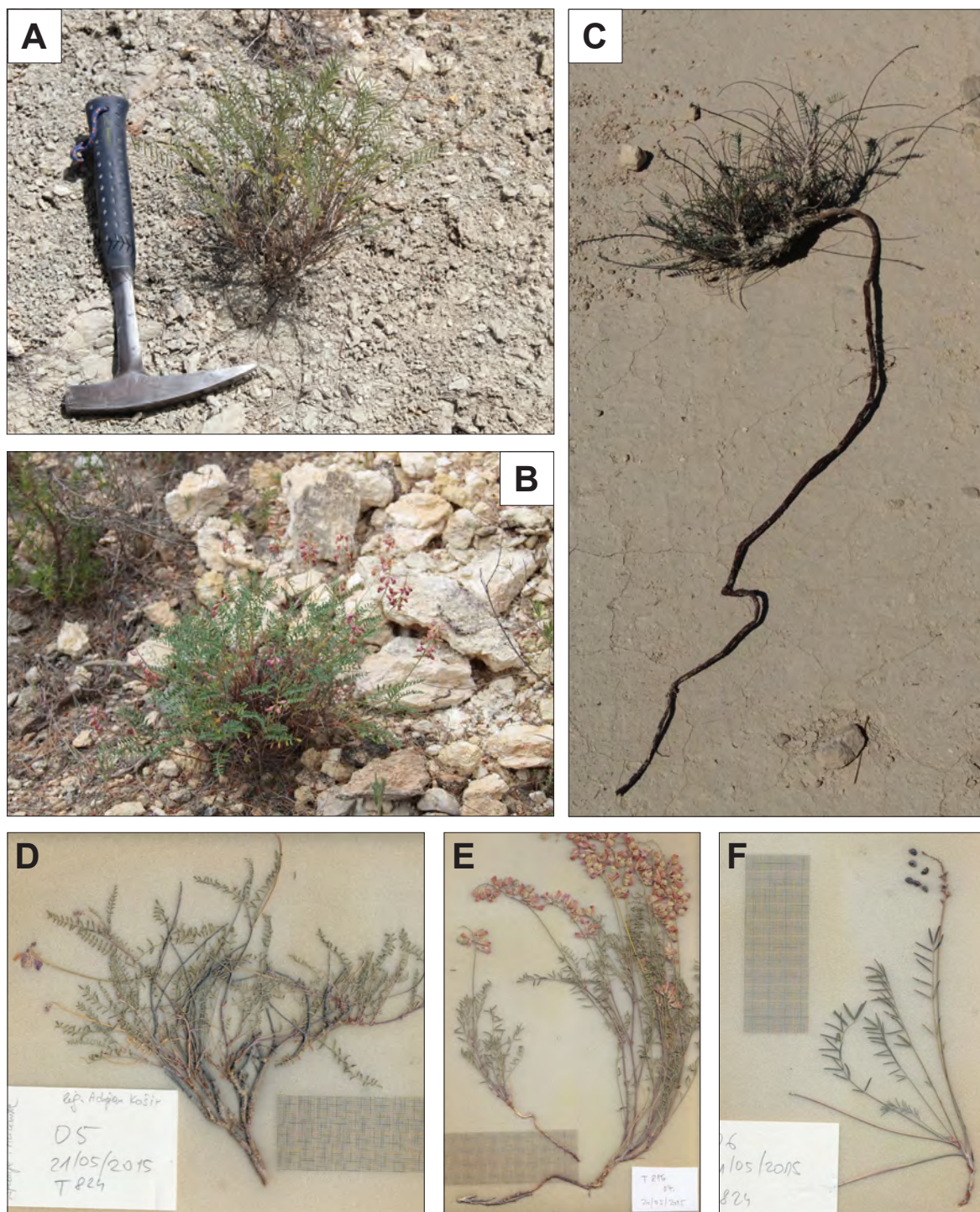


**Figure 4.6.** Field appearance and herbarium-dried specimens of legume plants from Hedysareae tribe from the Finestrat-Sella locality, corresponding to species/genera identified by DNA barcoding. Cf. Appendix A4-2. A and B) Small evergreen bushes (note flowers in B) collected in May 2015; C) Excavated small plant with a part of a long tap root. D, E) Specimens of *Hedysarum boveanum* ssp. *europaum*; F) Specimen of *Onobrychis* sp. Herbarium material was determined by Boštjan Surina, FAMNIT, University of Primorska, Koper/Capodistria.



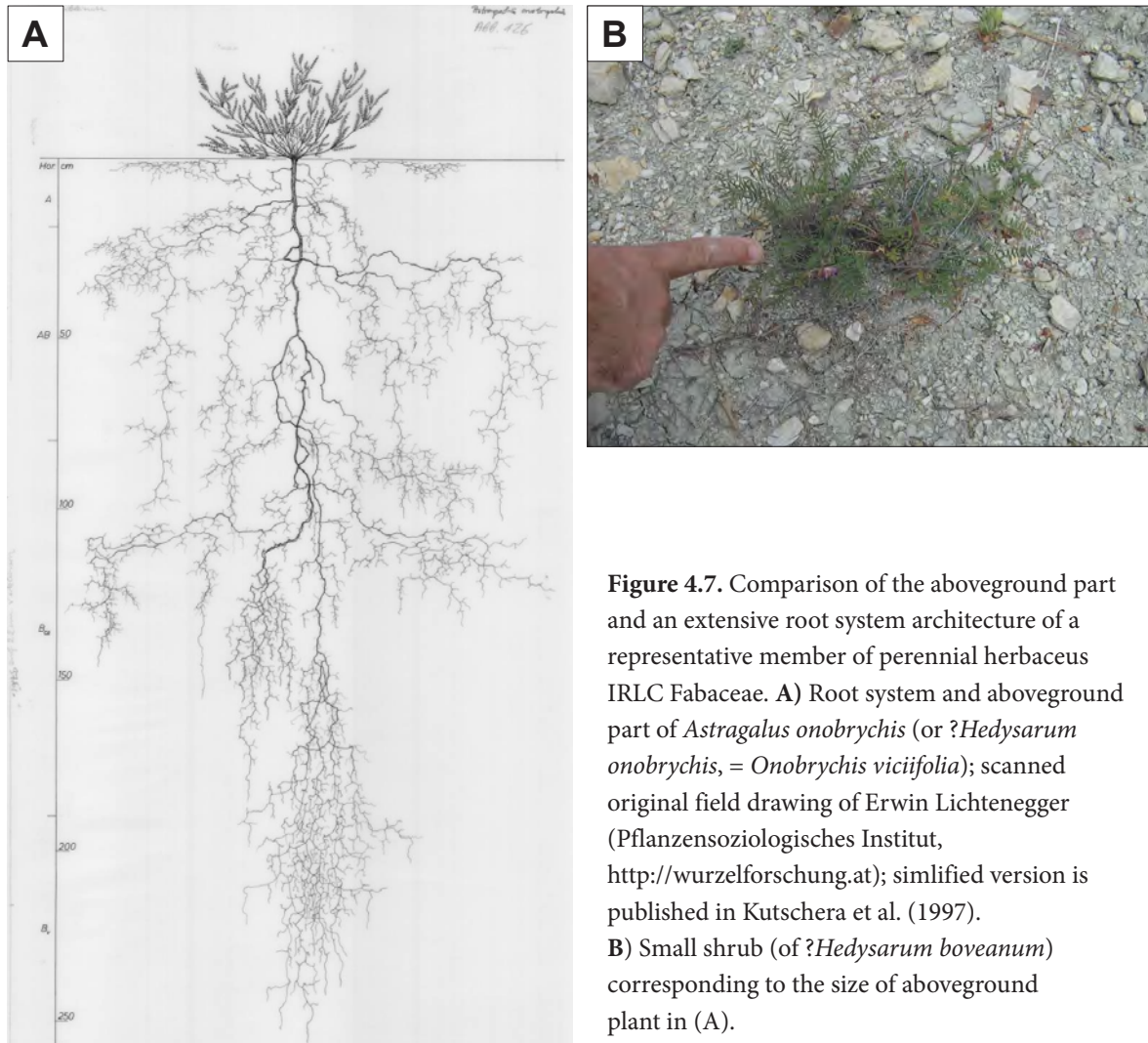


**Figure 4.7.** Comparison of the aboveground part and an extensive root system architecture of a representative member of perennial herbaceous IRLC Fabaceae. **A)** Root system and aboveground part of *Astragalus onobrychis* (or ?*Hedysarum onobrychis*, = *Onobrychis viciifolia*); scanned original field drawing of Erwin Lichtenegger (Pflanzensoziologisches Institut, <http://wurzelforschung.at>); simplified version is published in Kutschera et al. (1997). **B)** Small shrub (of ?*Hedysarum boveanum*) corresponding to the size of aboveground plant in (A).

Performed DNA barcoding of iCRs have provided highly promising results and indicated strength of the barcoding approach, particularly in that the methodology can be usefully applied for small amounts of plant tissues such as organic remains preserved in iCRs. Among the three DNA regions, recommended for plant barcoding (Hollingsworth et al. 2009) and applied in this study, *rbcL*a manifested the best performance. Unfortunately, *matK*, which offers high-resolution discriminating power, especially in combination with *rbcL*a, did not bring expected results. However, all three gene regions produced good quality sequences, therefore the further systematic genetic study of iCR and aboveground vegetation will likely be based on *rbcL*+*matK* as a standard 2-locus barcode, and supplemented by the ITS gene.

Unexpectedly, DNA barcoding results of iCRs from natural habitats are predominantly (or exclusively) matching with legumes. This is in agreement with (scarce) previous

research, which actually recognised intracellular carbonate biomineralisation only in roots of cultivated legume genera *Onobrychis* (Ross and Delaney) and *Hedysarum* (Tola 2009). Watt and Weston (2009) have emphasised the importance of (calcified) shovel roots of *H. coronarium* as one of the most outstanding examples with a highly specialised root development and biochemical mechanism to enable acquisition of very limiting soil resources. However, the small sample of iCRs used in the present DNA barcoding study and very limited obtained results do not enable any definite generalisation about the intracellular calcification being specific for only one taxonomic group.

#### 4.4 Conclusions

A test study of DNA barcoding performed on twenty-one samples of organic tissues, associated with iCRs, produced eight positive results. Among the three standard barcoding loci applied in DNA identification, *rbcLa* sequences showed best performance and were obtained in all successfully PCR-amplified samples, whereas ITS and *matK* sequences were reproduced only in 4 and 3 samples, respectively. Significantly, all three gene regions were successfully obtained in larger samples of root tissue, indicating the need for methodological improvement.

DNA barcodes of six samples showed good to excellent similarity (identity) with published sequences of the IRL clade (inverted repeat-lacking clade), a monophyletic group of Fabaceae. Three samples were reliably identified on a genus level: two samples as *Onobrychis* sp. and one as *Ononis* sp. The other four legume iCR samples apparently also belong to different species of the tribes Hedysareae and Trifolieae.

DNA barcodes of two samples showed perfect fit with published sequences of *Salvia rosmarinus* and *Erica* sp., both among the most common plants in the vegetation in the study area but not related to legumes. However, these results should be taken with care since the organic parts in these two samples were not undoubtedly related to associated iCR aggregates.

Results of the present study have provided a very good framework for a future systematic research on iCRs from natural habitats, including their DNA taxonomy and experimental investigation of intracellular CaCO<sub>3</sub> mineralisation in plant roots.

## Chapter 5: The *Microcodium* controversy

### 5.1 Introduction

*Microcodium* is a problematic fossil biogenic carbonate feature with a very distinctive cellular aggregate structure composed of individual polyhedral, elongate crystalline elements of calcite, typically arranged in a radial pattern. It has a long stratigraphic record but very discontinuous stratigraphic distribution spanning from the late Palaeozoic to Quaternary, with a peak occurrence in the late Cretaceous and particularly during the early Palaeogene.

In the original palaeontological description of material from the Tertiary (Miocene) marine facies of South Germany, the typical *Microcodium* was identified as a new genus of codiacean calcareous green algae and described with a type species named *M. elegans* (Glück 1912). Older literature mostly followed Glück in his nomenclature and interpretation of algal origin although *M. elegans* proved to be a junior synonym of *Paronipora penicillata* (Capeder 1904). The senior form *P. penicillata* was described as a favositid (tabulate) coral species from a Cretaceous-Eocene succession in Piedmont, Italy (Cherchi and Schroeder 1988).

Based on material from various French outcrops of Cretaceous and Palaeogene continental successions, Marie (1957) and Lucas and Montenat (1967) rejected previous interpretations of the marine origin of *Microcodium* and claimed against its relationship with algae. Their crucial observations showed that (1) *Microcodium* was a postdepositional phenomenon, (2) it could penetrate deeply into the limestone substratum through cracks and bedding plane partings, and (3) demonstrated in thin sections the ability [of the organism] “to corrode the rock on which they have settled” (Lucas and Montenat 1967).

Subsequent studies have mostly accepted that *Microcodium* is invariably associated with continental palaeoenvironments and soil formation (Bodergat 1974), and that even “when observed to corrode marine rock, [...] it is always situated below an erosional surface reflecting palaeoemersion” (Freytet & Plaziat 1982). As such, in its modern conception, it has been considered as a specific pedological feature and a reliable diagnostic criterion for recognition of past vadose environments.



Lucas and Montenat (1967) were the first authors suggesting heterotrophic life mode of the *Microcodium* organism(s), according to their interpretation probably related to filamentous soil bacteria, whereas Bodergat (1974), in one of the most thorough earlier micromorphological studies of *Microcodium*, suggested its link with (a consortium of) Actinobacteria (Actinomycetes). The hypothesis of root-related origin of *Microcodium*, put forward in the seminal work of Klappa (1978a), has been founded on extended range of morphologies described by Esteban (1972, 1974) and Bodergat (1974), which included atypical forms in the definition (diagnosis) of *Microcodium* (Appendix A5.2, Fig. A5-2.1). Re-evaluation of descriptions and original illustrations in the cited papers shows that all of the atypical *Microcodium* forms are actually (identical to) intracellularly calcified roots (Chapter 3) and originated in the same broad area of the Spanish Levante – in case of Bodergat (1974) from the Holocene (“Post-Thyrrenian”) of Jijona near Alicante, Klappa’s (1978a) material from Recent and Pleistocene calcrete profiles of the coastal region of SE Spain and the Island of Ibiza (Klappa 1987b), and Esteban’s (1974) examples from the Pleistocene of the Tarragona area (Catalonia, NE Spain). In their thorough study, Jaillard et al. (1991) highlighted significant morphological (structural) and ecological resemblance between modern calcified roots and the classic (fossil) *Microcodium* but emphasised that the hypothesis of their identity should be carefully re-examined. Further evidence in support of rhizogenic interpretation of *Microcodium* has been provided by Morin (1993), Wright et al. (1995), Alonso-Zarza et al. (1998) and Košir (2004).

Original descriptions and clear illustrations of Capeder (1904) and Glück (1912) undoubtedly show that both names refer to similar fossil forms with identical morphological characters. Despite the formal taxonomic priority of *P. penicillata*, highlighted by Cherchi and Schroeder (1988), the generic name *Microcodium* has predominantly remained in use also in the recent literature – regardless of genetic interpretation of the feature as a fossil or as a type of sedimentary (diagenetic) or soil fabric.

*Microcodium* has served as one of the most useful micromorphological features of palaeosols and subaerial exposure surfaces in carbonate successions, often easily recognizable already in outcrops and almost unambiguously in thin sections. Massive accumulations of *Microcodium* characterise continental carbonate and clastic deposits, especially in the peri-Mediterranean area, such as classic Paleocene (‘Vitrollian’) fluvial, lacustrine and palustrine facies of southern France (Freytet and Plaziat 1982 and references therein) and the non-marine Garumnian deposits of the Spanish Pyrenees (e.g. Rossi 1997;

Baceta et al. 2011; Pujalte et al. 2014, 2022). Rock-forming *Microcodium* deposits are locally so widespread that they have been given brand names such as *microcodiomite* (for a type of Lutetian architectural stone from Provence, France; Bodergat 1974) and *microcoditas* – for a facies, forming several metres thick beds, in the Paleocene continental successions of the Áger Basin (Rossi 1997).

*Microcodium* accumulations make important stratigraphic units and characterise boundaries of major depositional sequences in the eastern part of the French Pyrenees (Southern Corbières; Combes et al. 2004), palaeokarst cave systems in the Paleocene-Eocene carbonate platform system the Urbasa–Andia plateau (the Pyrenees, north Spain; Baceta et al. 2007), superregional palaeokarst unconformities of the Adriatic-Dinaric Carbonate Platform in Croatia and Slovenia (Otoničar 2007, 2021; Brlek et al. 2013; Brlek et al. 2014; Brlek and Glumac 2014 and references therein) and the Eocene *Microcodium* Formation (Faure-Muret and Fallot 1954; Varrone and Clari 2003) in the French-Italian Maritime Alps and Cretaceous-Palaeogene of Sardinia (Matteucci & Murru 2002; Murru et al. 2007; Murru et al. 2015).

Immense amounts of reworked *Microcodium* calcarenites were accumulated in a marine hemipelagic setting of the Subbetic Zone (Betic Cordillera, southern Spain; Vera et al. 2004; Molina et al. 2006; Pujalte et al. 2019a, b). Here the Danian–early Selandian succession (the Olivares and the Majalcorón Formation) is largely composed of calcarenites, comprising 60–90% of resedimented *Microcodium* grains, which are intercalated in hemipelagic marls rich in planktonic foraminifera (Rodríguez-Tovar et al. 2020).

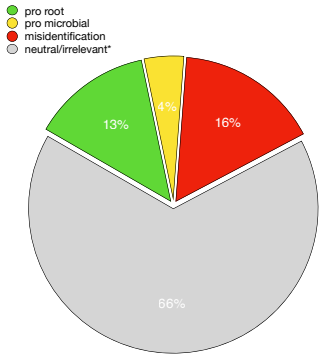
An intriguing Palaeozoic example is an unusually thick *Microcodium* occurrence in Early Permian carbonates from an unnamed oil field in the Timan Pechora Basin of northern Russia (Lapointe et al. 2005) associated with a multi-horizon oil-bearing reservoir, up to 30 metres thick; *Microcodium* horizons, up to 10 m thick, are reservoir prone where they have been leached by meteoric fluids below a major unconformity.

*Microcodium* has received a considerable interest in sedimentology, and soil and plant science. Major papers dealing with its controversial origin have been frequently cited (Table 5.1) although the largest part of citations (~66%; see pie chart in Table 5.1) is represented by papers merely mentioning *Microcodium* – commonly as an evidence for subaerial exposure and soil formation – without any in-depth discussion and palaeoecological or genetic implications of its occurrences. A strikingly large number of publications is based on misidentified *Microcodium*: this can cause considerable problems and flawed interpretations when, for example, a whole diagenetic sequence or a sequence stratigraphic correlation is

**Table 5.1.** Google scholar citation scores of major papers on *Microcodium*, explicitly dealing with its origin; \*updated on August 8th, 2021. Topic of references [5], [6] and [7] is broader, consequently, a considerable portion of citations included in the total does not relate to *Microcodium*.

Right: a pie chart showing proportions of papers either 1) supporting the root-related origin (green) or 2) microbial origin (yellow), 3) being neutral or inconclusive in interpretation (grey), and 4) those showing clear misidentification of *Microcodium* (red). Based on a semi-objective review of papers citing (at least one of the) references [1]-[4] or [8]-[11]; references obtained from the Web of Science Core Collection database (see data in Table A5.1-1 in Appendix A5.1).

major publications on <i>Microcodium</i>		Google Scholar Citations*
[1]	Lucas & Montenat 1967	24
[2]	Esteban 1974	126
[3]	Bodergat 1974	59
[4]	Klappa 1978	241
[5]	Freytet & Plaziat 1982	504
[6]	Jaillard et al. 1992	132
[7]	Wright et al. 1995	153
[8]	Rossi 1997	15
[9]	Alonso Zarza et al. 1998	86
[10]	Košir 2004	177
[11]	Kabanov et al. 2008	88
	total:	1605



The pie chart illustrates the distribution of citation interpretations for the papers listed in Table 5.1. The categories are: pro root (green, 13%), pro microbial (yellow, 4%), misidentification (red, 16%), and neutral/irrelevant\* (grey, 66%).

based on a supposed *Microcodium* as a crucial evidence for vadose environments during the diagenetic history; such problems are briefly discussed and summarised in Chapter 6.

This chapter is primarily aimed at (re)solving the controversy about the origin of *Microcodium*. Earlier work (Košir 2004; Appendix A5-2) documented examples of calcified plant roots and *Microcodium* from subaerial exposure profiles in a succession of Paleocene shallow-marine carbonates in southwestern Slovenia. Morphologies, intermediate between the typical *Microcodium* aggregates and calcified roots, observed in calcrete laminar horizons, provided micromorphological evidence in support of previous rhizogenic interpretations of *Microcodium* structures. Material of Košir (2004) is re-examined here and complemented by Cretaceous, Palaeogene and Quaternary material from Slovenia, Croatia, Spain, France and the Caribbean islands. The chapter is based on a detailed petrographic, morphological and ultrastructural study of a variety of *Microcodium* examples, integrated with a comparative carbon and oxygen stable isotope analysis. It discusses the arguments opposing the rhizogenic interpretations (see Chapter 1, Section 1.4), using discussion and conclusions of a subsequent paper of Kabanov et al. (2008) as a discourse concept. Since 'extant' examples of *Microcodium* have not been (yet) encountered in present-day soils, a considerable part is devoted to one of the youngest known examples – from a Holocene



beachrock from Providenciales, Turks and Caicos Islands, British West Indies (Dickson 2014).

The comprehensive review of Kabanov et al. (2008) presented important new data about the earliest firmly documented occurrences of unambiguous *Microcodium* in upper Palaeozoic carbonate successions and proposed an alternative general conceptual model about its formation. The central narrative of their paper has been directed towards reinterpretation of the origin of *Microcodium* from a widely accepted rhizogenic (root-related) hypothesis (see discussion by Košir 2004; Appendix A5-2) to a rather complex carbonate biomineralisation mechanism induced by (Actino)bacteria and/or fungi, an idea already advocated before – since the early studies of Lucas and Montenat (1967) and Bodergat (1974) to the succeeding works of Freytet and Plaziat (1982) and Verrecchia et al. (1995), amongst others.

Kabanov et al. (2008) have coherently confronted most of the previously published arguments in favour of the root origin and used their reasoning specifically to demonstrate an apparent morphological, physiological and (palaeo)ecological incompatibility between fundamental *Microcodium* attributes and structural traits of plant roots and intracellular  $\text{CaCO}_3$  mineralisation in their cortical cells. Their review has been based on well-known Palaeogene *Microcodium* occurrences from the Ebro Basin (Catalonia, NE Spain) and on so far mostly undocumented Upper Moscovian (Carboniferous) examples from the East European Craton, Russia. However, they have not provided any potential analogue (a micromorphological carbonate feature) from modern soils or young palaeosols, which would correspond to their speculative microbially induced *Microcodium* formation model.

The discussion section (5.8) is aimed to demonstrate that there are more apparent similarities between *Microcodium* and intracellularly calcified plant roots than substantial inconsistencies between the two features. Arguments proposed by Kabanov et al. (2008) are here used as a rough framework for a comparative analysis of architecture, morphology, crystal patterns and ultrastructure, and geochemical signatures of both phenomena. An important objective of this section is to show that the concept of functional traits\* (Freschet et al. 2021), which proved to be a valuable and well founded approach for understanding intracellular  $\text{CaCO}_3$  accumulation in fine roots (Section 3.4 of Chapter 3), can be applied in the same manner to explain the intriguing characteristics of *Microcodium*. Finally, some conspicuous modern examples of Actinobacteria-related carbonate features from vadose terrestrial environments are presented and compared to the model postulated by Kabanov et al. (2008).

## 5.2 Material and methods

In addition to material from Paleocene calcrete profiles from Slovenia (Košir 2004; Appendix 5-2), representative *Microcodium* examples were selected from published and unpublished material from the collection of the Institute of Palaeontology ZRC SAZU, Ljubljana, and supplemented by two sets of samples provided by others.

Uppermost Cretaceous, Paleocene and Eocene material from the Adriatic Carbonate Platform, External Dinarides (Slovenia, Italy, Croatia), has been collected at subaerial exposure surfaces in sections and discrete outcrops of the paralic carbonate complex of the Liburnian Formation, and shallow marine, foram-dominated platform successions of the Trstelj Formation and the Alveolina-Nummulites Limestone (localities with coordinates are shown in Appendix A5-3). These include sections logged along the motorway road cuts in the Kras Plateau between Čebulovica and Kozina (Zamagni et al. 2008; Zamagni et al. 2012), the Dolenja Vas locality (Drobne et al. 1988; Tewari et al. 2007), and in a road cut section at the Village of Padriče/Padricciano, Trieste Karst, Italy (Caffau et al. 1995; Brazzatti et al. 1996; Tewari et al. 2007). *Microcodium*-bearing calcretes have been collected from palaeokarst-related and paralic sediments at the Koromačno locality in Istria, Croatia (Santonian to lower Eocene; Otoničar & Košir 2016). Several examples come from cores T1-7 and T1-9 (Paleocene, Trstelj Formation), drilled for the project of geological assessment of construction sites for the second track of the Divača—Koper railway line (Celarc 2010).

Palaeosols with *Microcodium* have been sampled in Paleocene-Eocene “Garumnian” continental succession (The Tremp Group) in the Esplugafreda section, Noguera-Ribagorzana valley (Aragón, NE Spain). In this section, in addition to its known occurrences in various levels of the Danian Talarn Formation and the Thanetian Esplugafreda Formation (Schmitz and Pujalte 2003, 2007; Baceta et al. 2011; Adatte et al. 2014), *Microcodium* has also been discovered in the ‘Upper red beds’ unit of the Claret Formation (Ilerdian, lowermost Eocene; Figs. A5-3.4 and A5-3.4 in Appendix A5-3).

Similar palaeosol material was sampled in a road cut near the village of Fontjoncouse (Aude, Occitanie, southern France; Fig. A5-xX in Appendix A5-3) in Danian (lowermost Paleocene) continental succession, correlative to the nearby Albas site described by Wright et al. (1995) (also see Freytet et al. 1997). From the same continental basin system, a set of spectacular samples of lamellar *Microcodium* from Paleocene (‘Vitrollien’) breccia near Montpellier has been kindly provided by Michel Condomines, Université de Montpellier.

Studied Quaternary examples comprise material from San Salvador Island, the Bahamas, where individual fragmentary clusters of typical *Microcodium* have been encountered in thin sections of weakly-cemented Holocene carbonate aeolianite dunes of the North Point Member (Figure 2.XX, Section 2.x, Chapter 2 and Appendix A2-X; Carew and Mylroie 1995, 1997, their Fig. 3A-3; Mylroie and Carew 2010; Mylroie et al. 2012), and from a Holocene beachrock of Providenciales, Turks and Caicos Islands, British West Indies (Wanless et al. 1989; Dickson 2014; location in Appendix A5-3). Samples of the latter have been kindly provided by Tony (J.A.D.) Dickson, Cambridge University.

### 5.2.1. *Thin section preparation and petrography*

Non-porous *Microcodium*-bearing carbonates have been examined in more than 250 standard uncovered and unstained thin sections (from 30 to 60  $\mu\text{m}$  thick) prepared in the laboratory at the Institute of Palaeontology ZRC SAZU in Ljubljana. Selected thin sections for CL, SEM EDS and EPMA analysis were polished at the Thin Section Laboratory UCM (Departamento de Mineralogía y Petrología, Facultad de Ciencias Geológicas, Universidad Complutense Madrid, Spain).

Highly porous Quaternary samples from coastal outcrops of the Bahamas and Caicos were first cut into glass-slide size slices ( $\sim 1.5 \times 3$  cm) with parallel faces, several mm thick, using a precise Buehler Iso-Met low-speed diamond saw with propylene glycol as a cooling liquid to prevent mechanical damage of crystal ultrastructure. To remove the remains of sea salt from pores, slices were washed in slowly running tap water for 6 hours, followed by two baths (30 minutes each) in distilled water, and finally a bath of 70% ethanol for several minutes. Slices were air-dried at 40°C [4-6 hours] in a drying chamber and embedded (impregnated) with EpoTek 301-1 low-viscosity epoxy resin in a Struers EpoVac vacuum chamber. For selected samples, the resin was dyed by adding 1 wt% Keystone Oil blue dye (in powder). Resin-embedded slices were machine lapped on one side with silicon carbide abrasive powder (600F/mean grit size 25  $\mu\text{m}$ ) and then manually polished using a succession of silicon carbide (SiC) pads (Kemet, UK) P1200 (15  $\mu\text{m}$  grit size), P2500 (8  $\mu\text{m}$ ) and P4000 (5  $\mu\text{m}$ ). Polished faces were mounted at room temperature on glass slides using EpoTek 301-1 epoxy resin and a Logitech bonding jig. Mounted slices were trimmed and machine lapped at slow rotation to  $\sim 20$   $\mu\text{m}$  thickness, followed by manual polishing using a succession of same SiC pads, and finally machine-polished for 10–20 minutes with



1 µm diamond paste (SPI Diamond Compound, Structure Probe, Inc., West Chester, USA), dispersed on a polishing cloth mounted on aluminium plate, on a Logitech PM5 machine, producing ultra-thin sections (5–15 µm thick).

Thin sections were observed and photographed in transmitted light under conventional polarising microscopes and stereomicroscopes (an Olympus BX51 equipped with a digital camera Olympus SC180 and cellSens™ software; a Leitz Orhoplan and a Wild M420 equipped with a Leica DFC450 and LAS (Leica Application Suite) imaging software).

Transmitted light petrography was supplemented by cathodoluminescence (CL) imaging at the Institute of Karst Research ZRC SAZU, Postojna, Slovenia, using a Technosyn cold CL luminoscope (model CITL CL8200 MK4) with a 14-15 kV electron beam energy and an electron current of 350-400 µA, mounted on a Nikon Eclipse E600 petrographic microscope with either a Nikon DXM1200 or a Leica DFC450 digital camera and corresponding software suits. Most of the long-exposure CL images were digitally enhanced using Adobe Photoshop CS6 adjustments of exposure and brightness/contrast.

Selected polished thin sections were examined with fluorescence microscopy in the Microscopy Lab (SEES, Cardiff) using a Leica DML microscope in reflected light with filters for blue and green wavelength fluorescent light, fitted with Leica LAS imaging software.

### 5.2.2. Scanning electron microscopy

Scanning electron microscopy (SEM) was carried on a JEOL JSM 330A (see Appendix A5-2) and a JEOL JSM IT100 LV microscope at the Microscopy Laboratory ZRC SAZU in Ljubljana. SEM observation was performed on freshly broken surfaces of mm-to-cm sized rock fragments and isolated *Microcodium* aggregates (see below). Fragments were washed in distilled water in an ultrasonic bath and mounted onto standard aluminium holders with double adhesive tape or carbon paste. Uncoated specimens were observed and photographed in low-vacuum (LV) mode (20-40 Pa) with an accelerating voltage of 15 kV and 20 kV at a working distance from 9 to 11 mm. Photomicrographs were taken in topographic, compositional and shadow backscattered electron imaging (BET, BEC and BES) modes, whilst Au-coated samples (for 100-300 seconds using a Baltec SCD-50 Sputter Coater) were observed in high vacuum (HV) SED mode.

SEM images of polished thin sections were collected either in LV on uncoated surfaces in BEI mode or coated with carbon (for several seconds, using a JEOL JEC-530 Carbon

Coater) and observed in high vacuum with an accelerating voltage of 15 kV and 20 kV. Conventional backscattered electron imaging of uncoated thin sections was supplemented by Charge Contrast Images (CCI) performed in LV conditions (40–60 Pa) with a powerful beam (maximum accelerating voltage and high probe current) using a low-vacuum Secondary Electron Detector (LV SED) or a backscattered detector (see also methods in Chapter 3). Several impregnated double-polished thin sections were etched (decalcified) with diluted (5 %) HCl, washed with distilled water, air-dried and Au-coated for SEM analysis.

### 5.2.3. Elemental analysis

Qualitative and semiquantitative Energy Dispersive X-ray Spectroscopy elemental analysis (EDS) was performed on a JEOL JSM IT100 LV microscope at the same LV conditions as described above. Elemental spectra were obtained on uncoated thin sections using point or small area analysis with 100 seconds preset (live) time and automatic element identification mode. Elements selected from qualitative results were further analysed manually in (semi)quantitative (standardless) mode; results were calculated and reported in pure (non-oxide) form.

Elemental analyses of *Microcodium* were performed on polished thin sections on a JEOL JXA-8900 M WD/ED Electron Microprobe at the National Electronic Microscopy Centre (CNME) at the University Complutense Madrid. Microprobe was operating at 15 kV and 20 nA and employing an electron beam diameter of 5  $\mu\text{m}$  (for further analytical details see Appendix A5.4)

### 5.2.4. Sampling and stable isotope analysis of carbonate $\delta^{13}\text{C}$ and $\delta^{18}\text{O}$

From hard limestone, samples for stable isotope analysis were obtained from slices remaining from thin section preparation. Portions of slices rich in *Microcodium* were cut into ~0.2–0.5 mm thick platelets using a Buehler Iso-Met low-speed saw. Individual platelets were collected in glass vials, washed in distilled water, air-dried and set into a clean watch glass. Then they were covered with several drops of 70% ethanol and gently crushed using a glass stirring rod. Clear, limpid clusters of *Microcodium* devoid of visible remains of matrix or cement were manually picked from the watch glass under a stereomicroscope

(using a combination of transmitted and reflected light) with a precise tweezers or a fine brush, and collected in conical bottom vials, approximately 0.5 to 1 mm<sup>3</sup> per sample.

Soft, weakly cemented rock samples with *Microcodium* were processed by rough crushing of 100–200 g of sample into a glass beaker, soaking of material with water, and followed by agitation of a mixture for 5–10 minutes in an ultrasonic bath. The fines were washed under running water over a set of standard stainless steel sieves. Collected residues were air-dried. Individual well-preserved and clean *Microcodium* clusters without traces of matrix were collected from the  $\phi > 250 \mu\text{m}$  residue on a microfossil tray under a stereomicroscope into glass vials, 2–5 clusters per sample, yielding approximately 1 mm<sup>3</sup> of material. Clusters of individual samples were gently crushed and mixed (homogenised) inside the vials using a clean stirring rod.

Carbon and oxygen stable isotope analyses of *Microcodium* were performed at the Stable Isotope Laboratory of the School of Earth and Environmental Sciences, Cardiff University, with additional analyses carried out at the University of Graz, Austria (see Appendix A1-1). At Cardiff, isotopic determinations were performed on powdered samples using a ThermoFinnigan MAT 252 mass spectrometer with a Kiel IV carbonate preparation device. For an individual sample, repeated measurements (typically quadruplicates) were done on sets of separated sub-samples, approximately 20–100  $\mu\text{g}$  each. Isotope values are reported relative to Vienna Pee Dee Belemnite (VPDB) using the standard NBS-19. The average analytical precision of the standard analyses over the period of the investigation was  $\pm 0.05\text{‰}$  for <sup>18</sup>O and  $\pm 0.03\text{‰}$  for <sup>13</sup>C (G. Bianchi, personal communication).

At Graz, sample powders, 200–500  $\mu\text{g}$  each, were reacted with 100% phosphoric acid at 70°C in a Kiel II automated reaction system, and the evolved carbon dioxide gas was analysed with a Finnigan Delta Plus mass spectrometer with analytical precision  $< 0.05\text{‰}$  for  $\delta^{13}\text{C}$ ,  $< 0.1\text{‰}$  for  $\delta^{18}\text{O}$ . Likewise, the isotope values were corrected according to the NBS19 standard and reported relative to VPDB standard.



### 5.3. Morphology and architecture of *Microcodium*

A typical *Microcodium* structure (Bodergat 1974; Freytet and Plaziat 1982; Morin 1993) consists of a millimetric cellular aggregate composed of individual polyhedral, elongate crystalline elements of calcite (Fig. 5.1; Appendix A5-2, Fig. A5-2.1). These elements are polygonal in cross section and are usually strongly elongate, measuring 50–800  $\mu\text{m}$  in length (in rare examples  $> 1\text{ mm}$ ) and 20–100  $\mu\text{m}$  in width. Basic elements, simply termed *grains* by Klappa (1978) to avoid terminological confusion and genetic implications, are typically arranged in a distinctive radial pattern forming cylindrical and vermiform structures with grains arranged around a central tubular space termed *axial canal* (Bodergat 1974; Fig. 5.1, Fig. A5-2.1) Diameter of the axial canal is typically between 50 and 200  $\mu\text{m}$ , comparable to diameter of vascular cylinders of fine roots (Fig. 5.11; Appendix A5-2, Fig. A5-2.8; also see comparison with dimensions of iCRs in Appendix A3). Depending on the orientation, cylindrical *Microcodium* shapes have been compared to morphology of a corncob (in longitudinal directions; Figs. 5.1, 5.4, 5.5 and 5.7A, B) or rosettes (in cross section; Figs. 5.1, 5.5, 5.7A, B). This archetypal morphology has been described by Bodergat (1974) as *Microcodium* Type 1.

Another form, named Type 2, is characterised by layered arrangement of asymmetric aggregates, normally composed of strongly elongate grains. Such forms have been termed lamellar or mono-laminar (Freytet et al. 1997) or palisadic since they resemble palisade tissues (in biological sense, layers of parallel, often columnar cells having their long axes perpendicular to a surface; OED Online) that can be observed in certain directions in thin sections. As illustrated by Freytet and Plaziat (1982) and Morin (1993), there is a morphological continuum between both basic types with intermediate asymmetrical forms (Fig. A5-2.1).

The fundamental morphological characteristic of *Microcodium*, as opposed to ‘normal’ plant cellular materials, is a marked elongate, slender shape of its constitutive elements (grains). Most papers describe these elements as prisms (Bodergat 1974; Klappa 1978; Kabanov et al. 2008) although *Microcodium* elements are generally not prismatic (prism is a polyhedron with two end faces that are similar, equal, and parallel rectilinear figures, and whose sides are parallelograms or rectangles). As shown in Figure 5.2, prisms can only form (constitute) a planar monolayer of cells whereas in curved (folded) cellular monolayers, cells adopt a shape that can be simplified as frustum (plural frusta) – a truncated pyramidal polyhedron (Fig. 5.2B).

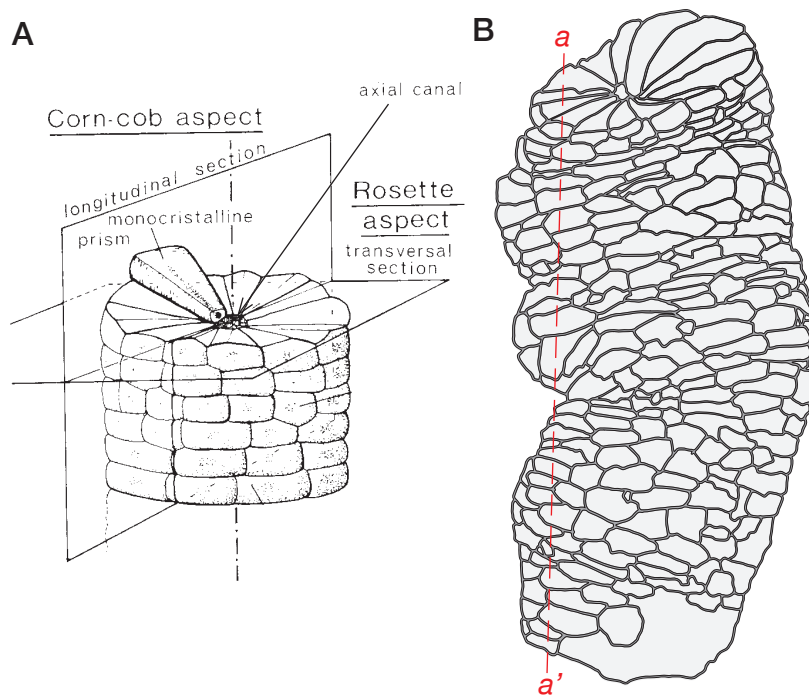


**Figure 5.1.** A) Reconstruction of a typical cylindrical *Microcodium* aggregate showing corn-cob shape in longitudinal section and rosette form in transversal section. From Freytet & Plaziat (1982).

B) Traced SEM image of a moderately contorted *Microcodium* fragment in Fig. 5.3C. Oblique or marginally placed 2D sections through the aggregate (e.g. along the marked red line a-a') would result in a series of apparently unconnected rosettes. Digitally traced with Adobe Illustrator CS6.

A simple growth model of a basic *Microcodium* architecture in Figure 5.3 assumes an initial ring (a single layer) of cells of similar diameter (Fig. 5.3B) around a tubular space (axial canal; in plant roots, that would correspond to a vascular cylinder). Non-uniform (asymmetric) increase of volume of some cells result in their radial (centrifugal) expansion (increase in  $r$ ) while the cell length ( $d$ ) remains unchanged (Fig. 5.3C). A typical *Microcodium* rosette, composed of regular, wedge-shaped polyhedral elements (Fig. 5.3D), can be derived from B by uniform radial cell growth (increase in  $r$ ), but, as in C, without cell expansion (elongation) in longitudinal direction ( $d$ ). Technically, polyhedra in D are prisms – but with their (short) axes oriented longitudinally (parallel to  $d$ ).

Yet, a typical shape of *Microcodium* grains can be best simplified as a frustum (Fig. 5.3E): such elements compose cellular structure of any curved, non-planar layer (Fig. 5.2B). Moreover, if cells grow (expand) radially (centrifugally) in a uniform way (in all directions), a resulting geometric shape is an aggregate of frusta.

Figure 5.4 illustrates a simple 2D model of cellular growth from a tubular monolayer of cells. A simple cylindrical shape (a corn cob form) can only result from uniform radial (but not longitudinal) extension of cells (at the same rate). Alternatively, non-uniform, competitive outward growth of cells from discrete points/centres (and suppressed/restrained growth between them) results in distorted/contorted cylindrical shapes. Such

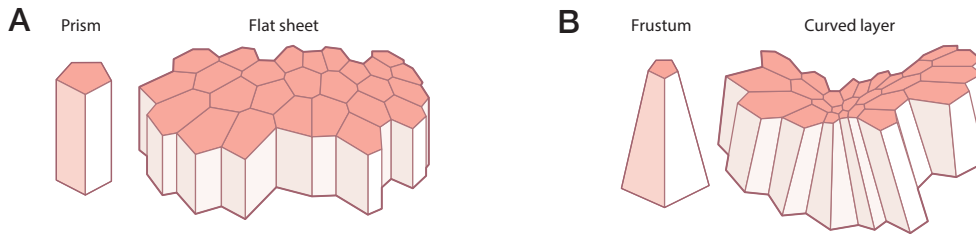


**Figure 5.2.** A) Scheme representing a planar monolayer of columnar cells. Cells are simplified as prisms. B) Scheme illustrating curved or folded cellular monolayer. Cells adopt a shape that would be geometrically simplified as frusta (note that walls of true biological cells are much more complex in shape and typically curved). Modified from Gómez-Gálvez et al. (2018) and Blanchard (2018).

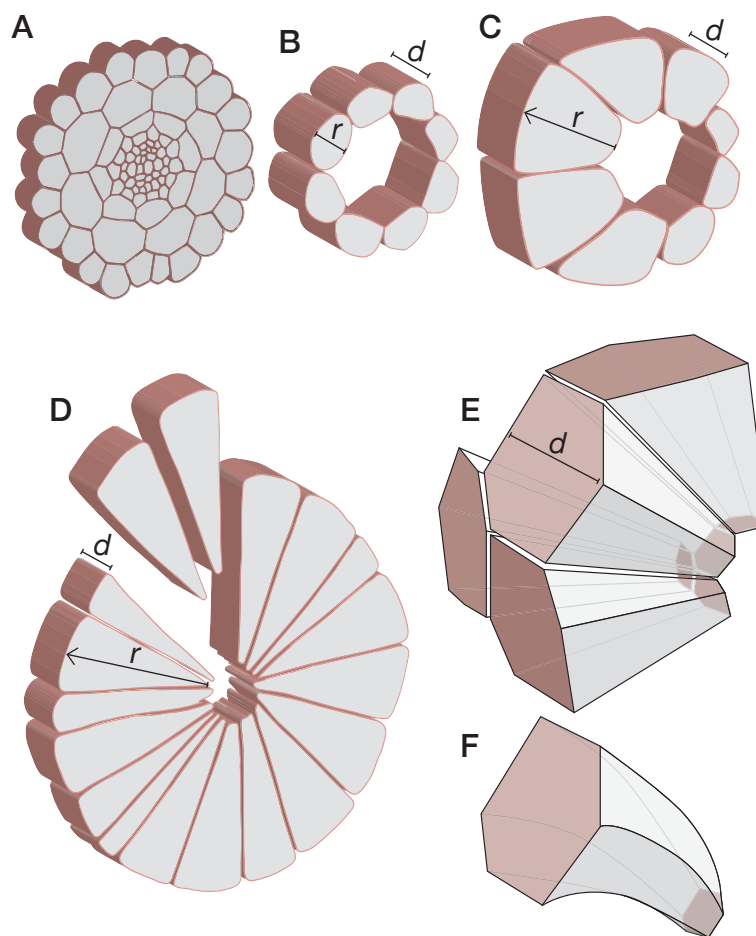


**Figure 5.3.** A) An example of a simple fine root cross-section of a model plant *Arabidopsis thaliana* (modified from Peret et al. 2009). B) A single layer of (cortical) cells with similar diameter ( $r$ ) and length ( $d$ ) extracted from fig. A. Cells do not show expanded radial growth. C) Same single layer of cells showing asymmetrical nonuniform enlargement of cell volume resulting in radial expansion of cells (increase in  $r$ ) while cell length ( $d$ ) remains unchanged. Cf. fig. 5.20B. D) A typical *Microcodium* rosette composed of regular, wedge-shaped polyhedral elements; such structure results from uniform radial cell growth (increase in  $r$ ) but no cell expansion (elongation) in longitudinal direction ( $d$ ). E) Schematic illustration of a structure, formed by uniform cell growth from a sphere or a folded surface, is composed of frusta - truncated pyramidal polyhedra. F) Scheme of a typical curved, often twisted *Microcodium* frustum with curved faces resulting from radial expansion of cellular elements at different growth rates.



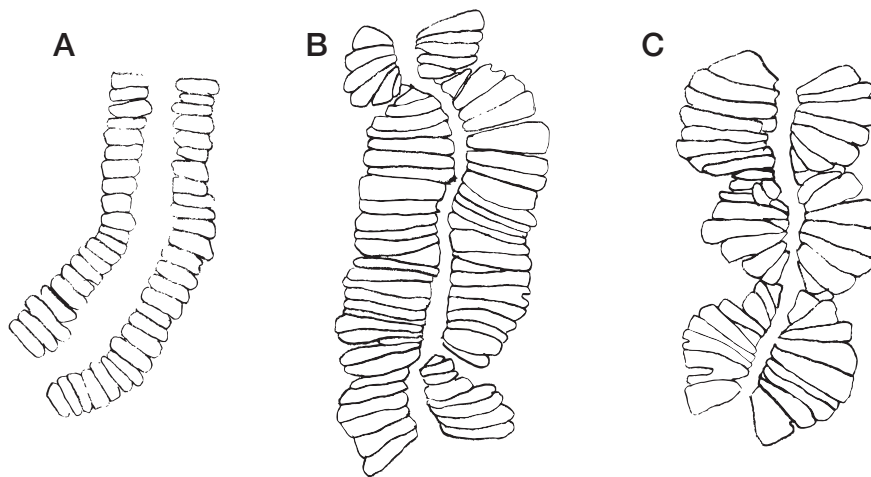


**Figure 5.4.** Sketches of longitudinal sections through cylindrical (type 1) *Microcodium* aggregates.

A) A corn-cob form resulting from simple, uniform growth of cellular elements symmetrically from a central canal (tube). B) Moderately distorted/contorted corn-cob shape, and C) strongly distorted shape, composed of connected rosettes. Distorted morphology is due to expanded radial growth of elements at certain points/centers along the axial canal and suppressed/restrained growth of cells between them.

a growth mode can produce irregular aggregates which, in particular longitudinal or oblique cross sections (illustrated in Fig. 5.1B), appear as a series of unconnected spheroids (rosettes; Figs. 5.8A-C) although they actually belong to a single distorted cylindrical aggregate (cf. SEM images in Fig. 5.5). Consequently, rosette *Microcodium* shapes are not merely corn-cob forms in cross sections.

*Microcodium* elements typically have slightly to considerably convex, rounded distal termination (Figs. 5.5 to 5.8, Figs. A5-4.01-4.03), whereas individual grains terminate with a distinctive pit (Figs. 5E, G, Fig. A5-4.03). Bulbous terminations of strongly elongate grains are also visible on lamellar *Microcodium* forms on sides directed towards the substrate (Fig. 5.6D, E).

Additional element of complexity, almost impossible to reconstruct in thin sections, is a fact that *Microcodium* aggregates in 3D often exhibit branching patterns (Figs. 5.5 and 5.6). There is a striking similarity between the lateral branches of *Microcodium* (Figs. 5.5D, E, G and Figs. 5.6A, B) and modern intracellularly calcified roots (Fig. 5.6C; see also Chapter 3) showing considerably lower diameter at the point of initiation of a lateral (branch). Both *Microcodium* and the calcified root in these examples exhibit an analogous topology where

branching is confined to the main axis whereas lamellar *Microcodium* examples in Figures 5.6 D and E show a clear dichotomous branching pattern.

Thin section photomicrographs in Figures 5.7 and 5.8 show examples of Type 1 *Microcodium* corncob and rosette morphologies corresponding to simplified models in Figure 5.4 and 3D SEM images in Figures 5.5 and 5.6. Simple aggregates generally do not express considerable radial elongation of grains (in longitudinal sections) and are composed of a relatively small number of cells in cross sections (Fig. 5.7) as compared to larger rosette aggregates (Fig. 5.8, Figs. A5-4.01 E, F, A5-4.02A-D).

Although the lamellar palisade forms (Type 2) have been used as one of the key arguments against the root-related origin of *Microcodium* (Freynet et al. 1997; Kabanov et al. 2008 and references therein), almost none of the papers following the well-illustrated book of Freynet and Plaziat (1982) have explicitly re-examined morphological attributes of these intriguing structures (a notable exception is an unpublished thesis of Morin 1993).

Spectacular examples of lamellar *Microcodium* presented here are from the Palaeogene of southern France. They have enabled further insight into the architecture of lamellar forms – reasonably comparable to certain forms of modern calcified roots, and together with the asymmetric intracellularly calcified roots presented in Chapter 3 provided a firm basis to compare and explain the mode of formation of both features. Lamellar forms illustrated in Figures 5.9 and 5.10 (also see Appendix A5-4, Figs. A5-4.04–07), all from a single locality of Paleocene breccia near Montpellier, France, are only weakly cemented and enable to easily exfoliate, with all details preserved, mm to cm size individual lamellae of *Microcodium* (Fig. 5.9). At a closer examination under SEM, grooved surfaces visible in hand-specimens (Figs. 5.9B, C) show an intricate branched architecture (Figs. 5.6D, E) with a clear cellular patterned surface. Thin section photomicrographs in Figures 5.10 and A5-4.06 (Appendix A5-4) show variably oriented sections through lamellae, from palisades (in longitudinal direction) to series of lobate asymmetric forms (in cross section) and irregular folding (convolution) and branching in oblique sections (Fig. 5.10B). Importantly, the asymmetric *Microcodium* forms are apparently *always* oriented with the elongate side (= growing direction) towards the substrate (Fig. 5.10A, Figs. A5-4.07) and with the axial canal placed opposite the contact with the substrate (compare with illustrations of Bodergat (1974) and Freynet and Plaziat (1982); Appendix A5-2, Fig. A5-2.1C). Centripetal (inward) growth and successive corrosion of the substrate is best seen in corroded pebbles (Fig. 5.9A) where *Microcodium* aggregates in all layers (lamellae) are oriented in the same direction (Figs. 5.10A, D, E). Analogous geometries are characteristic of flat, shovel morphologies



**Figure 5.5.** SEM photomicrographs of *Microcodium* aggregates from the Esplugafreda section, NE Spain (see Appendix A5-3). All images taken on uncoated specimens in backscattered low-vacuum mode. A-C) contorted corn-cob aggregates; D) two *Microcodium* fragments with considerably different diameter, stuck together; E-F) aggregates with short lateral branches; G) large, strongly distorted aggregate, in the upper part intermediate between corn-cob and rosette shape. Note deflated appearance (pitted surface) of individual grains in E and G.



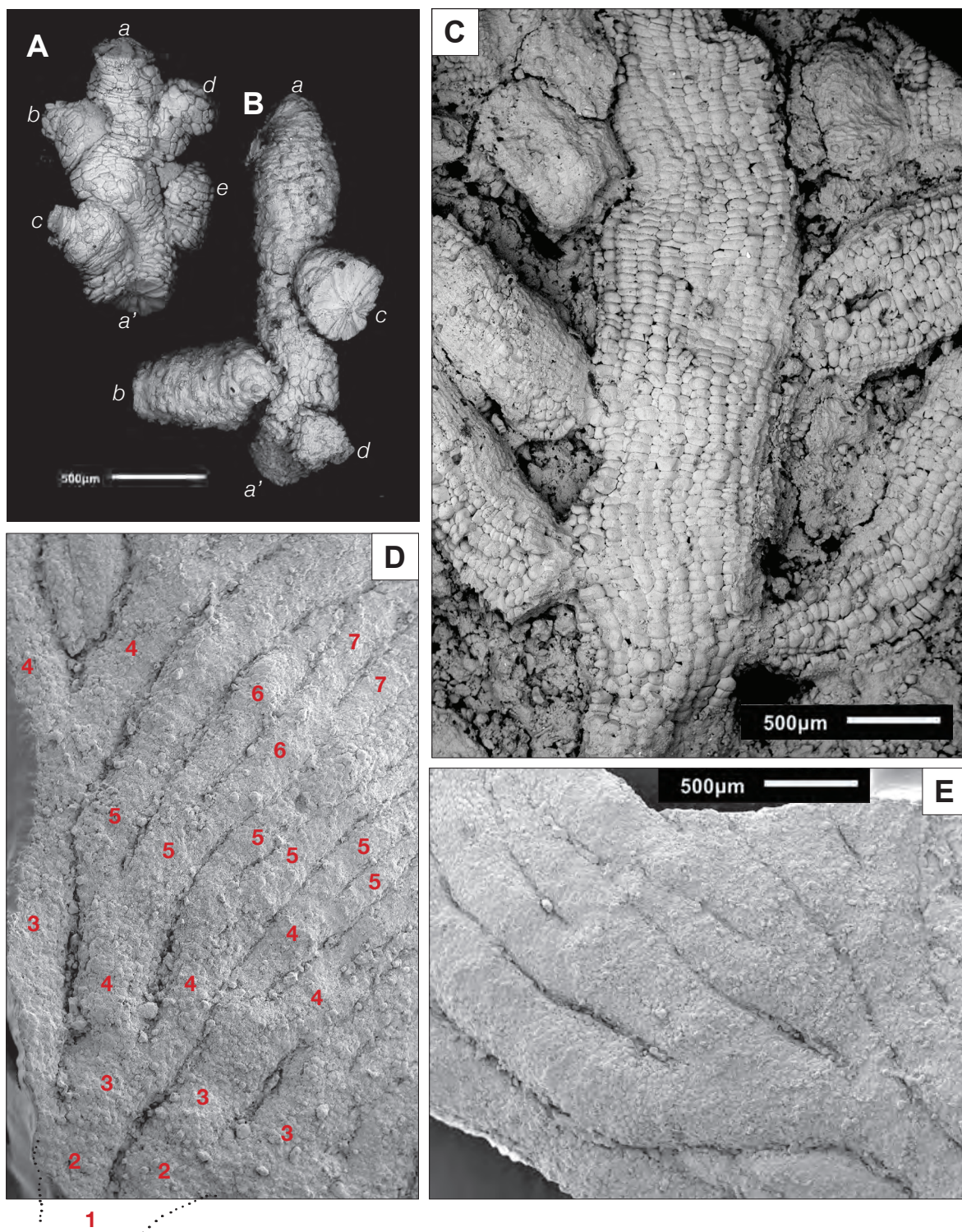


**Figure 5.6.** Branching patterns in *Microcodium* and intracellularly calcified roots; secondary electron SEM images, all at same magnification. **A)** Highly contorted, vermiform *Microcodium* aggregate (a-a') with short (broken) laterals (b, c, d, e), Eocene Claret Fm. **B)** Relatively straight and regular cylindrical aggregate (a-a') with short laterals (b, c, d); note significantly lower diameter of laterals at the point where they emerge from the 'parent' branch'. Paleocene Esplugafreda Formation, Spain. **C)** Herringbone branching pattern of intracellularly calcified root segment with a parent root (vertical) and lateral branches on both sides. Note reduced diameter of branches at the point of emergence from the parent root cortex, analogous to Figs. 5.6B and 5.5E-F. Modern soil, Finestrat, Spain. **D, E)** Dichotomous branching pattern of lamellar *Microcodium*. All branches in D (numbered in developmental orders from 2 to 7) originate from a single, lowest order branch (number 1, extrapolated out of the image). Cf. Fig. 5.9. Paleocene continental succession, Montpellier, France.



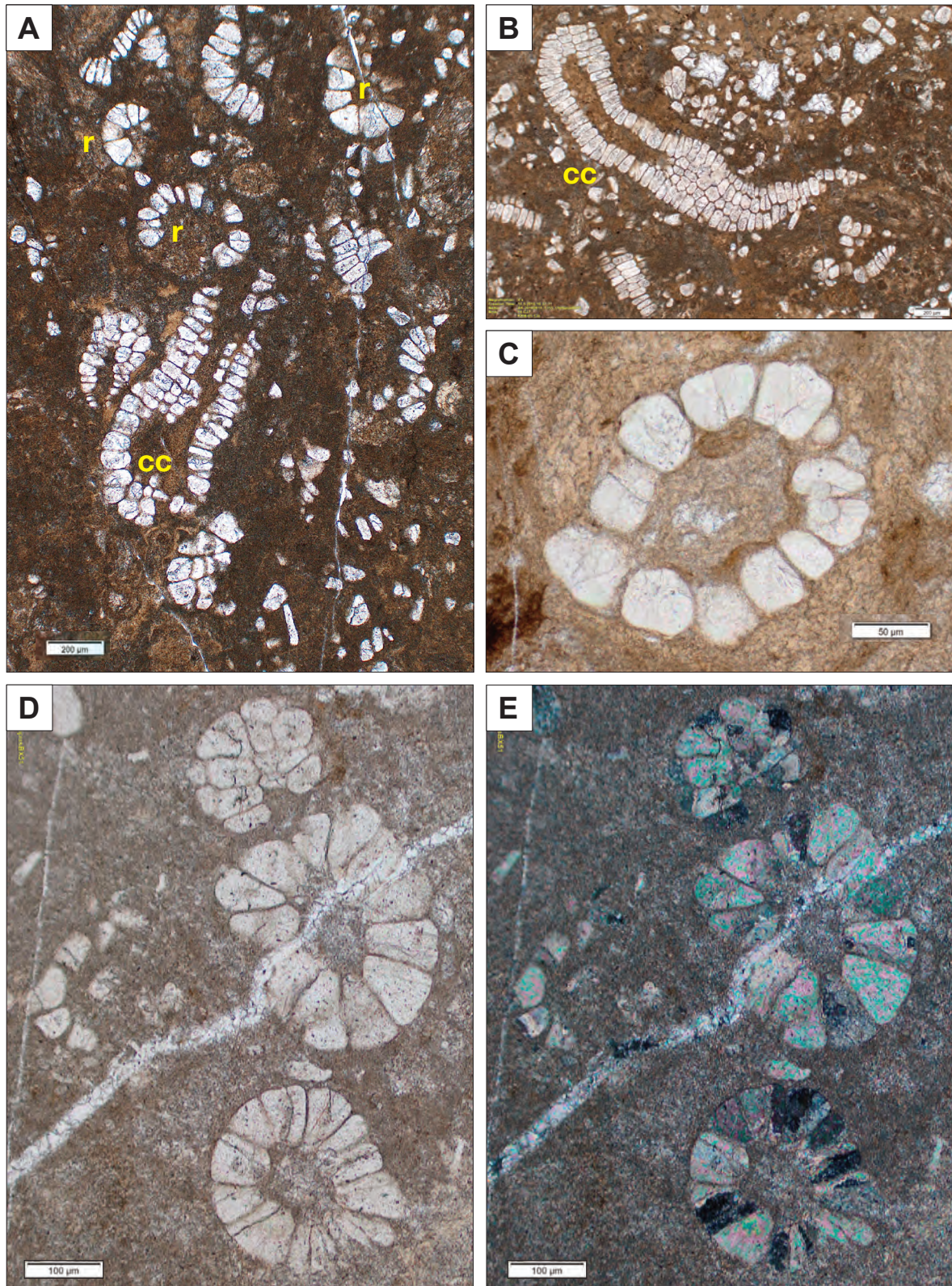


**Figure 5.7.** Thin section photomicrographs of cylindrical (type 1) *Microcodium* aggregates. A, B) Typical corn cob (cc) and rosette sections; partly disintegrated aggregates in micrite; lower Eocene calcrete, Koromačno, Istria. C) A rosette section composed of a single layer of non-elongate, isodiametric polyhedral cells (35-45 µm in diameter). Paleocene, Sv. Martin calcrete, sample SM1-Rh3-3. D, E) PPL/XPL pair showing cross sections of simple rosettes, composed of moderately elongate grains. Boundary interval (Paleocene/Eocene) between the Trstelj Formation and the Alveolina-Nummulites Limestone, Kremance locality.



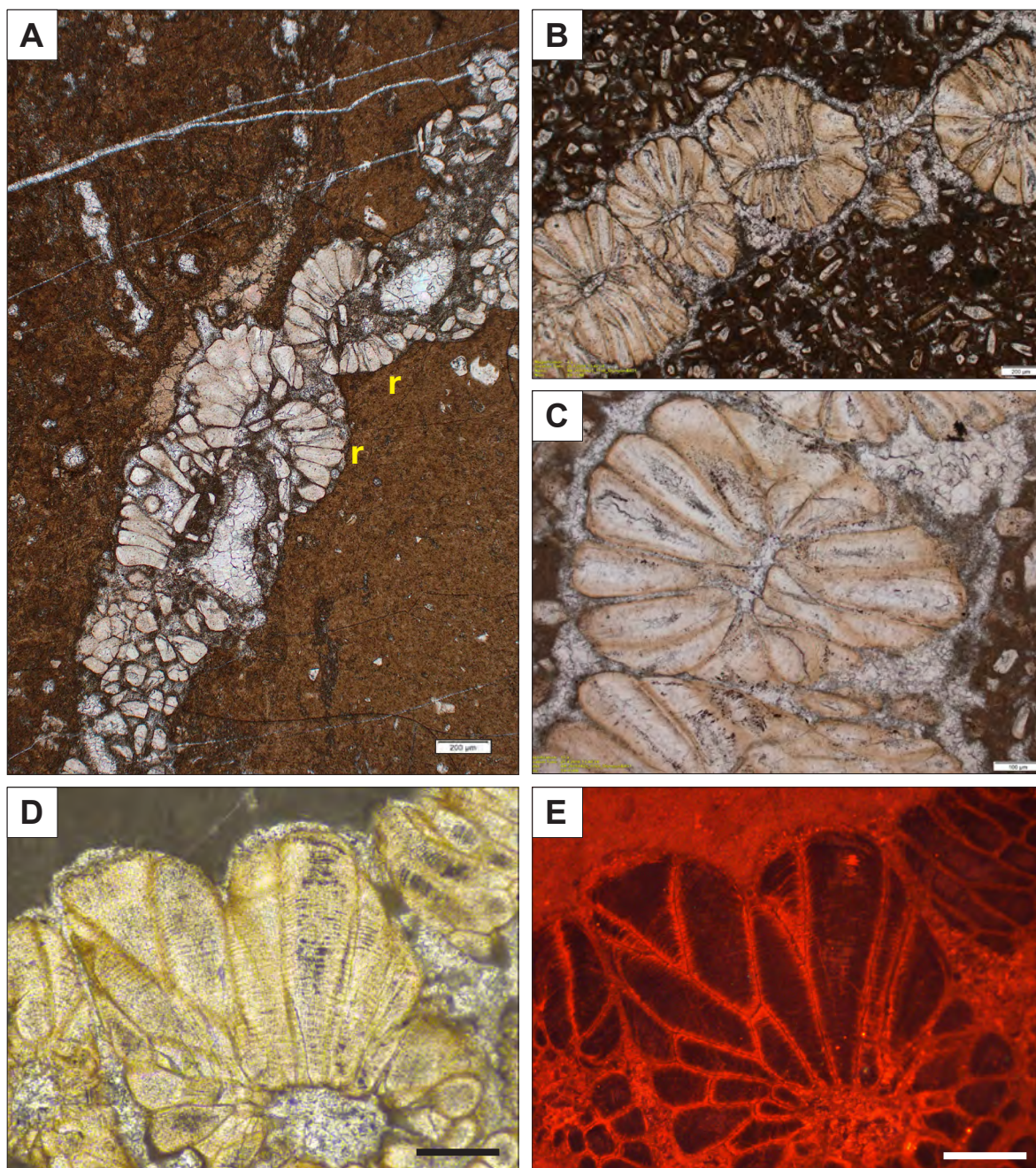


**Figure 5.8.** Thin section photomicrographs of type 1 *Microcodium* aggregates.

A) *Microcodium* corroding a fissure in massive calcrite; rosettes (r) are partly disaggregated. PPL, Paleocene, Sv. Martin calcrite. B) Discrete rosettes, probably belonging to a single distorted cylindrical aggregate (cf. Fig. 5.5). *Microcodium* grows in a fissure in an earlier stage calcrite, largely composed of smaller *Microcodium* grains, embedded in dark micrite. C) detail of B. Note two-layered (vaculate) structure of in grains and a (sparite-filled) space between *Microcodium* and the substrate. PPL, Paleocene, Section Divača AC. D, E) PPL/CL pair of a rosette section. Strongly elongate grains display clear concentric layered (striate) ultrastructure. CL image shows generally nonluminescent grains with red luminescent, thin outer layer, enclosing striate part. Polyhedral elements are separated by clearly distinguishable thin (several  $\mu\text{m}$  thick) nonluminescent 'walls'. Paleocene, Čebulovica II section (Appendix A5-3). Scale bar 100  $\mu\text{m}$ . Also see Figures A5-4.01 to A5-4.03 in Appendix A5-4.



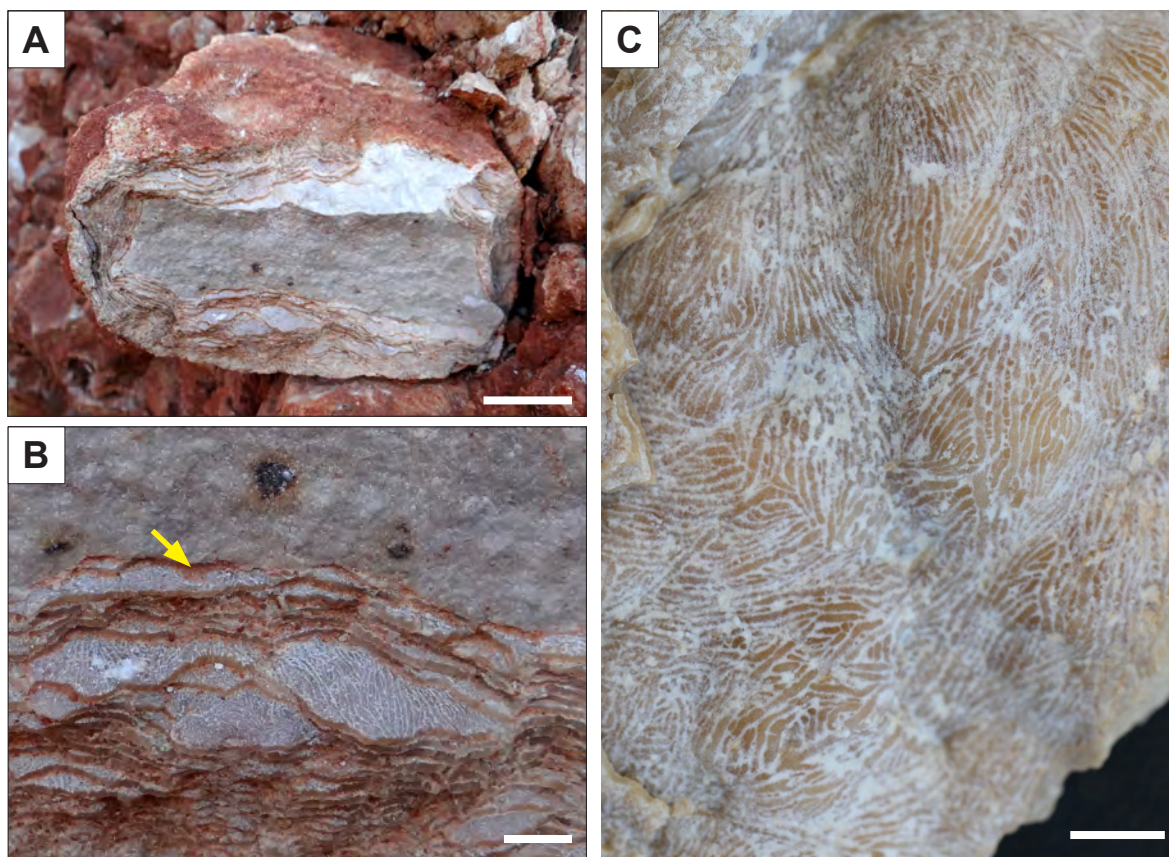


**Figure 5.9.** Lamellar *Microcodium* on a mesoscale. A) Limestone pebble intensively corroded by successive millimetric layers (lamellae) of *Microcodium*, growing centripetally. Scale bar 1 cm. B) Close up view of A showing intricately patterned surfaces of lamellae, corresponding to densely branched *Microcodium* structures. Detailed view under SEM is shown in Figs. 5.6 D, E. Arrow indicates red noncarbonate (insoluble) material concentrated between *Microcodium* lamellae. Scale bar 5 mm. C) Fragment of lamellar *Microcodium* (brownish colour) with white micritic interlayers. Scale bar 5 mm.

of intracellularly calcified roots with ectopic vascular cylinders (Figs. 3.17G, H, 3.20, 2.21, Section 3.4, and Figs. A3-4.02, 4.03, 4.04), particularly those composed of pronouncedly long cells.

In general, even the most asymmetric *Microcodium* forms with extremely elongate grains, constituting the lamellar aggregates, can be geometrically described with the same basic principles as set up for the radial growth process. The fundamental difference is that the cellular growth in asymmetric forms progressed predominantly (preferentially) or exclusively in only one direction. In cross sections, intermediate morphologies render a shape of an asymmetrical oval-shaped rosette with the axial canal placed eccentrically (Appendix A5-4, Fig. A5-4.07A), whereas in extremely elongate forms, axial canals occur marginally. Marginally placed axial canal constitute a longitudinal groove along an



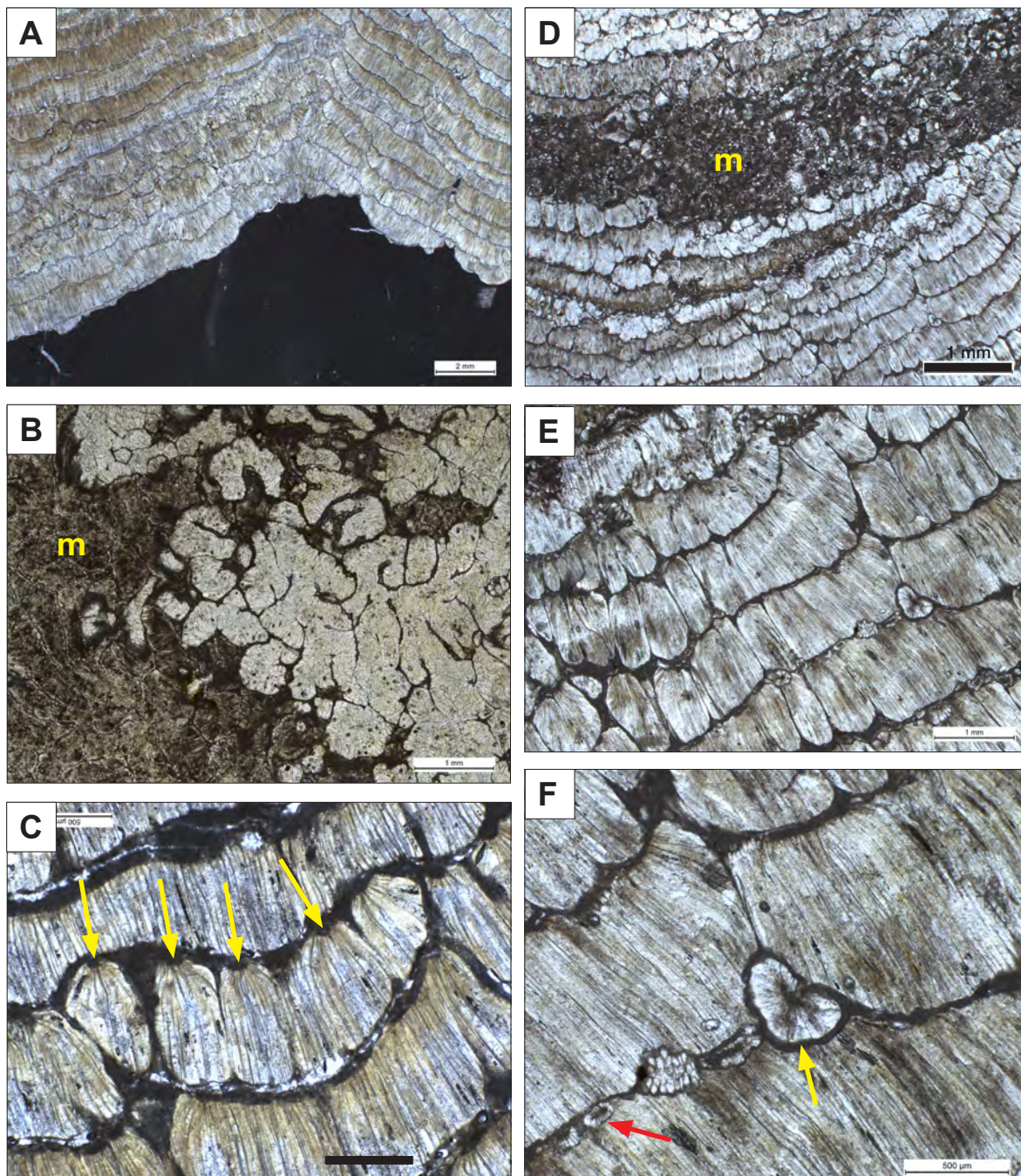


**Figure 5.10.** Lamellar *Microcodium* in thin sections, all in PPL. A) Cross-section through lamellar *Microcodium* in contact with corroded limestone (dark lower part). Excessively thick thin section. B) A section, cut slightly oblique to lamellae, showing cerebroid-like shape of aggregates. m - strongly micritised part. C) Transverse section through a lobate-shaped lamella, composed of several asymmetric aggregates; arrows indicate 'axial' canals placed marginally (distally to the substrate). Cf. Figs. 3.17G, H in Chapter 3. Scale bar 0.5 mm. D) Lamellar *Microcodium* with an interlayer, composed predominantly of micritised cylindrical (Type 1) aggregates (m). E, F) Lamellae of strongly asymmetric aggregates corroded by smaller, rosette-shaped *Microcodium*, protruding along (through) interlamellar partings. Yellow arrow: larger, fully developed aggregate (also note micrite-filled dissolutional void around the rosette); red arrow: an aggregate in incipient growth stage. All samples are from Paleocene breccia/conglomerate, Montpellier, France. Also see Figures A5-4.04 to A5-4.06 in Appendix A5-4.

aggregate and is visible as a pit on the edge of an elliptical cross section (Fig. 5.10C), placed distally (opposite) to the substrate.

In some sections, lamellar forms are associated with cylindrical (rosette) forms of *Microcodium* growing between and corroding previously formed lamellae (Figs. 5.10E, F). Cathodoluminescence petrography of lamellar forms often reveals cellular structure, not visible in plane polarised light (PPL), showing that individual layers of strongly elongate grains can be actually composed of multiple smaller grains or more than a single layer of elongate elements (Figs. A5-4.06E, F, A5-4.07). However, such a pattern may partly be an artefact of overly thick thin sections where individual grains can be clearly seen in reflected CL light but are not discernible in transmitted light due to their overlapping.

### 5.3.1 *Fine root rhizoliths, incipient Microcodium and intermediate morphologies*

Previous research (Košir 2004, Appendix A5-2) has shown that typical *Microcodium* morphology can be derived from anatomy of simple fine roots (Figs. A5-2.9, A5-2.10). Further evidence is shown in Figure 5.11 with fine root fabrics and incipient stages of *Microcodium*. Noncalcified fine roots with only partially preserved anatomical details (Fig. 5.11A) are associated with very fine roots, 100 to 200  $\mu\text{m}$  in diameter, with preserved cellular structure of the cortex, characterised by cloudy brownish calcite and simple structure, composed of only one or two layers of small cells, 20-25  $\mu\text{m}$  in diameter (Figs. 5.11B, C). Some sections of fine roots display individual, considerably enlarged (hypertrophied) outer cells which are typically lighter in colour and measure up to 100  $\mu\text{m}$ . Individual root sections exhibit preserved thin outermost cellular layer (Fig. 5.11C), apparently corresponding to epidermis. Well-developed *Microcodium* aggregates, up to 0.5 mm in diameter with elongate, 100-250  $\mu\text{m}$  long grains (Fig. 5.11D), are associated with incipient *Microcodium*, <200  $\mu\text{m}$  in diameter, composed of minute grains (20-30  $\mu\text{m}$ ). In spite of their small dimensions, some *Microcodium* rosettes in different stages of development, from incipient to fully developed forms (Fig. 5.11F), are composed of pyramidal grains with ultrastructure, characteristic of strongly elongate elements (see Section 5.5).



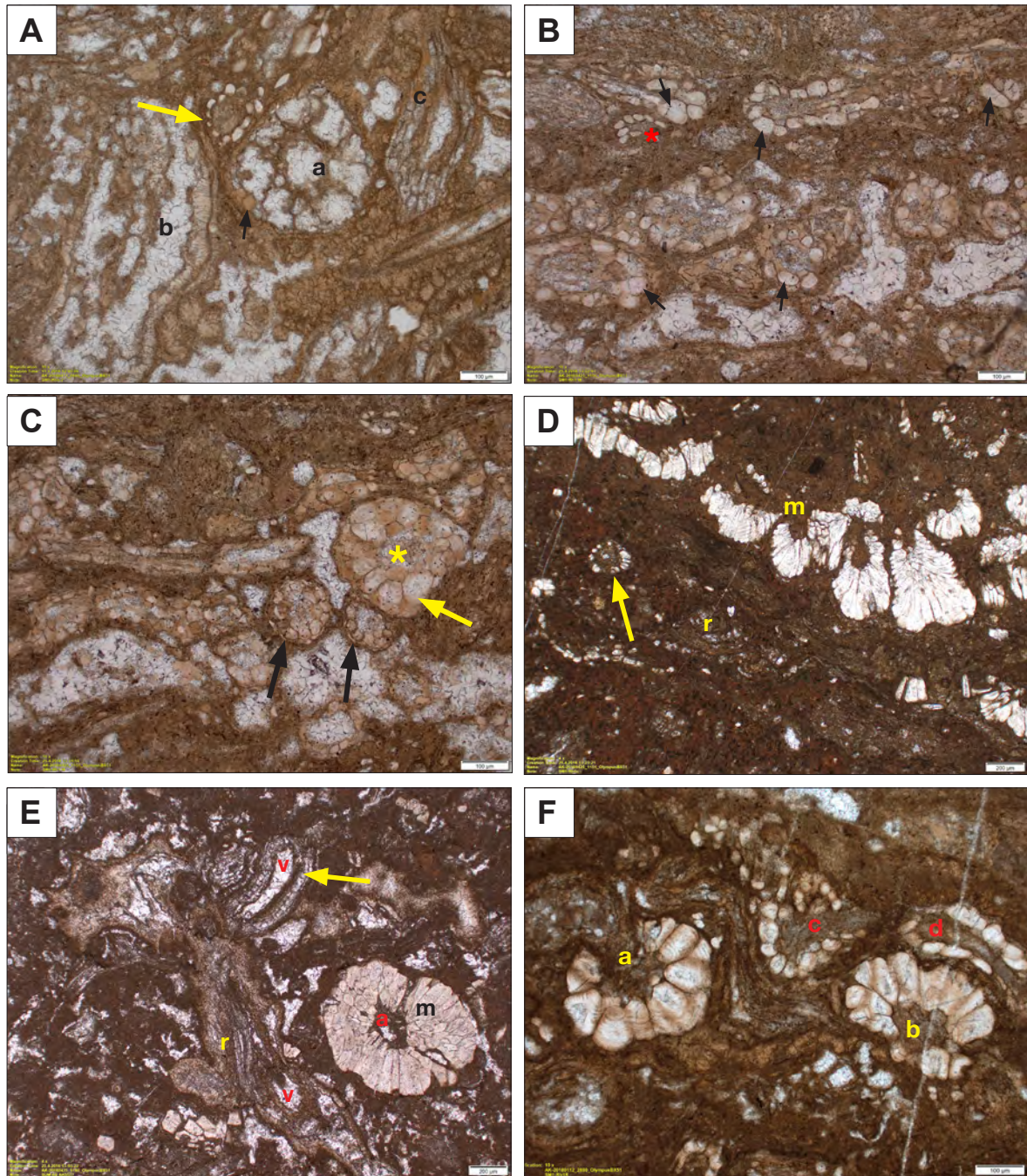


**Figure 5.11.** Fine root fabric and incipient stages of *Microcodium* from the Sv. Martin laminar calcrete. Thin section images in PPL. A) Noncalcified fine roots (a, b, c) with only partially preserved anatomical details: a - transverse section with the central tube corresponding to a vascular cylinder, surrounded by radial septate micrite fabric (cortex) with several preserved cells (black arrow); b - same as [a] but in longitudinal/oblique section; c - oblique section with preserved cellular structure of the cortex. Yellow arrow indicates a very fine root in cross section, composed of a single layer of small calcified cells (?embryonic stage of *Microcodium*). B) Sections of fine roots with individual enlarged (hypertrophied) calcified cells (black arrows). C) Black arrows indicate thin layers of partly preserved epidermal cells of very fine roots (<100  $\mu\text{m}$  diameter). Larger root (yellow asterisk) shows considerably enlarged cortical cells (yellow arrow), apparently merged (fused) with the epidermis. Cf. CL images in Figs. 5.18. D) Asymmetric *Microcodium* aggregates (m), micritic rhizoliths (r) and incipient *Microcodium* (yellow arrow). E) Branched rhizolith (r) with partially preserved anatomical details (arrow), associated with fully-developed *Microcodium* (m). Note similarity of diameter of rhizolith vascular cylinders (v) and the axial canal of *Microcodium* (a). F) Developed (a, b) and incipient (c, d) *Microcodium*.

#### 5.4 *Microcodium*-substrate relationships

A controversial aspect, which is commonly seen with all morphotypes, is the ability of *Microcodium* to dissolve and intensely corrode carbonate substrates. The most spectacular examples of corrosive nature of *Microcodium* are lamellar forms, centripetally corroding carbonate clasts (Fig. 5.9), and cylindrical aggregates in contact with bioclasts where *Microcodium* clearly cross-cut internal structures of fossils (Fig. 5.12E, Figs. A5-4.09, A5-4.10). *Microcodium* commonly grows along fractures and enlarge the voids by corroding the walls (Figs. 5.8A, 5.12 D, 5.13A; Fig. A5-4.01D). It often disaggregates, leaving empty voids which retain the corrosional outline (Fig. 5.12D). In-situ aggregates in direct contact with the substrate and protruding into it usually display intact structure (Fig. 5.12F) but apparently rapidly disintegrate to fragments and individual grains due to (soil) bioturbation (Figs. 5.13A, B, Fig. A5-4.09E, F).

Individual aggregates are commonly separated from the corroded substrate by a void, up to several 10  $\mu\text{m}$  wide, subsequently filled by cement or matrix (Figs. A5-4.10A-D), and occasionally associated with thin films of non-carbonate mineral or organic material (Fig. 5.12C). Dissolutional voids, considerably larger in diameter than aggregates themselves, are well expressed in cylindrical forms protruding through partings and corroding previously formed *Microcodium* lamellae (Fig. 5.10F). Exceptionally, *in situ Microcodium* aggregates are surrounded by tubular, spar-filled features, up to 50  $\mu\text{m}$  long and 10-20  $\mu\text{m}$  in diameter, protruding into the micritic substrate, corresponding in size and shape to root hairs (Figs. 5.12A, B). In some cases, depending on diagenetic alteration of material, similar features can be better recognisable under CL (Fig. A5-4.10E, F).

Disintegrated *Microcodium* grains are susceptible to reworking and resedimentation. *In situ Microcodium* aggregates are often associated with reworked material (Fig. 5.13A, Fig. A5-4.11A), locally forming packstone and grainstone textures, composed almost exclusively of *Microcodium* grains (Fig. 5.13C, Figs. A5-4.11B, C). Reworked grains can be incorporated in later stages of calcrete development (Fig. 5.13D, Figs. A5-4.11D, F). Furthermore, because of the constructive–destructive nature of many rhizogenic calcretes, *Microcodium* colonies can often be seen corroding indurated horizons from earlier stages of soil development (Fig. 5.13A).



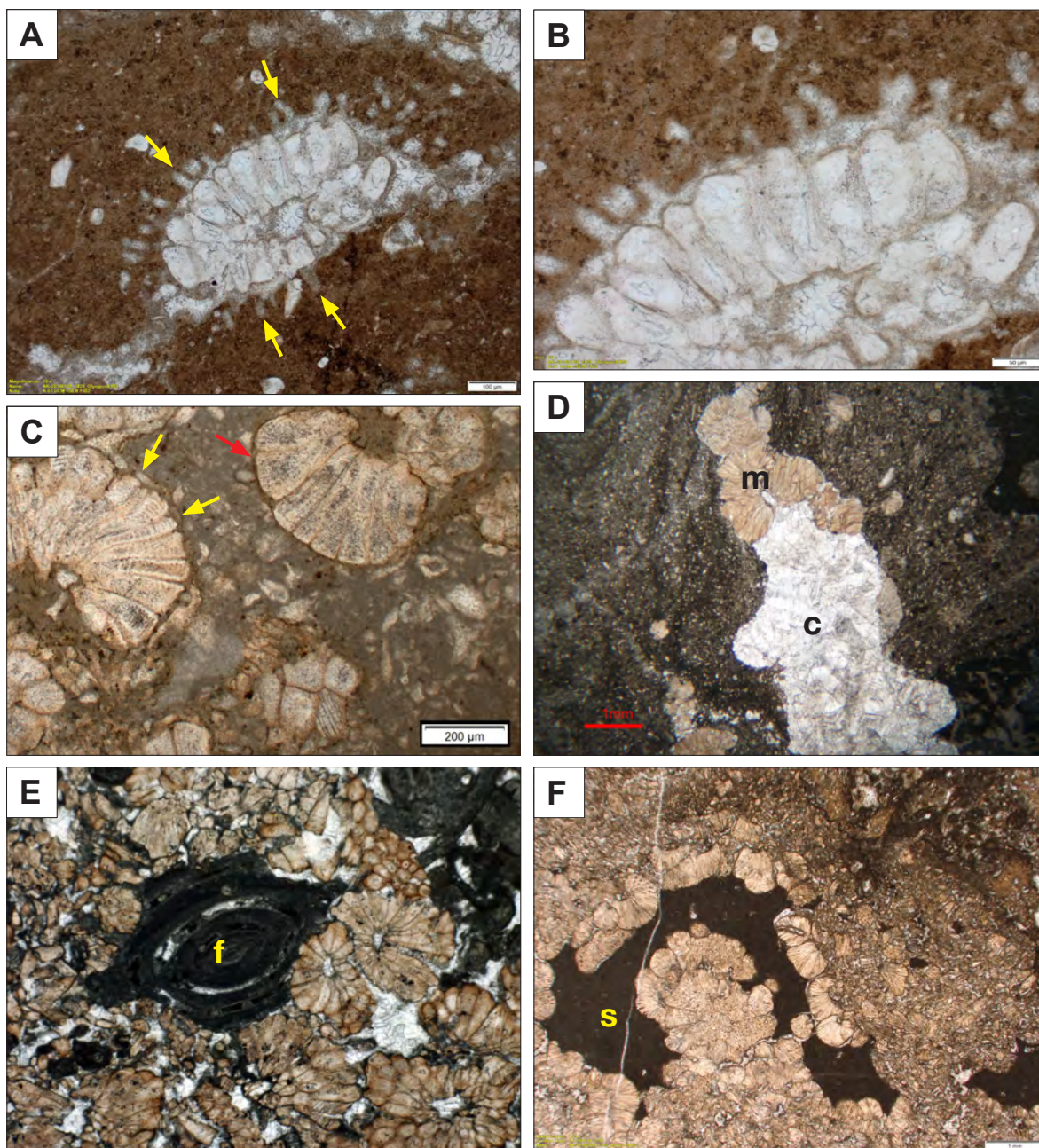


**Figure 5.12.** *Microcodium*-substrate relationships. Thin sections photomicrographs in PPL. A, B) *Microcodium* surrounded by tubular, spar-filled features (arrows), protruding into the micritic substrate, corresponding in size and shape to root hairs. Also note a void around the *Microcodium* rosette, possibly corresponding to decomposed root epidermis. C) *Microcodium* aggregates enclosed with a thin layer of brown, organic-rich material. Yellow arrows indicate possible remains of an epidermis, red arrow shows a thin film of non-carbonate/organic rich material. Paleocene, Dolenja Vas section. D) *Microcodium*, corroding fine-grained palustrine limestone. In-situ aggregates are preserved in the upper part (m) whereas *Microcodium* in the lower part had disintegrated and had been removed. The corresponding void, filled by sparite cement (c), retained the curved shape created by *Microcodium* dissolution. Paleocene, Šumka section. E) Miliolid foram (f) corroded by *Microcodium*. Paleocene, Čebulovica section. F) Intensively corroded mudstone with asymmetric, fan shaped *Microcodium* aggregates protruding into the substrate (s). *Microcodium* aggregates in contact with the mudstone substrate are intact but largely disintegrated in the surrounding. Liburnian Formation, Maastrichtian, Vrabcé locality. Also see Fig. A5-4.11.



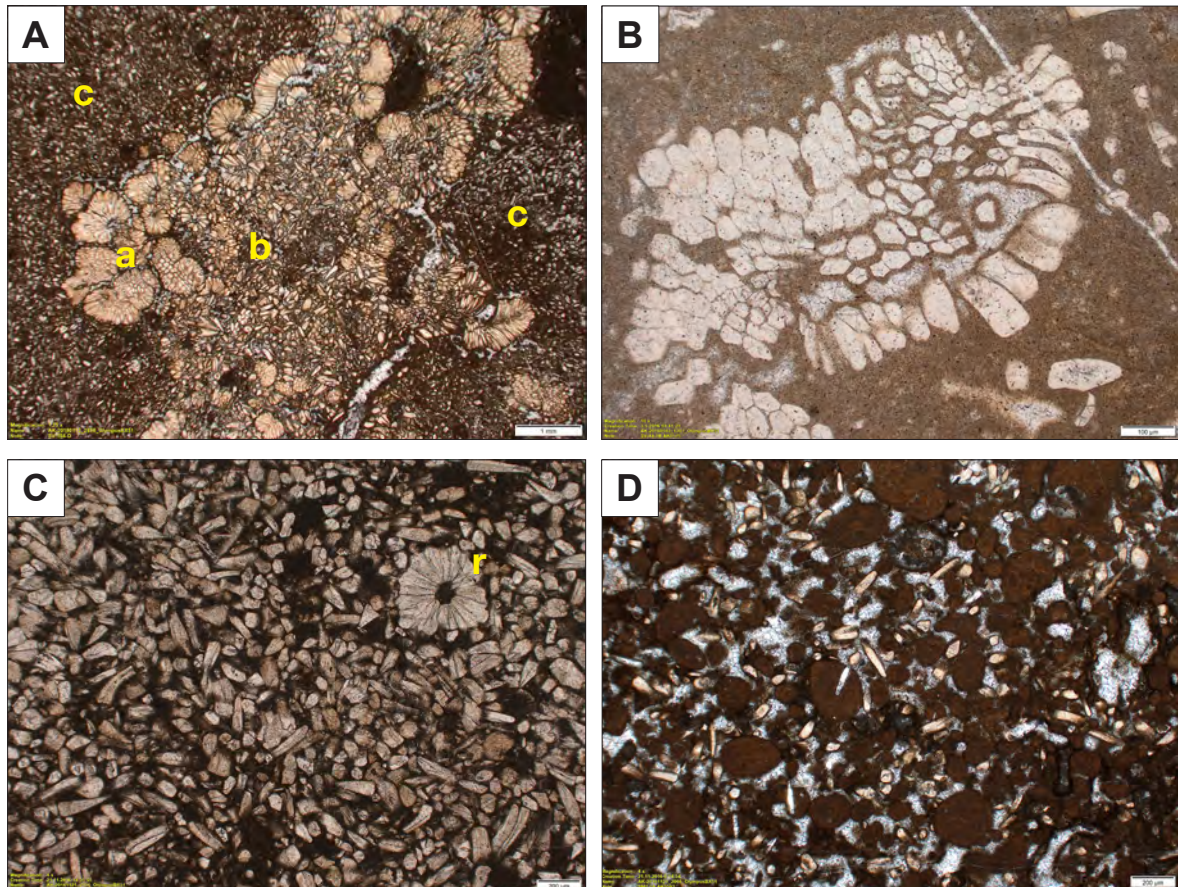


**Figure 5.13.** *Microcodium*-substrate relationships and disintegrated aggregates. Thin section photomicrographs in PPL. **A**) Several mm wide vertical corrosional structure in calcrete (c) made of *in-situ* asymmetric *Microcodium* aggregates (a) at the edge and disintegrated *Microcodium* in the central part (b). Paleocene, Divača AC locality. **B**) Partly disintegrated aggregate. Note early micrite cement enclosing the polyhedral grains. Sample SV-44, Divača, Paleocene. **C**) *Microcodium* packstone composed of separate elongate grains and an unbroken rosette (r). Slavnik locality, Maastrichtian. **D**) Individual elongate *Microcodium* grains incorporated in peloidal calcrete. Paleocene, Šumka section.

### 5.5 Ultrastructure and crystal morphology of *Microcodium* grains

Petrographic description of the rhizogenic microfabric presented by Košir (2004) has mainly concentrated on transitional morphologies between calcified roots and classic *Microcodium* features in thin sections from two adjacent laminar calcrete profiles (Appendix A5-2). The following analysis is based on a much wider variety of material from different settings and is complemented by optical cathodoluminescence (CL) using high-

sensitive digital cameras, and SEM petrography. Previous CL investigations (Appendix A5-2, Section A5-2.6.2) did not give results with sufficient resolution and contrast due to the limited light-capture sensitivity of the equipment.

Compared to numerous papers aimed at reconstructing the architecture of *Microcodium*, relatively few studies comprehensively examined the crystal ultrastructure and growth patterns of individual elements. Amongst these studies, the most thorough investigations have been provided by Lucas & Montenat (1967), Bodergat (1974), Roux (1985), Morin (1993) and Kabanov et al. (2008). As noted in Sections 3.4 and 5.1, material of Klappa's (1978) interpretation pertains mostly to Recent and Pleistocene intracellularly calcified roots (cf. Jaillard 1987 and Jaillard et al. 1991), whereas his petrographic analysis only briefly delineate the ultrastructure and crystallographic properties, intrinsic to classic pre-Quaternary *Microcodium*. An important issue in comparing both features is that modern calcified roots have not undergone significant diagenetic changes (but see the following section) whereas most *Microcodium* examples are from well-cemented rocks that were mostly subjected to multiple diagenetic phases in different realms.

A comparative list of petrographic features of *Microcodium* and intracellularly calcified roots, illustrated in Section 3.3, is given in Table 5.2. In general, typical elongate *Microcodium* grains (elements) exhibit (some of) the following characteristics:

1) Individual grains are predominantly monocrystalline, rarely polycrystalline, generally showing simple, uniform extinction, rarely undulose patterns in cross-polarised light (XPL) (Appendix A5-4, Figs. A5-4.12 and A5-4.13). Under XPL, apparently unique *Microcodium* grains can show aggregate, usually bipartite structure, composed of two or more parts with different crystal orientation and extinction (Figs. 5.15B, Appendix A5-4, Figs. A5-4.12B, A5-4.13B), similar to common structure of calcite in calcified root cells (Figs. 3xy-3.xz; Jaillard 1987, Jaillard et al. 1991).

2) Calcite in *Microcodium* grains is typically rich in minute dark, solid or fluid inclusions, and/or micropores (Fig. 5.14E, F), 0.5–2 µm in diameter (Appendix A5-4, Fig. A5-4.16D).

3) Elongate elements often show fibrous appearance in longitudinal section (Figs. 5.14A, F, Appendix A5-4, Figs. A5-4.12A, E), although prominent radial fibrous calcite fabric, reported by some other studies (e.g. Kabanov et al. 2008; see below) has not been observed by SEM examination of the studied material. In some cases, indistinctive radial fabric

**Table 5.2.** Comparative petrography of classic fossil *Microcodium* and modern intracellularly calcified roots (iCRs). Note that most petrographic information of *Microcodium* has been obtained by observation in thin sections whereas investigation of iCRs is typically performed on fragmental samples under SEM.

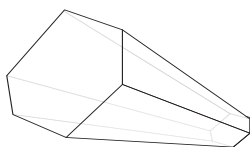
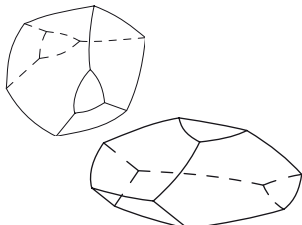
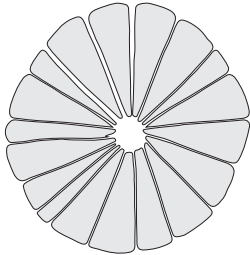
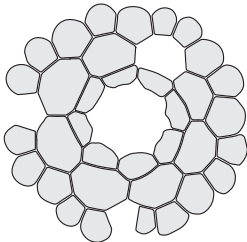
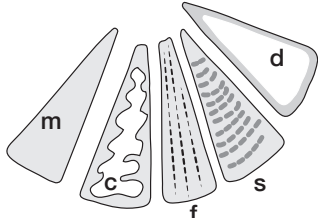
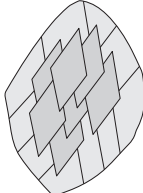
	<i>Microcodium</i>	iCRs	remarks
<b>mineralogical composition</b>	Low Mg calcite	Low Mg calcite	
<b>grain shape</b>	<p>Relatively regular polyhedra with flat sides and polygonal in cross section, generally simplified as frusta<sup>[1]</sup>, pyramids or prisms;</p> <p>Predominantly strongly elongate</p> 	<p>Complex polyhedra, often with curved and folded sides;</p> <p>Generally isodiametric to moderately elongate;</p> <p>Elongate in special cases</p> 	<sup>[1]</sup> see Figs. 5.2 and 5.3 and references therein
<b>grain arrangement</b>	<p>Generally monolayered, radially arranged, fitting pattern cellular structure</p> 	<p>Multilayered;</p> <p>Fitting pattern cellular structure; empty (non-calcified) cells common</p> 	also see Fig. 5.3
<b>crystal structure</b>	<p>Generally monocrystalline [m] but also composite polycrystalline structure, often two layered calcite elements, generally with darker, inclusion-rich outer part and more limpid centre, either with diffuse boundary [d] or central part of vacuolar/cisternate shape [c], or with indistinctive radial fibrous structure [f] <sup>[2]</sup>;</p> <p>Common radial striate features [s] <sup>[3]</sup></p> 	<p>Mono- to polycrystalline</p> <p>Lamellar, mesocrystalline and oriented-growth nanocrystalline structures observable under SEM</p> <p>In thin sections clear calcite without (organic) inclusions</p> 	<p><sup>[2]</sup> Kabanov et al. (2008) distinguish “prismatic” and “radial-fibrous” ultrastructure</p> <p><sup>[3]</sup> Figs. 5.21 and 5.22; see also discussion in Morin (1993)</p>



Table 5.2. (continued)

	<i>Microcodium</i>	iCRs	remarks
<b>structure of laminar aggregates</b>	Typically composed of strongly asymmetrical aggregates <sup>[4]</sup> ; layers/laminae composed of structures exhibiting dichotomous branching patterns <sup>[5]</sup> ; Aggregates oriented towards the corroded substrate with their thicker (ventral) side.	Layers/laminae composed of asymmetrical, fully calcified roots showing dense herringbone branching <sup>[6]</sup> . Aggregates oriented towards the corroded substrate with their thicker (ventral) side.	<sup>[4]</sup> see Fig. 5.6D, E; <sup>[5]</sup> Figs. 5.9, 5.10; <sup>[6]</sup> Figs. 5.6C, 3.9,
<b>relationships with substrate</b>	Clear corrosive (replacive) contacts	Clear corrosive (replacive) contacts	see Figs. 3.9, 3.11, 3.15A-D and Figs. 5.12-5.13
<b>optical properties</b>			
XPL extinction	Within a single grain (element) generally uniform, reported also sweeping <sup>[7]</sup> to aggregate <sup>[8]</sup> extinction patterns,	Fully calcified cells commonly composed of two or more parts with different crystal orientation and uniform or undulose extinction patterns	<sup>[7]</sup> Freydet and Plaziat 1982; <sup>[8]</sup> Klappa 1978b
cathodoluminescence and charge contrast imaging patterns	Internal structure often emphasised under CL with distinguishable layers / generations of calcite (e.g. folded, cisternoid vacuoles)  CL patterns of <i>Microcodium</i> (enlarged calcified cells) differ from nonluminescent permineralised root cells <sup>[9]</sup>	Internal structure not discernable under CL  SEM CCI may exhibit internal crystalline features (e.g. primary microlamellar structure)	<sup>[9]</sup> See Figs. 5.18, 5.19
fluorescence patterns	Non-fluorescent to weakly fluorescent; fluorescence filters may enhance the contrast between different calcite forms within a single grain	Weak fluorescence in individual grains probably related to secondary incorporated organic matter in microendolith borings	see Figs. 3.30A, B; A3-4.14L, J; A5-4.13.
calcite crystal inclusions	Common dark calcite, yellowish to pale brown in colour with cloudy appearance; Apparent inclusions of organic matter and fluids in submicrometric pores <sup>[10]</sup>	Generally limpid calcite without incorporated solid organic matter, rarely calcite with fluid inclusions	<sup>[10]</sup> see Appendix A5-4.16
<b>weathering patterns</b>	Common intensively micritised calcite by microendolith borings	Common intensively micritised calcite by microendolith borings	see Figs. 3.27-3.30, Figs. 5.20-5.22 and Figs. A5-4.19-4.21
<b>diagenetic alteration</b>	Affected by diagenetic history from early (meteoric) to late stages (deep burial)	Generally devoid of considerable diagenetic change	

appears to be enhanced by vesicular inclusions (pores) in calcite, often slightly elongated and preferentially aligned in series in radial direction (Fig. 5.14F).

4) *Microcodium* calcite grains are commonly yellowish to pale brown in colour (in standard, ~30 µm thick thin sections) and have cloudy appearance.

5) Brown calcite usually constitutes the outer layer of an individual grain whereas the central part is typically more limpid. Transition between the coloured and limpid calcite can be diffuse (Figs. 5.8B, C, 5.14C, E) or sharp, delineating a central lumen (vacuole) (Fig. 5.15A-C; Appendix A5-4, Fig. A5-4.13E, F).

6) In two-layered, vacuolar grains, the outer calcite layer is characterised by inclusion-rich, porous calcite, analogous to grains with radial fibrous appearance. In cross section, vacuoles exhibit circular shape (Figs. 5.15A-C) whereas in longitudinal sections through *Microcodium* elements, the vacuolar, central part displays conspicuously folded, convoluted to costate morphology (Figs. 5.15D-G). Complex vacuolar bodies display intricately folded shapes, which morphologically resemble (but are not genetically related to!) convoluted cell organelles such as endoplasmic reticulum and Golgi apparatus (Sparkes 2021, Evert 2006; these organelles are composed of a system of flattened, membrane-bounded vesicles, called cisternae). Similar cisternoid morphology can be deduced from well-oriented longitudinal sections through *Microcodium* grains in transmitted light in ultra-thin sections (diameter of vacuole is typically ~20 µm, i.e. smaller than a thickness of a standard thin section) as well as in backscattered electron (BEI) SEM images of polished thin sections (Figs. 5.15D, E). Cisternoid vacuolar features are often very clearly expressed in CL photomicrographs (Figs. 5.16 and 5.17) with non-luminescent outer layer and bright to dull orange or red luminescent internal vacuole. Equivalent ultrastructure, best seen in CL photomicrographs, can be observed in incipient *Microcodium* (Fig. 5.16C, D) and transitional forms, i.e. fine roots with individual, hypertrophied cortical cells (Fig. 5.18-5.19) which are invariably non-luminescent and occasionally exhibit complex (cisternoid) vacuolar structure. Such enlarged cortical cells have apparently formed by the same biomineralisation mechanism whereas larger fine roots, in spite of their well-preserved (permineralised) cellular tissues but lacking enlarged (calcified) cells, exhibit very different, indistinctive CL patterns (Fig. 5.19E, F, Figs. A5-4.17, A5-4.18).

7) *Microcodium* grains exhibit significant difference in chemical composition of calcite layers. Electron probe microanalysis (EPMA) of major and selected trace elements (Ca, Mg, Fe, Mn, Sr, P, S) of vacuolar *Microcodium* indicate presence (increased amount) of sulphur (0.14—0.43 wt% S) and magnesium (0.8—1.7 wt% Mg) in the outer, porous/inclusion-rich

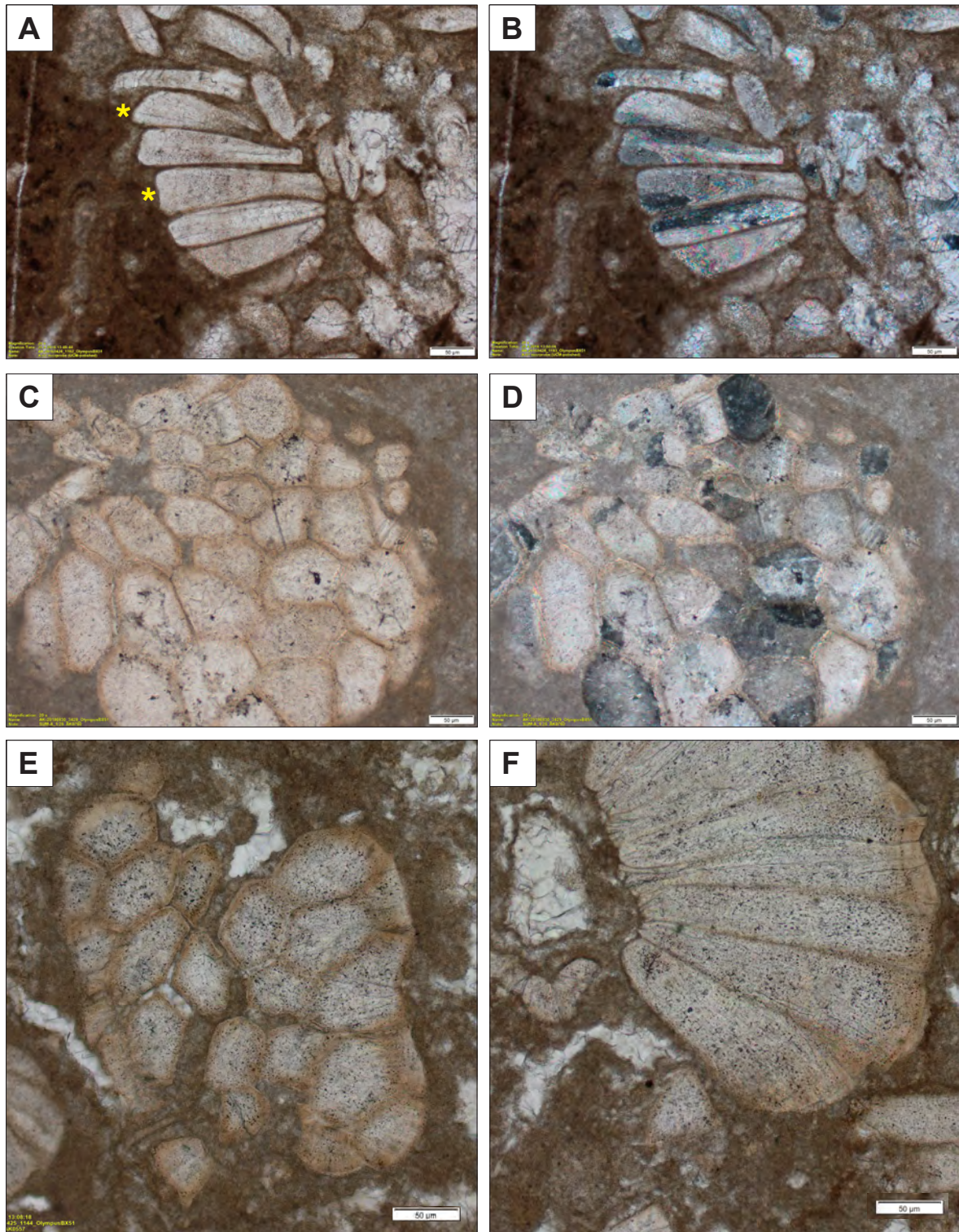


**Figure 5.14.** Ultrastructure and crystal morphology of *Microcodium* grains in thin sections. A) PPL photomicrograph of disaggregated, separated *Microcodium* grains in longitudinal section with indistinctive radial fibrous appearance, accentuated by minute, dark inclusions (micropores). B) XPL image of (A). Sv. Martin calcrite. C, D) PPL/XPL pair of a transverse section of an aggregate, composed of cloudy brownish, inclusion-rich calcite. E) Transverse section of an aggregate composed of grains with distinctive brownish outer layer and colourless internal part. Both layers contain inclusions/micropores, contact between the layers is diffuse. F) Longitudinal section of an aggregate; grains display indistinctive radial-fibrous texture, marked by slightly elongate, aligned inclusions (pores). Figs C-F: Paleocene, Šumka section.



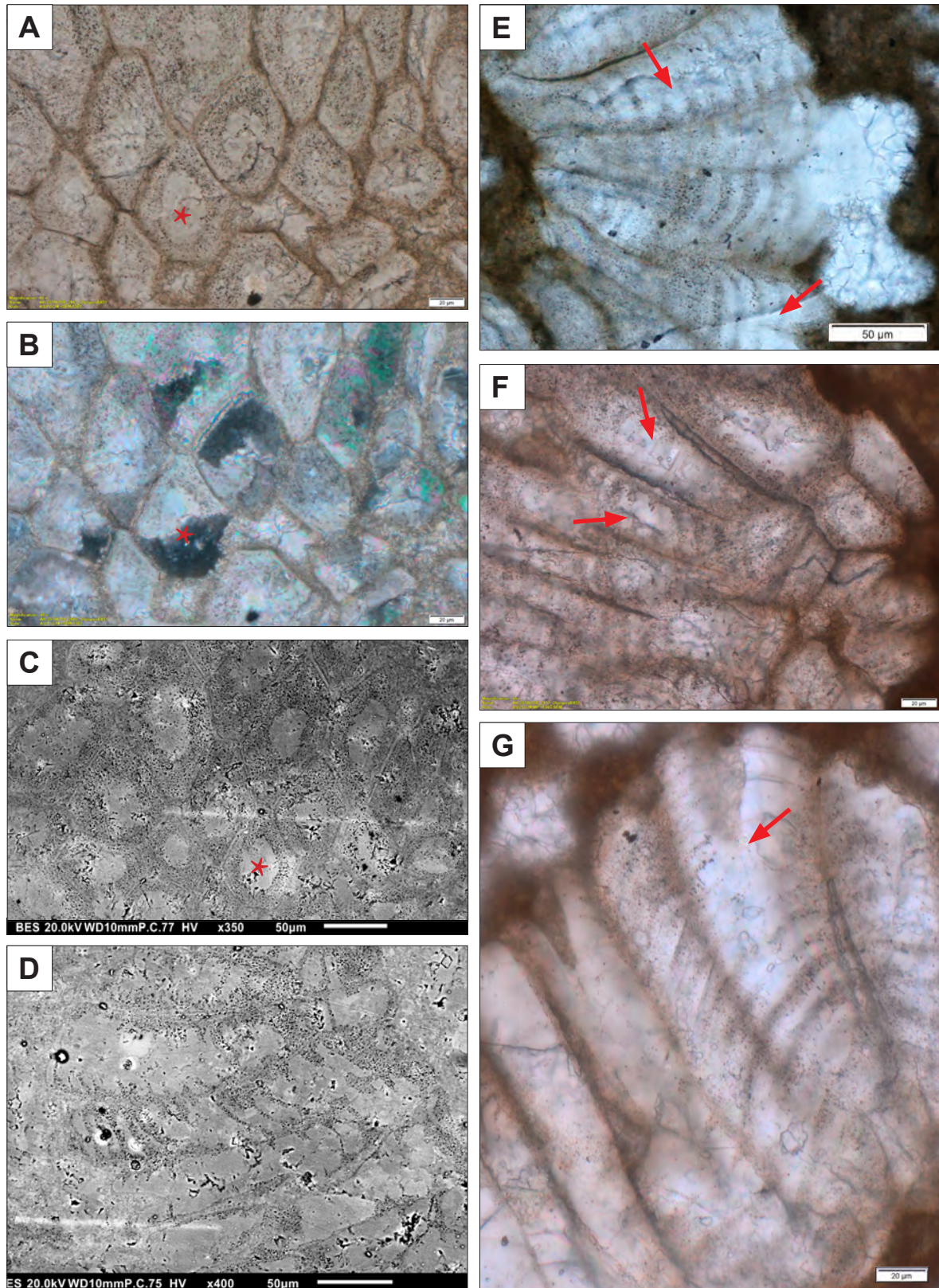


Figure 5.15. Please see caption on the following page.

**Figure 5.15.** (previous page)

Ultrastructure and crystal morphology of *Microcodium* grains: two-layered grains with vacuolar features. A, B, C) PPL, XPL and BES SEM photomicrographs of transverse section of an aggregate, composed of grains with a central vacuole (clear calcite) and an outer layer, rich in inclusions (pores). Boundaries between the layers are well discernable. Vacuoles exhibit rounded shape in cross section. Note polycrystalline structure visible in some grains under XPL (Fig. B), and crystal boundaries cross-cutting the vacuole/outer layer (asterisk). Sv Martin calcrete, Paleocene. Double-polished very thin section (~15 µm). D) BES SEM image of elongate grains in longitudinal section showing clearly-bounded contorted (folded) central vacuoles and the outer layer with micropores/inclusions (black). Also see higher magnification SEM image of the outer layer in Fig. A5-4.16D. Polished thin section. E, F, G) PPL photomicrographs of complex vacuolar grains in longitudinal section. Concentric layers of clear calcite correspond to vacuoles, enclosed in porous calcite. Individual sections along the axial part of grains (arrows) indicate that all the layers are interconnected in the median part, forming a cisternoid-like vacuole. Double-polished very thin section (~15 µm), Šumka section, Paleocene. Also see SEM images in Fig. A5-4.15 and PPL/fluorescence images in Fig. A5-4.13 E, F.

layer (Appendix A5-5) compared to 0.0—0.1 wt% S and 0.36—0.75 wt% Mg, respectively, in the inner layer. Backscattered electron SEM observations and EDS analysis of the same sample (Appendix A5-4, Fig. A5-4.15) correspond to EPMA results and indicate that the presence of sulphur is probably related to organic matter in vesicular pores (µm-size black spots in BES SEM images; Figs. 5.15C, D, Fig. A5-4.15C, D, Fig. A5-4.16D). Contents and ratio between Mn and Fe, which could provide explanation for contrasting CL response of calcite layers in vacuolar grains (e.g. Machel 2000; Barbin 2000), are close or below detection limit in all EPMA point measurements (Appendix A5-5).

8) Particularly strongly elongate *Microcodium* elements often show fine, 5-10 µm thick, concentric striations (Fig. 5.8D, E, Appendix A5-4, Figs. A5-4.02A-D, A5-4.10C). In the studied material, examples of *Microcodium* characterised by striate ultrastructure are relatively poorly preserved and have not provided further insight into this intriguing feature, interpreted by some previous researchers as an accretionary layering or successive growth lines (Roux 1995; Morin 1993 and references therein). However, exquisite microstructural details of concentric striae in calcite are preserved in Quaternary *Microcodium* material, described in Section 5.6 and further discussed in Section 5.8.3.

9) Many earlier works on *Microcodium* reported filamentous fabric occurring within the calcite crystals, composed of fine 'filaments' (i.e. tubular pores), 0.5-2 µm in diameter, organised in branching and fan-like patterns. Filamentous features have been one of the major matters in question in the *Microcodium* controversy and are, therefore, discussed separately in the following section (5.6) and compared to identical features observed in modern calcified root cells (Chapter 3, Section 3.4).



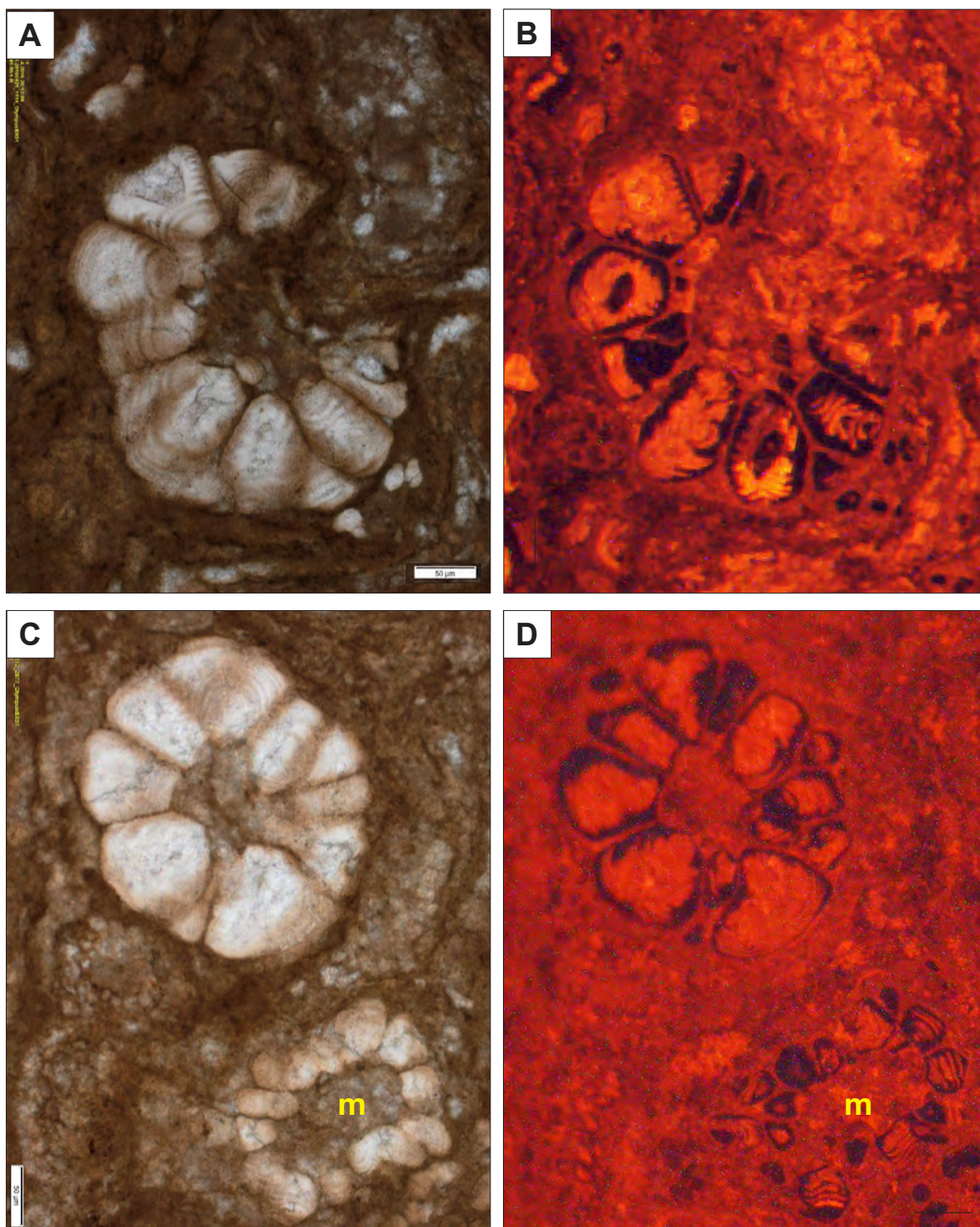


**Figure 5.16.** Ultrastructure and crystal morphology of *Microcodium* grains in different stages of development. A, C) PPL and B, D) CL images of a small rosette sections, composed of triangular (in 3D pyramidal) grains with concentric layered structure. Cisternoid vacuoles are clearly visible in CL (luminescent central parts of grains), distinguishable from nonluminescent (black) outer layer. Cisternate structure is noticeable also in small grains of incipient *Microcodium* (m) in Figs. C and D. Scale bars 50 μm. Sample SM1\_Rh-R, Paleocene, Sv. Martin calcrete.



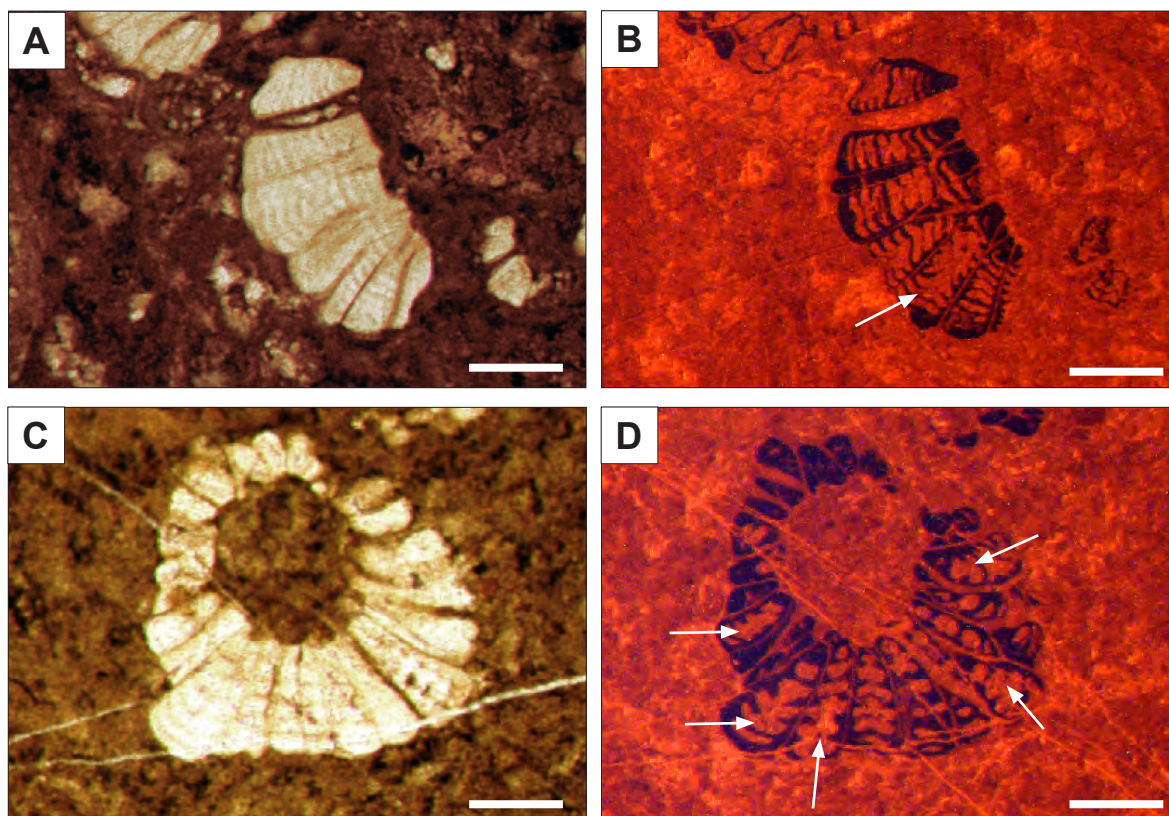


**Figure 5.17.** Ultrastructure and crystal morphology of *Microcodium* grains with complex vacuolar structures. A, C) PPL photomicrographs of excessively thick thin section ( $\sim 50 \mu\text{m}$ ) of tranverse section of *Microcodium* showing concentric layered ultrastructure of grains. In transmitted light, layers within a grain appear to be cseparate whereas in CL photomicrographs (B, D), some sections through central (median) parts of grains show that the layers are joined in a single cisternoid vacuole (white arrows) within nonluminescent (black) calcite.

Sample SM1-Rh6-B, Paleocene, Sv. Martin calcrete. Scale bar  $100 \mu\text{m}$ .

### 5.6 Internal filamentous microfabric of *Microcodium* grains

As noted in previous sections, the original interpretation of *Microcodium* as a product of calcite precipitation within plant cells in association with mycorrhizal fungi (Klappa 1978) was primarily based on Quaternary calcified roots, not *Microcodium* sensu stricto. However, well-preserved examples of Palaeogene and Holocene *Microcodium* have revealed micromorphology of intracrystalline filaments (tubular fabric) identical to features in modern intracellularly calcified roots, revealed by SEM analysis of resin-embedded samples, described in Chapter 3 (Section 3.3.5), apparently related to microbial (fungal) endoliths).

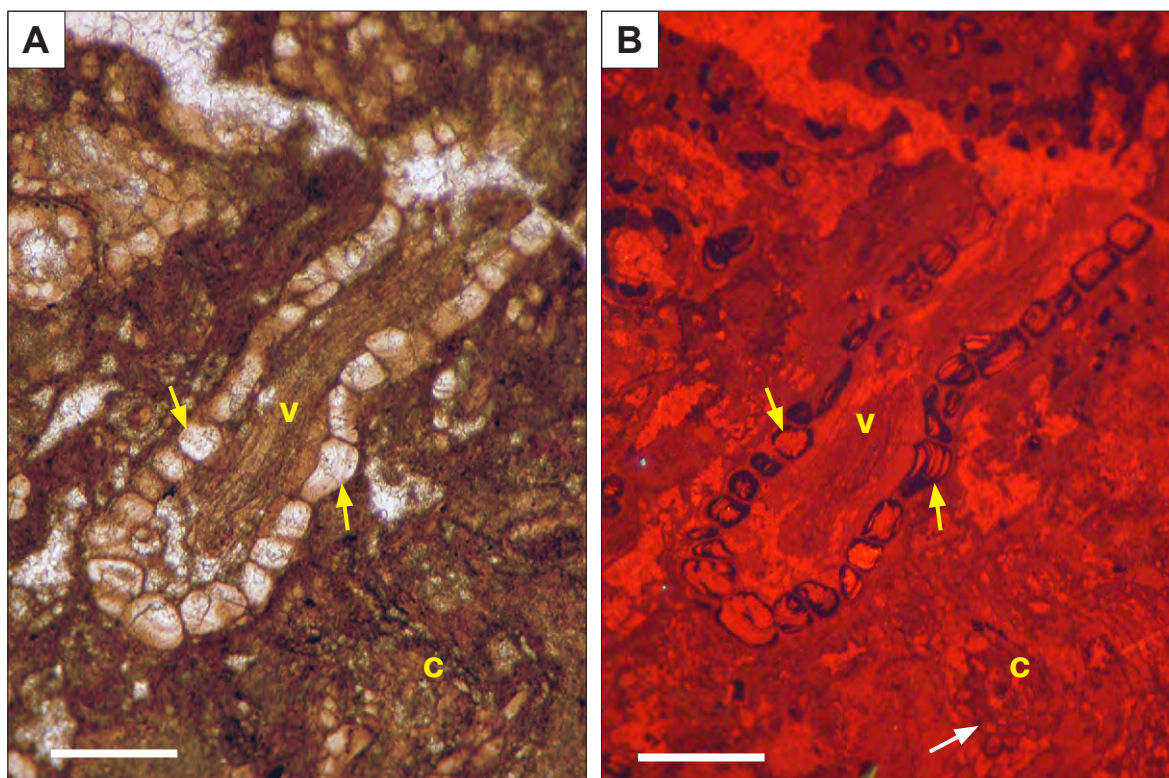


**Figure 5.18.** Permineralised fine roots and incipient *Microcodium* grains. PPL (A) and CL (B) photomicrographs of longitudinal section of a partly calcified fine root. Fabric, corresponding to cellular tissues of the vascular cylinder (xylem), is indistinctly visible in the central part (v) and in the fine root rhizolith in transverse section (c); cellular fabric is better seen under CL. Fine root has apparently a single layer of cortex, composed of large, hypertrophied calcified cells (yellow arrows); compare with size of noncalcified cells in c (white arrow). Internal structure of calcified cortical cells (= incipient *Microcodium*) is analogous to ultrastructure of well-developed, elongate *Microcodium* grains (Figs. 5.15, 5.16). Paleocene, Sv. Martin calcrete. Scale bar 100  $\mu$ m.

**Figure 5.19. (next page)**

Permineralised fine roots and incipient *Microcodium*. Thin sections photomicrographs in PPL and CL. A, B) Fine roots in trasverse sections (a, b) with individual calcified (hypetrophied) cortical cells appearing more limpid in PPL and nonluminescent in CL. Blue and yellow arrows locate the same calcified cells in PPL and CL. *Microcodium* (m) with indistinctive cisternoid vacuolar grains. C, D) As in A, B: several fine roots (a, b, c) with enlarged calcified cortical cells (black under CL). Arrow (d) indicates a non-calcified but permineralised fine root without enlarged cells. E, F) Yellow arrows: strongly enlarged "fat" (hypertrophied) calcified cortical cells in cross section and in longitudinal section (blue arrow). White arrow: small cell with cisternate vacuolar structure. R: oblique section of fine root lacking calcified cells but exhibiting relatively well discernible cellular structure in PPL (brown cells) and dull luminescence under CL. Paleocene, Sv. Martin calcrete. Scale bars: 100  $\mu$ m.



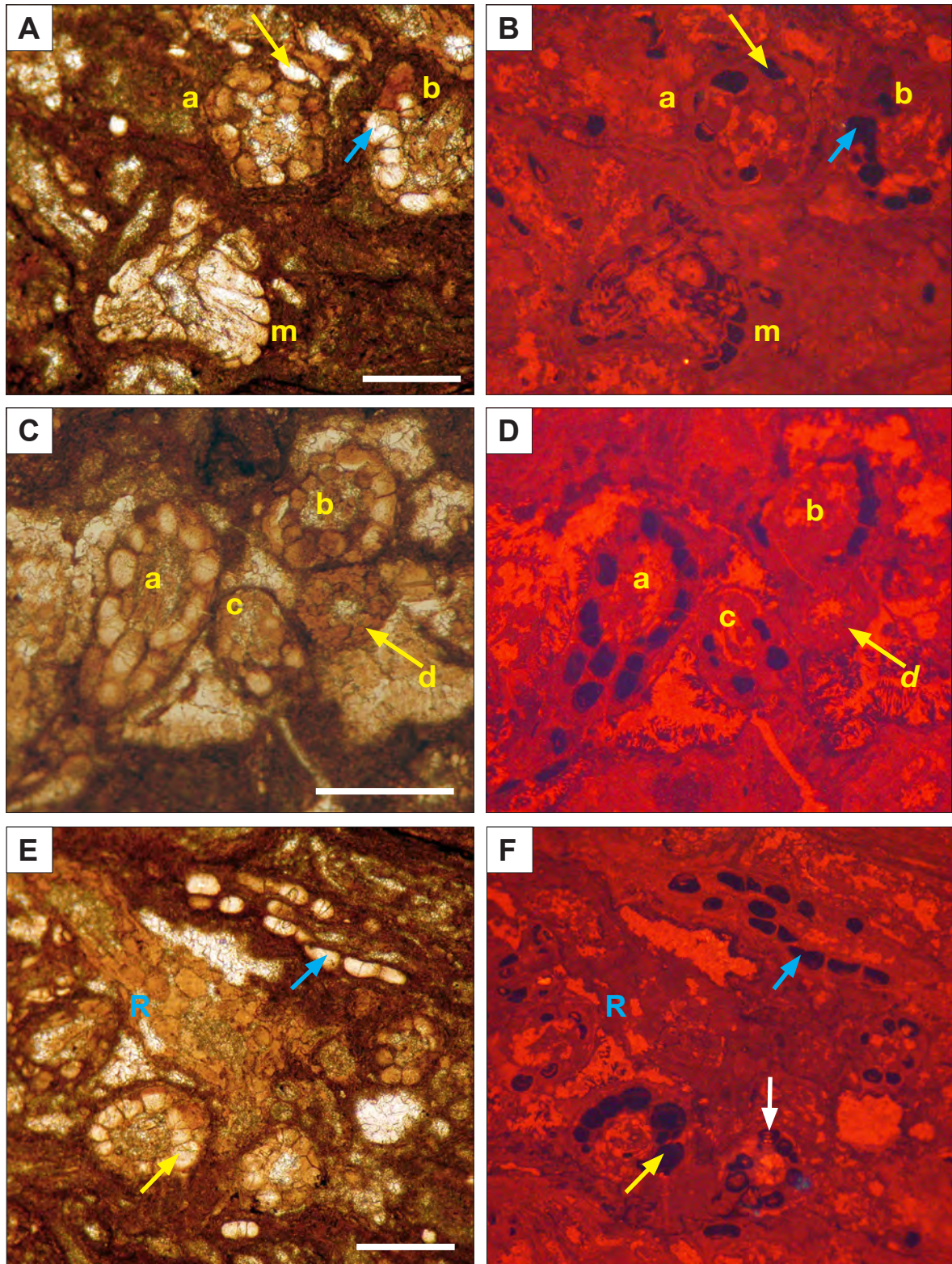


Figure 5.19. (Please see caption on the previous page)



Calcite of *Microcodium* aggregates is often opaque and appears to be intensively micritised. It is apparent from fabric, observed in ultrathin sections (Figs. 5.20 and 5.22), that the opaque micritic aspect, as seen in standard thin sections, results from dense, intertwined networks of microtubular features, typically approximately 1 µm in diameter (Figs. 5.20F-H; Fig. A5-4.19F). Grains in a single aggregate can exhibit very variable proportions of filamentous fabric, occurring in calcite – from individual straight, dichotomously branched and coiled filaments or a sparse veneer of tubules, centripetally protruding into the grain (Figs. 5.20C, 5.21C, D), to layered networks (Fig. 5.20 B), concentric striate structures (Figs. 5.21E, F, 5.22A, B) and radial swarms of filaments, following the axis of elongation of individual grains (Figs. 5.20E, F). Similar to the patterns observed in intracellularly calcified roots (Sections 3.4.4 and 3.5.4), the tubular networks appear to protrude into *Microcodium* grains from the external, intergranular space (Figs. 5.20A, C) and preferentially proliferate in particular, determined intracrystalline layers. Peculiar striate fabric of *Microcodium* appears to be a consequence of such growth strategy, i.e. selective infestation of parts (concentric layers) in *Microcodium* grains (Figs. 5.21E, F, 5.22A), seemingly advantageous to endolithic microorganisms by particular mineral properties, most probably due to higher amount of incorporated organic matter (Golubic et al. 2005). In addition to apparent similarity with the classic micritisation mechanism, creating micrite envelopes (Bathurst 1966, 1975), *Microcodium* grains can also exhibit opposite patterns, characterised by selectively micritised internal parts and less altered and better preserved thin outer layer (Fig. 5.21C). Such patterns appear to be associated with *Microcodium* grains with double-layered, vacuolar ultrastructure (Section 5.5).

---

**Figure 5.20. (next page)**

Filamentous features (microborings) in *Microcodium* calcite, all samples from Paleocene breccia, Montpellier. A) PPL photomicrograph of lamellar *Microcodium*. The outer layer of grains of an aggregate (yellow asterisk) shows dark filaments limited to the lower (internal) side of grains.

B) Transverse section of *Microcodium* aggregate showing different degree of calcite alteration in individual grains. Red arrow indicates a grain only slightly infested with microborings, yellow arrows indicate grains with curved filamentous structures, corresponding to intracrystalline irregularities/layers. C) Close up showing proliferation of endolithic microborings into calcite grains from the intergranular (intercellular) space.

D) High magnification PPL photomicrograph of microborings. E) PPL photomicrograph of radial microborings, concentrated on a distal side of a *Microcodium* grain. F) SEM photomicrograph of strongly acid-etched surface of vacuum-embedded thin section showing resin-filled casts of microborings (f).

G) Detail of F, scale bar 50 µm. H) Resin-embedded microborings with measurements.

Also see Figure A5-4.19 in Appendix A5-4.

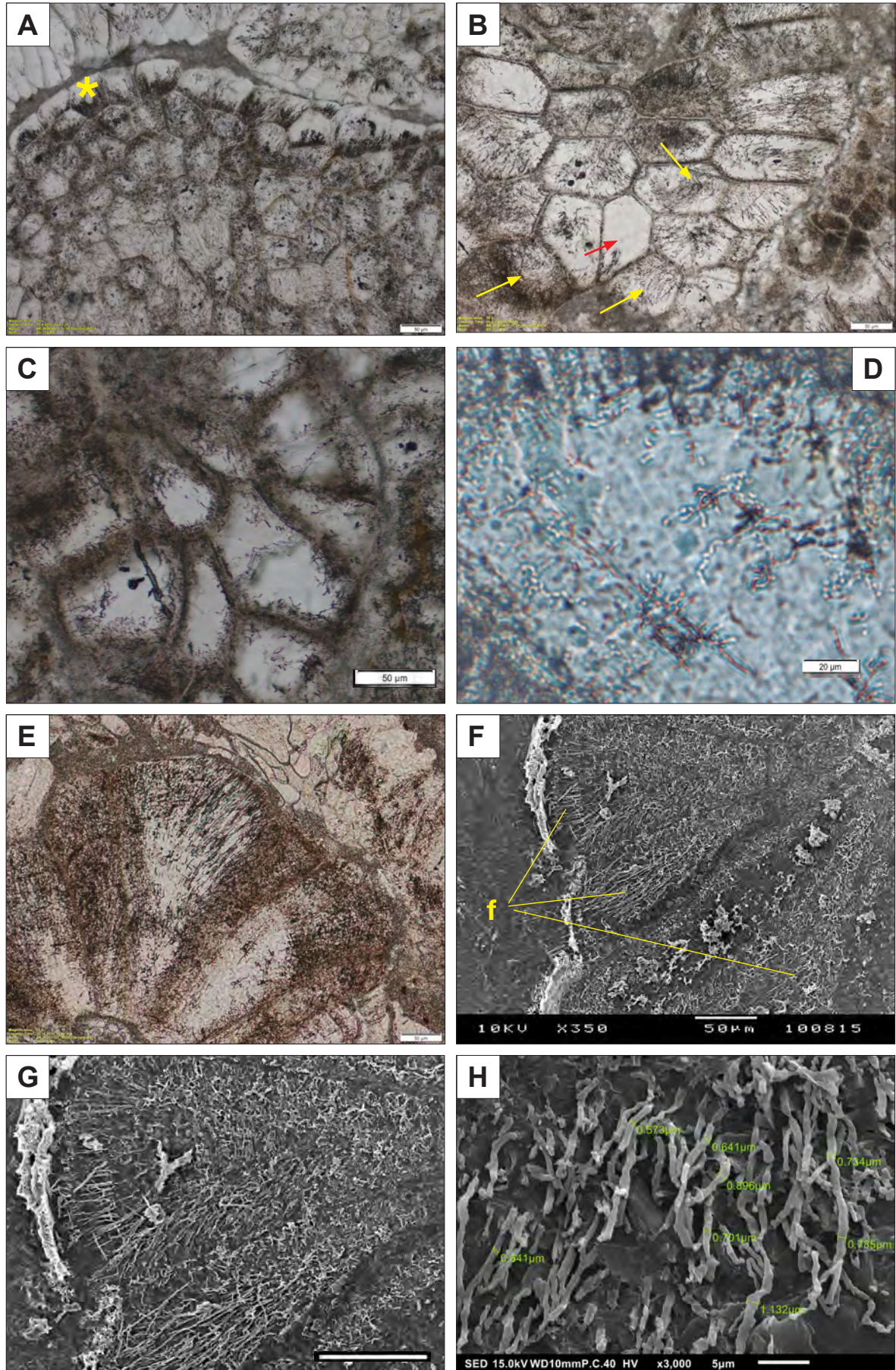
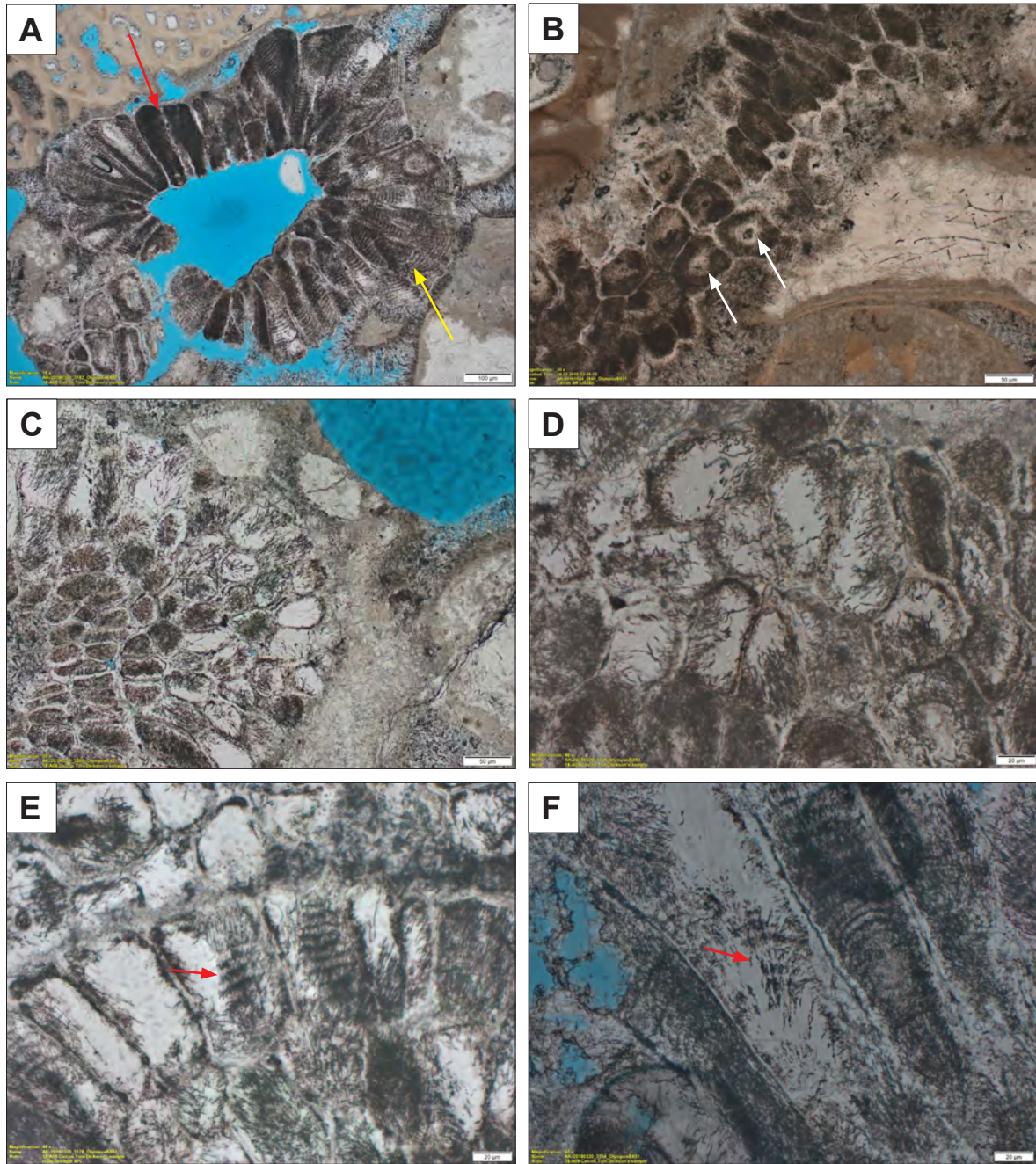


Figure 5.20. Please see caption on the previous page.





**Figure 5.21.** *Microcodium* from a Holocene beachrock of Providenciales, Turks and Caicos Islands. Blue resin-embedded ultrathin section photomicrographs in PPL. **A)** Intensively micritised ('endolithised') *Microcodium* aggregate, partly resulting in totally opaque grains, whereas most grains exhibit distinctive concentric layering (striation) in longitudinal sections, clearly enhanced by microborings. **B)** Strongly altered grains in transverse section. Some grains show apparently less affected internal parts (vacuoles), marked with white arrows. **C)** Transverse section of *Microcodium* aggregate showing different degree of endolithic alteration in individual calcite grains. Cf. Eocene example in Fig. 5.20B. **D)** Same as C at higher magnification. **E)** *Microcodium* grains in oblique/longitudinal section showing clear evidence of enhancement of striate ultrastructural patterns by preferential proliferation of endolithic borings (red arrow) in individual concentric layers within the calcite. **F)** Microborings in a radial/concentric pattern, probably following ultrastructural 'template' of calcite crystals (e.g. following lamellae of certain structure or composition). Also see Figs. A5-4.21 and A5-4.22.



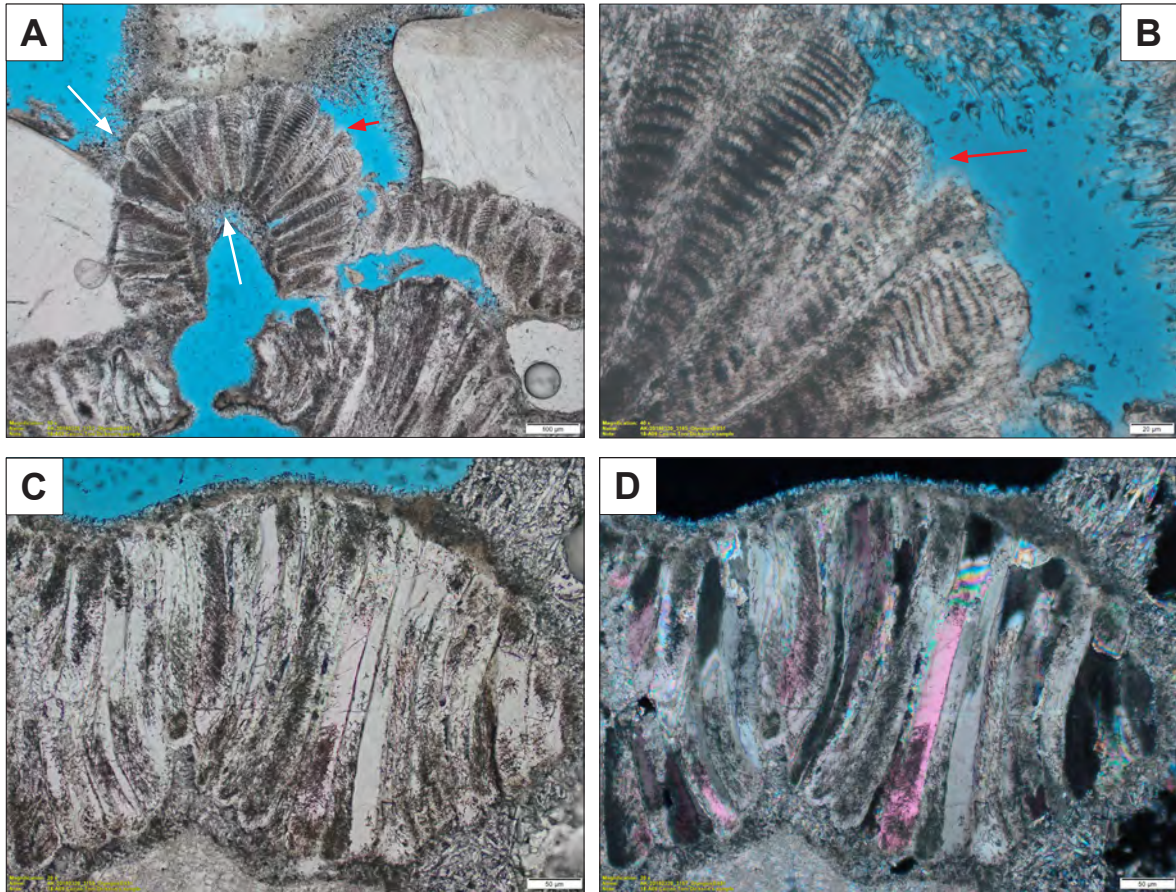


**Figure 5.22.** *Microcodium* from a Holocene beachrock of Providenciales, Turks and Caicos Islands. Blue resin-embedded ultrathin section. A) An aggregate with pronounced striate ultrastructure of elongate grains. White arrows indicate acicular aragonite cement post-dating formation of *Microcodium*. Dissolved outer margin of *Microcodium* elements (red arrow). B) detail of A. C, D) PPL and XPL photomicrographs of an aggregate composed of strongly elongate grains which exhibit different degrees of alteration by endolithic borings but no indication of striate (concentric) fabric. Also see Figs. A5-4.21 and A5-4.22.

### 5.7 Stable isotope analysis of $\delta^{13}\text{C}$ and $\delta^{18}\text{O}$

The analysis of carbon and oxygen stable isotopes has been focused on and limited to well-preserved *Microcodium* samples, visibly devoid of traces of matrix and/or cement (see methods in Section 5.2). The  $\delta^{13}\text{C}$  and  $\delta^{18}\text{O}$  results of a total of 51 measurements are shown in Appendix A5-6, Table A5-6.1. Values of  $\delta^{13}\text{C}$  range from  $-18.9\text{‰}$  to  $-4.7\text{‰}$  with an average of  $-11.0\text{‰}$  ( $\sigma \pm 2.97\text{‰}$ ), whereas  $\delta^{18}\text{O}$  values range from  $-8.0$  to  $-3.1\text{‰}$  and average at  $-5.8\text{‰}$  ( $\sigma \pm 1.26\text{‰}$ ). The  $\delta^{13}\text{C}$  and  $\delta^{18}\text{O}$  values are cross-plotted in Fig. 5.23. Two groups of extreme values correspond to two samples of Paleocene *Microcodium* from the Esplugafreda Formation, Spain ( $\delta^{13}\text{C} = -18.7 \pm 0.2\text{‰}$ ,  $\delta^{18}\text{O} = -7.8 \pm 0.2\text{‰}$ ), and of the Holocene *Microcodium* from beachrock from Caicos ( $\delta^{13}\text{C} = -4.8 \pm 0.15\text{‰}$ ,  $\delta^{18}\text{O} = -3.4 \pm 0.3\text{‰}$ ). Relatively positive values of the latter are most probably due to incorporation of marine cements in pores within the aggregates (see Fig. 5.22A, Fig. A5-4.20E).

Comparison of the  $\delta^{13}\text{C}$  and  $\delta^{18}\text{O}$  values of *Microcodium* with results of intracellularly calcified roots (Chapter 3, Figs. 3.33 and 3.34) and selected published data is shown in Figures 5.25 to 5.28 and discussed in Section 5.8.4.

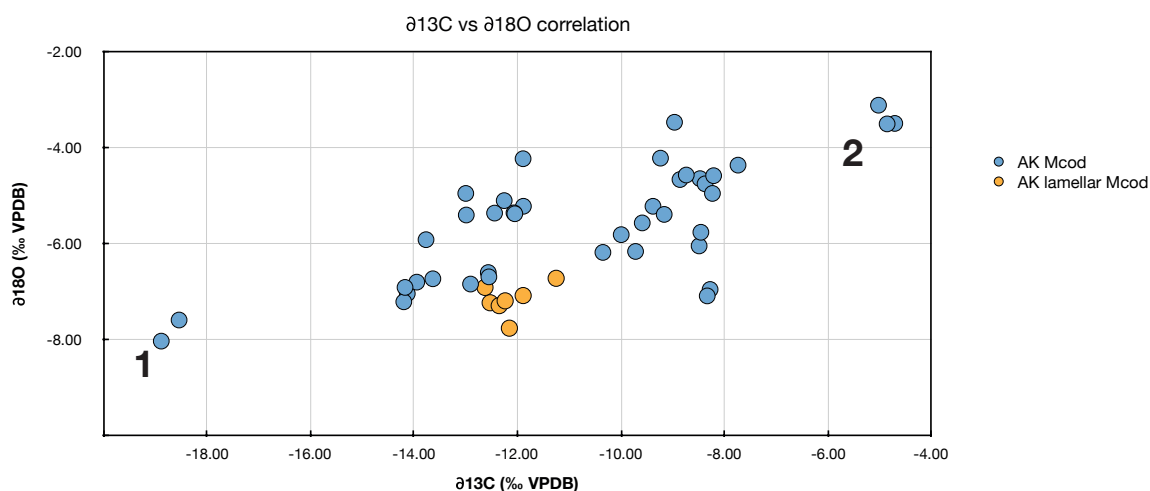


**Figure 5.23.** A cross plot of  $\delta^{13}\text{C}$  and  $\delta^{18}\text{O}$  values of *Microcodium* from this study. Extreme values correspond to (1) two samples of Paleocene material (also see Appendix A5-6, Table A5-6.1) and (2) Holocene *Microcodium* from beachrock from Caicos. Relatively positive values of the latter are most probably due to incorporation of marine cements within the aggregates.

## 5.8 Discussion: Ancient *Microcodium* and modern intracellularly calcified roots: similarities and differences

### 5.8.1 Architectural and morphological traits

As noted in Section 5.3, the atypical forms of *Microcodium*, i.e. Type 3 of Bodergat (1974) or form (b) of Esteban (1974), as well as the material used by Klappa (1978) are simply identical to modern intracellularly calcified roots and, in their original description, do not share fundamental attributes of *Microcodium* described in the previous section (Section 5.3). Kabanov et al. (2008) excluded these atypical varieties from the definition of *Microcodium* (*sensu stricto*): the evidence from this study concurs with that view, particularly since many of the published pre-Quaternary examples are highly ambiguous (e.g. Goldstein 1988). The early Eocene example of the Form (b) of Esteban (1972) appears to be merely a typical *Microcodium* in incipient stages of growth.

In terms of the morphological evidence against the root origin of *Microcodium*, the broad argument of Kabanov et al. (2008) can be summarised in several major points (directly quoted):

- (1) “The aggregate shape is extremely variable” (pp. 86, 96);
- (2) “[*Microcodium*] structures grew at expense of direct corrosion of the host substrate, whereas cortical root cells are separated by the epidermis and the root hair layer”;
- (3) “*Microcodium* is [usually] not associated with larger root remains”, and [its] “relation to small rootlet voids is facultative”;
- (4) Some “aggregates initiated their growth from some tiny, apparently non-root voids or even form a microcrystalline substrate”;
- (5) Individual “solitary grains and clusters of *Microcodium* grains are not always the products of aggregate breakdown and re-sedimentation, but often represent rudimentary stages of *in situ Microcodium*”;
- (6) “*Microcodium* concentrations sometimes occur without root structures at all; the most spectacular example being the thick laminar *Microcodium* in deep karst-associated penetrations”, and “the root-cell affiliation [sic] cannot explain the laminar *Microcodium* masses corroding hard substrates”.
- (7) “Morphology, corrosive contacts with substrates, and isotope signatures of *Microcodium* argue against its affiliation with root cells and/or mycorrhizae and encourages seeking its origin in the saprotrophic fungi or actinobacteria.”



Concerning their statement (1), it could be argued just the opposite: the external shape and the internal arrangement of elements in various *Microcodium* aggregates is relatively constant and uniform. The variability of aggregates, illustrated in figures above (Figs. 5.5-5.10; Fig. A5-4.7), can be elegantly explained with a few geometric principles and a common 'bauplan' equally applicable to all the different forms.

Regarding item (2), the corrosive nature of *Microcodium* ['at expense of the host substrate'] is indeed one of its basic attributes. This is exceptionally well expressed when it corrodes individual (bio)clasts or surfaces (examples in Fig. 5.12). However, regarding their contact with the substrate, there seems to be no difference between intracellularly calcified roots (Figs. 3.xy in Section 3.5x) and *Microcodium*. In both cases, there can be a prominent void, up to several 10 µm wide, between the calcified body and the substrate (Figs. 5.8B, C, 5.10F, 5.12C, Appendix A5-4, Fig. A5-4.10). Rarely, the substrate around *Microcodium* can show tubular structures, corresponding in their size and shape to (non-calcified) root hairs (Figs. 5.12A, Fig. A5-4.10E-F). Importantly, as has been shown in Section 3.4, clusters of modern intracellularly calcified roots are rarely preserved with (organic) epidermis and root hairs. Following precipitation of CaCO<sub>3</sub> in the cortex, calcified roots undergo rapid senescence associated with degradation of organic cell walls and final decay of cortex, epidermis and root hairs. Decomposition of non-lignified thin-walled tissues of fine roots is a rapid process (FitzPatrick 1990; Stolt and Lindbo 2010; Ismail-Meyer et al. 2018; Stoops 2021), particularly in normally oxic, biologically active soils.

When corroding substrates of mixed carbonate-siliciclastic lithologies, both *Microcodium* and intracellularly calcified roots often produce a thin 'decalcified' layer of insoluble material at the contact with the substrate. Such clayey layers are conspicuous in some lamellar *Microcodium* forms (Fig. 5.9B) and are often associated with intracellularly calcified roots growing in fractures of marl (Figs. 3.9, 3.12, 3.16), which appear embedded in an envelope of highly porous clayey-organic material, up to several 10's µm thick. Through complete decomposition of organic matter and soil compaction, such clayey envelopes are typically reduced to very thin, several µm thick films (Fig. 3.8D; Fig. A4-4.1).

A question of association of *Microcodium* with plant roots (3) is of little value if *Microcodium* is considered a form of calcified plant roots. But even if not, it has been repeatedly emphasised in the previous chapters that there is a fundamental functional and morphological difference between coarse roots and fine roots systems. Supposedly similar

mineralisation mechanisms observed in modern fine roots and ancient *Microcodium* do not require any direct involvement of higher order roots and are not related to preservation of coarse roots as “larger root remains” (rhizoliths; see Chapter 2). However, although not obligate (as contrasted with “facultative”), it has been shown that *Microcodium* often is associated with fine rhizoliths, particularly in laminar rhizolite calcretes (Fig. 5.11, Fig. A5-4.08). Furthermore, *Microcodium* structures themselves can exhibit branching patterns – a fundamental characteristic of roots, also considered as one of the principal diagnostic criteria for the recognition of rhizoliths (Appendix A5-3, Fig. A5-3.6).

On a microscale, a clear relationship between *Microcodium* and fine roots has been presented in earlier work (Košir 2004; Appendix A5-2, Figs. A5-2.9, A5-2.10). Further evidence of incipient growth forms of *Microcodium*, associated with roots, is shown in Figures 5.11A-C, where very fine roots with partly preserved, yet clearly visible cellular tissues, include distinct hypertrophied outer cortical cells identical in shape and ultrastructure to archetypal *Microcodium* grains (Fig. 5.16). Analogy between the typical *Microcodium* ultrastructure and the ultrastructure of hypertrophied cells is additionally displayed by distinguishing non-luminescent appearance and structural details seen under CL (Figs. 5.18-5.19), common to both forms.

Arguments (4) and (5) relate to a concept put forward by Kabanov et al. (2008) which considers an individual *Microcodium* grain as a discrete, independent item, not necessarily resulting from disintegration of an aggregate. Intense reworking of *Microcodium* grains often result in structureless deposits (Fig. 5.13, Appendix A5-4, Fig. A5-4.11) although, commonly, preserved fragments of aggregates can still be recognised (Fig. 5.13C). In the studied material, no individual *Microcodium* grains have been encountered, which could not be explained by reworking and incorporation in later stages of calcrete formation (Figs. 5.13D, A5-4.11). Moreover, the studied material has not given any indication of textural relationships of separate *Microcodium* grains, clasts, matrix and cement that would indicate replacive or displacive habit of an individual grain. Eventually, a perception of “solitary” grains and a mycelium-related growth model (Fig. 17 in Kabanov et al. 2008) can hardly provide any reasonable explanation of the polyhedral shape of *Microcodium* grains – if they would have grown in isolation – while on the contrary, a simple model of interactive mineral growth of adjacent cellular elements or compartments (Fig. 5.3) logically results in regular, polygonal aggregate structures.

Conclusions (6) of Kabanov et al. (2008) can similarly be disputed since individual layers of lamellar *Microcodium* forms can evidently show ramose (dendroid) layout (Figs. 5.6D, E), similar to dense ramifying patterns of root systems with high exploitation efficiency, e.g. roots spreading and filling-up planar fissures in soil (Figs. 3.8C, D, 3.10C, D, 3.14A, B, ). Dichotomous appearance of cylindrical and lamellar forms in suitable surfaces have already been noticed by Bodergat (1974; see also Freytet and Plaziat 1982), whereas Morin (1993, p. 51 - 53) illustrated impressive herringbone branching examples of Eocene *Microcodium*, morphologically virtually analogous (and more than functionally homologous?) to modern calcified root systems shown in Figures. 3.10-3.12, and 3.14).

Furthermore, a close similarity between asymmetric *Microcodium* aggregates and the unusual extremely flat (shovel) varieties of intracellularly calcified roots (Sections 3.3 and 3.4) demonstrates a need to perceive (fine) plant roots in a much broader manner than as simple tubular features. Soil horizons, composed entirely of laminae of flat calcified root aggregates (illustrated in Figures. 3.4E, F, 3.6E, F, 3.17) and strikingly resembling thick masses of lamellar *Microcodium* (e.g., Bodergat 1974 Freytet and Plaziat 1982), are hard to explain within the context of a 'common' root system architecture, yet it is beyond doubt that they form through  $\text{CaCO}_3$  mineralisation in an extraordinary type of plant roots, likely representing a specific morphological and physiological strategy to capture resources in calcareous soils (Košir 2004, Appendix A2, section A5-2.7.2; also see Section 3.4).

As quoted in the final point (7), Kabanov et al. (2008) have repeated the fundamental assertion of Freytet and Plaziat (1982) who found the corrosive nature of *Microcodium* incompatible with the activity of roots and proposed that *Microcodium* formed through symbiotic association of several microorganisms (probably fungi and bacteria), in which some might attack calcite and others might synthesize it. Both groups of authors interpreted *Microcodium* as “a soil or subsoil biogenic calcification”, a “corrosive agent” (Freytet et al. 1997), or, as expressed by Freytet and Plaziat (1982), an “iso-volumetric reorganization of calcite under the influence of microorganisms”. However, as it has been shown in Chapter 3, physiology of intracellular calcification in plant roots involves dissolution of carbonate substrate through extrusion of protons and intensive acidification of the rhizosphere. Corrosive activity of plant roots have been known and even experimentally demonstrated already in the nineteenth century (Hinsinger et al. 2003; Hinsinger 2013). Root-induced pH changes in the rhizosphere, associated carbonate rock weathering phenomena, and the



redistribution (reprecipitation) of Ca carbonate inside the root cells are driven by complex interactions, where several chemical processes co-occur (Lucas 2001, Hinsinger et al. 2005), however, they can be entirely explained by physiology of plant nutrient uptake mechanisms, without microbial involvement, e.g. in the form of microbially-induced carbonate mineralisation (Lambers et al. 2009).

The sub-point of (7) on *Microcodium* stable isotope signatures, supposedly inconsistent with intracellularly calcified roots, is discussed in Section 5.8.4 below.

### 5.8.2 Ultrastructure and crystal growth

As discussed in detail in Chapter 3 (Section 3.4), intracellular calcite mineralisation in plant roots consists of a rather complex array of processes – from possible precipitation of amorphous calcium carbonate precursor phases in presence of organic polymer matrices in confined vacuolar spaces, to complex mesocrystal formation and crystal (over)growth by nanoscale particle attachment. Likewise, we can assume that *Microcodium* formed through biomineralisation processes that shared similar physicochemical controls. However, despite of a broad comparability, certain ultrastructural attributes of *Microcodium* grains have not been observed in modern calcified roots cells. Some of these attributes are even mutually incompatible; hence, they can hardly be used for a general (bio)mineralisation model of *Microcodium*.

Radial fibrous ultrastructure, equivalent to fibrous appearance in elongate *Microcodium* grains, has not been encountered in modern CaCO<sub>3</sub> mineralised root cells. Apparent prevalence of fibrous structures in their material led Kabanov et al. (2008) to establish a general formation model of a basic *Microcodium* grain as composed of “slender, radiating prisms”, 1.5–4 µm wide, interlaced with “internal microvoids, represented by numerous microvugs, radial fissures and occasional canals of less than 1 µm, rarely up to 1.5 µm in diameter”. Their interpretation is predominantly based on SEM observation of acid-etched broken surfaces of *Microcodium* aggregates.

Kabanov et al. (2008) described their fibrous ultrastructural patterns as ‘prismatic’ and ‘radial’ and noted that “the radial growth [is] evident from concentric striations within some *Microcodium* grains”. Such terminology is inexact and can even contradict their interpretations. The term ‘prismatic’ [calcite], largely relating to biomineralisation,

has been used for highly organised microstructure patterns typical of, for example, ultrastructure of  $\text{CaCO}_3$  in molluscan skeletons (e.g. Mann 2001). Illustrations of Kabanov et al. (2008) and analysis of *Microcodium* ultrastructure herein do not show any resemblance with prismatic ultrastructure described in the literature. Similarly, the term 'radial' has a very specific meaning in carbonate petrography, denoting fibrous cements with distinctive morphology and optical orientation of subcrystals (e.g. Bathurst 1975), whereas fibrous structures presented by Kabanov et al. (2008) do not show such features.

*Microcodium* grains with large central voids have commonly been reported since the early works of Lucas and Montenat (1967), Esteban (1972) and Bodergat (1974) who named these voids vacuoles. These vacuoles within the calcite grains have been interpreted as secondary, dissolutional features (Freytet and Plaziat 1982), subsequently filled by spar cements. Kabanov et al. (2008) interpreted vacuoles as "areas [of the substrate] that have not been replaced by *Microcodium*" and are "filled with the remnants of the host sediment, commonly micrite or clear spar cement" (quoted from Kabanov et al. 2008, p. 86). Two-layer structure, composed of darker, inclusion-rich outer part and a limpid centre, illustrated in Figures 5.14 and 5.15A-C, has been mentioned in previous studies as a very common feature of *Microcodium* grains (Freytet and Plaziat 1982). Roux (1985) described tortuous series of vacuoles, arranged along the central part of *Microcodium* elements, but unfortunately did not provide any illustration of such features. Photomicrographs of *Microcodium* elements in ultra-thin sections, taken in transmitted light (Figs 5.15E-G) and under SEM in backscattered electron imaging (BEI) mode (Figs. 5.15c, D and A5-4.15), show relatively sharply separated internal lumina (vacuoles) and the outer layers. Cisternoid vacuolar bodies with intricately folded, convoluted shapes, most probably correspond to a membrane-bounded vesicle within a cell.

Whereas apparently structureless and finely striate grains of *Microcodium* are generally non-luminescent (Figs. 5.8E-F) under CL, complex vacuolar grains display distinctive non-luminescent outer part and red to orange luminescent cisternoid internal vacuole (Figs. 5.16 and 5.17). As noted in section 5.3, the same CL pattern can be discerned even in early (incipient) stages of *Microcodium* growth and in transitional forms, i.e. fine roots displaying sporadic individual hypertrophied (inflated) cells (Figs. 5.18 and 5.19).

Large striate *Microcodium* elements partially resemble elongate grains with complex vacuolar features. Individual layers in cisternoid vacuoles are typically ~20  $\mu\text{m}$  thick (Figs.

5.15E-G, 5.17), whereas concentric layers in striate forms are 10-15  $\mu\text{m}$  thick. The main problem with striate forms is that they are strongly altered with endolithic borings (Section 5.6, Figs. 5.20-5.22) obliterating original ultrastructure, which might have been identical to the cisternoid vacuolar fabric observed in well-preserved *Microcodium* grains. In fact, acid etching experiments performed by Morin (1993) have shown that, in certain cases, internal part of striate *Microcodium* grains consisted of seemingly interconnected concentric layers, similar in structure to cisternoid vacuoles described herein. However, due to their small dimensions, these ultrastructural features are mostly below resolution in standard (30  $\mu\text{m}$  thick) thin sections, therefore, a more comprehensive study would require petrographic analysis of precise, possibly double-polished ultrathin sections of well-preserved *Microcodium* material.

The biomineralisation model of *Microcodium* growth of Kabanov et al. (2008, Fig. 17) explained as “driven by fungal or actinobacterial substrate mycelium” has been primarily based on SEM observation of fine structures in acid-etched Moscovian samples (their Fig. 13). In SEM photomicrographs of grains in transverse sections, the authors have discerned radial fibrous crystalline fabric (termed ‘calcite prisms and threads’) associated with “fine internal voids [...], mostly represented by microvugs and radial fissures, with rare canal-like appearances”. Their model implies growth of fibrous crystal elements, several microns wide, along mycelia of “densely spaced hyphae that grew in one direction”. Such a model can hardly provide reasonable explanation of the common, if not prevailing, vacuolar structure of *Microcodium* grains. However, since the fibrous-filamentous structures illustrated by Kabanov et al. (2008) appear to be broadly consistent with material presented in earlier studies (Lucas and Montecat 1967; Bodergat 1974; Morin 1993), it can be presumed that, analogously, correspond to secondary processes, related to microbial endoliths, discussed below.

### ***5.8.3 Filamentous features: Evidence of mycorrhizae or nothing but microendolithic borings?***

Arbuscular mycorrhizal fungi (AMF) and vesicular-arbuscular mycorrhizal (VAM) associations with plant roots are extremely rarely preserved in fossil form. Arbuscular mycorrhizal fungi have not been found associated with  $\text{CaCO}_3$  biomineralised roots or fine roots preserved in palaeosol carbonates. An exception is the report of Sanz-Montero



and Rodriguez-Aranda (2012) on putative endomycorrhizal structures preserved in Miocene palaeosols through intracellular accumulation of dolomite in plant roots. However, the evidence for fossilised mycorrhizae and a mechanism of their preservation through supposedly intracellularly precipitated dolomite is difficult to derive from material presented in their study. Furthermore, the resemblance of their photomicrographs with micromorphology of extant or fossil plant root-VAM associations (e.g. Walker et al. 2018) is very speculative.

Almost all fossil examples of VAM are preserved by exceptional silica permineralisation and are known from classic Lagerstaetten (e.g. the Devonian Rhynie Chert and the Eocene Princeton Chert; Strullu-Derrien and Strullu 2007; Kenrick and Strullu-Derrien 2014; Strullu-Derrien et al. 2014; Taylor et al. 2015; Brundrett and Tedersoo 2018; Brundrett et al. 2018). Rarely, VAM structures occur in carbonate-permineralised peat in coal balls (e.g. Krings et al. 2011).

Preservation potential of VAM structures (arbuscules and hyphal coils) is extremely low because of the short lifespan of vesicular-arbuscular structures (days to weeks; Smith and Read 2008; Walker et al. 2018). Jaillard et al. (1991) have emphasised that mycorrhizal status has never been confirmed in modern intracellularly calcified roots. Moreover, occurrence and preservation of fungal structures, enclosed within the intracellular carbonate deposits, is highly improbable since mineralisation largely takes place inside cortical root cell vacuoles, which are not permeated by mycorrhizal fungi (Vierheilig et al. 2005). On the contrary, in a cell of the root cortex, occupied by a mycorrhizal fungus, there is a many-fold increase in cytoplasm volume while the vacuolar space is strongly reduced (Brundrett 2002).

As shown in Chapter 3, calcite in intracellularly calcified roots from Recent soils is strongly affected by soil microbial processes. Early modification of intracellular calcite include intensive microbial weathering of calcified cells, which appears to occur immediately after or during decomposition of organic parts of calcified roots. An analogy can be drawn between endolithic microborings in modern calcified roots (Sections 3.3 and 3.4, Figs. 3.27-3.30; Fig. A3-4.12) and the fabric observed in exceptionally well-preserved examples of *Microcodium* (Figs. 5.20-5.22). In both cases, tubular microstructures correspond to endolithic microborings that post-date precipitation of calcite. Filamentous fabrics commonly display preferential proliferation of microendolithic organisms in certain portions of crystals. In calcified cells, these seem to be intracrystalline lamellae with

incorporated (occluded) organic matter (fluorescence microscopy image in Figure A3-4.12E).

The filamentous fabric commonly observed in *Microcodium* and intracellularly calcified roots is evidently of microbial origin, however, in modern calcified roots and well-preserved *Microcodium* examples, there is no indication of microbial involvement in carbonate mineralisation processes. On the contrary, all the evidence shows that filamentous fabric formed post-mortem by endolithic boring of calcite grains – both in calcified cells and grains of *Microcodium* – most probably produced by fungi which possess enzymes capable of digesting organic matter, incorporated in calcite (Glaub et al. 2007; Golubic et al. 2005; McLouglin et al. 2007; Wisshak 2012; Taylor et al. 2015). This also accords with earlier observations of Roux (1985) and Jaillard et al. (1991), which showed that the tubular, filamentous fabric, considered by Klappa (1978) as a key evidence for mycorrhizae, resulted from a secondary biotic weathering of *Microcodium* and calcified roots.

#### 5.8.4 The $\delta^{13}\text{C}$ and $\delta^{18}\text{O}$ stable isotope signatures

There is a general lack of published data on the  $\delta^{13}\text{C}$  and  $\delta^{18}\text{O}$  composition of *Microcodium*. With the exception of the comprehensive study of Morin (1993), which included stable isotope analysis data of Bodergat (1974), and the review of Kabanov et al. (2008), there has been no systematic research focused on the stable isotope signatures of *Microcodium*, although some studies have included  $\delta^{13}\text{C}$  and  $\delta^{18}\text{O}$  of *Microcodium* in a broader context of assessing geochemical proxies of pedogenic carbonates, particularly biogenic calcretes (e.g. Brlek and Glumac 2014).

In addition to stable isotope analysis of *Microcodium* and its substrate, Morin (1993) analysed  $\delta^{13}\text{C}$  and  $\delta^{18}\text{O}$  composition of a larger number of Recent intracellularly calcified roots, whereas Kabanov et al. (2008) presented isotope analyses of Palaeozoic *Microcodium* samples and Palaeogene material.

Due to a relatively small number of stable isotope measurements of *Microcodium* performed in the framework of this study (Table A5-6), data of Morin (1993) and Kabanov et al. (2008) have been used to undertake a more comprehensive analysis. Comparison with stable isotope data for intracellularly calcified roots of this study (Chapter 3; Appendix A3-7, Table A3-7.1) has also been supplemented by selected data of Morin (1993) and Luo et al. (2020). Several other recent papers deal with  $\delta^{13}\text{C}$  and  $\delta^{18}\text{O}$  of calcified roots (Sections 3.3

and 3.4 and references therein) but do not provide datasets; therefore they have not been taken into account in this comparative analysis.

Figure 5.24 shows a cross-plot of  $\delta^{13}\text{C}$  and  $\delta^{18}\text{O}$  values of *Microcodium* and a box-and-whisker chart of  $\delta^{13}\text{C}$ , comparing ranges of values of different studies. Except for the anomalously positive values for Moscovian *Microcodium*, there is a strong overlap of ranges of values for individual data subsets (this study, Morin 1993, and Kabanov et al. 2008, respectively).

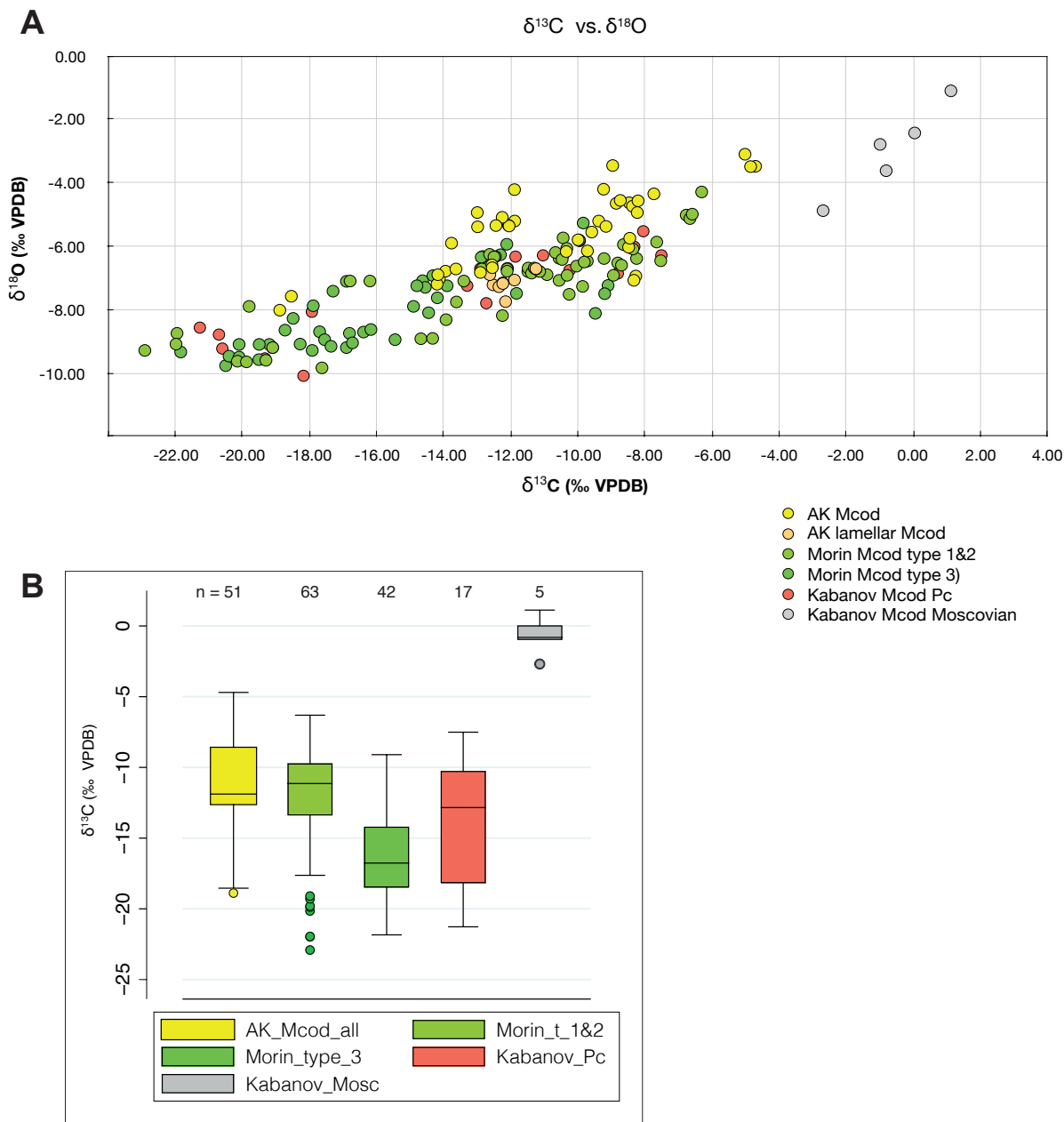
As shown in Figure 5.25, data of Morin (1993) exhibit strong correlation between  $\delta^{13}\text{C}$  and  $\delta^{18}\text{O}$ , whereas data obtained in this study show only weak positive covariation, by excluding extreme values, or moderate to strong correlation for the whole data set.

Figure 5.26 shows a cross-plot of  $\delta^{13}\text{C}$  of *Microcodium* and intracellularly calcified roots (vertical axis) vs.  $\delta^{13}\text{C}$  of the corresponding matrix (substrate). Data of the present study, which include Holocene *Microcodium* from Caicos (Appendix A5-6), selected examples of recent intracellularly calcified roots (iCRs) from the Alicante region (Sella-Finestrat), calcified roots of *Hedysarum coronarium* experimentally grown on a marl substrate (Appendix A3-X), are supplemented by data of Morin (1993) for both *Microcodium* and calcified roots (Appendix A5-7, Table A5-7.1) and their corresponding substrate. Available data does not exhibit any correlation between  $\delta^{13}\text{C}$  stable isotope composition of substrate and  $\delta^{13}\text{C}$  of *Microcodium* and/or calcified roots.

Comparison of  $\delta^{13}\text{C}$  composition of *Microcodium* and modern intracellularly calcified roots is presented in Figure 5.27 and on a cumulative  $\delta^{13}\text{C}$  and  $\delta^{18}\text{O}$  cross-plot (Fig. 5.28). Both plots of  $\delta^{13}\text{C}$  and of  $\delta^{18}\text{O}$  (Fig. 5.27A) show fully overlapping data sets with similar range of values and insignificant difference in central values (mean). Although the difference of the two groups has not been statistically evaluated, graphic presentation of datasets indicate strong similarity of variability and average values of *Microcodium* and intracellularly calcified roots.

The  $\delta^{13}\text{C}$  and  $\delta^{18}\text{O}$  values in Figure 5.28 indicate four groups of outliers (marked 1 to 4), significantly different from the main data cloud. The group Number 1 represents samples of *Microcodium* from Holocene beachrock that appear to be contaminated with remains of (aragonite) cements, characterised by very positive  $\delta^{13}\text{C}$  and  $\delta^{18}\text{O}$  values (from +4 to +5‰ and from -4 to +2.0‰, respectively) (Dickson 2014). Anomalously positive  $\delta^{13}\text{C}$  values of Palaeozoic *Microcodium* (Number 2) have been interpreted by Kabanov et al. (2008) as calcite predominantly precipitated from “carbon derived non-selectively from adjacent





**Figure 5.24.** Results of C and O stable isotope analysis of *Microcodium*.

A) The  $\delta^{13}\text{C}$  and  $\delta^{18}\text{O}$  values of *Microcodium* analysed in this study ('AK Mcod' (=type 1) and 'AK lamellar Mcod') compared with published data of Morin (1993; 'Morin Mcod type 1&2' correspond to cornocob and intermediate forms, 'Morin type 3' = lamellar forms) and Kabanov et al. (2008; 'Mcod Pc' = Paleocene, and 'Mcod-Moscovian' samples). Data from tables in Appendices: Table A5-6.1 (this study), Table A5-7.1 (data of Morin 1993), and Table A5-7-2 (Kabanov et al. 2008).

B) Box & whisker plot of  $\delta^{13}\text{C}$  values for the same data sets (except that the category "AK-Mcod\_all" includes values for both type 1 and type 2 forms). Boxes show the data range between 25<sup>th</sup> and 75<sup>th</sup> percentiles, the middle lines indicates median values, whiskers correspond to 'adjacent' data values (*min* and *max* in normal distribution), while separate circles represent outliers. (n = sample size/number of measurements).

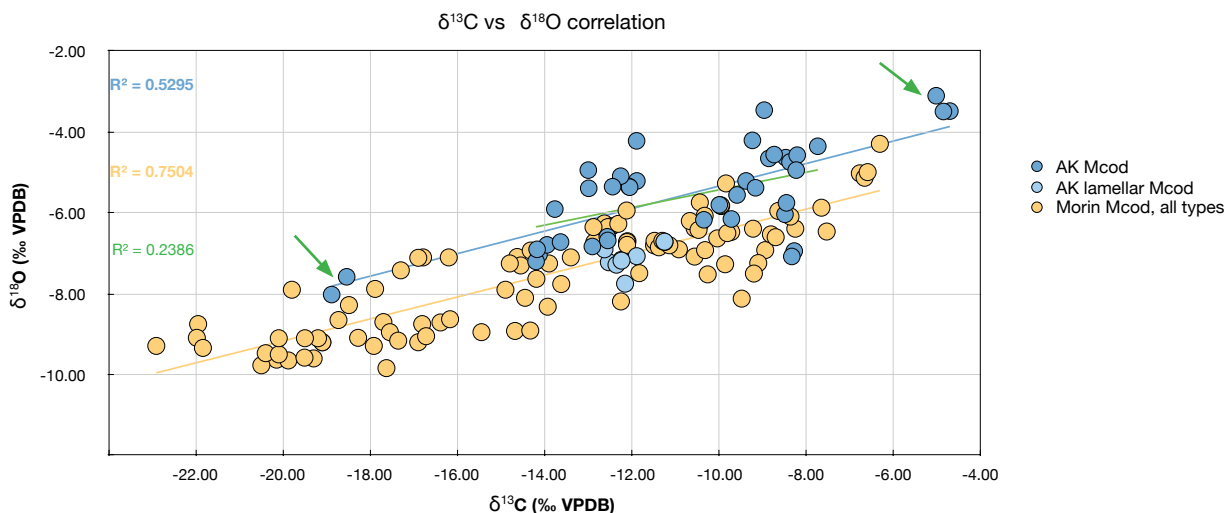


**Figure 5.25.** Correlation of  $\delta^{13}\text{C}$  and  $\delta^{18}\text{O}$  composition of *Microcodium*. Comparison of results of this study (darker and light blue circles and blue linear regression line with the corresponding  $R^2$  value) and data for all types of Morin (1993; beige circles and linear regression line and the corresponding  $R^2$  value). Green line is a linear regression line (with corresponding  $R^2$  value) of data from this study without extreme values (outliers), marked with green arrows.  $R^2$  ( $\sim 0.24$ ) indicates a weak positive correlation between  $\delta^{13}\text{C}$  and  $\delta^{18}\text{O}$  whereas cumulative data of Morin (1993) reveal very strong linear relationship ( $R^2 = 0.75$ ).

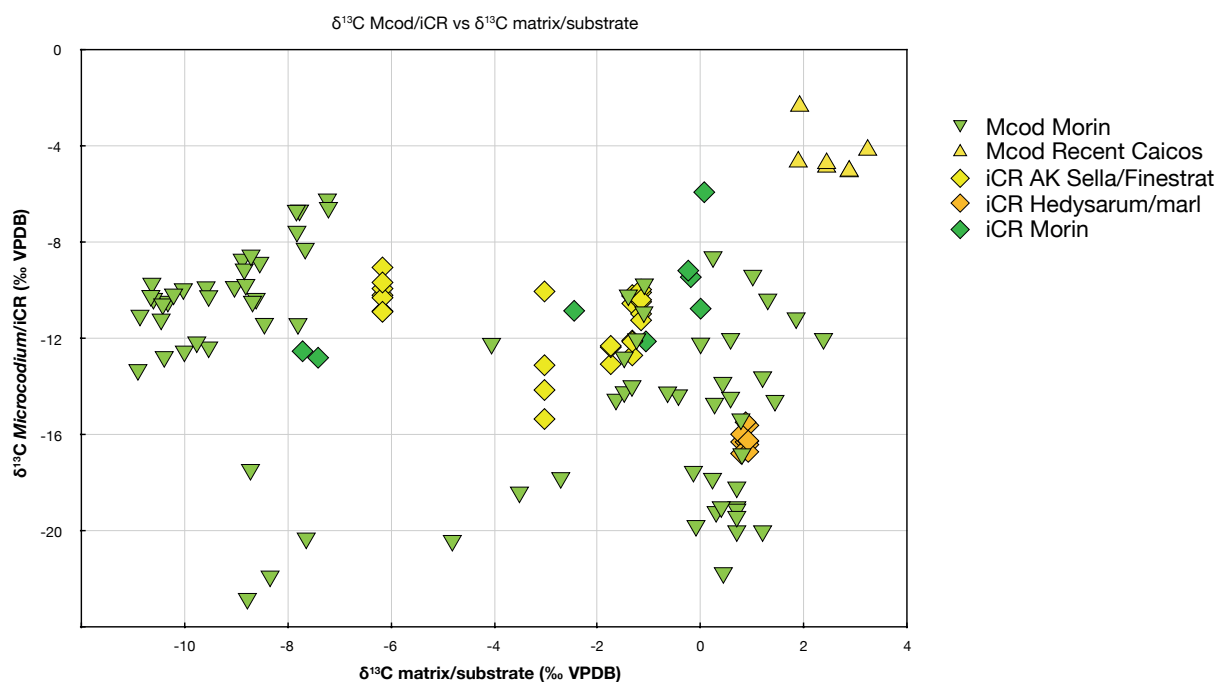


**Figure 5.26.** A cross plot of  $\delta^{13}\text{C}$  of *Microcodium* and intracellularly calcified roots (vertical axis) vs.  $\delta^{13}\text{C}$  of the corresponding matrix (substrate). Data of this study include Holocene *Microcodium* from Caicos (Appendix A5-6), recent intracellularly calcified roots (iCRs) from the Alicante region (Sella-Finestrat) and *Hedysarum coronarium* experimentally grown on marl substrate (Appendix A3-X), and data of Morin (1993) for both *Microcodium* and calcified roots (Appendix A5-7, Table A5-7.1) Available data does not exhibit any correlation between  $\delta^{13}\text{C}$  stable isotope composition of substrate and  $\delta^{13}\text{C}$  of *Microcodium* and/or calcified roots.

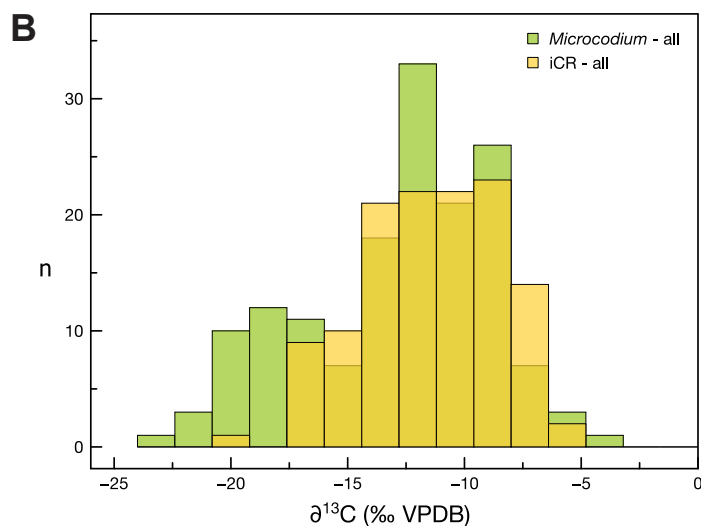
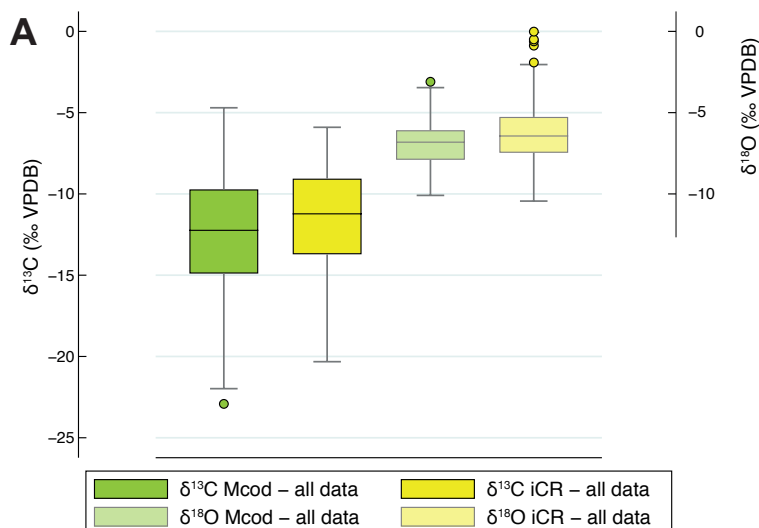


**Figure 5.27.** Comparison of stable isotope composition of *Microcodium* (Mcod) and modern intracellularly calcified roots (iCR).

A) Box & whisker plot of cumulative datasets of *Microcodium* (data of this study, and of Morin 1993, and Palaeogene data of Kabanov et al. 2008) and intracellularly calcified roots (data of this study (Appendix A3-X) and Morin 1993). Left: plots of  $\delta^{13}\text{C}$ , right: plots of  $\delta^{18}\text{O}$ . B) Histogram of  $\delta^{13}\text{C}$  values for *Microcodium* (green) and intracellularly calcified roots (yellow) showing strong overlap of both samples with similar range of values and central values (mean). A bimodal distribution of *Microcodium*  $\delta^{13}\text{C}$  is a consequence of a large subsample of Morin (1993) with strongly negative values (of lamellar forms).

marine limestone and possibly with minor incorporation of soil  $\text{CO}_2$ ”. However, except for this outlier, their range of  $\delta^{13}\text{C}$  and  $\delta^{18}\text{O}$  values for Palaeogene *Microcodium* entirely complies with the compiled dataset from this study and of Morin (1993), yet the authors have not presented explanation for such discrepancy.

Positive and negative  $\delta^{18}\text{O}$  outlier groups for intracellularly calcified roots in Figure 5.28 (3 and 4) have been attributed to climatic factors (Luo et al. 2020) and are discussed in Section 3.5.



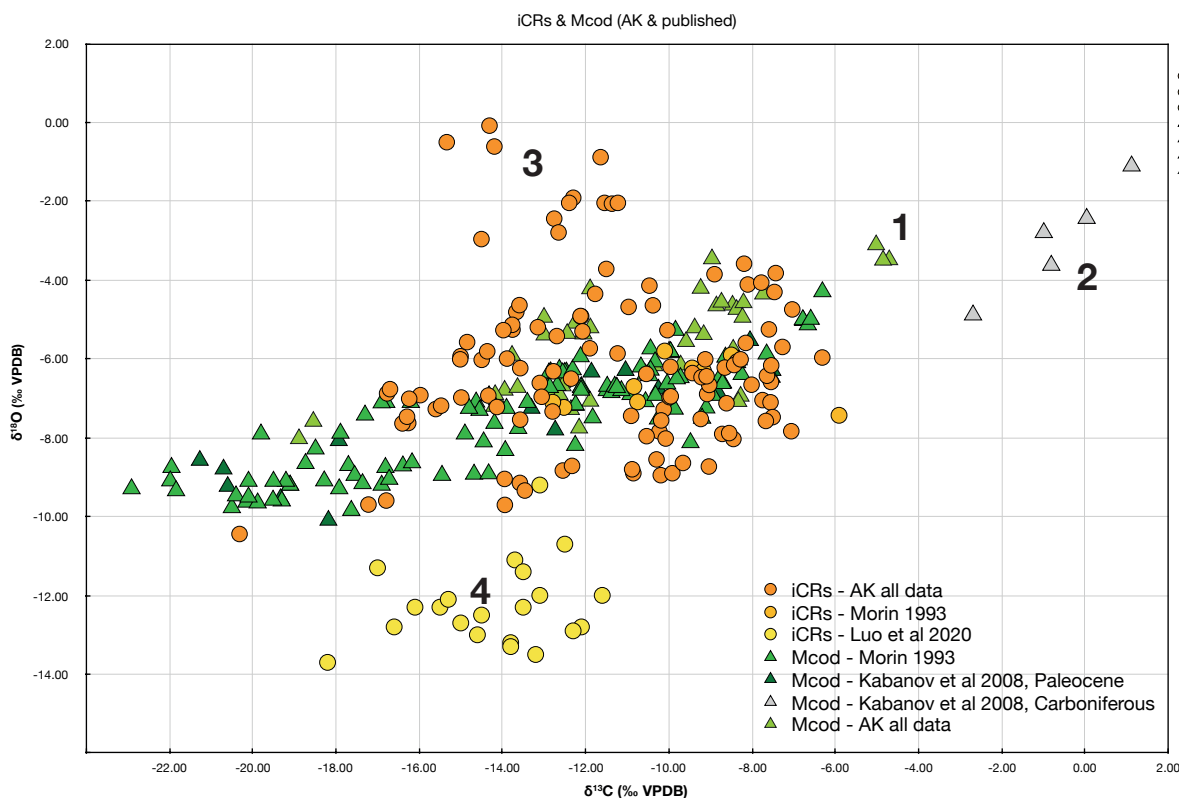


**Figure 5.28.** Cumulative cross-plot of  $\delta^{13}\text{C}$  and  $\delta^{18}\text{O}$  values of *Microcodium* (triangles, 'Mcod') and intracellularly calcified roots (circles, 'iCRs'), used in previous figures, with addition of data of Luo et al. (2020). Separated from the central data cloud are four major groups of outliers, marked with numbers: 1 - anomalously positive (both  $\delta^{13}\text{C}$  and  $\delta^{18}\text{O}$ ) values of Recent *Microcodium* from Caicos; 2 - group of outlier values corresponding to Palaeozoic *Microcodium* of Kabanov et al. (2008); 3 - strongly positive  $\delta^{18}\text{O}$  of iCRs (Chapter 3, this study), and 4 - anomalously negative  $\delta^{18}\text{O}$  of iCRs of Luo et al. (2020; supplementary data <https://doi.org/10.1016/j.jseaes.2020.104515>). See text for discussion.

A likely explanation is that the similarity between stable isotope signatures of *Microcodium* and intracellularly calcified roots is a result of similar (identical) biomineralisation physiology. Intracellular  $\text{CaCO}_3$  accumulation in plant roots presumably enhances production of protons (McConnaughey and Whelan 1997) through exchange of  $\text{Ca}^{2+}$  and  $2\text{H}^+$  using plant-respired  $\text{CO}_2$  (Appendix A5-2, Fig. A5-2.11).

A general diffusion-production (or diffusion-reaction) model of carbon stable isotope composition of modern soil and palaeosol carbonates (Cerling 1984, 1991) is based on specific predictions assuming that in precipitation of pedogenic carbonates isotopic equilibrium between the oxidized carbon species ( $\text{CO}_2$ ,  $\text{H}_2\text{CO}_3$ ,  $\text{HCO}_3^-$ ,  $\text{CO}_3^{2-}$ ,  $\text{CaCO}_3$ ) prevails and that complete isotopic exchange occurs during calcite dissolution-precipitation

in soils. Carbon pathways and isotopic fractionation of root-respired  $\text{CO}_2$  in formation of soil carbonates include: (1) diffusional  $^{13}\text{C}$  enrichment resulting in an end-member 4.4‰ fractionation for soil  $\text{CO}_2$  compared to soil-respired  $\text{CO}_2$ , and (2) temperature-dependent differentiation between soil-respired  $\text{CO}_2$  ( $\delta$ ) and soil carbonate ( $\Delta(\text{CaCO}_3 - \text{respired CO}_2) = \delta^{13}\text{C}_{\text{CaCO}_3} - \delta^{13}\text{C}_\delta$ ) resulting in  $^{13}\text{C}$  enrichment of 13 to 16.5‰ (Cerling 1999).

Pedogenic carbonate forms in soils when the solution becomes supersaturated with calcite (Cerling 1999; Cerling and Quade 1993) and are supposed to precipitate predominantly by physico-chemical mechanisms (evaporation and degassing) and evapotranspiration. Inheritance of carbon from the parent carbonate material of soils during dissolution/precipitation was considered a significant factor resulting in systematic enrichment of  $\delta^{13}\text{C}$  soil carbonates (Salomons and Mook 1986), however, mass balance models (Cerling 1984) have shown that that typical  $\text{CO}_2$  fluxes in soils are several orders of magnitude higher than the rates of soil carbonate formation (Cerling and Quade 1993). According to diffusion-production model, the rates of carbonate precipitation are low whereas the rates of exchange of carbon-bearing dissolved species ( $\text{CO}_2$ ,  $\text{H}_2\text{CO}_3$ ,  $\text{HCO}_3^-$ ,  $\text{CO}_3^{2-}$ ) are high, therefore, it is expected that there is an isotopic equilibrium between the carbon-bearing species. This implies that the isotopic composition of dissolved inorganic carbon is controlled by the soil respired  $\text{CO}_2$  without significant inheritance of carbon from dissolution of soil carbonate (Cerling 1999).

However, as emphasised by Wright and Vanstone (1991), if more direct biologically influenced carbonate precipitation was involved, significantly impoverishment in  $\delta^{13}\text{C}$  could result. The  $\delta^{13}\text{C}$  values of *Microcodium* and intracellularly calcified roots (Fig. 5.28) are to a large extent considerably lower than the theoretical lower limit for soil carbonates ( $\sim -11.5\text{‰}$ ), precipitated in equilibrium with soil respired  $\text{CO}_2$  resulting from  $\text{C}_3$  plant metabolism or organic matter corresponding to  $\text{C}_3$  plant biomass (Appendix A5-8). Biologically induced  $\text{CaCO}_3$  mineralisation processes occur rapidly and are typically associated with pronounced kinetic disequilibrium behavior in both photosynthetic and non-photosynthetic organisms (McConnaughey 1989b). Correlations of  $\delta^{13}\text{C}$  and  $\delta^{18}\text{O}$  values of *Microcodium* (Fig. 5.25) suggest strong non-equilibrium isotope partitioning and probable predominance of kinetic fractionation effects (McConnaughey 1989a, b). Kabanov et al. (2008) interpreted low values and remarkable dispersal of  $\delta^{13}\text{C}$  in their material as consistent with carbon sources from bacterial metabolism. However, as indicated in Figure 5.27B, there is a significant agreement in  $\delta^{13}\text{C}$  values of *Microcodium* and intracellularly

calcified roots, therefore, principles of carbon isotope fractionation (discrimination) mechanisms in plants (O'Leary 1981, Farquhar et al. 1989) discussed in Section 3.X may equally apply for interpretation of  $\delta^{13}\text{C}$  composition and variability of *Microcodium* calcite.

As noted in Chapter 3, the physiology and metabolic pathways involved in intracellular  $\text{CaCO}_3$  precipitation in plant roots remains largely unknown. Most of the studies dealing with calcified roots have interpreted intracellular accumulation of carbonate in root cortical cells with adaptation strategies of plants to cope with excessive calcium and bicarbonate concentrations in the soil solutions (Jaillard et al. 1991; Marschner 1995). In this case, intracellular  $\text{CaCO}_3$  mineralisation can be largely regarded as a sequestration mechanism for excessive Ca concentrations whereas the model of McConnaughey and Whelan (1997) links calcification with increased production of protons as an enhanced strategy of acquiring mineral nutrients, such as phosphorous and iron (Tola et al. 2009), through rhizosphere acidification and, consequentially, dissolution of calcareous substrate.

In comparison with slow precipitation of soil carbonates as predicted in the diffusion-reaction model of Cerling (1984, 1999), which disables significant incorporation of carbon from carbonate substrate (i.e. inheritance of  $^{13}\text{C}$  from dissolution of host-rock carbonate), intracellular  $\text{CaCO}_3$  precipitation is a very rapid process and occur simultaneously with rhizosphere mineral dissolution, however, the extent and mechanisms of possible incorporation of carbon from dissolved carbonate substrate have not been evaluated. However, it can be suggested, in analogy with presumed physiology of  $\text{CaCO}_3$  mineralisation in plant roots (Section 3.4), that  $\delta^{13}\text{C}$  of *Microcodium* carbonate predominantly reflects  $\delta^{13}\text{C}$  of plant respired  $\text{CO}_2$ . Presumably, rapid crystal growth of calcite in cell vacuoles, involving possible amorphous calcium carbonate precursors and phase changes, is primarily controlled by cell metabolism and secondary vacuolar metabolites and is likely associated with strong and variable kinetic disequilibria. Furthermore, multiple phases of crystal growth clearly observed in intracellularly calcified roots (Section 3.3, Figs. 3.23-3.25; Appendix A3-4, Figs. A3-4.06-4.08), probably also occurred in formation of *Microcodium*, as it can be deduced from its complex vacuolar forms, composed of calcite of different petrographic appearance and composition. It may be the case therefore that variability of *Microcodium*  $\delta^{13}\text{C}$  values reflects different ultrastructural varieties, however, available data do not permit any firm conclusions. Another, possibly even the most important factor in variability of  $\delta^{13}\text{C}$  and  $\delta^{18}\text{O}$  composition of *Microcodium*, is diagenetic change of primary carbonate. As illustrated in



Sections 5.6 and 5.8.3, pervasive micritisation of grains is caused by microbial endoliths: carbonate sediments and cements, precipitated in endolithic pores, can substantially change the isotopic composition of primary calcite. Moreover, published stable isotope analyses appear to be largely based on bulk samples (which invariably include non-*Microcodium* carbonate) or do not provide any details about the sampling procedures.

#### 5.8.5 *Can Microcodium be related to special root organs?*

Researchers who found morphology, anatomy and supposed calcification physiology of *Microcodium* incompatible with plant roots, have been apparently comparing it with the anatomy of archetypal, simple roots (Freytet et al. 1997; Kabanov et al. 2008). However, as clearly documented in Chapter 3, modern calcified roots and ancient *Microcodium* share many morphological and structural characteristics, which can be regarded as common functional traits. Moreover, it has been shown that intracellular calcification in modern roots often occur in specialised fine roots with characteristic, non-archetypal and substantially modified anatomy. Interestingly, as evidenced in several published reports and the pilot DNA identification study, presented in Chapter 4, intracellular  $\text{CaCO}_3$  mineralisation appears to be closely related with the Legume plant family, a large group, which is known for production of nodules (involved in N-fixation processes with symbiotic rhizobia), a specialised root organ with its specific internal structure. Similarly, flat asymmetrical (shovel; see Figs. A3-4.03 and 4.04 in Appendix A3-4) roots of calcifying legumes differ considerably from their parent 'normal' roots, which are not involved in biomineralisation. Another type on N-fixing mechanism, the actinorhizal symbiosis, involves association of roots of about 200 species of eight different angiosperm families with filamentous actinobacteria of the genus *Frankia* (Wall 2000; Pawlowski et al. 2012). Both legume-rhizobia and actinorhizal nodules are composed of cells, infected by bacterial threads, often showing considerably expanded infected cells in the nodule cortex (Pawlowski and Sprent 2008). Photomicrographs in Figure A5-4.16 (Appendix A5-4) show striking similarity between infection threads of rhizobia in cells of wild legume *Hedysarum glomeratum* nodules (reproduced from Muresu et al. 2008 and Marchetti et al. 2010) and transverse sections of vacuolar type of *Microcodium* elements with limpid central part and inclusion-rich outer layer. The resemblance includes size and shape of the cells, their internal structure, and also the size of inclusions in *Microcodium* calcite comparable with the size of bacteroid vesicles in nodule cells (Figs. A5-4.16D, E, F).

It is important to note that this comparison is not intended to imply any kind of genetic relationship between the two phenomena, nevertheless it demonstrates that *Microcodium* could be related to specific, yet unknown root forms and potentially involved symbiotic systems.

## 5.9 Summary and conclusions

The aim of this chapter was to show arguments for and against the opposing hypotheses on the origin of *Microcodium* using comparative analysis of *Microcodium* aggregates and intracellularly calcified roots, based on their architecture, morphology, crystal ultrastructure and  $\delta^{13}\text{C}$  and  $\delta^{18}\text{O}$  stable isotope signatures. Results support early studies, which interpreted *Microcodium* as a product of root calcification.

*Microcodium* and calcified roots share many architectural and morphological traits, such as the spatial configuration, branching patterns, size of aggregates and relationships with the substrate. Calcification in plant roots, associated with extrusion of protons and intensive corrosion of carbonate substrate, provides a strategy and a mechanism that can analogously explain formation of *Microcodium* and its corrosive aspect. Supposed incompatibility of the asymmetric forms of *Microcodium* with plant roots has been disproved by discovery of similar forms of modern calcified roots (Chapter 3).

This study has provided further examples of transitional forms, intermediate between non-calcified fine roots and typical *Microcodium* aggregates, supplemented by ultrastructural details observed under cathodoluminescence.

Although *Microcodium* grains and calcified cells share basic morphological and ultrastructural characteristics, particular fabric does not occur in both forms. Exclusive to *Microcodium* is an extraordinary, double-layered vacuolar structure, unknown in modern calcified roots, and often dark, inclusion-rich and microporous calcite, forming its grains. *Microcodium* grains often also exhibit concentric internal fabric (or similar vacuolar structure), which has not been encountered in calcified roots.

Calcite in both *Microcodium* and calcified root cells is often altered by endolithic microborings. This study has shown that the filamentous fabric, reported and differently interpreted in previous studies as involved in precipitation of calcite, post-dates biomineralisation and corresponds to microbial alteration of calcite.

Comparative analysis of  $\delta^{13}\text{C}$  and  $\delta^{18}\text{O}$  stable isotope signatures has not shown

significant difference between *Microcodium* and intracellularly calcified roots: on the contrary, analysed datasets indicate strong similarity of variability and average values.

Archetypal forms, found in Holocene beachrock deposits of Caicos, shows that future field research could reveal 'extant' *Microcodium*. Atypical asymmetric forms of modern calcified roots indicate that *Microcodium* could similarly correspond to specific, yet unknown root forms.



## ***Chapter 6: General conclusions and prospects***

One of the primary aims of the thesis is to emphasise that current concepts of rhizosphere and fine plant roots hold important implications for the interpretation of biogeochemical processes in calcretes and rhizoliths. The classical works, mostly published during the last decades of the previous century, have provided a strong conceptual framework for the use of root-related calcretes for the reconstruction of past ecosystems and environments, interpretation of sedimentary successions, including their tectonic, climatic and stratigraphic evolution. An updated review of rhizoliths and root-related calcretes should re-focus from morphology, facies, classification and petrographic recognition criteria, which have been central to the classic sedimentological and palaeontological approach, on metabolism and biomineralisation pathways in accumulation of soil carbonates in root systems, that is towards inherent subjects of geobiology. As stressed in many parts of the thesis, biogeochemical processes driven by plant roots and associated rhizosphere microbial communities are limited to fine root systems, which should form a central point of a revised conceptual re-evaluation of biomineralisation in modern soils and related phenomena in the sedimentary record.

A case study on laminar rhizolites from the Bahamas has shown that archetypal laminar rhizolite calcretes and finely laminated calcrete crusts may contain exceptionally preserved remains of fine root tissues. The presence of unambiguous anatomic details of fine roots is a very good indicator of plant roots as a major (f)actor in soil carbonate accumulation, however, petrographic analysis has also demonstrated that precipitated carbonate cannot be unequivocally attributed to root-induced mineralisation or is not necessarily connected with the rhizosphere processes, but most probably largely results from microbial decay-related accumulation of fibrous microcrystalline carbonate forms. The study has been based on 'fossil' material from outcrops where calcretes do not accumulate any more. However, a further research could focus on recognition of modern soil microenvironments, for example karstic soil pockets with growing plants and their root systems, presumably associated with accumulation of calcium carbonate within the fine root mats. The

Bahamian archipelago and other Caribbean island may provide an ideal regional setting because of a pronounced climatic gradient from a relatively humid climatic regime on the northern islands to the arid climate in the southern islands. Other prospective areas include the Mediterranean part of Spain with its thoroughly studied classical calcrete localities, as well as young carbonates in other parts of the Mediterranean basin.

The research, performed on original and previously unexplored material from the Mediterranean environments of the Alicante Province in southeastern Spain has revealed immense amounts of intracellularly calcified roots (iCRs) in modern calcareous soils as well as in Quaternary palaeosols. Architectural and morphological analysis of intracellularly calcified root systems revealed two morphological groups: symmetrical aggregates and asymmetrical, extremely flattened intracellularly calcified root forms with peripherally placed vascular cylinders. Such aberrant morphologies of calcified roots have not been previously reported in the literature. Detailed petrographic and micromorphological analysis of intracellularly calcified roots, integrated with mineralogical, elemental and stable isotope analysis of carbon and oxygen, has provided further evidence for close similarity of calcified roots with classical *Microcodium*. Architectural, morphological and physiological traits of intracellularly calcified roots and their stable isotope geochemical signatures are in agreement with the hypothesis that intracellular  $\text{CaCO}_3$  biomineralisation, coupled with proton extrusion, represents an efficient nutrient-acquiring mechanism and an adaptational strategy to nutrient-poor, highly calcareous soils.

A test study of DNA barcoding performed on twenty-one samples of organic tissues, associated with iCRs, produced eight positive results. Most of the obtained sequences showed very good similarity (identity) with published sequences of the IRL clade (inverted repeat-lacking clade), a monophyletic group of Fabaceae (legumes). Three samples were reliably identified on a genus level: two samples as *Onobrychis* sp. and one as *Ononis* sp. Results of the study have provided a very good framework for a future systematic research on iCRs from natural habitats, including their DNA taxonomy and experimental investigation of intracellular  $\text{CaCO}_3$  mineralisation in plant roots. Anticipated future research will be focused on systematic comparative DNA barcoding analysis of aboveground plants and their matching with DNA extracted from organic remains of calcified roots from the corresponding substrates. Another project should focus on experimental growth and biomineralisation in controlled, pot-grown plants of different

representatives of the Hedysareae tribe, which have been confirmed to produce intracellular calcium carbonate, growing in different substrates. A pilot experiment has already been set up using *Hedysarum coronarium* plants, growing in a natural marly limestone substrate and mixtures of organic soil with different Ca minerals, including calcite, portlandite ( $\text{Ca}(\text{OH})_2$ ), gypsum ( $\text{CaSO}_4 \cdot 2\text{H}_2\text{O}$ ), and wollastonite ( $\text{CaSiO}_3$ ), to estimate the potential of intracellular calcification processes in carbon sequestration.

The aim of the final chapter has been to show evidence for and against the arguments of the contrasting hypotheses about the origin of *Microcodium*, using comparative analysis of fossil *Microcodium* aggregates and modern intracellularly calcified roots, based on their architecture, morphology, crystal ultrastructure and  $\delta^{13}\text{C}$  and  $\delta^{18}\text{O}$  stable isotope signatures. Results support early studies, which interpreted *Microcodium* as a product of root  $\text{CaCO}_3$  biomineralisation. *Microcodium* and intracellularly calcified roots share many architectural and morphological traits, such as the spatial configuration, branching patterns, size of aggregates and relationships with the substrate. Calcification in plant roots, supposedly associated with extrusion of protons and intensive corrosion of carbonate substrate, provides a strategy and a mechanism that can analogously explain formation of *Microcodium* and its corrosive aspect. Supposed incompatibility of the asymmetric forms of *Microcodium* with plant roots has been disproved by discovery of similar forms of modern calcified roots. This study has provided further examples of transitional forms, intermediate between non-calcified fine roots and typical *Microcodium* aggregates, supplemented by ultrastructural details observed under cathodoluminescence.

Archetypal *Microcodium* forms, found in Holocene beachrock deposits of Caicos and in Holocene aeolianites of San Salvador, indicate that future, systematic field research of modern soils on young carbonates could potentially reveal 'extant' *Microcodium* forms. Atypical asymmetric forms of modern calcified roots have been reported only in several papers dealing with specific group of legume plants, whereas such forms of fine roots are virtually unknown in other groups of modern plants and in the fossil record. Similarly, asymmetric ancient *Microcodium* could correspond to a specific, yet unknown form of roots or special root organs, with architectural, morphological and physiological traits comparable to 'aberant' modern intracellularly calcified roots.



## References

- Abegg FE, Loope DB, Harris PM (2001) Carbonate Eolianites—Depositional Models and Diagenesis. In: Abegg FER, Loope DB, Harris PMM (eds) *Modern and Ancient Carbonate Eolianites: Sedimentology, Sequence Stratigraphy, and Diagenesis*. Special Publication 71. SEPM Society for Sedimentary Geology, Tulsa, pp 17-30. doi: 10.2110/pec.01.71.0017
- Adatte T, Khozyem H, Spangenberg JE, Samant B, Keller G (2014) Response of terrestrial environment to the Paleocene-Eocene Thermal Maximum (PETM), new insights from India and NE Spain. *Rendiconti Online della Società Geologica Italiana* 31:5-6. doi: /10.3301/ROL.2014.17
- Addadi L, Raz S, Weiner S (2003) Taking advantage of disorder: Amorphous calcium carbonate and its roles in biomineralization. *Advanced Materials* 15:959-970. doi: 10.1002/adma.200300381
- Adler PB, De Ros LF, Mansur KL, Ferrari AL, Fernandes LA, Sial AN (2021) Calcretes and travertines from the Palaeocene Itaborai Basin as evidence of the early evolution of the Southeastern Brazil Continental Rift. *Sedimentology* 68:477-511. doi: 10.1111/sed.12788
- AEMET (2015) Avance climatológico mensual (enero 2014-diciembre 2015). Resúmenes climatológicos. Comunitat Valenciana. Ministerio para la Transición Ecológica y el Reto Demográfico, Agencia Estatal de Meteorología. [http://www.aemet.es/es/serviciosclimaticos/vigilancia\\_clima/resumenes](http://www.aemet.es/es/serviciosclimaticos/vigilancia_clima/resumenes)
- Agostino M (2013) Introduction to the BLAST Suite and BLASTN. In: Agostino M (ed) *Practical Bioinformatics*. Garland Science, Boca Raton pp 47-71. doi: doi.org/10.1201/9780429258268
- Ahlborn M, Stemmen A L (2015) Depositional evolution of the Upper Carboniferous - Lower Permian Wordiekammen carbonate platform, Nordfjorden High, central Spitsbergen, Arctic Norway. *Norwegian Journal of Geology* 95:91-126
- Aizenberg J, Lambert G, Weiner S, Addadi L (2002) Factors involved in the formation of amorphous and crystalline calcium carbonate: A study of an ascidian skeleton. *Journal of the American Chemical Society* 124:32-39. doi: 10.1021/ja016990l
- Akkiraz MS, Akgun F, Orcen S (2011) Stratigraphy and palaeoenvironment of the Lower-”middle” Oligocene units in the northern part of the Western Taurides (Incesu area, Isparta, Turkey). *Journal of Asian Earth Sciences* 40:452-474. doi: 10.1016/j.jseaes.2010.09.010
- Alcaraz F (2017) The Arid Southeast. In: Loidi J (ed) *The vegetation of the Iberian Peninsula*. Springer International Publishing AG, Berlin, pp 249-274. doi: 10.1007/978-3-319-54867-8\_5
- Alonso-Zarza AM (1999) Initial stages of laminar calcrete formation by roots: examples from the Neogene of central Spain. *Sedimentary Geology* 126:177-191
- Alonso-Zarza AM (2003) Palaeoenvironmental significance of palustrine carbonates and calcretes in the geological record. *Earth-Science Reviews* 60:261-298. doi: 10.1016/s0012-8252(02)00106-x
- Alonso-Zarza AM (2018) Study of a modern calcrete forming in Guadalajara, Central Spain: An analogue for ancient root calcretes. *Sedimentary Geology* 373:180-190. doi: 10.1016/j.sedgeo.2018.06.006
- Alonso-Zarza AM, Arenas C (2004) Cenozoic calcretes from the Teruel Graben, Spain: microstructure, stable isotope geochemistry and environmental significance. *Sedimentary Geology* 167:91-108. doi: 10.1016/j.sedgeo.2004.02.001

- Alonso-Zarza AM, Genise JF, Cabrera MC, Mangas J, Martin-Perez A, Valdeolmillos A, Dorado-Valino M (2008) Megarhizoliths in Pleistocene aeolian deposits from Gran Canaria (Spain): Ichnological and palaeoenvironmental significance. *Palaeogeography Palaeoclimatology Palaeoecology* 265:39-51. doi: 10.1016/j.palaeo.2008.04.020
- Alonso-Zarza AM, Jones B (2007) Root calcrete formation on Quaternary karstic surfaces of Grand Cayman. *Geologica Acta* 5:77-88. doi: doi.org/10.1344/105.000000311
- Alonso-Zarza AM, Melendez A, Martin-Garcia R, Herrero MJ, Martin-Perez A (2012) Discriminating between tectonism and climate signatures in palustrine deposits: Lessons from the Miocene of the Teruel Graben, NE Spain. *Earth-Science Reviews* 113:141-160. doi: 10.1016/j.earscirev.2012.03.011
- Alonso-Zarza AM, Sanz ME, Calvo JP, Estevez P (1998) Calcified root cells in Miocene pedogenic carbonates of the Madrid Basin: evidence for the origin of *Microcodium* b. *Sedimentary Geology* 116:81-97. doi: 10.1016/s0037-0738(97)00077-8
- Alonso-Zarza AM, Wright VP (2010a) Calcretes. In: Alonso-Zarza AM, Tanner LH (eds) *Carbonates in Continental Settings*, vol 61, pp 225-267. doi: 10.1016/S0070-4571(09)06105-6
- Alonso-Zarza AM, Wright VP (2010b) Palustrine carbonates. In: Alonso-Zarza AM, Tanner LH (eds) *Carbonates in Continental Settings*, vol 61, pp 103-131. doi: 10.1016/S0070-4571(09)06102-0
- Altschul SF, Gish W, Miller W, Myers EW, Lipman DJ (1990) Basic Local Alignment Search Tool. *Journal of Molecular Biology* 215:403-410. doi: 10.1016/s0022-2836(05)80360-2
- Amundson R (2005) Soil Formation. In: J.I. D (ed) *Surface and Ground Water, Weathering, and Soils. Treatise on Geochemistry, Second Edition, Volume 5*, pp 1-35
- Amundson R, Richter DD, Humphreys GS, Jobbagy EG, Gaillardet J (2007) Coupling between biota and earth materials in the Critical Zone. *Elements* 3:327-332. doi: 10.2113/gselements.3.5.327
- Anderson KD, George AD (2020) Evolution of Pennsylvanian inner-platform phylloid algal reef mounds, Pha Nok Khao platform, northeastern Thailand. *Palaeogeography Palaeoclimatology Palaeoecology* 537. doi: 10.1016/j.palaeo.2019.109380
- Antoshkina AI (2006) Palaeoenvironmental implications of *Palaeomicrocodium* in Upper Devonian microbial mounds of the Chernyshev Swell, Timan-northern Ural region. *Facies* 52:611-625. doi: 10.1007/s10347-006-0083-z
- Antoshkina AI (2014) *Palaeomicrocodium*: A new view on its origin. *Paleontological Journal* 48:353-368. doi: 10.1134/s0031030114040030
- Aratman C, Ozkul M, Swennen R, Hollis C, Marques Erthal M, Claes H, Mohammadi Z (2020) The giant Quaternary Ballik travertine system in the Denizli Basin (SW Turkey): A palaeoenvironmental analysis. *Quaternaire* 31:91-116
- Arnott HJ (1982) Three systems of biomineralization in plants with comments on the associated organic matrix. In: Nancollas GH (ed) *Biological Mineralization and Demineralization, Dahlem Konferenzen 1982*. Springer-Verlag, Berlin, Heidelberg, New York, pp 199-218
- Arnott HJ (1995) Calcium oxalate in fungi. In: Khan SR (ed) *Calcium oxalate in biological systems*. CRC Press, Boca Raton, Fla. ; London, pp 73-111
- Arp G (1995) Lacustrine bioherms, spring mounds, and marginal carbonates of the Ries-impact-crater (Miocene, southern Germany). *Facies* 33:35-89. doi: 10.1007/bf02537444
- Arribas ME, Arribas J (2007) Interpreting carbonate particles in modern continental sands: An example from fluvial sands (Iberian Range, Spain). In: Arribas J, Critelli S, Johnsson MJ (eds)

- Sedimentary Provenance and Petrogenesis: Perspectives from Petrography and Geochemistry, pp 167-179. doi: 10.1130/2006.2420(11)
- Artieda O, Herrero J (2003) Pedogenesis in lutitic Cr horizons of gypsiferous soils. *Soil Science Society of America Journal* 67:1496-1506. doi: 10.2136/sssaj2003.1496
- Aurell M, McNeill DF, Guyomard T, Kindler P (1995) Pleistocene shallowing-upward sequences in New Providence, Bahamas: Signature of high-frequency sea-level fluctuations in shallow carbonate platforms. *Journal of Sedimentary Research Section B-Stratigraphy and Global Studies* 65:170-182
- Austin AT, Yahdjian L, Stark JM, Belnap J, Porporato A, Norton U, Ravetta DA, Schaeffer SM (2004) Water pulses and biogeochemical cycles in arid and semiarid ecosystems. *Oecologia* 141:221-235. doi: 10.1007/s00442-004-1519-1
- Azeredo AC, Wright VP, Mendonca J, Cabral MC, Duarte LV (2015) Deciphering the history of hydrologic and climatic changes on carbonate lowstand surfaces: calcrete and organic-matter/evaporite facies association on a palimpsest Middle Jurassic landscape from Portugal. *Sedimentary Geology* 323:66-91. doi: 10.1016/j.sedgeo.2015.04.012
- Baceta JI, Pujalte V, Wright VP, Schmitz B (2011) Carbonate platform models, sea-level changes and extreme climatic events during the Paleocene-early Eocene greenhouse interval: abasin-platform-coastal plain transect across the southern Pyrenean basin. In: Arenas C, Pomar L, Colombo F (eds) *Pree-Meeting Field trips Guidebook, 28th IAS Meeting, Zaragoza. Geo-Guías 7*. Sociedad Geológica de España, Zaragoza, pp 151-198
- Baceta JI, Wright VP, Beavington-Penney SJ, Pujalte V (2007) Palaeohydrogeological control of palaeokarst macro-porosity genesis during a major sea-level lowstand: Danian of the Urbasa-Andia plateau, Navarra, North Spain. *Sedimentary Geology* 199:141-169. doi: 10.1016/j.sedgeo.2007.01.024
- Baceta JI, Wright VP, Pujalte V (2001) Palaeo-mixing zone karst features from Palaeocene carbonates of north Spain: criteria for recognizing a potentially widespread but rarely documented diagenetic system. *Sedimentary Geology* 139:205-216. doi: 10.1016/s0037-0738(00)00166-4
- Bain RJ, Foos AM (1993) Carbonate microfabrics related to subaerial exposure and paleosol formation. In: Rezak R, Lavoie DL (eds) *Carbonate Microfabrics*. Springer-Verlag, New York, pp 17-27. doi: 10.1007/978-1-4684-9421-1\_2
- Banwart SA, Nikolaidis NP, Zhu YG, Peacock CL, Sparks DL (2019) Soil Functions: Connecting Earth's Critical Zone. *Annual Review of Earth and Planetary Sciences, Vol 47* 47:333-359. doi: 10.1146/annurev-earth-063016-020544
- Bao HM, Koch PL, Hepple RP (1998) Hematite and calcite coatings on fossil vertebrates. *Journal of Sedimentary Research* 68:727-738. doi: 10.2110/jsr.68.727
- Bao Y, Aggarwal P, Robbins NE, Sturrock CJ, Thompson MC, Tan HQ, Tham C, Duan LN, Rodriguez PL, Vernoux T, Mooney SJ, Bennett MJ, Dinneny JR (2014) Plant roots use a patterning mechanism to position lateral root branches toward available water. *Proceedings of the National Academy of Sciences of the United States of America* 111:9319-9324. doi: 10.1073/pnas.1400966111
- Barbéro M, Loisel R, Quézel P, Richardson DM, Romane F (1998) Pines of the Mediterranean Basin. In: Richardson DM (ed) *Ecology and Biogeography of Pinus*. Cambridge University Press, Cambridge, pp 153-170



- Barbin V (2000) Cathodoluminescence of carbonate shells: biochemical vs diagenetic process. In: Pagel M, Barbin V, Blanc P, Ohnenstetter D (eds) *Cathodoluminescence in Geosciences*. Springer, Berlin, Heidelberg, pp 303-329. doi: DOI: 10.1007/978-3-662-04086-7\_12
- Barbour MG, Burk JH, Pitts WD, Gilliam FS, Schwartz MW (1999) *Terrestrial plant ecology*, 3rd Edition edn. Addison Wesley Longman Inc., Menlo Park, California, 650 pp
- Bardgett RD, Mommer L, De Vries FT (2014) Going underground: root traits as drivers of ecosystem processes. *Trends in Ecology & Evolution* 29:692-699. doi: 10.1016/j.tree.2014.10.006
- Barta G (2011) Secondary carbonates in loess-paleosol sequences: a general review. *Central European Journal of Geosciences* 3:129-146. doi: 10.2478/s13533-011-0013-7
- Barta G (2014) Paleoenvironmental reconstruction based on the morphology and distribution of secondary carbonates of the loess-paleosol sequence at Sutto, Hungary. *Quaternary International* 319:64-75. doi: 10.1016/j.quaint.2013.08.019
- Batezelli A, Ladeira FSB, do Nascimento DL, Da Silva ML (2019) Facies and palaeosol analysis in a progradational distributive fluvial system from the Campanian-Maastrichtian Bauru Group, Brazil. *Sedimentology* 66:699-735. doi: 10.1111/sed.12507
- Bathurst RGC (1966) Boring Algae, Micrite Envelope and Lithification of Molluscan Biosparites. *Geological Journal* 5:15-32. doi: <http://dx.doi.org/10.1002/gj.3350050104>
- Bathurst RGC (1975) *Carbonate sediments and their diagenesis*. Elsevier, Amsterdam 658 pp
- Bauer P, Elbaum R, Weiss I (2011) Calcium and silicon mineralization in land plants: transport, structure and function. *Plant Science* 180:746-756. doi: 10.1016/j.plantsci.2011.01.019
- Becze Deak J, Langohr R, Verrecchia EP (1997) Small scale secondary CaCO<sub>3</sub> accumulations in selected sections of the European loess belt. Morphological forms and potential for paleoenvironmental reconstruction. *Geoderma* 76:221-252
- Berling DJ, Berner RA (2005) Feedbacks and the coevolution of plants and atmospheric CO<sub>2</sub>. *Proceedings of the National Academy of Sciences of the United States of America* 102:1302-1305
- Berling DJ, Butterfield NJ (2012) Plants and animals as geobiological agents. In: Knoll AH, Canfield DE, Konhauser KO (eds) *Fundamentals of geobiology*. Wiley-Blackwell, Oxford, pp 188-204. doi: 10.1002/9781118280874.ch11
- Benard P, Zarebanadkouki M, Brax M, Kaltenbach R, Jerjen I, Marone F, Couradeau E, Felde V, Kaestner A, Carminati A (2019) Microhydrological Niches in Soils: How Mucilage and EPS Alter the Biophysical Properties of the Rhizosphere and Other Biological Hotspots. *Vadose Zone Journal* 18. doi: 10.2136/vzj2018.12.0211
- Benard P, Zarebanadkouki M, Hedwig C, Holz M, Ahmed MA, Carminati A (2018) Pore-Scale Distribution of Mucilage Affecting Water Repellency in the Rhizosphere. *Vadose Zone Journal* 17. doi: 10.2136/vzj2017.01.0013
- Benison KC, Goldstein RH (2001) Evaporites and siliciclastics of the Permian Nippewalla Group of Kansas, USA: a case for non-marine deposition in saline lakes and saline pans. *Sedimentology* 48:165-188. doi: 10.1046/j.1365-3091.2001.00362.x
- Benjamini C (1979) Facies relationships in the Avedat Group (Eocene) in the northern Negev, Israel. *Israel Journal of Earth Sciences* 28:47-69
- Berman A (2008) Biomineralization of Calcium Carbonate. The Interplay with Biosubstrates. In: Sigel A, Sigel H, Sigel RKO (eds) *Biomineralization: From Nature to Application*. Metal Ions in Life Sciences, vol. 4. John Wiley & Sons, Ltd, Chichester, UK, pp 167-205. doi: 10.1002/9780470986325.ch5

- Berner EK, Berner RA, Moulton KL (2005) Plants and Mineral Weathering: Present and Past. In: Drever JI (ed) *Surface and Ground Water, Weathering, and Soils. Treatise on Geochemistry, Volume 5.* Elsevier, Amsterdam, pp 169-188. doi: 10.1016/B0-08-043751-6/05175-6
- Berner RA, Kothavala Z (2001) GEOCARB III: A revised model of atmospheric CO<sub>2</sub> over phanerozoic time. *American Journal of Science* 301:182-204. doi: 10.2475/ajs.301.2.182
- Berridge MJ, Bootman MD, Lipp P (1998) Calcium - a life and death signal. *Nature* 395:645-648. doi: 10.1038/27094
- Bignot G (1972) Recherches stratigraphiques sur les calcaires du cretace superieur et de l'eocene d'Istrie et des regions voisines. Essai revision du Liburnien. *Travaux du Laboratoire de micropaleontologie Paris* 2:1-353, 350 pls.
- Bignot G (1994) L'énigme des Microcodium. *Bulletin de la Société Géologique de Normandie et Amis du Muséum du Havre* 81:25-45
- Bignot G (1995) Les deux episodes a Microcodium du Paleogene parisien replaces dans un contexte peritethysien. *Newsletters On Stratigraphy* 32:79-89
- Bindschedler S, Cailleau G, Braissant O, Milliere L, Job D, Verrecchia EP (2014) Unravelling the enigmatic origin of calcitic nanofibres in soils and caves: purely physicochemical or biogenic processes? *Biogeosciences* 11:2809-2825. doi: 10.5194/bg-11-2809-2014
- Bindschedler S, Cailleau G, Verrecchia E (2016) Role of Fungi in the Biomineralization of Calcite. *Minerals* 6. doi: 10.3390/min6020041
- Bindschedler S, Milliere L, Cailleau G, Job D, Verrecchia EP (2009) Fungal implication in secondary calcium carbonate accumulation in soils and caves. *Geochimica Et Cosmochimica Acta* 73:A123-A123
- Bindschedler S, Milliere L, Cailleau G, Job D, Verrecchia EP (2012) An Ultrastructural Approach to Analogies between Fungal Structures and Needle Fiber Calcite. *Geomicrobiology Journal* 29:301-313. doi: 10.1080/01490451.2011.558565
- Birkeland PW (1999) *Soils and geomorphology*, 3rd ed. Oxford University Press, Oxford, 432 pp
- Blanchard GB (2018) A 3D cell shape found in sheets and tubes. *Nature* 561:182-183. doi: 10.1038/d41586-018-06162-1
- Blomeier D, Dustira A, Forke H, Scheibner C (2011) Environmental change in the Early Permian of NE Svalbard: from a warm-water carbonate platform (Gipshuken Formation) to a temperate, mixed siliciclastic-carbonate ramp (Kapp Starostin Formation). *Facies* 57:493-523. doi: 10.1007/s10347-010-0243-z
- Blomeier D, Scheibner C, Forke H (2009) Facies arrangement and cyclostratigraphic architecture of a shallow-marine, warm-water carbonate platform: the Late Carboniferous Ny Friesland Platform in eastern Spitsbergen (Pyefjellet Beds, Wordiekammen Formation, Gipsdalen Group). *Facies* 55:291-324. doi: 10.1007/s10347-008-0163-3
- Boardman MR, McCartney RF, Eaton MR (1995) Bahamian paleosols: Origin, relation to paleoclimate, and stratigraphic significance. In: Curran HA, White B (eds) *Terrestrial and Shallow Marine Geology of the Bahamas and Bermuda.* Geological Society of America Special Paper 300., Boulder, Colorado, pp 33-49. doi: 10.1130/0-8137-2300-0.33
- Bockelie JF (1994) Plant roots in core. In: Donovan SK (ed) *The Paleobiology of Trace Fossils.* Wiley, pp 177-199
- Bodergat AM (1974) Les Microcodiums. Milieux et modes de développement. *Documents des Laboratoires de Géologie de la Faculté des Sciences de Lyon, Notes et Mémoires* 62:173-235, pls. 71-110

- Boguckij AB, Lanczont M, Lacka B, Madeyska T, Zawidzki P (2006) Stable isotopic composition of carbonates in Quaternary sediments of the Skala Podil'ska sequence (Ukraine). *Quaternary International* 152:3-13. doi: 10.1016/j.quaint.2005.12.016
- Boix-Fayos C, Calvo-Cases A, Imeson AC, Soriano-Soto MD (2001) Influence of soil properties on the aggregation of some Mediterranean soils and the use of aggregate size and stability as land degradation indicators. *Catena* 44:47-67. doi: 10.1016/s0341-8162(00)00176-4
- Bover-Arnal T, Ferrandez-Canadell C, Aguirre J, Esteban M, Fernandez-Carmona J, Albert-Villanueva E, Salas R (2017) Late Chattian platform carbonates with benthic foraminifera and coralline algae from the SE Iberian Plate. *Palaios* 32:61-82. doi: 10.2110/palo.2016.007
- Bowen GJ, Bloch JI (2002) Petrography and geochemistry of floodplain limestones from the Clarks Fork basin, Wyoming, USA: carbonate deposition and fossil accumulation on a Paleocene-Eocene floodplain. *Journal of Sedimentary Research* 72:46-58. doi: 10.1306/061901720046
- Bown TM (1982) Ichnofossils and rhizoliths of the nearshore fluvial jebel-Qatrani Formation (Oligocene), Fayum Province, Egypt. *Palaeogeography Palaeoclimatology Palaeoecology* 40:255-309. doi: 10.1016/0031-0182(82)90031-1
- Bradak B, Kiss K, Barta G, Varga G, Szeberenyi J, Jozsa S, Novothny A, Kovacs J, Marko A, Meszaros E, Szalai Z (2014) Different paleoenvironments of Late Pleistocene age identified in Veroce outcrop, Hungary: Preliminary results. *Quaternary International* 319:119-136. doi: 10.1016/j.quaint.2013.11.035
- Braissant O, Cailleau G, Aragno M, Verrecchia EP (2004) Biologically induced mineralization in the tree *Milicia excelsa* (Moraceae): its causes and consequences to the environment. *Geobiology* 2:59-66. doi: 10.1111/j.1472-4677.2004.00019.x
- Braithwaite CJR (1983) Calcrete and other soils in Quaternary limestones - structures, processes and applications. *Journal of the Geological Society* 140:351-363. doi: 10.1144/gsjgs.140.3.0351
- Brantley SL, Goldhaber MB, Ragnarsdottir KV (2007) Crossing disciplines and scales to understand the Critical Zone. *Elements* 3:307-314. doi: 10.2113/gselements.3.5.307
- Brantley SL, Megonigal JP, Scatena FN, Balogh-Brunstad Z, Barnes RT, Bruns MA, Van Cappellen P, Dontsova K, Hartnett HE, Hartshorn AS, Heimsath A, Herndon E, Jin L, Keller CK, Leake JR, McDowell WH, Meinzer FC, Mozdzer TJ, Petsch S, Pett-Ridge J, Pregitzer KS, Raymond PA, Riebe CS, Shumaker K, Sutton-Grier A, Walter R, Yoo K (2011) Twelve testable hypotheses on the geobiology of weathering. *Geobiology* 9:140-165. doi: 10.1111/j.1472-4669.2010.00264.x
- Brantley SL, White TS, White AF, Sparks D, Richer D, Pregitzer K, Derry L, Chorover J, Chadwick O, April R, Anderson R, Amundson R (2006) *Frontiers in Exploration of the Critical Zone. Report of a workshop sponsored by the National Science Foundation (NSF), October 2015, Newark DE. National Science Foundation, Newark*
- Brasier AT (2011) Searching for travertines, calcretes and speleothems in deep time: Processes, appearances, predictions and the impact of plants. *Earth-Science Reviews* 104:213-239. doi: 10.1016/j.earscirev.2010.10.007
- Brazzatti T, Caffau M, Cozzi A, Cucchi F, Drobne K, Pugliese N (1996) Padriciano section (Karst of Trieste, Italy). In: Drobne K, Goričan Š, Kotnik B (eds) *The Role of Impact Processes in the Geological and Biological Evolution of Planet Earth, Workshop, Postojna, Ljubljana*, pp 189-198
- Brlek M, Glumac B (2014) Stable isotopic ( $\delta$  C-13 and  $\delta$  O-18) signatures of biogenic calcretes marking discontinuity surfaces: a case study from Upper Cretaceous carbonates of central Dalmatia and eastern Istria, Croatia. *Facies* 60:773-788. doi: 10.1007/s10347-014-0403-7



- Brllek M, Korbar T, Košir A, Glumac B, Grizelj A, Otoničar B (2014) Discontinuity surfaces in Upper Cretaceous to Paleogene carbonates of central Dalmatia (Croatia): Glossifungites ichnofacies, biogenic calcretes, and stratigraphic implications. *Facies* 60:467-487. doi: 10.1007/s10347-013-0378-9
- Brllek M, Korbar T, Tešović BC, Glumac B, Fuček L (2013) Stratigraphic framework, discontinuity surfaces, and regional significance of Campanian slope to ramp carbonates from central Dalmatia, Croatia. *Facies* 59:779-801. doi: 10.1007/s10347-012-0342-0
- Broadley M, Brown P, Cakmak I, Ma JF, Rengel Z, Zhao F (2012a) Chapter 8 - Beneficial Elements. In: Marschner P (ed) *Marschner's Mineral Nutrition of Higher Plants (Third Edition)*. Academic Press, San Diego, pp 249-269. doi: <https://doi.org/10.1016/B978-0-12-384905-2.00008-X>
- Broadley M, Brown P, Cakmak I, Rengel Z, Zhao F (2012b) Chapter 7 - Function of Nutrients: Micronutrients. In: Marschner P (ed) *Marschner's Mineral Nutrition of Higher Plants (Third Edition)*. Academic Press, San Diego, pp 191-248. doi: <https://doi.org/10.1016/B978-0-12-384905-2.00007-8>
- Brock AL, Buck BJ (2009) Polygenetic development of the Mormon Mesa, NV petrocalcic horizons: Geomorphic and paleoenvironmental interpretations. *Catena* 77:65-75. doi: 10.1016/j.catena.2008.12.008
- Brock-Hon AL, Robins CR, Buck BJ (2012) Micromorphological investigation of pedogenic barite in Mormon Mesa petrocalcic horizons, Nevada USA: Implication for genesis. *Geoderma* 179:1-8. doi: 10.1016/j.geoderma.2012.02.012
- Bromley RG (1996) *Trace fossils: biology, taphonomy and applications*, 2nd ed. Routledge/Taylor and Francis, London, 378 pp
- Brundrett M (1991) Mycorrhizas in natural ecosystems. *Advances in Ecological Research* 21:171-313. doi: 10.1016/s0065-2504(08)60099-9
- Brundrett M (2004) Diversity and classification of mycorrhizal associations. *Biological Reviews* 79:473-495. doi: 10.1017/s1464793103006316
- Brundrett MC (2002) Coevolution of roots and mycorrhizas of land plants. *New Phytologist* 154:275-304. doi: 10.1046/j.1469-8137.2002.00397.x
- Brundrett MC, Tedersoo L (2018) Evolutionary history of mycorrhizal symbioses and global host plant diversity. *New Phytologist* 220:1108-1115. doi: 10.1111/nph.14976
- Brundrett MC, Walker C, Harper CJ, Krings M (2018) Fossils of Arbuscular Mycorrhizal Fungi Give Insights Into the History of a Successful Partnership With Plants. In: Krings M, Harper CJ, Cúneo NR, Rothwell GW (eds) *Transformative Paleobotany. Papers to Commemorate the Life and Legacy of Thomas N. Taylor*. Academic Press, Elsevier, London, pp 461-480. doi: /10.1016/B978-0-12-813012-4.00019-X
- Brunner I, Brodbeck S, Buchler U, Sperisen C (2001) Molecular identification of fine roots of trees from the Alps: reliable and fast DNA extraction and PCR-RFLP analyses of plastid DNA. *Molecular Ecology* 10:2079-2087. doi: 10.1046/j.1365-294X.2001.01325.x
- Buggisch W, Blomeier D, Joachimski MM (2012) Facies, diagenesis and carbon isotopes of the Early Permian Gipshuken Formation (Svalbard). *Zeitschrift Der Deutschen Gesellschaft Fur Geowissenschaften* 163:309-321. doi: 10.1127/1860-1804/2012/0163-0309
- Buonocunto FP, D'Argenio B, Ferreri V, Sandulli R (1999) Orbital cyclostratigraphy and sequence stratigraphy of Upper Cretaceous platform carbonates at Monte Sant'Erasmus, southern Apennines, Italy. *Cretaceous Research* 20:81-95. doi: 10.1006/cres.1998.0138

- Buonocunto FP, Sprovieri M, Bellanca A, D'Argenio B, Ferreri V, Neri R, Ferruzza G (2002) Cyclostratigraphy and high-frequency carbon isotope fluctuations in Upper Cretaceous shallow-water carbonates, southern Italy. *Sedimentology* 49:1321-1337. doi: 10.1046/j.1365-3091.2002.00500.x
- Burford EP, Fomina M, Gadd GM (2003) Fungal involvement in bioweathering and biotransformation of rocks and minerals. *Mineralogical Magazine* 67:1127-1155
- Burford EP, Hillier S, Gadd GM (2006) Biomineralization of fungal hyphae with calcite (CaCO<sub>3</sub>) and calcium oxalate mono- and dihydrate in carboniferous limestone microcosms. *Geomicrobiology Journal* 23:599-611. doi: 10.1080/01490450600964375
- Burgess KS, Fazekas AJ, Kesnakurti PR, Graham SW, Husband BC, Newmaster SG, Percy DM, Hajibabaei M, Barrett SCH (2011) Discriminating plant species in a local temperate flora using the rbcL plus matK DNA barcode. *Methods in Ecology and Evolution* 2:333-340. doi: 10.1111/j.2041-210X.2011.00092.x
- Buser S (1968) Basic Geological Map of SFR Yugoslavia 1:100.000. Osnovna geološka karta SFRJ 1:100.000, sheet/list Gorica. Federal Geological Survey / Zvezni geološki Zavod, Beograd
- Buser S (1973) Basic geological map of SFR Yugoslavia 1:100.000, sheet Gorica, Explanatory text. Federal Geological Survey, Belgrade, 50 pp
- Bush DS (1995) Calcium regulation in plant-cells and its role in signaling. *Annual Review of Plant Physiology and Plant Molecular Biology* 46:95-122. doi: 10.1146/annurev.arplant.46.1.95
- Bustillo MA, Plet C, Alonso-Zarza AM (2013) Root calcretes and uranium-bearing silcretes at sedimentary discontinuities in the Miocene of the Madrid Basin (Toledo, Spain). *Journal of Sedimentary Research* 83:1130-1146. doi: 10.2110/jsr.2013.85
- Cabaleri NG, Benavente CA (2013) Sedimentology and paleoenvironments of the Las Chacritas carbonate paleolake, Canadon Asfalto Formation (Jurassic), Patagonia, Argentina. *Sedimentary Geology* 284:91-105. doi: 10.1016/j.sedgeo.2012.11.008
- Cabaleri NG, Benavente CA, Monferran MD, Narvaez PL, Volkheimer W, Gallego OF, Do Campo MD (2013) Sedimentology and palaeontology of the Upper Jurassic Puesto Almada Member (Canadon Asfalto Formation, Fossati sub-basin), Patagonia Argentina: Palaeoenvironmental and climatic significance. *Sedimentary Geology* 296:103-121. doi: 10.1016/j.sedgeo.2013.08.011
- Caffau M, Cucchi F, Drobne K, Galvani R, Pleničar M, Pugliese N, Turnšek D (1995) Stop 3: Padriciano. *Atti. Mus. Geol. Paleont. Monfalcone Quaderno Speciale* 3:123-133
- Cailleau G, Braissant O, Dupraz C, Aragno M, Verrecchia EP (2005) Biologically induced accumulations of CaCO<sub>3</sub> in orthox soils of Biga, Ivory Coast. *Catena* 59:1-17. doi: 10.1016/j.catena.2004.06.002
- Cailleau G, Braissant O, Verrecchia EP (2011) Turning sunlight into stone: the oxalate-carbonate pathway in a tropical tree ecosystem. *Biogeosciences* 8:1755-1767. doi: 10.5194/bg-8-1755-2011
- Cailleau G, Dadras M, Abolhassani-Dadras S, Braissant O, Verrecchia EP (2009a) Evidence for an organic origin of pedogenic calcitic nanofibres. *Journal of Crystal Growth* 311:2490-2495. doi: 10.1016/j.jcrysgro.2009.02.029
- Cailleau G, Verrecchia EP, Braissant O, Emmanuel L (2009b) The biogenic origin of needle fibre calcite. *Sedimentology* 56:1858-1875. doi: 10.1111/j.1365-3091.2009.01060.x
- Caja MA, Marfil R, Garcia D, Remacha E, Morad S, Mansurbeg H, Amorosi A, Martinez-Calvo C, Lahoz-Beltra R (2010) Provenance of siliciclastic and hybrid turbiditic arenites of the Eocene Hecho Group, Spanish Pyrenees: implications for the tectonic evolution of a foreland basin. *Basin Research* 22:157-180. doi: 10.1111/j.1365-2117.2009.00405.x

- Caldwell DR (2000) *Microbial physiology and metabolism*, 2nd ed edn. Star Publications, Belmont, xxv + 403 pp
- Callot G, Mousain D, Plassard C (1985) Concentrations de carbonate de calcium sur les parois des hyphes mycéliens. *Agronomie* 5:143-150
- Calvet F, Pomar L, Esteban M (1975) Las Rizocreaciones del Pleistoceno de Mallorca. . Instituto de Investigaciones geológicas, Universidad de Barcelona 30:35-60
- Calvet F, Wright VP, Gimenez J (1991) Microcodium: descripción y origen. Implicaciones paleogeográficas y paleogeomorfológicas Grupo Español del Terciario, Comunicaciones de Congreso, Vic, pp 50-51
- Calvo-Cases A, Boix-Fayos C, Imeson AC (2003) Runoff generation, sediment movement and soil water behaviour on calcareous (limestone) slopes of some Mediterranean environments in southeast Spain. *Geomorphology* 50:269-291. doi: 10.1016/s0169-555x(02)00218-0
- Canadell J, Jackson RB, Ehleringer JR, Mooney HA, Sala OE, Schulze ED (1996) Maximum rooting depth of vegetation types at the global scale. *Oecologia* 108:583-595
- Canaveras JC, SanchezMoral S, Calvo JP, Hoyos M, Ordonez S (1996) Dedolomites associated with karstification. An example of early dedolomitization in lacustrine sequences from the tertiary Madrid basin, central Spain. *Carbonates and Evaporites* 11:85-103. doi: 10.1007/bf03175788
- Candy I, Black S (2009) The timing of Quaternary calcrete development in semi-arid southeast Spain: Investigating the role of climate on calcrete genesis. *Sedimentary Geology* 218:6-15. doi: 10.1016/j.sedgeo.2009.03.005
- Cantarero I, Trave A, Alias G, Baques V (2010) Pedogenic products sealing normal faults (Barcelona Plain, NE Spain). *Journal of Geochemical Exploration* 106:44-52. doi: 10.1016/j.gexplo.2010.02.004
- Capeder G (1904) Sulla Paronipora penicillata. Nuovo genere di corallario fossile, appartenente alla famiglia delle Favositidi. *Rivista Italiana di Paleontologia e Stratigrafia* 10:59-61
- Carafoli E, Krebs J (2016) Why Calcium? How Calcium Became the Best Communicator. *Journal of Biological Chemistry* 291:20849-20857. doi: 10.1074/jbc.R116.735894
- Carew JL, Mylroie JE (1995) Depositional model and stratigraphy for the Quaternary geology of the Bahama Islands. In: Curran HA, White B (eds) *Terrestrial and Shallow Marine Geology of the Bahamas and Bermuda*. Geological Society of America Special Paper 300., Boulder, Colorado, pp 5-32. doi: 10.1130/0-8137-2300-0.5
- Carew JL, Mylroie JE (1997) Geology of The Bahamas. In: Vacher H, Quinn T (eds) *Geology and Hydrogeology of Carbonate Islands*. Developments in Sedimentology 54. Elsevier Science B.V., Amsterdam, pp 91-139
- Carew JL, Mylroie JE (2001) Quaternary carbonate eolianites of the Bahamas: Useful analogues for the interpretation of ancient rocks? In: Abegg FER, Loope DB, Harris PMM (eds) *Modern and Ancient Carbonate Eolianites: Sedimentology, Sequence Stratigraphy, and Diagenesis*. Special Publication 71. SEPM Society for Sedimentary Geology, Tulsa, pp 33-45
- Carminati A, Benard P, Ahmed MA, Zarebanadkouki M (2017) Liquid bridges at the root-soil interface. *Plant and Soil* 417:1-15. doi: 10.1007/s11104-017-3227-8
- Carminati A, Kroener E, Ahmed MA, Zarebanadkouki M, Holz M, Ghezzehei T (2016) Water for Carbon, Carbon for Water. *Vadose Zone Journal* 15. doi: 10.2136/vzj2015.04.0060
- Casado AI, Alonso-Zarza AM, La Iglesia A (2014) Morphology and origin of dolomite in paleosols and lacustrine sequences. Examples from the Miocene of the Madrid Basin. *Sedimentary Geology* 312:50-62. doi: 10.1016/j.sedgeo.2014.07.005



- Casanova J, Nury D (1989) Biosedimentology of the fluvio-lacustrine stromatolites from the Marseilles Oligocene graben. *Bulletin De La Societe Geologique De France* 5:1173-1184
- Celarc B (2010) Geološko – geomehanske raziskave in raziskave krasa za potrebe izdelave projektne dokumentacije za fazo PGD za drugi tir železniške proge Divača – Koper, odsek Divača – Črni Kal. Geološki zavod Slovenije, 49 pp
- Cerdà A (1997) Seasonal changes of the infiltration rates in a Mediterranean scrubland on limestone. *Journal of Hydrology* 198 209–225. doi: [https://doi.org/10.1016/S0022-1694\(96\)03295-7](https://doi.org/10.1016/S0022-1694(96)03295-7)
- Cerling TE (1984) The Stable isotopic composition of modern soil carbonate and its relationship to climate. *Earth and Planetary Science Letters* 71:229-240
- Cerling TE (1991) Carbon-Dioxide in the Atmosphere - Evidence from Cenozoic and Mesozoic Paleosols. *American Journal of Science* 291:377-400
- Cerling TE (1992) Further comments on using carbon isotopes in paleosols to estimate the CO<sub>2</sub> content of the palaeo-atmosphere. *Journal of the Geological Society* 149:673-675
- Cerling TE (1999a) Paleorecords of C<sub>4</sub> Plants and Ecosystems A2 - Sage, Rowan F. In: Monson RK (ed) C<sub>4</sub> Plant Biology. Academic Press, San Diego, pp 445-469. doi: <http://dx.doi.org/10.1016/B978-012614440-6/50014-8>
- Cerling TE (1999b) Stable carbon isotopes in palaeosol carbonates. In: Thiry M, Simon-Coinçon R (eds) Palaeoweathering, palaeosurfaces, and related continental deposits, Ias Special Publications 27, Blackwell Science, pp 43-60. doi: [10.1002/9781444304190.ch2](https://doi.org/10.1002/9781444304190.ch2)
- Cerling TE, Harris JM, MacFadden BJ, Leakey MG, Quade J, Eisenmann V, Ehleringer JR (1997) Global vegetation change through the Miocene/Pliocene boundary. *Nature* 389:153-158
- Cerling TE, Quade J (1993) Stable Carbon and Oxygen Isotopes in Soil Carbonates. In: Swart PK, Lohmann KC, Mckenzie J, Savin S (eds) Climate Change in Continental Isotopic Records. Geophysical Monographs 78. American Geophysical Union, Washington, DC, pp 217-231. doi: <https://doi.org/10.1029/GM078p0217>
- Cerling TE, Quade J, Wang Y, Bowman JR (1989) Carbon isotopes in soils and paleosols as ecology and paleoecology indicators. *Nature* 341:138-139. doi: [10.1038/341138a0](https://doi.org/10.1038/341138a0)
- Cerling TE, Solomon DK, Quade J, Bowman JR (1991) On the Isotopic Composition of Carbon in Soil Carbon-Dioxide. *Geochimica Et Cosmochimica Acta* 55:3403-3405
- Cerling TE, Wang Y, Quade J (1993) Expansion of C<sub>4</sub> Ecosystems as an indicator of global ecological change in the Late Miocene. *Nature* 361:344-345
- Chafetz HS, Butler JC (1980) Petrology of recent caliche pisolites, spherulites, and speleothem deposits from central Texas. *Sedimentology* 27:497-518. doi: [10.1111/j.1365-3091.1980.tb01644.x](https://doi.org/10.1111/j.1365-3091.1980.tb01644.x)
- Chafetz HS, Butler JC (1982) Comments on Petrology of recent caliche, pisolites, spherulites, and speleothem deposits from central Rexas - Reply. *Sedimentology* 29:443-445. doi: [10.1111/j.1365-3091.1982.tb01810.x](https://doi.org/10.1111/j.1365-3091.1982.tb01810.x)
- Chen JH, Curran HA, White B, Wasserburg GJ (1991) Precise chronology of the last interglacial period: 234U–230 Th data from fossil coral reefs in the Bahamas. *Geological Society of America Bulletin* 103:82–97
- Chen JT, Montanez IP, Qi YP, Wang XD, Wang QL, Lin W (2016) Coupled sedimentary and delta C-13 records of late Mississippian platform-to-slope successions from South China: Insight into delta C-13 chemostratigraphy. *Palaeogeography Palaeoclimatology Palaeoecology* 448:162-178. doi: [10.1016/j.palaeo.2015.10.051](https://doi.org/10.1016/j.palaeo.2015.10.051)

- Chenu C, Cosentino D (2011) Microbial Regulation of Soil Structure Dynamics. In: Ritz K, Young I (eds) *The architecture and biology of soils: life in inner space*. CABI, Wallingford, pp 37-69. doi: 10.1079/9781845935320.0037
- Cherchi A, Schroeder R (1988) Osservazioni sui microproblematici Paronipora Capeder, Microcodium Gluck, Baccanella Pantic e Palaeomicrocodium Mamet & Roux. *Bolletino della Societa Paleontologica Italiana* 27:79-81
- Cohen AL, McConnaughey TA (2003) Geochemical perspectives on coral mineralization. *Reviews in Mineralogy and Geochemistry* 54:151-187. doi: 10.2113/0540151
- Cohen AS (1982) Paleoenvironments of root casts from the Koobi Fora Formation, Kenya. *Journal of Sedimentary Petrology* 52:401-414
- Colfen H (2010) Biomineralization: A crystal-clear view. *Nature Materials* 9:960-961. doi: 10.1038/nmat2911
- Cölfen H, Antonietti M (2008) *Mesocrystals and Nonclassical Crystallization*. John Wiley & Sons Ltd, West Sussex. DOI:10.1002/9780470994603
- Collins DBG, Bras RL (2007) Plant rooting strategies in water-limited ecosystems. *Water Resources Research* 43:W06407. doi: 10.1029/2006wr005541
- Colodrón I, Ruiz V, Núñez A (1981) Mapa geológico y Memoria de la Hoja no. 847 (Villajoyosa). Mapa geológico de España E. 1:50.000 (MAGNA), Segunda Serie. IGME, 22 pp
- Combes PJ, Peybernes B, Fondécave-Wallez MJ (2004) Karsts polyphasés, faciès marins et continentaux dans le Paléocène de la partie orientale des Pyrénées françaises. *Eclogae Geologicae Helveticae* 97:155-174. doi: 10.1007/s00015-004-1120-y
- Coniglio M, Harrison RS (1983a) Facies and diagenesis of Late Pleistocene carbonates from Big Pine Key, Florida. *Bulletin of Canadian Petroleum Geology* 31:153-147
- Coniglio M, Harrison RS (1983b) Holocene and Pleistocene caliche from Big Pine Key, Florida. *Bulletin of Canadian Petroleum Geology* 31:3-13
- Correll DS (1979) The Bahama Archipelago and Its Plant Communities. *Taxon* 28:35-40
- Cousin M (1981) Les rapports Alpes-Dinarides Les confins de l'Italie et de la Yougoslavie. *Societe Geologique du Nord*. Publication no. 5, vol 1 and 2:521 + 521 pp
- Cramer MD, Hawkins HJ (2009) A physiological mechanism for the formation of root casts. *Palaeogeography Palaeoclimatology Palaeoecology* 274:125-133. doi: 10.1016/j.palaeo.2008.12.021
- Crang R, Lyons-Sobaski S, Wise R (2018) *Plant anatomy: a concept-based approach to the structure of seed plants*. Springer Nature Switzerland AG, Cham, xvi + 725 pp
- Crespo MB, Serra L (1993) A new Spanish species of the genus *Ononis* L. (Fabaceae). *Botanical Journal of the Linnean Society* 111:37-46
- Cui Y, Zhao Q, Hu S, Jiang LW (2020) Vacuole Biogenesis in Plants: How Many Vacuoles, How Many Models? *Trends in Plant Science* 25:538-548. doi: 10.1016/j.tplants.2020.01.008
- Curran HA, White B (2001) Ichnology of Holocene carbonate eolianites of the Bahamas. In: Abegg FER, Loope DB, Harris PMM (eds) *Modern and Ancient Carbonate Eolianites: Sedimentology, Sequence Stratigraphy, and Diagenesis*. Special Publication 71. SEPM Society for Sedimentary Geology, Tulsa, pp 47-56. doi: 10.2110/pec.01.71.0047
- Cutler DF (1987) *Root identification manual of trees and shrubs: A guide to the anatomy of roots of trees and shrubs hardy in Britain and Northern Europe*. Chapman and Hall, London, ix + 245 pp
- Cutler DF, Botha CEJ, Stevenson DW (2008) *Plant anatomy: an applied approach*. Blackwell Publishing, Malden, MA, vii + 302 pp

- Czarnes S, Hallett PD, Bengough AG, Young IM (2000) Root- and microbial-derived mucilages affect soil structure and water transport. *European Journal of Soil Science* 51:435-443. doi: 10.1046/j.1365-2389.2000.00327.x
- da Silva JH, Saraiva GD, Campelo SCM, Martinez JCC, Viana BC, Bezerra FI, Abagaro BTO, Freire PC (2019) Raman and infrared spectroscopy investigation of the root fossil (rhizoliths) from the Carboniferous period, Piauí Formation, Parnaíba Sedimentary Basin, Northeast Brazil. *Vibrational Spectroscopy* 100:117-122. doi: 10.1016/j.vibspec.2018.11.007
- da Silva ML, Batezelli A, Ladeira FSB (2017a) Micromorphology of Paleosols of the Marília Formation and their Significance in the Paleoenvironmental Evolution of the Bauru Basin, Upper Cretaceous, Southeastern Brazil. *Revista Brasileira De Ciencia Do Solo* 41. doi: 10.1590/18069657rbcs20160287
- da Silva ML, Batezelli A, Ladeira FSB (2017b) The mineralogy of paleosols in the Marília Formation and their importance in the environmental evolution of the Maastrichtian of the Bauru Basin in southeastern Brazil. *Brazilian Journal of Geology* 47:403-426. doi: 10.1590/2317-4889201720170101
- Danjon F, Stokes A, Bakker MR (2013) Root systems of woody plants. In: Eshel A, Beekman T (eds) *Plant Roots: the Hidden Half*, 4th Edition, pp 29-21-29-26. doi: 10.1201/b14550-34
- Dart RC, Barovich KM, Hill SM, Chittleborough DJ (2012) Sr-isotopes as a tracer of Ca sources and mobility in profiles hosting regolith carbonates from southern Australia. *Australian Journal of Earth Sciences* 59:373-382. doi: 10.1080/08120099.2012.662912
- Darwin C, Darwin F (1880) *The power of movement in plants*. John Murray, London
- Daugherty DR, Boardman MR, Metzler CV (1987) Characteristics and origins of joints and sedimentary dikes of the Bahama Islands. In: Curran HA (ed) *Proceedings of the Third Symposium on the Geology of the Bahamas CCFL Bahamian Field Station*, Fort Lauderdale, Florida, pp 45-65
- Davaud E, Septfontaine M (1995) Post-mortem onshore transportation of epiphytic foraminifera: recent example from the Tunisian coastline. *Journal of Sedimentary Research* A65:136-142.
- Davies WJ, Bacon MA (2003) Adaptations of roots to drought. In: de Kroon H., E.J.W. V (eds) *Root Ecology. Ecological Studies (Analysis and Synthesis)*, vol 168. Springer, Berlin, Heidelberg, pp 173-192. doi: 10.1007/978-3-662-09784-7\_1
- Dawson TE, Hahm WJ, Crutchfield-Peters K (2020) Digging deeper: what the critical zone perspective adds to the study of plant ecophysiology. *New Phytologist* 226:666-671. doi: 10.1111/nph.16410
- de Tombeur F, Cornelis J-T, Lambers H (2021) Silicon mobilisation by root-released carboxylates. *Trends in Plant Science*. doi: <https://doi.org/10.1016/j.tplants.2021.07.003>
- De Vere N, Rich TCG, Trinder SA, Long C (2015) DNA Barcoding for Plants. In: Batley J (ed) *Plant Genotyping: Methods and Protocols*. Springer New York, pp 101-118
- de Willigen P, Heinen M, van Noordwijk M (2017) Roots partially in contact with soil: Analytical solutions and approximation in models of nutrient and water uptake. *Vadose Zone Journal* 17:170060. doi: doi:10.2136/vzj2017.03.0060
- De Yoreo JJ, Gilbert P, Sommerdijk N, Penn RL, Whitlam S, Joester D, Zhang HZ, Rimer JD, Navrotsky A, Banfield JF, Wallace AF, Michel FM, Meldrum FC, Colfen H, Dove PM (2015) Crystallization by particle attachment in synthetic, biogenic, and geologic environments. *Science* 349. doi: 10.1126/science.aaa6760



- Dell B, Bartle JR, Tacey WH (1983) Root occupation and root channels of Jarrah Forest subsoils. *Australian Journal of Botany* 31:615–627
- Demidchik V, Shabala S, Isayenkov S, Cuin TA, Pottosin I (2018) Calcium transport across plant membranes: mechanisms and functions. *New Phytologist* 220:49–69. doi: 10.1111/nph.15266
- Dickison WC (2000) Integrative plant anatomy. Harcourt/Academic Press, San Diego, xvii, 533 pp
- Dickson JAD (2014) Marine Beachrocks. Carbonate Diagenesis Ltd., Apple iBooks 41 pp
- Dickson JAD, Saller AH (1995) Identification of subaerial exposure surfaces and porosity preservation in Pennsylvanian and Lower Permian shelf limestones, Eastern Central Basin Platform, Texas. In: Budd DA, Saller AH, Harris PM (eds) Unconformities and porosity in carbonate strata, AAPG memoir 63. American Association of Petroleum Geologists, Tulsa, Okla., pp 239–257
- DiMasi E, Gower LB (2014) Biomineralization sourcebook: characterization of biominerals and biomimetic materials. CRC Press, Taylor & Francis Group, Boca Raton, FL, xxxi, 387 pages pp
- DiMichele WA, Gastaldo RA (2008) Plant paleoecology in deep time. *Annals of the Missouri Botanical Garden* 95:144–198. doi: <https://doi.org/10.3417/2007016>
- do Nascimento DL, Batezelli A, Ladeira FSB (2019) The paleoecological and paleoenvironmental importance of root traces: Plant distribution and topographic significance of root patterns in Upper Cretaceous paleosols. *Catena* 172:789–806. doi: 10.1016/j.catena.2018.09.040
- Doblas-Miranda E, Martinez-Vilalta J, Lloret F, Alvarez A, Avila A, Bonet FJ, Brotons L, Castro J, Yuste JC, Diaz M, Ferrandis P, Garcia-Hurtado E, Iriondo JM, Keenan TF, Latron J, Llusia J, Loepfe L, Mayol M, More G, Moya D, Penuelas J, Pons X, Poyatos R, Sardans J, Sus O, Vallejo VR, Vayreda J, Retana J (2015) Reassessing global change research priorities in mediterranean terrestrial ecosystems: how far have we come and where do we go from here? *Global Ecology and Biogeography* 24:25–43. doi: 10.1111/geb.12224
- Dolan L, Davies J (2004) Cell expansion in roots. *Current Opinion In Plant Biology* 7:33–39. doi: 10.1016/j.pbi.2003.11.006
- Doyle JJ (1994) Phylogeny of the Legume family - an approach to understanding the origins of nodulation. *Annual Review of Ecology and Systematics* 25:325–349
- Driese SG, Mora CI (1993) Physicochemical environment of pedogenic carbonate formation in Devonian vertic paleosols, Central Appalachians, USA. *Sedimentology* 40:199–216. doi: 10.1111/j.1365-3091.1993.tb01761.x
- Drobne K (1977) Alvéolines paléogènes de la Slovénie et de l'Istrie. *Mémoires Suisses de Paléontologie* 77:132pp, 121 pls
- Drobne K, Ogorelec B, Pleničar M, Zucchi Stolfa ML, Turnšek D (1988) Maastrichtian, Danian and Thanetian beds in Dolenja vas (NW Dinarides, Yugoslavia). *Razprave IV. razr. SAZU* 29:147–224
- Duniway MC, Herrick JE, Monger HC (2007) The high water-holding capacity of petrocalcic horizons. *Soil Science Society Of America Journal* 71:812–819. doi: 10.2136/sssaj2006.0267
- Duniway MC, Herrick JE, Monger HC (2010) Spatial and temporal variability of plant-available water in calcium carbonate-cemented soils and consequences for arid ecosystem resilience. *Oecologia* 163:215–226. doi: 10.1007/s00442-009-1530-7
- Dupraz C, Reid RP, Braissant O, Decho AW, Norman RS, Visscher PT (2009) Processes of carbonate precipitation in modern microbial mats. *Earth-Science Reviews* 96:141–162. doi: 10.1016/j.earscirev.2008.10.005
- Durand N, Monger HC, Canti MG (2010) Calcium carbonate features. In: Stoops G, Marcelino V, Mees F (eds) Interpretation of Micromorphological Features of Soils and Regoliths. Elsevier, Amsterdam, pp 149–194. doi: 10.1016/B978-0-444-53156-8.00009-X

- Durand N, Monger HC, Canti MG, Verrecchia EP (2018) Calcium carbonate features. In: Stoops G, Marcelino V, Mees F (eds) *Interpretation of Micromorphological Features of Soils and Regoliths*. Second Edition. Elsevier, Amsterdam, pp 205-258. doi: /10.1016/B978-0-444-63522-8.00009-7
- Dutton MV, Evans CS (1996) Oxalate production by fungi: Its role in pathogenicity and ecology in the soil environment. *Canadian Journal of Microbiology* 42:881-895. doi: 10.1139/m96-114
- Ehleringer JR, Cerling TE (2002a) C3 and C4 photosynthesis. In: Mooney HA, Canadell JG (eds) *Encyclopedia of Global Environmental Change. Volume 2: The Earth system: biological and ecological dimensions of global environmental change*. Jon Wiley & Sons, Ltd, Chichester, pp 189-190
- Ehleringer JR, Cerling TE (2002b) Stable isotopes. In: Mooney HA, Canadell JG (eds) *Encyclopedia of Global Environmental Change. Volume 2: The Earth system: biological and ecological dimensions of global environmental change*. Jon Wiley & Sons, Ltd, Chichester, pp 544-550
- Ehleringer JR, Cerling TE, Helliker BR (1997) C-4 photosynthesis, atmospheric CO<sub>2</sub> and climate. *Oecologia* 112:285-299
- Ehrenberg SN, Pickard NAH, Svana TA, Oxtoby NH (2002) Cement geochemistry of Photozoan carbonate strata (Upper Carboniferous-Lower Permian), Finnmark Carbonate Platform, Barents Sea. *Journal of Sedimentary Research* 72:95-115. doi: 10.1306/050701720095
- Ehrenfeld JG (2001) Plant-Soil Interactions In: Levin SA (ed) *Encyclopedia of Biodiversity*. Elsevier, New York, pp 689-709. doi: <http://dx.doi.org/10.1016/B0-12-226865-2/00346-1>
- Ehrenfeld JG (2013) Plant-Soil Interactions. In: Levin SA (ed) *Encyclopedia of Biodiversity (Second Edition)*. Academic Press, Waltham, pp 109-128. doi: <http://dx.doi.org/10.1016/B978-0-12-384719-5.00179-9>
- Eissenstat DM (1992) Costs and benefits of constructing roots of small diameter. *Journal of Plant Nutrition* 15:763-782
- Eissenstat DM, Kucharski JM, Zadworny M, Adams TS, Koide RT (2015) Linking root traits to nutrient foraging in arbuscular mycorrhizal trees in a temperate forest. *New Phytologist* 208:114-124. doi: 10.1111/nph.13451
- Eissenstat DM, Volder A (2005) The efficiency of nutrient acquisition over the life of a root. In: BassiriRad H (ed) *Nutrient Acquisition by Plants. An Ecological Perspective*, vol 181. Springer-Verlag, Berlin, Heidelberg, pp 185-220. doi: 10.1007/3-540-27675-0\_8
- Eissenstat DM, Wells CE, Yanai RD, Whitbeck JL (2000) Building roots in a changing environment: implications for root longevity. *New Phytologist* 147:33-42
- Eissenstat DM, Yanai RD (1997) The ecology of root lifespan. *Advances in Ecological Research*, vol 27, pp 1-60. doi: 10.1016/S0065-2504(08)60005-7
- Eissenstat DM, Yanai RD (2002) Root life span, efficiency, and turnover. In: Waisel Y, Eshel A, Beekman T, Kafkafi U (eds) *Plant roots : the hidden half*, Third Edition. CRC Press, Boca Raton, pp 221-238. doi: 10.1201/9780203909423.ch13
- Ekart DD, Cerling TE, Montanez IP, Tabor NJ (1999) A 400 million year carbon isotope record of pedogenic carbonate: Implications for paleoatmospheric carbon dioxide. *American Journal of Science* 299:805-827
- El Kadiri K, Hlila R, De Galdeano CS, Lopez-Garrido AC, Chalouan A, Serrano F, Bahmad A, Guerra-Merchan A, Liemlahi H (2006) Regional correlations across the Internides-Externides front (northwestern Rif Belt, Morocco) during the Late Cretaceous-Early Burdigalian times: palaeogeographical and palaeotectonic implications. In: Moratti G, Chalouan A (eds) *Tectonics of the Western Mediterranean and North Africa*, vol 262, pp 193-+. doi: 10.1144/gsl.sp.2006.262.01.12

- Enstone DE, Peterson CA, Hallgren SW (2001) Anatomy of seedling tap roots of loblolly pine (*Pinus taeda* L.). *Trees-Structure and Function* 15:98-111. doi: 10.1007/s004680000079
- Epstein E (1973) Roots. *Scientific American* 228:48-58. doi: 10.1038/scientificamerican0573-48
- Epstein E, Bloom AJ (2005) *Mineral nutrition of plants: principles and perspectives*, 2nd edn. Sinauer Associates, Sunderland, Mass., xiv + 400 pp
- Eren M, Kadir S, Hatipoglu Z, Gul M (2008) Quaternary Calcrete Development in the Mersin Area, Southern Turkey. *Turkish Journal of Earth Sciences* 17:763-784
- Eren M, Kaplan MY, Kadir S, Kapur S (2018) Biogenic (beta-fabric) features in the hard laminated crusts of the Mersin and Adana regions, southern Turkey and the role of soil organisms in the formation of the calcrete profiles. *Catena* 168:34-46. doi: 10.1016/j.catena.2017.12.021
- Erickson DL, Spouge J, Resch A, Weigt LA, Kress WJ (2008) DNA barcoding in land plants: developing standards to quantify and maximize success. *Taxon* 57:1304-1316
- Eshel A, Beekman T (2013) *Plant roots : the hidden half*, 4th edn. Routledge/CRC Press, Boca Raton, 848 pp. doi: doi.org/10.1201/b14550
- Esperante R, Rodriguez-Tovar FJ, Nalin R (2021) Rhizoliths in Lower Pliocene alluvial fan deposits of the Sorbas Basin (Almeria, SE Spain). *Palaeogeography Palaeoclimatology Palaeoecology* 567. doi: 10.1016/j.palaeo.2021.110281
- Esteban M (1972) Una nueva forma de prismas de *Microcodium elegans* Glueck 1912 y su relación con el caliche del Eoceno Inferior, Marmella, provincia de Tarragona (España). *Revista de Instituto de Investigaciones Geológicas, Universidad de Barcelona* 27:65-81
- Esteban M (1974) Caliche textures and "Microcodium". *Bollettino Della Societa Geologica Italiana* v. 92 (Suppl. 1973):105-125
- Esteban M (1982) Comments on 'Petrology of recent caliche, spherulites, and speleothem deposits from central Texas' by H.S. Chafetz and J.C. Butler, Discussion. *Sedimentology* 29:441-443
- Esteban M, Klappa CF (1983) Subaerial exposure environment. In: Scholle PA, Bebout DG, Moore CH (eds) *Carbonate Depositional Environments*, vol 33, pp 1-54
- Eswaran H, Reich PF, Kimble JM, F.H. B, Padmanabhan E, Moncharoen P (2000) Global carbon stocks. In: Lal R, Kimble JM, Eswaran H, Stewart BA (eds) *Global Climate Change and Pedogenic Carbonates*. CRC Press, Lewis Publishers, Boca Raton, pp 15-26
- Evert RF (2006) *Esau's Plant anatomy. Meristems, cells, and tissues of the plant body, their structure, function, and development*, 3rd edition. Wiley-Interscience, Hoboken, NJ, xiv + 601 pp
- Fahn A (1982) *Plant anatomy*, 3rd rev. edn. Pergamon Press, Oxford ; New York, xi + 544 pp
- Farjon A, Styles BT (1997) *Pinus* (Pinaceae). *Flora Neotropica. Monographs of New York Botanical Garden* 75:1-291
- Farquhar GD, Ehleringer JR, Hubick KT (1989) Carbon isotope discrimination and photosynthesis. *Annual Review of Plant Physiology and Plant Molecular Biology* 40:503-537. doi: 10.1146/annurev.arplant.40.1.503
- Faucon MP, Houben D, Lambers H (2017) Plant Functional Traits: Soil and Ecosystem Services. *Trends in Plant Science* 20:385-394. doi: DOI: 10.1016/j.tplants.2017.01.005
- Faure-Muret A, Fallot P (1954) La formation a *Microcodium* au pourtour de l'Argentera-Mercantour. *Bulletin De La Societe Geologique De France* S6-IV:111-138. doi: /10.2113/gssgfbull.S6-IV.1-3.111
- Fazekas AJ, Kuzmina ML, Newmaster SG, Hollingsworth PM (2012) DNA Barcoding Methods for Land Plants. In: Kress WJ, Erickson DL (eds) *DNA Barcodes: Methods and Protocols. Methods in Molecular Biology* 858. Springer, pp 223-252. doi: 10.1007/978-1-61779-591-6\_11



- Fedoroff N, Coury MA, Lacroix E, Oleschko K (1994) Calcitic accretion on indurated volcanic materials (example of tepetates, Altiplano, Mexico). *Proc. XVth World Congress of Soil Sciences, Acapulco*, Vol. 6A:459-472
- Felton EA, Crook KAW, Keating BH (2000) The Hulopoe Gravel, Lanai, Hawaii: New sedimentological data and their bearing on the “giant wave” (mega-tsunami) emplacement hypothesis. *Pure and Applied Geophysics* 157:1257-1284. doi: 10.1007/s000240050025
- Field KJ, Pressel S, Duckett JG, Rimington WR, Bidartondo MI (2015) Symbiotic options for the conquest of land. *Trends in Ecology & Evolution* 30:477-486. doi: 10.1016/j.tree.2015.05.007
- Fimmen RL, Richter DD, Vasudevan D, Williams MA, West LT (2008) Rhizogenic Fe-C redox cycling: a hypothetical biogeochemical mechanism that drives crustal weathering in upland soils. *Biogeochemistry* 87:127-141. doi: 10.1007/s10533-007-9172-5
- Finlay R (2005) Action and interaction in the mycorrhizal hyphosphere – a re-evaluation of the role of mycorrhizas in nutrient acquisition and plant ecology. In: BassiriRad H (ed) *Nutrient Acquisition by Plants. An Ecological Perspective*, vol 181. Springer-Verlag, Berlin, Heidelberg, pp 221-276
- Finlay RD (2006) The fungi in soil. In: Elsas JDv, Jansson JK, Trevors JT (eds) *Modern soil microbiology*, 2nd Edition. CRC Press, Taylor & Francis, Boca Raton, pp 107-146
- Finlay RD, Mahmood S, Rosenstock N, Bolou-Bi EB, Kohler SJ, Fahad Z, Rosling A, Wallander H, Belyazid S, Bishop K, Lian B (2020) Reviews and syntheses: Biological weathering and its consequences at different spatial levels - from nanoscale to global scale. *Biogeosciences* 17:1507-1533. doi: 10.5194/bg-17-1507-2020
- Finlay RD, Thorn RG (2019) The fungi in soil. In: van Elsas JD, Jansson JK, Rosado AS, Nanniperi P (eds) *Modern soil microbiology*, Third edition. edn. CRC Press, Taylor & Francis, Boca Raton, pp 65-89. doi: <https://doi.org/10.1201/9780429059186>
- Fitter A (1996) Characteristics and function of root systems. In: Waisel Y, Eshel A, Kafkafi U (eds) *Plant roots : the hidden half*, Second Edition, 2nd edn. Marcel Dekker, New York, pp 1-20
- Fitter A (2002) Characteristics and function of root systems. In: Waisel Y, Eshel A, Beeckman T, Kafkafi U (eds) *Plant roots : the hidden half*, Third Edition. CRC Press, Boca Raton, pp 21-50. doi: 10.1201/9780203909423
- Fitter A, Hay RKM (2002) *Environmental physiology of plants*, 3rd edn. Academic Press, San Diego, xii + 367 pp
- Fitter AH, Stickland TR (1991) Architectural analysis of plant-root systems 2. Influence of nutrient supply on architecture in contrasting plant-species. *New Phytologist* 118:383-389. doi: 10.1111/j.1469-8137.1991.tb00019.x
- Fitter AH, Stickland TR, Harvey ML, Wilson GW (1991) Architectural analysis of plant-root systems 1. Architectural correlates of exploitation efficiency. *New Phytologist* 118:375-382. doi: 10.1111/j.1469-8137.1991.tb00018.x
- FitzPatrick EA (1990) Roots in thin sections of soils. In: Douglas LA (ed) *Soil micromorphology: a basic and applied science. Proceedings of the VIIIth International Working Meeting of Soil Micromorphology*, San Antonio 1988, vol 19. Elsevier, Amsterdam Oxford New York Tokio, pp 9-23. doi: 10.1016/S0166-2481(08)70311-8
- Fomina M, Burford EP, Hillier S, Kierans M, Gadd GM (2010) Rock-Building Fungi. *Geomicrobiology Journal* 27:624-629. doi: 10.1080/01490451003702974
- Foos AM, Bain RJ (1995) Mineralogy, chemistry, and petrography of soils, surface crusts, and soil stones, San Salvador and Eleuthera, Bahamas. In: Curran HA, White B (eds) *Terrestrial and*

- shallow marine geology of the Bahamas and Bermuda, Geological Society of America, Special Paper 300, pp 223-232. doi: <https://doi.org/10.1130/0-8137-2300-0.223>
- Ford D, Williams PW (2007) Karst hydrogeology and geomorphology. John Wiley, Chichester
- Franceschi V (2001) Calcium oxalate in plants. *Trends in Plant Science* 6:331-331. doi: 10.1016/s1360-1385(01)02014-3
- Franceschi VR, Horner HT (1980) Calcium-oxalate crystals in plants. *Botanical Review* 46:361-427. doi: 10.1007/bf02860532
- Franceschi VR, Loewus FA (1995) Oxalate biosynthesis and function in plants and fungi. In: Khan SR (ed) Calcium oxalate in biological systems. CRC Press, Boca Raton, Florida; London, pp 113-129
- Franceschi VR, Nakata PA (2005) Calcium oxalate in plants: Formation and function. *Annual Review of Plant Biology* 56:41-71
- Fratesi SE, Lynch FL, Kirkland BL, Brown LR (2004) Effects of SEM preparation techniques on the appearance of bacteria and biofilms in the carter sandstone. *Journal of Sedimentary Research* 74:858-867. doi: 10.1306/042604740858
- Freeman T, Rosell J, Obrador A (1982) Oncolites From Lacustrine Sediments In The Cretaceous Of Northeastern Spain. *Sedimentology* 29:433-436. doi: 10.1111/j.1365-3091.1982.tb01806.x
- Freschet GT, Pagès L, Iversen CM, Comas LH, Rewald B, Roumet C, Klimešová J, Zadworny M, Poorter H, Postma JA, Adams TS, Bagniewska-Zadworna A, Bengough AG, Blancaflor EB, Brunner I, Cornelissen JHC, Garnier E, Gessler A, Hobbie SE, Meier IC, Mommer L, Picon-Cochard C, Rose L, Ryser P, Scherer-Lorenzen M, Soudzilovskaia NA, Stokes A, Sun T, Valverde-Barrantes OJ, Weemstra M, Weigelt A, Wurzbürger N, York LM, Batterman SA, Gomes de Moraes M, Janeček Š, Lambers H, Salmon V, Tharayil N, McCormack ML (2021a) A starting guide to root ecology: strengthening ecological concepts and standardising root classification, sampling, processing and trait measurements. *New Phytologist* 232:973-1122. doi: <https://doi.org/10.1111/nph.17572>
- Freschet GT, Roumet C, Comas LH, Weemstra M, Bengough AG, Rewald B, Bardgett RD, De Deyn GB, Johnson D, Klimesova J, Lukac M, McCormack ML, Meier IC, Pages L, Poorter H, Prieto I, Wurzbürger N, Zadworny M, Bagniewska-Zadworna A, Blancaflor EB, Brunner I, Gessler A, Hobbie SE, Iversen CM, Mommer L, Picon-Cochard C, Postma JA, Rose L, Ryser P, Scherer-Lorenzen M, Soudzilovskaia NA, Sun T, Valverde-Barrantes OJ, Weigelt A, York LM, Stokes A (2021b) Root traits as drivers of plant and ecosystem functioning: current understanding, pitfalls and future research needs. *New Phytologist* 232:1123-1158. doi: 10.1111/nph.17072
- Freschet GT, Valverde-Barrantes OJ, Tucker CM, Craine JM, McCormack ML, Violle C, Fort F, Blackwood CB, Urban-Mead KR, Iversen CM, Bonis A, Comas LH, Cornelissen JHC, Dong M, Guo DL, Hobbie SE, Holdaway RJ, Kembel SW, Makita N, Onipchenko VG, Picon-Cochard C, Reich PB, de la Riva EG, Smith SW, Soudzilovskaia NA, Tjoelker MG, Wardle DA, Roumet C (2017) Climate, soil and plant functional types as drivers of global fine-root trait variation. *Journal of Ecology* 105:1182-1196. doi: 10.1111/1365-2745.12769
- Freytet P, Moissenet E (1983) Remains of algae identifiable in Plio-Quaternary calcrete of northeastern Spain. *Comptes Rendus De L Academie Des Sciences Serie Ii* 296:1563-1566
- Freytet P, Plaziat JC (1982) Continental carbonate sedimentation and pedogenesis : late Cretaceous and early Tertiary of southern France, Contributions to sedimentology 12. E. Schweizerbart, Stuttgart, 213 pp

- Freytet P, Plaziat JC, Verrecchia EP (1997) A classification of rhizogenic (root-formed) calcretes, with examples from the upper Jurassic lower Cretaceous of Spain and upper Cretaceous of southern France - Discussion. *Sedimentary Geology* 110:299-303. doi: 10.1016/s0037-0738(96)00090-5
- Froede CR (2002) Rhizolith evidence in support of a late Holocene sea-level highstand at least 0.5 m higher than present at Key Biscayne, Florida. *Geology* 30:203-206
- Frohlich MW (1984) Freehand Sectioning with Parafilm. *Stain Technology* 59:61-62. doi: 10.3109/10520298409113832
- Gadd GM (2006) *Fungi in biogeochemical cycles*. Cambridge University Press, Cambridge, xix + 469 pp. doi: 10.1017/CBO9780511550522
- Gadd GM (2007) *Geomycology: biogeochemical transformations of rocks, minerals, metals and radionuclides by fungi, bioweathering and bioremediation*. *Mycological Research* 111:3-49. doi: 10.1016/j.mycres.2006.12.001
- Gal A, Weiner S, Addadi L (2015) A perspective on underlying crystal growth mechanisms in biomineralization: solution mediated growth versus nanosphere particle accretion. *Crystengcomm* 17:2606-2615. doi: 10.1039/c4ce01474j
- Garcia-deblas B, Benito B, Rodriguez-Navarro A (2001) Plant cells express several stress calcium ATPases but apparently no sodium ATPase. *Plant and Soil* 235:181-192. doi: 10.1023/a:1011949626191
- Garvie LAJ (2003) Decay-induced biomineralization of the saguaro cactus (*Carnegiea gigantea*). *American Mineralogist* 88:1879-1888
- Garvie LAJ (2006) Decay of cacti and carbon cycling. *Naturwissenschaften* 93:114-118. doi: 10.1007/s00114-005-0069-7
- Genise JF, Alonso-Zarza AM, Krause JM, Sanchez MV, Sarzetti L, Farina JL, Gonzalez MG, Cosarinsky M, Bellosi ES (2010) Rhizolith balls from the Lower Cretaceous of Patagonia: Just roots or the oldest evidence of insect agriculture? *Palaeogeography Palaeoclimatology Palaeoecology* 287:128-142. doi: 10.1016/j.palaeo.2010.01.028
- Genise JF, Bellosi ES, Verde M, Gonzalez MG (2011) Large ferruginized palaeorhizospheres from a Paleogene lateritic profile of Uruguay. *Sedimentary Geology* 240:85-96. doi: 10.1016/j.sedgeo.2011.08.008
- Gibbons W, Moreno T (2002) Introduction and overview. In: Gibbons W, Moreno T (eds) *The Geology of Spain*. The Geological Society, London, pp 1-6
- Giménez-Font P (2013) La dinàmica del paisatge de terrasses de cultiu: algunes reflexions per al seu estudi a la Serra d'Aitana (País Valencià). *Quaderns Agraris* 34 83-98. doi: DOI: 10.2436/20.1503.01.23
- Giménez-Font P, Marco Molina JA (2017) La dinámica del paisaje en la Serra d'Aitana (Alacant, España): síntesis de transformaciones históricas en una montaña mediterránea (1600-2010). *Estudios Geográficos* 78:105-133. doi: 10.3989/estgeogr.201704
- Glaub I, Golubic S, Gektidis M, Radtke G, Vogel K (2007) Microborings and Microbial Endoliths: Geological Implications. In: Miller W (ed) *Trace Fossils: Concepts, Problems, Prospects*. Elsevier, Amsterdam, pp 368-381. doi: /doi.org/10.1016/B978-044452949-7/50147-9
- Glennie KW, Evamy BD (1968) Dikaka - plants and plant-root structures associated with aeolian sand. *Palaeogeography Palaeoclimatology Palaeoecology* 4:77-87. doi: 10.1016/0031-0182(68)90088-6
- Glück H (1912) Eine neue gesteinbildende Siphonee (Codiacee) aus dem marinen Tertiär von



- Südeuschland. Mitteilungen der Grossherzoglich Badischen Geologischen Landesanstalt, Heidelberg 7: 3-24
- Gocke M, Kuzyakov Y, Wiesenberg GLB (2010) Rhizoliths in loess - evidence for post-sedimentary incorporation of root-derived organic matter in terrestrial sediments as assessed from molecular proxies. *Organic Geochemistry* 41:1198-1206. doi: 10.1016/j.orggeochem.2010.08.001
- Gocke M, Peth S, Wiesenberg GLB (2014) Lateral and depth variation of loess organic matter overprint related to rhizoliths - Revealed by lipid molecular proxies and X-ray tomography. *Catena* 112:72-85. doi: 10.1016/j.catena.2012.11.011
- Gocke M, Pustovoytov K, Kuhn P, Wiesenberg GLB, Loscher M, Kuzyakov Y (2011) Carbonate rhizoliths in loess and their implications for paleoenvironmental reconstruction revealed by isotopic composition: delta C-13, (14)c. *Chemical Geology* 283:251-260. doi: 10.1016/j.chemgeo.2011.01.022
- Goebel M, Hobbie SE, Bulaj B, Zadworny M, Archibald DD, Oleksyn J, Reich PB, Eissenstat DM (2011) Decomposition of the finest root branching orders: linking belowground dynamics to fine-root function and structure. *Ecological Monographs* 81:89-102. doi: 10.1890/09-2390.1
- Goldstein RH (1988) Paleosols of Late Pennsylvanian cyclic strata, New Mexico. *Sedimentology* 35:777-803. doi: 10.1111/j.1365-3091.1988.tb01251.x
- Golubic S, Perkins RD, Lukas KJ (1975) Boring Microorganisms and Microborings in Carbonate Substrates. In: Frey RW (ed) *The Study of Trace Fossils*. Springer, Berlin, Heidelberg, pp 229-259. doi: [https://doi.org/10.1007/978-3-642-65923-2\\_12](https://doi.org/10.1007/978-3-642-65923-2_12)
- Golubic S, Radtke G, Le Campion-Alsumard T (2005) Endolithic fungi in marine ecosystems. *Trends in Microbiology* 13:229-235. doi: 10.1016/j.tim.2005.03.007
- Golubic S, Schneider J (2001) Microbial endoliths as internal biofilms Workshop on Fossil and Recent BioFilms, Oldenburg, pp 249-263
- Gomez-Galvez P, Vicente-Munuera P, Tagua A, Forja C, Castro AM, Letran M, Valencia-Exposito A, Grima C, Bermudez-Gallardo M, Serrano-Perez-Higuera O, Cavodeassi F, Sotillos S, Martin-Bermudo MD, Marquez A, Buceta J, Escudero LM (2018) Scutoids are a geometrical solution to three-dimensional packing of epithelia. *Nature Communications* 9. doi: 10.1038/s41467-018-05376-1
- Gorbushina AA, Krumbein WE, Volkmann M (2002) Rock surfaces as life indicators: New ways to demonstrate life and traces of former life. *Astrobiology* 2:203-213
- Goudie AS (1996) Organic agency in calcrete development. *Journal of Arid Environments* 32:103-110. doi: 10.1006/jare.1996.0010
- Gower LB (2008) Biomimetic Model Systems for Investigating the Amorphous Precursor Pathway and Its Role in Biomineralization. *Chemical Reviews* 108:4551-4627. doi: 10.1021/cr800443h
- Graham PH, Vance CP (2003) Legumes: Importance and constraints to greater use. *Plant Physiology* 131:872-877. doi: 10.1104/pp.017004
- Gregory MR, Martin AJ, Campbell KA (2004) Compound trace fossils formed by plant and animal interactions; Quaternary of northern New Zealand and Sapelo Island, Georgia (USA). *Fossils and Strata* 51:88-105
- Gregory PJ (2006) *Plant roots: growth, activity, and interaction with soils*. Blackwell Publishing, Oxford, Ames, Iowa, x + 318 pp
- Gregory PJ, Nortcliff S (2013) *Soil conditions and plant growth*. Wiley-Blackwell, Chichester, West Sussex, UK ix + 461 pp. doi: 10.1002/9781118337295
- Grosjean AS, Pittet B (2013) Facies analysis and depositional environments of the Taulanne

- Limestone Formation in the South Alpine Foreland Basin (Oligocene, southeastern of France). *Facies* 59:717-736. doi: 10.1007/s10347-012-0350-0
- Grosjean AS, Pittet B, Ferry S, Maheo G, Gardien V (2012) Reconstruction of Tertiary palaeovalleys in the South Alpine Foreland Basin of France (Eocene-Oligocene of the Castellane arc). *Sedimentary Geology* 275:1-21. doi: 10.1016/j.sedgeo.2012.05.022
- Grosjean AS, Pittet B, Gardien V, Leloup PH, Maheo G, Garcia JB (2017) Tectonic heritage in drainage pattern and dynamics: the case of the French South Alpine Foreland Basin (ca. 45-20Ma). *Basin Research* 29:26-50. doi: 10.1111/bre.12134
- Gušić I, Jelaska V (1990) Upper Cretaceous stratigraphy of the Island of Brač within the geodynamic evolution of the Adriatic Carbonate Platform. *Djela Jugoslavenske Akademije Znanost i Umjetnosti, Zagreb*, 69:160 p
- Hamon Y, Deschamps R, Joseph P, Garcia D, Chanvry E (2016) New insight of sedimentological and geochemical characterization of siliciclastic-carbonate deposits (Alveolina Limestone Formation, Graus-Tremp basin, Spain). *Bulletin De La Societe Geologique De France* 187:133-153
- Harrison RS (1977) Caliche profiles: indicators of near surface subaerial diagenesis, Barbados, West Indies. *Bulletin of Canadian Petroleum Geology* 25:123-173
- Hartl WP, Klapper H, Barbier B, Ensikat HJ, Dronskowski R, Muller P, Ostendorp G, Tye A, Bauer R, Barthlott W (2007) Diversity of calcium oxalate crystals in Cactaceae. *Canadian Journal Of Botany-Revue Canadienne De Botanique* 85:501-517. doi: 10.1139/b07-046
- Hasenmueller EA, Gu X, Weitzman JN, Adams TS, Stinchcomb GE, Eissenstat DM, Drohan PJ, Brantley SL, Kaye JP (2017) Weathering of rock to regolith: The activity of deep roots in bedrock fractures. *Geoderma* 300:11-31. doi: 10.1016/j.geoderma.2017.03.020
- Hawkesford M, Horst W, Kichey T, Lambers H, Schjoerring J, Møller IS, White P (2012) Chapter 6 - Functions of Macronutrients. In: Marschner P (ed) *Marschner's Mineral Nutrition of Higher Plants (Third Edition)*. Academic Press, San Diego, pp 135-189. doi: <https://doi.org/10.1016/B978-0-12-384905-2.00006-6>
- He HH, Bleby TM, Veneklaas EJ, Lambers H, Kuo J (2012) Precipitation of Calcium, Magnesium, Strontium and Barium in Tissues of Four Acacia Species (Leguminosae: Mimosoideae). *Plos One* 7. doi: 10.1371/journal.pone.0041563
- He HH, Kirilak Y, Kuo J, Lambers H (2015) Accumulation and precipitation of magnesium, calcium, and sulfur in two acacia (Leguminosae; Mimosoideae) species grown in different substrates proposed for mine-site rehabilitation. *American Journal of Botany* 102:290-301. doi: 10.3732/ajb.1400543
- He HH, Veneklaas EJ, Kuo J, Lambers H (2014) Physiological and ecological significance of biomineralization in plants. *Trends in Plant Science* 19:166-174. doi: 10.1016/j.tplants.2013.11.002
- Hearty PJ, Kindler P (1993) New perspectives on Bahamian geology - San Salvador island, Bahamas. *Journal Of Coastal Research* 9:577-594. doi: <https://www.jstor.org/stable/4298108>
- Heidari A, Mahmoodi S, Stoops G, Mees F (2005) Micromorphological characteristics of vertisols of Iran, including nonstnectitic soils. *Arid Land Research And Management* 19:29-46
- Hernández Samaniego A, Navarro Juli JJ, Pascual Muñoz H, Estevez Rubio A, López Arcos M (1993) Mapa geológico y Memoria de la Hoja no. 848 (Benidorm). Mapa geológico de España E. 1:50.000 (MAGNA), Segunda Serie. IGME, 73 pp
- Herrero J, Porta J (1987) Aridisols of Spain. In: Kimble JM (ed) *Proceedings of the 6th International Soil Correlation Meeting, Washington, DC*, pp 61-66

- Herrero J, Porta J (2000) The terminology and the concepts of gypsum-rich soils. *Geoderma* 96:47-61. doi: 10.1016/s0016-7061(00)00003-3
- Herrero J, Porta J, Fedoroff N (1992) Hypergypsic soil micromorphology and landscape relationships in northeastern Spain. *Soil Science Society of America Journal* 56:1188-1194
- Herve V, Clerc M, Cailleau G, Bueche M, Junier T, Verrecchia E, Junier P (2018) Carbonate Accumulation in the Bark of *Terminalia bellirica*: A New Habitat for the Oxalate-Carbonate Pathway. *Geomicrobiology Journal* 35:31-39. doi: 10.1080/01490451.2017.1309087
- Herve V, Simon A, Randevoson F, Cailleau G, Rajoelison G, Razakamanarivo H, Bindschedler S, Verrecchia E, Junier P (2021) Functional Diversity of the Litter-Associated Fungi from an Oxalate-Carbonate Pathway Ecosystem in Madagascar. *Microorganisms* 9. doi: 10.3390/microorganisms9050985
- Hinsinger P (1998) How do plant roots acquire mineral nutrients? Chemical processes involved in the rhizosphere. *Advances In Agronomy*, Vol 64, vol 64, pp 225-265
- Hinsinger P (2013) Plant-induced changes in soil processes and properties. In: Gregory PJ, Nortcliff S (eds) *Soil Conditions and Plant Growth*. Wiley-Blackwell, pp 323-365
- Hinsinger P, Bengough AG, Vetterlein D, Young IM (2009) Rhizosphere: biophysics, biogeochemistry and ecological relevance. *Plant and Soil* 321:117-152. doi: 10.1007/s11104-008-9885-9
- Hinsinger P, Gobran GR, Gregory PJ, Wenzel WW (2005) Rhizosphere geometry and heterogeneity arising from root-mediated physical and chemical processes. *New Phytologist* 168:293-303. doi: 10.1111/j.1469-8137.2005.01512.x
- Hinsinger P, Plassard C, Tang CX, Jaillard B (2003) Origins of root-mediated pH changes in the rhizosphere and their responses to environmental constraints: A review. *Plant and Soil* 248:43-59
- Hirsch AM, Lum MR, Downie JA (2001) What makes the rhizobia-legume symbiosis so special? *Plant Physiology* 127:1484-1492. doi: 10.1104/pp.127.4.1484
- Hladil J, Carew JL, Mylroie JE, Pruner P, Kohout T, Jell JS, Lacka B, Langrova A (2004) Anomalous magnetic susceptibility values and traces of subsurface microbial activity in carbonate banks on San Salvador Island, Bahamas. *Facies* 50:161-182. doi: 10.1007/s10347-004-0013-x
- Hodge A (2015) *Plant Responses to Phosphorus Availability*. eLS. John Wiley & Sons, Ltd, Chichester doi:10.1002/9780470015902.a0021258
- Hofmann BA, Farmer JD, Von Blanckenburg F, Fallick AE (2008) Subsurface filamentous fabrics: An evaluation of origins based on morphological and geochemical criteria, with implications for exopaleontology. *Astrobiology* 8:87-117. doi: 10.1089/ast.2007.0130
- Hollingsworth PM (2011) Refining the DNA barcode for land plants. *Proceedings of the National Academy of Sciences of the United States of America* 108:19451-19452. doi: 10.1073/pnas.1116812108
- Hollingsworth PM, Forrest LL, Spouge JL, Hajibabaei M, Ratnasingham S, van der Bank M, Chase MW, Cowan RS, Erickson DL, Fazekas AJ, Graham SW, James KE, Kim KJ, Kress WJ, Schneider H, van AlphenStahl J, Barrett SCH, van den Berg C, Bogarin D, Burgess KS, Cameron KM, Carine M, Chacon J, Clark A, Clarkson JJ, Conrad F, Devey DS, Ford CS, Hedderson TAJ, Hollingsworth ML, Husband BC, Kelly LJ, Kesanakurti PR, Kim JS, Kim YD, Lahaye R, Lee HL, Long DG, Madrinan S, Maurin O, Meusnier I, Newmaster SG, Park CW, Percy DM, Petersen G, Richardson JE, Salazar GA, Savolainen V, Seberg O, Wilkinson MJ, Yi DK, Little DP, Grp CPW (2009) A DNA barcode for land plants. *Proceedings of the National Academy of Sciences of the United States of America* 106:12794-12797. doi: 10.1073/pnas.0905845106



- Hollingsworth PM, Graham SW, Little DP (2011) Choosing and Using a Plant DNA Barcode. *Plos One* 6. doi: 10.1371/journal.pone.0019254
- Horner HT, Wagner BL (1995) Calcium oxalate formation in higher plants. In: Khan SR (ed) *Calcium oxalate in biological systems*. CRC Press, Boca Raton, Fla. ; London, pp 53-71
- Hornero Díaz JE, García Aróstegui JL, Aragón Rueda R, Rodríguez Estrella T (2009) *Acuíferos de Sierra Aitana y su entorno*. Diputación Provincial de Alicante, Instituto Geológico y Minero de España (IGME), Alicante, 65 pp. <https://ciclohídrico.com/download/el-agua-en-alicante-acuíferos-de-sierra-aitana-y-su-entorno/>
- Huguet A, Bernard S, El Khatib R, Gocke MI, Wiesenberg GLB, Derenne S (2020) Multiple stages of plant root calcification deciphered by chemical and micromorphological analyses. *Geobiology*. doi: 10.1111/gbi.12416
- Huguet A, Wiesenberg GLB, Gocke M, Fosse C, Derenne S (2012) Branched tetraether membrane lipids associated with rhizoliths in loess: Rhizomicrobial overprinting of initial biomarker record. *Organic Geochemistry* 43:12-19. doi: 10.1016/j.orggeochem.2011.11.006
- Huneke H, Joachimski M, Buggisch W, Lutzner H (2001) Marine carbonate facies in response to climate and nutrient level: The Upper Carboniferous and Permian of central Spitsbergen (Svalbard). *Facies* 45:93-135. doi: 10.1007/bf02668107
- HVMO (2021) Virtual Herbarium of the Western Mediterranean (Herbari Virtual del Mediterrani Occidental), Departament de Biologia, Universitat de les Illes Balears. <http://herbarivirtual.uib.es/en/> Retrieved: 23/06/2021
- IAEA (2015) Isotopic composition of precipitation in the Mediterranean Basin in relation to air circulation patterns and climate. Final report of a coordinated research project 2000–2004, IAEA TECDOC 1453, 223 pp
- Igawa T (2003) Microbial contribution to deposition of Upper Carboniferous and Lower Permian seamount-top carbonates, Akiyoshi, Japan. *Facies* 48:61-78. doi: 10.1007/bf02667530
- Imai H (2007) Self-organized formation of hierarchical structures. *Biomaterialization I: Crystallization and Self-Organization Process* 270:43-72. doi: 10.1007/128\_054
- Imai H (2016) Mesostructured crystals: Growth processes and features. *Progress in Crystal Growth and Characterization of Materials* 62:212-226. doi: 10.1016/j.pcrysgrow.2016.04.011
- Immenhauser A, Schlager W, Burns SJ, Scott RW, Geel T, Lehmann J, Van der Gaast S, Bolder-Schrijver LJA (1999) Late Aptian to late Albian sea-level fluctuations constrained by geochemical and biological evidence (Nahr Umr formation, Oman). *Journal of Sedimentary Research* 69:434-446. doi: 10.2110/jsr.69.434
- Immenhauser A, Schlager W, Burns SJ, Scott RW, Geel T, Lehmann J, Van der Gaast S, Bolder-Schrijver LJA (2000) Origin and correlation of disconformity surfaces and marker beds, Nahr Umr Formation, northern Oman. In: Alsharhan AS, Scott RW (eds) *Middle East Models of Jurassic/Cretaceous Carbonate Systems: SEPM Special Publication* 69, pp 209-225
- Ismail-Meyer K, Stolt MH, Lindbo DL (2018) Soil organic matter. In: Stoops G, Marcelino V, Mees F (eds) *Interpretation of Micromorphological Features of Soils and Regoliths*. Second Edition. Elsevier, Amsterdam, pp 471-512. doi: /10.1016/B978-0-444-63522-8.00017-6
- Itkin D, Goldfus H, Monger HC (2016) Human induced calcretisation in anthropogenic soils and sediments: Field observations and micromorphology in a Mediterranean climatic zone, Israel. *Catena* 146:48-61. doi: 10.1016/j.catena.2016.06.025
- IUSS Working Group WRB (2015) World Reference Base for Soil Resources 2014, update 2015. International soil classification system for naming soils and creating legends for soil maps.

- World Soil Resources Reports No. 106. International Union of Soil Sciences, FAO, Rome, 192 pp.  
<https://www.fao.org/3/i3794en/I3794en.pdf>
- Jackson RB, Canadell J, Ehleringer JR, Mooney HA, Sala OE, Schulze ED (1996) A global analysis of root distributions for terrestrial biomes. *Oecologia* 108:389-411
- Jackson RB, Moore LA, Hoffmann WA, Pockman WT, Linder CR (1999) Ecosystem rooting depth determined with caves and DNA. *Proceedings of the National Academy of Sciences of the United States of America* 96:11387-11392
- Jackson RB, Sperry JS, Dawson TE (2000) Root water uptake and transport: using physiological processes in global predictions. *Trends in Plant Science* 5:482-488. doi: 10.1016/s1360-1385(00)01766-0
- Jaillard B (1982) Relation entre dynamique de l'eau et organisation morphologique d'un sol calcaire. *Science du Sol* 20:31-52
- Jaillard B (1983) Mise en évidence de la calcitisation des cellules corticales de racines de Graminées en milieu carbonaté. Evidence of cortical cell calcitization of Gramineae roots in calcareous media. *Comptes Rendus de l'Académie des Sciences Paris, Serie II* 297:293-296
- Jaillard B (1984) Mise en évidence de la néogenèse de sables calcaires sous l'influence des racines: incidence sur la granulométrie du sol. Evidence for the neogenesis of calcareous sands under the influence of roots - incidence on soil granulometry. *Agronomie* 4:91-100
- Jaillard B (1985) Activité racinaire et rhizostructures en milieu carbonaté. *Pedologie* 35:297-313
- Jaillard B (1987a) Les structures rhizomorphes calcaires: modèle de réorganisation des minéraux du sol par les racines Institut National de la Recherche Agronomique, Laboratoire de Science du Sol, Montpellier, p 227
- Jaillard B (1987b) Techniques for studying the ionic environment at the soil/root interface 20th Colloquium of the International Potash Institute, Proceedings, Bern, pp 247-261
- Jaillard B (1992) Calcification des cellules corticales des racines en milieu calcaire. *Bulletin de la Société Botanique de France* 139:41-46
- Jaillard B, Callot G (1987) Action des racines sur la ségrégation minéralogique des constituants du sol. In: Fedoroff N, Bresson LM, Courty MA (eds) *Micromorphologie des Sols – Soil Micromorphology*. Association Française pour l'Étude du Sol, pp 371-375
- Jaillard B, Guyon A, Maurin AF (1991) Structure and composition of calcified roots, and their identification in calcareous soils. *Geoderma* 50:197-210. doi: 10.1016/0016-7061(91)90034-q
- Jaillard B, Hinsinger P (1993) Alimentation minérale des végétaux dans le sol. *Techniques Agricoles* 1210:1-13
- Jaillard B, Plassard C, Hinsinger P (2003) Measurements of H Fluxes and Concentrations in the Rhizosphere. In: Rengel Z (ed) *Handbook of Soil Acidity*. Marcel Dekker, Basel, New York, pp 231-266. doi: DOI: 10.1201/9780203912317.ch9
- James NP (1972) Holocene and Pleistocene calcareous crust (caliche) profiles, criteria for subaerial exposure. *Journal of Sedimentary Petrology* 42:817-836. doi: 10.1306/74d7263f-2b21-11d7-8648000102c1865d
- James NP (1979) Facies Models 11: Reefs. In: Walker RG (ed) *Facies Models*, Geoscience Canada Reprint Series 1. Geological Association of Canada, Toronto, pp 121-132
- James NP, Choquette PW (1984) Diagenesis 9. Limestones - the meteoric diagenetic environment. *Geoscience Canada* 11:161-194
- James NP, Jones B (2016) *Origin of carbonate sedimentary rocks*. AGU/John Wiley & Sons, Inc., Chichester, West Sussex, xiv + 446 pp

- Javid M, Ford R, Nicolas ME (2012) Tolerance responses of *Brassica juncea* to salinity, alkalinity and alkaline salinity. *Functional Plant Biology* 39:699-707. doi: 10.1071/fp12109
- Jenny H (1941) *Factors of soil formation : a system of quantitative pedology*. Reprinted Edition, 1994. Dover Publications : Constable, New York ; London, xviii, 281 p pp
- Jones B (1990) Tunicate spicules and their syntaxial overgrowths - examples from the Pleistocene Ironshore Formation, Grand Cayman, British West Indies. *Canadian Journal of Earth Sciences* 27:525-532. doi: 10.1139/e90-049
- Jones B (1992) Construction of spar calcite crystals around spores. *Journal of Sedimentary Petrology* 62:1054-1057. doi: 10.1306/D4267A46-2B26-11D7-8648000102C1865D
- Jones B (1994) Diagenetic processes associated with plant roots and microorganisms in karst terrains of the Cayman Islands, British West Indies. In: Wolf KH, Chilingarian GV (eds) *Diagenesis IV, Developments in Sedimentology*, vol 52. Elsevier, Amsterdam, pp 425-475
- Jones B, Kahle CF (1993) Morphology, relationship, and origin of fiber and dendrite calcite crystals. *Journal of Sedimentary Petrology* 63:1018-1031
- Jones B, Ng KC (1988) The structure and diagenesis of rhizoliths from Cayman Brac, British-West-Indies. *Journal of Sedimentary Petrology* 58:457-467
- Jones B, Peng X (2014) Abiogenic growth of needle-fiber calcite in spring towers at Shiqiang, Yunnan Province, China. *Journal of Sedimentary Research* 84:1021-1040. doi: 10.2110/jsr.2014.82
- Jones B, Renaut RW (2008) Cyclic development of large, complex, calcite dendrite crystals in the Clinton travertine, Interior British Columbia, Canada. *Sedimentary Geology* 203:17-35. doi: 10.1016/j.sedgeo.2007.10.002
- Jones B, Squair CA (1989) Formation of peloids in plant rootlets, Grand Cayman, British-West-Indies. *Journal of Sedimentary Petrology* 59:1002-1007. doi: 10.1306/212F90D4-2B24-11D7-8648000102C1865D
- Jurkovsek B, Biolchi S, Furlani S, Kolar-Jurkovsek T, Zini L, Jez J, Tunis G, Bavec M, Cucchi F (2016) Geology of the Classical Karst Region (SW Slovenia-NE Italy). *Journal of Maps* 12:352-362. doi: 10.1080/17445647.2016.1215941
- Jurkovšek B, Toman M, Ogorelec B, Šribar L, Drobne K, Poljak M, Šribar L (1996) Geological map of the southern part of the Trieste-Komen Plateau, 1:50.000. Institute of Geology, Geotechnics and Geophysics, Ljubljana, 143 pp
- Kabanov P (2003) The upper Moscovian and basal Kasimovian (Pennsylvanian) of central European Russia: Facies, subaerial exposures and depositional model. *Facies* 49:243-270
- Kabanov P, Anadon P, Krumbein WE (2008) Microcodium: An extensive review and a proposed non-rhizogenic biologically induced origin for its formation. *Sedimentary Geology* 205:79-99. doi: 10.1016/j.sedgeo.2008.02.003
- Kabanov PB (2005) Traces of terrestrial biota in the Upper Moscovian paleosols of central and northern European Russia. *Paleontological Journal* 39:372-385
- Kabanov PB, Alekseeva TV, Alekseeva VA, Alekseev AO, Gubin SV (2010) Paleosols In Late Moscovian (Carboniferous) Marine Carbonates Of The East European Craton Revealing "Great Calcimagnesian Plain" Paleolandscapes. *Journal of Sedimentary Research* 80:195-215. doi: 10.2110/jsr.2010.026
- Kaemmerer M, Revel JC (1991) Calcium-carbonate accumulation in deep strata and calcrete in Quaternary alluvial formations of Morocco. *Geoderma* 48:43-57
- Kaemmerer M, Revel JC (1996) New data on the laminar horizon genesis of calcretes developed on



- Morocco coarse Quaternary alluvium: consequences of the desertification processes. *Arid Soil Research and Rehabilitation* 10:107-123
- Kaemmerer M, Revel JC, Barlier JF (1991) Formation des amas friables et de nodules calcaires dans des sols argileux en régions tempérée et semi-aride. *Science du Sol* 29:1-12
- Kahle CF (1977) Origin of subaerial Holocene calcareous crusts: role of algae, fungi and sparmicritisation. *Sedimentology* 24:413-435. doi: <https://doi.org/10.1111/j.1365-3091.1977.tb00130.x>
- Karabourniotis G, Horner HT, Bresta P, Nikolopoulos D, Liakopoulos G (2020) New insights into the functions of carbon-calcium inclusions in plants. *New Phytologist* 228:845-854. doi: [10.1111/nph.16763](https://doi.org/10.1111/nph.16763)
- Kaygili S, Aksoy E, Jones B, Acar S (2019) The use of Microcodium to identify a paraconformity: An example from the Paleogene sequence of Malatya Basin (eastern Turkey). *Sedimentary Geology* 380:83-93. doi: [10.1016/j.sedgeo.2018.11.015](https://doi.org/10.1016/j.sedgeo.2018.11.015)
- Kelly EF, Chadwick OA, Hilinski TE (1998) The effect of plants on mineral weathering. *Biogeochemistry* 42:21-53. doi: [10.1023/a:1005919306687](https://doi.org/10.1023/a:1005919306687)
- Kenny R, Krinsley DH (1992) Silicified Mississippian paleosol microstructures - evidence for ancient microbial-soil associations. *Scanning Microscopy* 6:359-366
- Kenrick P, Strullu-Derrien C (2014) The Origin and Early Evolution of Roots. *Plant Physiology* 166:570-580. doi: [10.1104/pp.114.244517](https://doi.org/10.1104/pp.114.244517)
- Khalaf FI, Al-Zamel A (2016) Petrography, micromorphology and genesis of Holocene pedogenic calcrete in Al-Jabal Al-Akhdar, Sultanate of Oman. *Catena* 147:496-510. doi: [10.1016/j.catena.2016.07.044](https://doi.org/10.1016/j.catena.2016.07.044)
- Khan SR (1995) Calcium oxalate in biological systems. CRC Press, Boca Raton, Fla. ; London
- Khokhlova OS, Khokhlov AA, Kuznetsova AM, Stolpnikova EM, Kovaleva NO, Lyubin VP, Belyaeva EV (2016) Carbonate features in the uppermost layers of Quaternary deposits, Northern Armenia, and their significance for paleoenvironmental reconstruction. *Quaternary International* 418:94-104. doi: [10.1016/j.quaint.2015.07.035](https://doi.org/10.1016/j.quaint.2015.07.035)
- Khokhlova OS, Kovalevskaya I, Oleynik SA (2001a) Records of climatic changes in the carbonate profiles of Russian Chernozems. *Catena* 43:203-215
- Khokhlova OS, Sedov SN, Golyeva AA, Khokhlov AA (2001b) Evolution of Chernozems in the Northern Caucasus, Russia during the second half of the Holocene: carbonate status of paleosols as a tool for paleoenvironmental reconstruction. *Geoderma* 104:115-133
- Khormali F, Abtahi A, Stoops G (2006) Micromorphology of calcitic features in highly calcareous soils of Fars Province, Southern Iran. *Geoderma* 132:31-46
- Kindle EM (1923) Range and distribution of certain types of Canadian Pleistocene concretions. *Geological Society of America Bulletin* 34: 609-648. doi: <https://doi.org/10.1130/GSAB-34-609>
- Kindle EM (1925) A note on rhizocretions. *The Journal of Geology* 33:744-746. doi: <https://doi.org/10.1086/623245>
- Kindler P, Hearty PJ (1997) Geology of the Bahamas: Architecture of the Bahamian islands. In: Vacher H, Quinn T (eds) *Geology and Hydrogeology of Carbonate Islands*. *Developments in Sedimentology* 54. Elsevier Science B.V., Amsterdam, pp 141-160
- Kirkham MB (2014) Principles of soil and plant water relations. Academic Press, Elsevier, Amsterdam, 520 pp. <https://doi.org/10.1016/C2013-0-12871-1>
- Klappa CF (1978a) Biolithogenesis of Microcodium: elucidation. *Sedimentology* 25:489-522. doi: [10.1111/j.1365-3091.1978.tb02077.x](https://doi.org/10.1111/j.1365-3091.1978.tb02077.x)

- Klappa CF (1978b) Morphology, composition and genesis of quaternary calcretes from the Western Mediterranean: A petrographic approach. PhD Thesis, University of Liverpool
- Klappa CF (1979) Calcified filaments in Quaternary calcretes: organomineral interactions in the subaerial vadose environment. *Journal of Sedimentary Petrology* 49:955-968. doi: 10.2110/jsr.49.955
- Klappa CF (1980a) Brecciation textures and tepee structures in Quaternary calcrete (caliche) profiles from eastern Spain: the plant factor in their formation. *Geological Journal* 15:81-89.
- Klappa CF (1980b) Rhizoliths in terrestrial carbonates: classification, recognition, genesis and significance. *Sedimentology* 27:613-629. doi: 10.1111/j.1365-3091.1980.tb01651.x
- Koch PL (1998) Isotopic reconstruction of past continental environments. *Annual Review of Earth And Planetary Sciences* 26:573-613. doi: 10.1146/annurev.earth.26.1.573
- Kohn MJ, Cerling TE (2002) Stable isotope compositions of biological apatite. In: Kohn MJ, Rakovan J, Hughes JM (eds) *Phosphates. Geochemical, Geobiological, and Materials Importance. Reviews in Mineralogy and Geochemistry*, v. 48. Mineralogical Society of America, Washington, D. C., pp 455-488. doi: <https://doi.org/10.2138/rmg.2002.48.12>
- Kolo K, Claeys P (2005) In vitro formation of Ca-oxalates and the mineral glushinskite by fungal interaction with carbonate substrates and seawater. *Biogeosciences* 2:277-293
- Kolo K, Keppens E, Preat A, Claeys P (2007) Experimental observations on fungal diagenesis of carbonate substrates. *Journal of Geophysical Research-Biogeosciences* 112. doi: 10.1029/2006jg000203
- Kornicker LS (1958) Bahamian limestone crusts. *Gulf Coast Association of Geological Societies Transactions* 8:167-170
- Košir A (1997) Eocene platform-to-basin depositional sequence, southwestern Slovenia. *Gaea Heidelbergensis* 3:205
- Košir A (1998) Rhizogenic calcretes from a shallow-marine carbonate succession, Paleocene of SW Slovenia (abstract) British Sedimentology Research Group, 37th Annual Meeting, London, p 34
- Košir A (2004) Microcodium revisited: Root calcification products of terrestrial plants on carbonate-rich substrates. *Journal of Sedimentary Research* 74:845-857. doi: 10.1306/040404740845
- Košir A, Martín-Pérez A (2018) Growth mechanisms of needle fibre calcite : is microbial metabolism involved? (abstract) International Sedimentological Congress. A sedimentary journey through 3 billion years in the new world, Québec.
- Košir A, Otoničar B (2001) The evolution of Upper Cretaceous and Palaeogene synorogenic carbonate platforms in NW Dinaric foreland basin In: Dragičević I, Velić I (eds) *Carbonate Platform(s) of the Dinarides*, Abstracts. University of Zagreb, Zagreb, pp 62-63
- Kramer PJ (1983) *Water relations of plants*. Academic Press Inc., New York, xi + 489 pp
- Kraus MJ (1999) Paleosols in clastic sedimentary rocks: their geologic applications. *Earth-Science Reviews* 47:41-70. doi: 10.1016/S0012-8252(99)00026-4
- Kress WJ (2017) Plant DNA barcodes: Applications today and in the future. *Journal of Systematics and Evolution* 55:291-307. doi: 10.1111/jse.12254
- Kress WJ, Erickson DL (2007) A Two-Locus Global DNA Barcode for Land Plants: The Coding rbcL Gene Complements the Non-Coding trnH-psbA Spacer Region. *Plos One* 2. doi: 10.1371/journal.pone.0000508
- Kress WJ, García-Robledo C, Uriarte M, Erickson DL (2015) DNA barcodes for ecology, evolution, and conservation. *Trends in Ecology & Evolution* 30:25-35. doi: /10.1016/j.tree.2014.10.008

- Kress WJ, Wurdack KJ, Zimmer EA, Weigt LA, Janzen DH (2005) Use of DNA barcodes to identify flowering plants. *Proceedings of the National Academy of Sciences of the United States of America* 102:8369-8374. doi: 10.1073/pnas.0503123102
- Krings M, Taylor TN, Taylor EL, Dotzler N, Walker C (2011) Arbuscular mycorrhizal-like fungi in Carboniferous arborescent lycopsids. *New Phytologist* 191:311–314
- Krklec K, Dominguez-Villar D, Perica D (2015) Depositional environments and diagenesis of a carbonate till from a Quaternary paleoglacier sequence in the Southern Velebit Mountain (Croatia). *Palaeogeography Palaeoclimatology Palaeoecology* 436:188-198. doi: 10.1016/j.palaeo.2015.07.004
- Krumbein WE, Jens K (1981) Biogenic rock varnishes of the Negev Desert (Israel): An ecological study of iron and manganese transformation by cyanobacteria and fungi. *Oecologia* 50:25-38. doi: 10.1007/bf00378791
- Krumbein WE, Paterson DM, Zavarzin GA (2003) Fossil and recent biofilms : a natural history of life on Earth. Kluwer Academic Publishers, Dordrecht ; Boston, xxi, 482 p. pp
- Kumar P, Hallgren SW, Enstone DE, Peterson CA (2007) Root anatomy of *Pinus taeda* L.: seasonal and environmental effects on development in seedlings. *Trees-Structure and Function* 21:693-706. doi: 10.1007/s00468-007-0162-y
- Kump LR, Kasting JF, Crane RG (2010) *The earth system*, 3rd edn. Pearson - Prentice Hall, San Francisco, xi, 420 pp
- Kutschera L, Lichtenegger E (2013) *Wurzelatlas mitteleuropäischer Waldbäume und Straucher*, 6. Band der Wurzelatlas-Reihe, 2. Auflage, Graz-Stuttgart, 604 pp
- Kutschera L, Lichtenegger E, Sobotik M (1992) *Wurzelatlas mitteleuropäischer Grünlandpflanzen. Band 2: Pteridophyta und Dicotyledoneae (Magnoliopsida) Teil 2 Anatomie*. Gustav Fischer Verlag, Jena, 261 pp
- Kutschera L, Sobotik M, Haas D (1997) *Wurzeln: Bevurzelung von Pflanzen in verschiedenen Lebensräumen*. 5. Band der Wurzelatlas-Reihe. *Stapfia* 49, Linz, 331 pp
- Kuznetsov VG, Olenova KY (2012) Lower permian deposits in the northern Kolva megaswell (Timan-Pechora plate): Lithology, formation conditions, and structure of petroleum reservoirs. *Lithology and Mineral Resources* 47:334-354. doi: 10.1134/s0024490212040049
- Kuzyakov Y, Razavi BS (2019) Rhizosphere size and shape: Temporal dynamics and spatial stationarity. *Soil Biology & Biochemistry* 135:343-360. doi: 10.1016/j.soilbio.2019.05.011
- Labourdette R (2011) Stratigraphy and static connectivity of braided fluvial deposits of the lower Escanilla Formation, south central Pyrenees, Spain. *Aapg Bulletin* 95:585-617. doi: 10.1306/08181009203
- Labourdette R, Jones RR (2007) Characterization of fluvial architectural elements using a three-dimensional outcrop data set: Escanilla braided system, South-Central Pyrenees, Spain. *Geosphere* 3:422-434. doi: 10.1130/ges00087.1
- Lacka B, Lanczont M, Madeyska T (2009) Oxygen and carbon stable isotope composition of authigenic carbonates in loess sequences from the Carpathian margin and Podolia, as a palaeoclimatic record. *Quaternary International* 198:136-151. doi: 10.1016/j.quaint.2008.02.001
- Lal R (2003) Global potential of soil carbon sequestration to mitigate the greenhouse effect. *Critical Reviews in Plant Sciences* 22:151-184. doi: 10.1080/713610854
- Lal R (2004) Soil carbon sequestration impacts on global climate change and food security. *Science* 304:1623-1627. doi: 10.1126/science.1097396
- Lal R, Kimble JM (2000) Pedogenic carbonates and the global carbon cycle. In: Lal R, Kimble JM,



- Eswaran H, Stewart BA (eds) *Global Climate Change and Pedogenic Carbonates*. CRC Press, Lewis Publishers, Boca Raton, pp 1-14
- Lal R, Kimble JM, Eswaran H, Stewart BA (2000) *Global climate change and pedogenic carbonates*. Lewis Publishers, Boca Raton, Fla., 305 pp
- Lambers H, Mougél C, Jaillard B, Hinsinger P (2009) Plant-microbe-soil interactions in the rhizosphere: an evolutionary perspective. *Plant and Soil* 321:83-115. doi: 10.1007/s11104-009-0042-x
- Lambers H, Raven JA, Shaver GR, Smith SE (2008) Plant nutrient-acquisition strategies change with soil age. *Trends in Ecology & Evolution* 23:95-103. doi: 10.1016/j.tree.2007.10.008
- Lambers H, Shane MW, Cramer MD, Pearse SJ, Veneklaas EJ (2006) Root structure and functioning for efficient acquisition of phosphorus: Matching morphological and physiological traits. *Annals of Botany* 98:693-713. doi: 10.1093/aob/mcl114
- Landeweert R, Hoffland E, Finlay RD, Kuyper TW, van Breemen N (2001) Linking plants to rocks: ectomycorrhizal fungi mobilize nutrients from minerals. *Trends in Ecology & Evolution* 16:248-254. doi: 10.1016/s0169-5347(01)02122-x
- Landing E, Westrop SR, Bowring SA (2013) Reconstructing the Avalonia palaeocontinent in the Cambrian: A 519 Ma caliche in South Wales and transcontinental middle Terreneuvian sandstones. *Geological Magazine* 150:1022-1046. doi: 10.1017/s0016756813000228
- Landrein P, Loreau JP, Fleury JJ (2001b) Intra-Maastrichtian subaerial exposure of the Gavrovo-Tripolitza carbonate platform (Greece): effect on endemic associations of Rhapydionininae (Foraminifera, Alveolinacea). *Bulletin de la Societe Geologique de France* 172:85-98. doi: 10.2113/172.1.85
- Lapointe PA, Barnett AJ, Kabanov P (2005) Unusually Thick Microcodium Occurrences in Early Permian Carbonates, Timan Pechora Oil Field (CIS): Origin and Significance for Reservoir Properties. *AAPG Search and Discovery*, Article #90039
- Lauenroth WK, Gill R (2003) Turnover of root systems. In: de Kroon H, Visser EJW (eds) *Root ecology*. Springer, Berlin, pp 61-90. doi: DOI: 10.1007/978-3-662-09784-7\_3
- Laurain M, Meyer R (1979) Paleo-weathering and paleosol: pedological calcrete at the top of chalk under Eocene sediments in the Montagne-de-Reims. *Comptes Rendus Hebdomadaires Des Seances De L Academie Des Sciences Serie D* 289:1211-1214
- Lawrence E (2005) *Henderson's dictionary of biology*, 13th Edition. Pearson, Benjamin Cummings, London, 748 pp
- Leadbeater BSC, Riding R (1986) *Biom mineralization in Lower Plants and Animals*. Clarendon Press, Oxford
- Lee JA (1998) The calcicole—calcifuge problem revisited. *Advances in Botanical Research Incorporating Advances in Plant Pathology*, Vol 29 29:1-30. doi: 10.1016/S0065-2296(08)60306-7
- Legall B, Poncet J (1983) The Lizard Front (Cornwall, England) - a main tectonic contact underlined by paleozoic limestone slices. *Comptes Rendus De L Academie Des Sciences Serie Ii* 296:1683-&
- Lehman TM (1989) Upper Cretaceous (Maastrichtian) Paleosols In Trans Pecos Texas. *Geological Society of America Bulletin* 101:188-203. doi: 10.1130/0016-7606(1989) 101<0188:ucmpit> 2.3.co;2
- Lekach J, Amit R, Grodek T, Schick AP (1998) Fluvio-pedogenic processes in an ephemeral stream channel, Nahal Yael, southern Negev, Israel. *Geomorphology* 23:353-369. doi: 10.1016/s0169-555x(98)00015-4
- Leret Verdú G, Lendínez González A (1978) Mapa geológico y Memoria de la Hoja no. 872 (Alicante). Mapa geológico de España E. 1:50.000 (MAGNA), Segunda Serie. IGME, 33 pp

- Letsch D, Kiefer L (2017) A marine pebbly mudstone from the Swiss Alps: palaeotectonic implications and some consequences for the interpretation of Precambrian diamictites. *Swiss Journal of Geosciences* 110:753-776. doi: 10.1007/s00015-017-0275-2
- Li J, Hu XM, Garzanti E, BouDagher-Fadel M (2021) Climate-driven hydrological change and carbonate platform demise induced by the Paleocene-Eocene Thermal Maximum (southern Pyrenees). *Palaeogeography Palaeoclimatology Palaeoecology* 567. doi: 10.1016/j.palaeo.2021.110250
- Li R, Jones B (2014) Calcareous crusts on exposed Pleistocene limestones: A case study from Grand Cayman, British West Indies. *Sedimentary Geology* 299:88-105. doi: 10.1016/j.sedgeo.2013.10.003
- Li T, Li GJ (2014) Incorporation of trace metals into microcodium as novel proxies for paleo-precipitation. *Earth and Planetary Science Letters* 386:34-40. doi: 10.1016/j.epsl.2013.10.011
- Li ZL, Wang NA, Cheng HY, Ning K, Zhao LQ, Li RL (2015a) Formation and environmental significance of late Quaternary calcareous root tubes in the deserts of the Alashan Plateau, northwest China. *Quaternary International* 372:167-174. doi: 10.1016/j.quaint.2014.11.021
- Li ZL, Wang NA, Li RL, Ning K, Cheng HY, Zhao LQ (2015b) Indication of millennial-scale moisture changes by the temporal distribution of Holocene calcareous root tubes in the deserts of the Alashan Plateau, Northwest China. *Palaeogeography Palaeoclimatology Palaeoecology* 440:496-505. doi: 10.1016/j.palaeo.2015.09.023
- Li ZL, Zhu RX, Gao YH, Chim CH, Liao H (2020) Recrystallization of Holocene calcareous root tubes in the Tengger Desert, Northwest China and its effects on the reliability of paleoenvironmental reconstruction results. *Quaternary International* 562:85-93. doi: 10.1016/j.quaint.2020.07.005
- Liang T, Jones B (2015) Petrographic and geochemical features of sinkhole-filling deposits associated with an erosional unconformity on Grand Cayman. *Sedimentary Geology* 315:64-82. doi: 10.1016/j.sedgeo.2014.10.010
- Lidz BH, Shinn EA, Hudson JH, Multer HG, Halley RB, Robbin DM (2008) Controls on Late Quaternary coral reefs of the Florida Keys. In: Riegl BM, Dodge RE (eds) *Coral Reefs of the USA. Coral Reefs of the World, vol 1*. Springer Science + Business Media, Dordrecht, pp 9-74. doi: [https://doi.org/10.1007/978-1-4020-6847-8\\_2](https://doi.org/10.1007/978-1-4020-6847-8_2)
- Linder CR, Moore LA, Jackson RB (2000) A universal molecular method for identifying underground plant parts to species. *Molecular Ecology* 9:1549-1559
- Linnaeus C (1770) *Systema naturae per regna tria naturæ, secundum classes, ordines, genera, species*. Tomus III. Ioannis Thomae Trattner, Vienna, 236+ pp
- Lintern MJ (2015) The association of gold with calcrete. *Ore Geology Reviews* 66:132-199. doi: 10.1016/j.oregeorev.2014.10.029
- Liutkus CM (2009) Using petrography and geochemistry to determine the origin and formation mechanism of calcitic plant molds; rhizolith or tufa? *Journal of Sedimentary Research* 79:906-917. doi: 10.2110/jsr.2009.093
- Liutkus CM, Wright JD, Ashley GM, Sikes NE (2005) Paleoenvironmental interpretation of lake-margin deposits using delta C-13 and delta O-18 results from early Pleistocene carbonate rhizoliths, Olduvai Gorge, Tanzania. *Geology* 33:377-380. doi: 10.1130/g21132.1
- Loisy C, Verrecchia EP, Dufour P (1999) Microbial origin for pedogenic micrite associated with a carbonate paleosol (Champagne, France). *Sedimentary Geology* 126:193-204
- Lonoy A (1995) A Midcarboniferous, carbonate-dominated platform, central Spitsbergen. *Norsk Geologisk Tidsskrift* 75:48-63

- Loope DB (1988) Rhizoliths in ancient eolianites. *Sedimentary Geology* 56:301-314. doi: 10.1016/0037-0738(88)90058-9
- López B, Sabaté S, Gracia C (1998) Fine roots dynamics in a Mediterranean forest: effects of drought and stem density. *Tree Physiology* 18:601-606. doi: <https://doi.org/10.1093/treephys/18.8-9.601>
- Lowenstam HA (1981) Minerals formed by organisms. *Science* 211:1126-1131. doi: DOI: 10.1126/science.7008198
- Lowenstam HA, Weiner S (1989) *On biomineralization*. Oxford University Press, New York, ix, 324 pp. doi: 10.1093/oso/9780195049770.001.0001
- Lucas G, Montenat C (1967) Observations sur les structures internes et de développement des *Microcodium*. *Bulletin De La Societe Geologique De France* 7 909-918, pl 933b
- Lucas Y (2001) The role of plants in controlling rates and products of weathering: Importance of biological pumping. *Annual Review of Earth And Planetary Sciences* 29:135-163. doi: 10.1146/annurev.earth.29.1.135
- Luo X, Wang H, An ZS, Zhang ZK, Liu WG (2020) Carbon and oxygen isotopes of calcified root cells, carbonate nodules and total inorganic carbon in the Chinese loess-paleosol sequence: The application of paleoenvironmental studies. *Journal of Asian Earth Sciences* 201. doi: 10.1016/j.jseaes.2020.104515
- Luterbacher H-P, Eichenseer E, Betzler C, Van Den Hurk AM (1991) Carbonate-siliciclastic depositional systems in the Paleogene of the South Pyrenean foreland basin: a sequence stratigraphic approach. In: Macdonald DIM (ed) *Sedimentation, Tectonics and Eustasy; Sea Level Changes at Active Margins: International Association of Sedimentologists, Special Publication, vol 12*, pp 391-407. doi: 10.1002/9781444303896.ch21
- Lynch JP (2005) Root architecture and nutrient acquisition. In: BassiriRad H (ed) *Nutrient Acquisition by Plants. An Ecological Perspective*, vol 181. Springer-Verlag, Berlin, Heidelberg, pp 147-183
- Lynch JP, Chimungu JG, Brown KM (2014) Root anatomical phenes associated with water acquisition from drying soil: targets for crop improvement. *Journal of Experimental Botany* 65:6155-6166. doi: 10.1093/jxb/eru162
- Machel HG (2000) Application of cathodoluminescence to carbonate diagenesis. In: Pagel M, Barbin V, Blanc P, Ohnenstetter D (eds) *Cathodoluminescence in Geosciences*. Springer, Berlin, pp 271-301. doi: 10.1007/978-3-662-04086-7\_11
- Mack GH, James WC (1992) Calcic paleosols of the Pliopleistocene Camp Rice and Palomas Formations, Southern Rio-Grande Rift, USA. *Sedimentary Geology* 77:89-109. doi: 10.1016/0037-0738(92)90105-z
- Mack GH, James WC, Monger HC (1993) Classification of paleosols. *Geological Society of America Bulletin* 105:129-136. doi: 10.1130/0016-7606(1993)105<0129:cop>2.3.co;2
- Mackenzie FT, Lerman A (2006) *Carbon in the Geobiosphere. Earth's Outer Shell*. Springer, xxi + 402 pp
- Maeght JL, Rewald B, Pierret A (2013) How to study deep roots - and why it matters. *Frontiers in Plant Science* 4:14. doi: 10.3389/fpls.2013.00299
- Maestre FT, Cortina J (2004) Are *Pinus halepensis* plantations useful as a restoration tool in semiarid Mediterranean areas? *Forest Ecology and Management* 198:303-317. doi: 10.1016/j.foreco.2004.05.040
- Maestre FT, Cortina J, Bautista S, Bellot J (2003) Does *Pinus halepensis* facilitate the establishment of shrubs in Mediterranean semi-arid afforestations? *Forest Ecology and Management* 176:147-160. doi: 10.1016/s0378-1127(02)00269-4



- Mallol C (2006) What's in a beach? Soil micromorphology of sediments from the Lower Paleolithic site of 'Ubeidiya, Israel. *Journal of Human Evolution* 51:185-206. doi: 10.1016/j.jhevol.2006.03.002
- Mamet B, Preat A (1985) Presence Of Palaeomicrocodium (Alga-Questionable Incertae Sedis-Questionable) In The Lower Givetian Of Belgium. *Geobios* 18:389-&. doi: 10.1016/s0016-6995(85)80101-7
- Mamet BL, Roux A (1982) The Presence Of Microcodium (Alga, Incertae-Sedis) In The Upper Paleozoic Of The Canadian Arctic. *Canadian Journal of Earth Sciences* 19:357-363. doi: 10.1139/e82-027
- Mandic O, de Leeuw A, Vukovic B, Krijgsman W, Harzhauser M, Kuiper KF (2011) Palaeoenvironmental evolution of Lake Gacko (Southern Bosnia and Herzegovina): Impact of the Middle Miocene Climatic Optimum on the Dinaride Lake System. *Palaeogeography Palaeoclimatology Palaeoecology* 299:475-492. doi: 10.1016/j.palaeo.2010.11.024
- Mann S (2001) *Biom mineralization : principles and concepts in bioinorganic materials chemistry*. Oxford University Press, New York, xii, 198 p. pp
- Marchetti M, Capela D, Glew M, Cruveiller S, Chane-Woon-Ming B, Gris C, Timmers T, Poinso V, Gilbert LB, Heeb P, Medigue C, Batut J, Masson-Boivin C (2010) Experimental Evolution of a Plant Pathogen into a Legume Symbiont. *Plos Biology* 8. doi: 10.1371/journal.pbio.1000280
- Marco Molina JA, Alfaro P, Delgado J, Tomás R, Estévez A (2004) Sierra de Aitana. In: Alfaro P, Andreu JM, Estévez A, Tent-Manclús JE, Yébenes A (eds) *Geología de Alicante*. Universidad de Alicante, Instituto de Ciencias de la Educación, San Vicente del Raspeig, pp 201-224. doi: 10.13140/RG.2.1.3244.4000.
- Marie P (1957) Sur quelques gisements français à Microcodium. *Compte Rendu Sommaire des Séances de la Société Géologique de France* 10:171-175
- Marschner H (1995) *Mineral nutrition of higher plants*, 2nd edn. Academic Press, Amsterdam, London, xv + 889 pp
- Marschner P (2012) Chapter 15 - Rhizosphere Biology. In: Marschner P (ed) *Marschner's Mineral Nutrition of Higher Plants (Third Edition)*. Academic Press, San Diego, pp 369-388. doi: <https://doi.org/10.1016/B978-0-12-384905-2.00015-7>
- Marschner P, Rengel Z (2012) Chapter 12 - Nutrient Availability in Soils. In: Marschner P (ed) *Marschner's Mineral Nutrition of Higher Plants (Third Edition)*. Academic Press, San Diego, pp 315-330. doi: <https://doi.org/10.1016/B978-0-12-384905-2.00012-1>
- Marshall JD, Brooks JR, Lajtha K (2007) Sources of Variation in the Stable Isotopic Composition of Plants. In: Michener R, Lajtha K (eds) *Stable Isotopes in Ecology and Environmental Science*, Second Edition. Blackwell Publishing Ltd, Oxford, UK, pp 22-60. doi: <https://doi.org/10.1002/9780470691854.ch2>
- Martin G, Guggiari M, Bravo D, Zopfi J, Cailleau G, Aragno M, Job D, Verrecchia E, Junier P (2012) Fungi, bacteria and soil pH: the oxalate-carbonate pathway as a model for metabolic interaction. *Environmental Microbiology* 14:2960-2970. doi: 10.1111/j.1462-2920.2012.02862.x
- Martin RE (1999) *Taphonomy. A Process Approach*. Cambridge University Press, Cambridge, UK, xvi + 508 pp
- Martín-Pérez A, Košir A (2017a) Biogenicity of fibrous microcrystalline calcite in vadose terrestrial settings (abstract) *Sticking together : microbes and their role in forming sediments*. Abstract book. The Geological Society, London, p 87
- Martín-Pérez A, Košir A (2017b) The origin of fibrous microcrystalline calcite : abiotic, biotic

- or polymer induced? (abstract) Goldschmidt 2017 Conference, Paris, France, <https://goldschmidtabstracts.info/2017/2607.pdf>
- Martín-Pérez A, Košir A, Johnston VE, Mulec J, Franko M (2019a) Microbialites underground? Mafics, microbiology and water chemistry of moonmilk speleothems in Slovenian caves M-Fed, Microbialites: Formation, Evolution, Diagenesis Conference & Workshop, Dijon, October 2019, p 62
- Martín-Pérez A, Mulec J, Johnston VE, Skok S, Simič T, Košir A (2019b) Microbiological characterization of moonmilk speleothems from Snežna jama na Raduhi and Koševka Cave, Slovenia In: Blatnik M (ed) Karst hydrogeology - research trends and applications: abstracts & guide book, Postojna, p 114
- Martin-Martin M, Guerrero F, Tosquella J, Tramontana M (2020) Paleocene-Lower Eocene carbonate platforms of westernmost Tethys. *Sedimentary Geology* 404. doi: 10.1016/j.sedgeo.2020.105674
- Martin-Chivelet J, Gimenez R (1992) Paleosols In Microtidal Carbonate Sequences, Sierra-De-Utiel Formation, Upper Cretaceous, Se Spain. *Sedimentary Geology* 81:125-145. doi: 10.1016/0037-0738(92)90060-5
- Martínez del Olmo W, Colodrón Gómez I, Núñez Galiano A (1978) Mapa geológico y Memoria de la Hoja no. 846 (Castalla). Mapa geológico de España E. 1:50.000 (MAGNA), Segunda Serie. IGME, 32 pp
- Martinez F, Lazo YO, Fernandez-Galiano RM, Merino JA (2002) Chemical composition and construction cost for roots of Mediterranean trees, shrub species and grassland communities. *Plant Cell and Environment* 25:601-608. doi: 10.1046/j.1365-3040.2002.00848.x
- Martinez F, Merino O, Martín A, García Martín D, Merino J (1998) Belowground structure and production in a Mediterranean sand dune shrub community. *Plant and Soil* 201:209–216
- Marty F (1999) Plant vacuoles. *The Plant Cell* 11:587–599
- Matteucci R, Murru M (2002) Early Tertiary Microcodium from Sardinia, Italy. *Bollettino Della Societa Geologica Italiana* 121:289-296
- McConnaughey T (1989a) C-13 and O-18 isotopic disequilibrium in biological carbonates: 1. patterns. *Geochimica Et Cosmochimica Acta* 53:151-162
- McConnaughey T (1989b) C-13 and O-18 isotopic disequilibrium in biological carbonates: 2. Invitro simulation of kinetic isotope effects. *Geochimica Et Cosmochimica Acta* 53:163-171
- McConnaughey T (1998) Acid secretion, calcification, and photosynthetic carbon concentrating mechanisms. *Canadian Journal Of Botany-Revue Canadienne De Botanique* 76:1119-1126
- McConnaughey TA (2003) Sub-equilibrium oxygen-18 and carbon-13 levels in biological carbonates: carbonate and kinetic models. *Coral Reefs* 22:316-327
- McConnaughey TA (2012) Zooxanthellae that open calcium channels: implications for reef corals. *Marine Ecology Progress Series* 460:277-287. doi: 10.3354/meps09776
- McConnaughey TA, Whelan JF (1997) Calcification generates protons for nutrient and bicarbonate uptake. *Earth-Science Reviews* 42:95-117. doi: 10.1016/S0012-8252(96)00036-0
- McCormack ML, Dickie IA, Eissenstat DM, Fahey TJ, Fernandez CW, Guo DL, Helmisaari HS, Hobbie EA, Iversen CM, Jackson RB, Leppalammi-Kujansuu J, Norby RJ, Phillips RP, Pregitzer KS, Pritchard SG, Rewald B, Zadworny M (2015) Redefining fine roots improves understanding of below-ground contributions to terrestrial biosphere processes. *New Phytologist* 207:505-518. doi: 10.1111/nph.13363

- McCormick EL, Dralle DN, Hahm WJ, Tune AK, Schmidt LM, Chadwick KD, Rempe DM (2021) Widespread woody plant use of water stored in bedrock. *Nature* 597:225-+. doi: 10.1038/s41586-021-03761-3
- McCully M (1995) How do real roots work - some new views of root structure. *Plant Physiology* 109:1-6. doi: 10.1104/pp.109.1.1
- McCully ME (1999) Roots in soil: Unearthing the complexities of roots and their rhizospheres. *Annual Review of Plant Physiology and Plant Molecular Biology* 50:695-718
- McKee ED, Ward WC (1983) Eolian environment. In: Scholle PA, Bebout DG, Moore CH (eds) *Carbonate Depositional Environments: American Association of Petroleum Geologists, Memoir*, vol 33, pp 131-170
- McKee KL (2001) Root proliferation in decaying roots and old root channels: a nutrient conservation mechanism in oligotrophic mangrove forests? *Journal of Ecology* 89:876-887. doi: 10.1046/j.0022-0477.2001.00606.x
- McKenzie BE, Peterson CA (1995a) Root browning in *Pinus banksiana* Lamb. and *Eucalyptus pilularis* Sm. 1. Anatomy and permeability of the white and tannin zones. *Botanica Acta* 108:127-137. doi: 10.1111/j.1438-8677.1995.tb00842.x
- McKenzie BE, Peterson CA (1995b) Root browning in *Pinus banksiana* Lamb. and *Eucalyptus pilularis* Sm. 2. Anatomy and permeability of the cork zone. *Botanica Acta* 108:138-143. doi: 10.1111/j.1438-8677.1995.tb00842.x
- McLaren S (2004) Characteristics, evolution and distribution of quaternary channel Calcretes, Southern Jordan. *Earth Surface Processes and Landforms* 29:1487-1507. doi: 10.1002/esp.1135
- McLaren S, Gardner R (2004) Late quaternary vadose carbonate diagenesis in coastal and desert dune and beach sands: Is there a palaeoclimatic signal? *Earth Surface Processes and Landforms* 29:1441-1458. doi: 10.1002/esp.1132
- McLaren SJ (1995) Early Carbonate Diagenetic Fabrics In The Rhizosphere Of Late Pleistocene Aeolian Sediments. *Journal of the Geological Society* 152:173-181. doi: 10.1144/gsjgs.152.1.0173
- McLoughlin N, Brasier MD, Wacey D, Green OR, Perry RS (2007) On biogenicity criteria for endolithic microborings on early earth and beyond. *Astrobiology* 7:10-26. doi: 10.1089/ast.2006.0122
- Meldrum FC (2003) Calcium carbonate in biomineralisation and biomimetic chemistry. *International Materials Reviews* 48:187-224. doi: 10.1179/095066003225005836
- Meldrum FC, Colfen H (2008) Controlling Mineral Morphologies and Structures in Biological and Synthetic Systems. *Chemical Reviews* 108:4332-4432. doi: 10.1021/cr8002856
- Melim LA, Masferro JL (1997) Geology of the Bahamas: Subsurface geology of the Bahamas banks. Chapter 3. In: Vacher HL, Quinn T (eds) *Geology and Hydrogeology of Carbonate Islands. Developments in Sedimentology* 54, vol 54. Elsevier Science B.V., Amsterdam, pp 161-182. doi: DOI: 10.1016/S0070-4571(04)80025-6
- Melis MT, Loddo S (2012) Landforms and soils. In: Vogiatzakis IN (ed) *Mediterranean Mountain Environments*. John Wiley & Sons, Ltd., Chichester, West Sussex, Hoboken, NJ, pp 65-85
- Menezes MN, Araujo HI, Dal' Bo PE, Medeiros MAA (2019) Integrating ichnology and paleopedology in the analysis of Albian alluvial plains of the Parnaiba Basin, Brazil. *Cretaceous Research* 96:210-226. doi: 10.1016/j.cretres.2018.12.013
- Meyer CJ, Peterson CA (2013) Structure and function of three suberized cell layers: Epidermis, exodermis and endodermis. In: Eshel A, Beekman T (eds) *Plant Roots: The Hidden Half*, Fourth Edition. CRC Press, Boca Raton, pp 5-1 – 5-20



- Miller CR, James NP, Bone Y (2012) Prolonged carbonate diagenesis under an evolving late cenozoic climate; Nullarbor Plain, southern Australia. *Sedimentary Geology* 261:33-49. doi: 10.1016/j.sedgeo.2012.03.002
- Miller CR, James NP, Kyser TK (2013) Genesis of blackened limestone clasts at Late Cenozoic subaerial exposure surfaces, Southern Australia. *Journal of Sedimentary Research* 83:339-353. doi: 10.2110/jsr.2013.32
- Milliere L, Gussone N, Moritz T, Bindschedler S, Verrecchia EP (2019) Origin of strontium and calcium in pedogenic needle fibre calcite (NFC). *Chemical Geology* 524:329-344. doi: 10.1016/j.chemgeo.2019.06.022
- Milliere L, Hasinger O, Bindschedler S, Cailleau G, Spangenberg J, Verrecchia EP (2009) Tracing soil carbon cycle and the origin of needle fibre calcite. *Geochimica Et Cosmochimica Acta* 73:A882-A882
- Milliere L, Hasinger O, Bindschedler S, Cailleau G, Spangenberg JE, Verrecchia EP (2011a) Stable carbon and oxygen isotope signatures of pedogenic needle fibre calcite. *Geoderma* 161:74-87. doi: 10.1016/j.geoderma.2010.12.009
- Milliere L, Spangenberg JE, Bindschedler S, Cailleau G, Verrecchia EP (2011b) Reliability of stable carbon and oxygen isotope compositions of pedogenic needle fibre calcite as environmental indicators: examples from Western Europe. *Isotopes in Environmental and Health Studies* 47:341-358. doi: 10.1080/10256016.2011.601305
- Millo C (2001) *Microcodium*. *Natura Nascosta* 23:1-13
- Mircescu CV, Tamas T, Bucur II, Sasaran E, Ungureanu R, Mircescu V, Mircescu E, Oprisa A (2021) Upper Triassic-Lower Jurassic continental carbonates from the Apuseni Mountains, Romania: facies, lithology and paleoenvironments. *Facies* 67. doi: 10.1007/s10347-021-00622-3
- Miyajima R, Oaki Y, Kogure T, Imai H (2015) Variation in mesoscopic textures of biogenic and biomimetic calcite crystals. *Crystal Growth & Design* 15:3755-3761. doi: 10.1021/acs.cgd.5b00407
- Mojon PO, De Kaenel E, Kalin D, Becker D, Pirkenseer CM, Rauber G, Ramseier K, Hostettler B, Weidmann M (2018) New data on the biostratigraphy (charophytes, nannofossils, mammals) and lithostratigraphy of the Late Eocene to Early Late Miocene deposits in the Swiss Molasse Basin and Jura Mountains. *Swiss Journal of Palaeontology* 137:1-48. doi: 10.1007/s13358-017-0145-6
- Molina JM, Nieto LM (2008) *Microcodium* en calizas del Eoceno Medio (Luteciense) de la Sierra de la Pila (Prebético Interno, Murcia). *Geogaceta* 44:111-114
- Molina JM, Nieto LM (2010) Paleosuelos con calcretas, rizolitos y *Microcodium* en ambientes fluviales y aluviales (Oligoceno, Prebético, provincia de Murcia). *Geogaceta* 48:51-54
- Molina JM, Vera JA, Aguado R (2006) Reworked *Microcodium* calcarenites interbedded in pelagic sedimentary rocks (Paleocene, Subbetic, southern Spain): Paleoenvironmental reconstruction. In: Alonso-Zarza AM, Tanner LH (eds) *Paleoenvironmental record and applications of calcretes and palustrine carbonates*. Geological Society of America Special paper, vol 416, Boulder, pp 189-202. doi: 10.1130/2006.2416(12)
- Monferran MD, Cabaleri NG, Gallego OF, Armella C, Cagnoni M (2016) Spinicaudatans From The Upper Jurassic Of Argentina And Their Paleoenvironments. *Palaios* 31:405-420. doi: 10.2110/palo.2016.032
- Monger HC (2014) Soils as generators and sinks of inorganic carbon in geologic time. In: Hartemink AE, McSweeney K (eds) *Soil Carbon*. Progress in Soil Science. Springer International Publishing Switzerland, pp 27-36. doi: 10.1007/978-3-319-04084-4\_3

- Monger HC, Daugherty LA, Lindemann WC, Liddell CM (1991) Microbial precipitation of pedogenic calcite. *Geology* 19:997-1000. doi: 10.1130/0091-7613(1991)019<0997:mppoc>2.3.co;2
- Monger HC, Kraimer RA, Khresat S, Cole DR, Wang XJ, Wang JP (2015) Sequestration of inorganic carbon in soil and groundwater. *Geology* 43:375-378. doi: 10.1130/g36449.1
- Monje PV, Baran EJ (2002) Characterization of calcium oxalates generated as biominerals in cacti. *Plant Physiology* 128:707-713. doi: 10.1104/pp.010630
- Montanez IP (2013) Modern soil system constraints on reconstructing deep-time atmospheric CO<sub>2</sub>. *Geochimica Et Cosmochimica Acta* 101:57-75. doi: 10.1016/j.gca.2012.10.012
- Moraetis D, Al Kindi SS, Al Saadi SK, Al Shaibani A, Pavlopoulos K, Scharf A, Mattern F, Harrower MJ, Pracejus B (2020) Terrace agriculture in a mountainous arid environment - A study of soil quality and regolith provenance: Jabal Akhdar (Oman). *Geoderma* 363. doi: 10.1016/j.geoderma.2019.114152
- Moret L, Flandrin J (1961) Nouvelles observations de 'Microcodium' dans les Alpes Françaises. *Trav. Lab. Geol. Univ. Grenoble* 37:19-24
- Morin N (1993) Les Microcodium: architecture, structure et composition, comparaison avec les racines calcifiées. [Thesis]: University of Montpellier II, Montpellier, 132 pp
- Mottareale G (1898) Di alcuni organi particolari delle radici tubercolifere dello *Hedysarum coronarium* in relazione al *Bacillus radicolica* e alla *Phytomyxa leguminosarum*. *Atti del Reale Istituto d'Incoraggiamento alle Scienze Naturali di Napoli* 11:1-7
- Mount JE, Cohen AS (1984) Petrology and geochemistry of rhizoliths from Plio-Pleistocene fluvial and marginal lacustrine deposits, East Lake-Turkana, Kenya. *Journal of Sedimentary Petrology* 54:263-275
- Multer HG, Hoffmeister JE (1968) Subaerial laminated crusts of the Florida Keys. *Geological Society of America, Bulletin* 79:187-192
- Muresu R, Polone E, Sulas L, Baldan B, Tondello A, Delogu G, Cappuccinelli P, Alberghini S, Benhizia Y, Benhizia H, Benguedouar A, Mori B, Calamassi R, Dazzo FB, Squartini A (2008) Coexistence of predominantly nonculturable rhizobia with diverse, endophytic bacterial taxa within nodules of wild legumes. *Fems Microbiology Ecology* 63:383-400. doi: 10.1111/j.1574-6941.2007.00424.x
- Murru M, Ferrara C, Matteucci R (2015) Paleocene palustrine and ephemeral alluvial facies in southern Sardinia (Italy). *Italian Journal of Geosciences* 134:134-148. doi: 10.3301/ijg.2014.32
- Murru M, Ferrara C, Matteucci R, De Pelo S (2007) I depositi carbonatici calustri paleocenici della Sardegna Centro-Meridionale (Italia). *Geologica Romana* 40:201-213
- Myers R, Wade D, Bergh C (2004) Fire Management Assessment of the Caribbean Pine (*Pinus Caribaea*) Forest Ecosystems on Andros and Abaco Islands, Bahamas, the Global Fire Initiative. GFI publication no. 2004-1. The Nature Conservancy, Arlington, VA:1-17
- Myroie JE, Carew JL (1995) Karst development on carbonate islands. In: Budd DA, Saller AH, Harris PM (eds) *Unconformities and porosity in carbonate strata. Memoir 63. American Association of Petroleum Geologists*, pp 55-76. doi: 10.1306/M63592
- Myroie JE, Carew JL (2010) Field guide to the geology and karst geomorphology of San Salvador Island. Gerace Reserch Centre, San Salvador, The Bahamas, 89 pp
- Myroie JE, Carew JL, Curran HA, Godefroid F, Kindler P, Sealey NE (2012) Geology of New Providence Island, Bahamas: A Field Trip Guide. 16th Symposium on the Geology of the Bahamas and Other Carbonate Regions. Gerace Research Centre, San Salvador, Bahamas, 58 pp
- Myroie JE, Carew JL, Vacher HL (1995) Karst development in the Bahamas and Bermuda. In:

- Curran HA, White B (eds) *Terrestrial and Shallow Marine Geology of the Bahamas and Bermuda*. Geological Society of America Special Paper 300., Boulder, Colorado, pp 251-267. doi: 10.1130/0-8137-2300-0.5
- Nahon D, Ducloux J, Butel P, Augas C, Paquet H (1980) Néofonnations d'aragonite, premières étapes d'une suite évolutive dans les encroûtements calcaires. *Comptes Rendus Hebdomadaires des Seances de l'Academie des Sciences, Serie D* 291:725-727
- Nakata PA (2003) Advances in our understanding of calcium oxalate crystal formation and function in plants. *Plant Science* 164:901-909. doi: 10.1016/s0168-9452(03)00120-1
- Netterberg F (1969) Ages of Calcretes in Southern Africa. *The South African Archaeological Bulletin* 24:88-92
- Neumann G, Römheld V (2012) Chapter 14 - Rhizosphere Chemistry in Relation to Plant Nutrition. In: Marschner P (ed) *Marschner's Mineral Nutrition of Higher Plants (Third Edition)*. Academic Press, San Diego, pp 347-368. doi: <https://doi.org/10.1016/B978-0-12-384905-2.00014-5>
- Nickel E (1982) Alluvial-Fan Carbonate Facies With Evaporites, Eocene Guarga Formation, Southern Pyrenees, Spain. *Sedimentology* 29:761-796. doi: 10.1111/j.1365-3091.1982.tb00084.x
- Nordt LC, Wilding LP, Drees LR (2000) Pedogenic carbonate transformations in leaching soil systems: implications for the global C cycle. In: Lal R, Kimble JM, Eswaran H, Stewart BA (eds) *Global climate change and pedogenic carbonates*. Lewis Publishers, Boca Raton, Florida, pp 43-64
- North GB, Nobel PS (2000) Heterogeneity in water availability alters cellular development and hydraulic conductivity along roots of a desert succulent. *Annals of Botany* 85:247-255
- Northrop JI (1890) Notes on the geology of the Bahamas. *Transactions of the New York Academy of Sciences* 10:4-22
- Novakova AA, Dolzhikova AV, Novikov VM, Boeva NM, Zhegallo EA (2017) Comparative analysis of the structural and morphological features of biogenic and synthesized goethite nanoparticles. *Crystallography Reports* 62:971-975. doi: 10.1134/s1063774517060189
- Nyambe IA (1999) Sedimentology of the Gwembe Coal Formation (Permian), Lower Karoo Group, mid-Zambezi Valley, southern Zambia. In: Smith ND and Rogers J, Eds. *Fluvial Sedimentology VI* 409-434 pp. doi: 10.1002/9781444304213.ch29
- O'Leary MH (1981) Carbon isotope fractionation in plants. *Phytochemistry* 20:553-567. doi: 10.1016/0031-9422(81)85134-5
- O'Leary MH (1989) Carbon isotopes in photosynthesis: Fractionation techniques may reveal new aspects of carbon dynamics in plants. *BioScience* 38:328-336. doi: <https://doi.org/10.2307/1310735>
- Oaki Y, Imai H (2003) Experimental demonstration for the morphological evolution of crystals grown in gel media. *Crystal Growth & Design* 3:711-716. doi: 10.1021/cg034053e
- Ogorelec B, Dolenc T, Drobne K (2007) Cretaceous-Tertiary boundary problem on shallow carbonate platform: Carbon and oxygen excursions, biota and microfacies at the K/T boundary sections Dolenja Vas and Sopada in SW Slovenia, Adria CP. *Palaeogeography Palaeoclimatology Palaeoecology* 255:64-76. doi: 10.1016/j.palaeo.2007.02.041
- Ogorelec B, Drobne K, Jurkovšek B, Dolenc T, Toman M (2001) Paleocene beds of the Liburnia Formation in Čebulovica (Slovenia, NW Adriatic-Dinaric platform). *Geologija* 44:15-65
- Oldroyd GED, Murray JD, Poole PS, Downie JA (2011) The Rules of Engagement in the Legume-Rhizobial Symbiosis. *Annual Review of Genetics*, Vol 45 45:119-144. doi: 10.1146/annurev-genet-110410-132549



- Olszta MJ, Gajjeraman S, Kaufman M, Gower LB (2004) Nanofibrous calcite synthesized via a solution-precursor-solid mechanism. *Chemistry of Materials* 16:2355-2362
- Oordt AJ, Soreghan GS, Stemmerik L, Hinnov LA (2020) A Record Of Dust Deposition In Northern, Mid-Latitude Pangaea During Peak Icehouse Conditions Of The Late Paleozoic Ice Age. *Journal of Sedimentary Research* 90:337-363. doi: 10.2110/jsr.2020.15
- Ortega E, Lozano FJ, Martínez FJ, Bienes R, Gallardo JF, Asensio C (2016 ) Soils of the Mediterranean Areas. In: J. G (ed) *The Soils of Spain*. World Soils Book Series. Springer, Berlin, pp 163-188. doi: /10.1007/978-3-319-20541-0\_5
- Osmond KS, Sibout R, Hardtke CS (2007) Hidden branches: Developments in root system architecture. *Annual Review of Plant Biology* 58:93-113. doi: 10.1146/annurev.arplant.58.032806.104006
- Otoničar B (2007) Upper Cretaceous to Paleogene forbulge unconformity associated with foreland basin evolution (Kras, Matarsko Podolje and Istria; SW Slovenia and NW Croatia). *Acta Carsologica* 36:101-120. doi: <https://doi.org/10.3986/ac.v36i1.213>
- Otoničar B (2021) Speleogenesis and depositional history of paleokarst phreatic caves/cavities; Podgrad, SW Slovenia. *Acta Carsologica* 50:67-96. doi: 10.3986/ac.vi.9945
- Otoničar B, Košir A (1998) Upper Cretaceous – Paleogene palustrine carbonates of Liburnian Formation, SW Slovenija In: Cañaveras JC, Garcia del Cura MA (eds) 15th International Sedimentological Congress, Alicante, Abstracts, pp 475-476
- Otoničar B, Košir A (2016) Cretaceous-Tertiary paleokarst from Ubac Peninsula (Istria, NW Croatia): an example of paleokarstic phreatic cave. In: Otoničar B, Gostinčar P (eds) *Paleokarst: 24th International Karstological School Classical Karst. Abstracts & Guide Book*. Založba ZRC, Postojna, pp 88-99
- Owen RA, Owen RB, Renaut RW, Scott JJ, Jones B, Ashley GM (2008) Mineralogy and origin of rhizoliths on the margins of saline, alkaline Lake Bogoria, Kenya Rift Valley. *Sedimentary Geology* 203:143-163. doi: 10.1016/j.sedgeo.2007.11.007
- Pallardy SG (2008) *Physiology of woody plants*, 3rd Edition, 3rd edn. Elsevier, Amsterdam ; Boston, xiv, 454 p. pp
- Palmer AN (1991) Origin and morphology of limestone caves. *Geological Society of America Bulletin* 103:1-21. doi: 10.1130/0016-7606(1991)103<0001:OAMOLC>2.3.CO;2
- Palmer AN (2007 ) *Cave geology*. Cave Books, 454 pp
- Patacca E, Scandone P, Mazza P (2008) The Miocene land-vertebrate fossil site of Scontrone (Central Apennines, Italy). *Bollettino Della Societa Geologica Italiana* 127:51-73
- Pavlovec R (1963) Stratigrafski razvoj starejšega paleogena v južnozahodni Sloveniji. *Razprave IV. razr. SAZU* 7:419-556
- Pawlowski K, Demchenko KN (2012) The diversity of actinorhizal symbiosis. *Protoplasma* 249:967-979. doi: 10.1007/s00709-012-0388-4
- Pawlowski K, Sprent JI (2008) Comparison between actinorhizal and legume symbiosis. In: Pawlowski K, Newton WE (eds) *Nitrogen-fixing Actinorhizal Symbioses*. Springer, Dordrecht, pp 261-288. doi:10.1007/978-1-4020-3547-0\_10
- Pelechaty SM, James NP (1991) Dolomitized Middle Proterozoic Calcretes, Bathurst Inlet, Northwest Territories, Canada. *Journal of Sedimentary Petrology* 61:988-1001
- Peng X (2011) Anisotropy of soil physical properties. In: Gliński J, J. H, Lipiec J (eds) *Encyclopedia of Agrophysics*. Springer Science+Business Media B.V., pp A55-A57. doi: 10.1007/978-90-481-3585-1

- Péret B, De Rybel B, Casimiro I, Benková E, Swarup R, Laplaze L, Beeckman T, Bennett MJ (2009) Arabidopsis lateral root development: an emerging story. *Trends in Plant Science* 14:399-408. doi: 10.1016/j.tplants.2009.05.002
- Perkins RD (1977) Depositional framework of Pleistocene rocks in South Florida. In: Enos P, Perkins RD (eds) *Quaternary sedimentation in South Florida*. GSA Memoir 147, Tulsa, pp 131-198
- Peterson CA, Enstone DE, Taylor JH (1999) Pine root structure and its potential significance for root function. *Plant and Soil* 217:205-213. doi: 10.1023/a:1004668522795
- Pfefferkorn HW, Fuchs K (1991) A field classification of fossil plant substrate interactions. *Neues Jahrbuch fuer Geologie und Palaeontologie. Abhandlungen* 183:17-36
- Phillips SE, Milnes AR, Foster RC (1987a) Calcified filaments - an example of biological influences in the formation of calcrete in South Australia. *Australian Journal of Soil Research* 25:405-428. doi: 10.1071/sr9870405
- Phillips SE, Milnes AR, Foster RC (1987b) Calcified Filaments - An Example Of Biological Influences In The Formation Of Calcrete In South-Australia. *Australian Journal of Soil Research* 25:405-428. doi: 10.1071/sr9870405
- Phillips SE, Self PG (1987) Morphology, Crystallography And Origin Of Needle-Fiber Calcite In Quaternary Pedogenic Calcretes Of South-Australia. *Australian Journal of Soil Research* 25:429-444. doi: 10.1071/sr9870429
- Pipujol MD, Buurman P (1994) The Distinction Between Groundwater Gley And Surface-Water Gley Phenomena In Tertiary Paleosols Of The Ebro Basin, Ne Spain. *Palaeogeography Palaeoclimatology Palaeoecology* 110:103-113. doi: 10.1016/0031-0182(94)90112-0
- PiPujol MD, Buurman P (1997) Dynamics of iron and calcium carbonate redistribution and palaeohydrology in middle Eocene alluvial paleosols of the southeast Ebro Basin margin (Catalonia, northeast Spain). *Palaeogeography Palaeoclimatology Palaeoecology* 134:87-107
- Pirozynski KA, Dalpe Y (1989) Geological History Of The Glomaceae With Particular Reference To Mycorrhizal Symbiosis. *Symbiosis* 7:1-36
- Placer L (1981) Tectonic structure of southwest Slovenia / Geološka zgradba jugozahodne Slovenije. *Geologija* 24:27-60
- Plata JM, Rodriguez R, Preusser F, Boixadera J, Balasch JC, Antunez M, Poch RM (2021) Red soils in loess deposits of the Western Ebro Valley. *Catena* 204. doi: 10.1016/j.catena.2021.105430
- Plotnick RE, Kenig F, Scott AC (2015) Using the voids to fill the gaps: caves, time, and stratigraphy. In: Smith DG, Bailey RJ, Burgess PM, Fraser AJ (eds) *Strata and Time: Probing the Gaps in Our Understanding*. Geological Society Special Publications, 404. Geological Society, London, pp 233-250. doi: <http://dx.doi.org/10.1144/SP404.5>
- Pomar L (2020) Carbonate systems. In: Scarselli N, Adam J, Chiarella D, Roberts DG, Bally AW (eds) *Regional Geology and Tectonics (Second Edition) Volume 1: Principles of Geologic Analysis*. Elsevier, New York, pp 235-311. doi: <https://doi.org/10.1016/B978-0-444-64134-2.00013-4>
- Pomoni-Papaioannou F, Kostopoulou V (2008) Microfacies and cycle stacking pattern in Liassic peritidal carbonate platform strata, Gavrovo-Tripolitza platform, Peloponnesus, Greece. *Facies* 54:417-431. doi: 10.1007/s10347-008-0142-8
- Pomonipapaioannou F, Solakius N (1991) Phosphatic Hardgrounds And Stromatolites From The Limestone Shale Boundary Section At Prossilion (Maastrichtian-Paleocene) In The Parnassus-Ghiona Zone, Central Greece. *Palaeogeography Palaeoclimatology Palaeoecology* 86:243-254. doi: 10.1016/0031-0182(91)90083-4

- Pons MJ, Franchini M, Giusiano A, Patrier P, Beaufort D, Impiccini A, Rainoldi AL, Meinert L (2017) Alteration halos in the Tordillos sediment-hosted copper deposit of the Neuquen Basin, Argentina. *Ore Geology Reviews* 80:691-715. doi: 10.1016/j.oregeorev.2016.06.011
- Pons MJ, Rainoldi AL, Franchini M, Giusiano A, Cesaretti N, Beaufort D, Patrier P, Impiccini A (2015) Mineralogical signature of hydrocarbon circulation in Cretaceous red beds of the Barda Gonzalez area, Neuquen Basin, Argentina. *Aapg Bulletin* 99:525-554. doi: 10.1306/08131413170
- Poot P, Hopper SD, van Diggelen JMH (2012) Exploring rock fissures: does a specialized root morphology explain endemism on granite outcrops? *Annals of Botany* 110:291-300. doi: 10.1093/aob/mcr322
- Porta J, Herrero J (1988) Micromorfología de suelos con yeso. *Anales de Edafología y Agrobiología* 47:179-198
- POWO (2021) Plants of the World Online. Facilitated by the Royal Botanic Gardens, Kew <http://www.plantsoftheworldonline.org/> Retrieved: 12 September 2021
- Pregitzer KS (2002) Fine roots of trees - a new perspective. *New Phytologist* 154:267-270
- Pregitzer KS (2003) Woody plants, carbon allocation and fine roots. *New Phytologist* 158:421-424
- Proia AD, Brinn NT (1985) Identification of calcium-oxalate crystals using alizarin red-S stain. *Archives of Pathology & Laboratory Medicine* 109:186-189
- Pujalte V, Monechi S, Ortiz S, Orue-Etxebarria X, Rodriguez-Tovar F, Schmitz B (2019a) Microcodium-rich turbidites in hemipelagic sediments during the Paleocene-Eocene Thermal Maximum: Evidence for extreme precipitation events in a Mediterranean climate (Rio Gor section, southern Spain). *Global and Planetary Change* 178:153-167. doi: 10.1016/j.gloplacha.2019.04.018
- Pujalte V, Robador A, Payros A, Samsó JM (2016) A siliciclastic braid delta within a lower Paleogene carbonate platform (Ordesa-Monte Perdido National Park, southern Pyrenees, Spain): Record of the Paleocene-Eocene Thermal Maximum perturbation. *Palaeogeography Palaeoclimatology Palaeoecology* 459:453-470. doi: 10.1016/j.palaeo.2016.07.029
- Pujalte V, Schmitz B, Baceta JI (2014) Sea-level changes across the Paleocene-Eocene interval in the Spanish Pyrenees, and their possible relationship with North Atlantic magmatism. *Palaeogeography Palaeoclimatology Palaeoecology* 393:45-60. doi: 10.1016/j.palaeo.2013.10.016
- Pujalte V, Schmitz B, Payros A (2019b) Lower Paleocene Microcodium-rich calcarenites in hemipelagic areas of the Subbetic Zone, SE Spain: Sr isotopes, source area and palaeogeographic implications. *Geogaceta* 66:19-22
- Pujalte V, Schmitz B, Payros A (2022) A rapid sedimentary response to the Paleocene-Eocene Thermal Maximum hydrological change: New data from alluvial units of the Tremp-Graus Basin (Spanish Pyrenees). *Palaeogeography Palaeoclimatology Palaeoecology* 589:110818. doi: /10.1016/j.palaeo.2021.110818
- Pylro VS, de Freitas ALM, Otoni WC, da Silva IR, Borges AC, Costa MD (2013) Calcium Oxalate Crystals in Eucalypt Ectomycorrhizae: Morphochemical Characterization. *Plos One* 8:6. doi: 10.1371/journal.pone.0067685
- Quézel P (2000) Taxonomy and biogeography of Mediterranean pines (*Pinus halepensis* and *P. brutia*). In: Neñman G, Trabaud L (eds) *In Ecology, Biogeography and Management of Pinus halepensis and P. brutia Forest Ecosystems in the Mediterranean Basin*. Backhuys Publishers, Leiden, pp 1-12
- Radha AV, Forbes TZ, Killian CE, Gilbert P, Navrotsky A (2010) Transformation and crystallization energetics of synthetic and biogenic amorphous calcium carbonate. *Proceedings of the*



- National Academy of Sciences of the United States of America 107:16438-16443. doi: 10.1073/pnas.1009959107
- Rao VP (1990) On The Occurrence Of Caliche Pisolites From The Western Continental-Shelf Of India. *Sedimentary Geology* 69:13-19. doi: 10.1016/0037-0738(90)90097-d
- Raven JA (1991) Terrestrial rhizophytes and H<sup>+</sup> currents circulating over at least a millimeter: An obligate relationship? *New Phytologist* 117:177-185. doi: 10.1111/j.1469-8137.1991.tb04899.x
- Raven JA, Franco AA, de Jesus EL, Jacob-Neto J (1990) H<sup>+</sup> extrusion and organic-acid synthesis in N<sub>2</sub>-fixing symbioses involving vascular plants. *New Phytologist* 114:369-389. doi: 10.1111/j.1469-8137.1990.tb00405.x
- Raven JA, Giordano M (2009) Biomineralization by photosynthetic organisms: Evidence of coevolution of the organisms and their environment? *Geobiology* 7:140-154. doi: 10.1111/j.1472-4669.2008.00181.x
- Raven JA, Knoll AH (2010) Non-Skeletal Biomineralization by Eukaryotes: Matters of Moment and Gravity. *Geomicrobiology Journal* 27:572-584. doi: 10.1080/01490451003702990
- Rea PA (2018) Plant Vacuoles. eLS. doi: 10.1002/9780470015902.a0001675.pub3
- Read JF (1974) Calcrete deposits and Quaternary sediments, Edel Province, Shark Bay, Western Australia. In: Logan BW, Read JF, Hagan GM, Hoffman P, Brown RG, Woods PJ, Gebelein CD (eds) *Evolution and Diagenesis of Quaternary Carbonate Sequences, Shark Bay, Western Australia*. AAPG Memoir 22. AAPG, Tulsa, OK, pp 250-282
- Read JF (1976) Calcretes and their distinction from stromatolites. In: Walter MR (ed) *Stromatolites. Developments in Sedimentology* 20, vol Volume 20. Elsevier, pp 55-71. doi: [http://dx.doi.org/10.1016/S0070-4571\(08\)71129-4](http://dx.doi.org/10.1016/S0070-4571(08)71129-4)
- Reeves CC (1970) Origin, Classification, and Geologic History of Caliche on the Southern High Plains, Texas and Eastern New Mexico. *The Journal of Geology* 78:352-362. doi: <https://www.jstor.org/stable/30062094>
- Reijmer JJG (2021) Marine carbonate factories: Review and update. *Sedimentology* 68:1729–1796. doi: 10.1111/sed.12878
- Retallack GJ (1988) Field recognition of paleosols. In: Reinhardt J, Sigleo WR (eds) *Paleosols and Weathering through Geologic Time: Principles and Applications*, Geological Society of America, Special Paper, vol 216, pp 1-20
- Retallack GJ (1997) *A colour guide to paleosols*. Wiley, New York, xii + 175 pp
- Retallack GJ (2001) *Soils of the past. An introduction to paleopedology*. Blackwell Science, Oxford, UK, xi + 404 pp
- Retallack GJ (2012) Criteria For Distinguishing Microbial Mats And Earths. In: Noffke N, Chafetz H (eds) *Microbial Mats in Siliciclastic Depositional Systems through Time*, pp 139-152
- Retallack GJ (2021) Soil, soil processes, and paleosols. In: Alderton D, Elias SA (eds) *Encyclopedia of Geology (Second Edition)*. Academic Press, Elsevier, London, pp 690-707. doi: <https://doi.org/10.1016/B978-0-12-409548-9.12537-0>
- Retallack GJ, Smith RMH, Ward PD (2003) Vertebrate extinction across Permian-Triassic boundary in Karoo Basin, South Africa. *Geological Society of America Bulletin* 115:1133-1152. doi: 10.1130/b25215.1
- Richter DD, Markewitz D (1995) How deep is soil? *BioScience* 45:600-609
- Ridge RW, Emons AM (2000) *Root hairs: cell and molecular biology*. Springer, Tokyo ; New York, xvi, 336 pp
- Riera V, Anadon P, Oms O, Estrada R, Maestro E (2013) Dinosaur eggshell isotope geochemistry

- as tools of palaeoenvironmental reconstruction for the upper Cretaceous from the Tremp Formation (Southern Pyrenees). *Sedimentary Geology* 294:356-370. doi: 10.1016/j.sedgeo.2013.06.001
- Riera V, Oms O, Gaete R, Galobart A (2009) The end-Cretaceous dinosaur succession in Europe: The Tremp Basin record (Spain). *Palaeogeography Palaeoclimatology Palaeoecology* 283:160-171. doi: 10.1016/j.palaeo.2009.09.018
- Rivers JM, Skeat SL, Yousif R, Liu CJ, Stanmore E, Tai P, Al-Marri SM (2019) The depositional history of near-surface Qatar aquifer rocks and its impact on matrix flow and storage properties. *Arabian Journal of Geosciences* 12. doi: 10.1007/s12517-019-4498-6
- Robbin DM, Stipp JJ (1979) Depositional rate of laminated soilstone crusts, Florida Keys. *Journal of Sedimentary Petrology* 49:175-180
- Robbins NE, Dinneny JR (2015) The divining root: moisture-driven responses of roots at the micro- and macro-scale. *Journal of Experimental Botany* 66:2145-2154. doi: 10.1093/jxb/eru496
- Robbins NE, Dinneny JR (2018) Growth is required for perception of water availability to pattern root branches in plants. *Proceedings of the National Academy of Sciences of the United States of America* 115:E822-E831. doi: 10.1073/pnas.1710709115
- Roberts K (2007) *Handbook of plant science*, 2 vol. Wiley, Chichester, xxiii +1599 pp
- Robins CR, Deurlington A, Buck BJ, Brock-Hon AL (2015) Micromorphology and formation of pedogenic ooids in calcic soils and petrocalcic horizons. *Geoderma* 251:10-23. doi: 10.1016/j.geoderma.2015.03.009
- Robinson D, Hodge A, Fitter A (2003) Constraints on the Form and Function of Root Systems. In: de Kroon H., E.J.W. V (eds) *Root Ecology. Ecological Studies (Analysis and Synthesis)*, vol 168. Springer, Berlin, Heidelberg, pp 1-32. doi: 10.1007/978-3-662-09784-7\_1
- Rodrigues AG, Dal'Bo PF, Basilici G, Soares MVT, Menezes MN (2019) Biotic Influence In The Genesis Of Laminar Calcretes In Vertisols Of The Marilia Formation (Upper Cretaceous, Brazil). *Journal of Sedimentary Research* 89:440-458. doi: 10.2110/jsr.2019.22
- Rodriguez-Blanco JD, Shaw S, Benning LG (2011) The kinetics and mechanisms of amorphous calcium carbonate (ACC) crystallization to calcite, via vaterite. *Nanoscale* 3:265-271. doi: 10.1039/c0nr00589d
- Rodriguez-Navarro C, Kudlacz K, Cizer O, Ruiz-Agudo E (2015) Formation of amorphous calcium carbonate and its transformation into mesostructured calcite. *Crystengcomm* 17:58-72. doi: 10.1039/c4ce01562b
- Rodriguez-Tovar FJ, Pujalte V, Payros A (2020) Danian-lower Selandian Microcodium-rich calcarenites of the Subbetic Zone (SE Spain): Record of Nereites ichnofacies in a deep-sea, base-of-slope system. *Sedimentary Geology* 406. doi: 10.1016/j.sedgeo.2020.105723
- Rodríguez-Tovar FJ, Pujalte V, Payros A (2020) Danian-lower Selandian Microcodium-rich calcarenites of the Subbetic Zone (SE Spain): Record of Nereites ichnofacies in a deep-sea, base-of-slope system. *Sedimentary Geology* 406. doi: 10.1016/j.sedgeo.2020.105723
- Romanek CS, Grossman EL, Morse JW (1992) Carbon isotopic fractionation in synthetic aragonite and calcite: Effects of temperature and precipitation rate. *Geochimica Et Cosmochimica Acta* 56:419-430. doi: [https://doi.org/10.1016/0016-7037\(92\)90142-6](https://doi.org/10.1016/0016-7037(92)90142-6)
- Rosales-Dominguez MD, Bermudez-Santana JC, Aguilar-Pina M (1997) Mid and Upper Cretaceous foraminiferal assemblages from the Sierra de Chiapas, southeastern Mexico. *Cretaceous Research* 18:697-712. doi: 10.1006/cres.1997.0081
- Ross WD, Delaney RH (1977) Massive Accumulation Of Calcium-Carbonate And Its Relation To Nitrogen-Fixation Of Sainfoin. *Agronomy Journal* 69:242-246

- Rossi C (1997) Microcodium y trazas fosiles de invertebrados en facies continentales (Paleoceno de la Guenca de Ager, Lerida). *Revista de la Sociedad Geologica de España* 10:371-391
- Rossi C, Canaveras JC (1999) Pseudospherulitic fibrous calcite in paleo-groundwater, unconformity-related diagenetic carbonates (Paleocene of the Ager Basin and Miocene of the Madrid Basin, Spain). *Journal of Sedimentary Research* 69:224-238. doi: 10.2110/jsr.69.224
- Rossinsky V, Wanless HR (1992) Topographic and vegetative controls on calcrete formation, Turks and Caicos Islands, British West Indies. *Journal of Sedimentary Petrology* 62:84-98. doi: <https://doi.org/10.1306/D4267898-2B26-11D7-8648000102C1865D>
- Rossinsky V, Wanless HR, Swart PK (1992) Penetrative calcretes and their stratigraphic implications. *Geology* 20:331-334. doi: [https://doi.org/10.1130/0091-7613\(1992\)020<0331:PCATSI>2.3.CO;2](https://doi.org/10.1130/0091-7613(1992)020<0331:PCATSI>2.3.CO;2)
- Roulin F (1987) Geodynamic, Climatic And Geochemical Evolution In A Tertiary Continental Basin - Detrital Deposits, Silcretes, Calcretes And Associated Clays - The Eocene Apt Basin (Vaucluse, France). *Comptes Rendus De L Academie Des Sciences Serie Ii* 305:121-125
- Roux A (1985) Introduction à l'étude des Algues fossiles paléozoïques (de la bactérie à la tectonique des plaques). *Bull. Centres de Recherche Exploration Production, Elf-Aquitaine* 9:465-699
- Rovira P, Vallejo VR (2008) Changes in delta C-13 composition of soil carbonates driven by organic matter decomposition in a Mediterranean climate: A field incubation experiment. *Geoderma* 144:517-534. doi: 10.1016/j.geoderma.2008.01.006
- Rowley MC, Estrada-Medina H, Tzec-Gamboa M, Rozin A, Cailleau G, Verrecchia EP, Green I (2017) Moving carbon between spheres, the potential oxalate-carbonate pathway of *Brosimum alicastrum* Sw.; Moraceae. *Plant and Soil* 412:465-479. doi: 10.1007/s11104-016-3135-3
- Rowley MC, Grand S, Verrecchia EP (2018) Calcium-mediated stabilisation of soil organic carbon. *Biogeochemistry* 137:27-49. doi: 10.1007/s10533-017-0410-1
- Rundel PW, Cowling RM (2013) Mediterranean-Climate Ecosystems In: Levin SA (ed) *Encyclopedia of Biodiversity (Second Edition)*. Academic Press, Waltham, pp 212-222. doi: <http://dx.doi.org/10.1016/B978-0-12-384719-5.00245-8>
- Ryan BH, Kaczmarek SE, Rivers JM (2020) Early and pervasive dolomitization by near-normal marine fluids: New lessons from an Eocene evaporative setting in Qatar. *Sedimentology* 67:2917-2944. doi: 10.1111/sed.12726
- Ryan BH, Kaczmarek SE, Rivers JM (2021) Multi-episodic recrystallization and isotopic resetting of early-diagenetic dolomites in near-surface settings. *Journal of Sedimentary Research* 91:146-166. doi: 10.2110/jsr.2020.056
- Sablok G, Rosselli R, Seeman T, van Velzen R, Polone E, Giacomini A, La Porta N, Geurts R, Muresu R, Squartini A (2017) Draft Genome Sequence of the Nitrogen-Fixing *Rhizobium sullae* Type Strain IS123(T) Focusing on the Key Genes for Symbiosis with its Host *Hedysarum coronarium* L. *Frontiers in Microbiology* 8. doi: 10.3389/fmicb.2017.01348
- Salas-Saavedra M, Dechnik B, Webb GE, Webster JM, Zhao JX, Nothdurft LD, Clark TR, Graham T, Duce S (2018) Holocene reef growth over irregular Pleistocene karst confirms major influence of hydrodynamic factors on Holocene reef development. *Quaternary Science Reviews* 180:157-176. doi: 10.1016/j.quascirev.2017.11.034
- Salih N, Mansurbeg H, Kolo K, Preat A (2019) Hydrothermal Carbonate Mineralization, Calcretization, and Microbial Diagenesis Associated with Multiple Sedimentary Phases in the Upper Cretaceous Bekhme Formation, Kurdistan Region-Iraq. *Geosciences* 9. doi: 10.3390/geosciences9110459



- Saller AH (1986) Radiaxial Calcite In Lower Miocene Strata, Subsurface Enewetak-Atoll. *Journal of Sedimentary Petrology* 56:743-762
- Saller AH, Koepnick RB (1990) Eocene To Early Miocene Growth Of Enewetak Atoll - Insight From Strontium-Isotope Data. *Geological Society of America Bulletin* 102:381-390. doi: 10.1130/0016-7606(1990)102<0381:etemgo>2.3.co;2
- Salomons W, Mook WG (1986) Isotope geochemistry of carbonates in the weathering zone. In: Fritz P, Fontes JC (eds) *Handbook of Environmental Isotope Geochemistry* vol. 2, Terrestrial environment B. Elsevier, Amsterdam, pp 239-269. doi: <https://doi.org/10.1016/B978-0-444-42225-5.50011-5>
- Samuels T, Bryce C, Landenmark H, Marie-Loudon C, Nicholson N, Stevens AH, Cockell C (2020) Microbial Weathering of Minerals and Rocks in Natural Environments. *Biogeochemical Cycles*, pp 59-79. doi: <https://doi.org/10.1002/9781119413332.ch3>
- Samuelsberg TJ, Pickard NAH (1999) Upper Carboniferous to Lower Permian transgressive-regressive sequences of central Spitsbergen, Arctic Norway. *Geological Journal* 34:393-411. doi: 10.1002/(sici)1099-1034(199911/12)34:4<393::aid-gj831>3.0.co;2-g
- Sanchez MD, Manco BN, Blaise J, Corcoran M, Hamilton MA (2019) Conserving and restoring the Caicos pine forests: The first decade. *Plant Diversity* 41:75-83. doi: 10.1016/j.pld.2018.05.002
- Sandulli R (2004) The Barremian carbonate platform strata of the Montenegro Dinarids near Podgorica: a cyclostratigraphic study. *Cretaceous Research* 25:951-967. doi: 10.1016/j.cretres.2004.09.002
- Sano H (2006) Impact of long-term climate change and sea-level fluctuation on Mississippian to Permian mid-oceanic atoll sedimentation (Akiyoshi Limestone Group, Japan). *Palaeogeography Palaeoclimatology Palaeoecology* 236:169-189. doi: 10.1016/j.palaeo.2005.11.009
- Sano H, Fujii S, Matsuura F (2004) Response of Carboniferous-Permian mid-oceanic seamount-capping buildup to global cooling and sea-level change: Akiyoshi, Japan. *Palaeogeography Palaeoclimatology Palaeoecology* 213:187-206. doi: 10.1016/j.palaeo.2004.07.015
- Sanz-Montero ME, Rodriguez-Aranda JP (2012) Endomycorrhizae in Miocene paleosols: Implications in biotite weathering and accumulation of dolomite in plant roots (SW Madrid Basin, Spain). *Palaeogeography Palaeoclimatology Palaeoecology* 333:121-130. doi: 10.1016/j.palaeo.2012.03.013
- Sarjeant WA (1975) Plant trace fossils. In: Frey RW (ed) *The Study of Trace Fossils*. Springer, Berlin, Heidelberg, pp 163-179. doi: [https://doi.org/10.1007/978-3-642-65923-2\\_10](https://doi.org/10.1007/978-3-642-65923-2_10)
- Sarkar S (1988) Petrology Of Caliche-Derived Peloidal Calcirudite Calcarenite In The Late Triassic Maleri Formation Of The Pranhita-Godavari-Valley, South-India. *Sedimentary Geology* 55:263-282. doi: 10.1016/0037-0738(88)90134-0
- Schenk HJ, Jackson RB (2002) Rooting depths, lateral root spreads and below-ground/above-ground allometries of plants in water-limited ecosystems. *Journal of Ecology* 90:480-494
- Schenk HJ, Jackson RB (2005) Mapping the global distribution of deep roots in relation to climate and soil characteristics. *Geoderma* 126:129-140
- Schilt F, Verpoorte A, Antl W (2017) Micromorphology of an Upper Paleolithic cultural layer at Grub-Kranawetberg, Austria. *Journal of Archaeological Science-Reports* 14:152-162. doi: 10.1016/j.jasrep.2017.05.041
- Schlager W (2000) Sedimentation rates and growth potential of tropical, cool-water and mud-mound carbonate systems. In: Skelton PW, Palmer TJ, Insalaco E (eds) *Carbonate platform systems: components and interactions*, Geological Society special publication 178. Geological Society, pp 217-227. doi: <https://doi.org/10.1144/GSL.SP.2000.178.01.14>

- Schlager W (2005) Carbonate sedimentology and sequence stratigraphy. *SEPM Concepts in sedimentology and paleontology* 8, 200 pp
- Schmalenberger A, Duran AL, Bray AW, Bridge J, Bonneville S, Benning LG, Romero-Gonzalez ME, Leake JR, Banwart SA (2015) Oxalate secretion by ectomycorrhizal *Paxillus involutus* is mineral-specific and controls calcium weathering from minerals. *Scientific Reports* 5. doi: 10.1038/srep12187
- Schmitz B, Pujalte V (2003) Sea-level, humidity, and land-erosion records across the initial Eocene thermal maximum from a continental-marine transect in northern Spain. *Geology* 31. doi: 10.1130/g19527.1
- Schmitz B, Pujalte V (2007) Abrupt increase in seasonal extreme precipitation at the Paleocene-Eocene boundary. *Geology* 35. doi: 10.1130/g23261a.1
- Schwinnig S (2010) The ecohydrology of roots in rocks. *Ecohydrology* 3:238-245. doi: 10.1002/eco.134
- Schwinnig S (2013) Do we need new rhizosphere models for rock-dominated landscapes? *Plant and Soil* 362:25-31. doi: 10.1007/s11104-012-1482-2
- Schwinnig S (2020) A critical question for the critical zone: how do plants use rock water? *Plant and Soil* 454:49-56. doi: 10.1007/s11104-020-04648-4
- Scott AC (1992) Anatomical preservation of fossil plants. In: Briggs DEG, Crowther PR (eds) *Palaeobiology: A Synthesis*. Blackwell, Oxford, UK, pp 263-266
- Sealey NE (1994) *Bahamian Landscapes: An introduction to the Geography of the Bahamas*, Second edition. Media Publishing, Nassau, Bahamas, 128 pp
- Semeniuk V (2010) A note on calcite precipitates as encrustations around sea rush roots and rhizomes and as laminae in high tidal zones of western Leschenault Inlet estuary. *Journal of the Royal Society of Western Australia* 93:195-119
- Semeniuk V (2011) Microkarst, Palaeosols, and Calcrete along Subaerial Disconformities in the Ordovician Daylesford Limestone, Bowan Park, Central Western New South Wales. *Proceedings of the Linnean Society of New South Wales* 132:187-220
- Semeniuk V, Meagher TD (1981) Calcrete In Quaternary Coastal Dunes In Southwestern Australia - A Capillary-Rise Phenomenon Associated With Plants. *Journal of Sedimentary Petrology* 51: 47-68
- Setoguchi H, Okazaki M, Suga S (1989) Calcification in higher plants with special reference to cystoliths. In: Crick RE (ed) *Origin, Evolution, and Modern Aspects of Biomineralization in Plants and Animals*. Plenum Press, New York, pp 409-418
- Severini G (1908a) Particolarità morfologiche ed anatomiche nelle radici dell' *Hedysarum coronarium* L. *Annali di Botanica* 7: 75-82
- Severini G (1908b) Ricerche fisiologiche e batteriologiche sull' *Hedysarum coronarium* L. (volg. Sulla). *Annali di Botanica* 7:33-70
- Sheldon ND, Tabor NJ (2009) Quantitative paleoenvironmental and paleoclimatic reconstruction using paleosols. *Earth-Science Reviews* 95:1-52. doi: 10.1016/j.earscirev.2009.03.004
- Shinn EA (2019) So What? A Brief History of Robert N. Ginsburg. *The Depositional Record* 5:395-399. doi: <https://doi.org/10.1002/dep2.76>
- Shinn EA, Lidz BH (1988) Blackened Limestone Pebbles: Fire at Subaerial Unconformities. In: James NP, Choquette PW (eds) *Paleokarst*. Springer New York, New York, NY, pp 117-131. doi: 10.1007/978-1-4612-3748-8\_6

- Sigel A, Sigel H, Sigel RKO (2008) *Biom mineralization : from nature to application*. John Wiley & Sons, Chichester, xxvii + 671 pp
- Simkiss K, Wilbur KM (1989) *Biom mineralization: cell biology and mineral deposition*. Academic Press, San Diego, xiv, 337 pp
- Singh BP, Il Lee Y, Pawar JS, Charak RS (2007) Biogenic features in calcretes developed on mudstone: Examples from Paleogene sequences of the Himalaya, India. *Sedimentary Geology* 201:149-156. doi: 10.1016/j.sedgeo.2007.05.013
- Singh BP, Tandon SK, Singh GP, Pawar JS (2009) Palaeosols in early Himalayan foreland basin sequences demonstrate latitudinal shift-related long-term climatic change. *Sedimentology* 56:1464-1487. doi: 10.1111/j.1365-3091.2008.01042.x
- Sinha R, Tandon SK, Sanyal P, Gibling MR, Stuben D, Berner Z, Ghazanfari P (2006) Calcretes from a Late Quaternary interfluvium in the Ganga Plains, India: Carbonate types and isotopic systems in a monsoonal setting. *Palaeogeography Palaeoclimatology Palaeoecology* 242:214-239. doi: 10.1016/j.palaeo.2006.05.015
- Skinner HCV, Jahren AH (2005) Biom mineralization. In: Schlesinger WH (ed) *Biogeochemistry. Treatise on Geochemistry* vol. 8, vol 8. Elsevier, Amsterdam, pp 117-184
- Skinner HCW, Ehrlich H (2014) Biom mineralization. In: Holland HD, Turekian KK (eds) *Treatise on Geochemistry (Second Edition)*. Elsevier, Oxford, pp 105-162. doi: <https://doi.org/10.1016/B978-0-08-095975-7.00804-4>
- Smit J (1979) *Microcodium*, its earliest occurrence and other considerations. *Revue de Micropaléontologie* 22:44-50
- Smith DL (1982) Calcium oxalate and carbonate deposits in plant cells. In: Anghileri LJ, Tuffet-Anghileri AM (eds) *The Role of Calcium in Biological Systems*. CRC Press, Boca Raton, pp 253-261
- Smith FA, Smith SE, Timonen S (2003) Mycorrhizas. In: de Kroon H., E.J.W. V (eds) *Root Ecology. Ecological Studies (Analysis and Synthesis)*, vol 168. Springer, Berlin, Heidelberg, pp 257-295. doi: 10.1007/978-3-662-09784-7\_11
- Smith IK, Vankat JL (1992) Dry Evergreen Forest (Coppice) Communities of North Andros Island, Bahamas. *Bulletin of the Torrey Botanical Club* 119:181-191. doi: <https://www.jstor.org/stable/2997030>
- Smith JJ, Hasiotis ST, Woody DT, Kraus MJ (2008) Paleoclimatic implications of crayfish-mediated prismatic structures in paleosols of the Paleogene Willwood Formation, Bighorn Basin, Wyoming, USA. *Journal of Sedimentary Research* 78:323-334. doi: 10.2110/jsr.2008.040
- Smith SE, Read D (2008) *Mycorrhizal Symbiosis (Third Edition)*. Academic Press, London, xi + 800 pp. <http://dx.doi.org/10.1016/B978-012370526-6.50002-7>
- Song RQ, Colfen H (2010) Mesocrystals-Ordered Nanoparticle Superstructures. *Advanced Materials* 22:1301-1330. doi: 10.1002/adma.200901365
- Sooltanian N, Seyrafian A, Vaziri-Moghaddam H (2011) Biostratigraphy and paleo-ecological implications in microfacies of the Asmari Formation (Oligocene), Naura anticline (Interior Fars of the Zagros Basin), Iran. *Carbonates and Evaporites* 26:167-180. doi: 10.1007/s13146-011-0053-6
- Soriano P, Costa M (2017) The Coastal Levantine Area. In: Loidi J (ed) *The vegetation of the Iberian Peninsula*. Springer International Publishing AG, Berlin, pp 589-625. doi: DOI 10.1007/978-3-319-54784-8\_14
- Sorrel P, Eymard I, Leloup PH, Maheo G, Olivier N, Sterb M, Gourbet L, Wang GC, Jing W, Lu HJ,



- Li HB, Xu YD, Zhang KX, Cao K, Chevalier ML, Replumaz A (2017) Wet tropical climate in SE Tibet during the Late Eocene. *Scientific Reports* 7. doi: 10.1038/s41598-017-07766-9
- Spanicek J, Cosovic V, Mrinjek E, Vlahovic I (2017) Early Eocene evolution of carbonate depositional environments recorded in the Cikola Canyon (North Dalmatian Foreland Basin, Croatia). *Geologia Croatica* 70:11-25. doi: 10.4154/gc.2017.05
- Sparkes IA (2021) Plant Endoplasmic Reticulum. *eLS*, Vol 2:95–102 doi: 10.1002/9780470015902.a0029266
- Srivastava V, McKee LS, Bulone V (2017) Plant Cell Walls. *eLS*. John Wiley & Sons, Ltd, Chichester 10.1002/9780470015902.a0001682.pub3
- Stolt MH, Lindbo DL (2010) Soil organic matter. In: Stoops G, Marcelino V, Mees F (eds) *Interpretation of Micromorphological Features of Soils and Regoliths*. Elsevier, Amsterdam, pp 369-396. doi: 10.1016/B978-0-444-53156-8.00017-9
- Stoops G (2021) *Guidelines for Analysis and Description of Soil and Regolith Thin Sections, Second Edition*. Soil Science Society of America, Inc., John Wiley & Sons, Inc., Hoboken, NJ, xv + 240 pp
- Storey R, Jones RGW, Schachtman DP, Treeby MT (2003) Calcium-accumulating cells in the meristematic region of grapevine root apices. *Functional Plant Biology* 30:719-727
- Strullu-Derrien C, Kenrick P, Pressel S, Duckett JG, Rioult JP, Strullu DG (2014) Fungal associations in *Horneophyton ligneri* from the Rhynie Chert (c. 407 million year old) closely resemble those in extant lower land plants: novel insights into ancestral plant-fungus symbioses. *New Phytologist* 203:964-979. doi: 10.1111/nph.12805
- Strullu-Derrien C, McLoughlin S, Philippe M, Mork A, Strullu DG (2012) Arthropod interactions with bennettitalean roots in a Triassic permineralized peat from Hopen, Svalbard Archipelago (Arctic). *Palaeogeography Palaeoclimatology Palaeoecology* 348:45-58. doi: 10.1016/j.palaeo.2012.06.006
- Strullu-Derrien C, Strullu DG (2007) Mycorrhization of fossil and living plants (*La mycorrhization des plantes fossiles et actuelles*). *Comptes Rendus Palevol* 6:483-494. doi: /10.1016/j.crpv.2007.09.006
- Stubblefield SP, Taylor TN (1988) Recent Advances In Paleomycology. *New Phytologist* 108:3-25. doi: 10.1111/j.1469-8137.1988.tb00200.x
- Sun QF, Huguet A, Zamanian K (2021) Outcrop distribution and formation of carbonate rhizoliths in Badain Jaran Desert, NW China. *Catena* 197. doi: 10.1016/j.catena.2020.104975
- Sun QF, Wang H, Zamanian K (2019a) Radiocarbon age discrepancies between the carbonate cement and the root relics of rhizoliths from the Badain Jaran and the Tenggeri deserts, Northwest China. *Catena* 180:263-270. doi: 10.1016/j.catena.2019.04.011
- Sun QF, Xue WH, Zamanian K, Colin C, Duchamp-Alphonse S, Pei WT (2019b) Formation and paleoenvironment of rhizoliths of Shiyang River Basin, Tenggeri Desert, NW China. *Quaternary International* 502:246-257. doi: 10.1016/j.quaint.2018.06.046
- Sutherland JM, Sprent JI (1984) Calcium-oxalate crystals and crystal cells in determinate root-nodules of legumes. *Planta* 161:193-200. doi: 10.1007/bf00982912
- Suzuki T (2005) Observation of wet specimens: Simple freeze-dry and LV CRYO technique. *Application Notes*. JEOL User's Meeting, JEOL (Europe) S.A.
- Swart PK (2015) The geochemistry of carbonate diagenesis: The past, present and future. *Sedimentology* 62:1233-1304. doi: 10.1111/sed.12205
- Swart PK, Eberli GP, McKenzie JA (2009a) *Perspectives in Carbonate Geology: a Tribute to the*

- Career of Robert Nathan Ginsburg. IAS Special Publication 41. Wiley-Blackwell, Chichester, UK, xi+287 pp
- Swart PK, Eberli GP, McKenzie JA (2009b) Preface. In: Swart PK, Eberli GP, McKenzie JA (eds) Perspectives in Carbonate Geology: a Tribute to the Career of Robert Nathan Ginsburg. IAS Special Publication 41. Wiley-Blackwell, Chichester, UK, pp vii-x
- Syah MHF, Kano A, Iizuka T, Kakizaki Y (2019) Depositional and diagenetic history of limestones and dolostones of the Oligo-Miocene Kujung Formation in the Northeast Java Basin, Indonesia. *Island Arc* 28. doi: 10.1111/iar.12326
- Tabor NJ, Myers TS (2015) Paleosols as Indicators of Paleoenvironment and Paleoclimate. *Annual Review of Earth and Planetary Sciences*, Vol 43 43:333-361. doi: 10.1146/annurev-earth-060614-105355
- Tais L, Zeiger E (1998) *Plant Physiology*, Second Edition. Sinauer Associates Inc., Sunderland, Massachusetts, xxvi + 792 pp
- Taiz L, Zeiger E, Møller IM, Murphy A (2015) *Plant physiology and development*, Sixth edition edn. Sinauer Associates, Inc., Sunderland, Massachusetts, xxix + 761 pp
- Talavera S, Aedo C, Castroviejo S, Romero C, Sáez L, J. SF, Velayos M (2000) *Flora Iberica. Plantas vasculares de la Península Ibérica e Islas Baleares. Vol. 7/II Leguminosae (partim)*. Real Jardín Botánico, CSIC, Madrid, x1x + 1119 pp
- Taylor LL, Leake JR, Quirk J, Hardy K, Banwart SA, Beerling DJ (2009) Biological weathering and the long-term carbon cycle: integrating mycorrhizal evolution and function into the current paradigm. *Geobiology* 7:171-191. doi: 10.1111/j.1472-4669.2009.00194.x
- Taylor TN, Krings M, Taylor EL (2015) *Fossil Fungi*. Academic Press, Elsevier, Amsterdam etc., xv + 384 pp
- Tazaki K, Fukuyama A, Tazaki F, Takehara T, Nakamura K, Okuno M, Hashida Y, Hashida S (2017) Electron Microscopy Observation of Biomineralization within Wood Tissues of Kurogaki. *Minerals* 7. doi: 10.3390/min7070123
- Tewari VC, Stenni B, Pugliese N, Drobne K, Riccamboni R, Dolenc T (2007) Peritidal sedimentary depositional facies and carbon isotope variation across K/T boundary carbonates from NW Adriatic platform. *Palaeogeography Palaeoclimatology Palaeoecology* 255:77-86. doi: 10.1016/j.palaeo.2007.02.042
- Thomas SG, Tabor NJ, Yang W, Myers TS, Yang Y, Wang D (2011) Palaeosol stratigraphy across the Permian-Triassic boundary, Bogda Mountains, NW China: Implications for palaeoenvironmental transition through earth's largest mass extinction. *Palaeogeography Palaeoclimatology Palaeoecology* 308:41-64. doi: 10.1016/j.palaeo.2010.10.037
- Thompson WG, Curran HA, Wilson MA, White B (2011) Sea-level oscillations during the last interglacial highstand recorded by Bahamas corals. *Nature Geoscience* 4:684-687. doi: 10.1038/ngeo1253
- Thor K (2019) Calcium-Nutrient and Messenger. *Frontiers in Plant Science* 10. doi: 10.3389/fpls.2019.00440
- Timonen S, Marschner P (2006) Mycorrhizosphere concept. In: Mukerji KG, Manoharachary C, Singh J (eds) *Microbial Activity in the Rhizosphere*, vol 7. Springer, Berlin, pp 155-172
- Tinker PB, Nye PH (2000) *Solute movement in the rhizosphere*. Oxford University Press, New York, xix, 444 pp
- Todisco D, Bhiry N (2008) Micromorphology of periglacial sediments from the Tayara site, Qikirtaq Island, Nunavik (Canada). *Catena* 76:1-21. doi: 10.1016/j.catena.2008.08.002

- Tola E, Henriquez-Saba JL, Polone E, Dazzo FB, Concheri G, Casella S, Squartini A (2009) Shovel roots: a unique stress-avoiding developmental strategy of the legume plant *Hedysarum coronarium* L. *Plant and Soil* 322:25-37. doi: 10.1007/s11104-008-9861-4
- Tovar RE, Fastovsky DE, Benammi M (2012) Pedogenic calcrete in the Late Cretaceous of Michoacan, Mexico. *Boletin De La Sociedad Geologica Mexicana* 64:61-70
- Turner BR (1993) Paleosols In Permo-Triassic Continental Sediments From Prydz Bay, East Antarctica. *Journal of Sedimentary Petrology* 63:694-706
- Turner BR, Makhlof I (2005) Quaternary sandstones, northeast Jordan: Age, depositional environments and climatic implications. *Palaeogeography Palaeoclimatology Palaeoecology* 229:230-250. doi: 10.1016/j.palaeo.2005.06.024
- Turner EC, Jones B (2005) Microscopic calcite dendrites in cold-water tufa: implications for nucleation of micrite and cement. *Sedimentology* 52:1043-1066
- Tyree MT, Ewers FW (1991) The hydraulic architecture of trees and other woody plants. *New Phytologist* 119:345-360. doi: <https://doi.org/10.1111/j.1469-8137.1991.tb00035.x>
- Tyrell T, Young JR (2009) Coccolithophores. In: Thorpe SA, Turekian KK (eds) *Encyclopedia of Ocean Sciences*, Second Edition. Academic Press, Elsevier, Amsterdam, pp 606-614. doi: <https://doi.org/10.1016/B978-012374473-9.00662-7>
- Uren NC (2018) Calcium oxalate in soils, its origins and fate - a review. *Soil Research* 56:443-450. doi: 10.1071/sr17244
- Vacher HL, Quinn TM (1997) *Geology and hydrogeology of carbonate islands*. Developments in Sedimentology 54. Elsevier, Amsterdam
- van Breemen N, Finlay R, Lundstrom U, Jongmans AG, Giesler R, Olsson M (2000) Mycorrhizal weathering: A true case of mineral plant nutrition ? *Biogeochemistry* 49:53-67. doi: 10.1023/a:1006256231670
- Vance CP, Uhde-Stone C, Allan DR (2003) Phosphorus acquisition and use: critical adaptations by plants for securing a nonrenewable resource. *New Phytologist* 157:423-447. doi: <https://doi.org/10.1046/j.1469-8137.2003.00695.x>
- Van Driessche AES, Kellermeier M, Benning LG, Gerbauer D (2017) *New Perspectives on Mineral Nucleation and Growth: From Solution Precursors to Solid Materials*. Springer, Cham, Switzerland, 380 pp. 10.1007/978-3-319-45669-0
- van Elsas JD (2019) The soil environment. In: van Elsas JD, Jansson JK, Rosado AS, Nanniperi P (eds) *Modern soil microbiology*, Third edition. edn. CRC Press, Taylor & Francis, Boca Raton, pp 3-21. doi: <https://doi.org/10.1201/9780429059186>
- van Elsas JD, Jansson JK, Rosado AS, Nanniperi P (2019) *Modern soil microbiology*, Third edition. edn. CRC Press, Taylor & Francis, Boca Raton, xv + 516 pp
- Vanstone SD (1991) Early Carboniferous (Mississippian) Paleosols From Southwest Britain - Influence Of Climatic-Change On Soil Development. *Journal of Sedimentary Petrology* 61:445-457
- Vanstone SD (1998) Late Dinantian palaeokarst of England and Wales: implications for exposure surface development. *Sedimentology* 45:19-37. doi: 10.1046/j.1365-3091.1998.00132.x
- Varrone D, Clari P (2003a) Evolution stratigraphique et paleo-environnementale de la Formation a Microcodium et des Calcaires a Nummulites dans les Alpes Maritimes franco-italiennes: Stratigraphic and paleoenvironmental evolution of the Microcodium Formation and the Nummulitic Limestones in the French-Italian Maritimes Alps. *Geobios* 36:775-786



- Varrone D, Clari P (2003b) Stratigraphic and paleoenvironmental evolution of the Microcodium Formation and the Nummulitic Limestones in the French-Italian Maritimes Alps. *Geobios* 36:775-786. doi: 10.1016/j.geobios.2003.09.001
- Vartanian N (1996) The drought rhizogenesis. In: Waisel Y, Eshel A, Kafkafi U (eds) *Plant Roots: the Hidden Half*, 2nd Edition. Marcel Dekker Inc., New York, pp 471 – 481
- Vera JA (2004) Cordillera Bética y Baleares. In: Vera JA (ed) *Geología de España*. SGE-IGME, Madrid, pp 345-464
- Vera JA, Molina JM, Aguado R (2004) Calcarenitas de Microcodium (Formación Majalcorón, Paleoceno, Subbético): descripción, bioestratigrafía y significado en el Terciario de la Cordillera Bética. *Boletín Geológico y Minero* 115 453-468
- Verboom WH, Pate JS (2006) Bioengineering of soil profiles in semiarid ecosystems: the 'phytotarium' concept. A review. *Plant and Soil* 289:71-102. doi: 10.1007/s11104-006-9073-8
- Verrecchia E (1990a) Incidence de l'activité fongique sur l'induration des profils carbonatés de type calcrete pédologique. L'exemple du cycle oxalate-carbonate de calcium dans les encroûtements calcaires de Galilée (Israël). *Comptes Rendus de l'Academie Des Sciences, Serie II* 311:1367-1374
- Verrecchia E (2000) Fungi and sediments. In: Riding RE, Awramik SM (eds) *Microbial sediments*. Springer, New York, pp 68-75. doi: DOI: 10.1007/978-3-662-04036-2\_9
- Verrecchia EP (1990b) Litho-diagenetic implications of the calcium oxalate-carbonate biogeochemical cycle in semiarid calcretes, Nazareth, Israel. *Geomicrobiology Journal* 8:87-99
- Verrecchia EP (1994) L'origine biologique et superficielle des croûtes zonaires. *Bulletin De La Societe Geologique De France* 165:583-592
- Verrecchia EP (1996) Morphometry of microstromatolites in calcrete laminar crusts and a fractal model of their growth. *Mathematical Geology* 28:87-109
- Verrecchia EP (2011) Pedogenic carbonates. In: Reitner J, Thiel V (eds) *Encyclopedia of Geobiology*. Springer Berlin, pp 721-725. doi: 10.1007/978-1-4020-9212-1
- Verrecchia EP, Dumont JL, Verrecchia KE (1993) Role of calcium-oxalate biomineralization by fungi in the formation of calcretes - A case-study from Nazareth, Israel. *Journal of Sedimentary Petrology* 63:1000-1006
- Verrecchia EP, Freytet P, Verrecchia KE, Dumont JL (1995) Spherulites In Calcrete Laminar Crusts - Biogenic CaCO<sub>3</sub> Precipitation As A Major Contributor To Crust Formation. *Journal of Sedimentary Research Section a-Sedimentary Petrology and Processes* 65:690-700
- Verrecchia EP, Freytet P, Verrecchia KE, Dumont JL (1996) Spherulites in calcrete laminar crusts: Biogenic CaCO<sub>3</sub> precipitation as a major contributor to crust formation - Reply. *Journal of Sedimentary Research* 66:1041-1044
- Verrecchia EP, Ribier J, Patillon M, Rolko KE (1991) Stromatolitic Origin For Desert Laminar Limecrusts - A New Paleoenvironmental Indicator For Arid Regions. *Naturwissenschaften* 78:505-507. doi: 10.1007/bf01131398
- Verrecchia EP, Trombino L (2021) *A Visual Atlas for Soil Micromorphologists*. Springer Nature Switzerland AG, Cham, 177 pp. <https://doi.org/10.1007/978-3-030-67806-7>
- Verrecchia EP, Verrecchia KE (1994) Needle-fiber calcite - a critical-review and a proposed classification. *Journal of Sedimentary Research Section A - Sedimentary Petrology and Processes* 64:650-664
- Vierheilig H, Schweiger P, Brundrett M (2005) An overview of methods for the detection and observation of arbuscular mycorrhizal fungi in roots. *Physiologia Plantarum* 125:393-404. doi: 10.1111/j.1399-3054.2005.00564.x

- Viles HA (1984) Biokarst - Review And Prospect. *Progress in Physical Geography* 8:523-542. doi: 10.1177/030913338400800403
- Vogiatzakis IN (2012) *Mediterranean mountain environments*. Wiley, Chichester, West Sussex ; Hoboken, NJ, xii + 216 pp
- Volk TJ (2013) Fungi. In: Levin SA (ed) *Encyclopedia of Biodiversity (Second Edition)*, Volume 3. Academic Press, Waltham, pp 624-640. doi: <http://dx.doi.org/10.1016/B978-0-12-384719-5.00062-9>
- Waisel Y, Eshel A (2002) Functional diversity of various constituents of a single root. In: Waisel Y, Eshel A, Beeckman T, Kafkafi U (eds) *Plant roots : the hidden half*, Third Edition. CRC Press, Boca Raton, pp 157-174
- Waisel Y, Eshel A, Kafkafi U (1991) *Plant roots : the hidden half*. M. Dekker, New York, xiii, 948 pp
- Waisel Y, Eshel A, Kafkafi U (1996) *Plant roots : the hidden half*, 2nd edn. Marcel Dekker, New York, xvi, 1002 pp
- Waisel Y, Eshel A, Kafkafi U (2002) *Plant roots : the hidden half*, 3rd edn. M. Dekker, New York, xx, 1120 pp
- Walker C, Harper CJ, Brundrett MC, Krings M (2018) Looking for Arbuscular Mycorrhizal Fungi in the Fossil Record: An Illustrated Guide. In: Krings M, Harper CJ, Cúneo NR, Rothwell GW (eds) *Transformative Paleobotany. Papers to Commemorate the Life and Legacy of Thomas N. Taylor*. Academic Press, Elsevier, London, pp 481-517. doi: /10.1016/B978-0-12-813012-4.00020-6
- Wall LG (2000) The actinorhizal symbiosis. *Journal Of Plant Growth Regulation* 19:167-182
- Wallerius JG (1772) *Systema mineralogicum, quo corpora mineralia in classes ordines, genera et species, suis cum varietatibus divisa, describuntur, atque observationibus, experimentis et figuris æneis illustrantur, Tomus I. Laurentius Salvius, Stockholm, 423 pp*
- Wallerius JG (1778) *Systema mineralogicum, quo corpora mineralia in classes ordines, genera et species, suis cum varietatibus divisa, describuntur, atque observationibus, experimentis et figuris æneis illustrantur, Tomus II. Editio altera correctata. Officina Krausiana, Vienna, 640 pp*
- Wanas HA (2012) Pseudospherulitic fibrous calcite from the Quaternary shallow lacustrine carbonates of the Farafra Oasis, Western Desert, Egypt: A primary precipitate with possible bacterial influence. *Journal of African Earth Sciences* 65:105-114. doi: 10.1016/j.jafrearsci.2012.02.003
- Wang H, Greenberg SE (2007) Reconstructing the response of C-3 and C-4 plants to decadal-scale climate change during the late Pleistocene in southern Illinois using isotopic analyses of calcified rootlets. *Quaternary Research* 67:136-142. doi: 10.1016/j.yqres.2006.10.001
- Wang NA, Ning K, Li ZL, Wang YX, Jia P, Ma L (2016) Holocene high lake-levels and pan-lake period on Badain Jaran Desert. *Science China-Earth Sciences* 59:1633-1641. doi: 10.1007/s11430-016-5307-7
- Wang ZY, Gould KS, Patterson KJ (1994) Structure and development of mucilage-crystal idioblasts in the roots of 5 *Actinidia* species. *International Journal of Plant Sciences* 155:342-349. doi: 10.1086/297171
- Wanless HR, Dravis JJ, Tedesco LP, Rossinsky V (1989) *Carbonate Environments and Sequences of Calcos Platform, with an Introductory Evaluation of South Florida. Field Trip Guidebook T374. American Geophysical Union, Washington, iv + 75 pp*. doi:10.1002/9781118666791.ch1
- Ward WC (1975) Petrology and diagenesis of carbonate eolianites of northwestern Yucatan Peninsula, Mexico. In: Wantland KF, Pusey WC, III. (eds) *Belize Shelf Carbonate Sediments*,

- Clastic Sediments and Ecology: American Association of Petroleum Geologists, Studies in Geology 2, pp 500-571
- Watkinson SC, Boddy L, Money NP (2016) The fungi, 3rd edition, Third edition. edn. Elsevier, Amsterdam, xv + 449 pp
- Watt M, McCully ME, Canny MJ (1994) Formation and stabilization of rhizosheaths of *Zea-mays* L. Effect of soil-water content. *Plant Physiology* 106:179-186. doi: 10.1104/pp.106.1.179
- Watt M, Silk WK, Passioura JB (2006) Rates of root and organism growth, soil conditions, and temporal and spatial development of the rhizosphere. *Annals of Botany* 97:839-855. doi: 10.1093/aob/mcl028
- Watt M, Weston LA (2009) Specialised root adaptations display cell-specific developmental and physiological diversity. *Plant and Soil* 322:39-47. doi: 10.1007/s11104-009-0064-4
- Weaver JE (1919) The ecological relations of roots. Carnegie Institution of Washington, Washington, DC, 128 + 160 plates pp
- Webb MA (1999) Cell-mediated crystallization of calcium oxalate in plants. *Plant Cell* 11:751-761
- Webb MA, Cavaletto JM, Carpita NC, Lopez LE, Arnott HJ (1995) The intravacuolar organic matrix associated with calcium-oxalate crystals in leaves of *Vitis*. *Plant Journal* 7:633-648. doi: 10.1046/j.1365-313X.1995.7040633.x
- Weiner S, Addadi L (2011) Crystallization Pathways in Biomineralization. In: Clarke DR, Fratzl P (eds) *Annual Review of Materials Research*, Vol 41, vol 41, pp 21-40. doi: 10.1146/annurev-matsci-062910-095803
- Weiner S, Dove PM (2003) An overview of biomineralization processes and the problem of the vital effect. In: Dove PM, DeYoreo JJ, Weiner S (eds) *Biomineralization. Reviews in Mineralogy and Geochemistry* vol. 54, pp 1-29. doi: 10.2113/0540001
- Wells CE, Eissenstat DM (2002) Beyond the roots of young seedlings: The influence of age and order on fine root physiology. *Journal Of Plant Growth Regulation* 21:324-334
- West JB, Bowen GJ, Cerling TE, Ehleringer JR (2006) Stable isotopes as one of nature's ecological recorders. *Trends in Ecology & Evolution* 21:408-414
- Westphal H, Eberli GP, Smith LB, Grammer GM, Kislak J (2004) Reservoir characterization of the Mississippian Madison Formation, Wind River Basin, Wyoming. *Aapg Bulletin* 88:405-432. doi: 10.1306/12020301029
- Whitaker FF, Smart PL (1997) Hydrogeology of the Bahamian Archipelago. In: Vacher H, Quinn T (eds) *Geology and Hydrogeology of Carbonate Islands. Developments in Sedimentology* 54. Elsevier Science B.V., Amsterdam, pp 183-216. doi: 10.1016/S0070-4571(04)80026-8
- White B (1988) A Field Trip Guide to the Sue Point Fossil Coral Reef San Salvador Island, Bahamas. In: Mylroie J (ed) *Proceedings of the Fourth Symposium on the Geology of the Bahamas. Bahamian Field Station, San Salvador, Bahamas*, pp 353-365
- White B, Curran HA (1988) Mesoscale physical sedimentary structures and trace fossils In *Holocene carbonate eolianites from San-Salvador Island, Bahamas. Sedimentary Geology* 55:163-184. doi: 10.1016/0037-0738(88)90095-4
- White B, Curran HA (1997) Are the plant-related features in Bahamian Quaternary limestones trace fossils? Discussion, answers, and a new classification system. In: Curran HA (ed) *Guide to Bahamian Ichnology: Pleistocene, Holocene and Modern Environments. Bahamian Field Station San Salvador, Bahamas*, pp 47-54
- White B, Kurkky KA, Curran HA (1984) A shallowing-upward sequence in a Pleistocene coral reef and associated facies, San Salvador, Bahamas In: Teeter JW (ed) *Proceedings of the Second*



- Symposium on the Geology of the Bahamas. CCFL Bahamian Field Station, San Salvador, Bahamas, pp 53-70
- White PJ, Broadley MR (2003) Calcium in plants. *Annals of Botany* 92:487-511. doi: 10.1093/aob/mcg164
- Wieder M, Yaalon DH (1974) Effect of matrix composition on carbonate nodule crystallization. *Geoderma* 11:95-121. doi: 10.1016/0016-7061(74)90010-X
- Wilcox HE (1998) Mycorrhizae. In: Waisel Y, Eshel A, Kafkafi U (eds) *Plant Roots: the Hidden Half*, 2nd ed. Marcel Dekker Inc., New York, pp 689 – 721
- Wisshak M (2012) Chapter 8 - Microbioerosion. In: Knaust D, Bromley RG (eds) *Developments in Sedimentology*, vol 64. Elsevier, pp 213-243. doi: <https://doi.org/10.1016/B978-0-444-53813-0.00008-3>
- Wojciechowski MF, Lavin M, Sanderson MJ (2004) A phylogeny of legumes (Leguminosae) based on analyses of the plastid matK gene resolves many well-supported subclades within the family. *American Journal of Botany* 91:1846-1862. doi: 10.3732/ajb.91.11.1846
- Wolf SE, Gower LB (2017) Challenges and Perspectives of the Polymer-Induced Liquid-Precursor Process: The Pathway from Liquid-Condensed Mineral Precursors to Mesocrystalline Products. In: Van Driessche AES, Kellermeier M, Benning LG, Gerbauer D (eds) *New Perspectives on Mineral Nucleation and Growth: From Solution Precursors to Solid Materials*. Springer, pp 43-75. doi: 10.1007/978-3-319-45669-0\_3
- Woody DT, Smith JJ, Kraus MJ, Hasiotis ST (2014) Manganese-Bearing Rhizcretions In The Willwood Formation, Wyoming, Usa: Implications For Paleoclimate During The Paleocene-Eocene Thermal Maximum. *Palaios* 29:266-276. doi: 10.2110/palo.2013.105
- Wright VP (1982a) The Recognition And Interpretation Of Paleokarsts - 2 Examples From The Lower Carboniferous Of South-Wales. *Journal of Sedimentary Petrology* 52:83-94
- Wright VP (1982b) The recognition and interpretation of paleokarsts - Two examples from the Lower Carboniferous of South Wales. *Journal of Sedimentary Petrology* 52:83-94
- Wright VP (1983) A rendzina from the Lower Carboniferous of South-Wales. *Sedimentology* 30:159-179. doi: 10.1111/j.1365-3091.1983.tb00663.x
- Wright VP (1986) The Role Of Fungal Biomineralization In The Formation Of Early Carboniferous Soil Fabrics. *Sedimentology* 33:831-838. doi: 10.1111/j.1365-3091.1986.tb00985.x
- Wright VP (1988) Paleokarsts and Paleosols as Indicators of Paleoclimate and Porosity Evolution: A Case Study from the Carboniferous of South Wales. In: James NP, Choquette PW (eds) *Paleokarst*. Springer-Verlag, New York, pp 329-341
- Wright VP (1989) Terrestrial stromatolites and laminar calcretes: a review. *Sedimentary Geology* 65/1-2:1-13. doi: [https://doi.org/10.1016/0037-0738\(89\)90002-X](https://doi.org/10.1016/0037-0738(89)90002-X)
- Wright VP (1994) Paleosols In Shallow Marine Carbonate Sequences. *Earth-Science Reviews* 35:367-395. doi: 10.1016/0012-8252(94)90002-7
- Wright VP (2007) Calcrete. In: Nash DJ, McLaren SJ (eds) *Geochemical sediments and landscapes*. Blackwell Pub., Malden, MA, pp 10-45 doi: 10.1002/9780470712917.ch2
- Wright VP, Beck VH, SanzMontero ME (1996) Spherulites in calcrete laminar crusts: Biogenic CaCO<sub>3</sub> precipitation as a major contributor to crust formation - Discussion. *Journal of Sedimentary Research* 66:1040-1041
- Wright VP, Platt NH, Marriott SB, Beck VH (1995) A classification of rhizogenic (root-formed) calcretes, with examples from the Upper Jurassic Lower Cretaceous of Spain and Upper Cretaceous of southern France. *Sedimentary Geology* 100:143-158. doi: 10.1016/0037-0738(95)00105-0

- Wright VP, Platt NH, Marriott SB, Beck VH (1997) A classification of rhizogenic (root-formed) calcretes, with examples from the upper Jurassic lower Cretaceous of Spain and upper Cretaceous of southern France - Reply. *Sedimentary Geology* 110:305-307
- Wright VP, Platt NH, Wimbledon WA (1988) Biogenic laminar calcretes: evidence of calcified root-mat horizons in paleosols. *Sedimentology* 35:603-620. doi: 10.1111/j.1365-3091.1988.tb01239.x
- Wright VP, Sanz EM, Beck VH (1998) Rhizogenic origin for laminar-platy calcretes, Plioquaternary of Spain (abstract). In: Cañaveras JC, Garcia del Cura MA (eds) 15th International Sedimentological Congress, Alicante, Abstracts, p 827
- Wright VP, Tucker ME (1991) Calcretes: an introduction. In: Wright VP, Tucker ME (eds) *Calcretes*, vol 2, pp 1-22. doi: 10.1002/9781444304497.ch
- Wright VP, Vanstone SD (1991) Assessing The Carbon-Dioxide Content Of Ancient Atmospheres Using Palaeocalcretes - Theoretical And Empirical Constraints. *Journal of the Geological Society* 148:945-947. doi: 10.1144/gsjgs.148.6.0945
- Wright VP, Vanstone SD (1992) Further comments on using carbon isotopes in paleosols to estimate the CO<sub>2</sub> content of the palaeo-atmosphere. *Journal of the Geological Society* 149:675-676
- Yaalon DH (1997) Soils in the Mediterranean region: What makes them different? *Catena* 28:157-169. doi: 10.1016/s0341-8162(96)00035-5
- Yilmaz IO, Altiner D (2006) Cyclic palaeokarst surfaces in Aptian peritidal carbonate successions (Taurides, southwest Turkey): internal structure and response to mid-Aptian sea-level fall. *Cretaceous Research* 27:814-827. doi: 10.1016/j.cretres.2006.03.011
- York LM, Carminati A, Mooney SJ, Ritz K, Bennett MJ (2016) The holistic rhizosphere: integrating zones, processes, and semantics in the soil influenced by roots. *Journal of Experimental Botany* 67:3629-3643. doi: 10.1093/jxb/erw108
- Zacarias IA, Monferran MD, Martinez S, Gallego OF, Cabaleri NG, Armella C, Nieto DS (2019) Taphonomic analysis of an autochthonous fossil concentration in Jurassic lacustrine deposits of Patagonia, Argentina. *Palaeogeography Palaeoclimatology Palaeoecology* 514:265-281. doi: 10.1016/j.palaeo.2018.10.020
- Zadworny M, Eissenstat DM (2011) Contrasting the morphology, anatomy and fungal colonization of new pioneer and fibrous roots. *New Phytologist* 190:213-221. doi: 10.1111/j.1469-8137.2010.03598.x
- Zamagni J, Mutti M, Ballato P, Košir A (2012) The Paleocene-Eocene thermal maximum (PETM) in shallow-marine successions of the Adriatic carbonate platform (SW Slovenia). *Geological Society of America Bulletin* 124:1071-1086. doi: 10.1130/b30553.1
- Zamagni J, Mutti M, Košir A (2008) Evolution of shallow benthic communities during the late Paleocene-earliest Eocene transition in the northern Tethys (SW Slovenia). *Facies* 54:25-43. doi: 10.1007/s10347-007-0123-3
- Zamanian K, Pustovoytov K, Kuzyakov Y (2016) Pedogenic carbonates: Forms and formation processes. *Earth-Science Reviews* 157:1-17. doi: 10.1016/j.earscirev.2016.03.003
- Zenkner LJ, Kozłowski W (2017) Anomalous massive water-column carbonate precipitation (whittings) as another factor linking Silurian oceanic events. *Gff* 139:184-194. doi: 10.1080/11035897.2017.1332097
- Zhou J, Chafetz HS (2009) Biogenic caliches in Texas: The role of organisms and effect of climate. *Sedimentary Geology* 222:207-225. doi: 10.1016/j.sedgeo.2009.09.003
- Zhou J, Chafetz HS (2012) Caliche crusts: Microbially induced sedimentary structures on siliceous substrates. In: Noffke N, Chafetz H (eds) *Microbial Mats in Siliciclastic Depositional Systems through Time*, pp 191-198. doi: <https://doi.org/10.2110/sepmsp.101.191>

- Ziehen W (1980) Forschungen über Osteokollen I. *Mainzer Naturwissenschaftliches Archiv* 18:1-70
- Ziehen W (1981) Forschungen über Osteokollen II. *Mainzer Naturwissenschaftliches Archiv* 19:1-53
- Zobel RW (2003) Fine roots - discarding flawed assumptions. *New Phytologist* 160:276-279
- Zobel RW (2005a) Primary and secondary root systems. In: Zobel RW, Wright SF (eds) *Roots and Soil Management: Interactions between Roots and the Soil*. Agronomy Monograph no. 48. American Society of Agronomy, Crop Science Society of America, Soil Science Society of America, Madison, pp 3-14
- Zobel RW (2005b) Tertiary root systems. In: Zobel RW, Wright SF (eds) *Roots and Soil Management: Interactions between Roots and the Soil*. Agronomy Monograph no. 48. American Society of Agronomy, Crop Science Society of America, Soil Science Society of America, Madison, pp 35-56
- Zobel RW, Waisel Y (2010) A plant root system architectural taxonomy: A framework for root nomenclature. *Plant Biosystems* 144:507–512. doi: DOI: 10.1080/11263501003764483
- Zwieniecki MA, Newton M (1994) Root distribution of 12-year-old forests at rocky sites in southwestern Oregon: effects of rock physical properties. *Canadian Journal of Forest Research- Revue Canadienne De Recherche Forestiere* 24:1791–1796. doi: doi:10.1139/x94-231
- Zwieniecki MA, Newton M (1995) Roots growing in rock fissures - their morphological adaptation. *Plant and Soil* 172:181-187. doi: 10.1007/bf00011320
- Zwieniecki MA, Newton M (1996) Seasonal pattern of water depletion from soil-rock profiles in a Mediterranean climate southwestern Oregon. *Canadian Journal of Forest Research- Revue Canadienne De Recherche Forestiere* 26:1346-1352. doi: 10.1139/x26-150



## Appendices

## Appendix A1-1 Carbonate $\delta^{13}\text{C}$ and $\delta^{18}\text{O}$ stable isotope analysis data

### Laboratories and analytical details

*Stable Isotope Laboratory, School of Earth & Environmental Sciences, Cardiff University*  
(lab code Cf)

Isotopic determinations were performed on powdered samples using a ThermoFinnigan MAT 252 mass spectrometer with a Kiel IV carbonate preparation device. For an individual sample, repeated measurements (typically quadruplicates) were done on sets of separated sub-samples, approximately 20-100  $\mu\text{g}$  each. Isotope values are reported relative to Vienna Pee Dee Belemnite (VPDB) using the standard NBS-19. The average analytical precision of the standard analyses over the period of the investigation was  $\pm 0.05\text{‰}$  for  $\delta^{18}\text{O}$  and  $\pm 0.03\text{‰}$  for  $\delta^{13}\text{C}$  (G. Bianchi, personal communication 2005).

**GFZ. - GeoForschungsZentrum (GFZ) in Potsdam, Germany** (lab code GFZ)

Samples were analyzed by a ThermoFisher DELTA plus XL Finnigan GasBench II mass spectrometer. Stable isotope values were calculated with respect to the Vienna Peedee belemnite (VPDB) scale. Replicate analysis of standards (NBS19, CO1, CO8) indicated a precision of  $\pm 0.1\text{‰}$ .

Preparation: 100 %  $\text{H}_3\text{PO}_4$ , 75°C, 60 min, reference: NBS19, CO1, CO8 (VPDB);

Analytical precision:  $\delta^{13}\text{C}$  and  $\delta^{18}\text{O}$ :  $< 0.1\text{‰}$

**Graz University, Austria** (lab code Graz)

Methods : Sample powders were reacted with 100% phosphoric acid at 70°C in a Kiel II automated reaction system, and the evolved carbon dioxide gas was analysed with a Finnigan Delta Plus mass spectrometer at the University of Graz (analytical precision  $< 0.05\text{‰}$  for  $\delta^{13}\text{C}$ ,  $< 0.1\text{‰}$  for  $\delta^{18}\text{O}$ ). The  $\delta^{13}\text{C}$  and  $\delta^{18}\text{O}$  values are corrected according to the NBS19 standard and reported in per mill (‰) relative to the Vienna-PeeDee Belemnite (V-PDB) standard.

**Laboratorio de Isótopos Estables, Instituto de Geociencias (CSIC, UCM), Madrid**

(lab code UCM)

Instrument: Kiel IV Carbonate Device, ThermoScientific MAT253 Isotope Ratio Mass Spectrometer. Mass of the analysed sample: 45 to 60 µg of powdered sample reacted with 3 drops of 105% H<sub>3</sub>PO<sub>4</sub>, at 70° during 7 minutes. The result of each sample is an average of eight readings. δ<sup>13</sup>C and δ<sup>18</sup>O were calibrated to the IAEA standards NBS-19 and NBS-18 and Carrara marble as internal standard. Standard deviation is 0.04 for δ<sup>13</sup>C and 0.08 for δ<sup>18</sup>O for NBS-19 and Carrara marble and 0.04 for δ<sup>13</sup>C and 0.1 for δ<sup>18</sup>O, for NBS-18.

**Table A1-1.1.** Cumulative table of all stable isotope analysis results.

**Material types:** CC - chalky calcrete (bulk, pisoids); iCR - intracellularly calcified roots, unspecified and iCR-I - type I, iCR-II - type II, suffix-D - micritised/degraded iCRs; lam RhC - laminar calcrete (rhizolite); Mcod - *Microcodium*; NFC - pure needle fibre calcite; nod - calcrete nodule; rhizolith - individual rhizoliths (unspecified);

Lab	Sample ID	locality, material/ stratigraphic unit, age	sample name	material type	δ <sup>13</sup> C (VPDB)	δ <sup>18</sup> O (VPDB)
Cf	AK-03-003	Sella, modern soil	SLL-01	iCR	-13.15	-5.19
Cf	AK-03-004	Ibi, calcrete, ?Holocene	IBI-02	iCR	-13.94	-9.70
Cf	AK-03-006	Fontjouncouse, palaeosol, Paleocene	Fontjoncouse 01	Mcod	-8.27	-6.94
Cf	AK-03-007	Sella, modern soil	SLL-x	bulk CC	-6.29	-3.52
Cf	AK-03-008	Vrabče, palustrine limestone, Liburnian Fm. Maastrichtian	SV-81 Vrabče	Mcod	-9.38	-5.21
Cf	AK-03-009	Vrabče, palustrine limestone, Liburnian Fm. Maastrichtian	SV-81 Vrabče	Mcod	-9.16	-5.38
Cf	AK-03-010	Vrabče, palustrine limestone, Liburnian Fm. Maastrichtian	SV-81 Vrabče	Mcod	-9.59	-5.55
Cf	AK-03-010R	Vrabče, palustrine limestone, Liburnian Fm. Maastrichtian	SV-81 Vrabče	Mcod	-9.23	-4.20
Cf	AK-03-011	Vrabče, palustrine limestone, Liburnian Fm. Maastrichtian	SV-82 Vrabče	Mcod	-8.47	-4.63
Cf	AK-03-012	Vrabče, palustrine limestone, Liburnian Fm. Maastrichtian	SV-82 Vrabče	Mcod	-8.86	-4.65
Cf	AK-03-012R	Vrabče, palustrine limestone, Liburnian Fm. Maastrichtian	SV-82 Vrabče	Mcod	-8.96	-3.46
Cf	AK-03-013	Divača, calcrete in paralic limestone, Trstelj Fm, Paleocene	SV-84 Div-X-1	Mcod	-11.88	-5.21
Cf	AK-03-014	Divača, calcrete in paralic limestone, Trstelj Fm, Paleocene	SV-84 Div-X-1	Mcod	-12.07	-5.35



Table A1-1.1. (continued)

Lab	Sample ID	locality, material/ stratigraphic unit, age	sample name	material type	$\delta^{13}\text{C}$ (VPDB)	$\delta^{18}\text{O}$ (VPDB)
Cf	AK-03-014R	Divača, calcrete in paralitic limestone, Trstelj Fm, Paleocene	SV-84 Div-X-1	Mcod	-11.89	-4.22
Cf	AK-03-015	Divača, calcrete in paralitic limestone, Trstelj Fm, Paleocene	SV-84 Div-X-1	Mcod	-12.05	-5.36
Cf	AK-03-016	Fontjoncouse, palaeosol, Paleocene	Fontjoncouse 01	Mcod	-8.49	-6.03
Cf	AK-03-017	Fontjoncouse, palaeosol, Paleocene	Fontjoncouse 01	Mcod	-8.33	-7.08
Cf	AK-03-018	lbi, calcrete, ?Holocene	IBI-02	iCR-D	-7.50	-7.48
Cf	AK-03-018R	lbi, calcrete, ?Holocene	IBI-02	iCR-D	-7.67	-7.57
Cf	AK-03-019	lbi, calcrete, ?Holocene	IBI-02	iCR	-13.58	-9.15
Cf	AK-03-020	lbi, calcrete, ?Holocene	IBI-02	iCR	-13.57	-7.54
Cf	AK-03-021	lbi, calcrete, ?Holocene	IBI-02	iCR	-14.99	-6.98
Cf	AK-03-021R	lbi, calcrete, ?Holocene	IBI-02	iCR	-13.89	-5.99
Cf	AK-03-022	lbi, calcrete, ?Holocene	IBI-02	iCR	-14.34	-6.93
Cf	AK-03-023	Sella, modern soil	SLL-3	iCR- D	-9.43	-6.36
Cf	AK-03-024	Sella, modern soil	SLL-y	iCR	-13.67	-4.81
Cf	AK-03-024R	Sella, modern soil	SLL-y	iCR	-13.59	-4.63
Cf	AK-03-025	Sella, modern soil	SLL-2	iCR	-11.50	-3.72
Cf	AK-03-026	Sella, modern soil	SLL-X	iCR	-11.77	-4.35
Cf	AK-03-027	Benimantel, modern soil	BNM-01	iCR- D	-10.91	-7.44
Cf	AK-03-028	Benimantel, modern soil	BNM-01	iCR- D	-9.95	-6.95
Cf	AK-03-029	Polop, modern soil	PLP-01	iCR- D	-8.19	-3.58
Cf	AK-03-029R	Polop, modern soil	PLP-01	iCR- D	-8.10	-4.11
Cf	AK-03-030	Polop, modern soil	PLP-01	iCR- D	-7.78	-4.06
Cf	AK-03-030R	Polop, modern soil	PLP-01	iCR- D	-7.43	-3.82
Cf	AK-03-031	Sella, modern soil	SLL-x	iCR	-11.90	-5.73
Cf	AK-03-032	lbi, calcrete, ?Holocene	IBI-04	iCR-D	-9.21	-6.46
Cf	AK-03-033	lbi, calcrete, ?Holocene	IBI-06	iCR	-10.12	-7.28
Cf	AK-03-034	lbi, calcrete, ?Holocene	IBI-06	iCR	-14.50	-6.02
Cf	AK-03-035	lbi, calcrete, ?Holocene	IBI-06	iCR	-10.54	-6.38
Cf	AK-03-036	lbi, calcrete, ?Holocene	IBI-05	nod	-7.99	-5.24
Cf	AK-03-037	lbi, calcrete, ?Holocene	IBI-05	nod	-7.68	-5.31
Cf	AK-03-038	Sella, modern soil	SLL-09	NFC	-8.28	-5.36
Cf	AK-03-039	Sella, modern soil	SLL-09	NFC	-6.96	-5.01
Cf	AK-03-040	Sella, modern soil	SLL-09	bulk CC	-8.06	-4.96
Cf	AK-03-041	Sella, modern soil	SLL-09	bulk CC	-8.03	-5.32
Cf	AK-03-042	Sella, modern soil	SLL-09	NFC	-8.36	-5.44

Table A1-1.1. (continued)

Lab	Sample ID	locality, material/ stratigraphic unit, age	sample name	material type	$\delta^{13}\text{C}$ (VPDB)	$\delta^{18}\text{O}$ (VPDB)
Cf	AK-03-043	Sella, modern soil	SLL-09	NFC	-7.56	-5.14
Cf	AK-03-044	lbi, calcrete, ?Holocene	IBI-06	nod	-7.64	-5.31
Cf	AK-03-045	lbi, calcrete, ?Holocene	IBI-06	nod	-7.84	-5.44
Cf	AK-03-046	lbi, calcrete, ?Holocene	IBI-02	nod	-7.84	-5.41
Cf	AK-03-047	lbi, calcrete, ?Holocene	IBI-02	nod	-7.88	-5.36
Cf	AK-03-048	lbi, calcrete, ?Holocene	IBI-02	nod	-7.94	-5.47
Cf	AK-03-049	lbi, calcrete, ?Holocene	IBI-04	bulk CC	-8.31	-6.12
Cf	AK-03-050	lbi, calcrete, ?Holocene	IBI-04	bulk CC	-8.32	-6.21
Cf	AK-05-061	Dekani, modern soil on flysch marl	ACKS-Dekani	iCR	-17.22	-9.70
Cf	AK-05-062	Dekani, modern soil on flysch marl	ACKS-Dekani	iCR	-16.79	-9.59
Cf	AK-05-063	Dekani, modern soil on flysch marl	ACKS-Dekani	iCR	-13.95	-9.05
Cf	AK-05-064	Penàguila, calcrete, ?Holocene	PEN-01	iCR-II-D	-8.01	-6.65
Cf	AK-05-065	Penàguila, calcrete, ?Holocene	PEN-01	iCR-II-D	-8.45	-8.03
Cf	AK-05-066	Penàguila, calcrete, ?Holocene	PEN-01	iCR-II-D	-8.72	-7.90
Cf	AK-05-067	Penàguila, calcrete, ?Holocene	PEN-01	iCR-II-D	-8.43	-6.15
Cf	AK-05-068	Penàguila, calcrete, ?Holocene	PEN-01	iCR-II-D	-8.61	-7.12
Cf	AK-05-069	Penàguila, calcrete, ?Holocene	PEN-01	iCR-II-D	-8.55	-7.88
Cf	AK-05-070	Penàguila, calcrete, ?Holocene	PEN-01	iCR-II-D	-9.23	-7.52
Cf	AK-05-071	Relleu, modern soil	REL-AK-71	iCR-II-D	-7.46	-4.30
Cf	AK-05-072	Sella, modern soil	SLL-20/2	iCR	-15.00	-5.93
Cf	AK-05-073	Sella, modern soil	SLL-20/2	iCR	-14.85	-5.57
Cf	AK-05-074	Sella, modern soil	SLL-20/2	iCR	-13.76	-5.26
Cf	AK-05-075	Sella, modern soil	SLL-20/2	iCR	-14.36	-5.81
Cf	AK-05-076	Sella, modern soil	SLL-06	iCR	-14.50	-2.96
Cf	AK-05-078	Relleu, modern soil	REL- Relleu	iCR-II-D	-7.59	-5.25
Cf	AK-05-079	Relleu, modern soil	REL- Relleu	iCR-II-D	-6.31	-5.96
Cf	AK-05-080	Relleu, modern soil	REL-02	iCR-II-D	-7.64	-6.43
Cf	AK-05-081	Relleu, modern soil	REL-01	iCR-D	-7.55	-6.58
Cf	AK-05-082	Relleu, modern soil	REL-SICf-AK82	iCR-II-D	-7.03	-4.74
Cf	AK-05-083	Relleu, modern soil	REL-08	iCR-II-D	-7.54	-6.16
Cf	AK-05-084	Penàguila, calcrete, ?Holocene	PEN-01/02	iCR-II	-9.08	-6.89
GFZ	AK-06-227	Relleu, modern soil	Relleu	iCR-D	-7.06	-7.83
GFZ	AK-06-228	Dekani, modern soil on flysch marl	ACKS Dekani = AK-05-061, -62, -63 (Cf)	iCR	-20.32	-10.44
GFZ	AK-06-229	Sv. Martin calcrete, Trstelj Fm., Paleocene	SM1-Rh6-A	lam RhC	-5.04	-3.61

Table A1-1.1. (continued)

Lab	Sample ID	locality, material/ stratigraphic unit, age	sample name	material type	$\delta^{13}\text{C}$ (VPDB)	$\delta^{18}\text{O}$ (VPDB)
GFZ	AK-06-230	lbi, calcrete, ?Holocene	IBI-04	iCR-D	-9.12	-6.01
GFZ	AK-06-231	lbi, calcrete, ?Holocene	IBI-04	iCR-D	-7.27	-5.70
GFZ	AK-06-232	lbi, calcrete, ?Holocene	IBI-04	CC	-6.99	-5.92
GFZ	AK-06-233	lbi, calcrete, ?Holocene	IBI-04	iCR-D	-8.15	-5.59
GFZ	AK-06-234	La Mora/Tarragona, recent soil	La Mora	CC/pisoids	-7.46	-4.13
GFZ	AK-06-235	La Mora/Tarragona, Pleistocene calcrete	La Mora	CC/lam RhC	-10.19	-4.84
GFZ	AK-06-236	La Mora/Tarragona, Pleistocene calcrete	La Mora	CC/lam RhC	-10.33	-4.79
GFZ	AK-06-237	La Mora/Tarragona, recent soil	La Mora	CC/pisoids	-9.72	-4.42
GFZ	AK-06-238	Divača, calcrete in paralic limestone, Trstelj Fm, Paleocene	DIV-30	lam RhC	-5.84	-3.07
GFZ	AK-06-239	Divača, calcrete in paralic limestone, Trstelj Fm, Paleocene	DIV-30	lam RhC	-5.52	-3.63
GFZ	AK-06-240	Divača, calcrete in paralic limestone, Trstelj Fm, Paleocene	DIV-30	lam RhC	-6.79	-4.21
GFZ	AK-06-241	Divača, calcrete in paralic limestone, Trstelj Fm, Paleocene	DIV-30	lam RhC	-6.70	-4.82
GFZ	AK-06-243	Sv. Martin calcrete, Trstelj Fm., Paleocene	SM1-Rh4	lam RhC	-6.65	-4.01
GFZ	AK-06-244	Sv. Martin calcrete, Trstelj Fm., Paleocene	SM1-Rh4	lam RhC	-5.45	-3.62
GFZ	AK-06-245	Sv. Martin calcrete, Trstelj Fm., Paleocene	SM1-Rh4	lam RhC	-5.67	-3.79
GFZ	AK-06-246	Sv. Martin calcrete, Trstelj Fm., Paleocene	SM1-Rh4	lam RhC	-6.11	-3.70
GFZ	AK-06-247	Trstelj calcrete, Trstelj Fm/ Alveolina-nummulites limestone, Paleocene/Eocene	TRS - Trstelj calcrete	lam RhC	-2.16	-2.75
GFZ	AK-06-248	Nicholls Town, N Andros, calcrete on Pleistocene Cockburn Town Member	N Andros, NTW	lam RhC	-9.45	-2.26
GFZ	AK-06-249	Nicholls Town, N Andros, calcrete on Pleistocene Cockburn Town Member	N Andros, NTW	lam RhC	-9.83	-2.35
GFZ	AK-06-250	Nicholls Town, N Andros, calcrete on Pleistocene Cockburn Town Member	N Andros, NTW	lam RhC	-9.53	-3.17
GFZ	AK-06-251	Nicholls Town, N Andros, calcrete on Pleistocene Cockburn Town Member	N Andros, NTW	lam RhC	-9.76	-2.71
GFZ	AK-06-256	lbi, calcrete, ?Holocene	IBI-02 (=AK-03- 005???)	iCR	-12.55	-8.83



Table A1-1.1. (continued)

Lab	Sample ID	locality, material/ stratigraphic unit, age	sample name	material type	$\delta^{13}\text{C}$ (VPDB)	$\delta^{18}\text{O}$ (VPDB)
GFZ	AK-06-257	lbi, calcrete, ?Holocene	IBI-02 (=AK-03-019)	iCR	-13.46	-9.34
GFZ	AK-06-258	lbi, calcrete, ?Holocene	IBI-02 (=AK-03-020)	iCR	-12.33	-8.71
GFZ	AK-06-259	lbi, calcrete, ?Holocene	IBI-02 (=AK-03-021)	iCR	-13.57	-6.23
GFZ	AK-06-260	lbi, calcrete, ?Holocene	IBI-02 (=AK-03-022)	iCR	-12.77	-6.31
GFZ	AK-06-261	Sella, modern soil	SLL- (=AK-03-24)	iCR	-13.76	-5.13
GFZ	AK-06-262	lbi, calcrete, ?Holocene	IBI-05 (=AK-03-034)	iCR	-12.79	-7.33
Graz	AK-07-300	Vrabče, palustrine limestone, Liburnian Fm. Maastrichtian	SV-81 bulk mcod	mcod	-13.77	-5.90
Graz	AK-07-301	Vrabče, palustrine limestone, Liburnian Fm. Maastrichtian	SV-82 bulk mcod	mcod	-8.74	-4.56
Graz	AK-07-302	Divača, calcrete in paralic limestone, Trstelj Fm, Paleocene	DIV-33 dark laminae, bulk	lam RhC	-6.69	-4.47
Graz	AK-07-303	Divača, calcrete in paralic limestone, Trstelj Fm, Paleocene	DIV-33 dark laminae, bulk	lam RhC	-6.68	-4.46
Graz	AK-07-304	Divača, calcrete in paralic limestone, Trstelj Fm, Paleocene	DIV-33 dark laminae, bulk	lam RhC	-6.77	-5.23
Graz	AK-07-306	Divača, calcrete in paralic limestone, Trstelj Fm, Paleocene	DIV-33 host rock, base of clcrete, bulk	hostrock	-8.14	-5.05
Graz	AK-07-307	Divača, calcrete in paralic limestone, Trstelj Fm, Paleocene	DIV-33 host rock, base of clcrete, bulk	hostrock	-7.91	-5.27
Graz	AK-07-308	Divača, calcrete in paralic limestone, Trstelj Fm, Paleocene	DIV-33 host rock, = duplicate .-307	hostrock	-7.96	-5.15
Graz	AK-07-309	Divača, calcrete in paralic limestone, Trstelj Fm, Paleocene	DIV-33 Rh stromatol. dark laminae, bulk	lam RhC	-6.96	-4.30
Graz	AK-07-310	Divača, calcrete in paralic limestone, Trstelj Fm, Paleocene	DIV-33 Rh stromatol. dark laminae, bulk	lam RhC	-6.32	-4.56
Graz	AK-07-322	Slavnik, Liburnian Fm, ?Maastrichtian/Danian	lam cc Slavnik	lam RhC	-7.32	-3.57
Graz	AK-07-323	Slavnik, Liburnian Fm, ?Maastrichtian/Danian	lam cc Slavnik	lam RhC	-7.03	-3.17
Graz	AK-14-400	Sella-Finestrat, modern soil	T461-3-01 Sella/ Finestrat	iCR-I	-14.13	-7.22
Graz	AK-14-401	Sella-Finestrat, modern soil	T461-3-01	iCR-I	-10.03	-5.27
Graz	AK-14-402	Sella-Finestrat, modern soil	T461-3-01	iCR-I	-13.10	-6.61
Graz	AK-14-403	Sella-Finestrat, modern soil	T461-3-01	host, bulk	-3.02	-3.22

Table A1-1.1. (continued)

Lab	Sample ID	locality, material/ stratigraphic unit, age	sample name	material type	$\delta^{13}\text{C}$ (VPDB)	$\delta^{18}\text{O}$ (VPDB)
Graz	AK-14-404	Sella-Finestrat, modern soil	T461-3-01	iCR-I	-15.34	-0.50
Graz	AK-14-405	Sella-Finestrat, modern soil	T461-3-02	iCR-I	-13.98	-5.27
Graz	AK-14-406	Sella-Finestrat, modern soil	T461-3-02	iCR-I	-15.01	-6.01
Graz	AK-14-407	Sella-Finestrat, modern soil	T461-3-03	iCR-I	-13.06	-6.96
Graz	AK-14-408	Sella-Finestrat, modern soil	T461-3-03	iCR-I	-12.35	-6.50
Graz	AK-14-409	Sella-Finestrat, modern soil	T461-3-03	host, bulk	-1.74	-2.85
Graz	AK-14-410	Sella-Finestrat, modern soil	T461-3-06	iCR-I	-12.30	-1.91
Graz	AK-14-410-2	Sella-Finestrat, modern soil	T461-3-07	iCR-I	-12.75	-2.44
Graz	AK-14-411	Sella-Finestrat, modern soil	T461-3-06	iCR-I-D	-8.90	-3.85
Graz	AK-14-412	Sella-Finestrat, modern soil	T461-3-08	iCR-I	-11.64	-0.88
Graz	AK-14-413	Sella-Finestrat, modern soil	T461-3-09	iCR-I	-11.54	-2.04
Graz	AK-14-414	Sella-Finestrat, modern soil	T461-3-10	iCR-I	-14.31	-0.08
Graz	AK-14-414-2	Sella-Finestrat, modern soil	T461-3-10	iCR-I	-14.19	-0.61
Graz	AK-14-415	Sella-Finestrat, modern soil	T461-3-11	iCR-I	-12.39	-2.04
Graz	AK-14-415-2	Sella-Finestrat, modern soil	T461-3-11	iCR-I	-12.65	-2.79
Graz	AK-14-416	Sella-Finestrat, modern soil	T461-3-11	iCR-I	-11.37	-2.06
Graz	AK-14-416-2	Sella-Finestrat, modern soil	T461-3-11	iCR-I	-11.22	-2.04
Graz	AK-14-417	Sella-Finestrat, modern soil	T462-02 Sella/ Finestrat	iCR-II	-12.12	-4.91
Graz	AK-14-418	Sella-Finestrat, modern soil	T462-02	iCR-II	-12.07	-5.30
Graz	AK-14-418-2	Sella-Finestrat, modern soil	T462-02	iCR-II	-12.69	-5.42
Graz	AK-14-419	Sella-Finestrat, modern soil	T462-03	iCR-II	-10.23	-7.84
Graz	AK-14-419-2	Sella-Finestrat, modern soil	T462-03	iCR-II	-10.18	-7.56
Graz	AK-14-419-3	Sella-Finestrat, modern soil	T462-03	iCR-II	-10.53	-7.96
Graz	AK-14-420	Sella-Finestrat, modern soil	T462-03	host/matrix (marl)	-1.32	-2.44
Graz	AK-14-421	Sella-Finestrat, modern soil	T462-08	iCR-II	-9.03	-6.66
Graz	AK-14-421-2	Sella-Finestrat, modern soil	T462-08	iCR-II	-9.98	-6.97
Graz	AK-14-422	Sella-Finestrat, modern soil	T462-16	iCR-II	-10.97	-4.68
Graz	AK-14-423	Sella-Finestrat, modern soil	T462-16	host, bulk	-1.15	-2.29
Graz	AK-14-424	Sella-Finestrat, modern soil	T462-18	iCR-II	-10.08	-8.02
Graz	AK-14-425	Sella-Finestrat, modern soil	T462-18	iCR-II	-11.23	-5.86
Graz	AK-14-425-2	Sella-Finestrat, modern soil	T462-18	iCR-II	-9.96	-6.20
Graz	AK-14-426	Sella-Finestrat, modern soil	T462-18	iCR-II	-10.47	-4.14
Graz	AK-14-426-2	Sella-Finestrat, modern soil	T462-18	iCR-II	-10.38	-4.64
Graz	AK-14-427	Sella-Finestrat, modern soil	T462-10	iCR-II	-10.19	-8.95
Graz	AK-14-427-2	Sella-Finestrat, modern soil	T462-10	iCR-II	-9.92	-8.90
Graz	AK-14-427-3	Sella-Finestrat, modern soil	T462-10	iCR-II	-10.85	-8.90
Graz	AK-14-427-4	Sella-Finestrat, modern soil	T462-10	iCR-II	-10.30	-8.55

Table A1-1.1. (continued)

Lab	Sample ID	locality, material/ stratigraphic unit, age	sample name	material type	$\delta^{13}\text{C}$ (VPDB)	$\delta^{18}\text{O}$ (VPDB)
Graz	AK-14-427-5	Sella-Finestrat, modern soil	T462-10	iCR-II	-10.88	-8.80
Graz	AK-14-428	Sella-Finestrat, modern soil	T462-10	iCR-II	-9.04	-8.73
Graz	AK-14-428-2	Sella-Finestrat, modern soil	T462-10	iCR-II	-9.66	-8.64
Graz	AK-14-429	Sella-Finestrat, modern soil	T462-10	host, bulk	-6.16	-4.19
Graz	AK-14-430	Penàguila, calcrete, ?Holocene	T458-01 Penaguila	iCR-II-D	-8.28	-6.01
Graz	AK-14-431	Penàguila, calcrete, ?Holocene	T458-17 Penaguila	iCR-D	-8.36	-6.07
Graz	AK-14-432	Penàguila, calcrete, ?Holocene	T458-05 Penaguila	iCR-D	-9.09	-6.44
Graz	AK-14-433	Penàguila, calcrete, ?Holocene	T458-26 Penaguila	iCR-D	-8.66	-6.22
Graz	AK-14-434	Montpellier, 'Vitrollien', unknown conglomerate unit, Eocene	M-7 M.Condomines/ lam. mcod	mcod	-12.16	-7.75
Graz	AK-14-435	Montpellier, 'Vitrollien', unknown conglomerate unit, Eocene	M-7 M.Condomines/ lam. mcod	mcod	-12.53	-7.22
Graz	AK-14-435-2	Montpellier, 'Vitrollien', unknown conglomerate unit, Eocene	M-7 M.Condomines/ lam. mcod	mcod	-12.35	-7.28
Graz	AK-14-435-3	Montpellier, 'Vitrollien', unknown conglomerate unit, Eocene	M-7 M.Condomines/ lam. mcod	mcod	-11.89	-7.07
Graz	AK-14-435-4	Montpellier, 'Vitrollien', unknown conglomerate unit, Eocene	M-7 M.Condomines/ lam. mcod	mcod	-12.63	-6.90
Graz	AK-14-435-5	Montpellier, 'Vitrollien', unknown conglomerate unit, Eocene	M-7 M.Condomines/ lam. mcod	mcod	-12.24	-7.18
Graz	AK-14-435-6	Montpellier, 'Vitrollien', unknown conglomerate unit, Eocene	M-7 M.Condomines/ lam. mcod	mcod	-11.25	-6.71
Graz	AK-14-436	Esplugafreda Section, Claret Fm, lowermost Eocene	T449; Claret Fm	mcod	-14.13	-7.03
Graz	AK-14-436-2	Esplugafreda Section, Claret Fm, lowermost Eocene	T449; Claret Fm	mcod	-13.95	-6.79
Graz	AK-14-436-3	Esplugafreda Section, Claret Fm, lowermost Eocene	T449; Claret Fm	mcod	-14.20	-7.20
Graz	AK-14-436-4	Esplugafreda Section, Claret Fm, lowermost Eocene	T449; Claret Fm	mcod	-13.64	-6.72
Graz	AK-14-436-5	Esplugafreda Section, Claret Fm, lowermost Eocene	T449; Claret Fm	mcod	-14.17	-6.90
Graz	AK-14-437	Esplugafreda Section, Claret Fm, lowermost Eocene	T449; Claret Fm	mcod	-12.56	-6.59
Graz	AK-14-437-2	Esplugafreda Section, Claret Fm, lowermost Eocene	T449; Claret Fm	mcod	-12.55	-6.68



Table A1-1.1. (continued)

Lab	Sample ID	locality, material/ stratigraphic unit, age	sample name	material type	$\delta^{13}\text{C}$ (VPDB)	$\delta^{18}\text{O}$ (VPDB)
Graz	AK-14-437-3	Esplugafreda Section, Claret Fm, lowermost Eocene	T449; Claret Fm	mcod	-12.91	-6.83
Graz	AK-14-438	Esplugafreda Section, Esplugafreda Fm, Paleocene	T441 Espulgafrada	mcod	-9.72	-6.15
Graz	AK-14-439	Esplugafreda Section, Esplugafreda Fm, Paleocene	T441 Espulgafrada	mcod	-8.45	-5.75
Graz	AK-14-440	Esplugafreda Section, Esplugafreda Fm, Paleocene	T441 Espulgafrada	mcod	-10.35	-6.17
Graz	AK-14-440-2	Esplugafreda Section, Esplugafreda Fm, Paleocene	T441 Espulgafrada	mcod	-9.99	-5.80
Graz	AK-14-441	Esplugafreda Section, Esplugafreda Fm, Paleocene	T436 Espulgafrada	mcod	-8.37	-4.74
Graz	AK-14-441-2	Esplugafreda Section, Esplugafreda Fm, Paleocene	T436 Espulgafrada	mcod	-8.21	-4.57
Graz	AK-14-441-3	Esplugafreda Section, Esplugafreda Fm, Paleocene	T436 Espulgafrada	mcod	-8.23	-4.94
Graz	AK-14-442	Esplugafreda Section, Esplugafreda Fm, Paleocene	T422 (!) Fontllonga	mcod	-7.73	-4.35
Graz	AK-14-443	Esplugafreda Section, Esplugafreda Fm, Paleocene	T430 Espulgafrada	mcod	-18.54	-7.58
Graz	AK-14-443-2	Esplugafreda Section, Esplugafreda Fm, Paleocene	T430 Espulgafrada	mcod	-18.89	-8.02
Graz	AK-14-444	Esplugafreda Section, Esplugafreda Fm, Paleocene	T430 Espulgafrada	mcod	-13.00	-4.94
Graz	AK-14-444-2	Esplugafreda Section, Esplugafreda Fm, Paleocene	T430 Espulgafrada	mcod	-12.99	-5.39
Graz	AK-14-444-3	Esplugafreda Section, Esplugafreda Fm, Paleocene	T430 Espulgafrada	mcod	-12.26	-5.09
Graz	AK-14-444-4	Esplugafreda Section, Esplugafreda Fm, Paleocene	T430 Espulgafrada	mcod	-12.44	-5.35
Graz	AK-14-445	Lab-grown <i>Hedysarum coronarium</i>	<i>Hedysarum coronarium</i> PkT5	marl/host rock	0.78	-3.04
Graz	AK-14-445-2	Lab-grown <i>Hedysarum coronarium</i>	<i>Hedysarum coronarium</i> PkT5	marl/host rock	0.92	-2.95
Graz	AK-14-446	Lab-grown <i>Hedysarum coronarium</i>	<i>Hedysarum coronarium</i> PkT5	marl/host rock	0.92	-2.88
Graz	AK-14-446-2	Lab-grown <i>Hedysarum coronarium</i>	<i>Hedysarum coronarium</i> PkT5	marl/host rock	0.87	-2.95
Graz	AK-14-447	Lab-grown <i>Hedysarum coronarium</i>	<i>Hedysarum coronarium</i> PkT5	iCR	-16.29	-7.59
Graz	AK-14-447-2	Lab-grown <i>Hedysarum coronarium</i>	<i>Hedysarum coronarium</i> PkT5	iCR	-16.26	-7.63
Graz	AK-14-447-3	Lab-grown <i>Hedysarum coronarium</i>	<i>Hedysarum coronarium</i> PkT5	iCR	-16.40	-7.64
Graz	AK-14-447-4	Lab-grown <i>Hedysarum coronarium</i>	<i>Hedysarum coronarium</i> PkT5	iCR	-16.29	-7.47
Graz	AK-14-448	Lab-grown <i>Hedysarum coronarium</i>	<i>Hedysarum coronarium</i> PkT5	iCR	-16.77	-6.87

Table A1-1.1. (continued)

Lab	Sample ID	locality, material/ stratigraphic unit, age	sample name	material type	$\delta^{13}\text{C}$ (VPDB)	$\delta^{18}\text{O}$ (VPDB)
Graz	AK-14-448-2	Lab-grown Hedysarum coronarium	Hedysarum coronarium PkT5	iCR	-16.70	-6.77
Graz	AK-14-449	Lab-grown Hedysarum coronarium	Hedysarum coronarium PkT5	iCR	-15.60	-7.27
Graz	AK-14-449-2	Lab-grown Hedysarum coronarium	Hedysarum coronarium PkT5	iCR	-15.47	-7.19
Graz	AK-14-450	Lab-grown Hedysarum coronarium	Hedysarum coronarium PkT5	iCR	-15.97	-6.92
Graz	AK-14-450-2	Lab-grown Hedysarum coronarium	Hedysarum coronarium PkT5	iCR	-16.24	-7.01
Graz	AK-15-502	Caicos, beachrock, ?Holocene	Caicos Beachrock, pure mcod	mcod	-5.02	-3.10
Graz	AK-15-502-2	Caicos, beachrock, ?Holocene	Caicos Beachrock, pure mcod	mcod	-4.70	-3.48
Graz	AK-15-503	Caicos, beachrock, ?Holocene	Caicos Beachrock, 50-75% mcod	mcod & host	-4.15	-3.07
Graz	AK-15-503-2	Caicos, beachrock, ?Holocene	Caicos Beachrock, 50-75% mcod	mcod & host	-1.23	-2.39
Graz	AK-15-503-3	Caicos, beachrock, ?Holocene	Caicos Beachrock, 50-75% mcod	mcod & host	-1.97	-2.31
Graz	AK-15-503-4	Caicos, beachrock, ?Holocene	Caicos Beachrock, 50-75% mcod	mcod & host	-2.63	-2.50
Graz	AK-15-504	Caicos, beachrock, ?Holocene	Caicos Beachrock, bulk + mcod	mcod & host	-1.98	-2.59
Graz	AK-15-504-2	Caicos, beachrock, ?Holocene	Caicos Beachrock, bulk + mcod	mcod & host	-5.04	-3.74
Graz	AK-15-504-3	Caicos, beachrock, ?Holocene	Caicos Beachrock, bulk + mcod	mcod & host	-1.63	-2.25
Graz	AK-15-504-4	Caicos, beachrock, ?Holocene	Caicos Beachrock, bulk + mcod	mcod & host	-3.17	-3.14
Graz	AK-15-504-5	Caicos, beachrock, ?Holocene	Caicos Beachrock, bulk + mcod	mcod & host	-4.64	-3.35
Graz	AK-15-505	Caicos, beachrock, ?Holocene	Caicos Beachrock, bulk, +/- no mcod	hostrock	3.24	-0.89
Graz	AK-15-505-2	Caicos, beachrock, ?Holocene	Caicos Beachrock, bulk, +/- no mcod	hostrock	2.88	-0.40

Table A1-1.1. (continued)

Lab	Sample ID	locality, material/ stratigraphic unit, age	sample name	material type	$\delta^{13}\text{C}$ (VPDB)	$\delta^{18}\text{O}$ (VPDB)
Graz	AK-15-505-3	Caicos, beachrock, ?Holocene	Caicos Beachrock, bulk, +/- no mcod	hostrock	1.89	-1.61
Graz	AK-15-505-4	Caicos, beachrock, ?Holocene	Caicos Beachrock, bulk, +/- no mcod	hostrock	1.92	-1.44
Graz	AK-15-505-5	Caicos, beachrock, ?Holocene	Caicos Beachrock, bulk, +/- no mcod	hostrock	2.44	-1.05
Graz	AK-15-506	Caicos, beachrock, ?Holocene	Caicos Beachrock, mcod ~90%	mcod & host	-2.32	-2.65
Graz	AK-15-507	Caicos, beachrock, ?Holocene	Caicos Beachrock, mcod ~90%	mcod	-4.85	-3.49
Graz	AK-15-510	Sella-Finestrat, modern soil	Sella-Finestrat, at Dutchs; T823, small	iCR-D	-7.7	-7.0
Graz	AK-15-510-2	Sella-Finestrat, modern soil	Sella-Finestrat, at Dutchs; T823, small	iCR-D	-7.6	-7.1
Graz	AK-15-511	Sella-Finestrat, modern soil	Sella-Finestrat, T829, chalky nod.	NFC/CC	-6.5	-6.1
Graz	AK-15-511-2	Sella-Finestrat, modern soil	Sella-Finestrat, T829, chalky nod.	NFC/CC	-6.5	-6.1
Graz	AK-15-512	Sella-Finestrat, modern soil	Sella-Finestrat, T826-1; pisoids, NFC	NFC/CC/ pisoids	-6.0	-4.1
Graz	AK-15-512-2	Sella-Finestrat, modern soil	Sella-Finestrat, T826-1; pisoids, NFC	NFC/CC/ pisoids	-7.1	-4.6
Graz	AK-15-512-3	Sella-Finestrat, modern soil	Sella-Finestrat, T826-1; pisoids, NFC	NFC/CC/ pisoids	-4.9	-3.7
Graz	AK-15-512-4	Sella-Finestrat, modern soil	Sella-Finestrat, T826-1; pisoids, NFC	NFC/CC/ pisoids	-5.6	-3.8
Graz	AK-15-512-5	Sella-Finestrat, modern soil	Sella-Finestrat, T826-1; pisoids, NFC	NFC/CC/ pisoids	-5.7	-4.1
Graz	AK-15-512-6	Sella-Finestrat, modern soil	Sella-Finestrat, T826-1; pisoids, NFC	NFC/CC/ pisoids	-5.2	-3.9
Graz	AK-15-513	Sella-Finestrat, modern soil	Sella-Finestrat, T819-01; pine roots & carbonate	NFC/CC/ pisoids	-7.4	-5.0
Graz	AK-15-513-2	Sella-Finestrat, modern soil	Sella-Finestrat, T819-01; pine roots & carbonate	NFC/CC/ pisoids	-7.0	-4.9
Graz	AK-15-513-3	Sella-Finestrat, modern soil	Sella-Finestrat, T819-01; pine roots & carbonate	NFC/CC/ pisoids	-7.2	-4.9



Table A1-1.1. (continued)

Lab	Sample ID	locality, material/ stratigraphic unit, age	sample name	material type	$\delta^{13}\text{C}$ (VPDB)	$\delta^{18}\text{O}$ (VPDB)
Graz	AK-15-513-4	Sella-Finestrat, modern soil	Sella-Finestrat, T819-01; pine roots & carbonate	NFC/CC/ pisoids	-6.2	-4.6
Graz	AK-15-513-5	Sella-Finestrat, modern soil	Sella-Finestrat, T819-01; pine roots & carbonate	NFC/CC/ pisoids	-7.3	-5.0
Graz	AK-15-513-6	Sella-Finestrat, modern soil	Sella-Finestrat, T819-01; pine roots & carbonate	NFC/CC/ pisoids	-7.3	-5.0
Graz	AK-15-514	Sella-Finestrat, modern soil	Sella-Finestrat, T819-03; as --513	NFC/CC/ pisoids	-6.7	-5.1
Graz	AK-15-514-2	Sella-Finestrat, modern soil	Sella-Finestrat, T819-03; as --514	NFC/CC/ pisoids	-6.6	-5.0
UCM	AK-17-601	Nicholls Town, N Andros, calcrete on Pleistocene Cockburn Town Member	NTW-E lam CC	lam RhC	-9.77	-3.44
UCM	AK-17-602	Nicholls Town, N Andros, calcrete on Pleistocene Cockburn Town Member	NTW-E lam CC	lam RhC	-9.54	-3.58
UCM	AK-17-603	Nicholls Town, N Andros, calcrete on Pleistocene Cockburn Town Member	NTW-E lam CC	lam RhC	-9.97	-2.83
UCM	AK-17-604	Doukkala, Morocco, recent aeolianite	Doukkala rhizolith T16-127B	rhizolith	-7.6	-3.38
UCM	AK-17-605	Doukkala, Morocco, recent aeolianite	Doukkala rhizolith T16-127B	rhizolith	-8.4	-3.62
UCM	AK-17-606	Doukkala, Morocco, recent aeolianite	Doukkala rhizolith T16-126	rhizolith	-7.91	-3.69
UCM	AK-17-607	Doukkala, Morocco, recent aeolianite	Doukkala rhizolite T16-117 hard	lam RhC	-9.24	-4.04
UCM	AK-17-608	Doukkala, Morocco, recent aeolianite	Doukkala rhizolite T16-117 porous	lam RhC	-9.1	-3.83
UCM	AK-17-609	San Salvador, Pleistocene- Holocene	SanSal SSAL-08 - lam cc/rhizolite, hard layer	lam RhC	-5.91	-2.62
UCM	AK-17-610	San Salvador, Pleistocene- Holocene	SanSal SSAL-08 - lam cc/rhizolite, porous	lam RhC	-7.03	-2.94
UCM	AK-17-611	San Salvador, Pleistocene- Holocene	SanSal SSAL-04, rhizolith, internal part	rhizolith	-2.68	-2.75

## Appendix A2-1 Rhizolites of the Bahamas: Climatic setting, location maps and complementary field photographs

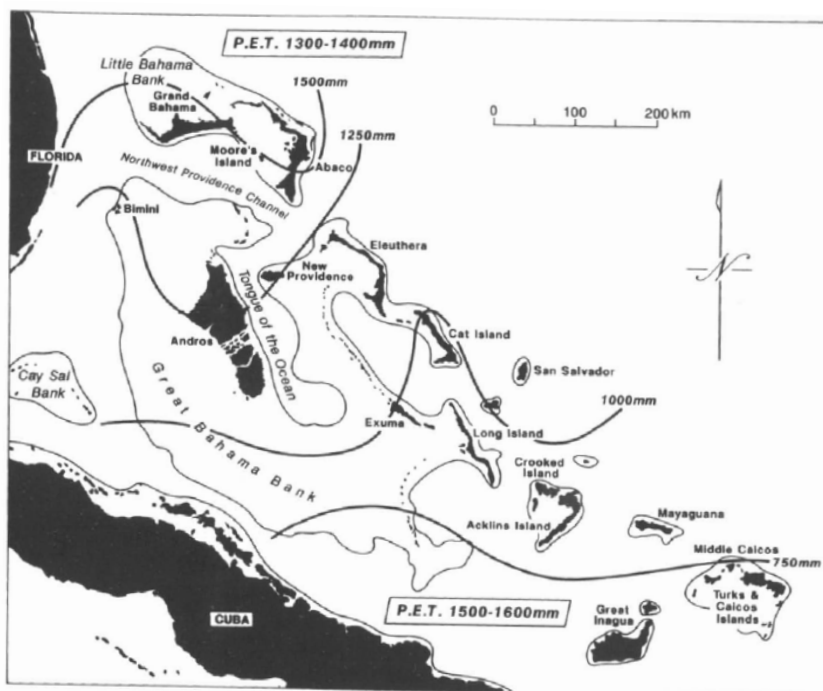


Fig. A2-1.01. Map of the Bahamian archipelago showing regional variation in mean annual rainfall (lines every 250 mm/y) and potential evapotranspiration data (P.E.T.). From Whitaker and Smart (1997) after Sealey (1994).

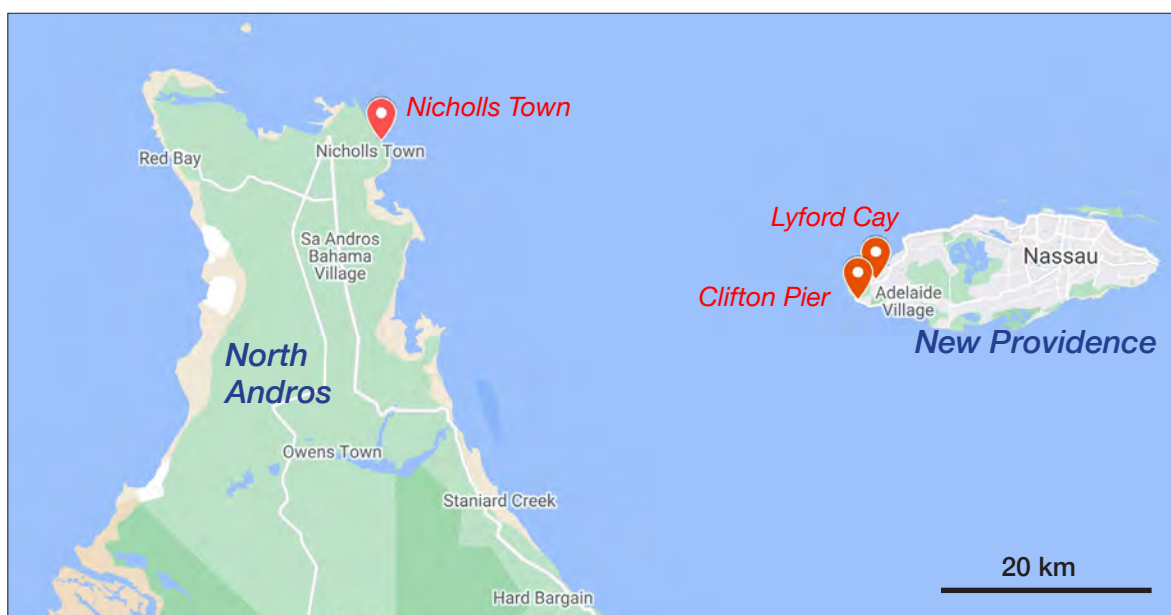


Fig. A2-1.02. Map of North Andros and New Providence Island with studied localities. Base map copied from GoogleMaps.

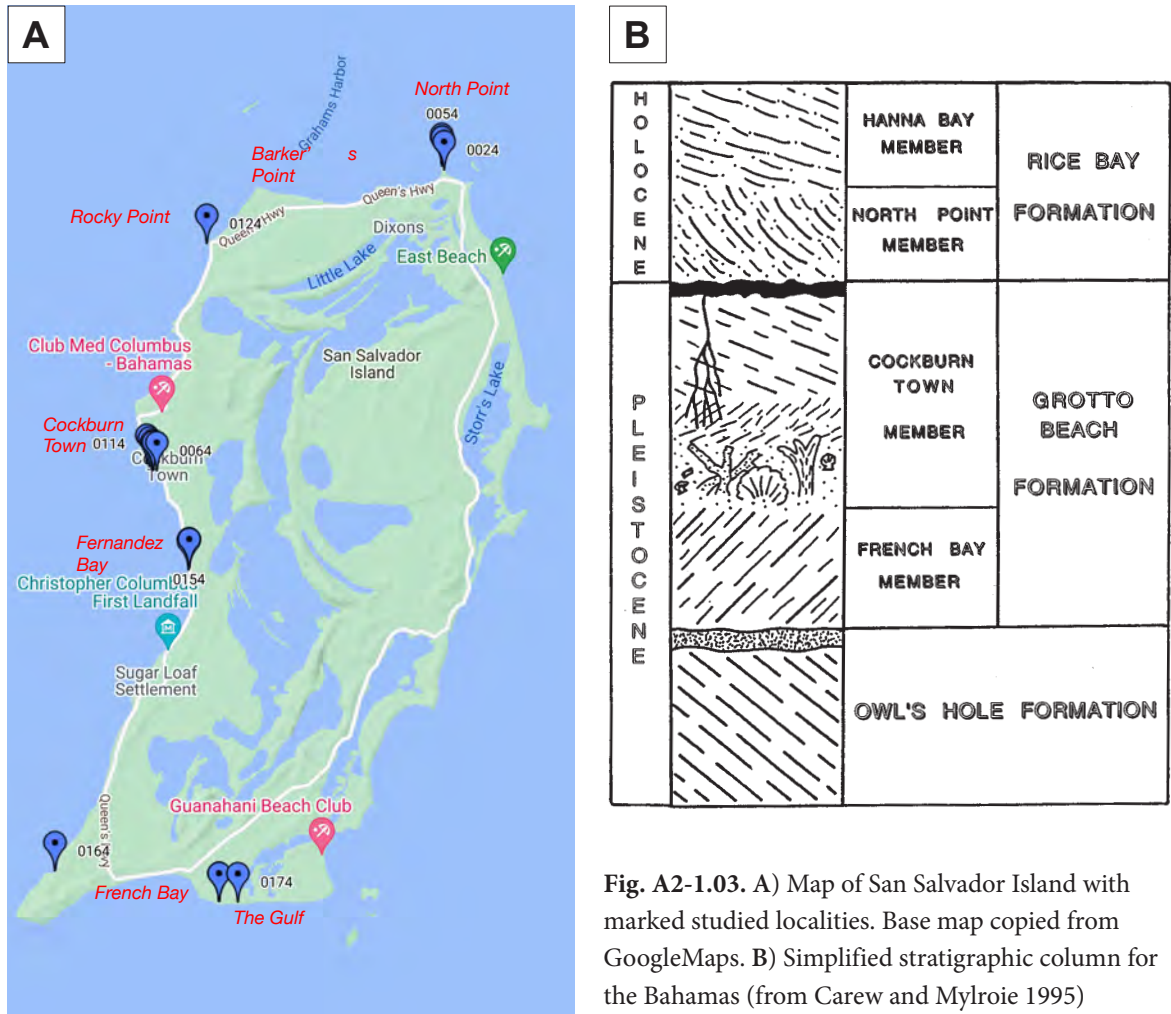
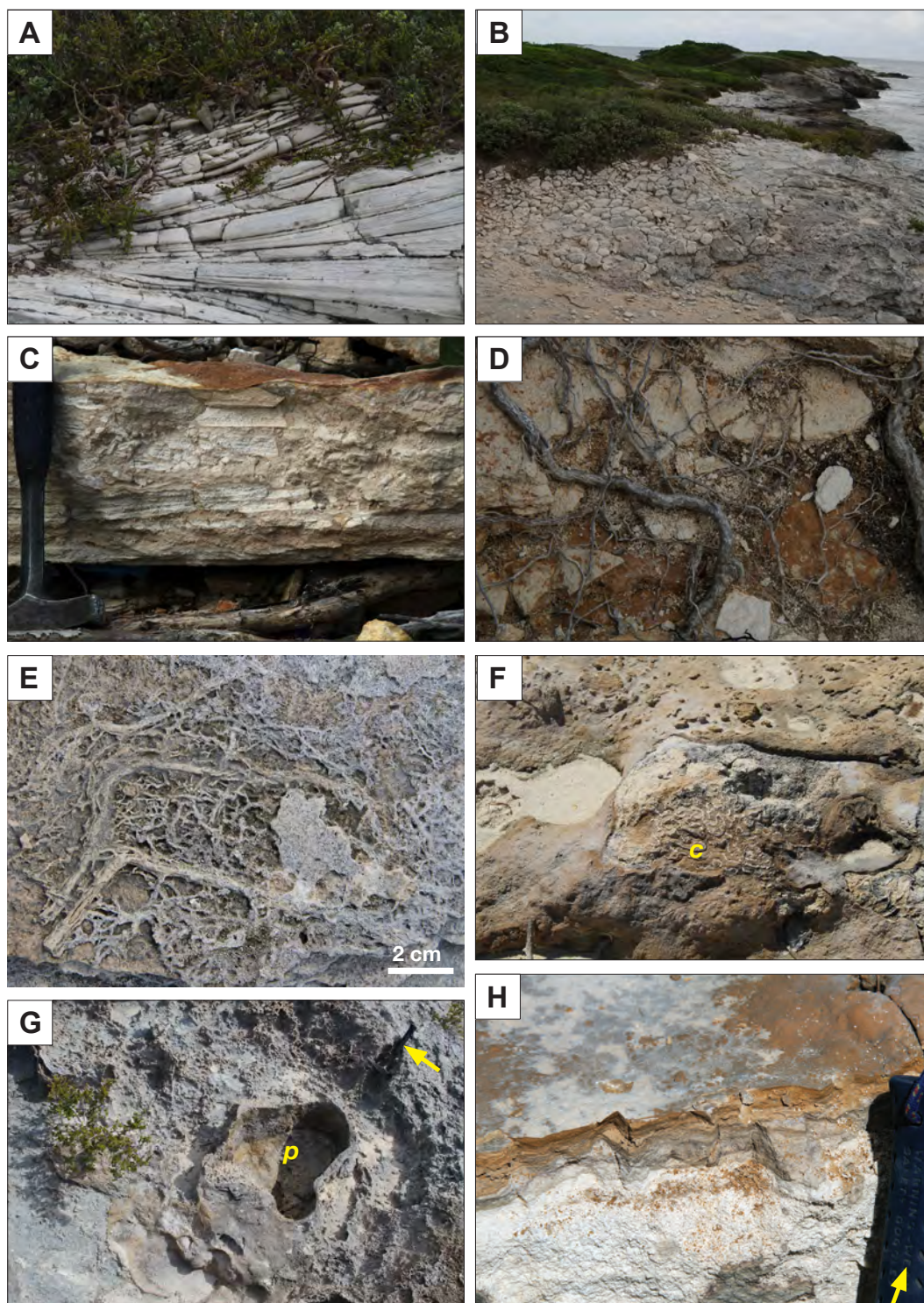


Fig. A2-1.03. A) Map of San Salvador Island with marked studied localities. Base map copied from GoogleMaps. B) Simplified stratigraphic column for the Bahamas (from Carew and Mylroie 1995)





**Fig. A2-1.04.** San Salvador Island, the Bahamas. **A, B)** Outcrops of aeolianite of the Rice Bay Formation at the North Point. **A:** cross-bedded aeolianite with plant roots penetrating along and enlarging bedding plane partings and joints, cross-cutting the bedding. **B:** exposed boxwork-like brecciation of aeolianite beds, produced by root growth. **C)** Palaeosol bed, composed of displaced, subparallel flat clasts of aeolianite in beige matrix. Pleistocene ?Cockburn Town Member, French Bay. **D)** Coarse and fine roots penetrating weakly cemented holocene aeolianite, French Bay. **E)** Rhizoliths from a weathered bedding plane in aeolianite, corresponding to a part of a root system. French Bay. **F)** Lamellar rhizolite coating coral rubble. Northwest Point, New Providence Island. **G)** Calcrete-lined solution pipe from eroded, weakly-cemented aeolian sand. Coast E of French Bay. **H)** Finely laminar red-brown calcrete, coating bioclastic limestone, Grotto Beach Formation, Pleistocene.



### Appendix A2-2 Holocene/Recent composite rhizoliths from Doukkala, Morocco

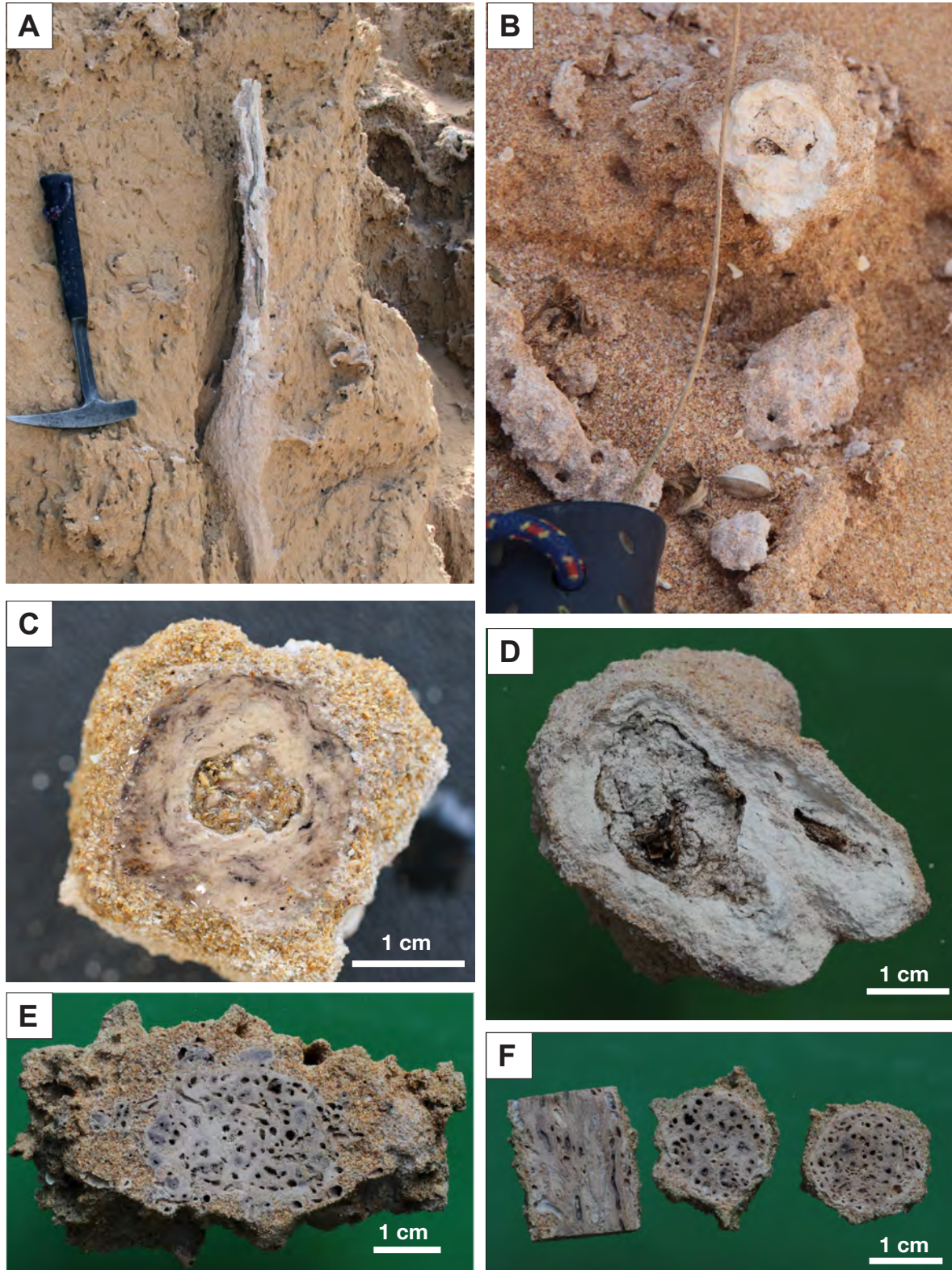
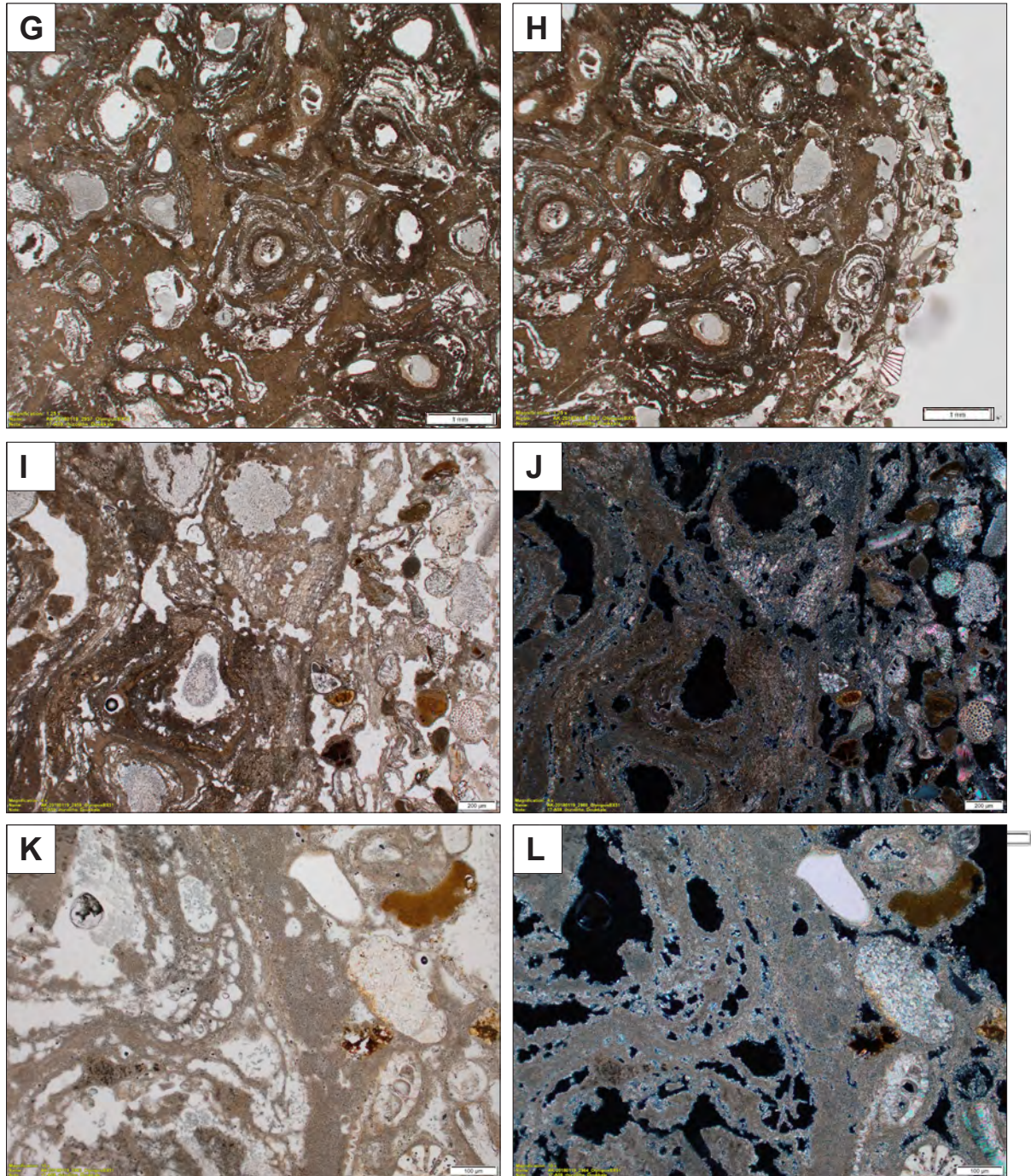


Fig. A2-2.01. (continued on next page)





**Fig. A2-2.01.** Composite rhizoliths from Holocene/Recent aeolian dunes near Oualidia (Doukkala region, Morocco). A-B) Vertical rhizoliths, several cm in diameter, forming in a void of former coarse tap root. C, D) Cross section of large rhizolith showing centripetal growth and progressive filling-up the void by carbonate precipitated around fine roots. E, F) Cut pieces of composite rhizoliths. G-L) PPL and XPL thin section photomicrograph pairs of a composite rhizolith.



### Appendix A2-3 Potential analogues of fine root mineralisation and taphonomy from modern soils of the Province of Alicante, Spain, and modern aeolianites of the Doukkala region, Morocco

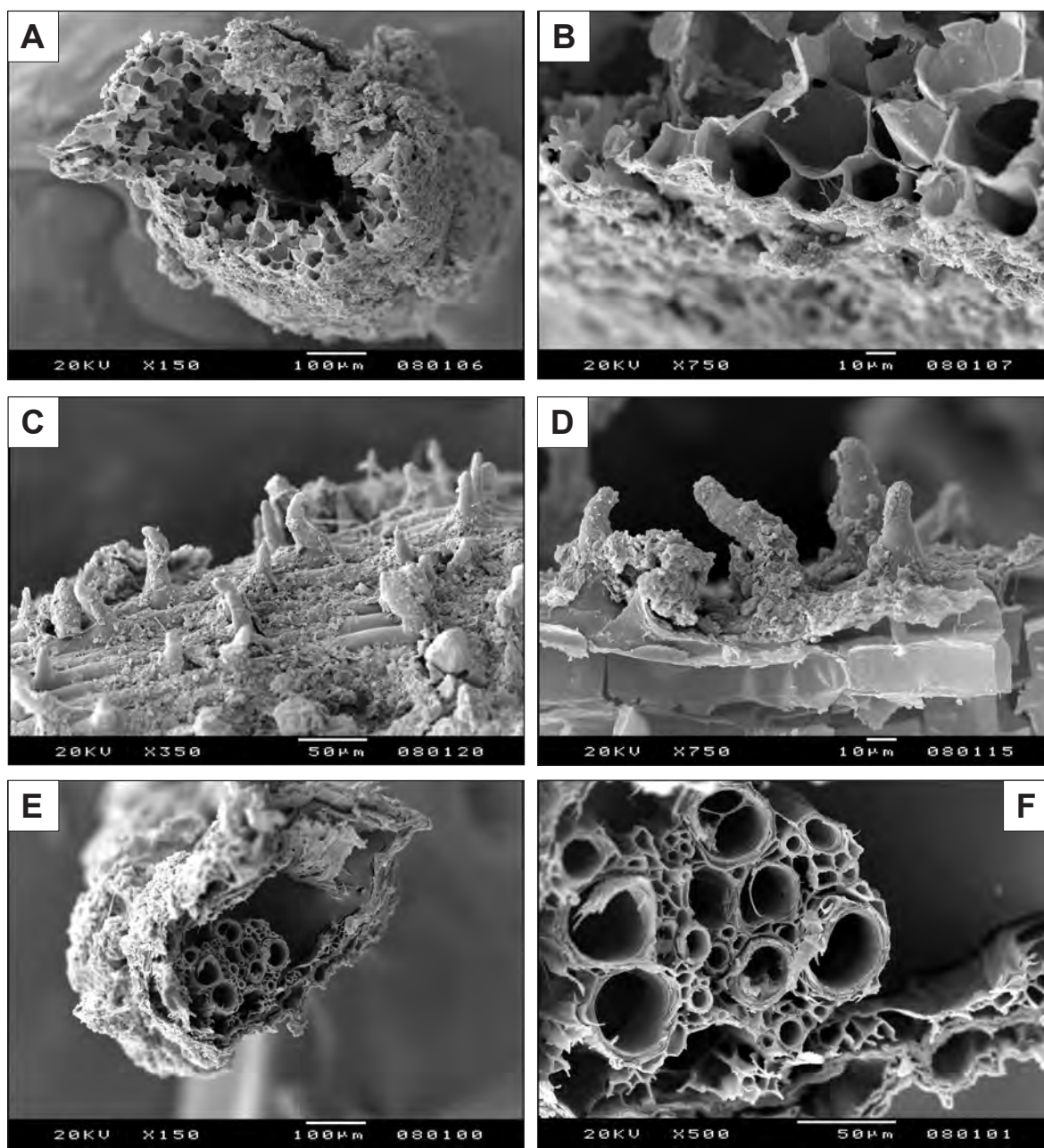


**Figure A2-3.01.** Dry, relatively well-preserved organic remains of fine roots from calcareous soil near Sella (see localities in Appendix 3-1). A, B) Fine root with thin and discontinuous coating of micrite, possibly not precipitated but attached to the root surface. C, D) Short root hairs. E, F) Partly collapsed root with degraded cortex but well-preserved vascular cylinder.

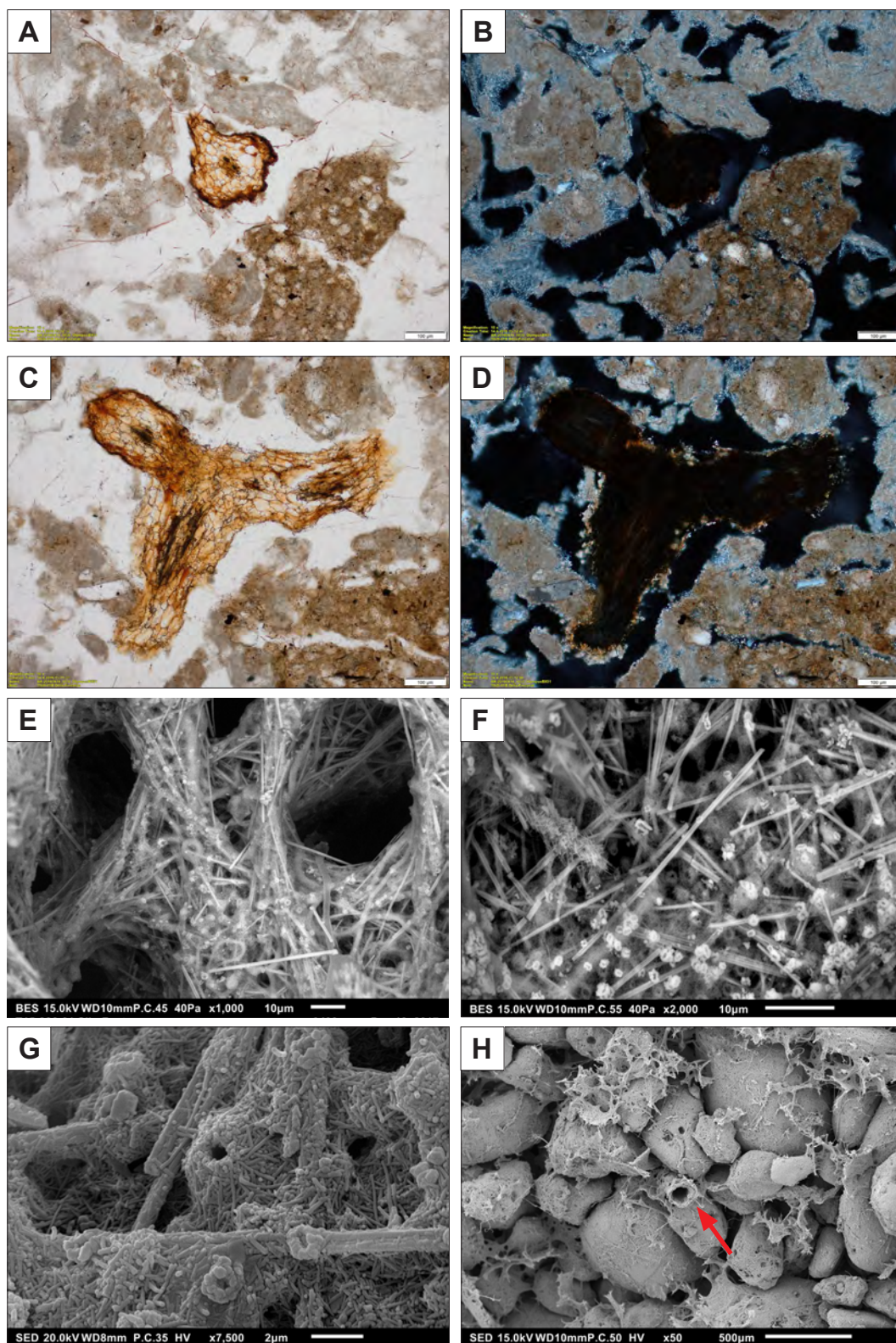


**Figure A2-3.02.** Photomicrographs of remains of short pine roots and associated carbonate accumulations. A-H: Finestrat-Sella; H - S'Estanyol. A-D) PPL/XPL pairs. E, F) Low vacuum BES photomicrographs of alveolar septal structure, composed of needle fibre calcite (NFC), calcite nanofibres, and calcified bacterial nest-like features. G) Higher magnification SED detail of Fig. F. H) Sand grains, cemented by alveolar septal structure, composed of NFC. Arrow indicates a tubule, left after decayed very fine root.



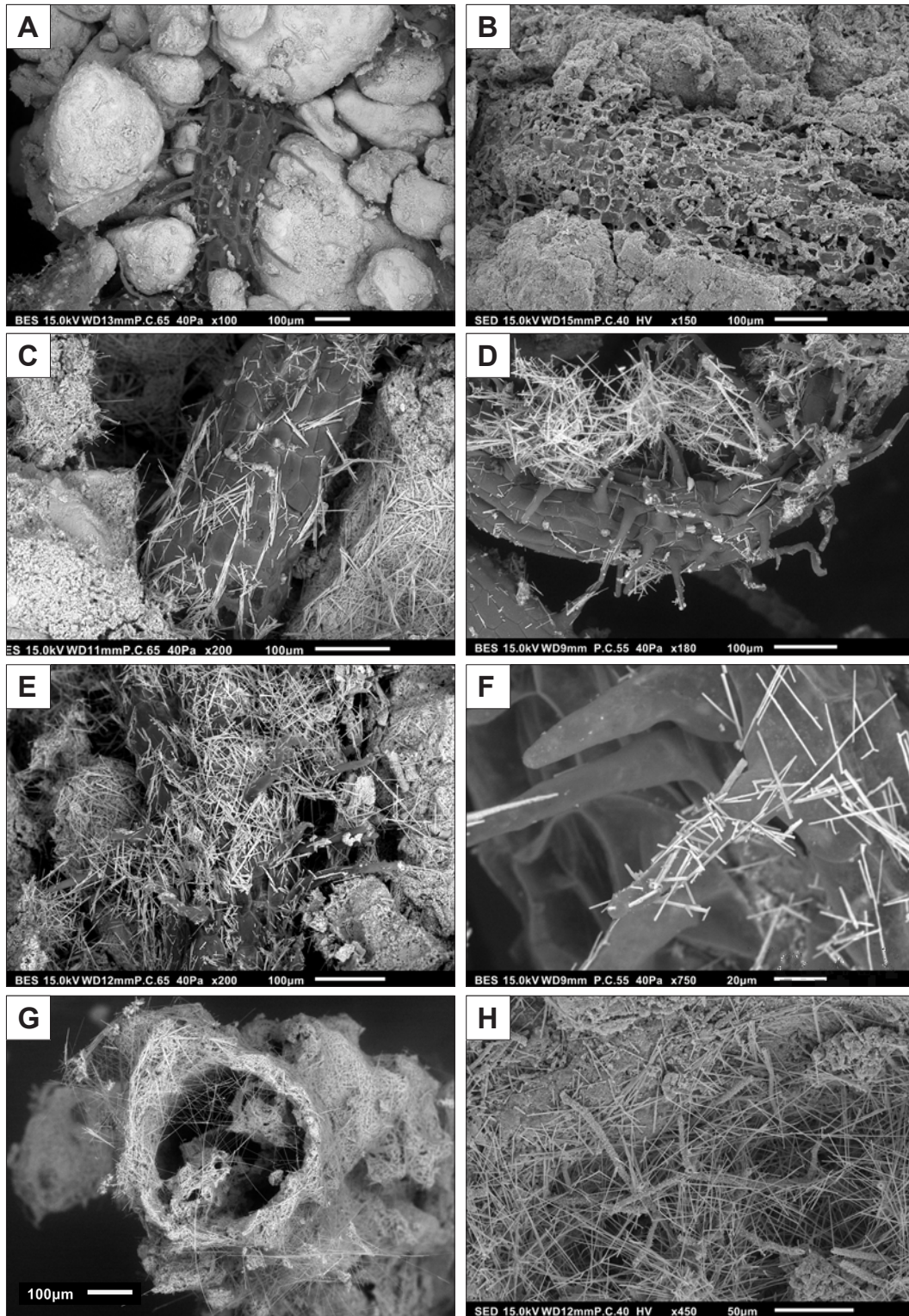


**Figure A2-3.03.** A-F) Fine roots from incipient sub-mm diameter rhizoliths in modern aeolianite, Doukkala, Morocco. Well-preserved epidermis and root hairs with NFC. G, H) Fine root rhizolith almost exclusively composed of NFC. H) Internal part of a rhizolith showing abundant mineralised fungal hyphae and open structure of NFC.



## Appendix A2-4 Examples of live or non-decayed fine root mats in present-day soils

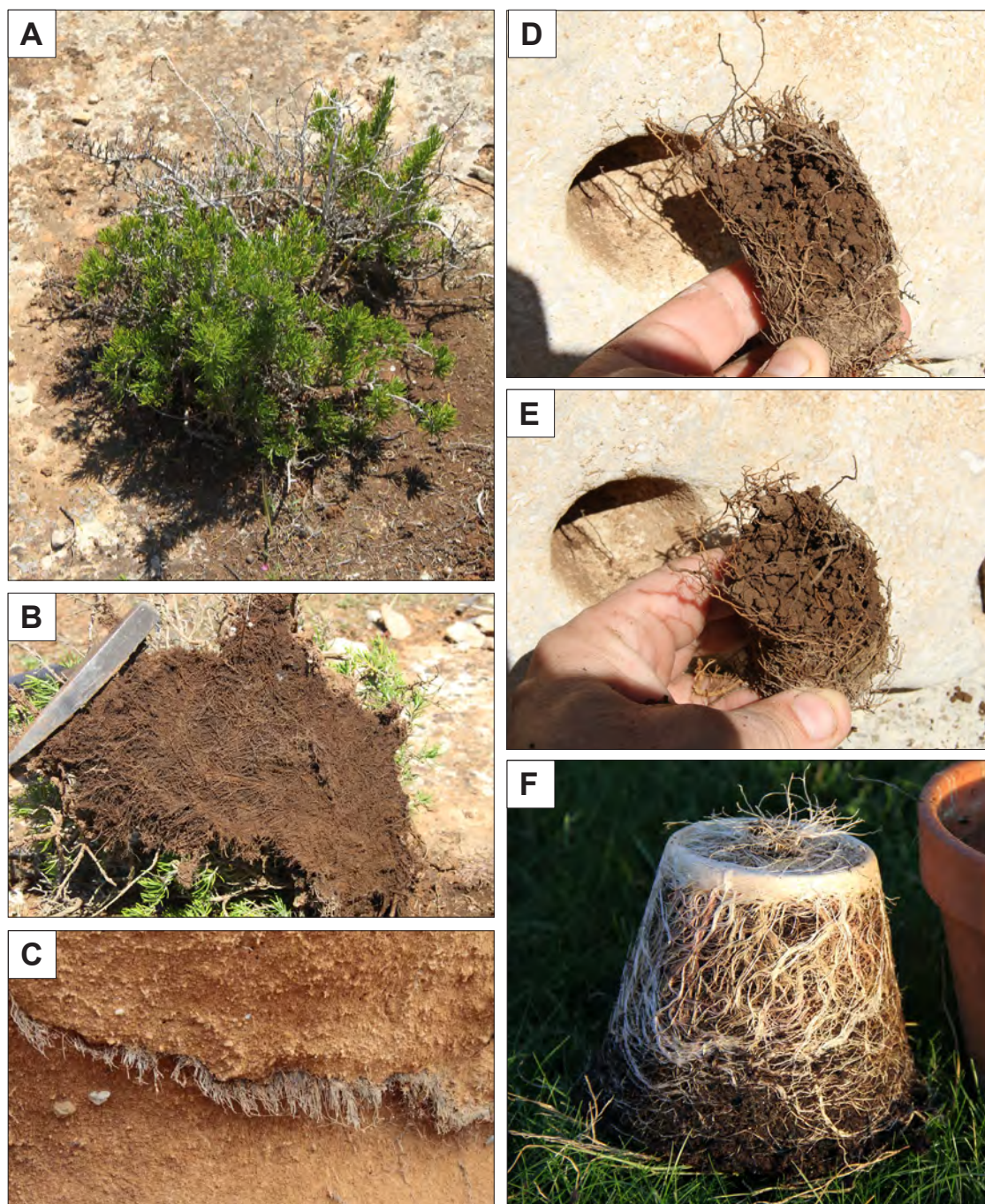


**Figure A2-4.01.** A, B) Small bush of *Salvia rosmarinus* with part of the root system growing in cracks in limestone and a thin root mat spreading over the surface (Cala Pi, Mallorca). Hammer for scale. C) Fine root mat of unknown plant(s), proliferating through a fissure in pedogenically altered aeolianite. Colònia de Sant Pere, Mallorca. Roots are 0.5-1 mm in diameter. D, E) Roots from a brown soil-filled karstic dissolution void, preferentially aligned along the rock surface, probably for efficient water capture. Črni kal, Slovenia. F) Fibrous fine root system of a pot-grown *Ocimum basilicum* - a model for root mats in natural settings such as soil pockets? Home herb garden.

## Appendix A2-5 $\delta^{13}\text{C}$ and $\delta^{18}\text{O}$ stable isotope analysis data of the Bahamian laminar rhizolites and comparative material

**Table A2-5.1.**  $\delta^{13}\text{C}$  and  $\delta^{18}\text{O}$  data for laminar rhizolites from the Bahamas and comparative Quaternary root-related calcretes from Spain, Morocco and selected samples of Palaeogene laminar calcretes from Slovenia. Also see sample details in Appendix A1-1, Table A1-1.1.

Lab	Sample ID	sample/material	type	$\delta^{13}\text{C}$ (VPDB)	$\delta^{18}\text{O}$ (VPDB)
GFZ	AK-06-248	Andros, NTW, lam CC	lam RhC	-9.45	-2.26
GFZ	AK-06-249	Andros, NTW, lam CC	lam RhC	-9.83	-2.35
GFZ	AK-06-250	Andros, NTW, lam CC	lam RhC	-9.53	-3.17
GFZ	AK-06-251	Andros, NTW, lam CC	lam RhC	-9.76	-2.71
UCM	AK-17-601	Andros, NTW-E lam CC	lam RhC	-9.77	-3.44
UCM	AK-17-602	Andros, NTW-E lam CC	lam RhC	-9.54	-3.58
UCM	AK-17-603	Andros, NTW-E lam CC	lam RhC	-9.97	-2.83
UCM	AK-17-609	SanSal SSAL-08 - lam cc/ rhizolite, hard layer	lam RhC	-5.91	-2.62
UCM	AK-17-610	SanSal SSAL-08 - lam cc/ rhizolite, porous	lam RhC	-7.03	-2.94
UCM	AK-17-604	Doukkala rhizolith T16-127B	rhizolith	-7.6	-3.38
UCM	AK-17-605	Doukkala rhizolith T16-127B	rhizolith	-8.4	-3.62
UCM	AK-17-606	Doukkala rhizolith T16-126	rhizolith	-7.91	-3.69
UCM	AK-17-607	Doukkala rhizolite T16-117 hard	lam RhC	-9.24	-4.04
UCM	AK-17-608	Doukkala rhizolite T16-117 porous	lam RhC	-9.1	-3.83
GFZ	AK-06-232	IBI-04	chalky/lam RhC	-6.99	-5.92
GFZ	AK-06-234	La Mora	pisolitic calcrete	-7.46	-4.13
GFZ	AK-06-235	La Mora	chalky/lam RhC	-10.19	-4.84
GFZ	AK-06-236	La Mora	chalky/lam RhC	-10.33	-4.79
GFZ	AK-06-237	La Mora	pisolitic calcrete	-9.72	-4.42
Graz	AK-15-511	Sella-Finestrat, T829, chalky nod.	NFC/chalky	-6.5	-6.1
Graz	AK-15-511-2	Sella-Finestrat, T829, chalky nod.	NFC/chalky	-6.5	-6.1
Graz	AK-15-512	Sella-Finestrat, T826-1; pisoids, NFC	NFC/chalky/piso	-6.0	-4.1
Graz	AK-15-512-2	Sella-Finestrat, T826-1; pisoids, NFC	NFC/chalky/piso	-7.1	-4.6
Graz	AK-15-512-3	Sella-Finestrat, T826-1; pisoids, NFC	NFC/chalky/piso	-4.9	-3.7
Graz	AK-15-512-4	Sella-Finestrat, T826-1; pisoids, NFC	NFC/chalky/piso	-5.6	-3.8

Table A2-5.1. (continued)

Lab	Sample ID	sample/material	type	$\delta^{13}\text{C}$ (VPDB)	$\delta^{18}\text{O}$ (VPDB)
Graz	AK-15-512-5	Sella-Finestrat, T826-1; pisoids, NFC	NFC/chalky/piso	-5.7	-4.1
Graz	AK-15-512-6	Sella-Finestrat, T826-1; pisoids, NFC	NFC/chalky/piso	-5.2	-3.9
Graz	AK-15-513	Sella-Finestrat, T819-01; pine roots & carbonate	NFC/chalky/piso	-7.4	-5.0
Graz	AK-15-513-2	Sella-Finestrat, T819-01; pine roots & carbonate	NFC/chalky/piso	-7.0	-4.9
Graz	AK-15-513-3	Sella-Finestrat, T819-01; pine roots & carbonate	NFC/chalky/piso	-7.2	-4.9
Graz	AK-15-513-4	Sella-Finestrat, T819-01; pine roots & carbonate	NFC/chalky/piso	-6.2	-4.6
Graz	AK-15-513-5	Sella-Finestrat, T819-01; pine roots & carbonate	NFC/chalky/piso	-7.3	-5.0
Graz	AK-15-513-6	Sella-Finestrat, T819-01; pine roots & carbonate	NFC/chalky/piso	-7.3	-5.0
Graz	AK-15-514	Sella-Finestrat, T819-03; as --513	NFC/chalky/piso	-6.7	-5.1
Graz	AK-15-514-2	Sella-Finestrat, T819-03; as --514	NFC/chalky/piso	-6.6	-5.0
GFZ	AK-06-229	SM1-Rh6-A	lam RhC	-5.04	-3.61
GFZ	AK-06-238	DIV-30	lam RhC	-5.84	-3.07
GFZ	AK-06-239	DIV-30	lam RhC	-5.52	-3.63
GFZ	AK-06-240	DIV-30	lam RhC	-6.79	-4.21
GFZ	AK-06-241	DIV-30	lam RhC	-6.70	-4.82
GFZ	AK-06-243	SM1-Rh4	lam RhC	-6.65	-4.01
GFZ	AK-06-244	SM1-Rh4	lam RhC	-5.45	-3.62
GFZ	AK-06-245	SM1-Rh4	lam RhC	-5.67	-3.79
GFZ	AK-06-246	SM1-Rh4	lam RhC	-6.11	-3.70
GFZ	AK-06-247	TRS CC	lam RhC	-2.16	-2.75
Graz	AK-07-302	DIV-33 dark laminae, bulk	lam RhC	-6.69	-4.47
Graz	AK-07-303	DIV-33 dark laminae, bulk	lam RhC	-6.68	-4.46
Graz	AK-07-304	DIV-33 dark laminae, bulk	lam RhC	-6.77	-5.23
Graz	AK-07-309	DIV-33 Rh stromatol. dark laminae, bulk	lam RhC	-6.96	-4.30
Graz	AK-07-310	DIV-33 Rh stromatol. dark laminae, bulk	lam RhC	-6.32	-4.56
Graz	AK-07-322	lam cc Slavnik	lam RhC	-7.32	-3.57
Graz	AK-07-323	lam cc Slavnik	lam RhC	-7.03	-3.17



## Appendix A3-1 Localities in the Alicante Region

**Table A3-1.1.** List of sampling localities in the Alicante Region (2014-2015) with coordinates.

Site #	Locality	Position (GPS)	Elevation (GPS)
T14-454	Relleu; Road CV-755 Relleu - Aïgues	N38° 31' 48.8 W0° 20' 40.7'''	455 m
T14-455	Relleu; Road CV-755 Relleu - Aïgues	N38° 31' 49.2 W0° 20' 39.8'''	473 m
T14-456	Relleu; Road CV-755 Relleu - Aïgues	N38° 31' 48.4 W0° 20' 37.3'''	477 m
T14-457	Penàguila; Road CV-770, Barranc del Seguró	N38° 37' 37.3 W0° 18' 44.4'''	702 m
T14-458	Penàguila; Road CV-770, Barranc del Seguró	N38° 37' 37.8 W0° 18' 43.0'''	708 m
T14-459	Penàguila; Road CV-770, Barranc del Seguró	N38° 37' 37.0 W0° 18' 45.7'''	722 m
T14-460	Torre de Arriba; Road CV-70 Benimantel- Benidorm	N38° 38' 33.4 W0° 09' 48.4'''	409 m
T14-461	Finestrat-Sella; unpaved forest road, N of Puig Campana	N38° 36' 46.8 W0° 12' 33.2'''	671 m
T14-462	Finestrat-Sella; unpaved forest road, N of Puig Campana	N38° 37' 01.9 W0° 12' 25.4'''	687 m
T14-463	Sella, The Site; unpaved road along Barranc de l'Arc	N38° 37' 34.6 W0° 13' 33.5'''	559 m
T14-464	Ibi; Road CV-806	N38° 37' 37.7" W0° 33' 03.0"	806 m
T14-464-1	Ibi; side road SE of A-7 Motorway	N38° 37' 29.7" W0° 32' 56.2"	810 m
T15-816	Sella, The Site; unpaved road along Barranc de l'Arc	N38° 37' 34.9 W0° 13' 33.1'''	567 m
T15-817	Pas del Comptador, unpaved road Sella-Guadalest	N38° 38' 18.5 W0° 11' 17.3'''	863 m
T15-818	Guadalest; forest road	N38° 39' 10.7" W0° 11' 37.9"	818 m
T15-819	Guadalest; forest road	N38° 39' 10.5" W0° 11' 33.9"	814 m
T15-820	Finestrat; E of Puig Capana	N38° 34' 54.3" W0° 12' 44.0"	416 m
T15-821	Finestrat; E of Puig Capana	N38° 36' 19.5" W0° 13' 09.8"	505 m
T15-822	Finestrat; E of Puig Capana	N38° 34' 54.8" W0° 12' 42.4"	351 m
T15-823	Finestrat-Sella; unpaved forest road, N of Puig Campana	N38° 36' 50.9" W0° 12' 43.6"	701 m



**Figure A3-1.01**  
 Topographic and road map (Google Maps) showing main localities, named after the nearby towns (Finestrat, Sella, Guadalest, Rellu, Penàguila, Ibi). Coordinates of the sampling points are listed in Table A3-1.1.

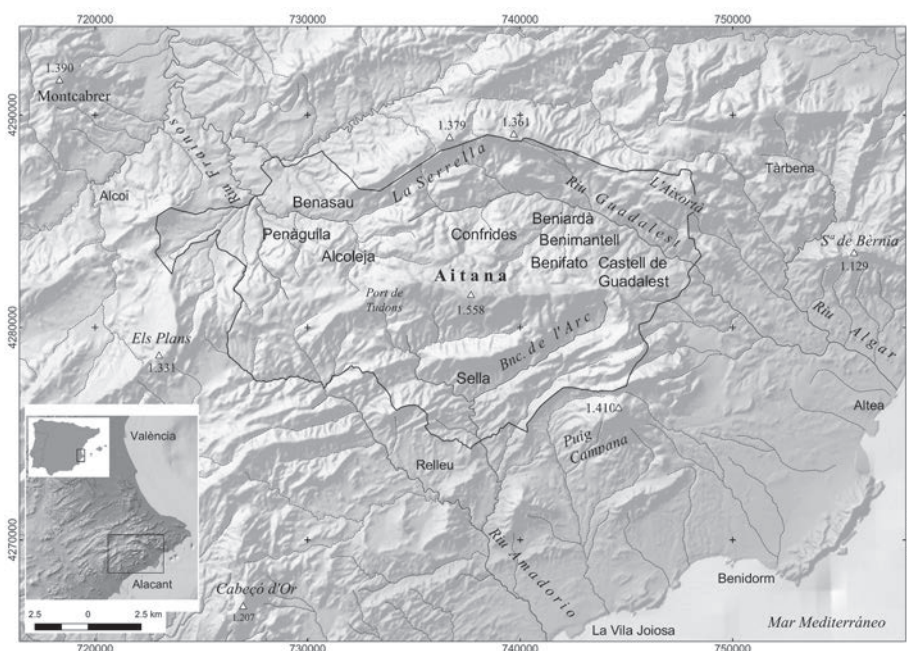


**Figure A3-1.02.** Topographic map showing drainage basins of three of the four major river in the main study area (Riu Amadorio, Riu Guadalest (a major tributary of Riu Algar), and Riu Frainos). From Giménez-Font and Marco Molina (2017). Riu Montnegre (Riu Verde) of the Ibi locality (SW of Alcoi) is not shown on the map.

## Appendix A3-2 Geological and climatic setting of the studied localities

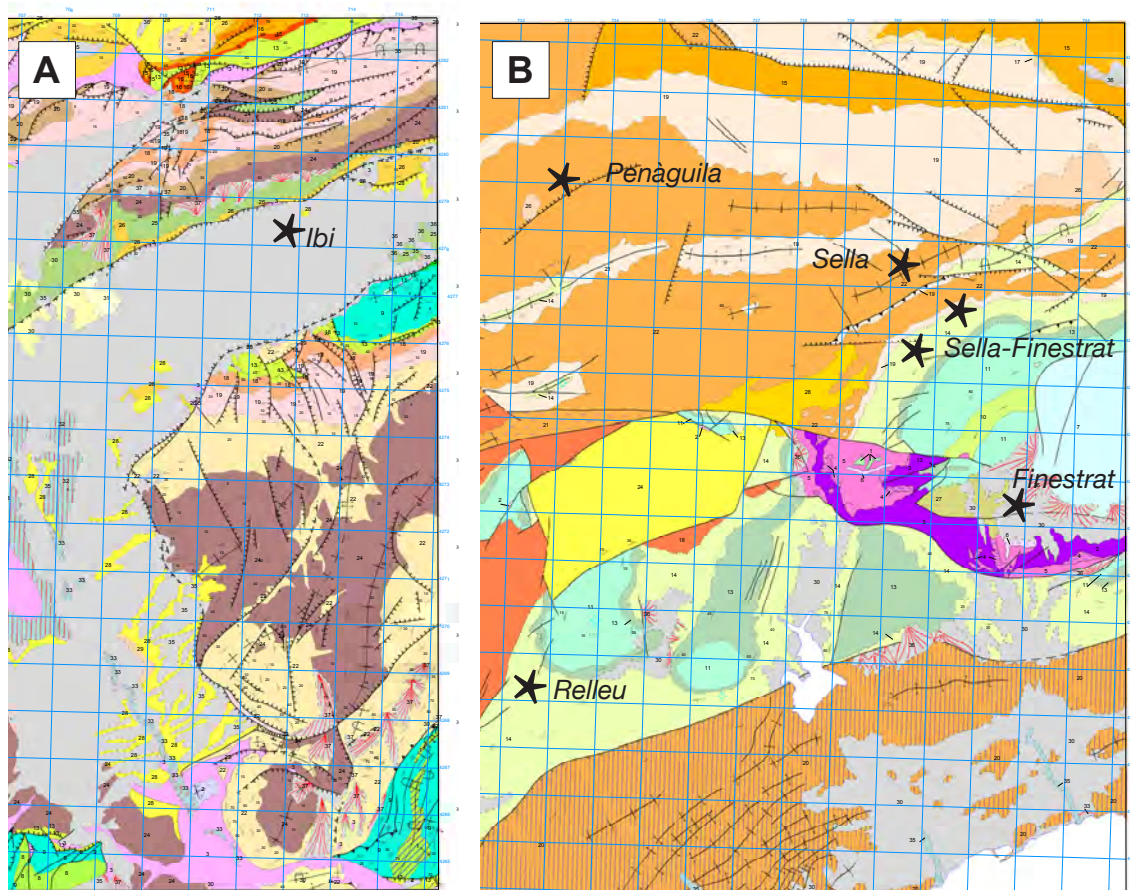


**Figure A3-2.01.** Geological maps with marked main sampling areas; extracted from Geological Map of Spain (Mapa geológico de España, 1: 50.000, 2ª Serie). A) Excerpt from the sheet Castalla (Hoja 846; Martínez del Olmo et al. 1978). [http://info.igme.es/cartografiadigital/datos/magna50/pdfs/d8\\_G50/Magna50\\_846.pdf](http://info.igme.es/cartografiadigital/datos/magna50/pdfs/d8_G50/Magna50_846.pdf) B) Excerpt from the sheet Villajoyosa (Hoja 847; Calodron et al. 1981) of the area between the Villajoyosa coast and Serra d'Aitana mountains. [http://info.igme.es/cartografiadigital/datos/magna50/pdfs/d8\\_G50/Magna50\\_847.pdf](http://info.igme.es/cartografiadigital/datos/magna50/pdfs/d8_G50/Magna50_847.pdf)



## Appendix A3-3 Sample preparation methods for intracellularly calcified roots

### Freeze drying and SEM observation of fresh root samples

#### Procedure:

- 1) Aluminium sample holder (30 or 51 mm diameter, thickness 10 mm; Fig. A3-3.1B) were immersed in a polystyrene bath, filled with liquid N<sub>2</sub>.
- 2) The holder was let cool to N<sub>2</sub> temperature and set onto PTFE holder, fixed into the SEM sample holder (Fig. A3-3.1A).
- 3) A fragment of fresh root was separately immersed in liquid N<sub>2</sub> and rapidly placed onto the cooled holder (Fig. A3-3.1B).
- 4) Sample holder was placed in the SEM chamber, closed as rapidly as possible to prevent ice formation from the air moisture, and evacuated to 20 to 40 Pa low vacuum conditions.
- 5) Samples were observed during freeze drying process and after complete ice sublimation (10-30 minutes) and kept at low vacuum for several hours to complete the drying process.

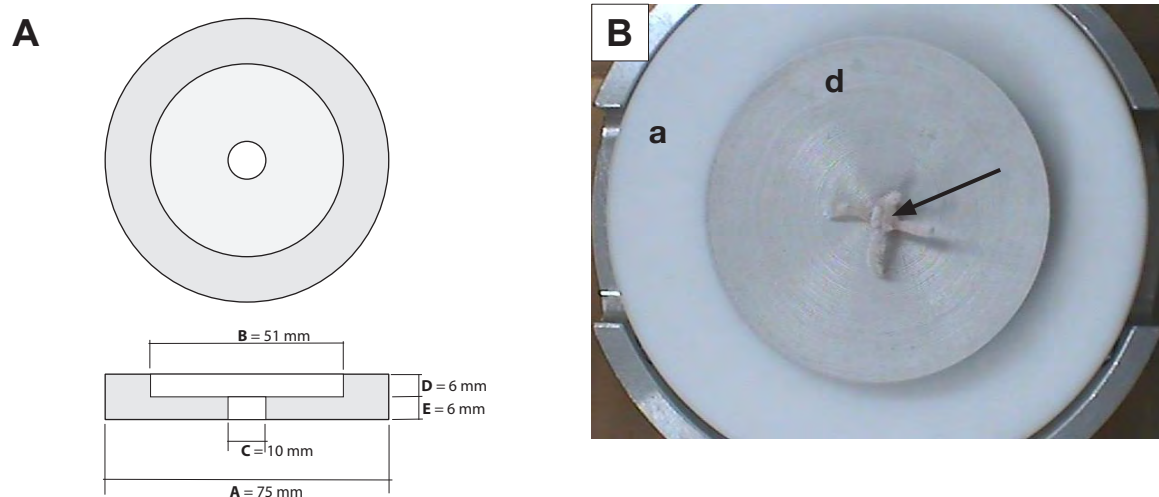


**Figure A3-3.1.**

A) Sketch of an adapter made of polytetrafluoroethylene (PTFE) to hold a standard SEM aluminium disc (stub) sample holder (diameter 51 mm, thickness 10 mm); above: top view, below: side view with dimensions. B) SEM holder with PTFE adapter (a) holding a pre-cooled aluminium disc (d) with a fragment of fine root (arrow), frozen in liquid nitrogen.

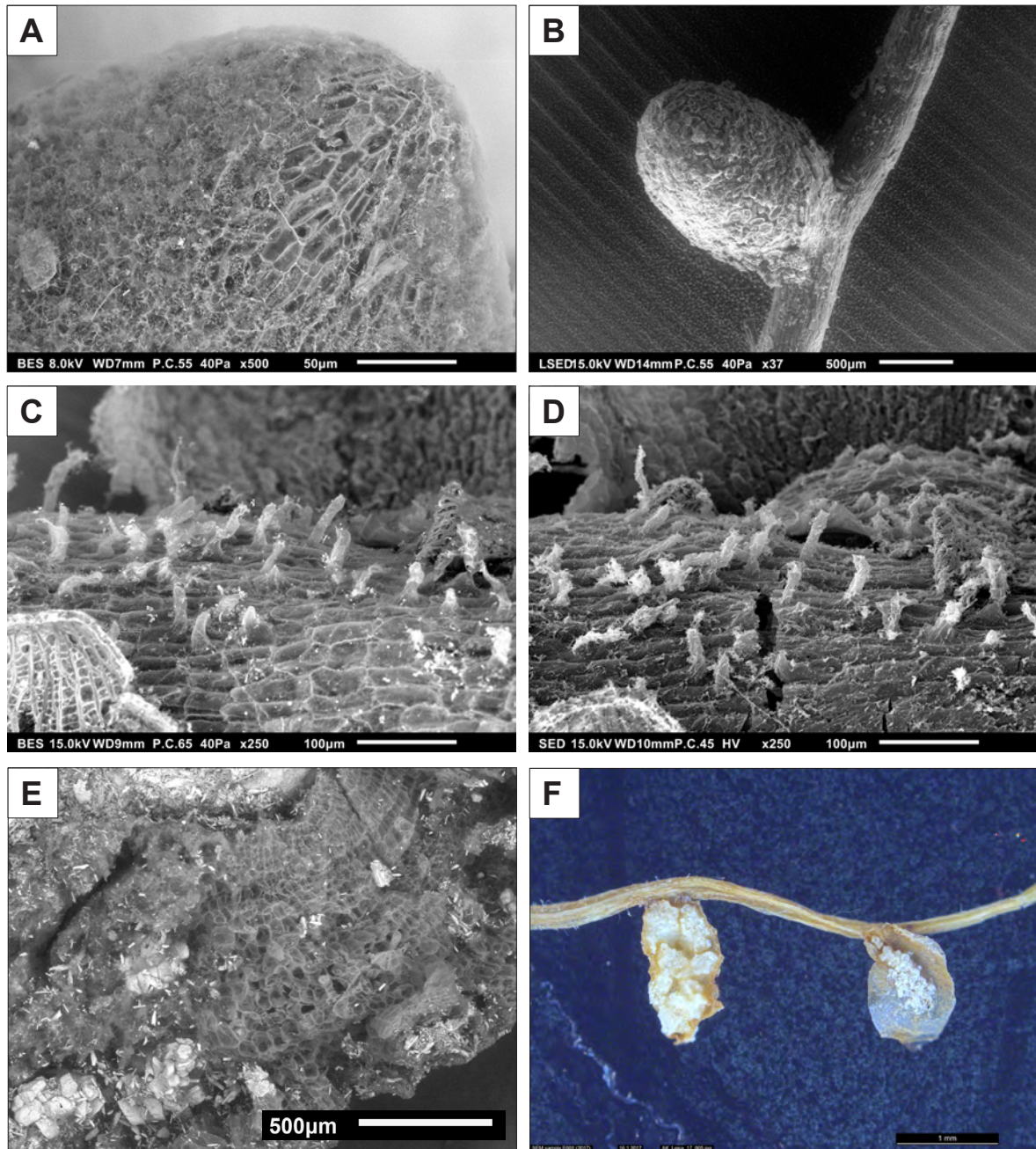


**Figure A3-3.3.** A-E) LV BES SEM photomicrographs of liquid-nitrogen frozen fragment of partly calcified root, observed during freeze-drying (ice sublimation) in the SEM chamber. F) An example of partly calcified roots of the same sample, collapsed after letting dry at room temperature and pressure. Stereomicroscope photomicrograph.



### Appendix A3-4 Intracellularly calcified roots: complementary figures

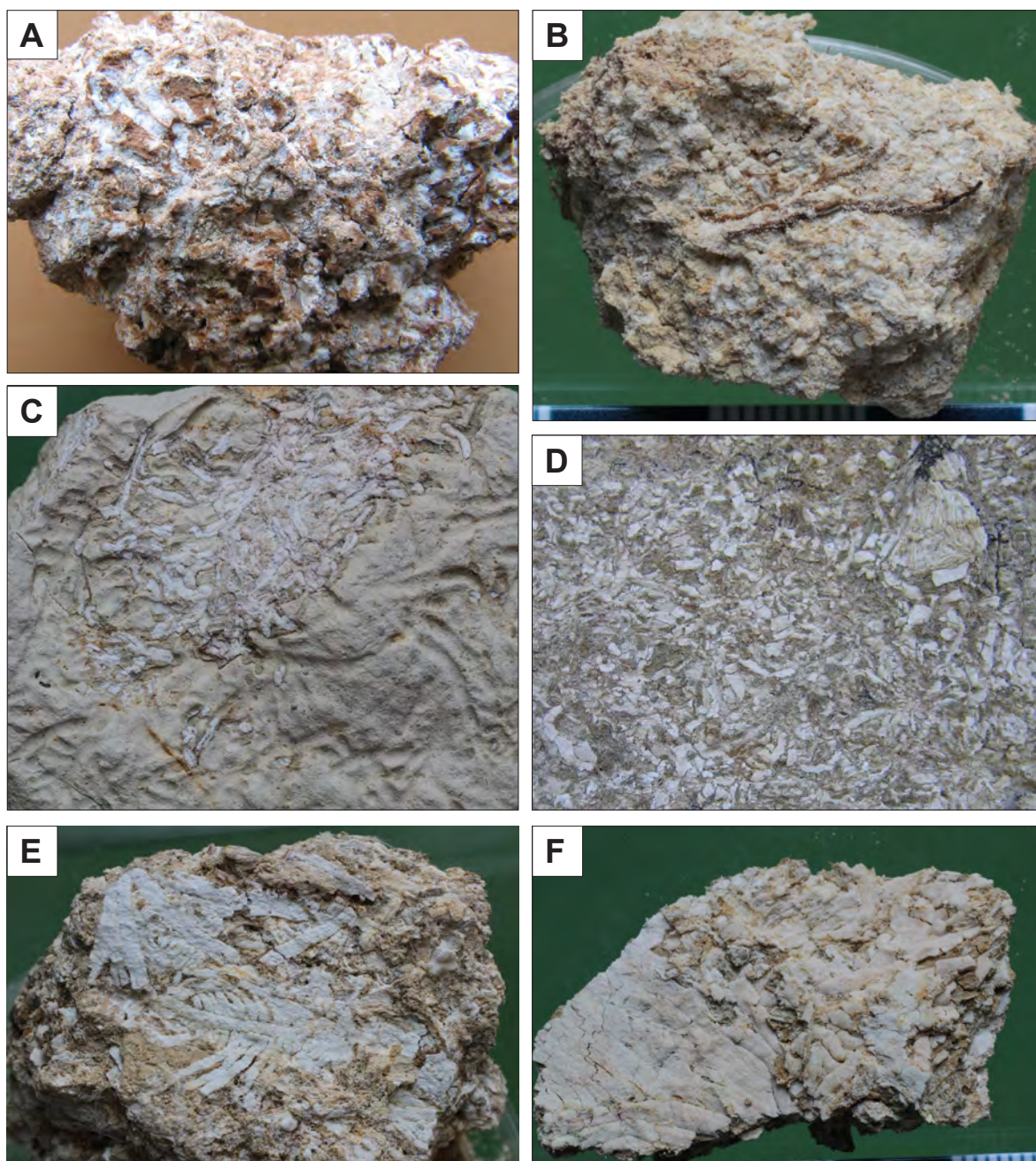
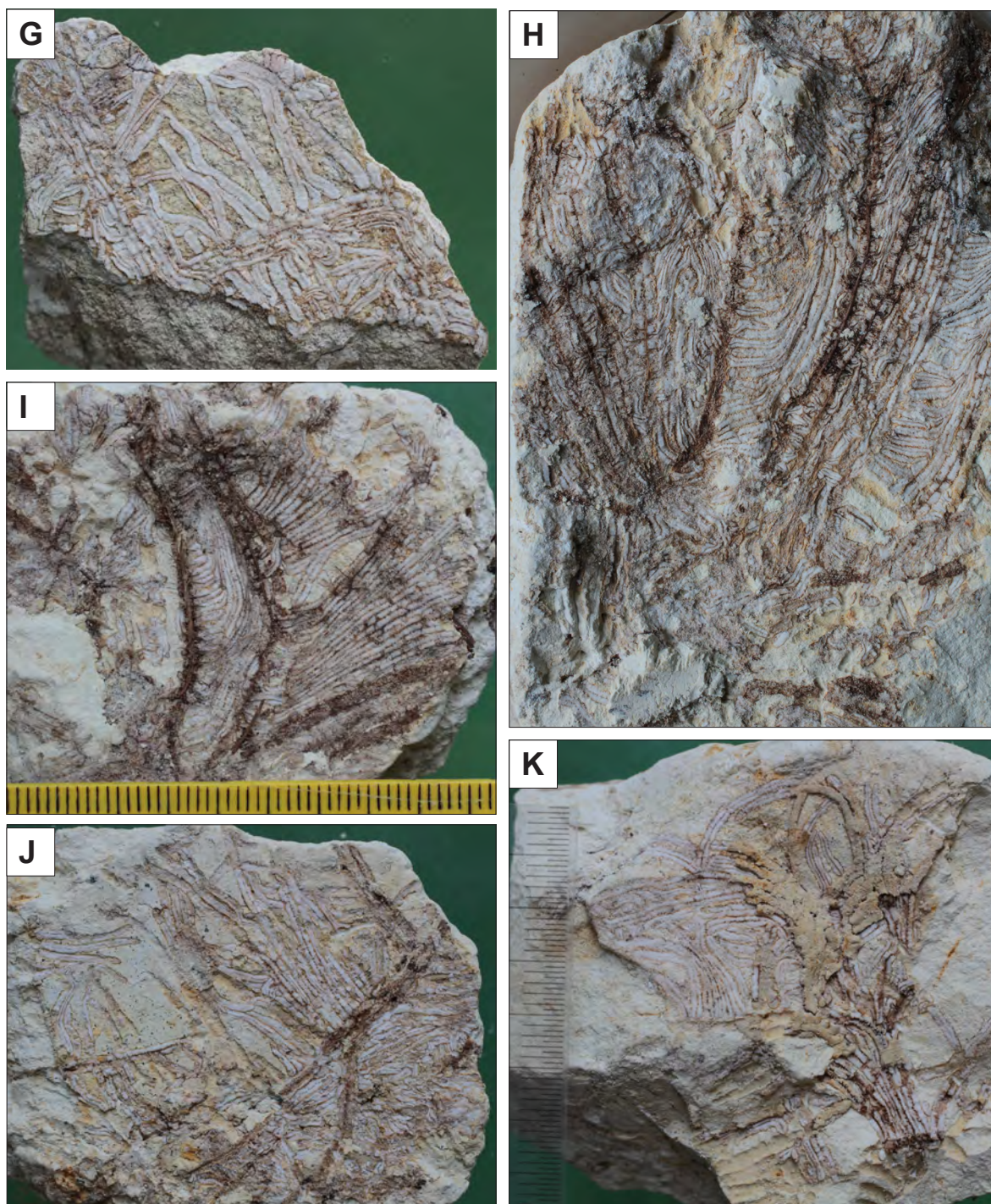


Figure A3-4.01. (continued on next page)





**Figure A3-4.01.** Type I and Type II iCR root systems in hand-specimens (supplement to Figs. 3.2-3.7 and 3.10-3.12). A and B) Type I clusters of mostly disintegrated iCRs. Ibi (A) and Sella (B) localities. C) Corroded surface of a marly limestone pebble with *in situ* preserved iCRs. Finestrat-Sella. D) Fragments of flat, Type 2 iCRs, embedded with clayey matrix. Finestrat-Sella. E-K) Well-preserved iCR systems showing relatively open or dense (fitted) herringbone branching patterns. E, F: Penaguila, G-K: Sella locality.



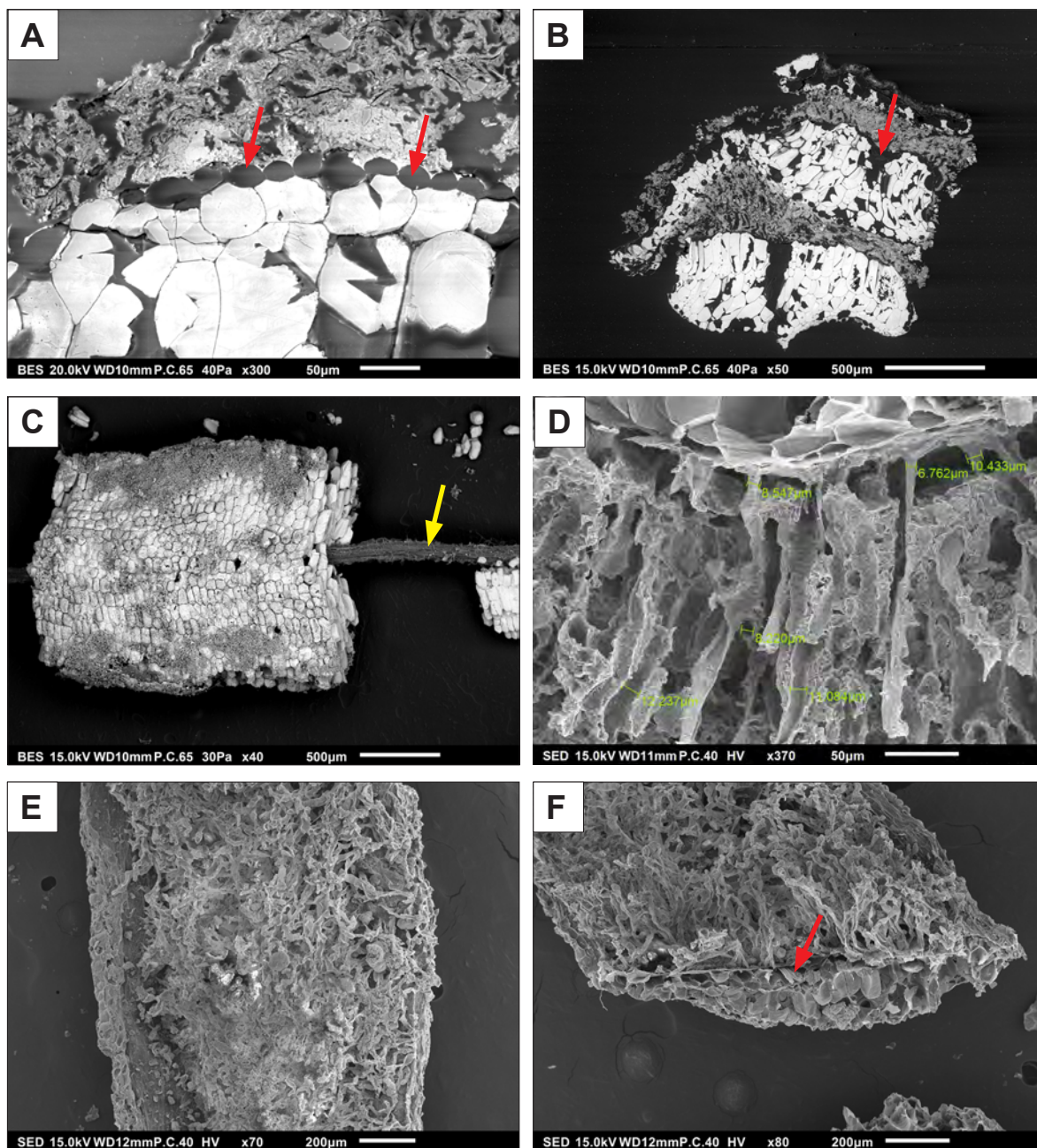


**Figure A3-4.02.** SEM photomicrographs of asymmetrical type II iCRs. A) BES SEM photomicrograph of a thin section of a resin-embedd iCR fragment. Arrows indicate empty, non-calcified (resin-filled) epidermal cells. B) Same as in Fig A. Arrow indicates partly preserved organic remain of a vascular cylinder. C) Fragment of iCR with preserved vascular cylinder (arrow). BES photomicrograph. D-F) SED photomicrographs of root-hair side of a flat, shovel-type iCR. Note dimensions of root hairs in D and ectopic (marginally placed) vascular cylinder in F (arrow). All samples from Finestrat-Sella locality.

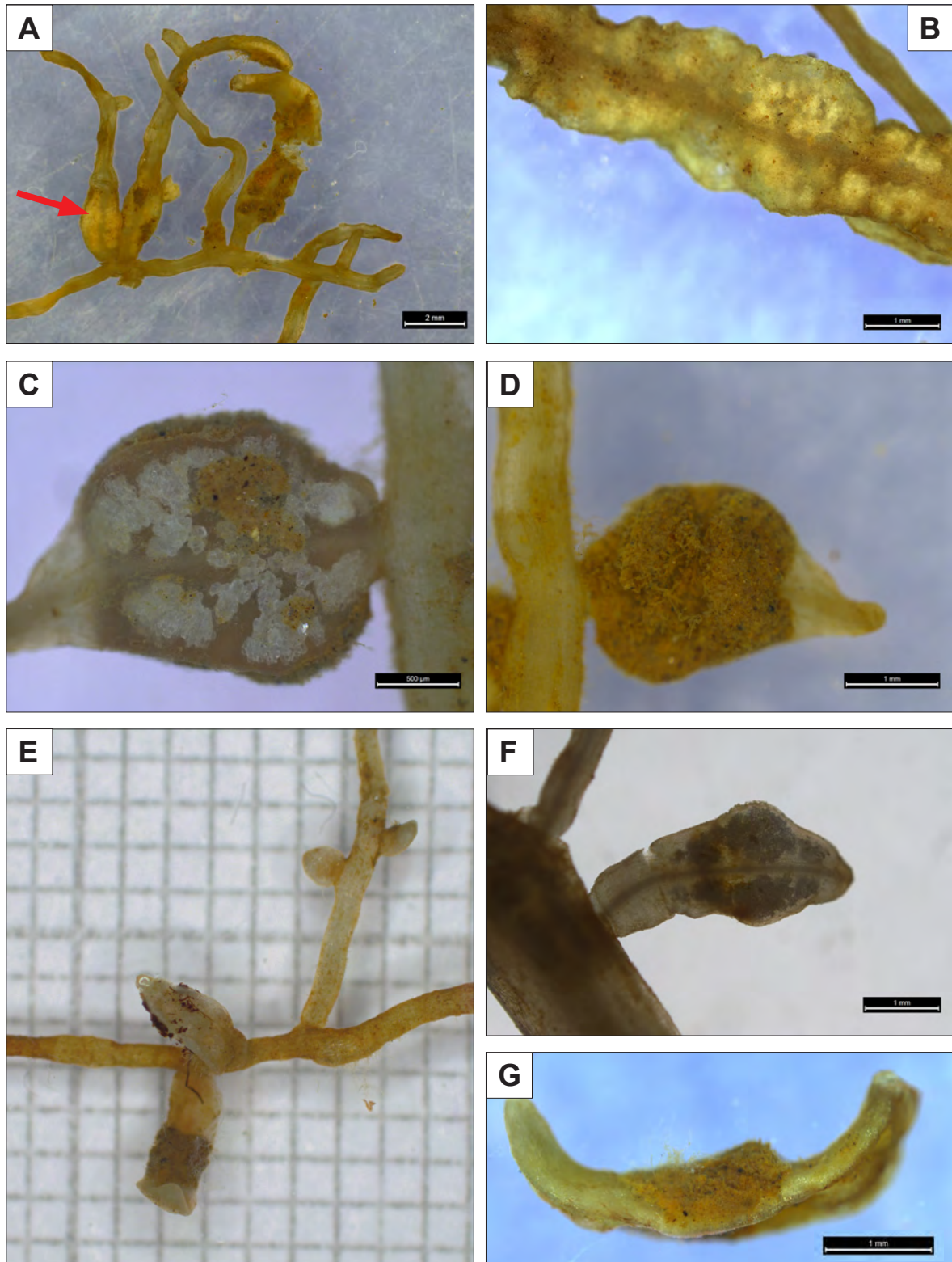


**Figure A3-4.03.** Asymmetric, Type II (shovel) live roots of pot-grown *Hedysarum coronarium*, partly calcified. A, B) Note the difference in diameter between non-calcified, lower-order root branches and flat, terminal branches with calcified dells. C and D) Short shovel root showing calcified cortex, seen through the epidermis (C) and opposite side covered with root hairs and clayey material. E-G) Longer shovels, showing typical curved (bent) shape due to asymmetric expansion of cells on one side of the root.



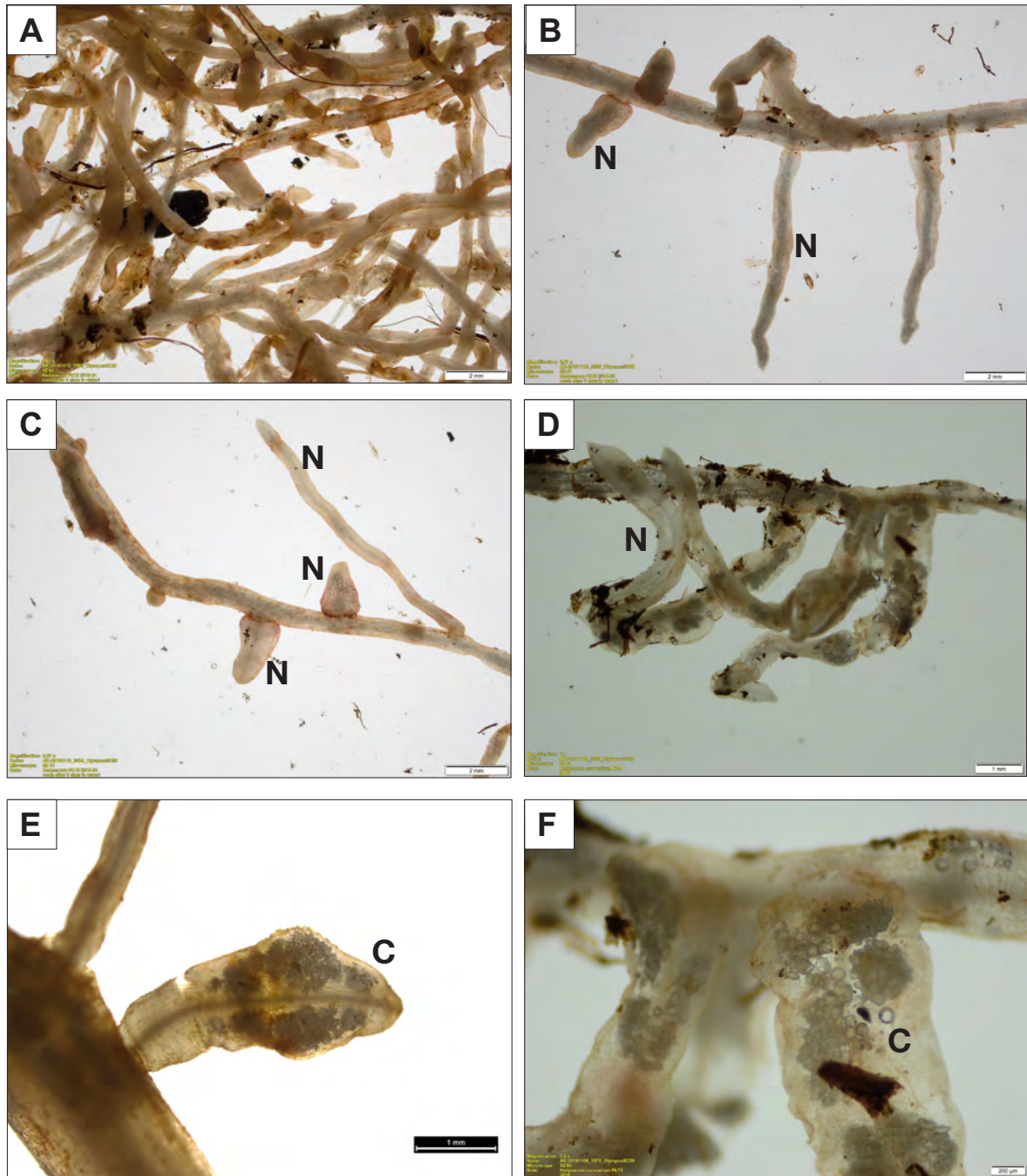


**Figure A3-4.04.** Type II (shovel) partly calcified live roots of pot-grown *Hedysarum coronarium*. Same material as in Fig. A3-4.03. Parts of root systems with noncalcified lower-order root branches and terminal, shovel-shaped noncalcified (N) or partly calcified roots (C).

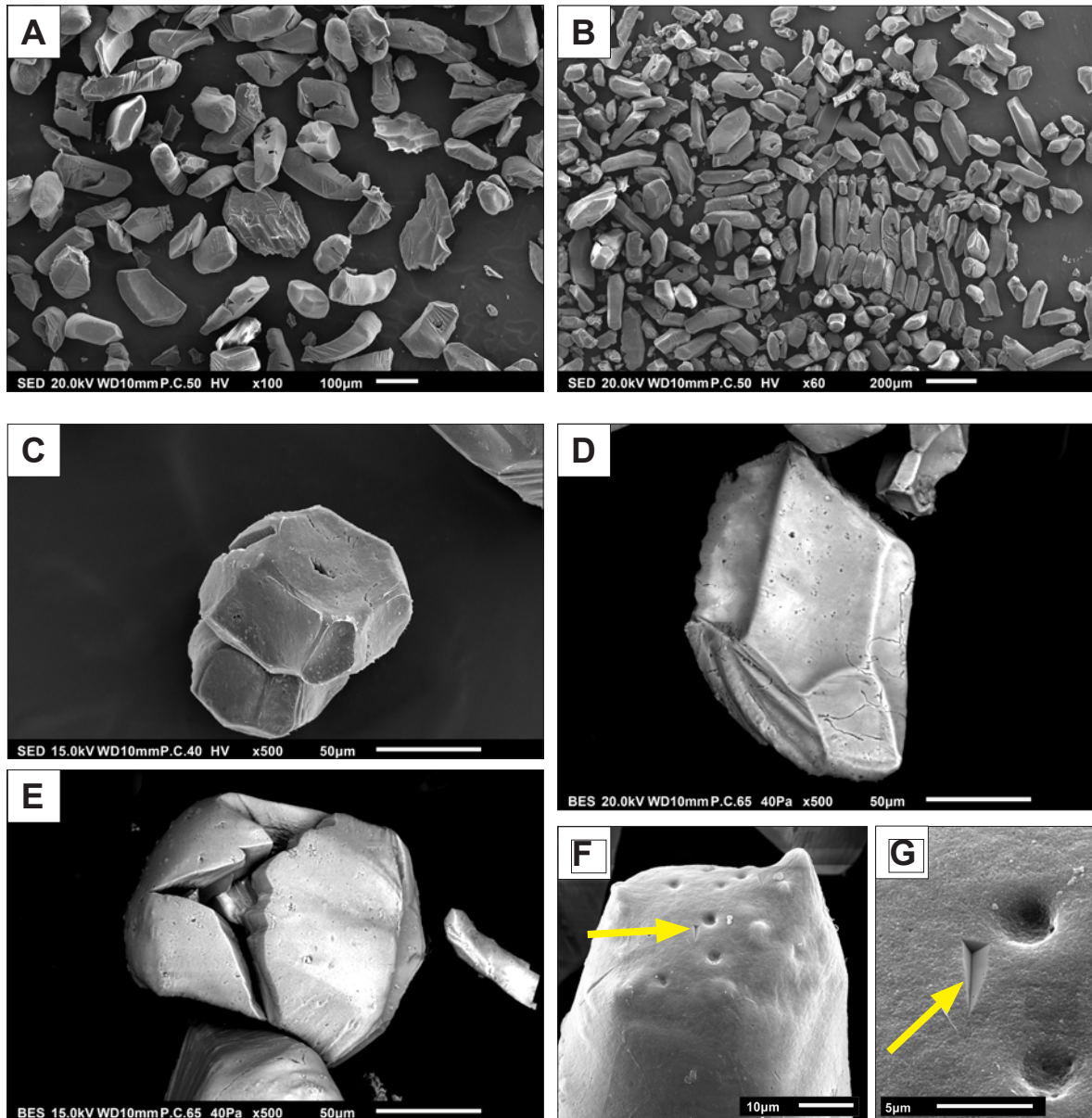


**Figure A3-4.05.** A-E) Morphological details of isolated calcified cells, showing curved polyhedral shapes, often with folded surface, corresponding to the folded surface of a cell wall. F, G) Smooth surface of a fully-calcified cell with hollows and protuberances and irregularities in the basal crystal (arrow), not (yet) overlain by the external, nanocrystalline layer.



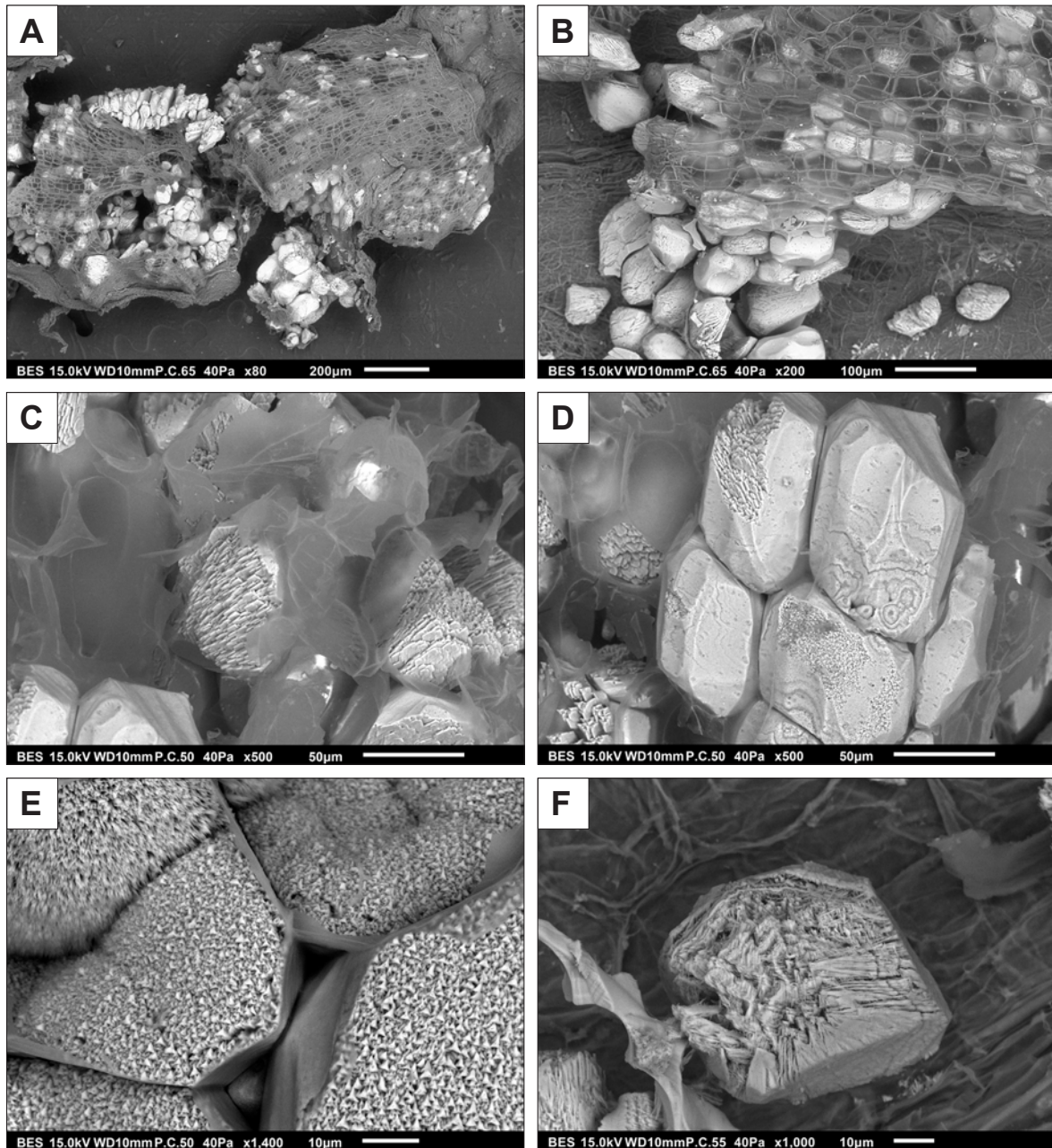


**Figure A3-4.06.** Low vacuum BES photomicrographs of partly calcified live root showing morphology and ultrastructure of partly calcified cells. Note transparent appearance of cell walls under BES SEM conditions in Figs. A-D. See captions in Figs. 3.23 and 3.24 for details.



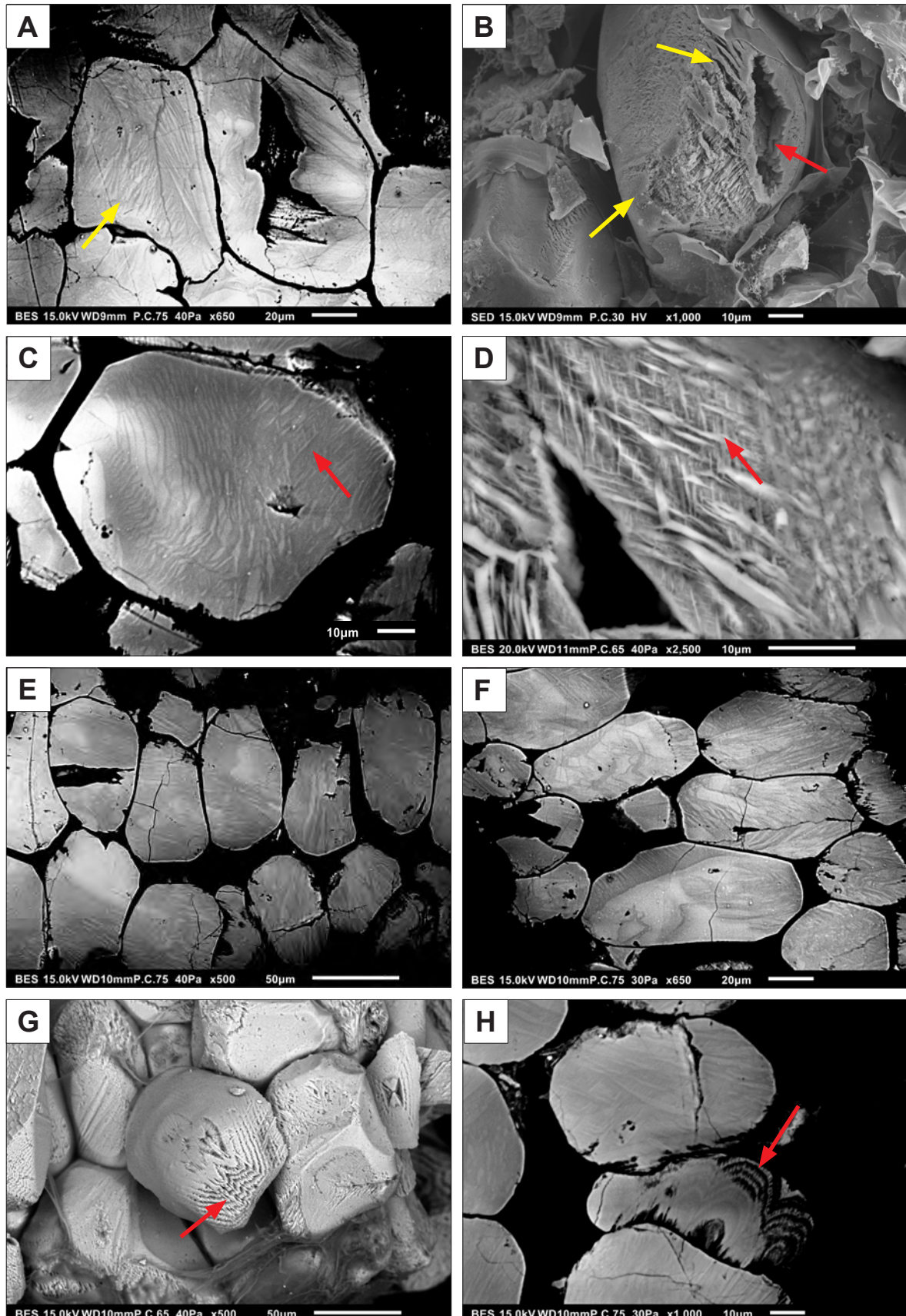
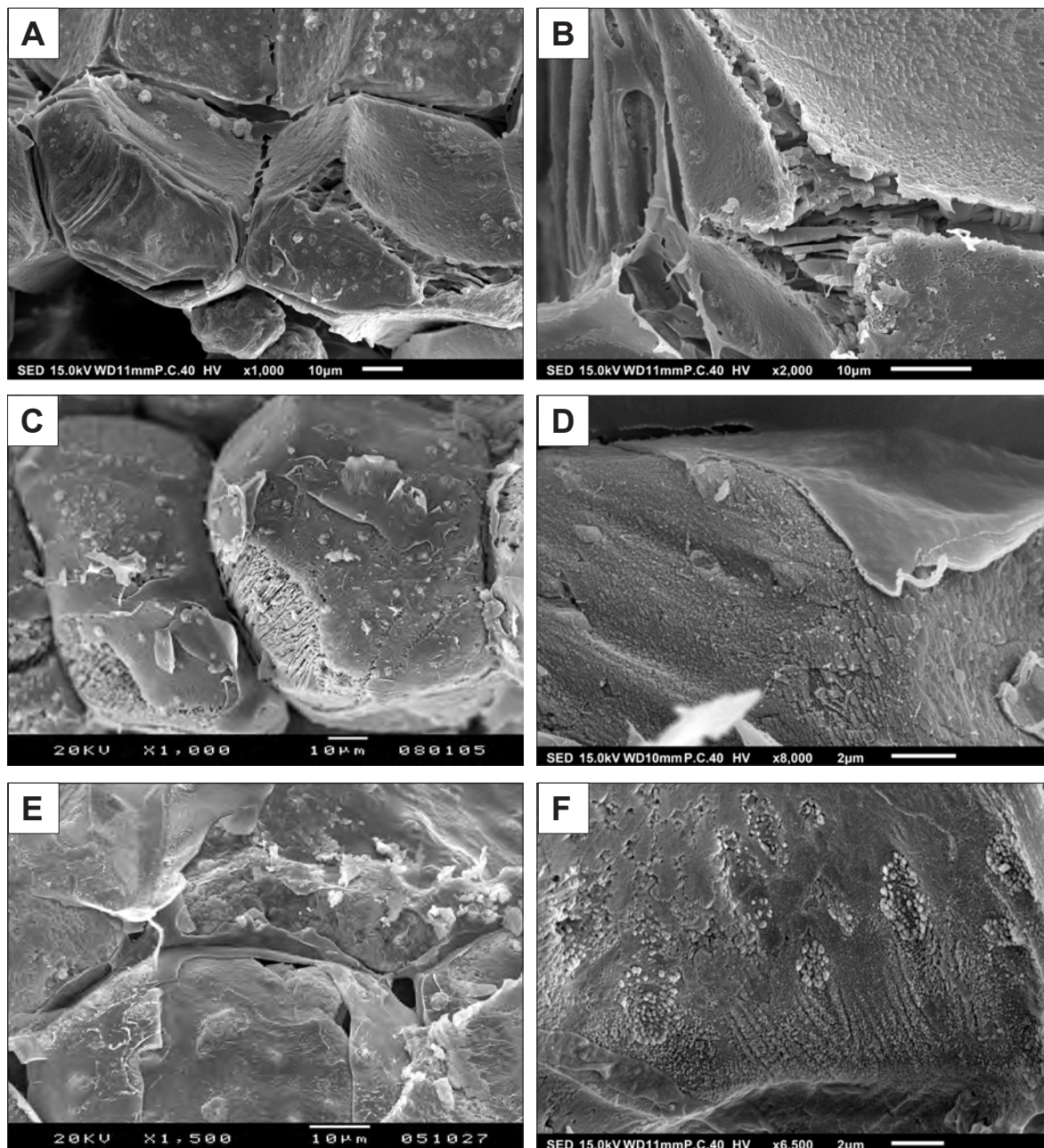


Figure A3-4.07. See caption on the next page.

**Figure A3-4.07.** (previous page) Ultrastructure of calcified cells under SEM. Calcified cells exhibiting parallel microlamellar and crossed (interlaced) lamellar ultrastructure. A, C, E, F) Charge contrast images (CCI) of polished thin sections. Ultrastructure of fully-calcified cells characterised by cross-lamellar microstructure, analogous to cells in Figs. B and D. G, H) SED and CCI BES photomicrographs of porous, incompletely calcified cell composed of microlamellar calcite . Sella, site T14-463. Also see caption in Fig. 3.23.



**Figure A3-4.08.** Ultrastructure of calcified cells under SEM. Ultrastructural details of external layer. See section 3.4.4 and caption in Fig. 3.25.



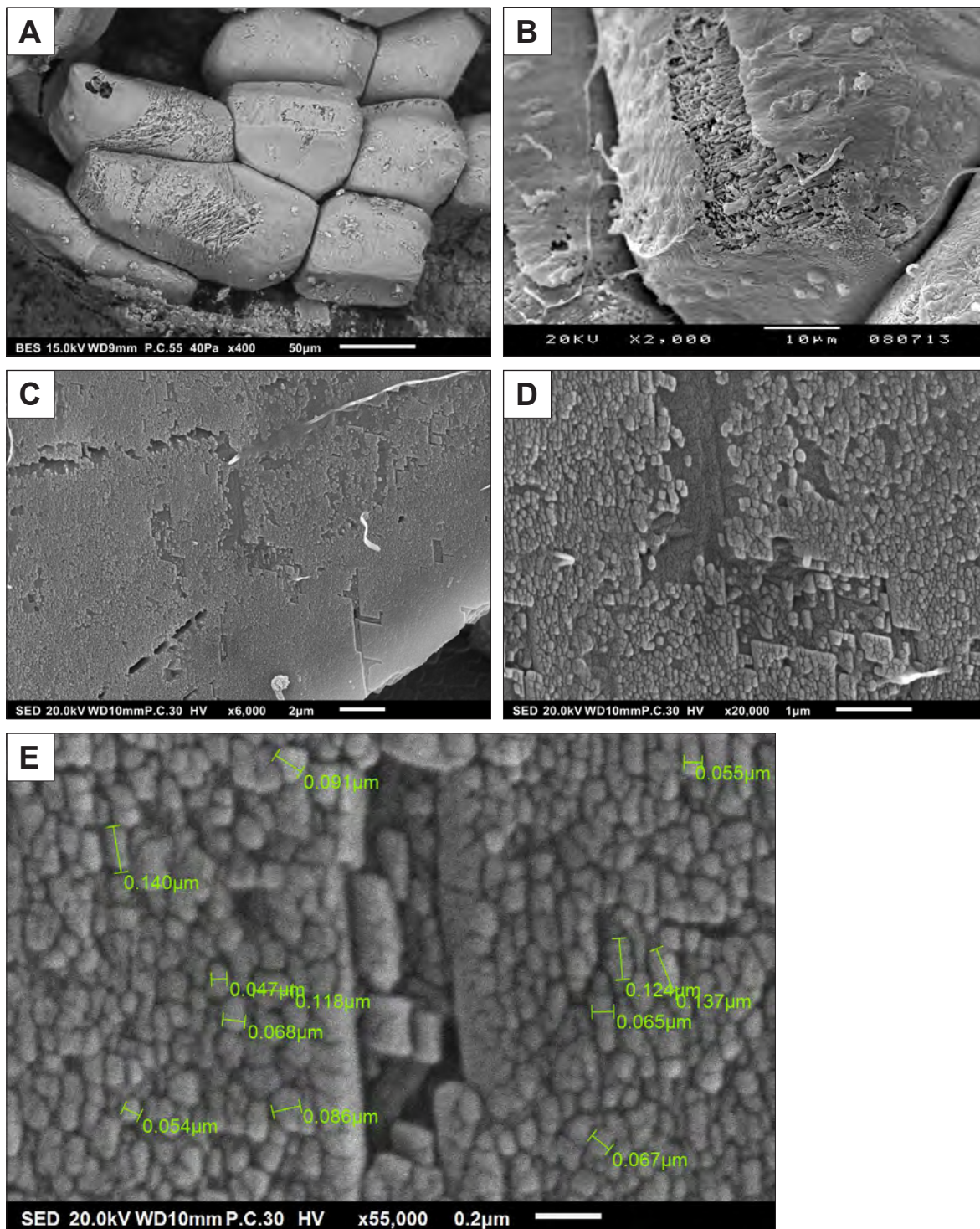


**Figure A3-4.09.** A-D) SEM photomicrographs of the external calcite layer formed by aggregation of globular (possibly amorphous or poorly crystalline) nanosized particles. E) High-magnification detail of the surface layer of iCR showing dimensions of the nanoparticles. See section 3.4.4. and caption in Fig. 3.25.



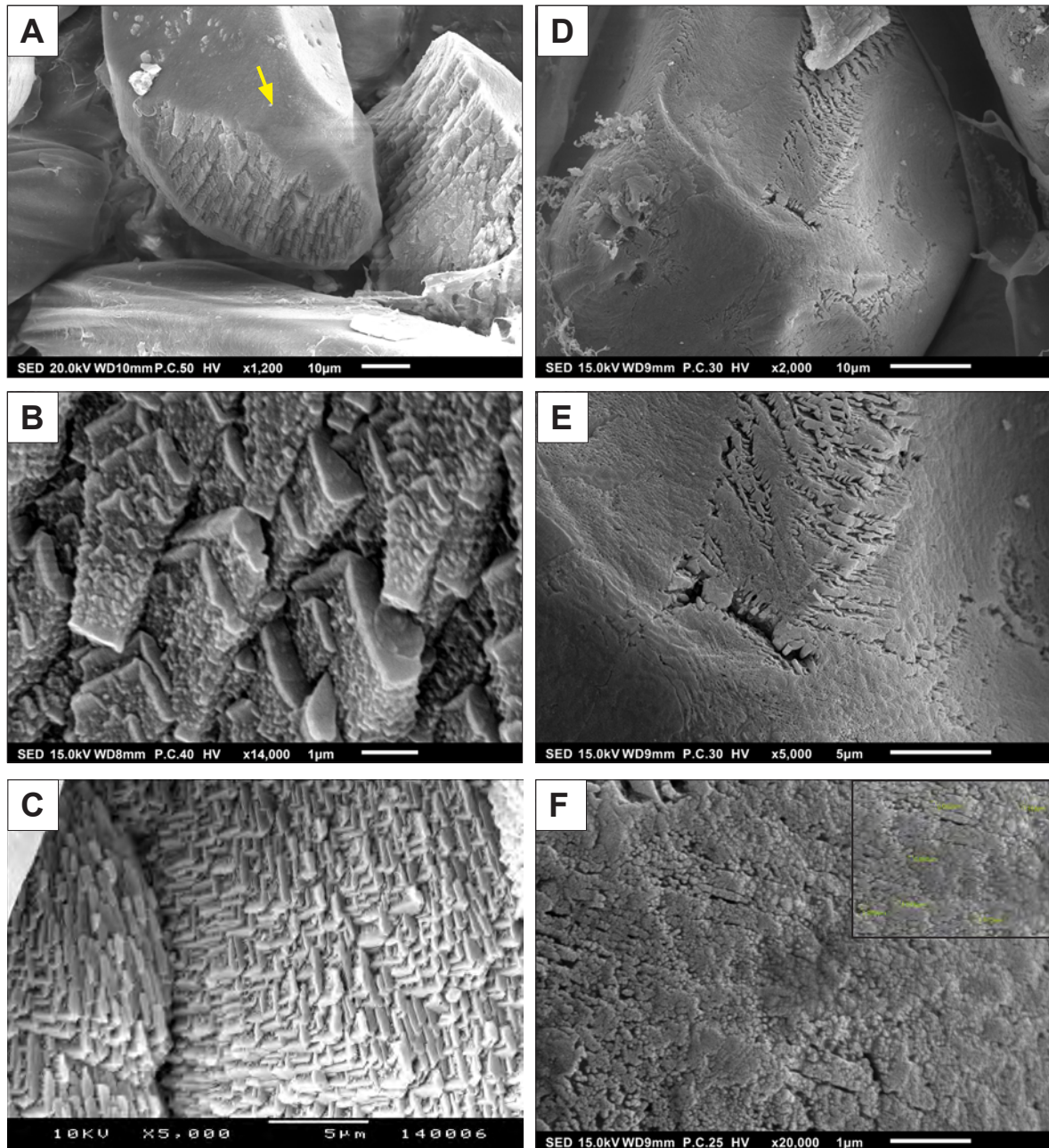


**Figure A3-4.10.** Vacuolar crystal maturation and microstructure of external layer of iCR cells.

All images taken in HV SED mode of Au-coated samples. A-C) Calcified cell composed of mesocrystalline calcite, incompletely covered by a layer of nanocrystalline calcite (arrow in A). D-F) Calcified cell composed of lammellar calcite with external layer made of irregular, nanocrystalline aggregates. See caption in Fig. 3.25.

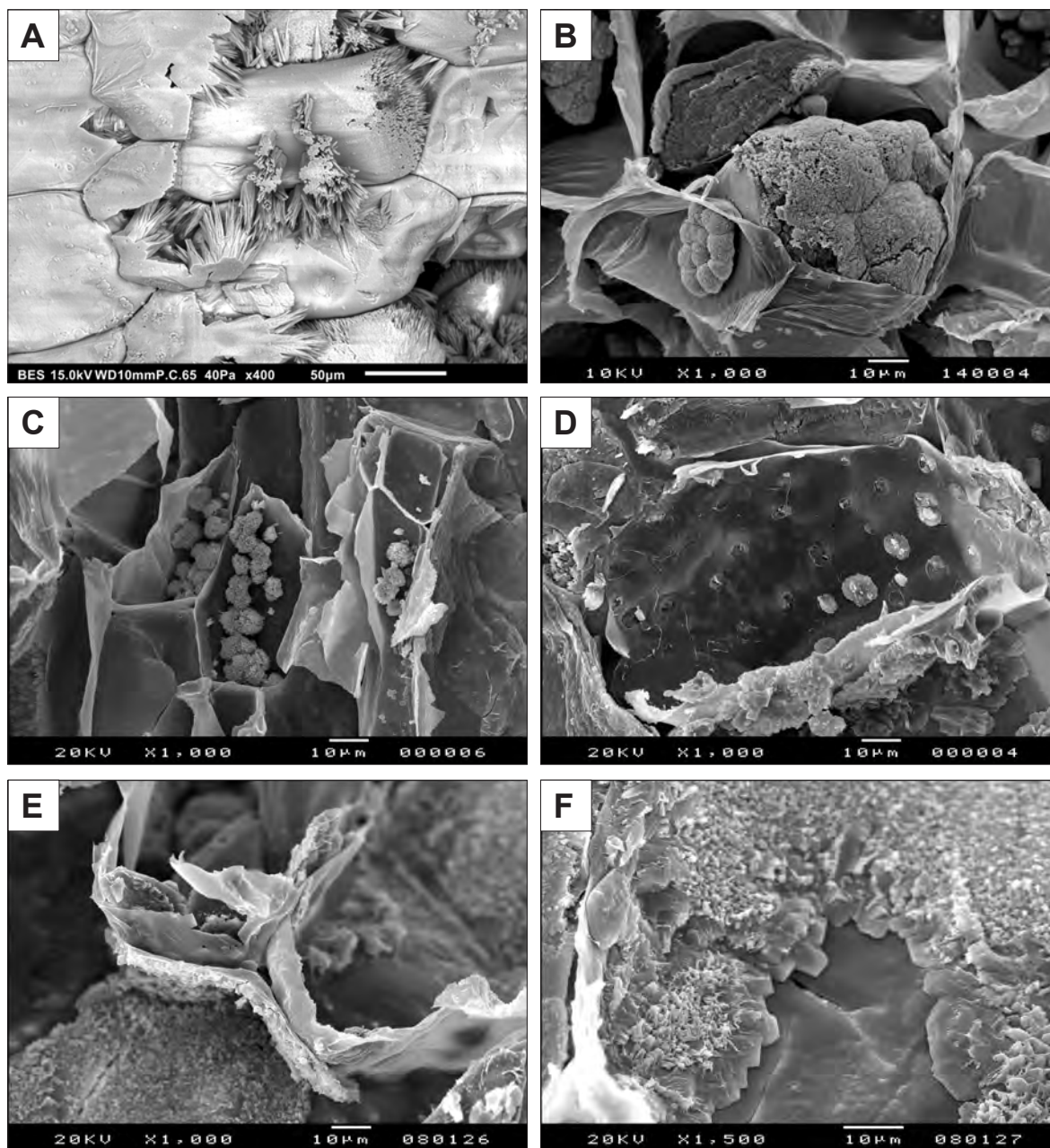


**Figure A3-4.11.** SEM photomicrographs of non-vacuolar, small-scale crystal forms. Also see caption in Fig. 3.26. A) Acicular crystal clusters growing perpendicular to cell walls, probably formed in an empty, non-calcified cell. B-D) Cell interiors with disc-shaped crystal bodies, 5-10 µm in diameter, formed on the surface of the cell wall. Sella, site T14-463. Cf. forms illustrated by Jaillard (1987), their Figs. 5-11c-f. E, F) Several micrometres thick calcite crust, coating the cell wall, probably formed by coalescence of clusters illustrated in Figs. C and D.



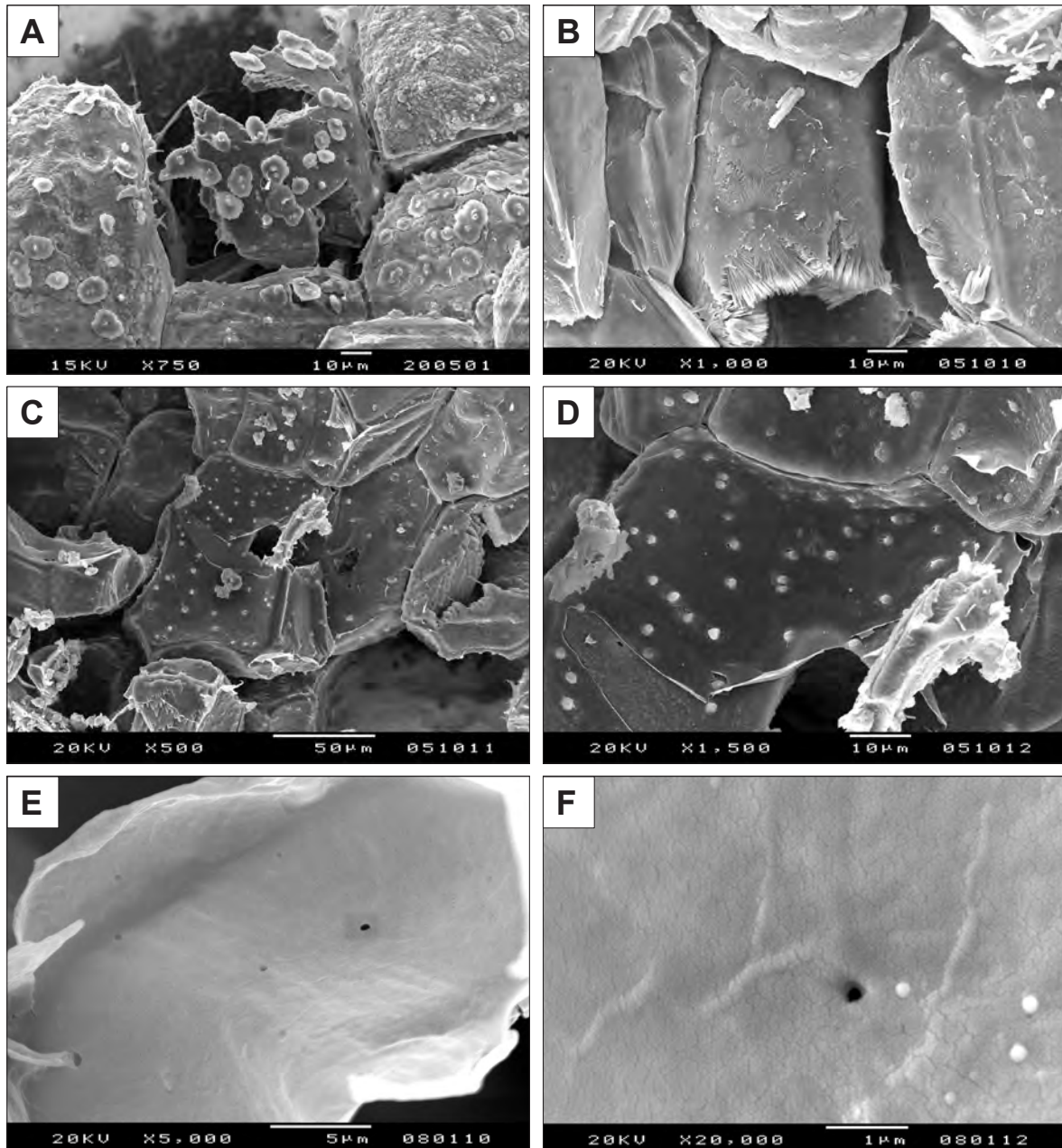


**Figure A3-4.12.** SEM photomicrographs of non-vacuolar, small-scale crystal forms. A) Disc-shaped i crystal bodies, 5-10 μm in diameter, formed on the surface of the cell wall, seen from the lower side (cf. Figs. 3.26D and A3-4.11D). B) Surface of a calcified cell showing lower (outer) side of acicular clusters illustrated in Fig. A3-4.11A. C, D) Mine mineral precipitates in hollows in the cell wall. E, F) Sub-micron size hollows in cell walls (?plasmodesmata) without associated mineral precipitates. Also see caption in Fig. 3.26.



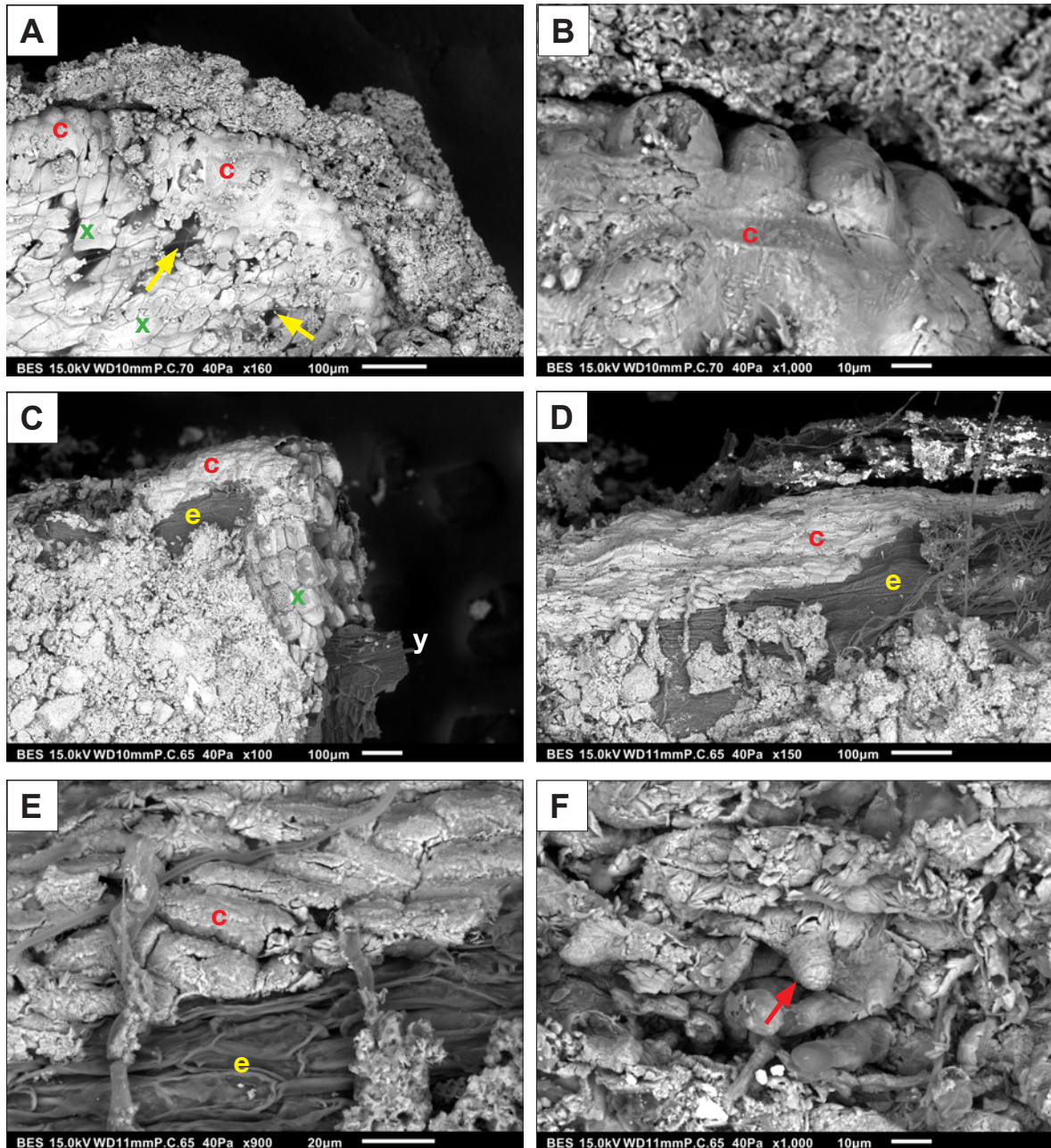


**Figure A3-4.13.** Small-scale Ca carbonate (and ?oxalate) precipitated externally on the epidermal cells, including some root hairs, of incompletely calcified iCRs. Lov vacuum BES photomicrographs. Finestrat-Sella. A) Thin crust (c); x - calcified cortex cells; yellow arrows: remains of cell walls. B) Detail of A showing arched epidermis cells coated by thin, ~1  $\mu\text{m}$  thick mineral layer (c). C-F) Detailed views showing the calcified layer (c), epidermis (e), vascular cylinder (y), and ?calcified root hair (red arrow in F).



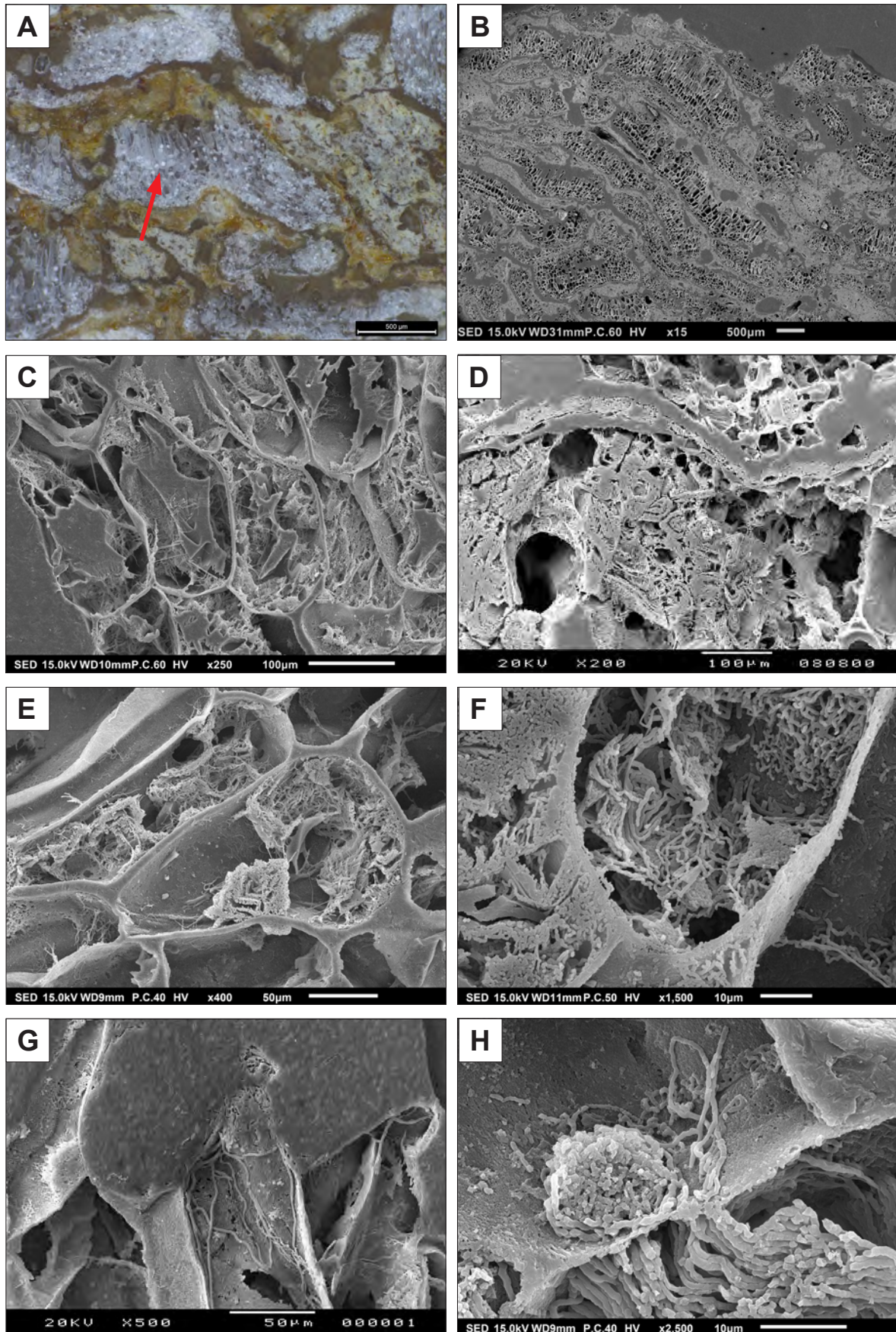
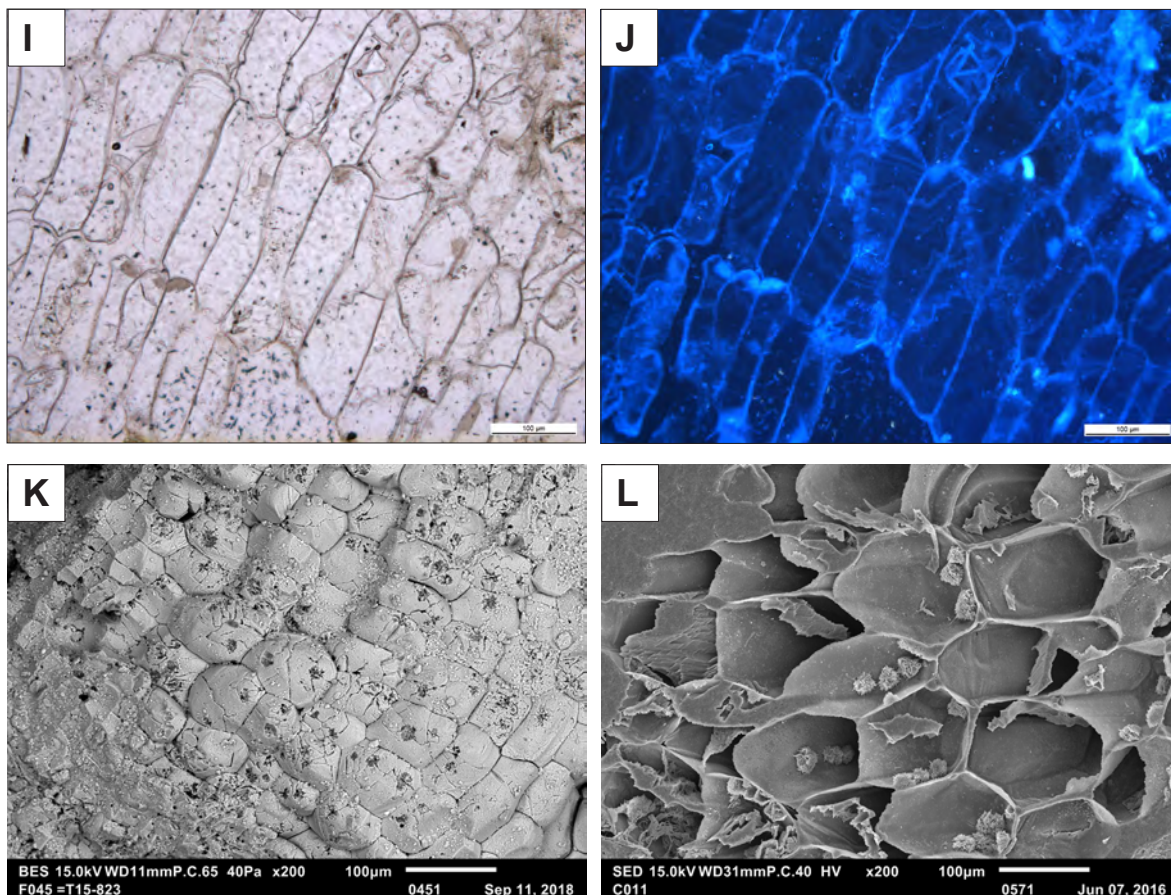


Figure A3-4.14. See continuation and caption on the next page.





**Figure A3-4.14.** Endolithic microborings in iCR calcite. Also see captions in Figs. 3.27 to 3.30.

A) Polished slab remaining from thin section preparation showing limpid calcified cells with white dots (arrow) corresponding to arbuscular structures in iCR calcite produced by endolithic microorganisms (cf. Fig. 3.30). B-H) Acid-etched polished, resin-embedded sample of iCRs with endolithic microborings. I, J) PPL and blue fluorescence pair of a thin section showing small clusters (?arbuscular structures) of endolith borings. K, L) SEM photomicrographs of iCR material similar to Figs I and J: K: surface of iCR showing hollows in calcified cells; L: analogous features seen in resin casts.



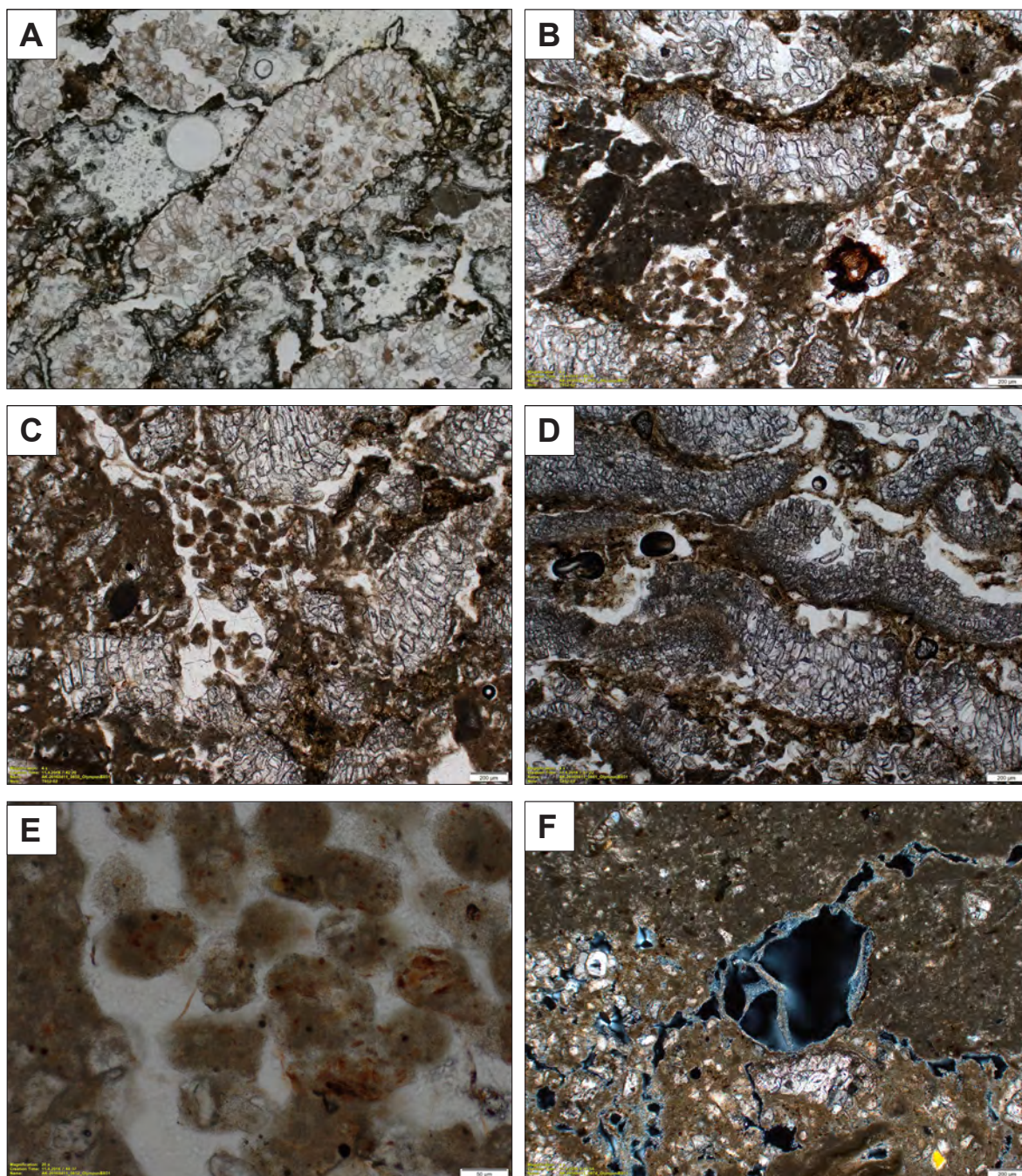


**Figure A3-4.15.** Thin section photomicrographs of partly weathered (degraded) iCRs. A-D) iCRs with partly micritised cells (altered by microendolithic borings). E) Peloids (faecal pellets), detail of Fig. C. F) Cavity with alveolar septal structure (NFC) in calcareous soil material largely composed of micritised iCR cells.

A



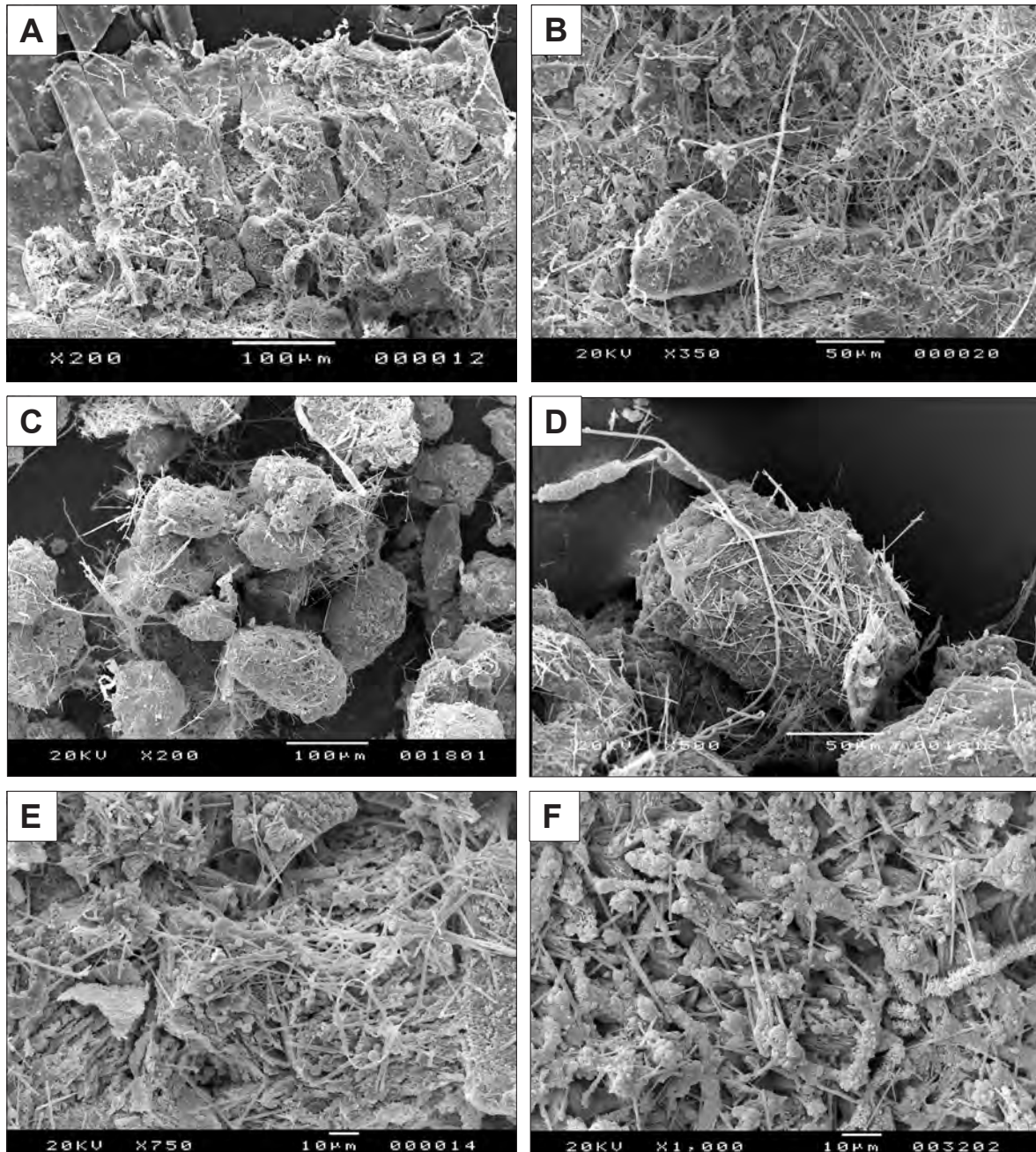


**Figure A3-4.16.** SEM photomicrographs of weathered (degraded) iCRs. A, B) A fragment of a type I iCR, etched and coated with needle fiber calcite (NFC), and numerous Ca-oxalate mineralised fungal hyphae. Sella, site T15-816. C, D) Weathered iCR cells, partly 'replaced' by NFC crystals. Penàguila, site T14-458. E, F) Extremely weathered calcified cells, covered by a film of NFC, nanofibres, mineralised bacteria and fungal hyphae. Sella, site T15-816. All images taken on Au-coated material in HV SED mode.

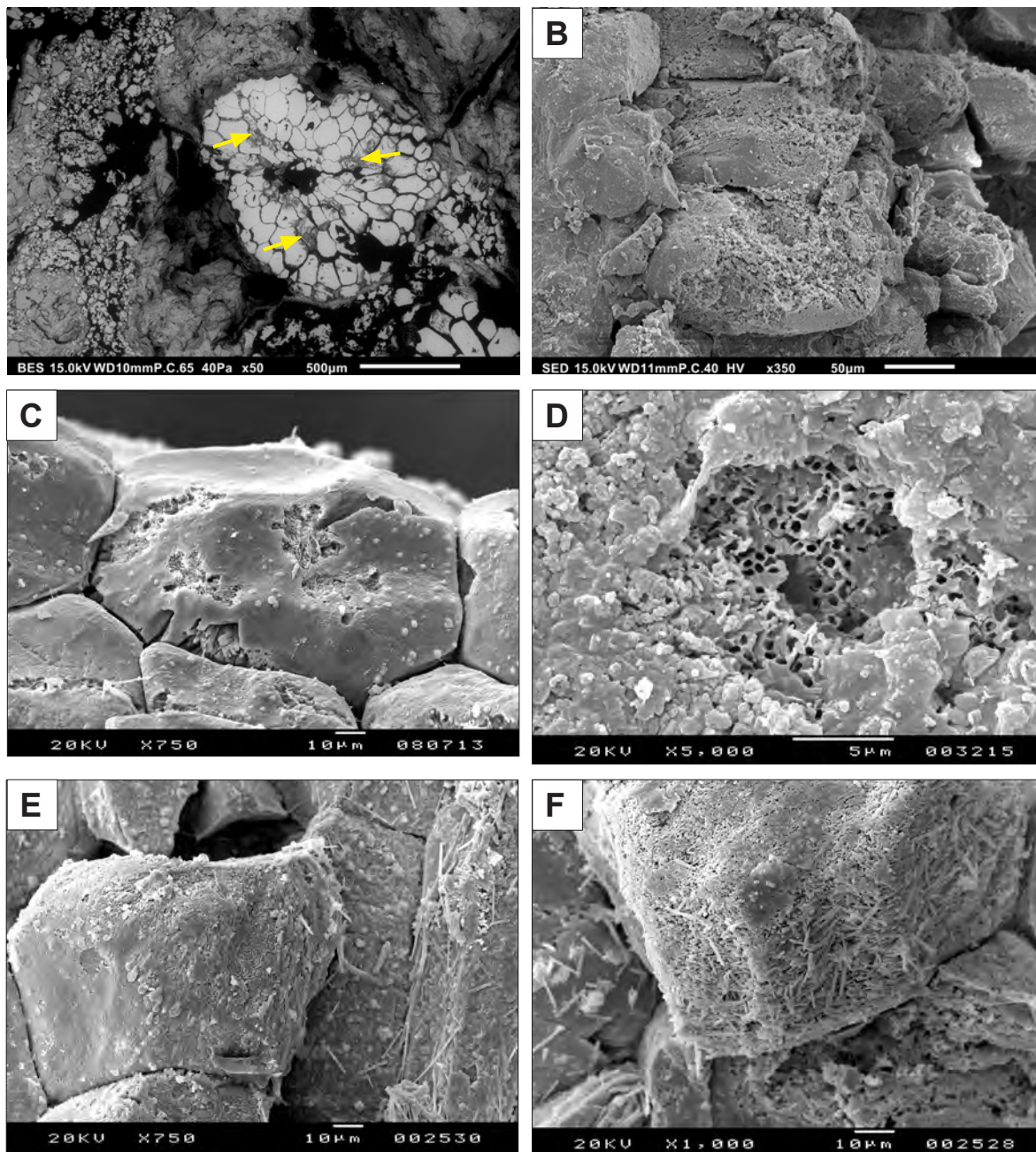


**Figure A3-4.17.** SEM photomicrographs of weathered (degraded) iCRs. A) BES SEM photomicrograph of a polished thin section showing Type I iCR in cross section. Arrows indicate cells strongly affected by microendolithic borings. C-F) SED photomicrographs of strongly weathered (etched) iCR cells with, probably microbially formed, dissolutional cavities, associated with secondary NFC (in Fig. F). Also see caption in Fig. 3.31.



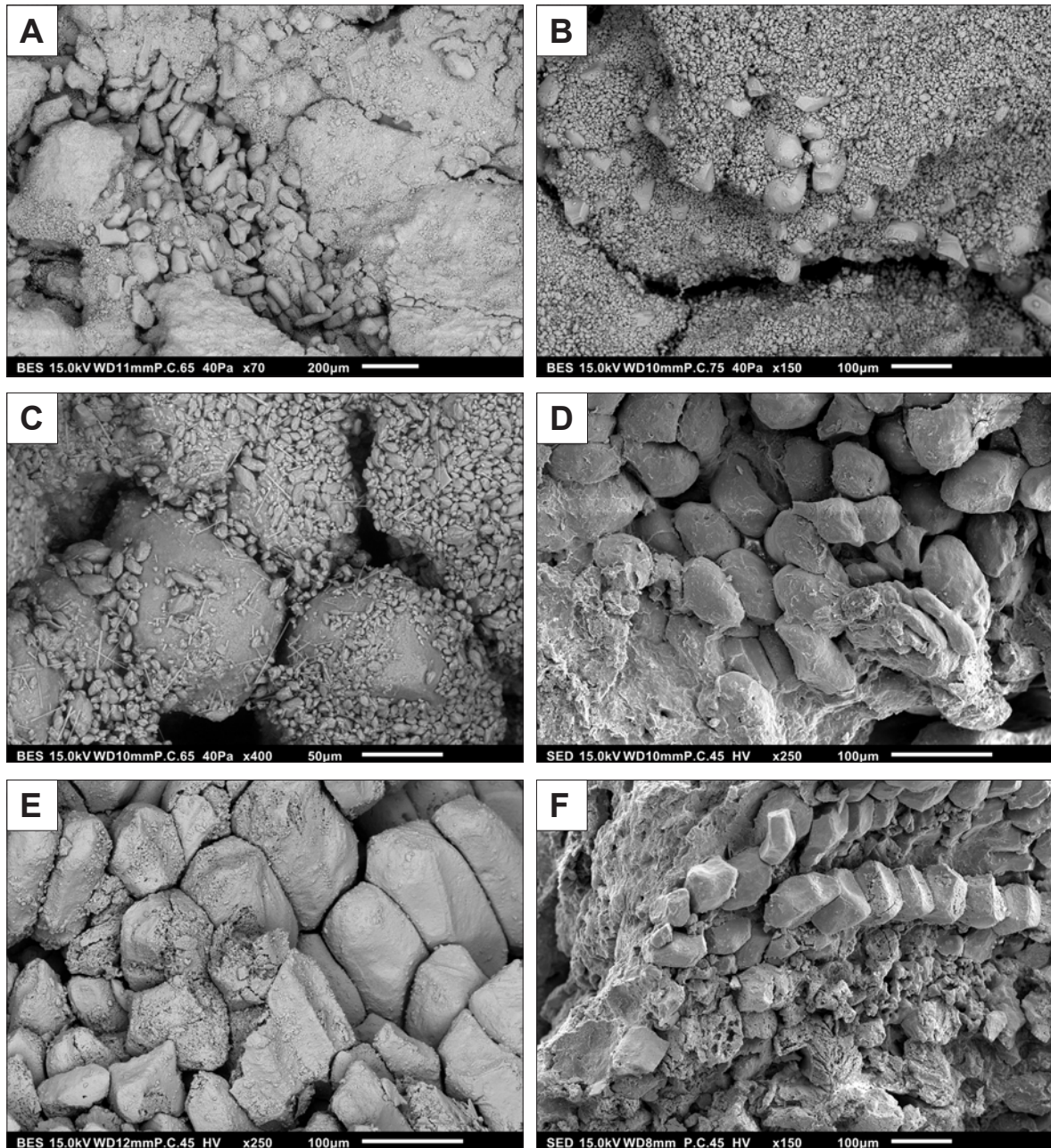


**Figure A3-4.18.** SEM (BES and SED) photomicrographs of weathered (degraded) iCRs. A-D) Disintegrated iCRs; individual calcified cells are incorporated in microsparite nodules. Penàguila locality. E, F) Etched (partly and selectively dissolved) iCR clusters. Ibi locality.

## Appendix A3-5 XRD and FTIR analysis of iCRs

**Figure A3-5.01.** XRD diffractograms of representative samples of intracellularly calcified roots. SLL-04, SLL-23; Sella, REL-05: Relleu, IBI-06: Ibi, PEN-01: Penàguila.

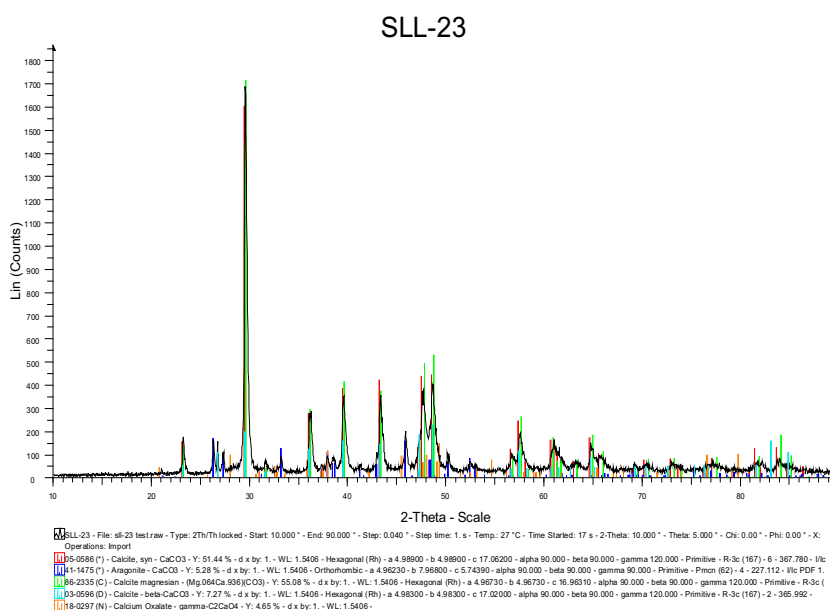
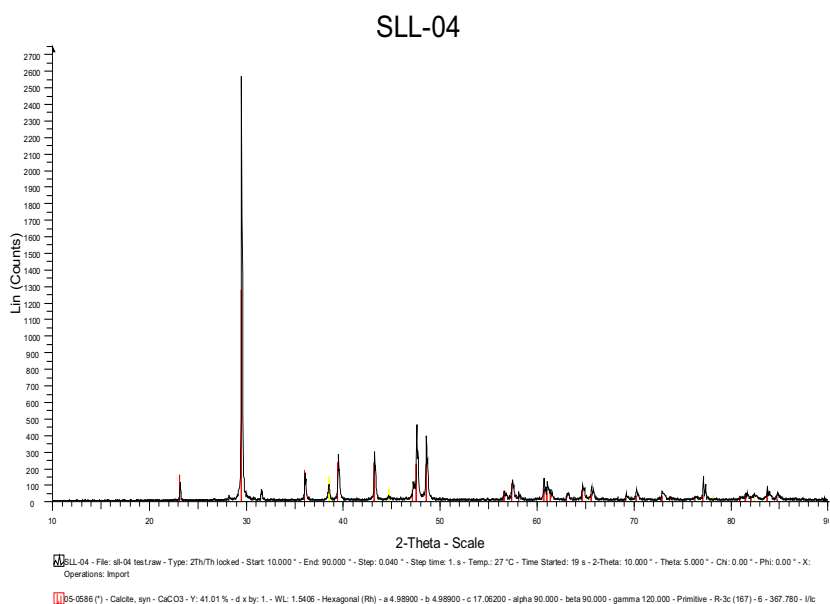
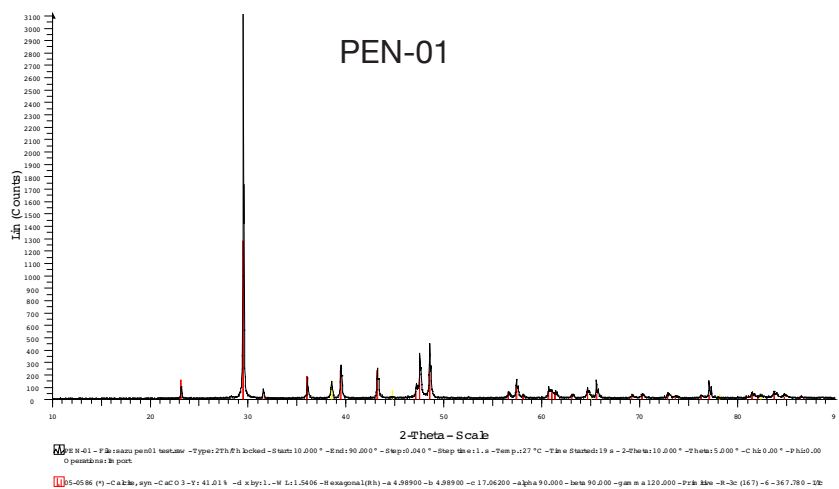
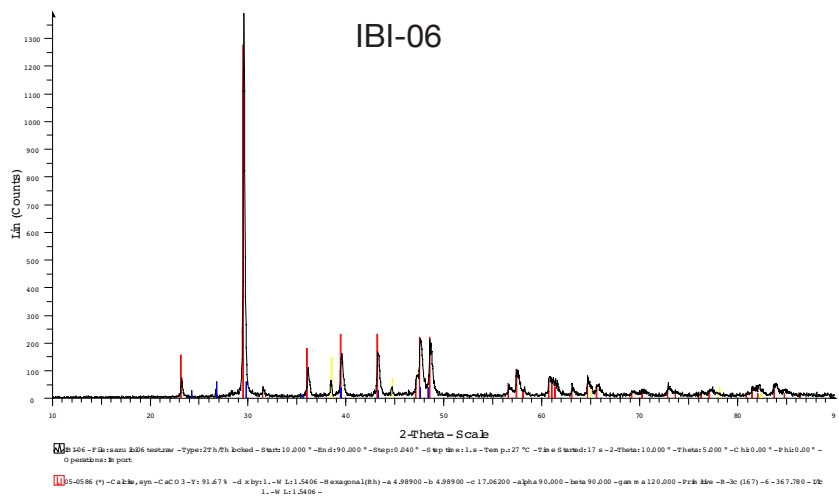
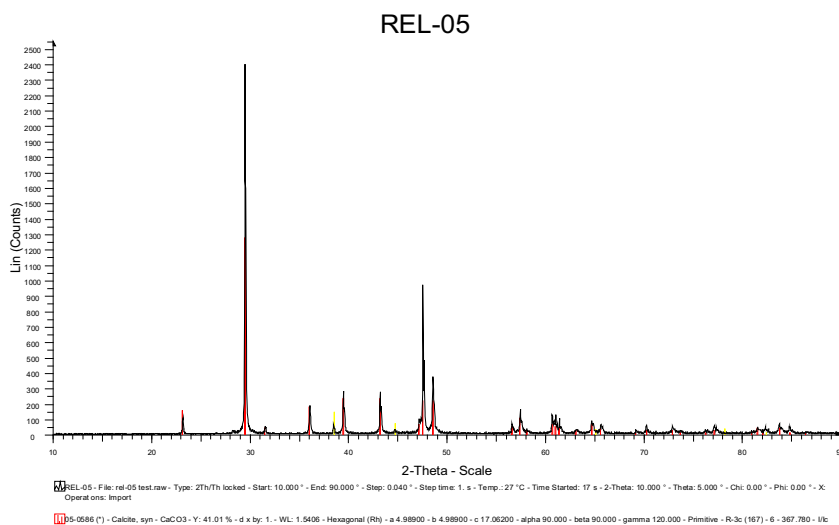
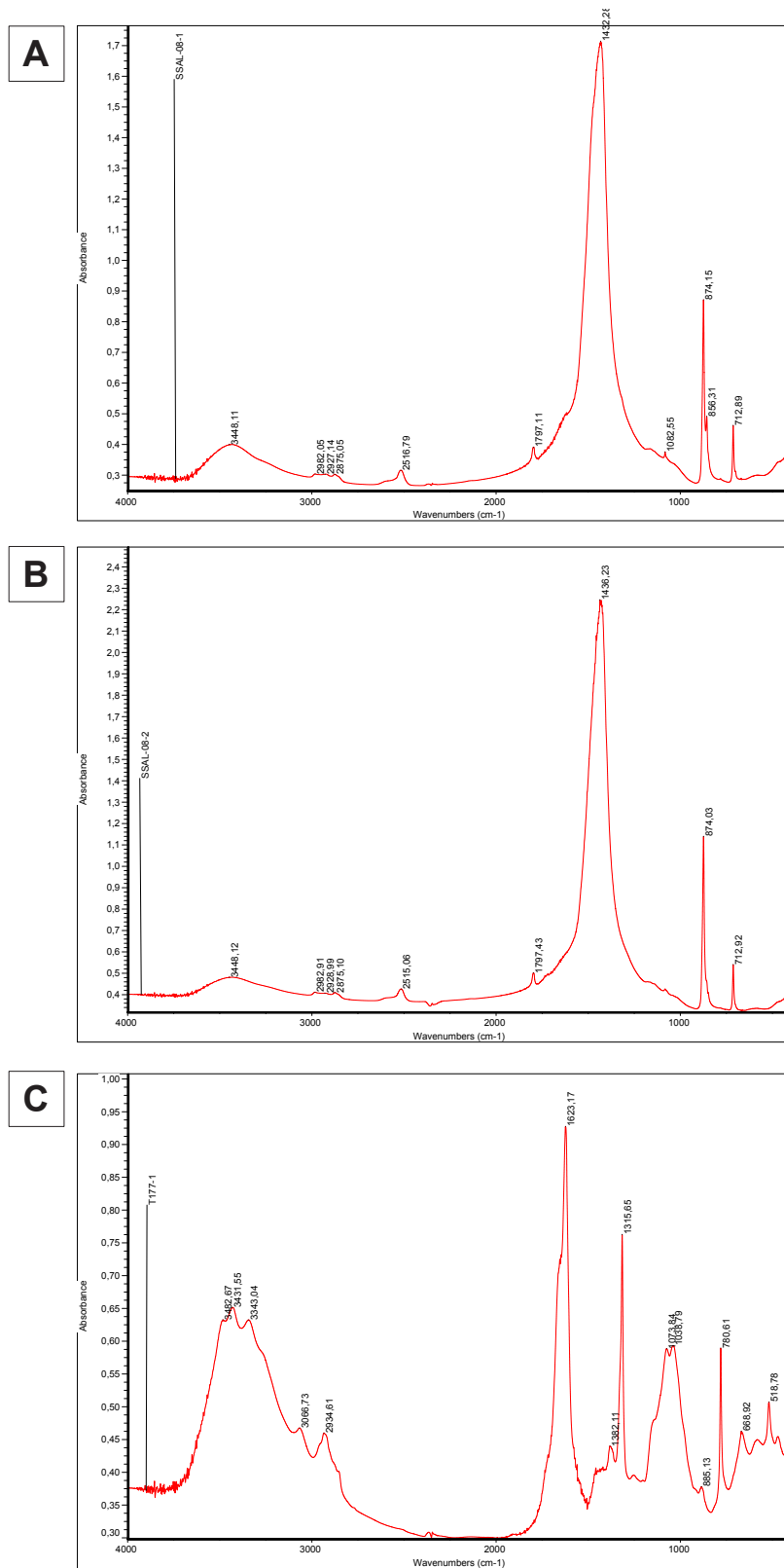


Figure A3-5.01. (continued).





**Figure A3-5.02.** FTIR spectra of two samples of iCR (A - IBI-06; B - SL-04), showing typical calcite patterns, and a spectrum (C) of a comparative sample of oxalate deposits on lichens (Lanzarote), showing a spectrum comparable to weddelite (Ca oxalate).



## Appendix A3-6 Results of EPMA analysis of iCRs

Elemental analyses were performed on polished thin sections on a JEOL JXA-8900 M WD/ED Electron Microprobe (CNME, University Complutense Madrid) operating at 15 kV and 20 nA and employing an electron beam diameter of 5 µm. The limits of detection for the analysed elements/oxides were: Ca 145 ppm, Mg 125 ppm, Fe 295 ppm, Mn 240 ppm, Sr 175 ppm, P, S 330 ppm, SiO<sub>2</sub> 400 ppm, Al<sub>2</sub>O<sub>3</sub> 170 ppm.

**Table A3-6.1.** Microprobe results, thinsections A03 and A04 in oxides form; iCR - intracellularly calcified roots, hst\_rck - hostrock.

thin section	material	pt #	CaO	MgO	FeO	MnO	SrO	P2O5	SO3	SiO2	Al2O3
A04	iCR	16	47.287	0.633	0.125	0.033	0.317	0.045	1.645	0.054	0.104
A04	iCR	17	52.206	1.097	0.046	0	0.554	0.022	0.018	0.012	0
A04	iCR	18	53.983	0.376	0	0.033	0.438	0.055	0.046	0.004	0.007
A04	hst_rck	19	31.288	1.085	1.372	0	0	0.139	0.083	17.925	7.279
A04	hst_rck	20	41.119	0.529	0.618	0	0	0.054	0.022	8.289	4.001
A04	hst_rck	21	0.492	0.907	4.109	0.027	0	0.023	0.019	20.435	4.812
A04	hst_rck	22	50.228	0.193	0.213	0.093	0.056	0.029	0.055	2.169	1.185
A04	iCR	23	55.661	0.75	0	0.033	0.266	0.009	0	0	0
A04	iCR/resin	24	35.272	0.134	0.046	0.016	0.172	0.062	0.047	0.021	0.088
A03	iCR	1	54.817	0.285	0.003	0.008	0.196	0.029	0.007	0	0.165
A03	iCR	2	53.201	0.493	0	0.026	0.263	0.055	0	0.005	0.005
A03	iCR	3	55.82	0.302	0.01	0	0.181	0.004	0	0.007	0
A03	iCR	4	52.953	0.415	0	0.049	0.339	0	0.044	0.056	0
A03	iCR	5	53.814	0.371	0.035	0	0.287	0.015	0	0	0
A03	iCR	6	54.98	0.388	0	0.083	0.371	0.049	0.045	0.034	0

**Table A3-6.2.** Microprobe results of thin section A04; elements in wt%. BES images show positions of the measurement points.

thin section - point #	material	Ca	Mg	Fe	Mn	Sr	P	S	Si	Al
A04 - 16	iCR	33.796	0.382	0.097	0.026	0.268	0.020	0.659	0.025	0.055
A04 - 17	iCR	37.311	0.662	0.036	0.000	0.468	0.010	0.007	0.006	0.000
A04 - 18	iCR	38.581	0.227	0.000	0.026	0.370	0.024	0.018	0.002	0.004
A04 - 19	hst_rck	22.361	0.654	1.066	0.000	0.000	0.061	0.033	8.379	3.852
A04 - 20	hst_rck	29.387	0.319	0.480	0.000	0.000	0.024	0.009	3.875	2.117
A04 - 21	hst_rck	0.352	0.547	3.194	0.021	0.000	0.010	0.008	9.553	2.547
A04 - 22	hst_rck	35.898	0.116	0.166	0.072	0.047	0.013	0.022	1.014	0.627
A04 - 23	iCR	39.781	0.452	0.000	0.026	0.225	0.004	0.000	0.000	0.000

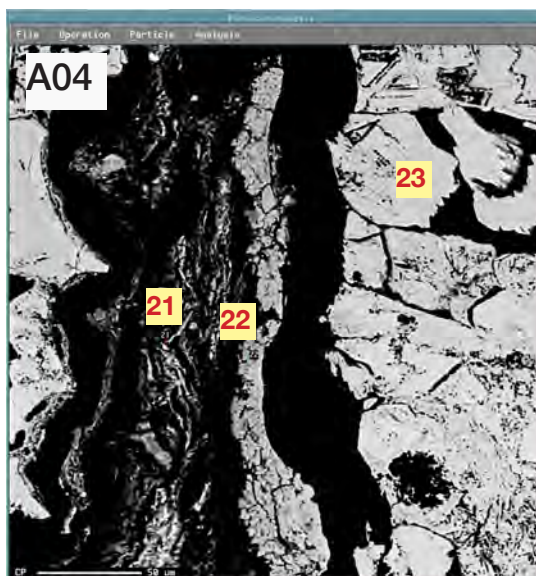
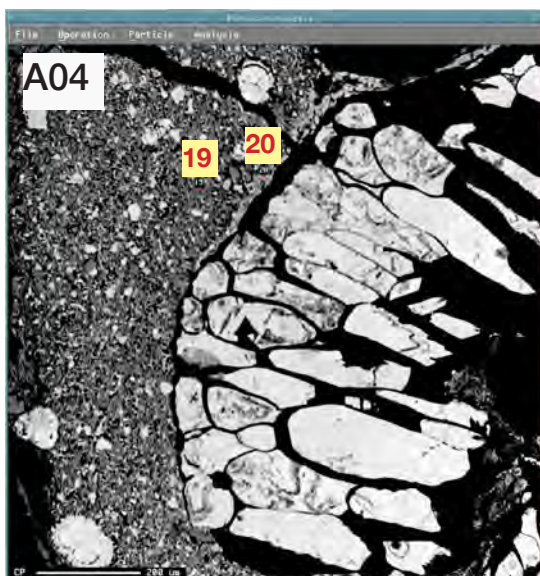
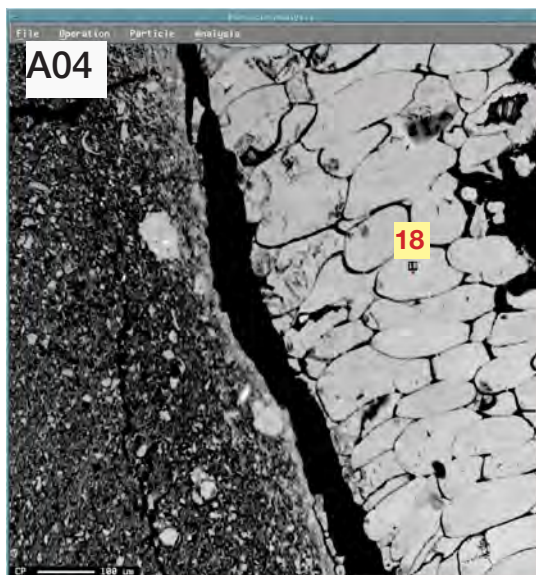
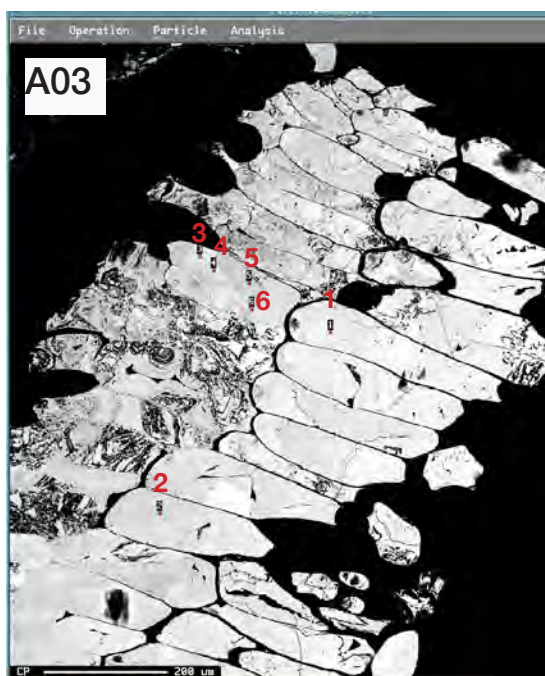




**Table A3-6.3.** Microprobe results of thin section A03. Elements in wt%. BES image shows positions of the measurement points.

thin section - point #	material	Ca	Mg	Fe	Mn	Sr	P	S
A03 - 1	iCR	39.177	0.172	0.002	0.006	0.166	0.013	0.003
A03 - 2	iCR	38.022	0.297	0.000	0.020	0.222	0.024	0.000
A03 - 3	iCR	39.894	0.182	0.008	0.000	0.153	0.002	0.000
A03 - 4	iCR	37.845	0.250	0.000	0.038	0.287	0.000	0.018
A03 - 5	iCR	38.461	0.224	0.027	0.000	0.243	0.007	0.000
A03 - 6	iCR	39.294	0.234	0.000	0.064	0.314	0.021	0.018



## Appendix A3-7 $\delta^{13}\text{C}$ and $\delta^{18}\text{O}$ stable isotope analysis of iCRs

**Table A3-7.1.** Data of  $\delta^{13}\text{C}$  and  $\delta^{18}\text{O}$  stable isotope results expressed in ‰ VPDB of pure iCRs.

Sample types: iCR: unspecified morphological type. iCR-I, iCR-II: type I and type II iCRs; iCR-D: weathered (degraded) iCRs. Morphologically unspecified samples, marked iCR\*, are from pot-grown calcified roots of *H. coronarium*. For sample and analytical procedure details see Appendix A1-1, Table A1-1.1.

Sample #	type	$\delta^{13}\text{C}$ (‰ VPDB)	$\delta^{18}\text{O}$ (‰ VPDB)	(cont.)	type	$\delta^{13}\text{C}$	$\delta^{18}\text{O}$
AK-03-003	iCR	-13.1	-5.2	AK-05-072	iCR	-15.0	-5.9
AK-03-004	iCR	-13.9	-9.7	AK-05-073	iCR	-14.8	-5.6
AK-03-018	iCR-D	-7.5	-7.5	AK-05-074	iCR	-13.8	-5.3
AK-03-018R	iCR-D	-7.7	-7.6	AK-05-075	iCR	-14.4	-5.8
AK-03-019	iCR	-13.6	-9.1	AK-05-076	iCR	-14.5	-3.0
AK-03-020	iCR	-13.6	-7.5	AK-05-078	iCR-II-D	-7.6	-5.3
AK-03-021	iCR	-15.0	-7.0	AK-05-079	iCR-II-D	-6.3	-6.0
AK-03-021R	iCR	-13.9	-6.0	AK-05-080	iCR-II-D	-7.6	-6.4
AK-03-022	iCR	-14.3	-6.9	AK-05-081	iCR-D	-7.5	-6.6
AK-03-023	iCR-D	-9.4	-6.4	AK-05-082	iCR-II-D	-7.0	-4.7
AK-03-024	iCR	-13.7	-4.8	AK-05-083	iCR-II-D	-7.5	-6.2
AK-03-024R	iCR	-13.6	-4.6	AK-05-084	iCR-II	-9.1	-6.9
AK-03-025	iCR	-11.5	-3.7	AK-06-227	iCR-D	-7.1	-7.8
AK-03-026	iCR	-11.8	-4.3	AK-06-228	iCR	-20.3	-10.4
AK-03-027	iCR	-10.9	-7.4	AK-06-230	iCR-D	-9.1	-6.0
AK-03-028	iCR-D	-10.0	-6.9	AK-06-231	iCR-D	-7.3	-5.7
AK-03-029	iCR-D	-8.2	-3.6	AK-06-233	iCR-D	-8.2	-5.6
AK-03-029R	iCR-D	-8.1	-4.1	AK-06-256	iCR	-12.5	-8.8
AK-03-030	iCR-D	-7.8	-4.1	AK-06-257	iCR	-13.5	-9.3
AK-03-030R	iCR-D	-7.4	-3.8	AK-06-258	iCR	-12.3	-8.7
AK-03-031	iCR	-11.9	-5.7	AK-06-259	iCR	-13.6	-6.2
AK-03-032	iCR-D	-9.2	-6.5	AK-06-260	iCR	-12.8	-6.3
AK-03-033	iCR	-10.1	-7.3	AK-06-261	iCR	-13.8	-5.1
AK-03-034	iCR	-14.5	-6.0	AK-06-262	iCR	-12.8	-7.3
AK-03-035	iCR	-10.5	-6.4	AK-14-400	iCR-I	-14.1	-7.2
AK-05-061	iCR	-17.2	-9.7	AK-14-401	iCR-I	-10.0	-5.3
AK-05-062	iCR	-16.8	-9.6	AK-14-402	iCR-I	-13.1	-6.6
AK-05-063	iCR	-13.9	-9.0	AK-14-404	iCR-I	-15.3	-0.5
AK-05-064	iCR-II-D	-8.0	-6.7	AK-14-405	iCR-I	-14.0	-5.3
AK-05-065	iCR-II-D	-8.4	-8.0	AK-14-406	iCR-I	-15.0	-6.0
AK-05-066	iCR-II-D	-8.7	-7.9	AK-14-407	iCR-I	-13.1	-7.0
AK-05-067	iCR-II-D	-8.4	-6.2	AK-14-408	iCR-I	-12.3	-6.5
AK-05-068	iCR-II-D	-8.6	-7.1	AK-14-410	iCR-I	-12.3	-1.9
AK-05-069	iCR-II-D	-8.6	-7.9	AK-14-410-2	iCR-I	-12.8	-2.4
AK-05-070	iCR-II-D	-9.2	-7.5	AK-14-411	iCR-D	-8.9	-3.9
AK-05-071	iCR-II-D	-7.5	-4.3	AK-14-412	iCR-I	-11.6	-0.9

Table A3-7.1 (continued)

(cont.)	type	$\delta^{13}\text{C}$	$\delta^{18}\text{O}$
AK-14-413	iCR-I	-11.5	-2.0
AK-14-414	iCR-I	-14.3	-0.1
AK-14-414-2	iCR-I	-14.2	-0.6
AK-14-415	iCR-I	-12.4	-2.0
AK-14-415-2	iCR-I	-12.7	-2.8
AK-14-416	iCR-I	-11.4	-2.1
AK-14-416-2	iCR-I	-11.2	-2.0
AK-14-417	iCR-II	-12.1	-4.9
AK-14-418	iCR-II	-12.1	-5.3
AK-14-418-2	iCR-II	-12.7	-5.4
AK-14-419	iCR-II	-10.2	-7.8
AK-14-419-2	iCR-II	-10.2	-7.6
AK-14-419-3	iCR-II	-10.5	-8.0
AK-14-421	iCR-II	-9.0	-6.7
AK-14-421-2	iCR-II	-10.0	-7.0
AK-14-422	iCR-II	-11.0	-4.7
AK-14-424	iCR-II	-10.1	-8.0
AK-14-425	iCR-II	-11.2	-5.9
AK-14-425-2	iCR-II	-10.0	-6.2
AK-14-426	iCR-II	-10.5	-4.1
AK-14-426-2	iCR-II	-10.4	-4.6
AK-14-427	iCR-II	-10.2	-9.0
AK-14-427-2	iCR-II	-9.9	-8.9
AK-14-427-3	iCR-II	-10.9	-8.9
AK-14-427-4	iCR-II	-10.3	-8.6
AK-14-427-5	iCR-II	-10.9	-8.8
AK-14-428	iCR-II	-9.0	-8.7
AK-14-428-2	iCR-II	-9.7	-8.6
AK-14-430	iCR-II-D	-8.3	-6.0
AK-14-431	iCR-D	-8.4	-6.1
AK-14-432	iCR-D	-9.1	-6.4
AK-14-433	iCR-D	-8.7	-6.2
AK-14-447	iCR*	-16.3	-7.6
AK-14-447-2	iCR*	-16.3	-7.6
AK-14-447-3	iCR*	-16.4	-7.6
AK-14-447-4	iCR*	-16.3	-7.5
AK-14-448	iCR*	-16.8	-6.9
AK-14-448-2	iCR*	-16.7	-6.8
AK-14-449	iCR*	-15.6	-7.3
AK-14-449-2	iCR*	-15.5	-7.2
AK-14-450	iCR*	-16.0	-6.9
AK-14-450-2	iCR*	-16.2	-7.0
AK-15-510	iCR-D	-7.7	-7.0
AK-15-510-2	iCR-D	-7.6	-7.1



## Appendix A4-1 DNA Barcoding results

### Bare sequences of obtained gene fragments for 8 samples

(8 rbcLa, 3 matK, and 4 ITS, respectively). See sample codes in Table 4.1.

#### \*\*\*A01 –rbcLa, matK, ITS

##### >A01\_rbcLa

AACAGAGACTAAAGCAAGTGTGGGTTCAAAGCTGGTGTAAAGATTATAGATTGACTTATTATACTCCTGAAT  
ATGAAACCAAGGATACTGATATCTTGGCAGCATTCCGAGTCACTCCTCAACCAGGAGTTCCCTCCTGAAGAAGCC  
GGTGTGCGGTAGCTGCCGAATCTTCCACTGGGACATGGACCACTGTGTGGACCGATGGGCTTACCAGTCTTG  
ATCGTTATAAAGGACGATGCTACCACATTGAACCCGTTGCTGGAGAAGAAAGTCAATTTATTGCTTATGTAGCT  
TATCCCTTAGACCTTTTTGAAGAAGTTCTGTTACTAACATGTTTACCTCCATTGTTGGTAATGTATTTGGGTTCA  
AGGCCTTACGCGCTCTACGTCTGGAGGATTTGCGAATCCCGGTTGCTTATGTTAAAACTTTCCAAGGTCTCCTC  
ACGGAATCCAAGTTGAGAGAGATAAATTGAACAAGTATGGTCGCTCTATTGGGATGTAATTAACCGAAA  
TTGGGATTATCCGCTAAGAATTACGGTCGAGCAGTTTATGAATGTCTTCGCGGT

##### >A01\_matK

TTTACATATTTAAATTATGTGTCAGATATACGAATACCCTATCCGATCCATCTGGAAATCTTAATTCAAATCCTTC  
GATACTGGGTAAAAGATGCCCTTTTTTTCATTTATTACGGTTGTTCTTTATAATTTTTGTAATTGGAATAGTTT  
GATTACTCCAAAATCTACTTTTTCAAAAAGTAATCCGAGATTATTCTTGTTCCCTATAATTGTTATGTATGTGAA  
TATGAATCTATCTTCTTTTTCTACGTAAAAAATCCTCTCATTTACGATTCAAATCTTTTAGCGTTTTTTTTGAGCG  
AATCTTTTTTATGCAAAAAGAGAACATCTTGTAGAAGTCCTTGATAAGGATTTTTCGTCTACCTAACATTCTTC  
AAGGATCCTCTCATTATTATGTTAGATATCAAGGAAAATCCATTCTGGCTTCAAAGAATGCGCCTCTTTGATG  
AATAAATGGAAACACTATTTTATCCATTTATGGCAATGTTTTTTGATATTTGGTCTGAACCAGGAACGGTTCAT  
ATAAACCAATTATCCGAACATTCATTTACCTTTTAGGCTATTTTTCAAATGTTGCGATAAATCCTTCAGTAGTAC  
GGAGTCAAATGTTACAAAATACATTCCTAATCGAAATTGGTAGCAAAAACTGGATATAATAGTTCCAATTATTC  
CTTTAATTAGATCATTGGCTAAAGAGAAAATTTGTAATGTCTTAGGTCATCCTATTAGTAAGCCGGTCTGGGCCG  
ATTCATCCGATTTGGATATTATTGACCGATTTTTGCGAATATCCAGAAATCTTCTCATTATTATAATGGATCCTC  
AAAAAAAAA

##### >A01\_ITS

GCTTATTGATGCTTAAATTCAGCGGTAGCCCCGCTGACCTGGGGTCTCGTCATGAGCATCCAAGGACGCTAG  
TGGGTCATAGAGGCCAAATCTGGTAAGAGCTGGCGCATGATCGGTCTCGTGGGTCACACAACCACCATCTATC  
ATGGCACACACCCTACCAAGGACTCAGTTTTAGCCAACCATGAGACAACWATTCTCACGGGAAGCCACCATTG  
GCCCTACACAGCCTATCAATAGGCATTGGGCAACGATATGTGACGCCAGGCAGACGTGCCCTCAACCTAATG  
GCTTCGGGCGCAACTTGCCTTCAAAAACGATGGTTACGGGATTCTGCAATTCACACCAAGTATCGCATTTT  
GCTACGTTCTTCATCGATGCAAGAGCCTAGATATCCGTTGCCGAGAGTCGTTTATATATACCATGCATCAAAA  
CTCCCAGAGGGCACCCTCCGGTCCCAAGAGGGGCGCACTGAACCAATTTAGTTTCTTGGCACACTCAGTG  
CCGGGTTTTGGTTTTGGTTGGGAGGGGAGCGCACAACTGGCTGCCCTGCCAACCAAGGGTGGACGAGGA  
GTTGAACACCAAGAGCCATCCCAACGATTCAAACAGATTACGAGTTGATCTACATGTAAGGCATCGACAATG  
ATCCTTCCGCGAGTTACCTACGGAAACCTTGTACGACT

#### Sample \*A02 – rbcLa

##### >A02\_rbcLa

AACAGAGACTAAAGCAAGTGTGGATTCAAAGCTGGTGTAAAGAGTACAAATTGACTTATTATACTCCTGAaT  
ATCAAACCAAGGATACTGATATATTGGCAGCATTCCGAGTCACTCCTCAACWGGAGTTCCCTCCTGAAGAAGCC  
GGTGTGCGGTAGCTGCCGAATCTTACTGGKACATGGACCACTGTGTGGACCGATGGACTTACCAGTCTTGA  
TCGTTACAAAGGGCGATGCTACCGCATTGAGCGTGTGTTGGAGAAAAAGATCAATATATTGCTTATGTAGCTT  
ACCTTTAGACCTTTTTGAAGAAGTTCCGTTACCAACATGTTTACTTCCATTGTAGTAATGTATTTGGGTTCAA  
AGCCCTGCGCGCTCTACGTCTGGAAGATTTGCGAATCCCTGTTGCTTATATTAATAACTTTCCAAGGTCTCCTCA  
TGGGATCCAAGTTGAAAGAGATAAATTGAACAAGTACGGTCGTCCTGTTGGGATGTAC

**Sample \*\*\*A03 - rbcLa, matK, ITS****>A03\_rbcLa**

AACAGAGACTAAAGCAAGTGTGGGTTCAAAGCTGGTGTAAAGATTATAGATTGACTTATTATACTCCTGAAT  
ATGAAACCAAGGATACTGATATCTTGGCAGCATTCCGAGTCACTCCTCAACCAGGAGTTCCTCCTGAAGAAGCC  
GGTGTGCGGTAGCTGCCGAATCTTCCACTGGGACATGGACCACTGTGTGGACCGATGGGCTTACCAGTCTTG  
ATCGTTATAAAGGACGATGCTACCACATTGAACCCGTTGCTGGAGAAGAAAGTCAATTTATTGCTTATGTAGCT  
TATCCCTTAGACCTTTTTGAAGAAGTTCTGTTACTAACATGTTACCTCCATTGTTGGTAATGTATTTGGGTTCA  
AGGCCTTACGCGCTCTACGTCTGGAGGATTTGCGAATCCCCGTTGCTTATGTTAAAACCTTTCCAAGGTCCTCCTC  
ACGGAATCCAAGTTGAGAGAGATAAATTGAACAAGTATGGTCGCTCCTATTGGGATGTACTATTAACCGAAA  
TTGGGATTATCCGCTAAGAATTACGGTCGAGCAGTTTATGAATGTCTTCGCGGT

**>A03\_matK**

TATTTAAATTATGTGTCAGATATACGAATACCCTATCCGATCCATCTGGAAATCTTAATCAAATCCTTCGATACT  
GGGTAAGATGCCCTTTTTTTCATTTATTACGGTTGTTTCTTTATAATTTTTGTAATTGGAATAGTTTGACTACT  
CCAAAATCTACTTTTTCAAAAAGTAATCCGAGATTATTCTTGTCTCTATAATTGTTATGTATGTGAATATGAAT  
CTATCTTCTTTTTCTACGTAAAAAATCCTCTCATTTACGATTCAAATCTTTAGCGTTTTTTTTGAGCGAATCTTTT  
TTTATGCAAAAAGAGAACATCTGTAGAAGTCTTGATAAGGATTTTTCGTCTACCTAACATTCTTCAAGGATC  
CTCTCATTATTATGTTAGATATCAAGGAAAATCCATTCTGGCTTCAAAGAATGCGCCTCTTTTGATGAATAAAT  
GGAAACACTATTTTATCCATTTATGGCAATGTTTTTTTGTATTTGGTCTGAACCAGGAACGGTTCATATAAACC  
AATTATCCGAACATTCATTTACCTTTTAGGCTATTTTTCAAATGTTCCGATAAATCCTTCAGTAGTACGGAGTCA  
AATGTTACAAAATACATTCCTAATCGAAATTGGTAGCAAAAAACTGGATATAATAGTTCCAATTATTCCTTTAAT  
TAGATCATTGGCTAAAGAGAAATTTTGAATGTCTTAGGTATCCTATTAGTAAGCCGGTCTGGGCCGATTATC  
CGATTTGGATATTATTGACCGATTTTTGCGAATATCCAGAAATCTTCTCATTATTATAATGGATCCTCAAAAAA  
AAAA

**>A03 ITS**

TCCGCTTATTGATGCTTAAATTCAGCGGGTAGCCCCGCTGACCTGGGGTCTCGTCATGAGCATCCAAGGACGC  
TAGTGGGTCATAGAGGCCAAATCTGGTAAGAGCTGGCGCATGATCGGTCTCGTGGGTACACAACCACCATCT  
ATCATGGCACACACCCTACCAAGGACTCAGTTTTAGCCAACCATGAGACAACAATTCTCACGGGAAGCCACCA  
TTCCGCCCTACACAGCCTATCAATAGGCATTGGGCAACGATATGTGACGCCAGGCAGACGTGCCCTCAACCTAA  
TGGCTTCGGGCGCAACTTGCCTTCAAAAACCTCGATGGTTACGGGATTCTGCAATTCACACCAAGTATCGCATT  
TCGCTACGTTCTTCATCGATGCAAGAGCCTAGATATCCGTTGCCGAGAGTCGTTTATATATACCATGCATCAAAA  
CACTCCCAGGAGGGCACCCTCCGGTCCCAAGAGGGGCGCACTGAACCAATTTTAGTTCTTGGCACACTCAG  
TGCCGGGGTTTTGGTTTTGGTTGGGAGGGGAGCGCACACGTTGGCTGCCCTGCCAACCAAGGGTGGACGAG  
GAGTTGAACACCAAGAGCCATCCCAACGATTCAAACAGATTACGAGTTGATCTACATGTAAGGCATCGACAA  
TGATCCTTCGCAGGTTACCTACGAAACCTTGTACGACTTCTCCT

**Sample \*A04 - rbcLa****>A04\_rbcLa**

AGAGACTAAAGCAAGTGTGGGTTCAAAGCTGGTGTAAAGATTACAAATTGACTTATTATACTCCTGAATACG  
AAATCAAGGATACTGATATCTTGGCAGCATTCCGAGTCACTCCTCAACCAGGAGTTCCTCCCGAAGAAGCCGGG  
GCTGCGGTAGCTGCCGAATCTTCCACTGGKACATGGACCACTGTGTGGACCGATGGACTTACCAGTCTTGATCG  
TTACAAAGGGCGATGCTACCACATTGAGGCCGTTGTTGGAGAAGAAAATCAATTTATTGCTTATGTAGCTTATC  
CYTTAGACCTTTTTGAAGAAGTTCTGTTACTAACATGTTTACTTCCATTGTGGGTAATGTATTTGGTTTCAARGC  
CTTACGMGCTCTACGTCTGGAGGATTTGCGAATCCCACTTCTTATTCCAAAACCTTTCCAAGGTCCTCCTCACGG  
CATTCAAGTTGAAAGAGATAAATTGAACAAGTATGGTCGCTCCCTATTGGGATGCACTATTAACCAAAAATTGG  
GATTATCTGCAAAAAAATTACGGTAGAGCGGTTTATGAATGTCT

**Sample \*\*\*A05 - rbcLa, matK, ITS****>A05\_rbcLa**

AACAGAGACTAAAGCAAGTGTGGATTCAAAGCGGGTGTTAAAGAGTACAAATTGACTTATTATACTCCTGAAT  
ACGAAACCAAAGATACTGATATCTTGGCAGCATTCCGAGTAACTCCTCAACCCGGAGTTCCACCTGAAGAAGCA  
GGGGCCGCGGTAGCTGCCGAATCTTCTACTGGTACATGGACAACCTGTGTGGACCGATGGACTTACCAGCCTTG  
ATCGTTACAAAGGGCGATGCTACCACATTGAGCCCGTTCTGGAGAAAAAGATCAATATATCTGTTATGTAGCT  
TACCCTTTAGACCTTTTTGAAGAAGTTCTGTTACTAACATGTTTACTTCCATTGTAGGAAATGTATTTGGATTCA  
AAGCCCTACGTGCTCTACGTCTGGAAGATCTGCGAATTCTGTTGCTTATGTTAAAACCTTCCAAGGCCCGCCTC  
ATGGGATCCAAGTTGAGAGAGATAAATTGAACAAGTACGGTCCTCTGCTGGGATGTACTATTAACCTAAA  
TTGGGGTTATCTGCTAAAACTATGGTAGAGCGGTTTATGAATGTCTTCGCGGT

**>A05\_matk**

AATTCATTCAATATTTCCATTTTTAGAGGACAATTTTTACATTTAAATTTGTGTTAGATATACTAATATCTCGCT  
CTGTCCATGTGGAAATCTTGATTCAAACCTTTCGCCTTTGGGTAAAAGATGTTTCTTCTTGCATTTATTACGAGT  
CTTCTCAACGAATATTGGAATAGTGTCTTACTCGAAAGAAAGTAAGCTTCTTTGTCAAAAAGAAATCAAAG  
GTTATTTTTTTTCTATATAATTCTCATGTATGTGAATACGAATCTATTTTCGCTTTTCTACGTAACCAATTTTTCA  
TTTACGATCAACATCTTCTGGAGTTCTTCTGAACGAATTTATTTCTCTATAAAAATAGAACGTCTTATGAACGGC  
TTTGTAAAGGATTTTCGGACCAACCTAGGGTTGGTTGAGGAACCTGCATGCATTATATCAGGTATCAAAGAAA  
ATCCATTCTGGCTTCAAAGGGACATCCCTTTTCATGAATAAATGGAATTTTACCTTGTCACTTTTTGGCAATGG  
CATTTTTCGGTGTGGTTTCATCCAAGAAGGATTTGATAAACCAATTTTCCAAGCATTCCCTTCAAATTTTGGCT  
ATCTTTCAAACGTGCAAATGAACCTTCCGTGGTACGGAGTCAAATTCTAGAAAATGCATTTCTAATCAATAATG  
CTATTAAGAAGCTCGATACCCTTGTCCAATTATCCTCTGATTGCGGAATTGGCTAAAGCGAAATTTGTAACG  
TATTGGGGCATCCATTAGTAAGCCGATTCGGGCTGATTTATCAGATTCTAATATTATTGACCGGTTTTCGCGTA  
TATGCAGAAATATTTCTCATTATCATAGCGGATCTGCAAAAAA

**>A05 ITS**

TTATTGATGCTAAACTCAGCGGGTAATCCCGCCTGACCTGGGGTCGCGGTGCAAGGTAGAGCGCCCTAAGGC  
ACCATAACCATTGGGTGATTGATGGATGCCATGCGGACGACGACGTGGCACGACGCGCGCGAGATTGAGTTG  
TTCAACCACCACTTATCGTGACACGAGTCGCGGAGGGATCGCATTTGGGCCAACCGCGCATCGAGACGCACGG  
GAGGCCAATATCCGCCCAACACCGCTGCTTACGCTGGGATGGGGGGCGACGCGATGCGTGACGCCAGGC  
AGACGTGCCCTCGGCCTAATGGCTTCGGGCGCAACTTGCCTTCAAAGACTCGATGGTTACGGGATTCTGCAAT  
TCACACCAAGTATCGATTTGCTACGTTCTTATCGATGCGAGAGCCGAGATATCCGTTGCCGAGAGTCGTTTT  
GACATTTGACAGACATCCGATCCCCACGCACGTTCCGCGAACGGGGTGGGGGAGGCGGACGCTTCTTTAGTT  
TTCCTTGGCGCATTCCGCGCCGGGGTTCTTAGCCCGCACGACATGGCCGAGGGAACATGCCGGGCGGGGG  
GCCGTTGGCACGATGGGGGTTGCCCCACGTCGTGCCCCGATGGCGTTAAACACGTGTTTCGCGGTCTGCTTT  
GCAGGTTNCGACAATGATCCTTCCGCAGGTTACCTACGGAAACCTTGTTA

**Sample \*A06 - rbcLa****>A06\_rbcLa**

AACAGAGACTAAAGCAAAGTTGGGTTAAAGCTGGTGTTAAAGATTACAAATTGACTTATTATACTCCTGACT  
ATCAAATCAAAGATACTGATATCTTGGCAGCATTCCGAGTAACTCCTCAACCTGGAGTTCCGCCGAAGAAGCA  
GGGGCTGCGGTAGCTGCCGAATCTTCTACTGGGACATGGACAACCTGTGTGGACCGATGGACTTACCAGTCTTG  
ATCGTTACAAAGRGCATGCTACCACATCGAGGCCGTTGTTGGaAAGAAAATCAATWTATTGCTTATGTAGCT  
TATCCTTTAGACCTTTTTGAAGAAGTTCTGTTACTAACATGTTTACCTCCATTGTGGGTAATGTATTTGGTTTCA  
AAGCCTTGCAGCTCTACGTCTGGAAGATTTGCGAATTTCCAATTTTAAAACCTTCCAAGGYCCTCCTCA  
CGGCATTCAAGTTGAAAGAGATAAATTGAACAAGTATGGACGTCCCTATTGGGATGCACTATTAACCAAAAT  
TGGGATTATCCGCTAAAAATAATGGTAGAGCGGTTTATGAATGTCTCCGCGG



**Sample \*\*A07** – rbcLa, ITS**>A07\_rbcLa**

AACAGAGACTAAAGCAAAGGTTGGGTTCAAAGCTGGTGTAAAGATTATAAATTGACTTATTATACTCCTGACT  
ATCAAACCAAAGATACTGATATCTTGGCAGCATTCCGAGTAAGTCCTCAACCTGGAGTCCGCCTGAAGAAGCA  
GGTGCAGCGGTAGCTGCCGAATCTTCTACTGGGACATGGACAACCTGTGTGGACCGATGGACTTACCAGTCTTG  
ATCGTTATAAAGGACGCTGCTACCACATCGAGCCTGTTGCTGGAGAAGATAGTCAATTTATTGCTTATGTAGCTT  
ATCCCTTAGACCTTTTTGAAGAAGGTTCTGTTACGAACATGTTTACCTCCATCGTAGGTAATGTATTTGGGTTCA  
AGGCCTTGC GCGCTCTACGTCTGGAAGATTTGCGAATCCCTAATGCTTATGTTAAAACCTTCCAAGGTCCTCCTC  
ACGGAATCCAAGTTGAGAGAGATAAATTGAACAAGTATGGACGTCCCTATTGGGATGTACTATTAACCCAAA  
ATTGGGTTTATCCGCTAAGAATTATGGTAGAGCAGTTTATGAATGTCTCCGCGGT

**>A07\_ITS**

TCCGCTTATTGATGCTTAAATTCAGCGGGTAGCCCCGCTGACCTGAGGTCTCATCACGAGCGTTAAGAAACGC  
AAAATGGGTAAGAGAGGCCACATTCAGCAGAGTAGTGATGATTTTCAAGTCTCGTGGGTCACACAACCACCA  
TCTATCATGGCACACCCTACCAAGTCTCAATTTTCAACCAACCGTGAGCCAAAAGAGTTCACGGGAGGCCAAC  
ATTCGCCATGCTCAATACCTATGAATAGGATATTGGCAAGAGGCTTCGATATGTGACACCCAGGCAGACGTGCC  
CTCAACCTAAATGGCATCGGGCGCAACTTGC GTTCAAAGACTCGATGGTTCACGGGATTCTGCAATTCACACCA  
AGTATCGATTTTCGCTACGTTCTTCATCGATGCAAGAGCCTAGATATCCGTTGCCGAGAGTCATTCTAATATCAT  
GTGTCCAAACACAACCCACACGAAAACCGTCTCCAGTGCCATGTGGGTGCGCTAAGAGCAAATTTAAATTCCT  
TGACGCATTACGCGCCGGGTTTGAGTTTTTGGCACGAAGGAGAACGCACTAAGTCGCCACCTTCAAACCCAG  
AGGTAAGCCTGAGGTGTGGAACAACCTCAAGCAAACCCAGTATGTTGAAACTGATTCACGTGTTGTTTAGCATG  
TAAGGCATCGACAATGATCCTTCCGCAGGTTACCTACGGAACCTTGTTACGACTTCCTCCT

**Sample \*A08****>A08\_rbcLa**

AACAGAGACTAAAGCAAAGTGTGGATTCAAAGCTGGTGTAAAGATTACAAATTGACTTATTATACTCCTAACT  
ATGAAACCAAAGATACTGATATCTTGGCAGCATTCCGAGTAACCCCTCAACCGGGAGTTCACCTGAAGAAGCA  
GGGGCCGCGGTAGCTGCCGAATCTTCTACTGGTACATGGACAACAGTGTGGACTGATGGACTTACTAGCCTTG  
ATCGTTACAAAGGGCGATGCTACCACATCGAGCCTGTTGCTGGAGACGAAAATCAATATATTGCTTATGTAGCT  
TATCCTTTAGACCTTTTTGAAGAGGTTCTGTTACTAATATGTTTACTTCCATTGTGGGTAATGTATTTGGATTCA  
AAGCCCTGCGCGCTCTACGTCTGGAAGATCTAAGAATCCCTACAGCGTATGTTAAAACGTTCCAAGGACCGCCT  
CATGGTATCCAAGTTGAAAGAGATAAATTGAACAAATACGGCCGTCCCTGTTGGGATGTACAATTAACCTAA  
ATTGGGTTATCTGCTAAAAACTATGGGAGAGCTGTTTATGAATGTCTACGCGGT

## Appendix A4-2 DNA Barcoding results

### Significant BLASTN alignment results for rbcLa sequences (samples A01-A08)

RID: CZ5PPE5J013  
 Job Title: **A01 rbcLa + matK**  
 Program: BLASTN  
 Database: nt Nucleotide collection (nt)  
 Query #1: Query ID: lcl|Query\_1863 Length: 1416

>Onobrychis viciifolia voucher L.Duan 2018014 (IBSC) chloroplast, complete genome  
 Sequence ID: NC\_053934.1 Length: 121932 >Onobrychis viciifolia voucher L.Duan 2018014  
 (IBSC) chloroplast, complete genome  
 Sequence ID: MW007721.1 Length: 121932 Range 1: 2076 to 2917  
 Score:1511 bits(818), Expect:0.0,  
 Identities:834/842(99%), Gaps:0/842(0%), Strand: Plus/Minus

Query	575	TTACATATTTAAATTATGTGTCAGATATACGAATACCTATCCGATCCATCTGGAAATC	634
Sbjct	2917	TTACATATTTAAATTATGTGTCAGATATACGAATACCTATCCGATCCATCTGGAAATC	2858
Query	635	TTAATTCAAATCCTTCGATACTGGGTAAAAGATGCCCTtttttttCATTATTACGGTTG	694
Sbjct	2857	TTAATTCAAATCCTTCGATACTGGGTAAAAGATGTCCCTTTTTTTCATTATTACGGTTG	2798
Query	695	TTCTTTATAATTTTGTAAATGGAATAGTTGATTACTCCAAAATCTACTTTTCAAAA	754
Sbjct	2797	TTCTTTATAATTTTGTAAATGGAATAGTTGATTACTCCAAAATCTACTTTTCAAAA	2738
Query	755	AGTAATCCGAGATTATCTTGTTCCTCTATAATGTTATGTATGTGAATATGAATCTATC	814
Sbjct	2737	AGTAATCCGAGATTATCTTGTTCCTCTATAATGTTATGTATGTGAATATGAATCTATC	2678
Query	815	TTCCTTTTCTACGTAAAAAATCCTCTCATTACGATTCAAATCTTTTAGCGttttttt	874
Sbjct	2677	TTCCTTTTCTACGTAAAAAATCCTCTCATTACGATTCAAATCTTTTAGCGTTTTTTTT	2618
Query	875	GAGCGAATCtttttttATGCAAAAAGAGAACATCTTGTAGAAGTCCTTGATAAGGATTTT	934
Sbjct	2617	GAGCGAATCtttttttATGCAAAAAGAGAACATCTTGTAGAAGTTTTGATAAGGATTTT	2558
Query	935	TCGTCTACCTTAACATTCTTCAAGGATCCTCTCATTATTATGTTAGATATCAAGGAAAA	994
Sbjct	2557	TCGTCTACCTTAACATTCTTCAAGGATCCTCTCATTATTATGTTAGATATCAAGGAAAA	2498
Query	995	TCCATTCTGGCTTCAAAGAATGCGCCTCTTTTGATGAATAAATGGAAACACTATTTTATC	1054
Sbjct	2497	TCCATTCTGGCTTCAAAGAATGCGCCTCTTTTGATGAATAAATGGAAACACTATTTTATC	2438
Query	1055	CATTTATGGCAATGtttttttGATATTTGGTCTGAACCAGGAACGGTTCATATAAACCAA	1114
Sbjct	2437	CATTTATGGCAATGtttttttGATATTTGGTCTGAACCAGGAACGGTTCATATAAACCAA	2378
Query	1115	TTATCCGAACATTCATTTACCTTTTAGGCTATTTTTCAAATGTTCCGATAAAATCCTTCA	1174
Sbjct	2377	TTATCCGAACATTCATTTACCTTTTAGGCTATTTTTCAAATGTTCCGATAAAATCCTTCA	2318
Query	1175	GTAGTACGGAGTCAAATGTTACAAAATACATTCTTAATCGAAATGGTAGCAAAAACTG	1234
Sbjct	2317	GTAGTACGGAGTCAAATGTTACAAAATACATTCTTAATCGAAATGGTAGCAAAAACTG	2258
Query	1235	GATATAATAGTTCCAATTATTCCTTTAATTAGATCATTGGCTAAAGAGAAATTTGTAAT	1294
Sbjct	2257	GATATAATAGTTCCAATTATTCCTTTAATTAGATCATTGGCTAAAGAGAAATTTGTAAT	2198

```

Query 1295 GTCTTAGGTCATCCTATTAGTAAGCCGGTCTGGGCCGATTCATCCGATTGGATATTATT 1354
          |||
Sbjct 2197 GTCTTAGGTCATCCTATTAGTAAGCCGGTCTGGGCCAATTCATCCGATTGGATATTATT 2138

Query 1355 GACCGATTTTTGCGAATATCCAGAAATCTTCTCATTATTATAATGGATCCTCaaaaaaa 1414
          |||
Sbjct 2137 GACCGATTTTTGCGAATATCCAGAAATCTTCTCATTATTATAATGGATCCTCAAAAAAA 2078

Query 1415 aa 1416
          ||
Sbjct 2077 AA 2076
    
```

-----

```

RID: DKENNFAC016
Job Title: A02_Sp_A_rbcLa (Fabaceae_IRLC)
Program: BLASTN
Database: nt Nucleotide collection (nt)
Query #1: A02_Sp_A_(Fabaceae_IRLC_clade) Query ID: lcl|Query_56465 Length: 507
    
```

```

>Melilotus sp. MP 711 ribulose-1,5-bisphosphate carboxylase/oxygenase large subunit (rbcL)
gene, partial cds; chloroplast
Sequence ID: MN216789.1 Length: 561
Range 1: 1 to 503
Score:734 bits(397), Expect:0.0,
Identities:467/503(93%), Gaps:0/503(0%), Strand: Plus/Plus
    
```

```

Query 5 GAGACTAAAGCAAGTGTGGATTCAAAGCTGGTGTAAAGAGTACAAATTGACTTATTAT 64
          |||
Sbjct 1 GAGACTAAAGCAAGTGTGGATTCAAAGCTGGTGTAAAGATTATAAATTGACTTATTAT 60

Query 65 ACTCCTGAATATCAAACCAAGGATACTGATATATTGGCAGCATCCGAGTCACTCCTCAA 124
          |||
Sbjct 61 ACTCCTGACTATGAAACCAAGATACTGATATCTTGGCAGCATCCGAGTAACTCCTCAA 120

Query 125 CCWGGAGTTCCTCCTGAAGAAGCCGGTGTGCGGTAGCTGCCGAATCTTCTACTGGKACA 184
          |||
Sbjct 121 CCTGGAGTTCCTGCTGAAGAAGCAGGGGAGCGGTAGCTGCCGAATCTTCTACTGGTACA 180

Query 185 TGGACCACTGTGTGGACCGATGGACTTACCAGTCTTGATCGTTACAAAGGGCGATGCTAC 244
          |||
Sbjct 181 TGGACAACCTGTGTGGACCGATGGACTTACCAGTCTTGATCGTTATAAAGGACGATGCTAC 240

Query 245 CGCATTGAGCGTGTGTGGAGAAAAAGATCAATATATTGCTTATGTAGCTTACCCTTTA 304
          |||
Sbjct 241 CACATCGAGCCTGTGCTGGAGAAGAAAATCAATATATTGCTTATGTAGCTTATCCTTTA 300

Query 305 GACCTTTTTGAAGAAGGTTCCGTTACCAACATGTTTACTTCCATTGTAGGTAATGTATTT 364
          |||
Sbjct 301 GACCTTTTTGAAGAAGGTTCTGTTACTAACATGTTTACTTCCATTGTGGGTAATGTATTT 360

Query 365 GGGTTCAAAGCCCTGCGCGCTCTACGTCTGGAAGATTTGCGAATCCCTGTGCTTATATT 424
          |||
Sbjct 361 GGGTTCAAAGCCCTGCGCGCTCTACGTCTGGAAGATTTGCGAATCCCAGTTGCTTATGTT 420

Query 425 AAAACTTTCCAAGGTCCTCCTCATGGGATCCAAGTTGAAAGAGATAAATTGAACAAGTAC 484
          |||
Sbjct 421 AAAACTTTCCAAGGACCTCCTCACGGAATCCAAGTTGAGAGAGATAAATTGAACAAGTAT 480

Query 485 GGTCGTCCCCTGTTGGGATGTAC 507
          ||
Sbjct 481 GGACGTCCCCTATTGGGATGTAC 503
    
```

-----



RID: CZ5X235T013  
 Job Title: **A03 rbcLa**  
 Program: BLASTN  
 Database: nt Nucleotide collection (nt)  
 Query #1: Query ID: lcl|Query\_9863 Length: 574

Sequences producing significant alignments:

>Onobrychis ptolemaica voucher EDNA15-0042803 ribulose-1,5-bisphosphate carboxylase/oxygenase large subunit (rbcL) gene, partial cds; chloroplast  
 Sequence ID: KX282909.1 Length: 580  
 Range 1: 3 to 576  
 Score:1011 bits(547), Expect:0.0,  
 Identities:565/574(98%), Gaps:0/574(0%), Strand: Plus/Plus

```

Query 1 AACAGAGACTAAAGCAAGTGTGGGTTCAAAGCTGGTGTAAAGATTATAGATTGACTTA 60
      |
Sbjct 3 AACAGAGACTAAAGCAAGTGTGGGTTCAAAGCTGGTGTAAAGATTATAGATTGACTTA 62

Query 61 TTATACTCCTGAATATGAAACCAAGGATACTGATATCTTGGCAGCATTCCGAGTCACTCC 120
      |
Sbjct 63 TTATACTCCTGAATATGAAACCAAGGATACTGATATCTTGGCAGCATTCCGAGTCACTCC 122

Query 121 TCAACCAGGAGTTCCTCCTGAAGAAGCCGGTGTGCGGTAGCTGCCGAATCTTCCACTGG 180
      |
Sbjct 123 TCAACCAGGAGTTCCTCCTGAAGAAGCTGGTGTGCGGTAGCTGCTGAATCTTCCACTGG 182

Query 181 GACATGGACCACTGTGTGGACCGATGGGCTTACCAGTCTTGATCGTTATAAAGGACGATG 240
      |
Sbjct 183 GACATGGACCACTGTGTGGACCGATGGACTTACCAGTCTTGATCGTTATAAAGGACGATG 242

Query 241 CTACCACATTGAACCCGTTGCTGGAGAAGAAAGTCAATTTATTGCTTATGTAGCTTATCC 300
      |
Sbjct 243 CTACCACATTGAGCCCGTTGCTGGAGAAGAAACTCAATTTATTGCTTATGTAGCTTATCC 302

Query 301 CTTAGACCTTTTTGAAGAAGGTTCTGTTACTAACATGTTTACCTCCATTGTTGGTAATGT 360
      |
Sbjct 303 CTTAGACCTTTTTGAAGAAGGTTCTGTTACTAACATGTTTACCTCCATTGTTGGTAATGT 362

Query 361 ATTTGGGTTCAAGGCCTTACGCGCTCTACGTCTGGAGGATTTGCGAATCCCCGTTGCTTA 420
      |
Sbjct 363 ATTTGGGTTCAAGGCCTTACGCGCTCTACGTCTGGAGGATTTGCGAATCCCCACTGCTTA 422

Query 421 TGTTAAAACCTTTCCAAGGTCCTCCTCACGGAATCCAAGTTGAGAGAGATAAATTGAACAA 480
      |
Sbjct 423 TACTAAAACCTTTCCAAGGTCCTCCTCACGGAATCCAAGTTGAGAGAGATAAATTGAACAA 482

Query 481 GTATGGTCGTCTCTATTGGGATGTACTATTAACCGAAATGGGATTATCCGCTAAGAA 540
      |
Sbjct 483 GTATGGTCGTCTCTATTGGGATGTACTATTAACCGAAATGGGATTATCCGCTAAGAA 542

Query 541 TTACGGTCGAGCAGTTTATGAATGTCTTCGCGGT 574
      |
Sbjct 543 TTACGGTCGAGCAGTTTATGAATGTCTTCGCGGT 576
    
```

>Onobrychis viciifolia ribulose-1,5-bisphosphate carboxylase/oxygenase large subunit (rbcL) gene, partial cds; chloroplast  
 Sequence ID: KX942280.1 Length: 1419  
 Range 1: 3 to 576  
 Score:1000 bits(541), Expect:0.0,  
 Identities:563/574(98%), Gaps:0/574(0%), Strand: Plus/Plus

```

Query 1 AACAGAGACTAAAGCAAGTGTGGGTTCAAAGCTGGTGTAAAGATTATAGATTGACTTA 60
      |
Sbjct 3 AACAGAACTAAAGCAAGTGTGGGTTCAAAGCTGGTGTAAAGATTATAGATTGACTTA 62

Query 61 TTATACTCCTGAATATGAAACCAAGGATACTGATATCTTGGCAGCATTCCGAGTCACTCC 120
      |
Sbjct 63 TTATACTCCTGAATATGAAACCAAGGATACTGATATCTTGGCAGCATTCCGAGTCACTCC 122

Query 121 TCAACCAGGAGTTCCTCCTGAAGAAGCCGGTGTGCGGTAGCTGCCGAATCTTCCACTGG 180
      |
Sbjct 123 TCAACCAGGAGTTCCTCCTGAAGAAGCCGGTGTGCGGTAGCTGCCGAATCTTCCACTGG 182
    
```

```

Query 181  GACATGGACCACTGTGTGGACCGATGGGCTTACCAGTCTTGATCGTTATAAAGGACGATG 240
          |||
Sbjct 183  GACATGGACCACTGTGTGGACCGATGGGCTTACCAGTCTTGATCGTTATAAAGGACGATG 242

Query 241  CTACCACATTGAACCCGTTGCTGGAGAAGAAAGTCAATTTATTGCTTATGTAGCTTATCC 300
          |||
Sbjct 243  CTACCACATTGAGCCCGTTGCTGGAGAAGAAAGTCAATTCATTGCTTATGTAGCTTATCC 302

Query 301  CTTAGACCTTTTTGAAGAAGGTTCTGTTACTAACATGTTTACCTCCATTGTTGGTAATGT 360
          |||
Sbjct 303  CTTAGATCTTTTTGAAGAAGGTTCTGTTACTAACATGTTTACCTCCATTGTTGGTAATGT 362

Query 361  ATTTGGGTTCAAGGCCTTACGCGCTCTACGCTCTGGAGGATTTGCGAATCCCCGTTGCTTA 420
          |||
Sbjct 363  ATTTGGGTTCAAGGCCTTACGCGCTCTACGCTCTGGAGGATTTGAGAATCCCCCTGCTTA 422

Query 421  TGTTAAACTTTCCAAGGTCCTCCTCACGGAATCCAAGTTGAGAGAGATAAAATGAACAA 480
          |
Sbjct 423  TACTAAACTTTCCAAGGTCCTCCTCACGGAATCCAAGTTGAGAGAGATAAAATGAACAA 482

Query 481  GTATGGTCGTCCTCTATTGGGATGTACTATTAACCGAAATGGGATTATCCGCTAAGAA 540
          |||
Sbjct 483  GTATGGTCGTCCTCTATTGGGATGTACTATTAACCGAAATGGGACTATCCGCTAAGAA 542

Query 541  TTACGGTCGAGCAGTTTATGAATGTCTTCGCGGT 574
          |||
Sbjct 543  TTACGGTCGAGCAGTTTATGAATGTCTTCGTTGGT 576
    
```

-----

```

RID: DKBP1CPA01R
Job Title:A04_Sp._B_rbcL_(Fabaceae_IRLC)
Program: BLASTN
Database: nt Nucleotide collection (nt)
Query #1: A04_Sp._B_(Fabaceae_IRLC_Clade_Wojciechowski_et_al_2004) Query ID:
lcl|Query_109467 Length: 565
    
```

Your search is limited to records that include: Fabaceae (taxid:3803)

Sequences producing significant alignments:

```

>Onobrychis ptolemaica voucher EDNA15-0042982 ribulose-1,5-bisphosphate carboxylase/
oxygenase large subunit (rbcL) gene, partial cds; chloroplast
Sequence ID: KX282911.1 Length: 566
Range 1: 1 to 564
Score:850 bits(460), Expect:0.0,
Identities:529/565(94%), Gaps:1/565(0%), Strand: Plus/Plus
    
```

```

Query 1  AGAGACTAAAGCAAGTGTGGGTTCAAAGCTGGTGTAAAGATTACAAATGACTTATTA 60
          |||
Sbjct 1  AGAGACTAAAGCAAGTGTGGGTTCAAAGCTGGTGTAAAGATTATAGATTGACTTATTA 60

Query 61  TACTCCTGAATACGAAATCAAGGATACTGATATCTTGGCAGCATTCCGAGTCACTCCTCA 120
          |||
Sbjct 61  TACTCCTGAATATGAAACCAAGGATACTGATATCTTGGCAGCATTCCGAGTCACTCCTCA 120

Query 121  ACCAGGAGTTCTCCCGAAGAAGCCGGGCTGCGGTAGCTGCCGAATCTTCCACTGGKAC 180
          |||
Sbjct 121  ACCAGGAGTTCTCTCTGAAGAAGCTGGTGTGCTGCGGTAGCTGCTGAATCTTCCACTGGGAC 180

Query 181  ATGGACCACTGTGTGGACCGATGGACTTACCAGTCTTGATCGTTATAAAGGGCGATGCTA 240
          |||
Sbjct 181  ATGGACCACTGTGTGGACCGATGGACTTACCAGTCTTGATCGTTATAAAGGACGATGCTA 240

Query 241  CCACATTGAGCCCGTTGCTGGAGAAGAAACTCAATTTATTGCTTATGTAGCTTATCCYTT 300
          |||
Sbjct 241  CCACATTGAGCCCGTTGCTGGAGAAGAAACTCAATTTATTGCTTATGTAGCTTATCCCTT 300

Query 301  AGACCTTTTTGAAGAAGGTTCTGTTACTAACATGTTTACTTCCATTGTGGTAATGTATT 360
          |||
Sbjct 301  AGACCTTTTTGAAGAAGGTTCTGTTACTAACATGTTTACTTCCATTGTGGTAATGTATT 360
    
```

```

Query 361  TGGTTTCAARGCCTTACGMGCTCTACGTCTGGAGGATTGCGAATCCCACCTTCTTATTC 420
          ||| ||||| ||||| ||||| ||||| ||||| ||||| ||||| ||||| ||||| |||||
Sbjct 361  TGGGTTC AAGGCCTTACGCGCTCTACGTCTGGAGGATTGCGAATCCCACCTGCTTATAC 420

Query 421  CAAAACCTTCCAAGGTCCTCCTCACGGCATTCAAGTTGAAAGAGATAAATTGAACAAGTA 480
          ||||| ||||| ||||| ||||| ||||| ||||| ||||| ||||| ||||| ||||| |||||
Sbjct 421  TAAAACCTTCCAAGGTCCTCCTCACGGCATTCAAGTTGAGAGAGATAAATTGAACAAGTA 480

Query 481  TGGTCGTCCCCTATTGGGATGCACTATTAACCCAAAATTGGGATTATCTGCaaaaaaTT 540
          ||||| ||||| ||||| ||||| ||||| ||||| ||||| ||||| ||||| ||||| |||||
Sbjct 481  TGGTCGTCTCTATTGGGATGTACTATTAACCCGAAATTGGGATTATCCGCTAAG-AATT 539

Query 541  ACGGTAGAGCGGTTTATGAATGTCT 565
          ||||| ||||| ||||| ||||| |||||
Sbjct 540  ACGGTCGAGCAGTTTATGAATGTCT 564
    
```

-----

```

RID: CZ6MWR97016
Job Title:A05 rbcLa
Program: BLASTN
Database: nt Nucleotide collection (nt)
Query #1: Query ID: lcl|Query_56557 Length: 574
    
```

```

Alignments:
>Salvia rosmarinus chloroplast, complete genome
Sequence ID: KR232566.1 Length: 152462
Range 1: 55384 to 55957
Score:1061 bits(574), Expect:0.0,
Identities:574/574(100%), Gaps:0/574(0%), Strand: Plus/Plus
    
```

```

Query 1      AACAGAGACTAAAGCAAGTGTGGATTCAAAGCGGGTGTAAAGAGTACAAATTGACTTA 60
          ||||| ||||| ||||| ||||| ||||| ||||| ||||| ||||| ||||| |||||
Sbjct 55384   AACAGAGACTAAAGCAAGTGTGGATTCAAAGCGGGTGTAAAGAGTACAAATTGACTTA 55443

Query 61     TTATACTCCTGAATACGAAACCAAAGATACTGATATCTTGGCAGCATTCCGAGTAACTCC 120
          ||||| ||||| ||||| ||||| ||||| ||||| ||||| ||||| ||||| |||||
Sbjct 55444   TTATACTCCTGAATACGAAACCAAAGATACTGATATCTTGGCAGCATTCCGAGTAACTCC 55503

Query 121    TCAACCCGGAGTCCACCTGAAGAAGCAGGGGCCGCGGTAGCTGCCGAATCTTCTACTGG 180
          ||||| ||||| ||||| ||||| ||||| ||||| ||||| ||||| ||||| |||||
Sbjct 55504   TCAACCCGGAGTCCACCTGAAGAAGCAGGGGCCGCGGTAGCTGCCGAATCTTCTACTGG 55563

Query 181    TACATGGACAACCTGTGTGGACCGATGGACTTACCAGCCTTGATCGTTACAAAGGGCGATG 240
          ||||| ||||| ||||| ||||| ||||| ||||| ||||| ||||| ||||| |||||
Sbjct 55564   TACATGGACAACCTGTGTGGACCGATGGACTTACCAGCCTTGATCGTTACAAAGGGCGATG 55623

Query 241    CTACCACATTGAGCCCGTTCCCTGGAGAAAAAGATCAATATATCTGTTATGTAGCTTACCC 300
          ||||| ||||| ||||| ||||| ||||| ||||| ||||| ||||| ||||| |||||
Sbjct 55624   CTACCACATTGAGCCCGTTCCCTGGAGAAAAAGATCAATATATCTGTTATGTAGCTTACCC 55683

Query 301    TTTAGACCTTTTTGAAGAAGGTTCTGTTACTAACATGTTTACTTCCATTGTAGGAAATGT 360
          ||||| ||||| ||||| ||||| ||||| ||||| ||||| ||||| ||||| |||||
Sbjct 55684   TTTAGACCTTTTTGAAGAAGGTTCTGTTACTAACATGTTTACTTCCATTGTAGGAAATGT 55743

Query 361    ATTTGGATTCAAAGCCCTACGTGCTCTACGTCTGGAAGATCTGCGAATCCTGTTGCTTA 420
          ||||| ||||| ||||| ||||| ||||| ||||| ||||| ||||| ||||| |||||
Sbjct 55744   ATTTGGATTCAAAGCCCTACGTGCTCTACGTCTGGAAGATCTGCGAATCCTGTTGCTTA 55803

Query 421    TGTTAAAACCTTCCAAGGCCCGCCTCATGGGATCCAAGTTGAGAGAGATAAATTGAACAA 480
          ||||| ||||| ||||| ||||| ||||| ||||| ||||| ||||| ||||| |||||
Sbjct 55804   TGTTAAAACCTTCCAAGGCCCGCCTCATGGGATCCAAGTTGAGAGAGATAAATTGAACAA 55863

Query 481    GTACGGTCGTCTCTGCTGGGATGTACTATTAACCTAAATGGGGTTATCTGCTAAAAA 540
          ||||| ||||| ||||| ||||| ||||| ||||| ||||| ||||| ||||| |||||
Sbjct 55864   GTACGGTCGTCTCTGCTGGGATGTACTATTAACCTAAATGGGGTTATCTGCTAAAAA 55923

Query 541    CTATGGTAGAGCGGTTTATGAATGTCTTCGCGGT 574
          ||||| ||||| ||||| ||||| |||||
Sbjct 55924   CTATGGTAGAGCGGTTTATGAATGTCTTCGCGGT 55957
    
```



-----

RID: DKB8M50301R  
 Job Title: **A06\_rbcLa** rptd  
 Program: BLASTN  
 Database: nt Nucleotide collection (nt)  
 Query #1: Query ID: lcl|Query\_139325 Length: 573  
 Your search is limited to records that include: Fabaceae (taxid:3803)

>Ononis reclinata voucher EDNA15-0042385 ribulose-1,5-bisphosphate carboxylase/oxygenase large subunit (rbcL) gene, partial cds; chloroplast  
 Sequence ID: KX282912.1 Length: 577  
 Range 1: 3 to 575  
 Score:848 bits(459), Expect:0.0,  
 Identities:534/573(93%), Gaps:0/573(0%), Strand: Plus/Plus

```

Query 1 AACAGAGACTAAAGCAAAGGTTGGGTTTAAAGCTGGTGTAAAGATTACAAATTGACTTA 60
      |||
Sbjct 3 AACAGAGACTAAAGCGAAGGTTGGGTTCAAAGCTGGTGTAAAGATTATAAATTGACTTA 62

Query 61 TTATACTCCTGACTATCAAATCAAAGATACTGATATCTTGGCAGCATTCCGAGTAACTCC 120
      |||
Sbjct 63 TTATACTCCTGACTATGAAACCAAAGATACTGATATCTTGGCAGCATTCCGAGTAACTCC 122

Query 121 TCAACCTGGAGTTCCGCCGAAGAAGCAGGGGCTGCGGTAGCTGCCGAATCTTCTACTGG 180
      |||
Sbjct 123 TCAACCTGGAGTTCCGCCCTGAAGAAGCAGGTGCAGCGGTAGCTGCCGAATCTTCCACTGG 182

Query 181 GACATGGACAACCTGTGTGGACCGATGGACTTACCAGTCTTGATCGTTACAAGGRCGATG 240
      |||
Sbjct 183 GACATGGACAACCTGTGTGGACCGATGGACTTACCAGTCTTGATCGTTATAAAGGACGCTG 242

Query 241 CTACCACATCGAGGCCGTTGTTGGAGAAGAAAATCAATWTATTGCTTATGTAGCTTATCC 300
      |||
Sbjct 243 CTACCACATCGAGCCCTGTGCTGGAGAAGATAATCAATTTATTGCTTATGTAGCTTATCC 302

Query 301 TTTAGACCTTTTTGAAGAAGGTTCTGTTACTAACATGTTTACCTCCATTGTGGGTAATGT 360
      |||
Sbjct 303 CTTAGACCTTTTTGAAGAAGGTTCTGTTACTAACATGTTTACCTCCATTGTAGGTAATGT 362

Query 361 ATTTGGTTTCAAAGCCTTGCGCGCTCTACGTCTGGAAGATTTGCGAATCCCAATCTTTA 420
      |||
Sbjct 363 ATTTGGGTTCAAAGCCTTGCGTGCTCTACGTCTGGAAGATTTGCGAATCCCTAATGCTTA 422

Query 421 TTTCAAACTTTCCAAGGYCCTCCTCACGGCATTCAAGTTGAAAGAGATAAATTGAACAA 480
      |||
Sbjct 423 TGTTAAAACCTTTCCAAGTCTCCTCACGGAATCCAAGTTGAGAGAGATAAATTGAACAA 482

Query 481 GTATGGACGTCCCTTATGGGATGCACTATTAACCAAATTTGGGATTATCCGCTAAAAA 540
      |||
Sbjct 483 GTATGGACGTCCCTTATGGGATGTACTATTAACCAAATTTGGGTTTATCCGCTAAGAA 542

Query 541 TAATGGTAGAGCGGTTTATGAATGTCTCCGCGG 573
      |||
Sbjct 543 TTATGGTCGAGCAGTTTATGAATGTCTACGCGG 575
    
```

-----

RID: CZ7X1RY9013  
 Job Title: **A07 rbcLa**  
 Program: BLASTN  
 Database: nt Nucleotide collection (nt)  
 Query #1: Query ID: lcl|Query\_63453 Length: 574

>Ononis reclinata voucher EDNA15-0042385 ribulose-1,5-bisphosphate carboxylase/oxygenase large subunit (rbcL) gene, partial cds; chloroplast  
 Sequence ID: KX282912.1 Length: 577  
 Range 1: 3 to 576  
 Score:1011 bits(547), Expect:0.0,  
 Identities:565/574(98%), Gaps:0/574(0%), Strand: Plus/Plus

```

Query 1 AACAGAGACTAAAGCAAAGGTTGGGTTCAAAGCTGGTGTAAAGATTATAAAATTGACTTA 60
      |||
Sbjct 3 AACAGAGACTAAAGCGAAGGTTGGGTTCAAAGCTGGTGTAAAGATTATAAAATTGACTTA 62

Query 61 TTATACTCCTGACTATCAAACCAAAGATACTGATATCTTGGCAGCATTCCGAGTAAGTCC 120
      |||
Sbjct 63 TTATACTCCTGACTATGAAACCAAAGATACTGATATCTTGGCAGCATTCCGAGTAAGTCC 122

Query 121 TCAACCTGGAGTTCGGCCTGAAGAAGCAGGTGCAGCGGTAGCTGCCGAATCTTCTACTGG 180
      |||
Sbjct 123 TCAACCTGGAGTTCGGCCTGAAGAAGCAGGTGCAGCGGTAGCTGCCGAATCTTCCACTGG 182

Query 181 GACATGGACAACCTGTGTGGACCGATGGACTTACCAGTCTTGATCGTTATAAAGGACGCTG 240
      |||
Sbjct 183 GACATGGACAACCTGTGTGGACCGATGGACTTACCAGTCTTGATCGTTATAAAGGACGCTG 242

Query 241 CTACCACATCGAGCCTGTTGCTGGAGAAGATAGTCAATTTATTGCTTATGTAGCTTATCC 300
      |||
Sbjct 243 CTACCACATCGAGCCTGTTGCTGGAGAAGATAATCAATTTATTGCTTATGTAGCTTATCC 302

Query 301 CTTAGACCTTTTTGAAGAAGGTTCTGTTACGAACATGTTTACCTCCATCGTAGGTAATGT 360
      |||
Sbjct 303 CTTAGACCTTTTTGAAGAAGGTTCTGTTACTAACATGTTTACCTCCATGTAGGTAATGT 362

Query 361 ATTTGGGTTCAAGGCCTTGGCGCTCTACGTCTGGAAGATTTGCGAATCCCTAATGCTTA 420
      |||
Sbjct 363 ATTTGGGTTCAAGGCCTTGGCGTCTCTACGTCTGGAAGATTTGCGAATCCCTAATGCTTA 422

Query 421 TGTAAAACCTTTCCAAGGTCCTCCTCACGGAATCCAAGTTGAGAGAGATAAAATTGAACAA 480
      |||
Sbjct 423 TGTAAAACCTTTCCAAGGTCCTCCTCACGGAATCCAAGTTGAGAGAGATAAAATTGAACAA 482

Query 481 GTATGGACGTCCCTATTGGGATGTACTATTAACCAAATTTGGGTTTATCCGCTAAGAA 540
      |||
Sbjct 483 GTATGGACGTCCCTATTGGGATGTACTATTAACCAAATTTGGGTTTATCCGCTAAGAA 542

Query 541 TTATGGTAGAGCAGTTTATGAATGTCTCCGCGGT 574
      |||
Sbjct 543 TTATGGTCGAGCAGTTTATGAATGTCTACGCGGT 576
    
```

-----

RID: CZ3C3RY7013  
 Job Title: **A08 rbcLa**  
 Program: BLASTN  
 Database: nt Nucleotide collection (nt)  
 Query #1: Query ID: lcl|Query\_52587 Length: 574

>Erica tetralix ribulose-1,5-biphosphate carboxylase/oxygenase large subunit gene, partial  
 cds; chloroplast  
 Sequence ID: KP737718.1 Length: 1493  
 Range 1: 3 to 576  
 Score:1044 bits(565), Expect:0.0,  
 Identities:571/574(99%), Gaps:0/574(0%), Strand: Plus/Plus

```

Query 1 AACAGAGACTAAAGCAAGTGTGGATTCAAAGCTGGTGTAAAGATTACAAATTGACTTA 60
      ||||| ||||| ||||| ||||| ||||| ||||| ||||| ||||| ||||| |||||
Sbjct 3 AACAGAACTAAAGCAAGTGTGGATTCAAAGCTGGTGTAAAGATTACAAATTGACTTA 62

Query 61 TTATACTCCTAACTATGAAACCAAAGATACTGATATCTTGGCAGCATTCCGAGTAACCCC 120
      ||||| ||||| ||||| ||||| ||||| ||||| ||||| ||||| ||||| |||||
Sbjct 63 TTATACTCCTAACTATGAAACCAAAGATACTGATATCTTGGCAGCATTCCGAGTAACCCC 122

Query 121 TCAACCGGGAGTTCCACCTGAAGAAGCAGGGGCGCGGTAGCTGCGGAATCTTCTACTGG 180
      ||||| ||||| ||||| ||||| ||||| ||||| ||||| ||||| ||||| |||||
Sbjct 123 TCAACCGGGAGTTCCACCTGAAGAAGCAGGGGCGCGGTAGCTGCGGAATCTTCTACTGG 182

Query 181 TACATGGACAACAGTGTGGACTGATGGACTTACTAGCCTTGATCGTTACAAAGGCGATG 240
      ||||| ||||| ||||| ||||| ||||| ||||| ||||| ||||| ||||| |||||
Sbjct 183 TACATGGACAACAGTGTGGACTGATGGACTTACTAGCCTTGATCGTTACAAAGGCGATG 242

Query 241 CTACCACATCGAGCCTGTGCTGGAGACGAAAATCAATATATTGCTTATGTAGCTTATCC 300
      ||||| ||||| ||||| ||||| ||||| ||||| ||||| ||||| ||||| |||||
Sbjct 243 CTACCACATCGAGCCTGTGCTGGAGACGAAAATCAATATATTGCTTATGTAGCTTATCC 302

Query 301 TTTAGACCTTTTTGAAGAGGGTCTGTTACTAATATGTTTACTTCCATTGTGGTAATGT 360
      ||||| ||||| ||||| ||||| ||||| ||||| ||||| ||||| ||||| |||||
Sbjct 303 TTTAGACCTTTTTGAAGAGGGCTCTGTTACTAATATGTTTACTTCCATTGTGGTAATGT 362

Query 361 ATTTGGATTCAAAGCCCTGCGCGCTCTACGTCTGGAAGATCTAAGAATCCCTACAGCGTA 420
      ||||| ||||| ||||| ||||| ||||| ||||| ||||| ||||| ||||| |||||
Sbjct 363 ATTTGGATTCAAAGCCCTGCGCGCTCTACGTCTGGAAGATCTACGAATCCCTACAGCGTA 422

Query 421 TGTAAAAACGTTCCAAGGACCGCCTCATGGTATCCAAGTTGAAAGAGATAAATTGAACAA 480
      ||||| ||||| ||||| ||||| ||||| ||||| ||||| ||||| ||||| |||||
Sbjct 423 TGTAAAAACGTTCCAAGGACCGCCTCATGGTATCCAAGTTGAAAGAGATAAATTGAACAA 482

Query 481 ATACGGCCGTCGCCCTGTTGGGATGTACAATTAACCTAAATTGGGGTTATCTGCTAAAAA 540
      ||||| ||||| ||||| ||||| ||||| ||||| ||||| ||||| ||||| |||||
Sbjct 483 ATACGGCCGTCGCCCTGTTGGGATGTACAATTAACCTAAATTGGGGTTATCTGCTAAAAA 542

Query 541 CTATGGGAGAGCTGTTTATGAATGTCTACGCGGT 574
      ||||| ||||| ||||| ||||| ||||| ||||| ||||| ||||| |||||
Sbjct 543 CTATGGGAGAGCTGTTTATGAATGTCTACGCGGT 576
    
```



## Appendix A4-3 DNA Barcoding results

### Significant BLASTN alignment results for ITS sequences

(samples A01, A03, A07)

RID: CZ30AD3U013  
 Job Title: **A01 ITS**  
 Program: BLASTN  
 Database: nt Nucleotide collection (nt)  
 Query #1: Query ID: lcl|Query\_52201 Length: 703

>Onobrychis viciifolia isolate c1208 18S ribosomal RNA gene, partial sequence; internal transcribed spacer 1, 5.8S ribosomal RNA gene, and internal transcribed spacer 2, complete sequence; and 28S ribosomal RNA gene, partial sequence  
 GeSequence ID: HM542570.1 Length: 645  
 Range 1: 1 to 645  
 Score:1155 bits(625), Expect:0.0,  
 Identities:638/645(99%), Gaps:0/645(0%), Strand: Plus/Minus

Query	41	CTGGGGTCTCGTCATGAGCATCCAAGGACGCTAGTGGGTCATAGAGGCCAAATCTGGTAA	100
Sbjct	645	CTGGGGTCTCGTCATGAGCATCCAAGGACGCTAGTGGGTCACAGAGGCCAAATCTGGTAA	586
Query	101	GAGCTGGCGCATGATCGGTCTCGTGGGTCACACAACCACCATCTATCATGGCACACACCC	160
Sbjct	585	GAGCTGGCACATGATCGGTCTCGTGGGTCACACAGCCACCATCTATCATGGCACACACCC	526
Query	161	TACCAAGGACTCAGTTTTTCAGCCAACCATGAGACAACWATTCTCACGGGAAGCCACCATT	220
Sbjct	525	TACCAAGGACTCAGTTTTTCAGCCAACCATGAGACAACAATGCTCACGGGAAGCCACCATT	466
Query	221	CGCCCTACACAGCCTATCAATAGGCATTGGGCAACGATATGTGACGCCAGGCAGACGTG	280
Sbjct	465	CGCCCTACACAGCCTATCAATAGGCATTGGGCAACGATATGTGACGCCAGGCAGACGTG	406
Query	281	CCCTCAACCTAATGGCTTCGGGCGCAACTTGC GTTCAAAAAC TCGATGGTTCACGGGATT	340
Sbjct	405	CCCTCAACCTAATGGCTTCGGGCGCAACTTGC GTTCAAAAAC TCGATGGTTCACGGGATT	346
Query	341	CTGCAATTCACACCAAGTATCGCATTTTCGCTACGTTCTTCATCGATGCAAGAGCCTAGAT	400
Sbjct	345	CTGCAATTCACACCAAGTATCGCATTTTCGCTACGTTCTTCATCGATGCAAGAGCCTAGAT	286
Query	401	ATCCGTTGCCGAGAGTCGTTTATATATACCATGCATCAAAACACTCCC GCAAGGGCACCG	460
Sbjct	285	ATCCGTTGCCGAGAGTCGTTTATATATACCATGCATCAAAACACTCCC GCAAGGGCACCG	226
Query	461	TCTCCGGTCCCAAGAGGGGCGCACTGAACCAATTTAGTTCCTTGGCACA CT CAGTGCCG	520
Sbjct	225	TCTCCGGTCCCAAGAGGGGCGCACTGAACCAATTTAGTTCCTTGGCACA CT CAGTGCCG	166
Query	521	GGGTTTGGGTTTGGTTGGGAGGGGAGCGCACAACTGGCTGCCCTGCCA ACCCAAGGGT	580
Sbjct	165	GGGTTTGGGTTTGGTTGGGAGGGGAGCGCACAACTGGCTGCCCTGCCA ACCCAAGGGT	106
Query	581	GGACGAGGAGTTGAACACCAAGGCCATCCCAACGTATTC AAACAGATT CACGAGTTGAT	640
Sbjct	105	GGACGAGGAGTTGAACCCCAAGGCCATCCCAACGTATTC AAACAGATT CACGAGTTGAT	46
Query	641	CTACATGTAAGGCATCGACAATGATCCTTCCGCAGGTTACCTAC	685
Sbjct	45	CTACATGTAAGGCATCGACAATGATCCTTCCGCAGGTTACCTAC	1

RID: CZ67WSPG013  
 Job Title: **A03\_ITS**  
 Program: BLASTN  
 Database: nt Nucleotide collection (nt)  
 Query #1: Query ID: lcl|Query\_36029 Length: 712

>Onobrychis viciifolia isolate c1208 18S ribosomal RNA gene, partial sequence;  
 internal transcribed spacer 1, 5.8S ribosomal RNA gene, and internal transcribed  
 spacer 2, complete sequence; and 28S ribosomal RNA gene, partial sequence  
 Sequence ID: HM542570.1 Length: 645  
 Range 1: 1 to 645

Score:1158 bits(627), Expect:0.0,  
 Identities:639/645(99%), Gaps:0/645(0%), Strand: Plus/Minus

```

Query 44 CTGGGGTCTCGTCATGAGCATCCAAGGACGCTAGTGGGTCATAGAGGCCAAATCTGGTAA 103
          |||
Sbjct 645 CTGGGGTCTCGTCATGAGCATCCAAGGACGCTAGTGGGTCACAGAGGCCAAATCTGGTAA 586

Query 104 GAGCTGGCGCATGATCGGTCTCGTGGGTACACAACCACCATCTATCATGGCACACACC 163
          |||
Sbjct 585 GAGCTGGCACATGATCGGTCTCGTGGGTACACAGCCACCATCTATCATGGCACACACC 526

Query 164 TACCAAGGACTCAGTTTTTCAGCCAACCATGAGACAACAATTTCTACGGGAAGCCACCATT 223
          |||
Sbjct 525 TACCAAGGACTCAGTTTTTCAGCCAACCATGAGACAACAATGCTCAGGGGAAGCCACCATT 466

Query 224 CGCCCTACACAGCCTATCAATAGGCATTGGGCAACGATATGTGACGCCCAGGCAGACGTG 283
          |||
Sbjct 465 CGCCCTACACAGCCTATCAATAGGCATTGGGCAACGATATGTGACGCCCAGGCAGACGTG 406

Query 284 CCCTCAACCTAATGGCTTCGGGGCGCAACTTGCGTTCAAAAACCTCGATGGTTCACGGGATT 343
          |||
Sbjct 405 CCCTCAACCTAATGGCTTCGGGGCGCAACTTGCGTTCAAAAACCTCGATGGTTCACGGGATT 346

Query 344 CTGCAATTACACCAAGTATCGCATTTCGCTACGTTCTTCATCGATGCAAGAGCCTAGAT 403
          |||
Sbjct 345 CTGCAATTACACCAAGTATCGCATTTCGCTACGTTCTTCATCGATGCAAGAGCCTAGAT 286

Query 404 ATCCGTTGCCGAGAGTCGTTTATATATATACCATGCATCAAAACACTCCCGCAAGGGCACCG 463
          |||
Sbjct 285 ATCCGTTGCCGAGAGTCGTTTATATATATACCATGCATCAAAACACTCCCGCAAGGGCACCG 226

Query 464 TCTCCGGTCCCAAGAGGGGCGCACTGAACCAATTTAGTTCTTGGCACACTCAGTGCCG 523
          |||
Sbjct 225 TCTCCGGTCCCAAGAGGGGCGCACTGAACCAATTTAGTTCTTGGCACATTCAGTGCCG 166

Query 524 GGGTTTGGGTTTGGTTGGGAGGGGAGCGCACAACTGGCTGCCCTGCCAACCAAGGGT 583
          |||
Sbjct 165 GGGTTTGGGTTTGGTTGGGAGGGGAGCGCACAACTGGCTGCCCTGCCAACCAAGGGT 106

Query 584 GGACGAGGAGTTGAACACCAAGGCCATCCCAACGTATTCAAACAGATTCACGAGTTGAT 643
          |||
Sbjct 105 GGACGAGGAGTTGAACCCCAAGGCCATCCCAACGTATTCAAACAGATTCACGAGTTGAT 46

Query 644 CTACATGTAAGGCATCGACAATGATCCTTCCGCAGGTTACCTAC 688
          |||
Sbjct 45 CTACATGTAAGGCATCGACAATGATCCTTCCGCAGGTTACCTAC 1
    
```

RID: KPDH4KHC013  
 Job Title: **A07 ITS**  
 Program: BLASTN  
 Database: nt Nucleotide collection (nt)  
 Query #1: Query ID: lcl|Query\_1925 Length: 728

>Ononis tridentata subsp. tridentata internal transcribed spacer 1, partial sequence; 5.8S ribosomal RNA gene and internal transcribed spacer 2, complete sequence; and 26S ribosomal RNA gene, partial sequence  
 Sequence ID: GQ488530.1 Length: 588  
 Range 1: 1 to 588  
 Score:1033 bits(559), Expect:0.0,  
 Identities:580/590 (98%), Gaps:2/590 (0%), Strand: Plus/Minus

```

Query 52   TCATCACGAGCGTTAAGAAACGCAAAATGGGTAAGAGAGGCCACATTCAGCAGAGTAGTG 111
          |||
Sbjct 588   TCATCACGAGCGTCAAGAAACGCAAAATGGGTAAGAGAGGCCACATTCAGCAGAGTAGTG 529

Query 112  TATGATTTTCAAGTCTCGTGGGTCACACAACCACCATCTATCATGGCACACCCTACCAAG 171
          |||
Sbjct 528   TATGATTTT-AAGTCTCGTGGGTCACACAACCACCATCTATCATGGCACACCCTACCAAG 470

Query 172  GTCTCAATTTTCAACCAACCGTGAGCCAAAAGAGTTTACGGGAGGCCAACATTCGCCATG 231
          |||
Sbjct 469   GTCTCGATTTTCAACCAACCGTGAGCCAAAAGAGTTTACGGGAGGCCAACATTCGCCATG 410

Query 232  CTCAATACCTATGAATAGGATATTGGCAAGAGGCTTCGATATGTGACACCCAGGCAGACG 291
          |
Sbjct 409   CACAATACCTATGAATAGGATATTGGCAAGAGGCTTCGATATGTGACACCCAGGCAGACG 350

Query 292  TGCCCTCAACCTAAATGGCATCGGGCGCAACTTGC GTTCAAAGACTCGATGGTTCACGGG 351
          |||
Sbjct 349   TGCCCTCAACCTAA-TGGCATCGGGCGCAACTTGC GTTCAAAGACTCGATGGTTCACGGG 291

Query 352  ATTCTGCAATTCACACCAAGTATCGCATTTTCGCTACGTTCTTCATCGATGCAAGAGCCTA 411
          |||
Sbjct 290   ATTCTGCAATTCACACCAAGTATCGCATTTTCGCTACGTTCTTCATCGATGCAAGAGCCTA 231

Query 412  GATATCCGTTGCCGAGAGTCATTCTAATATCATGTGTCCAAACACAACCCACACGAAAAC 471
          |||
Sbjct 230   GATATCCGTTGCCGAGAGTCATTCTAATATCATGTGTCCAAACACAACCCACACGAAAAC 171

Query 472  CGTCTCCAGTGCCATGTGGGTGCGCTAAGAGCAAATTTAAATTCCTTGACGCATTCAGC 531
          |||
Sbjct 170   CGTCTCCAGTGCCATGCGGGTGCCTAAGAGCAAATTTAAATTCCTTGACGCATTCAGC 111

Query 532  GCCGGGGTTTGTAGTTTTTGGCACGAAGGAGAACGCACTAAGTCGCCCACCTTCAAACCAG 591
          |||
Sbjct 110   GCCGGGGTTTGTAGTTTTTGGCACGAAGGAGAACGCACTAAGTCGCCCACCTTCAAACCAG 51

Query 592  AGGTAAGCCTGAGGTGTGGAACAACCTCAAGCAAACCCAGTATGTTGAAA 641
          |||
Sbjct 50   AGGTAAGCCTGAGGTGTGGAACAACCTCAAGCAAACCCAGTATGTTGAAA 1
    
```



## Appendix A4-4 *rbcLa* sequences (in FASTA format) of selected species of Mediterranean Fabaceae

FASTA *rbcLa* sequences from NCBI GenBank® (<https://www.ncbi.nlm.nih.gov/>) of selected (representative) species of common Mediterranean legumes. GenBank does not contain data for *Hedysarum boveanum*, therefore sequences of *H. alpinum*, *H. boreale* and *H. coronarium* are used.

>MK925491.1\_*Onobrychis viciifolia*\_NMW7573

```
AAGTGTGGGTTCAAAGCTGGTGTAAAGATTATAGATTGACTTATTATACTCCTGAATATGAAACCAAGGATACTGATA
TCTTGGCAGCATTCCGAGTCACTCCTCAACCAGGAGTTCCCTCCTGAAGAAGCCGGTGCTGCGGTAGCTGCCGAATCTTC
ACTGGGACATGGACCACTGTGTGGACCGATGGGCTTACCAGTCTTGATCGTTATAAAGGACGATGCTACCACATTGAGCC
CGTTGCTGGAGAAGAAAGTCAATTCATTGCTTATGTAGCTTATCCCTTAGATCTTTTGAAGAAGGTTCTGTTACTAACA
TGTTTACCTCCATTGTTGGAATGTATTTGGGTTCAAGGCCTTACGCGCTTACGCTGGAGGATTTGAGAATCCCCCTT
GCTTATACTAAAACCTTCCAAGGCTCCTCCTCACGGAATCCAAGTTGAGAGAGATAAATTGAACAAGTATGGTCGTCCTT
ATTGGGATGTACTATTAACCGAAATTGGGACTATCCGCTAAGAATTACGGTCGAGCAGTTT
```

>KJ746267.1\_*Onobrychis viciifolia*\_2

```
AAGATTATAGATTGACTTATATACTCCTGAATATGAAACCAAGGATACTGATATCTTGGCAGCATTCCGAGTCACTCCT
CAACCAGGAGTTCCCTCCTGAAGAAGCCGGTGCTGCGGTAGCTGCCGAATCTTCCACTGGGACATGGACCACTGTGTGGAC
CGATGGGCTTACCAGTCTTGATCGTTATAAAGGACGATGCTACCACATTGAGCCCGTTGCTGGAGAAGAAAGTCAATTC
TTGCTTATGTAGCTTATCCCTTAGATCTTTTGAAGAAGGTTCTGTTACTAACATGTTTACCTCCATTGTTGGTAATGTA
TTTTGGGTTCAAGGCCTTACGCGCTTACGCTGGAGGATTTGAGAATCCCCCTGCTTATACTAAAACCTTCCAAGGTC
TCCTCACGGAATCCAAGTTGAGAGAGATAAATTGAACAAGTATGGTCGCTCTATTGGGATGTACTATTAACCGAAAT
TGGGACTATCCGCTAAGAATTACGCTCGAGCAGTTTATGAATGCTTTCGTTGGTGGACTTGATTTTACCAAAGATGATGAA
AATGTGAACCTCCAGCCATTTATGCGTTGGAGAGATCGTTTCTTATTTGTGCCGAAGCAATTTATAAAGCACAGGCCGA
AACAGGTGAAATCAAAGG
```

>MF158773.1\_*Onobrychis arenaria*

```
CAGAGACTAAAGCAAGTGTGGGTTCAAAGCTGGTGTAAAGATTATAGATTGACTTATTATACTCCTGAATATGAAAC
AAGGATACGTATCTTGGCAGCATTCCGAGTCACTCCTCAACCAGGAGTTCCCTCCTGAAGAAGCCGGTGCTGCGGTAGC
TGCCGAATCTTCCACTGGGACATGGACCACTGTGTGGACCGATGGGCTTACCAGTCTTGATCGTTATAAAGGACGATGCT
ACCACATTGAGCCCGTTGCTGGAGAAGAAAGTCAATTCATTGCTTATGTAGCTTATCCCTTAGATCTTTTGAAGAAGG
TCTGTTACTAACATGTTTACCTCCATTGTTGGTAATGTATTTGGGTTCAAGGCCTTACGCGCTTACGCTGGAGGATTT
GAGAATCCCCCTGCTTATACTAAAACCTTCCAAGGCTCCTCCTCACGGAATCCAAGTTGAGAGAGATAAATTGAACAAG
ATGGTCGTCCTCTATTGGGATGTACTATTAACCGAAATTGGGACTATCCGCTAAGAATTACGGTCGAGCAGTTTATGAA
TGCTTTCG
```

>KX942279.1\_*Onobrychis caput-galli*

```
TTACCAGTCTTGATCGTTATAAAGGACGATGCTACCACATGAGCCCGTTGCTGGAGAAGAAAGTCAATT
TATTGCTTATGTAGCTTATCCCTTAGATCTTTTGAAGAAGGTTCTGTTACTAACATGTTTACCTCCATT
GTTGGTAATGATTTGGGTTCAAAGGCTTACGCGCTTACGCTGGAGGATTTGAGAATCCCCCTGCTT
ATATTAACCTTCCAAGGCTCCTCCTCACGGAATCCAAGTTGAGAGAGATAAATTGAACAAGTATGGTCG
TCCCTATTTGGGATGTACTATTAACCGAAATTGGGACTATCCGCTAAGAATTACGGTCGAGCAGTTTAT
GAATGCTTTCGTTGGACTTGTATTTTACCAAAGATGATGAAATGTGAACCTCCAGCCATTTATGCGTT
GGAGAGATCGTTTCTTATTTGTGCGGAAGCAATTTATAAAGCACAGGCCGAAACAGGTGAAATCAAAGG
ACATTTATTTGAATGTACTCGGCTACATGTGAAGAAATGATAAAGAGCTGTATTTGCTAGAGAAATTG
GGTGTTCCTATCGTCATGCATGACTACTTAACAGGGGATTCCTGCAAACTAGTTTGGCTCATTATT
GCCGTGATAATGGCTTACTTCTTTCATATCCACCGTCAATGCATGCAATTCGATAGACAGAAAAACCA
TGGTATGCACTTTCGTTATAGCTAAAGCATTACGTTTGTCTGGTGGAGATCATATTCACGCTGGGACT
GTAGTAGGTAACCTTGAAGGAGAAAGGAAATTAATTTAGGTTTTGTTGATTTACTACGTGATGATTTG
TTGAAAAGATAGAAGCCGAGGATTTATTTCACTCAGGATTTGGGTTCTTTACCAGGTGTTTACCCTG
TGCTTCGGGGGATTTACGCTTGGCATATGCCGCTCTGACCGAGATTTGGAGATGATTCCTGACTT
CAATTCGGTGGAGGAACCTTAGGACACCTTGGGGGAATGCACCAGGTGCCGTAGCTAATCGAGTAGCTC
TTGAGCATGTGTACAAGCTCGAAATGAGGACGCTGATCTTGCTCGTGGGGTAATGACATTTATCCGTGA
AGCTTGCAAAATGGAGTCTGAATTAGCTGCTGCTTGTGAAGTATGGAAGGAAATCAAATTTGAATTC
CAAATGGATACCTTTGTAA
```

>MG249537.1 *Hedysarum alpinum*

AGTGTGGGTTCAAAGCTGGTGTAAAGATTATAGATTGACTTATTATACCTCTGAATATGAAACCAAGGATACTGATAT  
CTTGGCAGCATTCCGAGTAACTCCTCAACCAGGAGTTCCTCCTGAAGAAGCAGGTGCTGCGGTAGCTGCCGAATCTTCCA  
CTGGGACATGGACCACTGTGTGGACCGATGGGCTTACCAGTCTTGATCGTTATAAAGGACGATGTACCACATTGAGCCC  
GTTGCTGGAGAAGAAAATCAATTTATGCTTATGTAGCTTATCCCTTAGACCTTTTGAAGAAGGTTCTGTTACTAACAT  
GTTTACCTCCATTGTTGGTAATGTATTTGGGTTCAAGGCTTACGCGCTCCTACGTTGGAGGATTTGCGAATCCCCCTG  
CTTATACTAAACTTTCCAAGGCTCCTCACGGAATCCAAGTTGAGAGAGATAAATGAACAAGTATGGTCGTCTCTA  
TTGGGATGTACTATTAACCAAAATTTGGGATTATCCGCTAAGAATTACGGTCGAGCAGTTTATGAATGTCCTT

>MG246751.1 *Hedysarum boreale*

AGTGTGGCTCAAAGCTGGTGTAAAGATTATAGATTGACTTATTATACCTCTGAATATGAAACCAAGG  
ATACTGATATCTTGGCAGCATTCCGAGTACTCCTCAACCAGGAGTTCCTGCTGAAGAAGCAGGTGCTGC  
GGTAGCTGCCGAATCTCCACTGGGACATGGACTACTGTGTGGACCGATGGGCTTACCAGTCTTGATCGT  
TATAAAGGACGATGTACCACATGTATTTGGGTTCAAGGCTTACGCGCTCCTACGTTGGAGGATTTGCGAATCCCCCTGCTTATACTAAACTTTCCAA  
ATCCCTTAGACCTTTTGAAGAAGGTTCTGTTACTAACATGTTTACCTCCATTGTTGGTAATGTATTTGG  
GTTCAAGGCTTACGCGCTCCTACGTTGGAGGATTTGCGAATCCCCCTGCTTATACTAAACTTTCCAA  
GGTCTCCTCACGGAATCCAAGTTGAGAGAGATAAATGAACAAGTATGGTCGTCTCTATTTGGGATGTA  
CTATTAACCAAAATTTGGGATTATCCGCTAAGAATTATGGTCGAGCAGTTTATGAATGTCCTT

>KC700659.1 *Hedysarum coronarium*

GATTATAGATTGACTTATTATACCTCTGAATATGAAACCAAGGATACTGATATCTTGGCAGCATTCCGAGTAACTCCTCA  
ACCAGGAGTTCCTGCTGAGGAAGCAGGTGCTGCGGTAGCTGCCGAATCTTCCACCGGGACATGGACCACTGTGTGGACCG  
ATGGCTTACCAGTCTTGATCGTTATAAAGGACGATGCTACCACATTGAGCTGTTCCTGGAGAAGAAAAGTCAATTTATT  
GCTTATGTAGCTTATCCCTTAGACCTTTTGAAGAAGGTTCTGTTACTAACATGTTTACCTCCATTGTTGGTAATGTATT  
TGGGTTCAAAGCTTACGCGCTCCTACGTTGGAGGATTTACGAATCCCCCTGCTTATGTTAAAACCTTTCCAAGGCTCTC  
CTCACGGAATCCAAGTTGAGAGAGATAAATGAACAATAATGGTCGTCTCTATTTGGGATGTACTATTAACCAAAATTTG  
GGTTATCCGCTAAGAATTACGGTAGAGCAGTTTATGAATGTCTTTCGCGGTGC

>KX282912.1 *Ononis reclinata*

CCAACAGAGACTAAAGCGAAGGTTGGGTTCAAAGCTGGTGTAAAGATTATAAATTGACTTATTATACTCCTGACTATGA  
AACCAAGATACTGATATCTTGGCAGCATTCCGAGTAAAGTCTCAACCTGGAGTTCCGCCTGAAGAAGCAGGTGCAGCGG  
TAGCTGCCGAATCTTCCACTGGGACATGGACAACGTGTGGACCGATGGACTTACCAGTCTTGATCGTTATAAAGGACGC  
TGCTACCACATCGAGCCTGTGTGCTGGAGAAGATAAATCAATTTATTGCTTATGTAGCTTATCCCTTAGACCTTTTGAAGA  
AGGTTCTGTTACTAACATGTTTACCTCCATTGTAGGTAATGTATTTGGGTTCAAAGGCTTCCGCTCCTACGTTGGAGGAT  
ATTTGCCAATCCCTAATGCTTATGTATAAAGCTTTCCAAGGCTTCCGCTCCTACGTTGGAGGATTTGCGAATCCCCCTG  
AAGTATGGACGTCCTTATTTGGGATGTACTATTAACCAAAATTTGGGTTTATCCGCTAAGAATTATGGTCGAGCAGTTTA  
TGAATGTCTACGCGGTG

>JN890828.1 *Ononis spinosa*

GAAGTTGGGTTCAAAGCTGGTGTAAAGATTATAAATTGACTTATTATACTCCTGACTATGAAACCAAGATACTGATA  
TCTTGGCAGCATTCCGAGTAAAGTCTCAACCTGGAGTTCACCTGAAGAAGCAGGTGCAGCGGTAGCTGCCGAATCTTCC  
ACTGGGACATGGACAACCTGTGTGGACCGATGGACTTACCAGTCTTGATCGTTATAAAGGACGCTGCTACCACATCGAGCC  
TGTTGCTGGAGAAGATAAATCAATTTATTGCTTATGTAGCTTATCCCTTAGACCTTTTGAAGAAGGTTCTGTTACTAAC  
ATTTTACCTCCATTGTAGGTAATGTATTTGGGTTCAAAGGCTTCCGCTCCTACGTTGGAGGATTTGCGAATCCCCCTG  
GCTTATGTTAAAACCTTTCCAAGGCTCCTCACGGAATCCAAGTTGAGAGAGATAAATGAACAAGTATGGACGTCCTCCT  
ATTTGGGATGTACTATTAACCAAAATTTGGGTTTATCCGCTAAGAATTATGGTCGAGCAGTTT

>MF572164.1 *Astragalus onobrychis*

ACAGAGACTAAAGCGACTGTGGGGTTCAAAGCTGGTGTAAAGATTATAGATTGACGTATTATACCTCCTG  
AGTACGAAACCAAGATACTGATATCTTGGCAGCATTCCGAGTAACTCCTCAACCCTGGGGTTCTGCTGA  
AGAAGCTGGTGTGCGGTAGCTGCCGAATCTTCCACTGGGACATGGACAACGTGTTGGACCGATGGTCTT  
ACCAGTCTTGATCGTTATAAAGGACGATGCTACCACATCGAGCCGTTCCGAGAGAAGAAAGTCAATTTA  
TTGCTTATGTAGCTTATCCCTTAGACCTTTTGAAGAAGGTTCTGTTACTAACATGTTTACCTCCATTGT  
TGGTAATGTATTTGGATTCAAGGCTTTCGCGCTCCTACGTTGGAGGATTTGCGAATCCCCACTGCTTAT  
GTTAAAACCTTTCCAAGGCTCCGCTCACGGAATCCAAGTTGAGAGAGATAAATGAACAAGTATGGACGTC  
CCCTATTTGGGATGTACCATTAAACCTAAATTTGGGTTATCCGCTAAGAATTACGGTAGAGCAGTTTATGA  
ATGCTTTCGCGGT

>Z95550.1:12-581 *Astragalus sparsus*

AACAGAGACGAAAGCAAGTGCAGGGTTCAAAGCTGGTGTAAAGATTATAAATTGACGTATTATACTCCTGATTATGAAA  
CCAAAGATACTGATATCTTGGCAGCATTCCGAGTAACTCCTCAACCTGGAGTTCCACCAGAAGAAGCAGGTGCTGCGGTA  
GCTGCCGAATCTTCCACTGGGACATGGACAACGTGTGTGGACCGATGGGCTTACCAGTCTTGATCGTTATAAAGGACGATG  
CTACCACATCGAGCCGTTCTGGAGAAGAAAGTCAATTTATTGCTTATGTAGCTTATCCCTTAGACCTTTTGAAGAAG  
GTTCTGTTACTAACATGTTTACCTCCATTGTTGGTAATGTATTTGGATTCAAGGCTTTCGCGCTCCTACGTTGGAGGAT  
TTGCGAATCCCTACTGTTAAAGCTTTCCAAGGCTCCGCTCACGGAATCCAAGTTGAGAGAGATAAATGAACAAGTATGAACA  
GTATGGACGTCCTTATTTGGGATGTACCATTAAACCTAAATTTGGGCTTATCCGCTAAGAATTACGGTAGAGCAGTTTATGA  
AATGCTCTCCG

>KC700631.1 *Medicago truncatula*

GATTATAGATTGACTTATTATACTCCTGACTATGAAACCAAAGATACTGATATCTTGGCAGCATTCCGAG  
TAAGTCCCTCAACCTGGAGTTCGGCTGAAGAAGCAGGTGCAGCGGTAGCTGCCGAATCTCCACTGGGAC  
ATGGACAACCGTGTGGACCGATGGACTTACCAGTCTTGATCGTTATAAAGGACGCTGCTACCACATCGAA  
CCTGTTGCTGGAGAAGAGAGTCAATTTATTGCTTATGTAGCTTATCCCTTAGACCTTTTTGAAGAAGGTT  
CTGTTACTAACATGTTTACCTCCATGTAGGTAATGTATTTGGGTCAAGGCCTTGCCTGCTCAGTCT  
GGAAGATTTGCGAATCCCGTGTGCTTATGTAAAACCTTCCAAGGTCCCTCACGGAATCCAAGTTGAG  
AGAGATAAATTGAACAAATATGGACGTCCCTATTGGGATGTACTATTAACCTAAATTGGGTTTATCCG  
CTAAAAATTACGGTAGAGCAGTTTATGAATGTCTACGCGGTGG

>KJ204375.1 *Medicago sativa*

TTGGGTTCAAAGCTGGTGTAAAGATTATAGATTGACTTATTATACTCCTGACTATGAAACCAAAGATAC  
TGATATCTTGGCAGCATTCCGAGTAAGTCCGCAACCTGGAGTTCGGCTGAAGAAGCAGGTGCAGCGGTA  
GCTGCCGAATCTTCCACTGGGACATGGACAACCTGTGTGGACCGATGGACTTACCAGTCTTGATCGTTATA  
AAGGACGCTGCTACCACATCGAACCTGTTGCTGGAGAAGAGACTCAATTTATTGCTTATGTAGCTTATCC  
CTTAGACCTTTTTGAAGAAGGTTCTGTTACTAACATGTTTACCTCCATTGTAGGTAATGTATTTGGGTT  
AAGGCCTTGCCTGCTCCTACGCTTGGAGATTTGCGAATCCCGTGTGCTTATGTAAAACCTTCCAAGGTC  
CTCCTCAGGAATCCAAGTTGAGAGAGATAAATTGAACAAATATGGACGTCCCTATTGGGATGTACTAT  
TAAACCTAAATTGGGTTTATCCGCTAAAAATTACGGTAGAGCAGTTTATGAATGTCTA

>MG249858.1 *Trifolium subterraneum*

AAGGTTGGGTTCAAAGCTGGTGTAAAGATTATAGATTGACTTATTATACTCCTGACTATGAAACCAAAG  
ATACTGATACTTTGGCAGCATTCCGAGTAACCTCCTCAACCCGAGTTCGGCCGAAGAAGCAGGTGCAGC  
GGTAGCTGCCGAATCTCCACTGGGACATGGACAACCTGTGTGGACCGATGGACTTACCAGTCTTGATCGT  
TATAAAGGACGCTGCTATACATCGAGCCTGTTGCTGGAGAAGATACTCAATTTATTGCTTATGTAGCTT  
ATCCCTTAGACCTTTTTGAAGAAGGTTCTGTTACTAACATGTTTACCTCTATTGTAGGTAATGTATTTGG  
ATTCAAAGCCTTGCCTGCTCCTACGCTTGGAGATTTGCGAATCCCGTGTGCTTATGTAAAACCTTCCA  
GGTCTCCTCACGGAATCCAAGTTGAGAGAGATAAATTGAACAAGTATGGACGTCCCTATTGGGATGTA  
CTATTAACCTAAATTGGGTTTATCCGCTAAGAATTATGGTAGAGCTGTTTACGAATGTCTA

>KX282521.1 *Alhagi graecorum*

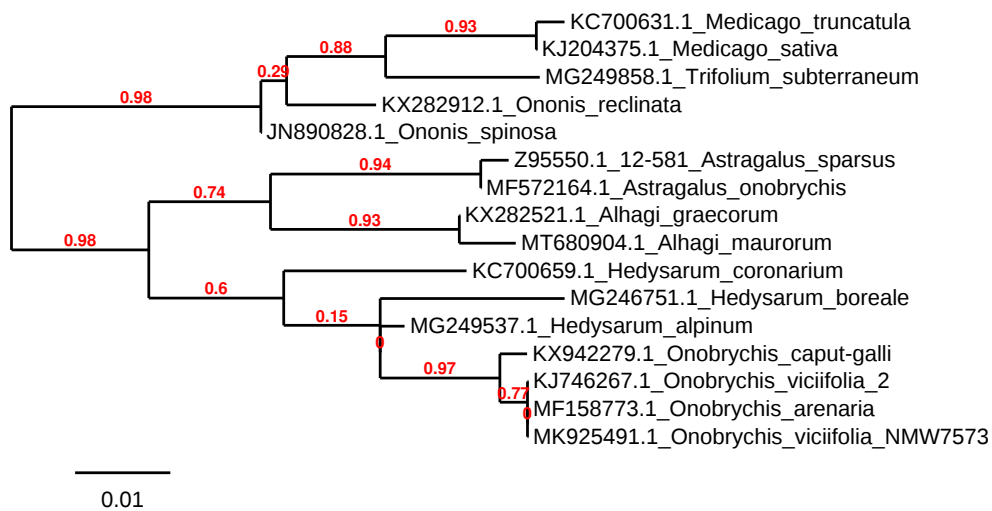
AAAGCTGGTGTAAAGATTATAGATTGACTTATTATACTCCTCAATATGAAACCAAAGATACTGATATCT  
TGGCAGCATTCGAGTAACCTCAACCTGGAGTTCGGCTGAGGAAGCAGGTGCCTGCGGTAGCTGCCGA  
ATCTTCCACTGGGACATGGACAACCTGTGTGGACCGATGGGCTTACCAGTCTTGATCGTTATAAAGGACGA  
TGCTACCACATCTGGACCCGTTGCTGGAGAAGAAAATCAATATATTGCTTATGTAGCTTATCCCTTAGACC  
TTTTTGAAGAAGGTTCTGTTACTAACATGTTTACCTCCATTGTTGGTAATGTATTTGGGTTCAAGGCCTT  
GCGGCTCTACGTTTGGAGGATTTGCGAATCCCTACTTCTTATATTAACCTTCCAAGGTCCGCTCAC  
GGAATCCAAGTTGAGAGAGATAAATTGAACAAGTATGGTCTCCACTATTGGGATGTACTATTAACCAA  
AATTAGGGTTATCCGCTAAGAATTACGGTAGAGCAG

>MT680904.1 *Alhagi maurorum*

AGCTGGTGTAAAGATTATAGATTGACTTATTATACTCCTCAATATGAAACCAAAGATACTGATATCTTG  
GCAGCATTCGAGTAACCTCAACCTGGAGTTCGGCTGAGGAAGCAGGTGCCTGCGGTAGCTGCCGAAT  
CTTCCACTGGGACATGGACAACCTGTGTGGACCGATGGGCTTACCAGTCTTGATCGTTATAAAGGACGATG  
CTACCACATCGAGCCGTTGCTGGAGAAGAAAATCAATATATTGCTTATGTAGCTTATCCCTTAGACCTT  
TTTTGAAGAAGGTTCTGTTACTAACATGTTTACTTCCATTGTTGGTAATGTATTTGGGTTCAAGGCCTTGC  
GCGCTCTACGTTTGGAGGATTTGCGAATCCCTACTTCTTATATTAACCTTCCAAGGTCCGCTCACGG  
AATCCAAGTTGAAAGAGATAAATTGAACAAGTATGGTCTCCACTATTGGGATGTACTATTAACCAA  
TTAGGGTTATCCGCTAAGAATTACGGTAGAGCAGTTTATGAATGTCTCCGCGGTGGACTTG



## Appendix A4-5 Phylogenetic tree of selected species of Mediterranean Fabaceae



The calculation and tree construction is based on BLAST rbcLa sequences listed in Appendix A4-4 and produced by Online Phlogeny Analysis programme (<http://www.phylogeny.fr/>).

## Appendix A5-1 Papers citing *Microcodium*

**Table A5-1.1** Data obtained from WoS (Clarivate™, webofscience.com) on April 15, 2021, include all papers citing (at least one of the) references [1]-[4] or [8]-[11] listed in Table 5.1 (main text). References are sorted from newest to oldest.

Categories: R (plant roots) - *Microcodium* interpreted as a product of plant root calcification; M (microbial) - papers supporting microbial origin of *Microcodium*; N - inconclusive or neutral interpretation about the origin; ≠- obvious misidentification of other microfeatures as *Microcodium*.

Reference	plant roots [R]	microbial [M]	neutral* [O]	misidentified [≠]
Sun et al. 2021			×	
Ryan et al. 2021				×
Mircescu et al. 2021			×	
Li et al. 2021			×	
Esperante et al. 2021			×	
Adler et al. 2021			×	
Ryan et al. 2020				×
Rodriguez-Tovar et al. 2020	×			
Oordt et al. 2020			×	
Moraetis et al. 2020				×
Martin-Martin et al. 2020			×	
Luo et al. 2020			×	
Li et al. 2020			×	
Aratman et al. 2020			×	
Anderson & George 2020			×	
Zacarias et al. 2019			×	
Syah et al. 2019				
Sun et al. 2019			×	
Sun et al. 2019			×	
Salih et al. 2019			×	

cont.	R	M	O	≠
Rodrigues et al. 2019				×
Rivers et al. 2019				×
Pujalte et al. 2019	×			
Milliere et al. 2019			×	
Menezes et al. 2019				×
Kaygili et al. 2019			×	
da Silva et al. 2019			×	
Batezelli et al. 2019				×
Salas-Saavedra et al. 2018			×	
Mojon et al. 2018		×		
Eren et al. 2018				×
Alonso-Zarza 2018	×			
Zenkner & Kozlowski 2017				×
Tazaki et al. 2017			×	
Spanicek et al. 2017			×	
Sorrel et al. 2017				×
Schilt et al. 2017			×	
Pons et al. 2017			×	
Novakova et al. 2017			×	
Letsch & Kiefer 2017			×	
Grosjean et al. 2017			×	
da Silva et al. 2017				×
da Silva et al. 2017				×
Bover-Arnal et al. 2017			×	

<i>cont.</i>	<b>R</b>	<b>M</b>	<b>O</b>	<b>≠</b>	<i>cont.</i>	<b>R</b>	<b>M</b>	<b>O</b>	<b>≠</b>
Wang et al. 2016			×		Sanz-Montero & Rodriguez-Aranda 2012				×
Pujalte et al. 2016	×				Retallack 2012			×	
Monferran et al. 2016			×		Miller et al. 2012			×	
Khokhlova et al. 2016			×		Kuznetsov & Olenova 2012			×	
Khalaf & Al-Zamel 2016	×				Javid et al. 2012			×	
Jurkovsek et al. 2016			×		Huguet et al. 2012			×	
Itkin et al. 2016			×		Grosjean et al. 2012			×	
Hamon et al. 2016			×		Dart et al. 2012			×	
Chen et al. 2016				×	Buggisch et al. 2012	×			
Robins et al. 2015				×	Brock-Hon et al. 2012				×
Pons et al. 2015				×	Alonso-Zarza et al. 2012	×			
Murru et al. 2015			×		Thomas et al. 2011				×
Lintern 2015			×		Sooltanian et al. 2011			×	
Liang & Jones 2015			×		Semeniuk 2011			×	
Li et al. 2015			×		Mandic et al. 2011			×	
Li et al. 2015			×		Labourdette 2011			×	
Krklec et al. 2015			×		Gocke et al. 2011			×	
Azeredo et al. 2015			×		Brasier 2011			×	
Ahlborn & StemmenKA 2015				×	Blomeier et al. 2011			×	
Woody et al. 2014			×		Barta 2011			×	
Pujalte et al. 2014	×				Akkiraz et al. 2011			×	
Li & Li 2014	×				Kabanov et al. 2010		×		
Gocke et al. 2014			×		Cantarero et al. 2010				×
Casado et al. 2014			×		Caja et al. 2010			×	
Brelek et al. 2014	×				Zhou & Chafetz 2009			×	
Brelek & Glumac 2014	×				Singh et al. 2009				×
Antoshkina 2014		×			Riera et al. 2009			×	
Riera et al. 2013			×		Lambers et al. 2009	×			
Miller et al. 2013			×		Candy & Black 2009			×	
Landing et al. 2013		×			Brock & Buck 2009			×	
Grosjean & Pittet 2013		×			Blomeier et al. 2009			×	
Cabaleri et al. 2013			×		Zamagni et al. 2008	×			
Cabaleri & Benavente 2013			×		Todisco & Bhiry 2008			×	
Bustillo et al. 2013			×		Pomoni-Papaioannou & Kostopoulou 2008			×	
Brelek et al. 2013	×				Patacca et al. 2008			×	
Zhou & Chafetz 2012			×		Owen et al. 2008			×	
Zamagni et al. 2012	×				Kabanov et al. 2008	×			
Wanas 2012				×					
Tovar et al. 2012			×						



<i>cont.</i>	R	M	O	≠	<i>cont.</i>	R	M	O	≠
Hofmann et al. 2008			×		Baceta et al. 2001	×			
Eren et al. 2008			×		Felton et al. 2000			×	
Alonso-Zarza et al. 2008			×		Samuelsberg & Pickard 1999			×	
Wang & Greenberg 2007			×		Rossi & Canaveras 1999			×	
Tewari et al. 2007			×		Nyambe 1999			×	
Singh et al. 2007				×	Immenhauser et al. 1999			×	×
Otonicar 2007	×				Buonocunto et al. 1999			×	
Ogorelec et al. 2007			×		Lekach et al. 1998			×	
Labourdette & Jones 2007			×		Bao et al. 1998			×	
Baceta et al. 2007	×				Alonso-Zarza et al. 1998	×			
Arribas & Arribas 2007			×		RosalesDominguez et al. 1997			×	
Alonso-Zarza & Jones 2007			×		Freytet et al. 1997		×		
Yilmaz & Altiner 2006				×	Goudie 1996		×		
Verboom & Pate 2006			×		Canaveras et al. 1996			×	
Sinha et al. 2006				×	Wright et al. 1995	×			
Sano 2006			×		Verrecchia et al. 1995			×	
Mallol 2006			×		McLaren 1995			×	
El Kadiri et al. 2006			×		Lonoy 1995			×	
Antoshkina 2006			×		Arp 1995			×	
Turner & Makhlof 2005			×		Wright 1994	×			
Kabanov 2005		×			Pipujol & Buurman 1994			×	
Westphal et al. 2004			×		Turner 1993			×	
Sano et al. 2004			×		Driese & Mora 1993			×	
Sandulli 2004			×		Martinchivelet & Gimenez 1992	×			
McLaren 2004			×		Mack & James 1992			×	
Kosir 2004	×				Kenny & Krinsley 1992			×	
Alonso-Zarza & Arenas 2004	×				Wright & Vanstone 1991	×			
Varrone & Clari 2003			×		Verrecchia et al. 1991			×	
Retallack et al. 2003			×		Pomonipapaioannou & Solakius 1991			×	
Kabanov 2003			×		Pelechaty & James 1991			×	
Igawa 2003			×		Monger et al. 1991				×
Artieda & Herrero 2003			×		Jaillard et al. 1991	×			
Alonso-Zarza 2003	×				Saller & Koepnick 1990			×	
Ehrenberg et al. 2002			×		Rao 1990				×
Buonocunto et al. 2002			×		Jones 1990			×	
Bowen & Bloch 2002			×		Pirozynski & Dalpe 1989		×		
Landrein et al. 2001			×		Lehman 1989				×
Huneke et al. 2001			×						
Benison & Goldstein 2001			×						

<i>cont.</i>	<b>R</b>	<b>M</b>	<b>O</b>	<b>≠</b>
Casanova & Nury 1989			×	
Stubblefield & Taylor 1988		×		
Sarkar 1988				×
Goldstein 1988				×
Roulin 1987			×	
Phillips & Self 1987			×	
Phillips et al. 1987			×	
Wright 1986			×	
Saller 1986			×	
Mamet & Preat 1985				×
Viles 1984			×	
James & Choquette 1984			×	
Legall & Poncet 1983			×	
Freytet & Moissenet 1983				×
Wright 1982			×	
Nickel 1982			×	
Mamet & Roux 1982				×
Freeman et al. 1982			×	
Chafetz & Butler 1982				×

<i>cont.</i>	<b>R</b>	<b>M</b>	<b>O</b>	<b>≠</b>
Semeniuk & Meagher 1981			×	
Krumbein & Jens 1981			×	
Nahon et al. 1980			×	
Klappa 1980	×			
Chafetz & Butler 1980				×
Laurain & Meyer 1979			×	
Klappa 1979			×	
Benjamini 1979			×	
Klappa 1978	×			
<i>count</i>	<b>30</b>	<b>10</b>	<b>148</b>	<b>36</b>

## Appendix A5-2 **Microcodium revisited: root calcification products of terrestrial plants on carbonate-rich substrates**

### A5-2.1 Introduction

Plant roots and associated microorganisms in the rhizosphere produce important accumulations of calcium carbonate in near-surface terrestrial settings. Root calcification structures are among the most prominent features in many soils and palaeosols and may actually constitute the dominant fabrics in some forms of calcrete (Wright et al. 1995).

Criteria for the recognition of root calcification macrofeatures in the rock record are relatively well established (Klappa 1980b; Esteban and Klappa 1983; Retallack 1988; Wright and Tucker 1991) and are based on well-documented Quaternary examples. However, some biogenic microstructures found commonly in palaeosols and at palaeo-exposure surfaces lack reliable modern analogues, and consequently, their origin is highly controversial (e.g. Verrecchia et al. 1995, 1996; Freytet et al. 1997; Wright et al. 1996; Wright et al. 1997; Wright et al. 1998; Alonso-Zarza et al. 1998).

*Microcodium* is one such problematic feature, especially in early Palaeogene and Miocene continental and marine successions (see, e.g., Klappa 1978; Wright and Tucker 1991, and references therein). *Microcodium* structures consist of cellular aggregates composed of individual crystals of calcite. A root origin for *Microcodium* was proposed by Klappa (1978), who interpreted it as a calcification product of a mycorrhizal (fungal and plant root) association. Support for this rhizogenic interpretation has been presented by Jaillard (1987a, 1992) and Jaillard et al. (1991), who described intracellularly calcified root cells from present-day soils that closely resemble *Microcodium* structures.

Freytet and Plaziat (1982) disagreed with the interpretation of Klappa (1978) because they found the root origin unable to explain laminar forms of *Microcodium*. Furthermore, Freytet et al. (1997) have argued that in spite of their obvious morphological similarity, the multilayer cell arrangement in modern calcified roots described by Jaillard and co-workers (e.g., Jaillard 1983, 1987a; Jaillard and Callot 1987; Jaillard et al. 1991) differs significantly from that of the typical ancient *Microcodium* aggregates, which are composed of a single layer of elongate crystals.



This paper documents examples of calcified plant roots and *Microcodium* from subaerial exposure profiles in a succession of Palaeocene shallow-marine carbonates in southwestern Slovenia. A crudely laminar horizon in one of the studied profiles contains abundant calcite aggregates which exhibit exquisitely preserved structural details of plant root tissues, and thus provide direct and unambiguous evidence for their rhizogenic origin. Moreover, morphologies intermediate between the typical *Microcodium* aggregates and calcified roots were observed in this laminar horizon and this observation supports previous rhizogenic interpretations of *Microcodium* structures. The aim of this paper is to present the morphological evidence for the root origin of *Microcodium*, as well as to discuss its palaeoecologic significance and the processes and causative factors for precipitation of calcium carbonate in the root cells of terrestrial plants inhabiting carbonate-rich substrates.

#### **A5-2.2 Calcification products of plant roots and the problem of *Microcodium***

Root calcification structures (rhizoliths, rhizcretions, rhizomorphs; see review of terminology by Klappa 1980b) exhibit various degrees of biological activity responsible for their formation. Except for their gross morphology, some forms may show no biologically influenced fabrics (for example, simple root molds left after roots have decayed and subsequently filled with a cement), whereas others are characterized by biologically controlled precipitation of calcium carbonate in, on, or around roots (Klappa 1980b; Jones and Ng 1988; Jones 1994; Wright et al. 1995; Alonso-Zarza 1999). With regard to location, two styles of calcification processes can be distinguished: (1) rhizosphere calcification (extracellular calcification of Wright et al. 1995), i.e. accumulation of calcium carbonate in the area immediately surrounding and influenced by plant roots; and (2) intracellular calcification. The former process is mediated mainly by the root-associated microorganisms in the soil (Jones 1994), but the latter is controlled directly by plants through the precipitation of calcium carbonate within their cortical root cells (Jaillard 1987a, 1992; see below). The term calcification, as used throughout this paper, denotes deposition of calcium salts (carbonate) in living tissue.

Intracellular calcification of roots appears to be a common phenomenon in modern soils. Products of intracellular root calcification are widespread in some present-day calcareous soils and may represent up to a quarter of the soil mass (Jaillard 1984, 1992; Jaillard et al. 1991). Active calcification in the living cortical root cells has also been reported in experimental work performed by Jaillard (1987a, 1987b, 1992) and Ross and

Delaney (1977). Calcified root cells may constitute significant quantities of secondary carbonate in Quaternary loess, loess palaeosols (Becze-Deák et al. 1997 and references therein), and chernozems (Khokhlova et al. 2001a; Khokhlova et al. 2001b), whereas pre-Quaternary unambiguous examples of intracellularly calcified plant roots are rare (Goldstein 1988; Alonso-Zarza et al. 1998; Alonso-Zarza 1999; Bowen and Bloch 2002).

Intracellular calcification of roots has also been considered as a mechanism creating *Microcodium* structures (Klappa 1978; Wright et al. 1995). *Microcodium* does not appear to exist today, although it has been reported from Quaternary carbonate eolianites on Isla Contoy, off the Yucatan Peninsula (Ward 1975; McKee and Ward 1983), the Mediterranean island of Mallorca (Calvet et al. 1975), and from calcrete crusts on San Salvador, Bahamas (Bain and Foos 1993; Foos and Bain 1995). Accumulations of *Microcodium* are abundant in Cretaceous, Palaeogene, and Miocene continental and marine carbonate successions, especially in the peri-Mediterranean area. These accumulations can form stratigraphic levels, several meters in thickness, composed almost entirely of in situ *Microcodium* aggregates (Freytet and Plaziat 1982; Wright et al. 1995; Rossi and Cañaveras 1999). *Microcodium* can be the dominant component in palaeo-calcretes (Esteban 1974; Wright et al. 1995) and is also common in palaeosols and palaeokarstic horizons, as well as within floodplain and palustrine deposits (Bodergat 1974; Freytet and Plaziat 1982; Wright et al. 1995; Alonso Zarza 2003).

Typical *Microcodium* structures (Bodergat 1974; Freytet and Plaziat 1982; Morin 1993) consist of millimetric aggregates composed of a single layer of individual cell-like crystals of calcite (Figs. A5-2.1A, B, C, A5-2.2B). These pyramidal or prismatic crystals are polygonal in cross section and are usually strongly elongate, measuring 100–800  $\mu\text{m}$  in length and 20–70  $\mu\text{m}$  in width (Freytet and Plaziat 1982). *Microcodium* aggregates occur in two basic forms (Bodergat 1974; Freytet and Plaziat 1982): (1) in root-like growths composed of cylindrical (“corn-cob”) aggregates (Fig. 5.1A) or connected or unconnected spheroids (rosettes; Fig. 5.1B), both with the polyhedral elements arranged in a radiating pattern around a hollow central channel, and as (2) laminar (lamellar) structures composed of layers of asymmetrical aggregates (Fig. 5.1C).

Bodergat (1974) and Esteban (1972, 1974) extended the definition of *Microcodium* to include atypical forms (Fig. A5-2.1D), called “*Microcodium* type 3” by Bodergat (1974), and “*Microcodium* (b)” by Esteban (1972, 1974), which consist of several layers of isodiametric crystals. The structure of these atypical forms resembles the morphology of modern plant roots (Fig. A5-2.1E; Klappa 1978; Jaillard et al. 1991; Alonso-Zarza et al. 1998) but differs

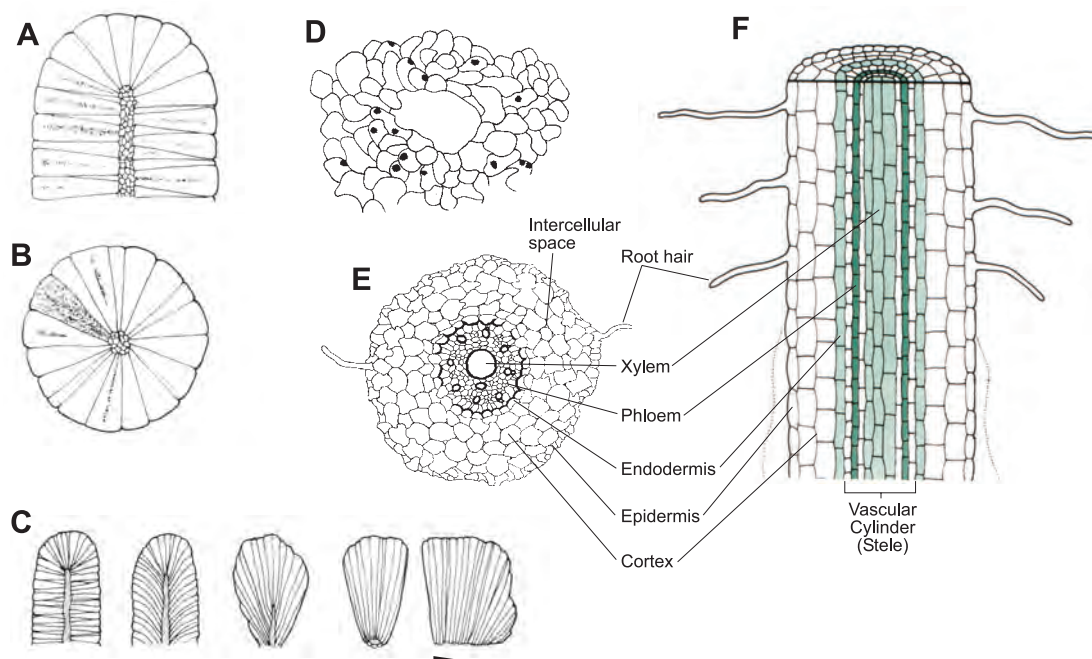


**Figure A5-2.1** Morphotypes of *Microcodium* and the structure of plant roots. Typical *Microcodium* structure is composed of a single layer of elongate calcite prisms forming root-like growths composed of A) cylindrical “corn-cob” aggregates, or B) spheroidal (rosette) aggregates. C) Morphological continuum between ‘corn-cob’ and laminar *Microcodium* morphologies (from Freytet and Plaziat 1982). D) Sketch of multilayer cell arrangement in *Microcodium* type 3 of Bodergat (1974) (= *Microcodium* (b) of Esteban 1974; from Bodergat 1974). E) Cross section of a root (Fahn 1982) and F) diagrammatic longitudinal section of a primary root, showing major structural elements of the root tissue (Tais and Zaiger 1998).

considerably from the shape of “cells” and their organization in “classical” *Microcodium* aggregates (Freytet and Plaziat 1982; Freytet et al. 1997). The original rhizogenic interpretation of *Microcodium* (Klappa 1978) was derived from Holocene material which appears to be identical to the calcified roots described by Jaillard (1987a) and Jaillard et al. (1991) (their figs. 3-5; compare with figs. 2-4 in Klappa 1978). This fundamental morphological difference between the cell architecture in calcified roots and *Microcodium* aggregates (Fig. A5-2.1A-E) appears to be the main issue in the controversy about the rhizogenic origin of *Microcodium* (Freytet et al. 1997; Wright et al. 1997). Comparison of the two morphologies is also shown in Figure A5-2.2.

Another problematic feature which is commonly seen with all morphotypes is the ability of *Microcodium* to dissolve and intensely corrode carbonate substrates. Freytet and Plaziat (1982) found the corrosive nature of *Microcodium* incompatible with the activity of roots and proposed that *Microcodium* formed through symbiotic association of several microorganisms (probably fungi and bacteria), in which some might attack calcite and others might synthesize it.



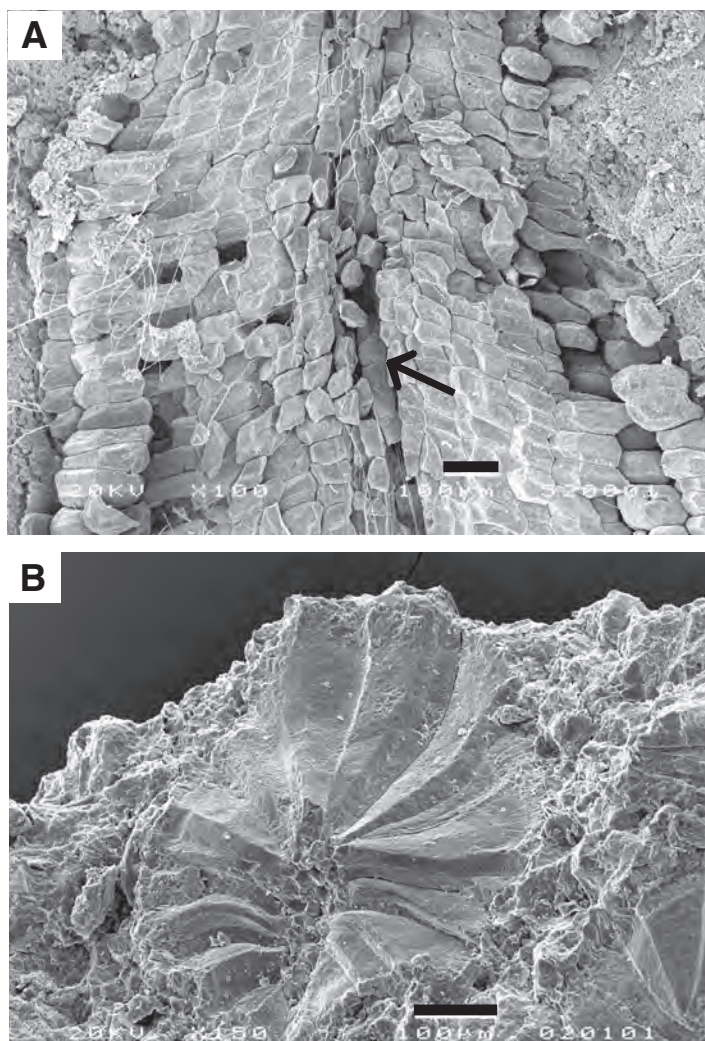


**Figure A5-2.2**

Scanning electron microscope photographs, showing a fundamental difference in cell organization between modern calcified roots and ancient *Microcodium*.

A) Longitudinal section through the calcified root from a Quaternary calcrete at Sella, SE Spain. Note the multilayer architecture of calcified cortical cells. Darker part in the middle of the root (arrow) corresponds to noncalcified vascular cylinder. Scale bar 100  $\mu\text{m}$ .

B) Broken *Microcodium* aggregate (“rosette”) from the Palaeocene fluvial deposits at Fontjoncouse, southern France, composed of a radiating pattern of elongate calcite pyramids. Axial channel is filled with microsparite. Scale bar 100  $\mu\text{m}$ .

In situ aggregates or disaggregated elements have been found in a great variety of facies (Klappa 1978; Freytet and Plaziat 1982; Wright and Tucker 1991; Wright 1994), making palaeoecological interpretation of *Microcodium* extremely difficult. To add to the controversy, some spheroidal carbonate microfeatures and forms of diagenetic calcite have been confused with *Microcodium* although they are obviously different in microstructure, morphology, and size (e.g., Chafetz and Butler 1980; Esteban 1982; Chafetz and Butler 1982; Monger et al. 1991; see discussion in Verrecchia et al. 1995 and Rossi and Cañaveras 1999).

### A5-2.3 Geological setting

The material studied in this paper occurs within a succession of Upper Palaeocene (Thanetian) shallow-marine limestones of the Trstelj Formation, which represent the middle part of the Kras Group (Košir and Otoničar 2001). The Kras Group is a widespread carbonate unit throughout the northeastern Adriatic coastal region, particularly in

southwestern Slovenia (Fig. A5-2.3A). It corresponds to the terminal megasequence of the Adriatic-Dinaric Carbonate Platform and overlies a major regional unconformity expressed by a palaeokarst and bauxite deposits. This megasequence was deposited during major tectonic events in the Late Cretaceous and Early Palaeogene when the carbonate platform was subaerially exposed, subsequently reestablished, and finally buried by prograding deep-water clastics (flysch) (Cousin 1981; Drobne 1977; Košir and Otoničar 2001).

A generalized stratigraphic column of the Upper Cretaceous, Palaeocene, and Eocene deposits in southwestern Slovenia is shown in Figure 5.3B (for more detailed stratigraphy and facies characteristics of these formations see Pavlovec 1963; Bignot 1972; Drobne 1977; Jurkovšek et al. 1996; and Ogorelec et al. 2001). The lower part of the Kras Group

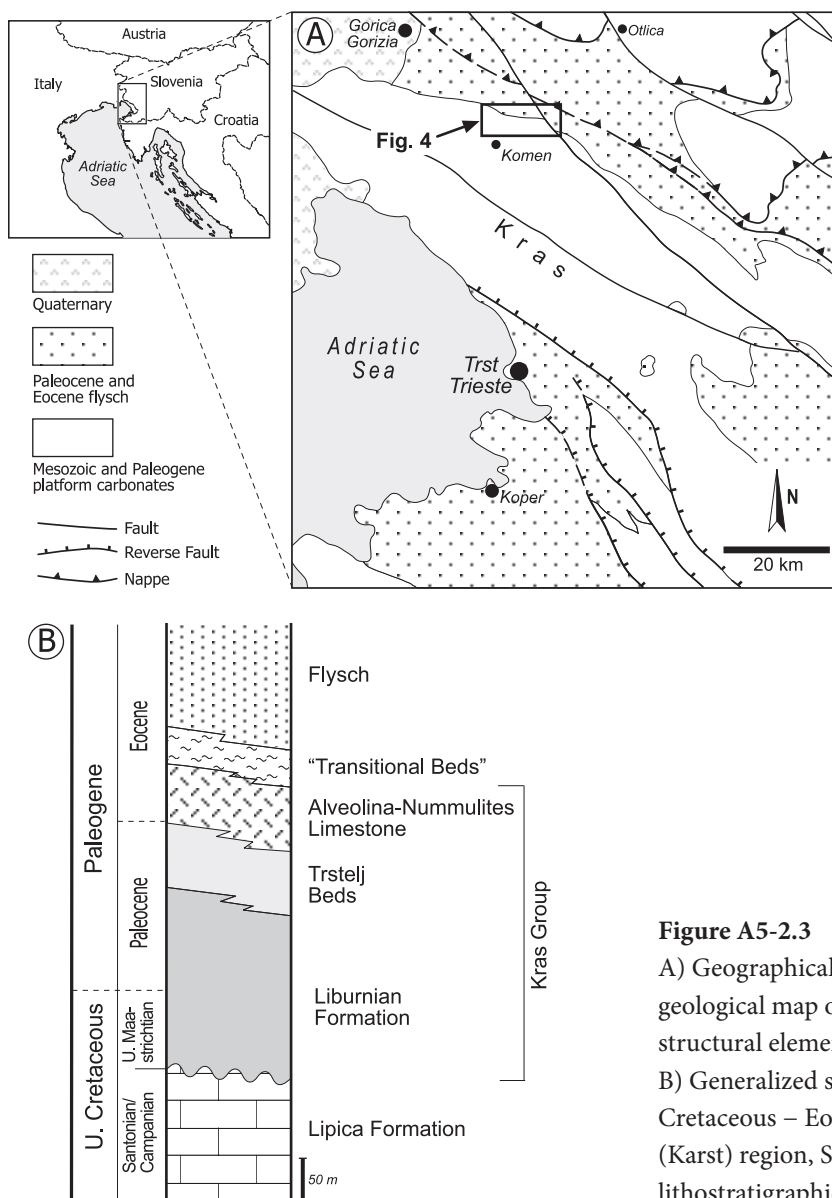


**Figure A5-2.3**  
 A) Geographical position and simplified geological map of SW Slovenia showing major structural elements (modified from Placer 1981).  
 B) Generalized stratigraphic column of upper Cretaceous – Eocene succession in the Kras (Karst) region, SW Slovenia, showing major lithostratigraphic units.

(i.e., The Liburnian Formation of Maastrichtian and early Palaeocene age) is characterized by restricted, marginal marine and palustrine carbonates, which show pedogenic modifications, including root-related laminar calcrete horizons and massive accumulations of *Microcodium* (Otoničar and Košir 1998). Prominent subaerial exposure surfaces, including calcretes, occur also in a succession of Upper Palaeocene and Lower Eocene bioclastic limestones of the Trstelj Formation and Alveolina-Nummulites Limestone. The calcrete profiles described herein occur in a succession of miliolid-dominated packstone and grainstone facies, typical of inner-ramp depositional settings (Luterbacher et al. 1991; Davaud and Septfontaine 1995; Košir 1997), which were deposited in a relatively high-energy, barrier-related depositional environment on a foram-dominated carbonate ramp.

#### **A5-2.4 Material and methods**

Subaerial exposure profiles were studied in well-exposed outcrops of the Trstelj Formation, situated along forest roads on the northern margin of the Kras Plateau (Figs. 5.3A and 5.4; Appendix A5-1). Two calcrete profiles were sampled in detail. Calcrete macrofabric was studied in outcrops and in polished slabs. Calcrete microfabric was analyzed in more than 150 thin sections, using standard transmitted light microscope. Standard thin-section petrography was supplemented with cathodoluminescence (CL) and UV fluorescence petrography. Nine selected thin sections were polished and examined under cathodoluminescence on CITL cold cathode luminoscope (model CL8200 Mk4) at the Karst Research Institute ZRC SAZU, Postojna, Slovenia, operating at approximately 15 kV beam energy and 400 mA beam current. Three polished thin sections were studied in reflected light under Opton-Axiophot (Zeiss) microscope, linked to a fluorescence-inducing blue light source. The chemical composition of four uncoated polished thin sections was obtained from electron microprobe analyses performed at the National Building and Civil Engineering Institute, Ljubljana, using an energy dispersive spectrometer (EDS), linked to a JEOL 5500 LV low-vacuum SEM. Elemental spectra were acquired at 20 kV and pressure of approximately 12 Pa. Scanning electron observation of broken surfaces and polished and etched slabs was carried on a JEOL JSM 330A microscope at the Institute of Palaeontology ZRC SAZU, Ljubljana.



### A5-2.5 Calcrete profiles

Most subaerial exposure surfaces from the studied succession of the Trstelj Formation are characterized by root-influenced fabric but differ in form and stage of development. The following profiles provide two examples of well developed calcretes with distinctive laminar horizons, composed almost entirely of root-calcification structures.

#### A5-2.5.1 Trstelj calcrete

The Trstelj calcrete was studied in several small outcrops along a forest road, NW of Trstelj Hill (Fig. A5-2.4). The calcrete caps the Trstelj Formation and corresponds to the boundary with the overlying Alveolina-Nummulites Limestone. The calcrete is developed on gray bioclastic grainstones and packstones, which are composed mostly of miliolid and small rovaliid forams, echinoderm fragments, and peloids. Thickness of the calcrete ranges from 10 to 30 cm. A schematic section of the calcrete profile, composed of three layers, is shown in Figure A5-2.5A. The lower unit is represented by distinctive dark mottles which occur in a layer, 10-15 cm thick, of grainstones and packstones below the massive calcrete horizon. Thin sections of the mottled limestone exhibit distinctive dark micritic coatings on the bioclasts and abundant alveolar septal structure in the intergranular spaces. The mottled horizon gradually passes upwards into the beige to dark gray colored massive/brecciated horizon. Thin sections of the massive horizon show dense microfabric of intensively micritized bioclasts, micrite cements, and pores with alveolar septal structure. Brecciation

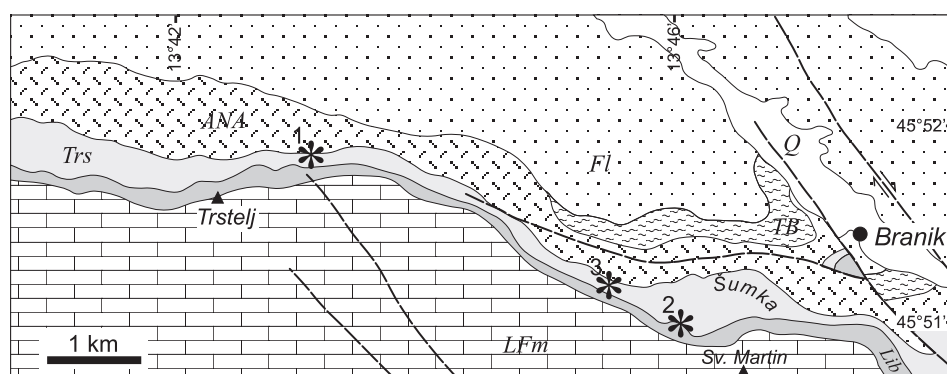


**Figure A5-2.4** Geological map of the studied area (modified from Buser 1968). Position of the area is indicated on the map in Figure 5.3A. Asterisks indicate position of Trstelj calcrete (1), Sv. Martin calcrete profile (2) and the Šumka section (3). Key to stratigraphic units: LFm, Lipica Formation; Lib, Liburnian Formation; Trs, Trstelj Formation; ANA, Alveolina-Nummulites Limestone; TB, Transitional Beds (Globigerina Marl); Fl, Flysch. For the stratigraphic range of the lithostratigraphic units see Figure A5-2.3B.

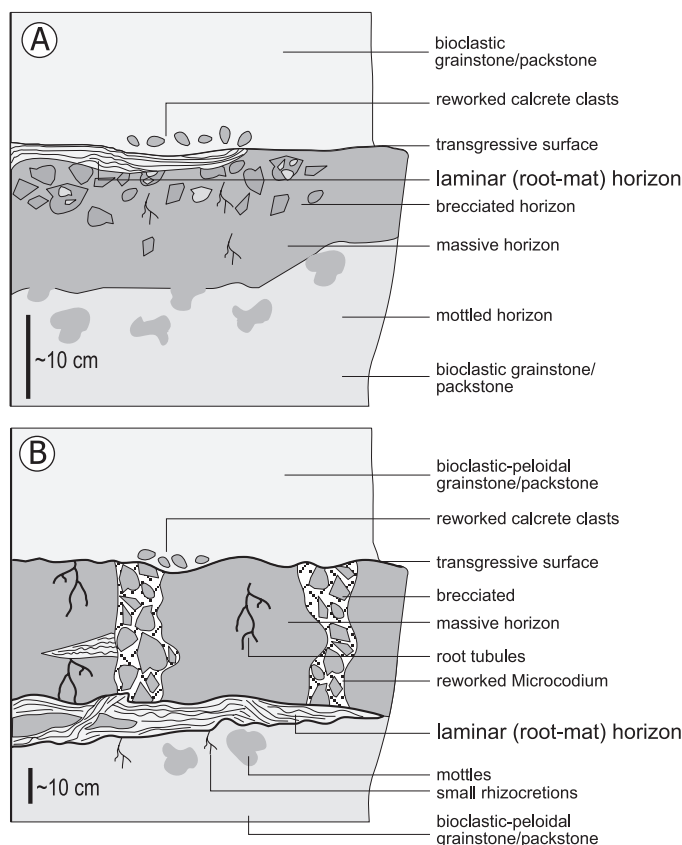


**Figure A5-2.5** Schematic diagram showing stratigraphy and major macrofeatures of the studied calcrete profiles. A) Trstelj calcrete profile. B) Sv. Martin profile.

is mostly restricted to the upper part of the horizon but can also constitute almost the entire horizon. Highly irregular to subrounded clasts in the brecciated part differ in color but exhibit microfabric characteristics similar to the matrix and the non-brecciated, massive part. Composite clasts (Fig. A5-2.6A) indicate that the horizon formed through multiple phases of brecciation and subsequent cementation by micrite. Root traces within the brecciated horizon indicate that the brecciation probably resulted from penetrative growth of roots (Klappa 1980a). Root-induced brecciation is further evidenced by root tubules, observed in cracks which penetrate into clasts.

The brecciated horizon is capped by a discontinuous, laminar horizon up to 4 cm thick (Fig. A5-2.6A). The laminar fabric also fills cavities several centimeters deep in the brecciated horizon. The lamination pattern results from the alternation of millimetric gray peloidal layers and dark brown to black layers, composed of intertwined tubules with micritic walls (Fig. A5-2.7A). Some micritic tubules exhibit indistinctive cellular structure, composed of thin arcuate septa (alveolar septal structure), which rarely show the well-preserved structure of root tissues (Fig. A5-2.7B). In parts of the laminar horizon, distinctive layers containing abundant isolated polygonal or slightly elongate calcite elements (Fig. A5-2.7C) occur within the peloidal and tubular laminae. These calcite

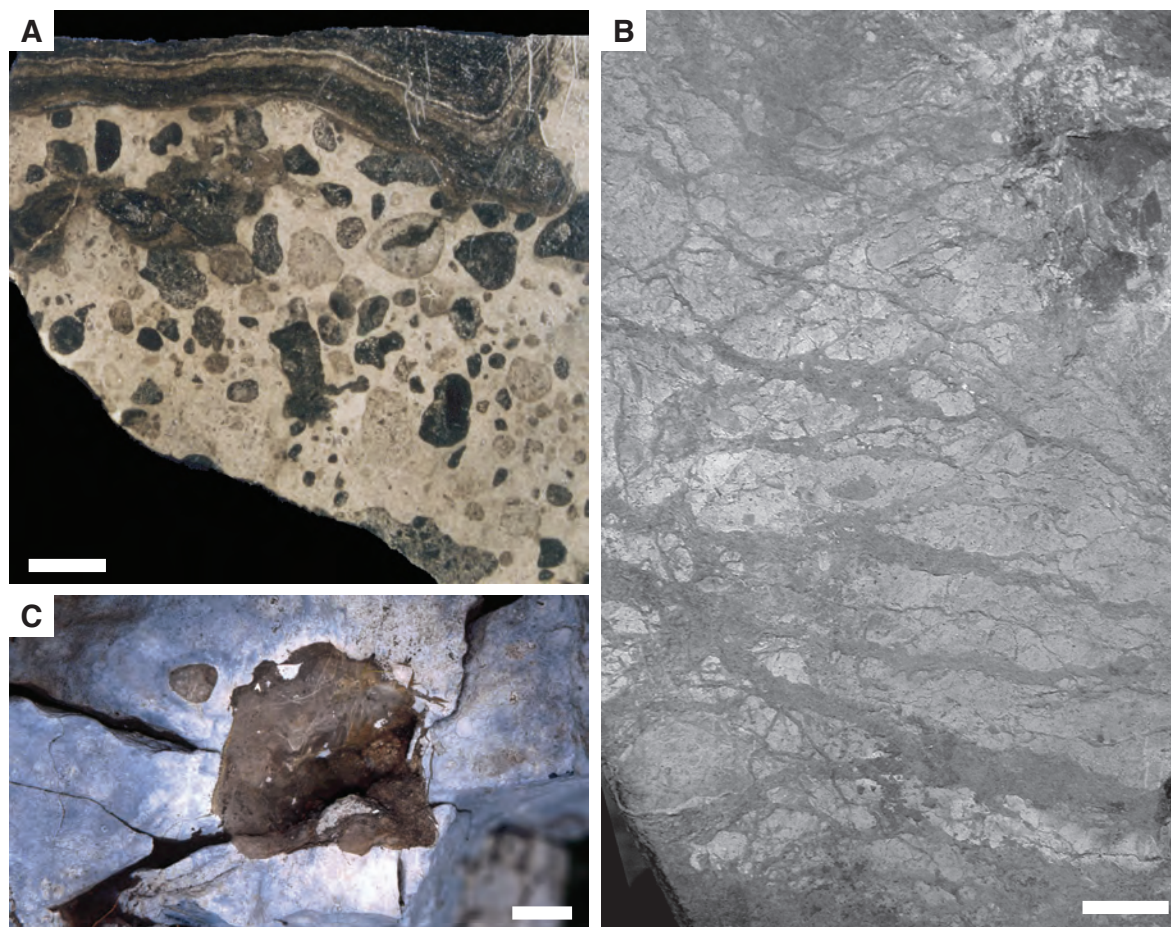


**Figure A5-2.6** A) Polished slab of the upper part of the Trstelj calcrete. Distinctive laminar horizon overlying the brecciated horizon. Scale bars in all figures 1 cm. B) Weathered surface of the crudely laminar horizon of the Sv. Martin calcrete, showing anastomosing pattern of subhorizontal to subvertical laminae, composed mostly of calcified roots (see photomicrograph in Fig. A5-2.7D, C) Subcircular void (dark) on the upper bedding surface of the massive horizon of the Sv. Martin calcrete, representing a mold of a large subvertical root that penetrates through the massive carbonate. The cavity is filled by dark micrite containing abundant disaggregated *Microcodium* elements and small calcrete clasts.

elements are rarely joined in small radial aggregates forming incomplete *Microcodium* rosettes (Fig. A5-2.7C) or are arranged in seriate structures that resemble laminar (lamellar) *Microcodium* colonies (Freytet and Plaziat 1982). The calcrete profile is directly overlain by bioclastic grainstone, composed of alveolinids and coral fragments and, in the basal part, with a transgressive lag of centimeter-size clasts of calcrete.

The Trstelj calcrete profile exhibits characteristic structure of well developed calcretes (Wright and Tucker 1991). The tubular microfabric of the laminar layer, capping the massive and brecciated horizon, is typical of root-mat calcretes (Wright et al. 1988). The micromorphology of the laminar crust is dominated by features that can be interpreted as products of calcification in the rhizosphere (Wright et al. 1995). The unique feature is the occurrence of *Microcodium* aggregates within the laminar calcrete fabric (see below).



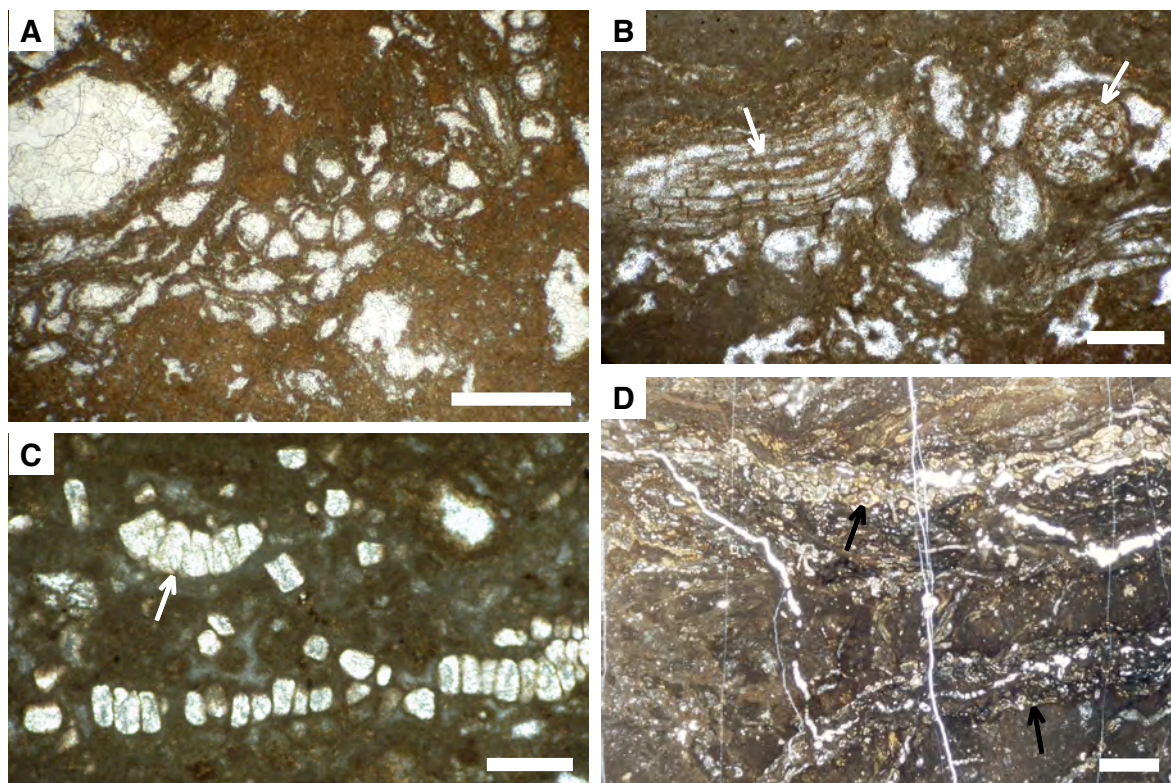


**Figure A5-2.7** A) Photomicrograph of the laminar horizon of the Trstelj calcrete (see Fig. A5-2.6A). Porous laminar microfabric is composed of spar-filled tubules within dark, microlaminar matrix. Plane-polarized light, scale bar 3 mm. B) Calcified micritic tubules with preserved root structure (arrows) in the Trstelj laminar crust. Plane-polarized light, scale bar 200  $\mu\text{m}$ . C) Layer of isolated calcified root cells within the peloidal-laminar horizon of the Trstelj calcrete and an incomplete *Microcodium* aggregate (arrow). Plane-polarized light, scale bar 0.5 mm. D) Photomicrograph of the laminar horizon of the Sv. Martin calcrete showing abundant intracellularly calcified roots (mainly in cross sections; arrows) in intertwined, irregular root laminae in a subhorizontal root mat. Thin section in plane-polarized light. Scale bar 4 mm.

#### A5-2.5.2 Sv. Martin calcrete

The second studied calcrete profile is exposed in a section along a forest road-cut below Sv. Martin Hill, about 2.5 km SW of Branik Village (Fig. A5-2.4). The calcrete appears as a bed, 60-80 cm thick, of dark brown limestone within gray bioclastic (skeletal) grainstones and packstones, which are composed mainly of miliolid and small rotaliid forams, dasycladacean algae, coral fragments, and peloids. Two distinctive calcrete horizons can be recognized in the profile (Fig. A5-2.5B): (1) the lower, crudely laminar horizon (Fig. A5-2.6B) which is overlain by (2) massive and partly brecciated horizon.

The crudely laminar horizon is 5-25 cm thick. Its lateral extent cannot be determined because of the small extent of the outcrop, but it appears to pinch out laterally. The crudely laminar fabric consists of intertwined and anastomosing millimeter-thick subhorizontal to subvertical sheets and stringers. The laminar horizon is dark, almost black, and the

laminae can be seen only on strongly weathered rock surfaces (Fig. A5-2.6B). Thin sections exhibit dense networks of millimeter- and submillimeter-size tubiform cylinders with dark micritic (laminar) walls (Fig. A5-2.7D). These tubular structures are filled with a drusy cement and are commonly associated with the alveolar septal structure which occurs within and between the tubules (Fig. A5-2.8A). However, the most characteristic and abundant microfeatures of the laminar horizon are: 1) calcitic cylinders which display exceptionally well-preserved details of root cellular structure (Fig. A5-2.8B-F); 2) typical *Microcodium* aggregates (Fig. A5-2.9); and 3) intermediate forms between the former two features (Fig. A5-2.10).

The massive horizon consists of a dark brown limestone which shows no distinctive macrostructures in the outcrop. Thin sections show that it is composed of a dense and partly microbrecciated micrite. The micrite includes rare, almost completely micritized, but still recognizable bioclasts, mostly miliolid and rovaliid forams, fragmented gastropod shells, and scattered, disaggregated *Microcodium* prisms. The massive horizon is cut by irregular subvertical fissures, several centimeters to decimeters wide, filled by brecciated limestone (Fig. A5-2.5B), and more regular cylindrical voids (Fig. A5-2.6C). The latter most probably represent infilled molds of large subvertical roots. The brecciated parts are composed of centimeter-size angular to subangular clasts of massive micrite, and a complex matrix of *Microcodium* fragments, micritic coatings, internal sediments, drusy sparite cement, and subordinate clayey material.

Most of the macrofeatures and microfeatures observed in the Sv. Martin calcrete profile can be interpreted as due to the activity of plants. Well-preserved calcified roots provide obvious and unambiguous evidence for the rhizogenic origin of the laminar horizon. Its occurrence below the massive calcrete horizon suggests that it represents a penetrative calcified root mat, whereas the brecciation of the massive horizon was most probably caused by the penetrative growth of roots (cf. Klappa 1980a). Similar calcrete profiles that have been interpreted as a result of constructive and destructive processes in the rhizosphere have been described from the Quaternary soils of the Turks and Caicos islands (Rossinsky and Wanless 1992; Rossinsky et al. 1992).



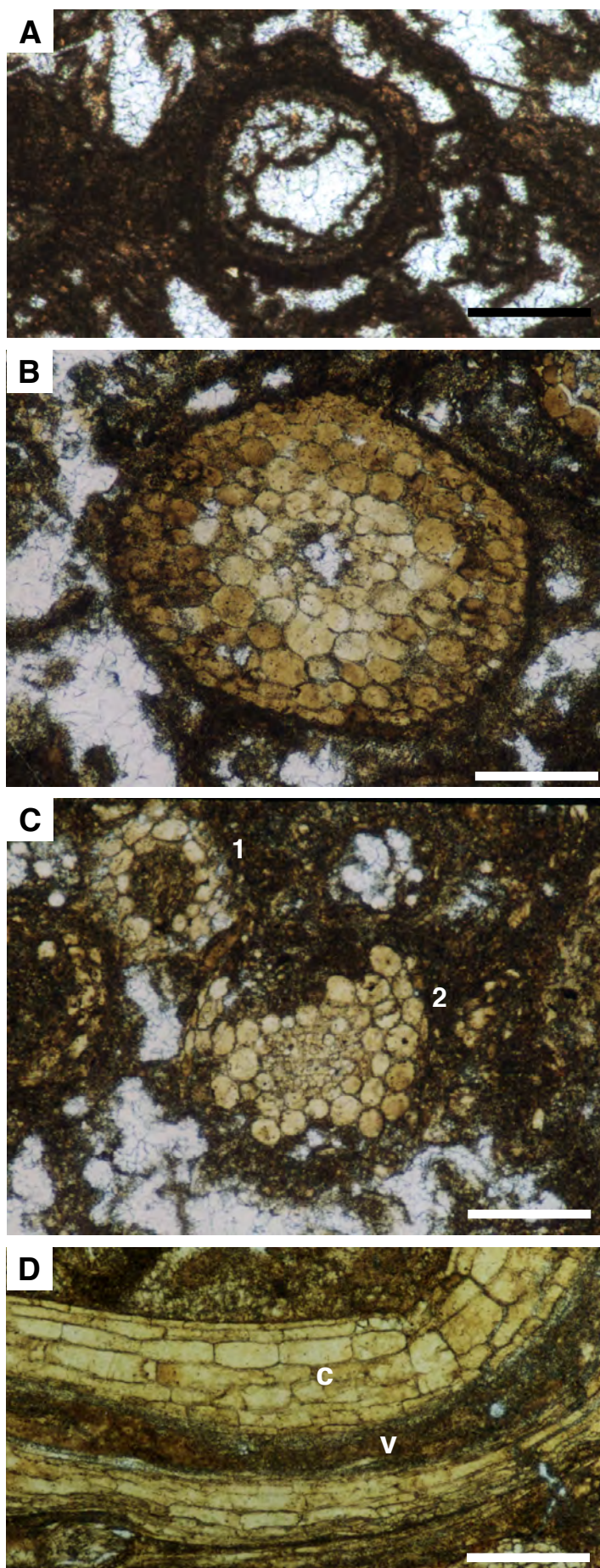


**Figure A5-2.8**

Photomicrographs of calcified roots from the Sv. Martin calcrete, all in plane-polarized light. A) Cross section of a root tubule, formed through precipitation of dark micrite around a root. The tubular void which mark the position of a decayed root is filled with sparry calcite cement and shows no evidence of intracellular calcification. Note prominent alveolar septal structure in and around the root tubule. Scale bar 200  $\mu\text{m}$ . B) Completely intracellularly calcified root in cross section. Almost the entire volume of this root is composed of calcified cortical cells. Small central part of the root, corresponding to the vascular cylinder, is filled by sparry calcite cement. The root is coated by a layer of dark micrite. Scale bar 200  $\mu\text{m}$ . C) Two incompletely calcified roots in cross section. Central part of (1) is filled by micrite. Indistinctive cellular microstructure can be seen in the central cylinder of the other root (2), probably representing calcified xylem vessels. Scale bar 200  $\mu\text{m}$ . D) Longitudinal section of a root, showing longitudinally elongate calcified cortical cells (c), and noncalcified central cylinder (v); compare with schematic root section in Fig. 5.1F. Scale bar 200  $\mu\text{m}$ . (continued on next page)



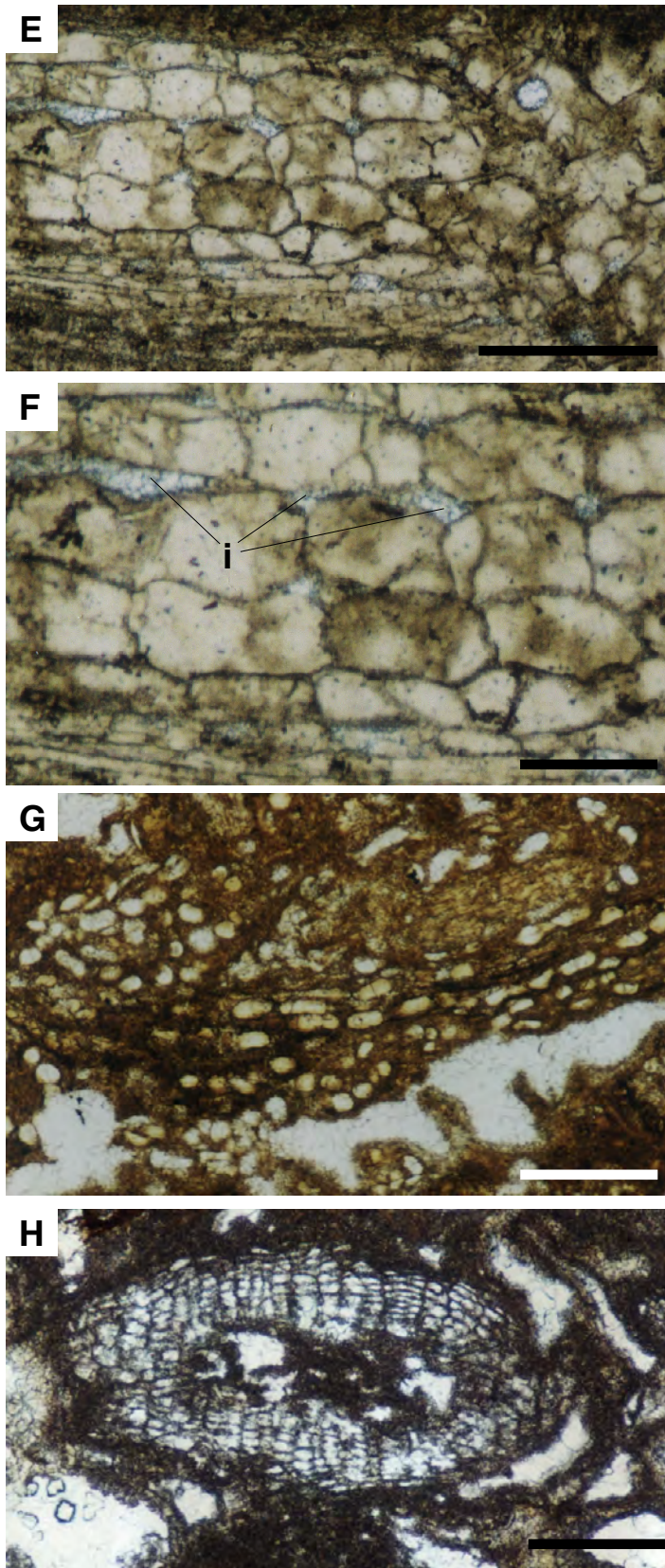


**Figure A5-2.8 (continued)**

E) Longitudinal section of a calcified root cortex. Scale bar 200 μm. F) detail of part E showing intercellular spaces in the cortex (i), filled by sparite cement. Scale bar 100 μm. G) Individual calcified root cells, representing several roots in longitudinal section with incompletely calcified root cortex. Scale bar 500 μm. H) Permineralised root in cross section. Although the cellular structure is well preserved, this root differs essentially from the calcified roots in parts B-G in that it exhibits no evidence of active, plant-controlled intracellular calcification but only impregnation of lignified cellular tissue by sparite cement. Scale bar 200 μm.

## A5-2.6 Rhizogenic microfabric

### A5-2.6.1 Intracellularly calcified roots

Calcified roots from the laminar horizon of the Sv. Martin calcrete exhibit high variability in size, shape, and structure (Fig. A5-2.8). The diameter of roots, as seen in cross sections, varies from 150  $\mu\text{m}$  to more than 1 mm. The length of calcified roots ranges from several millimeters to more than 1 cm. The maximum observed length of a longitudinal root section was more than 2 cm. The shape of the roots can be straight or curved, rarely showing branching and development of lateral roots. In plane-polarized light, the calcified root cells are most commonly light pale brown or yellow in color owing to dark inclusions in the calcite. Under crossed polars, the calcite in the root cells typically shows monocrystalline structure with uniform or sweeping extinction, or an aggregate pattern, composed of several calcite crystals.

Many of the calcified roots in thin sections exhibit perfectly preserved original cellular structure of the root cortex (Fig. A5-2.8B-F). The arrangement of cortical cells in individual roots is highly variable. The cortex can be composed of two to more than ten layers of cells. As seen in many longitudinal and cross sections, all the cells of the cortex are completely calcified (Fig. A5-2.8B, D, E, F), whereas some root sections are calcified incompletely (Fig. A5-2.8B) or only show few individual calcified cortical cells (Fig. A5-2.8G) without any other distinguishable elements of the root structure.

Except the cortex, other parts of the root exhibit almost no evidence of calcification. The central part of the root, corresponding to the vascular cylinder (stele; see Fig. A5-2.1E, F), is not calcified. This area is usually subsequently filled by dark brown micrite (Fig. A5-2.8C, D) or sparry calcite cement (Fig. A5-2.8B). In some cases, indistinctive cellular structures can be seen in the central cylinder; these may represent relicts of xylem vessels (Fig. 5.8C). Thin outermost cells, observable only in few sections of roots (Fig. A5-2.8D), probably represent calcified epidermis (cf. Fig. A5-2.1E, F). Significantly, calcified roots from the Sv. Martin calcrete exhibit no evidence of secondary growth (development of root tissues resulting from secondary thickening), indicating that the calcification was limited to the young parts of the fine roots.

#### A5-2.6.2 *Microcodium*, calcified roots and intermediate morphologies

The typical architectural elements of *Microcodium* structures, as defined above (Fig. A5-2.1A, B, C), are elongate polyhedrons (pyramids or prisms) of calcite. Calcified cortical root cells described and illustrated in the previous section (Fig. A5-2.8B-G) are generally isodiametric in shape in transverse cross sections but can be distinctly elongate in longitudinal sections (Fig. A5-2.8D, G; compare with Fig. A5-2.1F). However, many examples of calcified roots from the crudely laminar horizon of the Sv. Martin calcrete exhibit strong radial elongation of outer cortical cells, thus creating features which appear to be identical to “classical” *Microcodium* aggregates. Actually, a complete range of intermediate morphologies can be observed (Figs. A5-2.9, A5-2.10).

Some of the root cross sections exhibit only slightly increased size of individual cells in the outer layer of the cortex (Fig. A5-2.10A, B) but still display recognizable root cellular structure. Other examples show significantly enlarged single cortical cells which have isodiametric or polygonal morphology in cross section. The root in Figure A5-2.10B exhibits a completely modified single cortical layer consisting of strongly enlarged cells of quadrangular shape.

Outer cortical cells in some root sections show only an accentuated elongate shape (Fig. A5-2.10C). Many examples, however, consist of strongly radially elongate pyramidal (Fig. A5-2.9A, B) or prismatic cells (Fig. A5-2.9C) characteristic of *Microcodium*. Relicts of the root structure can be seen in some of these sections (Fig. A5-2.9A, B), whereas most of the sections exhibit no evidence of multilayer cellular structure (Fig. A5-2.9C) as seen in nonmodified roots. Aggregates composed of elongate polyhedral cells can be radially symmetrical, forming “rosette” structures with a noncalcified axial canal (Fig. A5-2.10B, C), or of strongly asymmetrical shapes, exhibiting subparallel orientation of cells typical of laminar forms of *Microcodium* (Freytet and Plaziat (1982).

Petrographically, the modified cells and prisms do not differ significantly from non-modified calcified root cells except that they can be clearer and of lighter color, and contain fewer dark inclusions in the calcite. Strongly elongate polyhedral cells from the Sv. Martin calcrete (Fig. A5-2.9) have the typical microstructure of *Microcodium* (Klappa 1978; Freytet and Plaziat 1982). The monocrystalline pyramids or prisms frequently exhibit a distinctive central part, composed of more limpid or fine-grained calcite (Fig. A5-2.9A, B). Rare longitudinal sections through the internal part of the pyramids show indistinctive filamentous structure similar to filaments (striae) documented by Lucas and Montenat (1967), Freytet



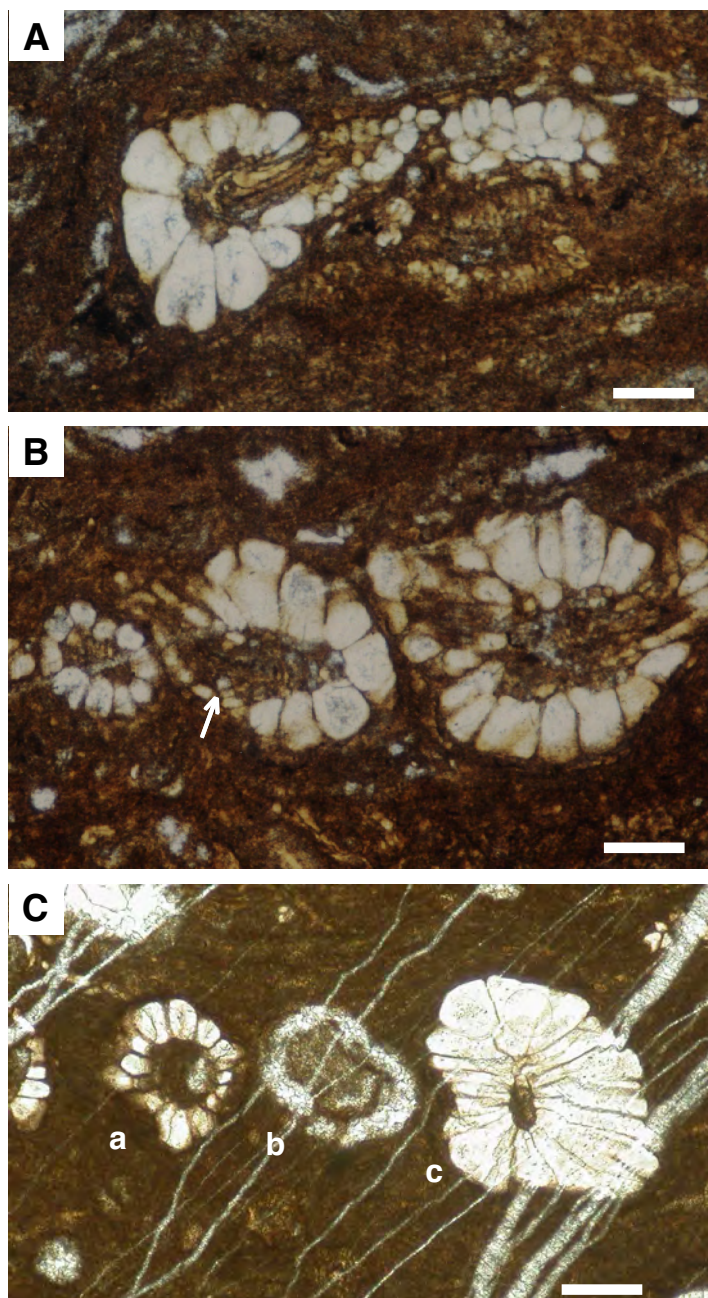


**Figure A5-2.9**

Photomicrographs of modified roots, all in plane-polarized light. Scale bar in all figures 100  $\mu\text{m}$ . A, B) Calcified root structures composed of elongate prismatic cells, creating typical *Microcodium* structure. Relicts of a multilayer root structure can be seen in some sections (arrow). C) Cross sections of three roots, exhibiting different degree of calcification and cell elongation; (a) is composed of a single layer of isodiametric to slightly elongated cells; (b) noncalcified root tubule; (c) typical *Microcodium* (“rosette”) structure.

and Plaziat (1982), and Morin (1993).

Different phases of calcite precipitation are most clearly seen in plane-polarized light. Both isodiametric calcified root cells and elongate morphologies are composed of light brown or yellowish calcite with cloudy appearance which differs significantly from clear white spar mosaics that fill individual pores and vascular cylinders and surround individual calcified roots (Fig. A5-2.8A, B). Under cathodoluminescence both the cell-filling calcite and clear spar are either nonluminescent or exhibit hardly distinguishable variations of dull red luminescence. Under UV fluorescence calcified cells and *Microcodium* prisms rarely show very weak brown fluorescence. Weak yellow fluorescence was observed in thin layers

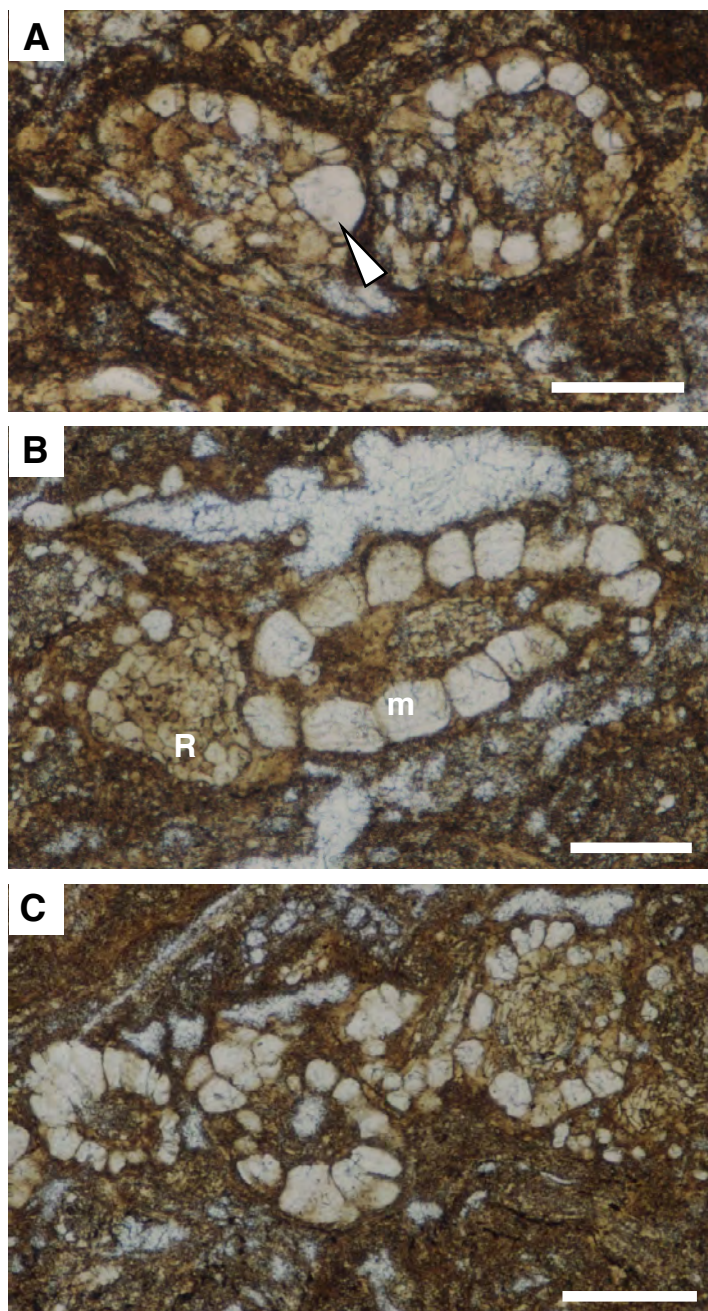


**Figure A5-2.10**

Photomicrographs of modified roots from the Sv. Martin calcrete, all in plane-polarized light. Sections of calcified roots show different degrees of cell elongation and increase in size. A) Single enlarged cell in the outer cortical layer (arrow). Scale bar 100  $\mu\text{m}$ .

B) Strongly enlarged quadrangular cells (m) and smaller, normal-sized cells (R). Scale bar 100  $\mu\text{m}$ .

C) Several cross sections of calcified roots with enlarged and elongated cortical cells.

Scale bar 150  $\mu\text{m}$ .

surrounding the roots, which are dark brown in transmitted light and probably correspond to the remnants of organic matter of the root epidermis.

Electron microprobe and SEM EDS microanalyses revealed that all calcite generations consist of low-Mg calcite with 0.2–0.8 mol %  $\text{MgCO}_3$  (see also Appendix A5-5). No significant variation was observed between different forms of calcite except minor amounts of sulfur (less than 0.3 wt %  $\text{SO}_3$ ) which have been detected in several calcified root cells and *Microcodium* prisms. The presence of sulfur indicates that dark inclusions in calcite of the calcified roots consist of sulfur-rich organic matter.



## A5-2.7 Discussion

### A5-2.7.1 Calcification and morphological modification of cortical root cells: Development of *Microcodium*

Abundant calcite aggregates in the crudely laminar horizon of the Sv. Martin calcrete (Fig. A5-2.8) and calcified tubules in the Trstelj laminar crust (Fig. A5-2.7) exhibit perfectly preserved structural details of plant root tissues. In both cases, the root textures provide direct proof for the rhizogenic origin of these laminar horizons. Importantly, the exceptional preservation of root structural details in the Sv. Martin laminar horizon is not just a consequence of favorable physicochemical conditions in the soil, leading to permineralization of plant tissues (Fig. A5-2.8H; Scott 1992; Martin 1999; Retallack 1997, 2001) but results from biologically controlled precipitation of calcite in living cortical cells of plant roots.

Active calcification (biomineralization) in living roots is indicated by selective (incomplete) calcification seen in some sections, in which only some of the cortical cells are calcified (Fig. A5-2.8C, G). This is particularly true of noncalcified intercellular spaces in the root cortex (Fig. A5-2.8F) that are filled by clear sparite, identical to sparite cements in larger pores and between the individual calcified roots.

The most important features of the Sv. Martin laminar calcrete are morphologies intermediate between the typical *Microcodium* aggregates and intracellularly calcified roots. These forms provide unambiguous evidence for the root origin of *Microcodium* and thus support previous rhizogenic interpretations (Klappa 1978; Morin 1993; Wright et al. 1995; Alonso-Zarza et al. 1998). However, most of the previous studies which considered *Microcodium* as a product of calcification of plant roots are based on atypical material, which either closely resembles the structure of plant roots (Alonso-Zarza et al. 1998) or is identical to the recent calcified roots (Klappa 1978) but does not exhibit the single-layered structure of strongly elongate cells, which are the main characteristics of *Microcodium*.

The morphological continuum of calcification structures described herein provides a missing link between modern calcified roots (e.g., Jaillard et al. 1991) and atypical forms of *Microcodium* (Bodergat 1974; Esteban 1972, 1974; Klappa 1978; Goldstein 1988; Alonso-Zarza et al. 1998) on one side, and the typical ancient *Microcodium* structures on the other. The intermediate forms show that the typical *Microcodium* aggregates formed through the morphological transformation of the root cortical cells. These transitional forms actually

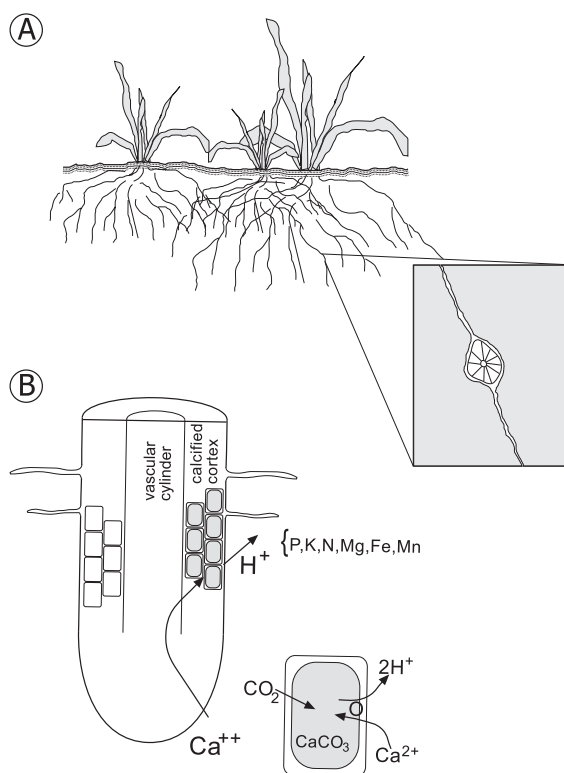


show calcified roots in different stages of *Microcodium* development. Characteristically, the process of morphological modification starts with the increase in size of the cells in the outermost cortical layer, producing large cells of relatively isodiametric shape (Fig. A5-2.10C). With the continuation of growth in radial direction, the cortical cells develop elongate pyramidal (polyhedral) shape. The polygonal arrangement of elements, similar to honeycomb structures, appears to be a consequence of a densely packed structure formed through the increased radial growth of cells. This kind of morphology, size, and arrangement of root cells has not been observed in modern plants, but there is a large body of evidence for the morphological transformation of the root structure and production of special forms of roots due to the adaptation of plants to specific ecological conditions (e.g., Fahn 1982; Vartanian 1996). Although the shape and structure of *Microcodium* may reflect distortion of the normal root cells prior to calcification, it is more likely that it developed by growth of the calcite within the cells, which distorted the cell shape, creating strongly elongate polyhedral forms. Similar but less pronounced radial distortion (elongation) of the cortical cells has also been documented in modern calcified roots (Jaillard 1987a).

#### A5-2.7.2 *Physiology of root calcification*

Calcification of roots presumably enhances production of protons (McConnaughey and Whelan 1997) through exchange of  $\text{Ca}^{2+}$  and  $2\text{H}^+$  using plant-respired  $\text{CO}_2$  (Fig. A5-2.11). Considerable proton effluxes from roots, often encountered in the rhizosphere, represent one of the modes of rhizosphere acidification as a profitable strategy for acquiring mineral nutrients. Rhizosphere acidification strategies are particularly evident in plants that grow preferentially on carbonate-rich alkaline soils of high acid-neutralizing capacity (Marschner 1995; Hinsinger 1998).

Significantly, modern calcified roots and virtually all occurrences of *Microcodium* are typically, although not exclusively (e.g., Alonso-Zarza et al. 1998), associated with nutrient-poor calcareous soils and carbonate substrates (Jaillard 1987a; Jaillard et al. 1991; Freytet and Plaziat 1982; Wright 1994; Wright et al. 1995). Calcification within the vacuoles of root cortical cells, coupled with extrusion of protons (Fig. 5.11B), thus most probably represents an effective mechanism for the nutrient acquisition (Jaillard and Hinsinger 1993; McConnaughey and Whelan 1997; McConnaughey 1998; Hinsinger 1998). Proton (acid) secretion in itself enables plants to mobilize sparingly soluble nutrients in the rhizosphere and to cope with constraints on mineral nutrition, such as low iron and zinc availability

**Figure A5-2.11**

A) Roots penetrate into fissures and dissolve carbonate substrate through acid secretion into the rhizosphere and simultaneous calcification of root cells, creating *Microcodium* structures.

B) Diagrammatic longitudinal section of the apical region of a root. Calcification within the vacuoles of root cortical cells act as a proton generator, allowing the plant to acidify the rhizosphere and thus acquire mineral nutrients from the soil. Production of protons is enhanced through exchange of  $\text{Ca}^{2+}$  and  $2\text{H}^+$  using plant-respired  $\text{CO}_2$ , (from McConnaughey and Whelan 1997).

(Marschner 1995). Carbonate precipitation in the vacuoles of cortical cells may additionally increase production of protons, which are potentially useful for nutrient assimilation (McConnaughey and Whelan 1997). Simultaneously, accumulation of  $\text{CaCO}_3$  in the root tissue might reflect protection of the plant from excessive calcium and bicarbonate concentrations in the soil solutions (Marschner 1995).

This nutrient-acquiring mechanism can explain both the motivations for carbonate precipitation in living root cells of terrestrial plants and the ability of *Microcodium* to dissolve and corrode carbonate substrate (Fig. A5-2.12A, B). The latter effect has actually been observed in modern calcified plant roots as well. In concert with rhizosphere acidification, calcified roots in calcareous soils are often surrounded by a decalcified rhizocylinder of aluminosilicate clayey matrix (Jaillard 1985, 1992; Jaillard and Callot 1987; Jaillard and Hinsinger 1993). Subsequent disintegration of the calcified roots can create distinctive channels on the surface of corroded hard carbonate substrate (Fig. A5-2.12C), analogous to corrosive features typical of *Microcodium* (e.g., Freytet and Plaziat 1982; Morin 1993).

Calcification in the root cells of modern plants appears to be a rapid process. Jaillard (1987a) showed in *in vitro* experiments under controlled conditions that living roots of oilseed rape were able to precipitate calcite in the cortical cells within only a few hours, and

that fully calcified cells were developed in a few days. Presumably, *Microcodium* structures also formed relatively rapidly under favorable conditions.

Most higher plant species facilitate the acquisition of mineral nutrients by the association of mycorrhizal fungi with the root system (Marschner 1995, Wilcox 1996). Klappa (1978) interpreted *Microcodium* as a calcification product of a mycorrhizal association. Indication of mycorrhizal symbiotic association has also been noted by Alonso-Zarza (1999), who recognized the common occurrence of fungal filaments in the external parts of calcified roots in Miocene laminar calcretes from central Spain. However, Jaillard (1987a, 1992) and Jaillard et al. (1991) found no evidence of mycorrhizae in calcified cells from present-day calcareous soils but only traces of post-mortem taphonomic alteration of calcite crystals by endolithic microorganisms. Likewise, there is no clear evidence of mycorrhizae in *Microcodium* structures. Calcification products of fungi (e.g., needle-fiber calcite forming alveolar septal structure; Wright 1986; Verrecchia and Verrecchia 1994; Verrecchia 2000) are one of the most prominent biogenic constituents of calcretes and are often associated with *Microcodium* and calcified roots, but there is no direct proof for the role of fungi in precipitation of calcium carbonate within the root cells and formation of *Microcodium*.

#### *A5-2.7.3 Environmental significance of calcified roots and Microcodium*

Recent calcified roots almost invariably occur in calcareous soils in semiarid regions with pronounced seasonal moisture regime (Jaillard et al. 1991). Similarly, *Microcodium* is most abundant in calcic palaeosols and calcretes that have been interpreted as a product of seasonal semiarid climate (Wright 1994; Wright et al. 1998). In general, calcite precipitates in extracellularly calcified roots (rhizcretions) are formed through evapotranspiration and calcification mediated by root-associated microorganisms in the rhizosphere during relatively dry periods with a net moisture deficit (Jones and Ng 1988; Wright 1994). In contrast, calcified root cells and *Microcodium*, as supposed products of a nutrient-acquiring mechanism, most probably formed through increased metabolic activity of plant roots during times when the soil was adequately moist and, correspondingly, when the soil environmental conditions became favorable for growth and proliferation of fine roots (e.g., North and Nobel 2000).

Palaeoenvironmental distribution of *Microcodium* is characterized by two important attributes. First, as noted above, occurrence of *Microcodium* is almost invariably associated



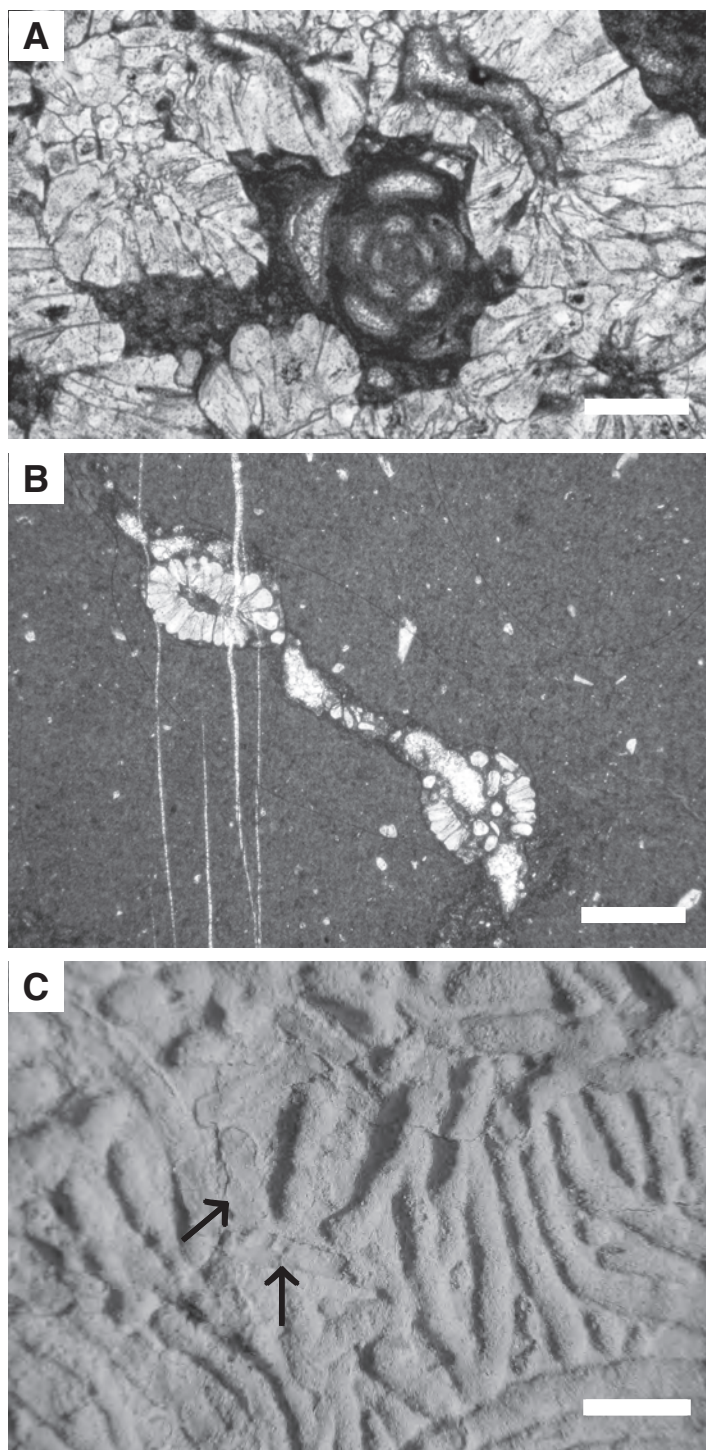


**Figure A5-2.12**

A) *Microcodium* corroding miliolid foram in a relatively unaltered bioclastic packstone. Thin section in plane-polarized light. Scale bar 0.5 mm.

B) Typical *Microcodium* corrosion fissure in the massive calcrete of the Sv. Martin profile. Thin section in plane-polarized light, scale bar 1 mm.

C) Surface of a clast of marly limestone from the Quaternary calcrete at Sella, SE Spain, showing distinctive corrosive channels left after disintegration of calcified roots. Remnants of calcified roots are still preserved in some channels (arrows). Scale bar 3 mm.

with carbonate rocks and calcareous soils. Second, most of the accumulations of *Microcodium* occur within continental depositional settings that are affected by pedogenesis and/or calcrete formation within palustrine, fluvial, and, rarely, karstic settings (Freytet and Plaziat 1982; Wright and Tucker 1991; Wright 1994; Alonso-Zarza 2003). The presence of disaggregated *Microcodium* in shallow marine deposits (Appendix A5-3, Fig. A5-3.3) may

result from erosion of a subaerial exposure surface during transgression and subsequent incorporation of eroded material into the overlying marine sediments, whereas in situ occurrence of *Microcodium* aggregates in shallow marine facies always indicates subaerial exposure and pedogenic modification of the sediment.

Examples of the *Microcodium* occurrences in almost unaltered shallow-marine limestones (Fig. A5-2.5.12A; Košir 1998) indicate that its formation took place during early stages of calcrete development. Similar association of *Microcodium* with early stages of soil development in the Upper Cretaceous peritidal carbonates has been noted by Martin-Chivelet and Gimenez (1992). However, aggregates of *Microcodium* can be reworked and included in more developed calcretes. Furthermore, because of the constructive-destructive nature of many rhizogenic calcretes, *Microcodium* colonies can often be seen corroding indurated horizons from earlier stages of soil development (Figs. A5-2.12B, A5-3.01).

Accumulations of *Microcodium* probably reflect a specific type of vascular plants of a pioneer community (i.e., initial stage of a primary plant succession; Barbour et al. 1999) which were able to colonize carbonate substrates during early phases of subaerial exposure. Calvet et al. (1991) suggested that *Microcodium* represents the product of garrigue (scrub) vegetation, whereas Wright et al. (1995) mentioned that it was likely associated with riparian vegetation. Jaillard (1984, 1992), Becze-Deák et al. (1997), and Alonso-Zarza (1999) noted a possible relationship of modern and fossil calcified roots with Graminae. However, there is no conclusive evidence for the relationship of *Microcodium* and even modern calcified roots with any specific group of plants. It is likely that the root calcification is and was used by plant species of different, and probably not even closely related, taxonomic groups.

Similarly, *Microcodium* may reflect a specific vegetation type and possibly mycorrhizal or non-mycorrhizal symbiotic association that appeared by the Mesozoic. The fossil record of *Microcodium* is unusual, with its peak occurrence in the early Palaeogene (especially the Palaeocene and early Eocene), and later in the Miocene (Wright and Tucker 1991; see also review of geographical and stratigraphical distribution in Klappa 1978). Smit (1979) and Bignot (1994, 1995) stated that *Microcodium* did not appear before the early Palaeocene, arguing that its appearance in Cretaceous rocks resulted from a deep penetration of *Microcodium* into the older rocks from the overlying Tertiary formations. However, there are numerous unambiguous and well-documented reports on *Microcodium* from the Upper Cretaceous carbonate successions of the peri-Tethyan region (Martin-Chivelet and Gimenez 1992; Gušić and Jelaska 1990; Landrein et al. 2001; amongst others), whereas most

of the older records are not reliable and/or are based on material that neither resembles typical *Microcodium* aggregates (e.g., Goldstein 1988; Immenhauser et al. 2000) nor exhibits the structure of non-modified calcified roots.

#### A5-2.8 Summary and conclusions

The crudely laminar calcrete horizon from the succession of Paleocene shallow-marine carbonates of the Trstelj Formation contains calcite aggregates which exhibit perfectly preserved structural details of plant root tissues. Morphology and structure of these aggregates indicate that they formed through biologically controlled precipitation of calcium carbonate within the root cortical cells. Furthermore, morphologies intermediate between the typical *Microcodium* aggregates and intracellularly calcified roots provide unambiguous evidence for the root origin of *Microcodium* and thus support previous rhizogenic interpretations. These transitional forms show that *Microcodium* aggregates formed as a consequence of morphological transformation of root cortical cells due to growth of the calcite within the cells, which distorted the cell shape in the radial direction. The morphological continuum of observed calcification structures provides a missing link between the cellular structure of fine roots in modern plants, typically composed of several layers of isodiametric cells, and the architecture of classical *Microcodium*, which is characterized by a single layer of elongate pyramidal or prismatic crystals of calcite.

Calcification of cortical cells and creation of *Microcodium* structures can be explained as an effective mechanism used for nutrient absorption by certain type(s) of vascular plants. Formation of *Microcodium* and intracellular calcification of roots in general most probably represent a special adaptational strategy of plants that enhance mobilization of elements on nutrient-poor calcareous substrates through proton secretion into the rhizosphere. This mechanism explains both the motivations for carbonate precipitation in living root cells of terrestrial plants and the ability of *Microcodium* to corrode carbonate substrate.

The widespread occurrence of *Microcodium* in almost unaltered shallow-marine limestones indicates that its formation took place during early stages of calcrete development. Accumulations of *Microcodium* probably reflect specific types of vascular plants of a pioneer community which had the capacity to colonize carbonate substrates during early phases of subaerial exposure.



## Appendix A5-3 Localities of *Microcodium* material described and illustrated in Chapter 5

**Table A5-3.1.** *Microcodium* localities. \*SI - Slovenia

locality*	setting	lithostratigraphic unit	Age	coordinates/ remarks
Trstelj (Kras, SI)	calcrete	Trstelj Fomation/ Alveolina-Nummulite Limestone (ANL)	Paleocene/Eocene	45°51'54"N 13°42'12"E
Sv. Martin (Kras, SI)	calcrete	Trstelj Fm	Paleocene	45°50'56"N 13°45'42"E
Šumka section (SI)	subaerial exposure surfaces in shallow marine limestone	Trstelj Fm	Upper Paleocene	45°51'05"N 13°45'15"E
Kremance (Kras, SI)	calcrete/ disconformity	Trstelj Fm/ANL	Paleocene/Eocene	N45.872490, E13.659269
Vrabče (Kras, SI)	palustrine limestone	Liburnian Fm	?Maastrichtian	N45.664592 E13.966706
Dolenja Vas (Kras, SI)	palustrine limestone	Liburnian Fm	Maastrichtian/ Paleocene	N45.664592 E13.966706
Pusto brdo Section, Trstelj (Kras, SI)	calcrete	Trstelj Fomation/ Alveolina-Nummulite Limestone (ANL)		N45.664592 E13.966706
Slavnik (Kras, SI)	laminar calcrete (rhizolite)	Liburnian Fm	?Upper Maastrichtian	N45.562779, E13.973458
Gabrak AC section (SI)	laminar calcrete (rhizolite) in paralic carbonate succession	Liburnian Fm	Paleocene	N45.689771 E13.977170
Divača AC section (SI)	laminar calcrete (rhizolite) in paralic carbonate succession	Liburnian Fm	Paleocene	N45.664592 E13.966706
Čebulovica section (SI)	subaerial exposure surfaces in paralic and shallow marine limestone	Liburnian Fm, Trstelj Fm	Paleocene	Figs. A5-3.02B and A5-3.03
Kozina section (SI)	subaerial exposure surfaces in shallow marine limestone	Trstelj Fm	Paleocene	Figs. A5-3.02C and A5-3.03
2TDK T1-7 core (SI)	subaerial exposure surfaces in shallow marine limestone	Trstelj Fm	Paleocene	See map in Figs. A5-3.02A

Table A5-3.1. (continued)

locality	setting	lithostratigraphic unit	Age	coordinates/ remarks
2TDK T1-9 core (SI)	subaerial exposure surfaces in shallow marine limestone	Liburnian Fm, Trstelj Fm	Paleocene (Thanetian)	See map in Figs. A5-3.02A
Koromačno, Istria (Croatia)	palaeokarst	/	Lower Eocene	N44.965916, E14.099531
Padriče (Kras, Italy)	subaerial exposure surfaces, paralic carbonates	Liburnian Fm	Cretaceous (Maastrichtian), Paleocene (Danian, Thanetian)	N45.656927, E13.830718
Fontjoncouse, France	palaeosol	“Garumnian”	Paleocene (Danian)	N43.04, E2.82
Esplugafreda, Spain	palaeosols	Talarn Fm Esplugafreda Fm Claret Fm	Paleocene, Eocene	GPS points T14-425 to T14-446 (Fig. A5-3.04)
Montpellier, France	breccia in a continental succession	‘Vitrollien’	Paleocene	43°39’00” N; 3°51’46” E
San Salvador, The Bahamas	aeolianite	North Point Member	Holocene	see Appendix A2-01.
Providenciales, Turks & Caicos	beach rock/calcrete	/	?Holocene	see Dickson (2014)

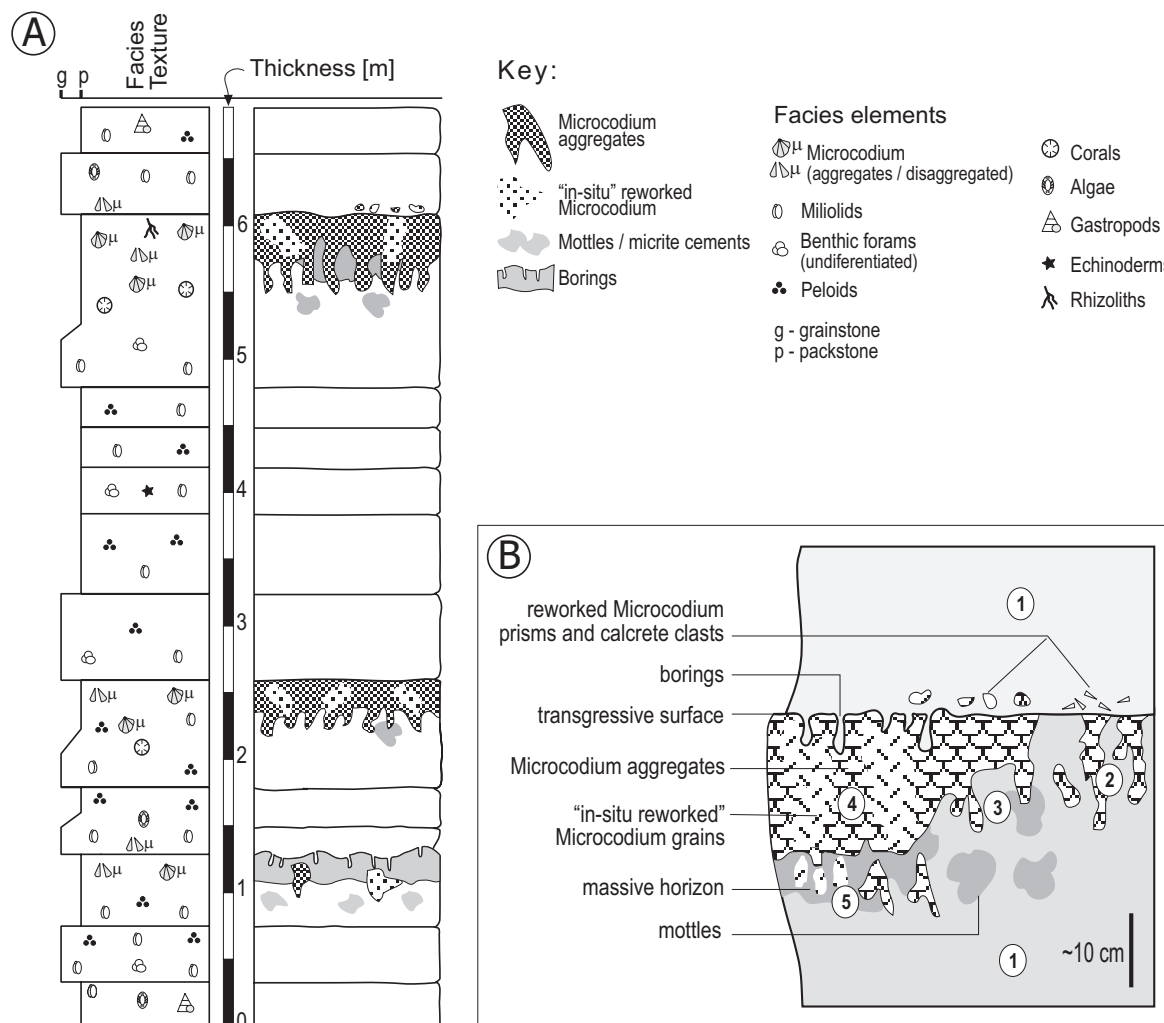


**Figure A5-3.01** Part of the Šumka section (see position in Fig. A5-2.4 and coordinates in Table A5.3-1) showing several subaerial exposure horizons within the succession of shallow-marine foram-dominated facies. **B)** Composite diagram showing major subaerial exposure features at different stages of development. *Microcodium* structures are the most common feature in all subaerial exposure profiles. *Microcodium* aggregates and disaggregated polyhedral elements may represent the only evidence for subaerial exposure (2) within relatively unaltered bioclastic packstone and grainstone (1). In some profiles, *Microcodium* forms massive accumulations which are almost completely composed of whole aggregates, corroding the cemented or uncemented substrate (3), and 'in-situ reworked' mass of disaggregated elements (4). The most developed horizons exhibit typical biogenic (beta) calcrite fabrics dominated by micrite coatings and cements, alveolar septal fabric, strongly micritized grains, and *Microcodium* which commonly occurs in two generations. Isolated *Microcodium* elements, which were formed during early stages of soil development, are embedded in dense micrite which form massive calcrite horizons. These massive horizons are cut through by a second generation of *Microcodium* (5), which formed in later stages of profile development.



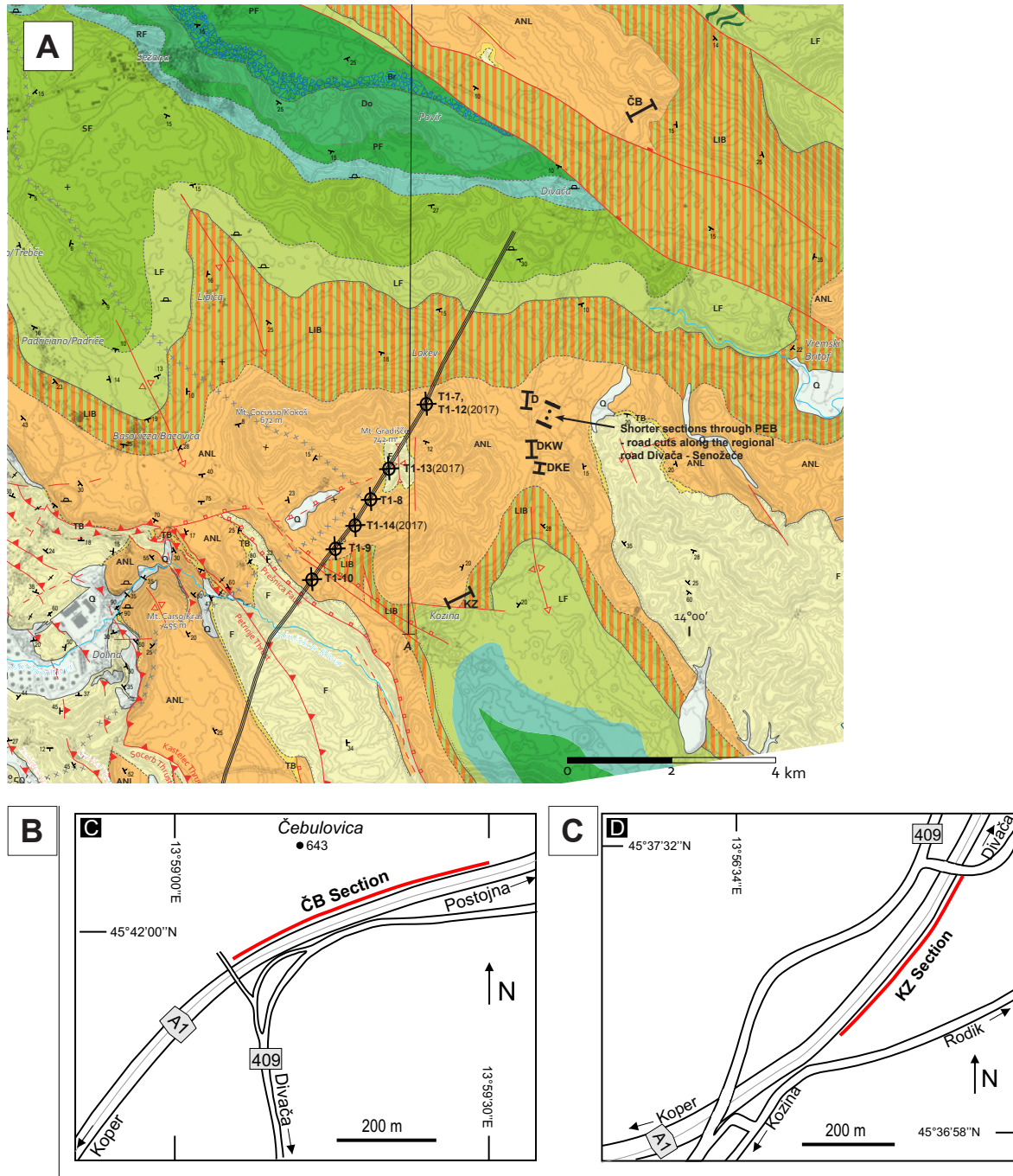


**Figure A5-3.02** A) Part of the geological map of the Trieste-Kome plateau of Jurkovšek et al. (2014) with marked localities (see Table A5-3.1.) B, C) Location maps of the motorway sections Čebulovica and Kozina (Zamagni et al. 2012)

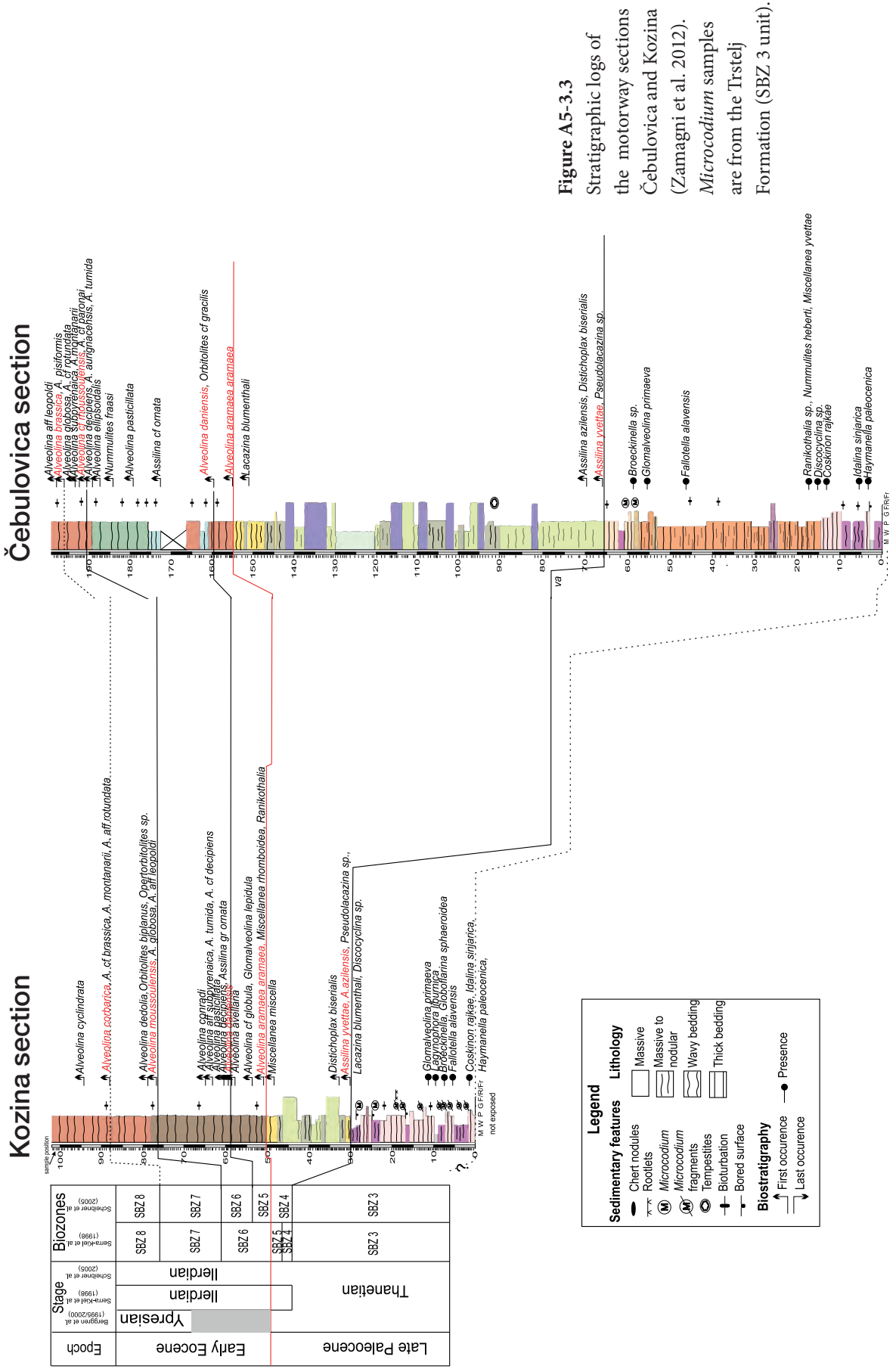


**Figure A5-3.3**  
Stratigraphic logs of the motorway sections of the motorway sections Čebulovica and Kozina (Zamagni et al. 2012). *Microcodium* samples are from the Trstelj Formation (SBZ 3 unit).



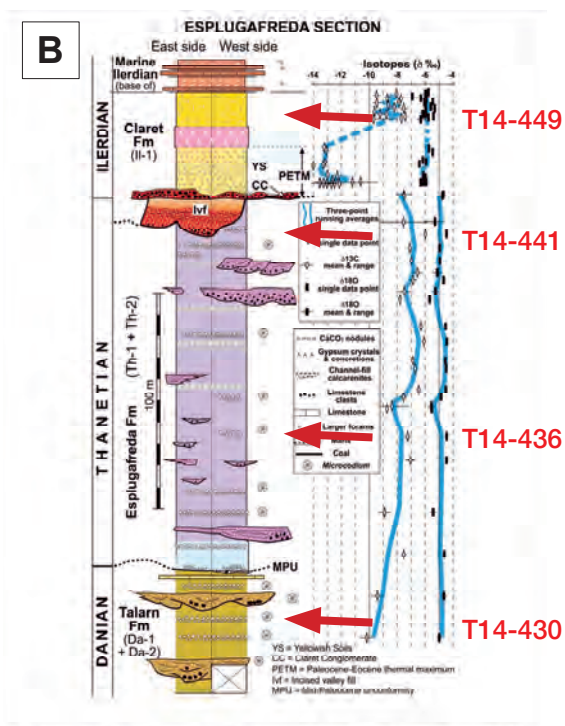
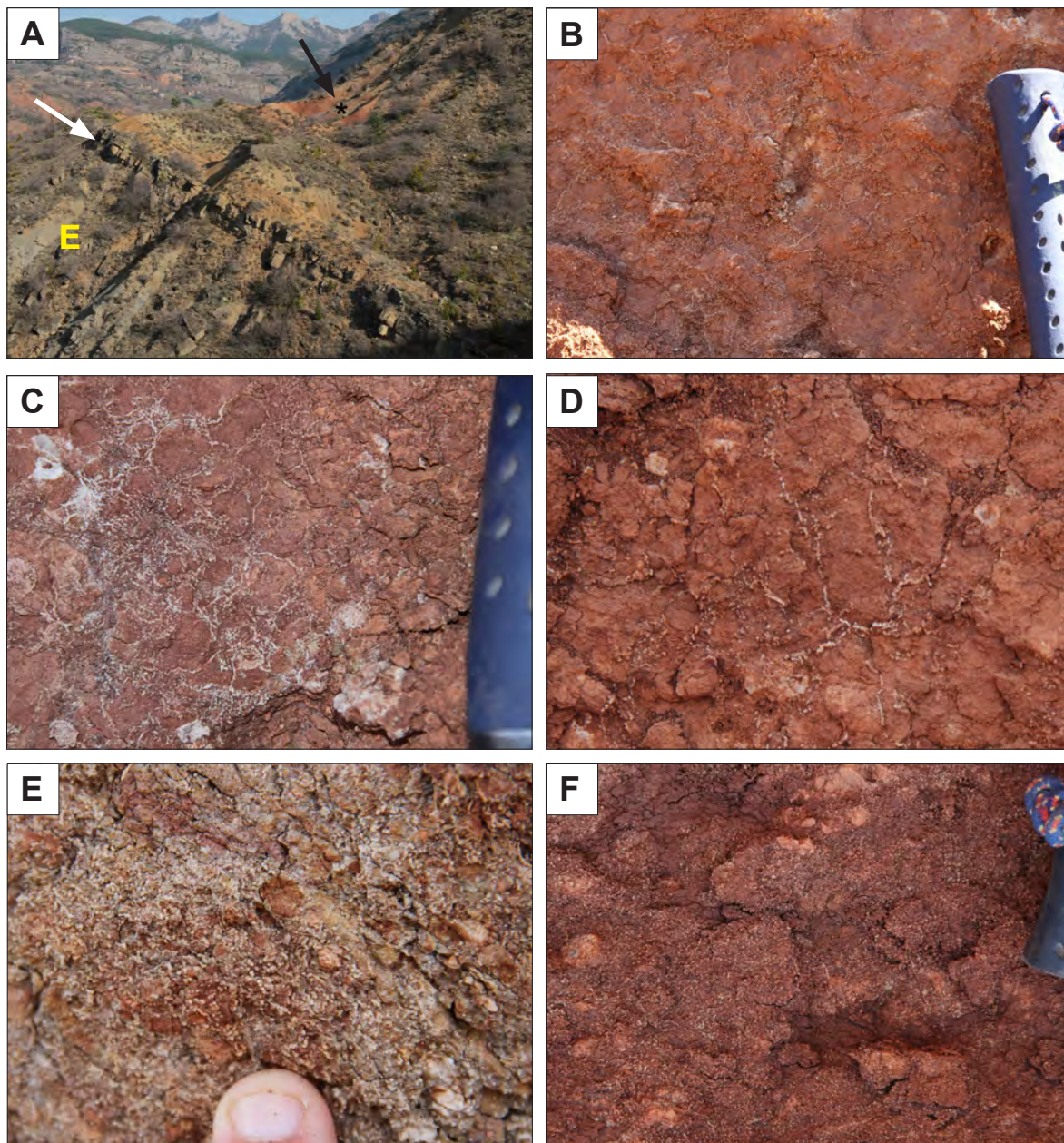


Fig. 18. Esplugafreda: columnar section of the Paleocene and lower Ilredian succession (location in Fig. 7A) and vertical  $\delta^{13}C$  isotopic profile (after Schwilz and Pupillo, 2003).

Figure A5-3.04 A) Google Maps satellite image of southern slopes of the Esplugafreda valley. Yellow points mark sampling locations of *Microcodium* for stable isotope analysis (see Section 5.7) B) Stratigraphic column for the Danian-Ilredian successions in the Esplugafreda location with marked *Microcodium* isotope samples. , From Baceta et al. (2011).





**Figure A5-3.05.**

A) Esplugafreda section (see Fig. A5-3.4B): Esplugafreda Formation (E) and Claret Formation (Claret conglomerate (white arrow), Upper red beds (black arrow). B-D) Anastomosing and branching *Microcodium* structures. E) Mottled palaeosol (GPS point T14-426) and F) dark red paleosol, both rich in partly disintegrated *Microcodium* aggregates. Cf. aggregates of Recent intracellularly calcified roots in Figs. 3.7D, 3.8A. All photos Paleocene, Esplugafreda Fm., Barranc d'Esplugafreda.



## Appendix A5-4 Petrography of *Microcodium*: Complementary material

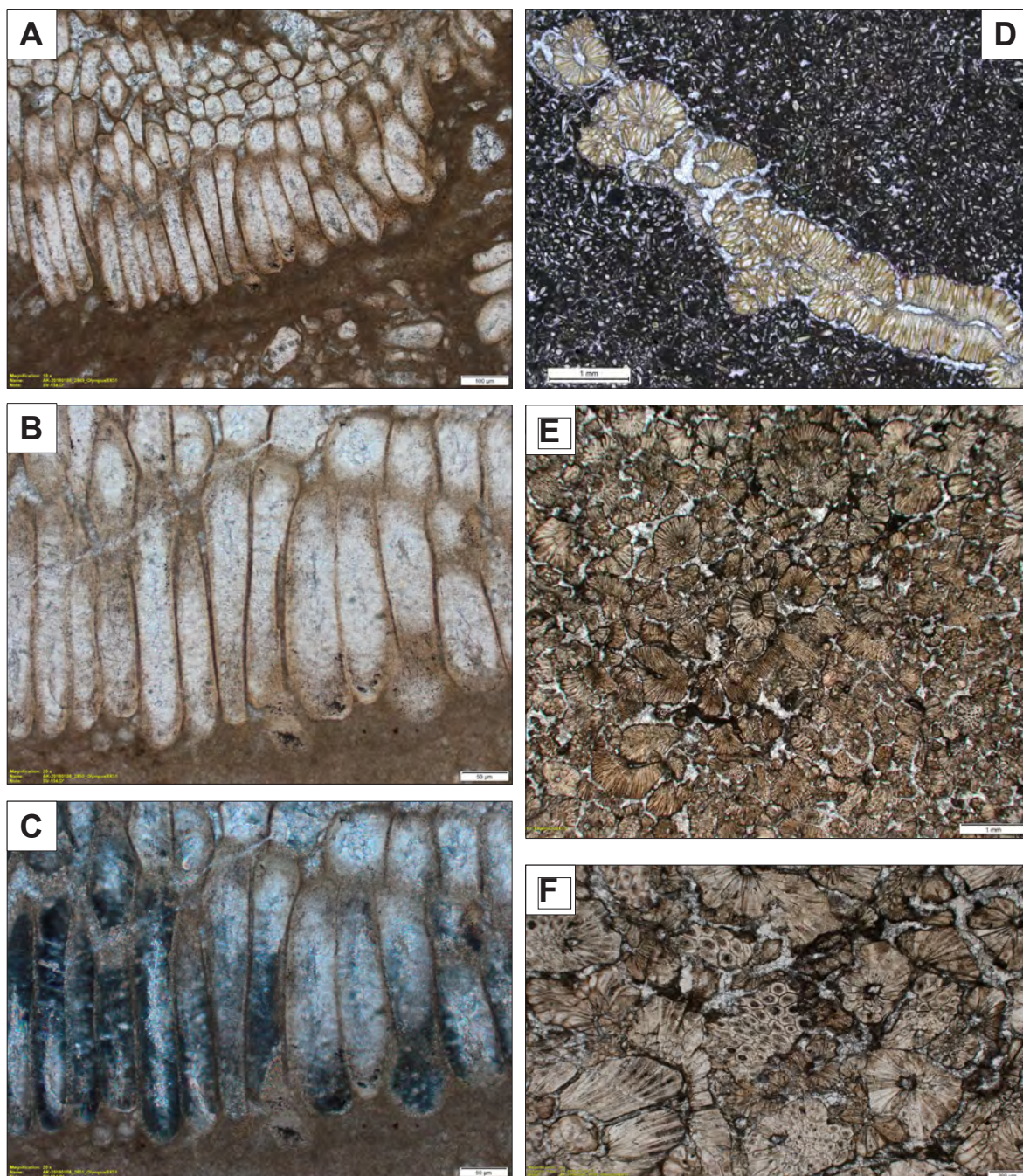


**Figure A5-4.01.** Morphology, architecture and crystal ultrastructure of *Microcodium*. A, B) PPL photomicrographs of *Microcodium* corn-cob aggregate with grains in cross section (upper part) and in longitudinal section with indistinctive radial two-layered ultrastructure, accentuated by minute, dark inclusions (micropores) in the darker, outer layer. Note rounded shape of cells! C) XPL of B. Divača AC Section, Lower part of the Trstelj Formation. D) *Microcodium* corroding a fissure in massive calcrete; PPL, Paleocene, Šumka. E, F) Pure microcodium limestone. Liburnian Formation, Vrabče locality.



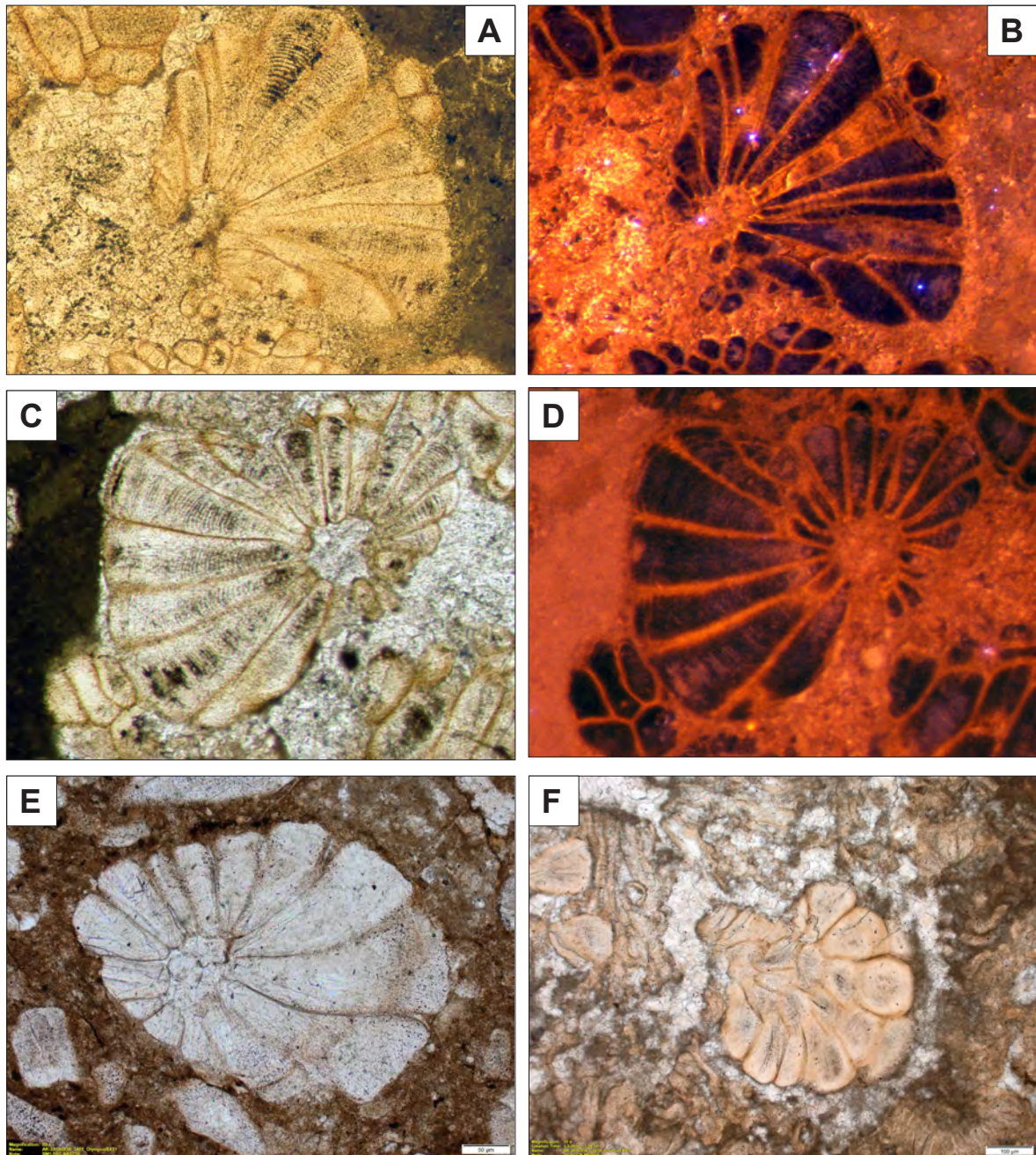


**Figure A5-4.02.** Morphology, ultrastructure and crystal morphology of *Microcodium* grains in thin sections. A-D) PPL/CL pairs of *Microcodium* rosettes composed of pyramidal elements, showing concentric striate ultrastructure. E, F) PPL photomicrographs of asymmetric *Microcodium* rosettes with inclusion-rich cloudy calcite. See sections 5.3 - 5.5 and captions in Figs. 5.13-5.19.



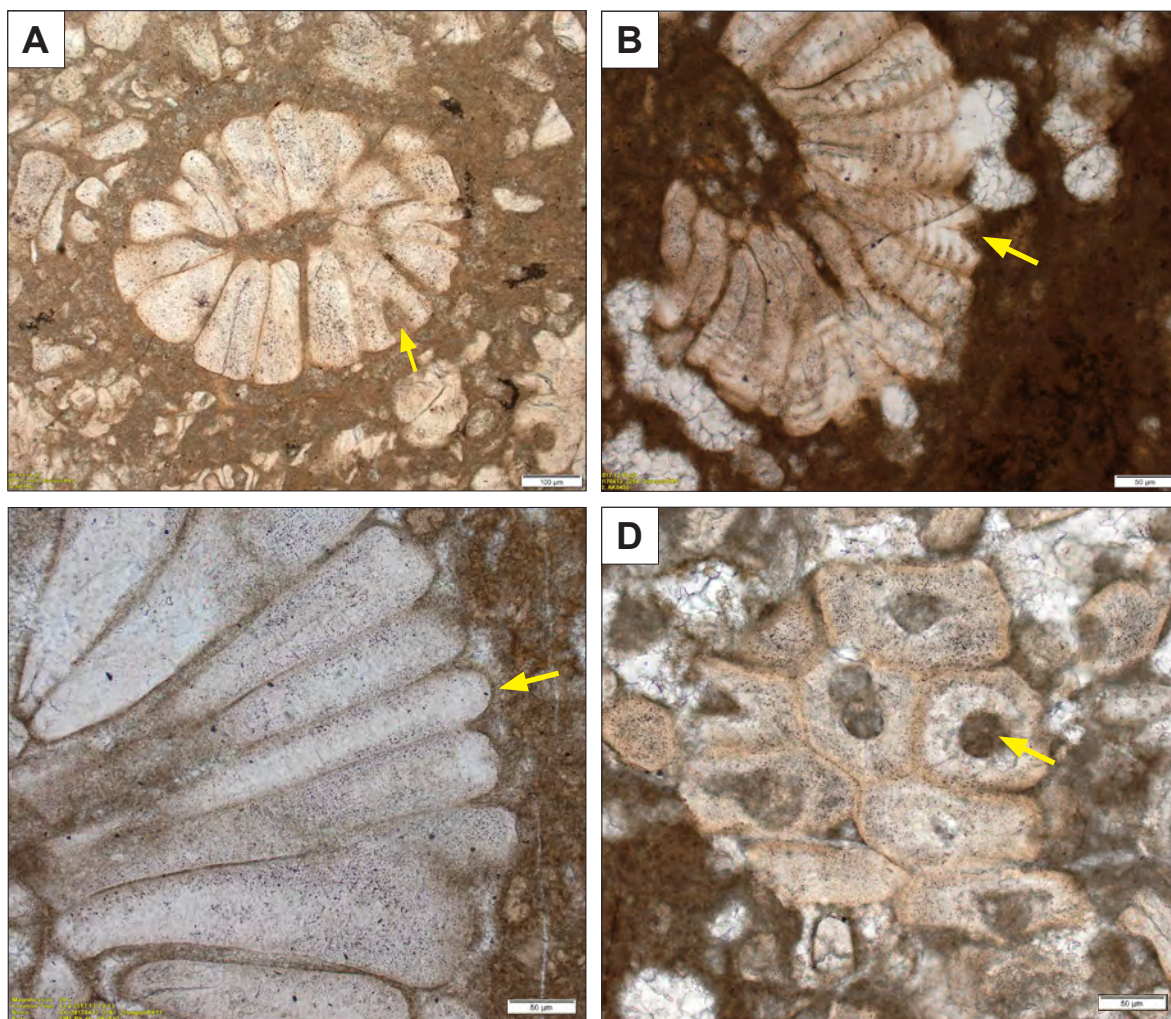


**Figure A5-4.03.** Morphology and ultrastructure of *Microcodium* grains, PPL photomicrographs. A) Rosette section, composed of pyramidal elements with indistinctive fibrous structure and B) rosette with elements with cisternoid vacuolar structure (see Fig. 5.15), both having individual grains showing pitted terminations. A: Liburnian Formation, Čebulovica section; B: Trstelj Formation, Šumka locality. C) Strongly elongate elements with pronounced rounded terminations (arrow). Sv. Martin calcrete. D) Transverse section through polyhedral (pyramidal) grains composed of inclusion-rich calcite. Note outer brown layer and hollows (terminal pits?) in the internal part. Trstelj Formation, Divača section.



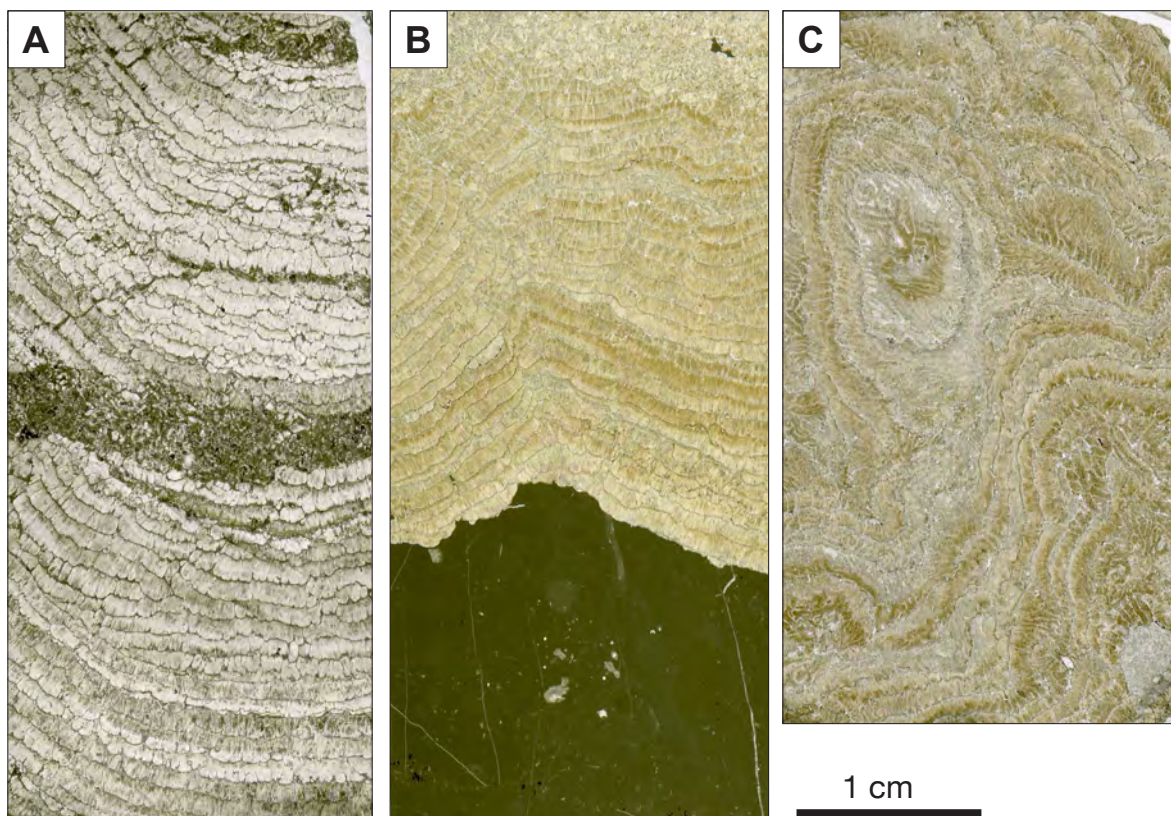


**Figure A5-4.04.** Morphology and architecture of lamellar (type 2) *Microcodium*. Thin sections scanned with a flatbed scanner. A and B) cross sections, C) section parallel to oblique to lamellae. All samples from breccia in Paleocene ('Vitrollian') continental succession near Montpellier, France.

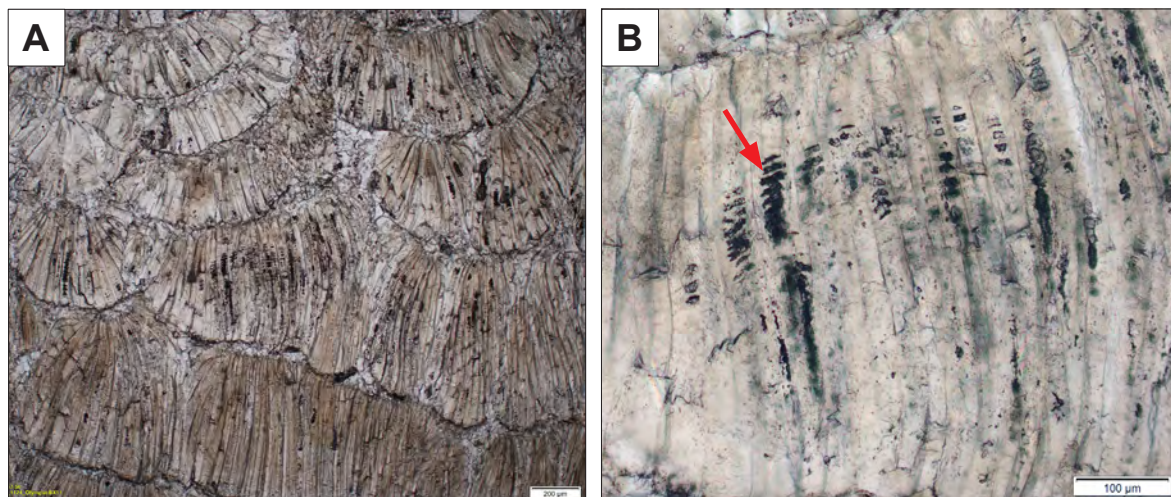


**Figure A5-4.05.** Lamellar *Microcodium*, thin section in PPL.

A and B) Aggregates composed of limpid, strongly elongate prismatic elements, some of them containing dark internal structures (red arrow in B), analogous to vacuoles shown in Figs. 5.15-5.18. Breccia in Paleocene ('Vitrollian') continental succession near Montpellier, France.



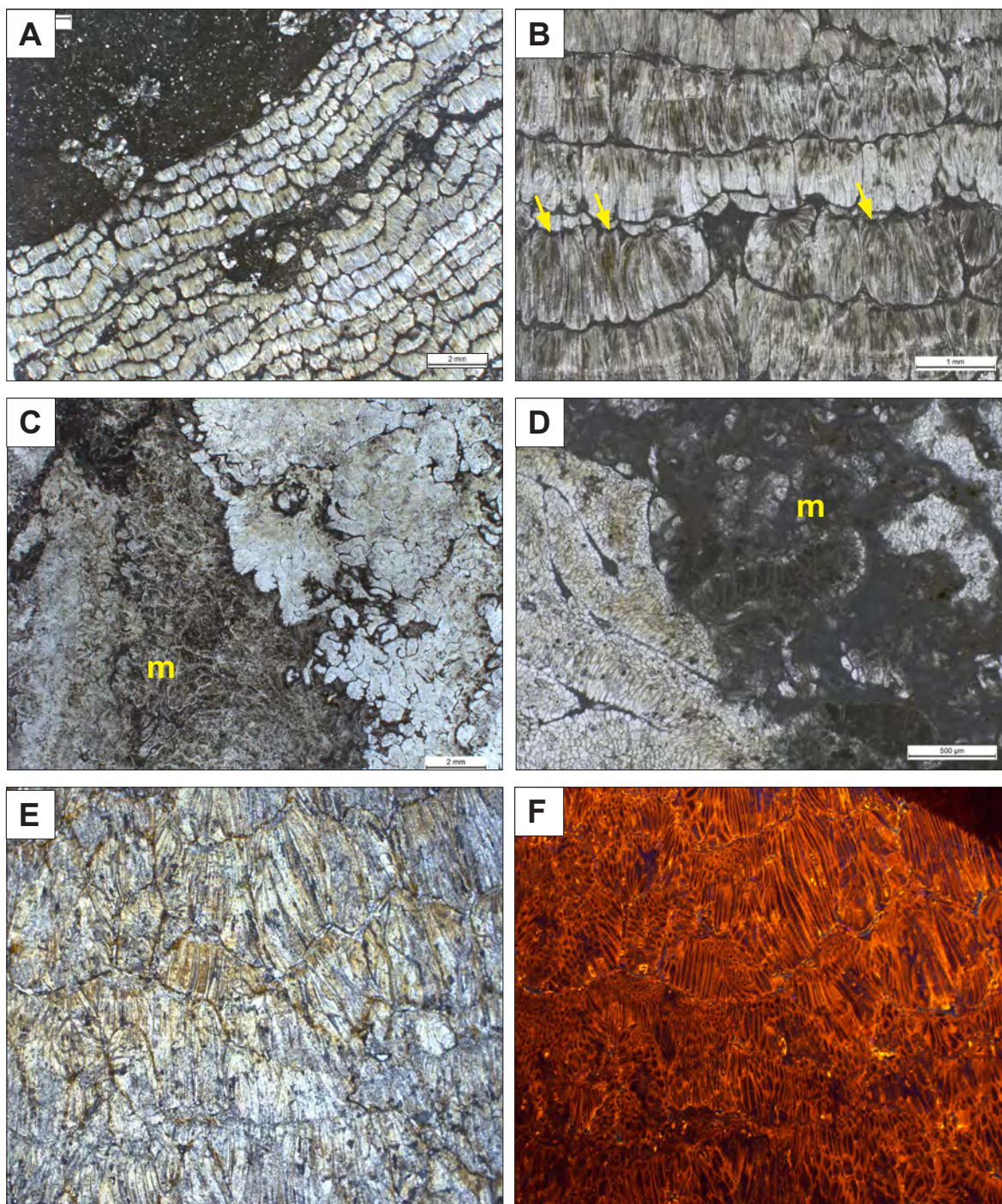


**Figure A5-4.06.** Morphology and architecture of lamellar *Microcodium* forms.

A) PPL image of lamellar *Microcodium* structure in cross section. Note mostly clearly distinguishable (separated) asymmetric aggregates organised in divisible layers. B) Cross section of dense lamellar structure composed of strongly elongate aggregates. Arrows indicate some of the aggregates with marginal grooves, corresponding to (ectopic) central/axial canals. C and D) sections parallel to slightly oblique to lamellae exhibiting cerebroid-like, folded and branched patterns. Label **m** marks opaque, more or less strongly micritised parts. E and F) PPL and CL image pair of densely packed lamellar structures. Note cellular fabric in some aggregates, clearly visible under CL (fig. F) but not discernible in PPL (fig. E). All samples from Paleocene breccia near Montpellier, France.



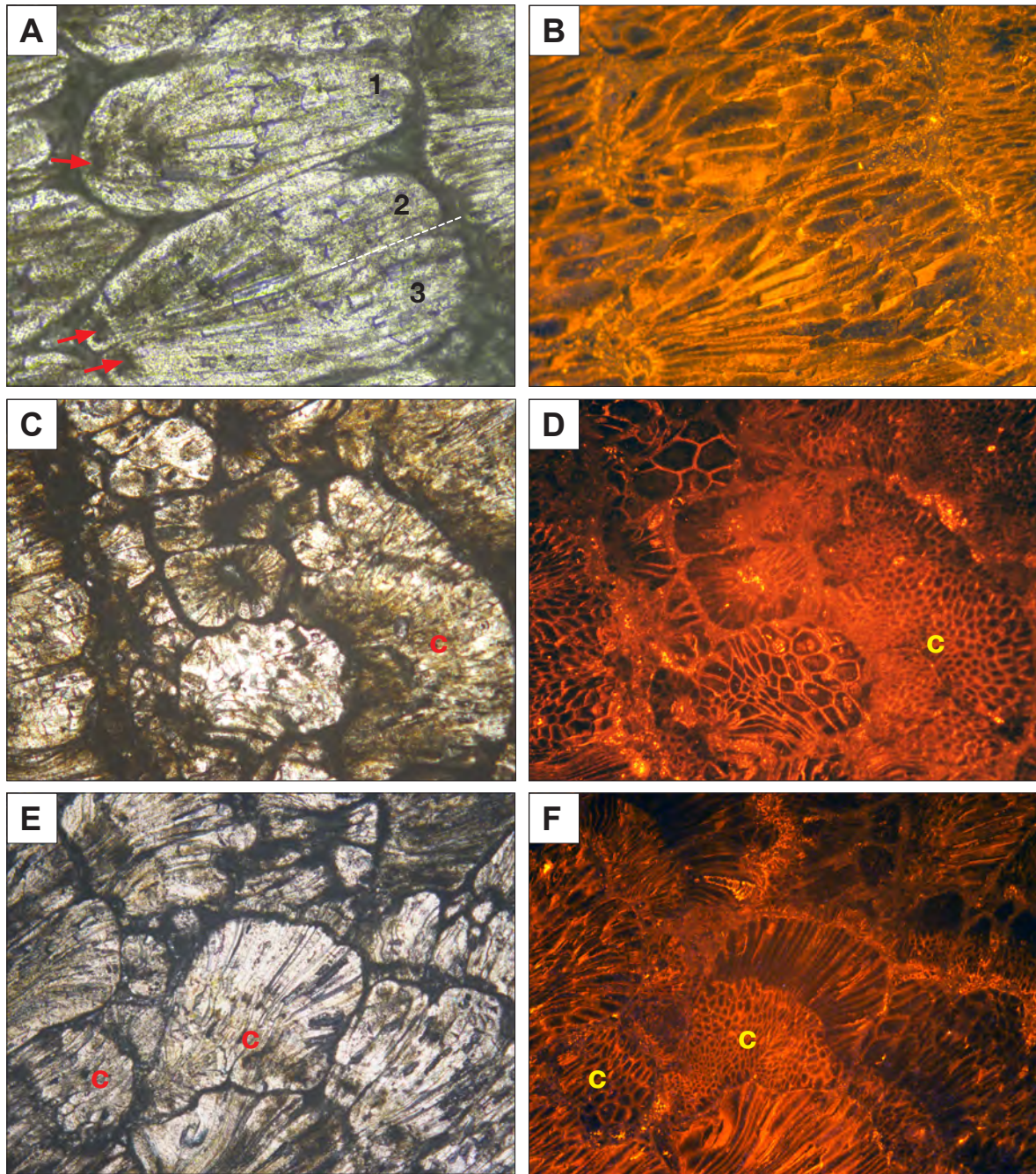


**Figure A5-4.07.** PPL and CL image pairs of strongly asymmetrical *Microcodium* aggregates.

A, B) Arrows indicate axial canals located close to the margin of asymmetric aggregates (numbered 1-3).  
 C-F) Labels c indicate aggregates apparently composed of elongate, prismatic elements under PPL (figs. C and E) while showing an obvious cellular texture in CL counterparts (figs. D and F), indicating that individual elongate prismatic grains are composed of multiple elements.



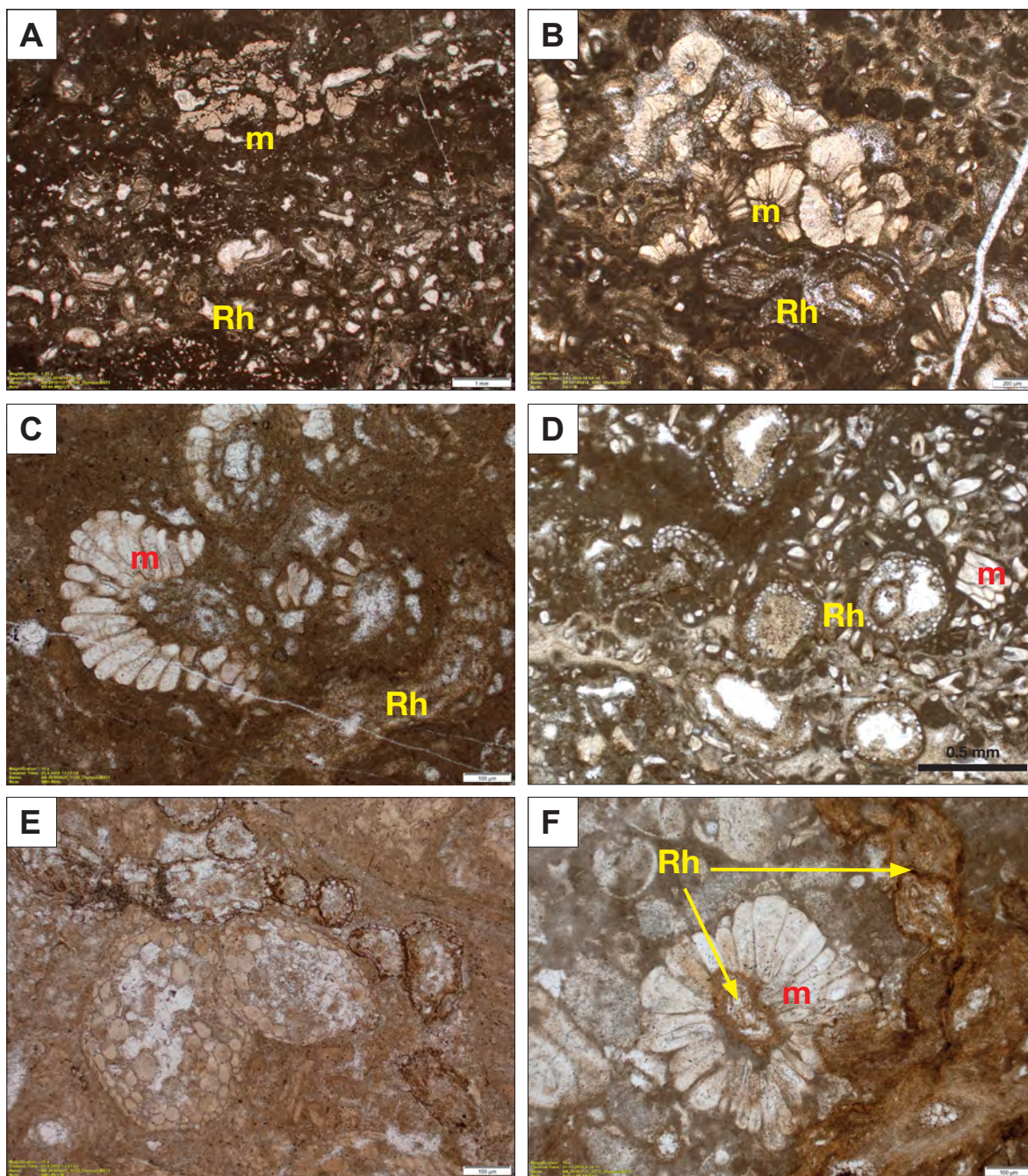


**Figure A5-4.08.** Association of fine root rhizoliths (Rh) and *Microcodium* (m) in laminar calcretes (rhizolites) from Paleocene Liburnian Formation (A, B) and Trstelj Formation (C-F). See explanation in captions of Figs. 5.19-5.20.



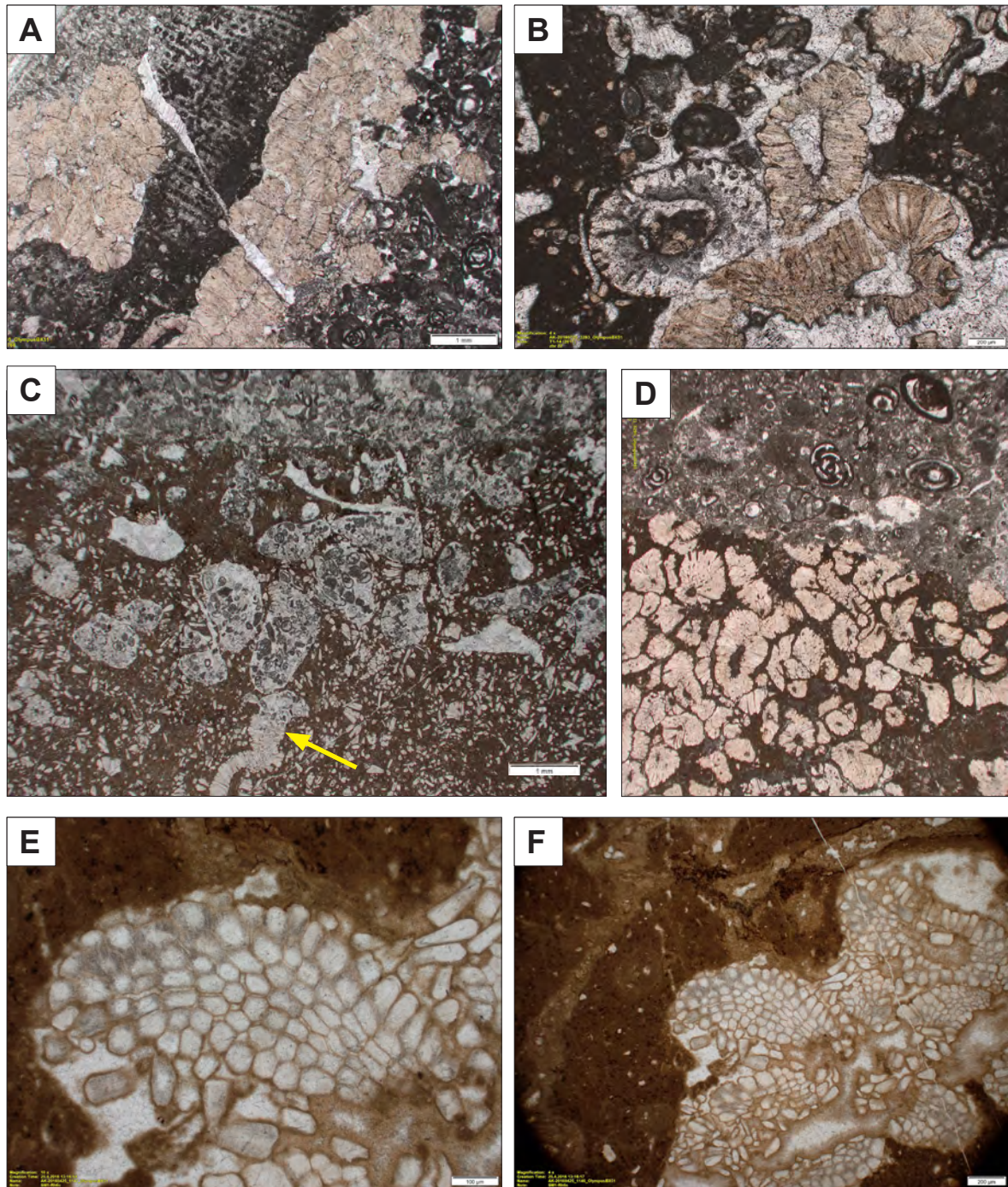


**Figure A5-4.09.** *Microcodium*-substrate relationships. See captions in Figs. 5.12 and 5.13. *Microcodium* corroding a coral clast (A) and lithified (?calcretised) bioclastic sediment (B). A: Šumka section. B: T1-9 core (see table in Appx. A5-3. C, D) Subaerial exposure surface, overlain by marine bioclastic grainstone/packstone, showing voids/borings corresponding to *Microcodium* (partly preserved in the lower part of fig. C). Šumka section. E, F) In situ partial disintegration of *Microcodium* aggregates in massive calcrete. Sv. Martin calcrete.



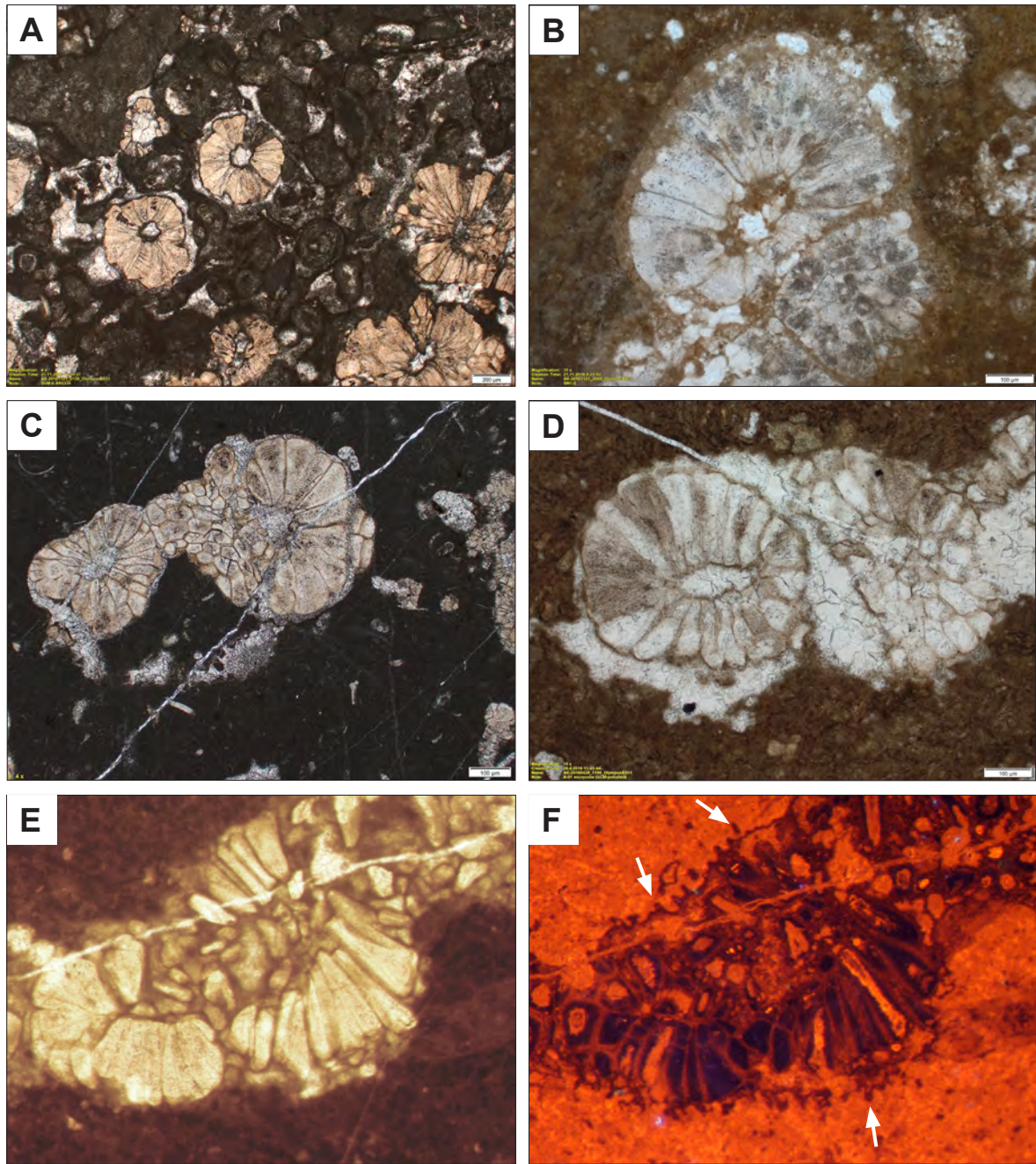


**Figure A5-4.10.** *Microcodium*-substrate relationships. A-D) Rosette cross-sections of *Microcodium* aggregates showin more or less pronounced void around the rosette, possibly corresponding to decomposed (root) epidermal layer. E, F) PPL/CL pair of (thick) thin section. Note features in CL image, but not visible in PPL, possibly corresponding to root hairs (cf. Fig. 5.12A, B). A: Šumka section; B, D, E, F: Sv. Martin calcrete; C: Čebulovica section.



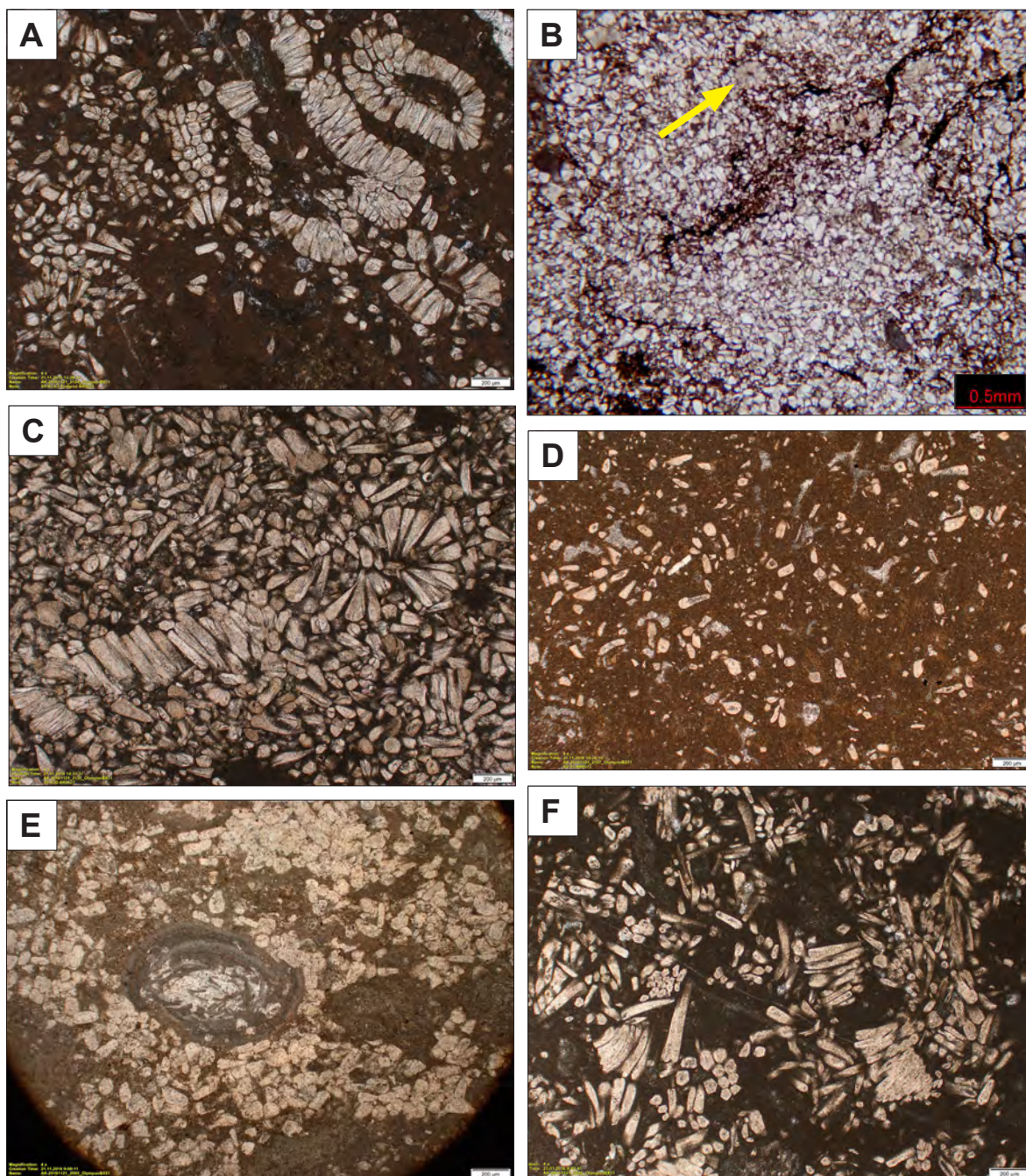


**Figure A5-4.11.** Disintegrated and resedimented *Microcodium*. All thin section photomicrographs in PPL. A) Whole and partly disintegrated corn-cob aggregates. Sample SV-44, Divača. B) *Microcodium* 'packstone' composed of almost of lightly elongate grains. Note preserved aggregate (rosette) marked with arrow. Čebulovica section. C) *Microcodium* packstone composed of separate elongate grains and an almost unbroken rosette. Liburnian Formation, Slavnik locality, Maastrichtian. D) Massive to peloidal calcrete with 'floating' *Microcodium* grains. E) Isodiametric *Microcodium* grains surrounding weathered miliolid foram. Trstelj calcrete. F) Strongly elongate pyramidal grains embedded in micrite. Padriče locality (see Table A5-3.1).



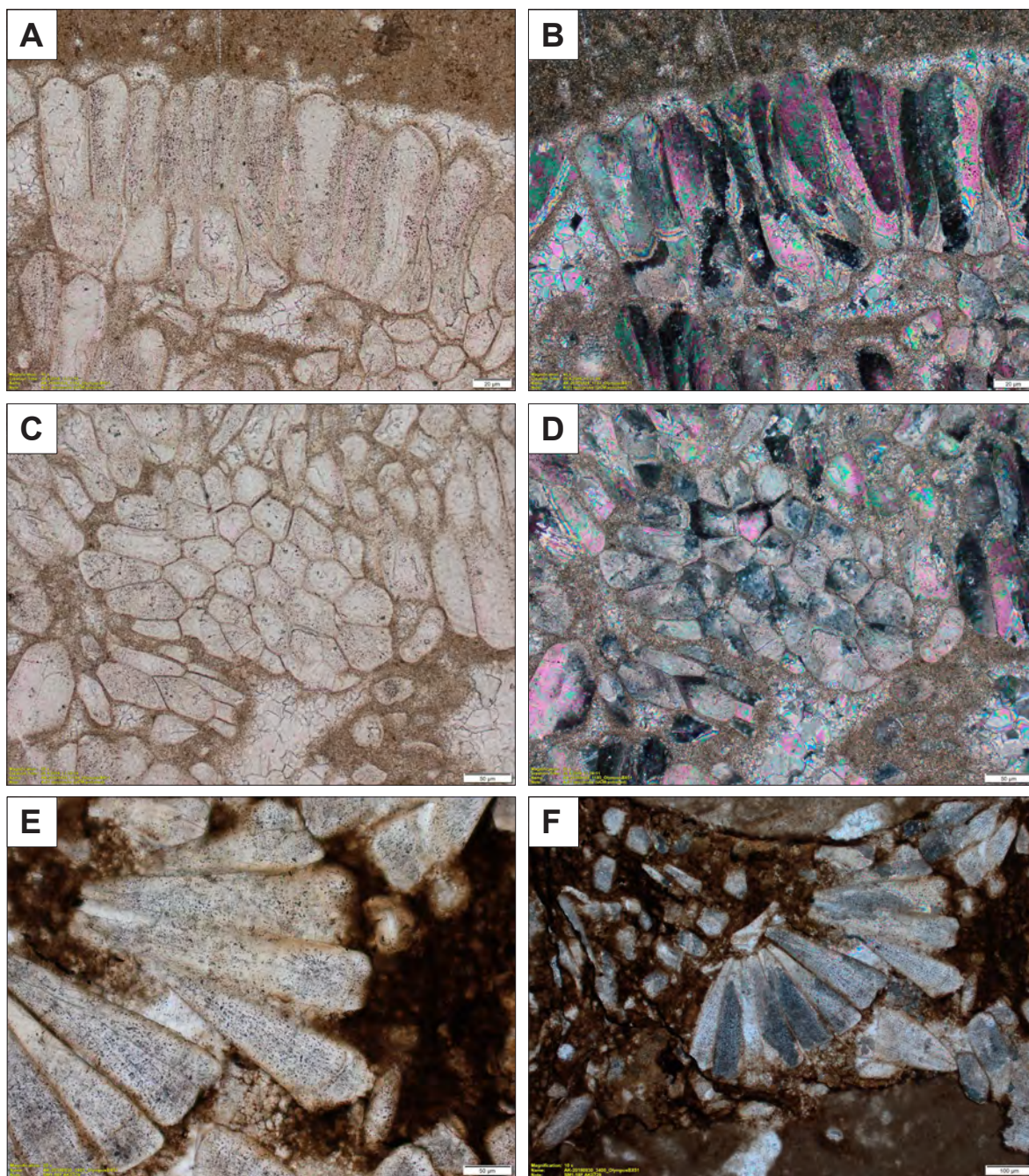


**Figure A5-4.12.** Ultrastructure and crystal morphology of *Microcodium* grains. PPL/XPL photomicrograph pairs of thin sections. See captions in Fig. 5.14.



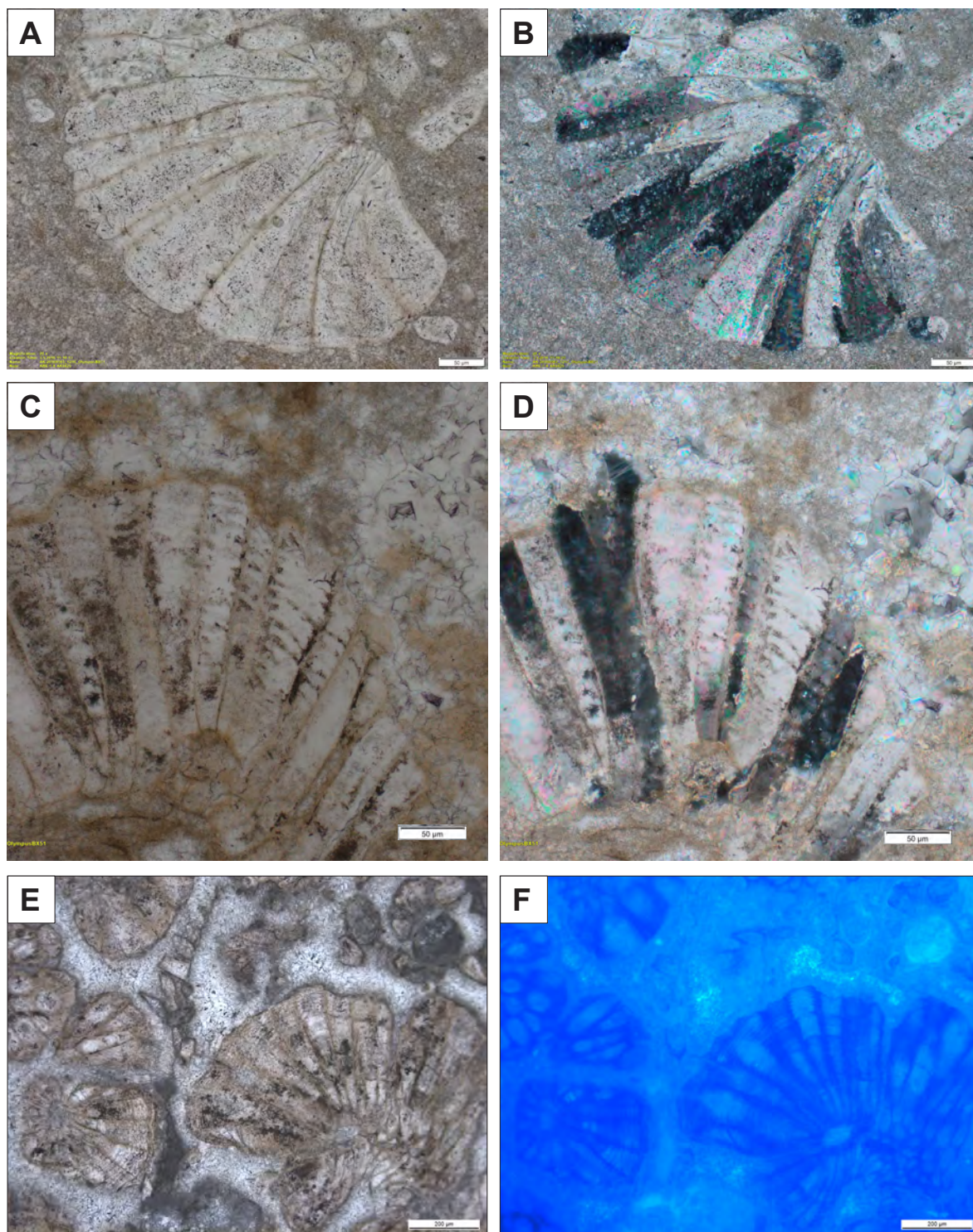


**Figure A5-4.13.** Ultrastructure and crystal morphology of *Microcodium* grains, thin section photomicrographs A, B and C, D) PPL/XPL pairs. E, F) PPL and fluorescence (blue light filter) photomicrographs of 'striate' *Microcodium*.



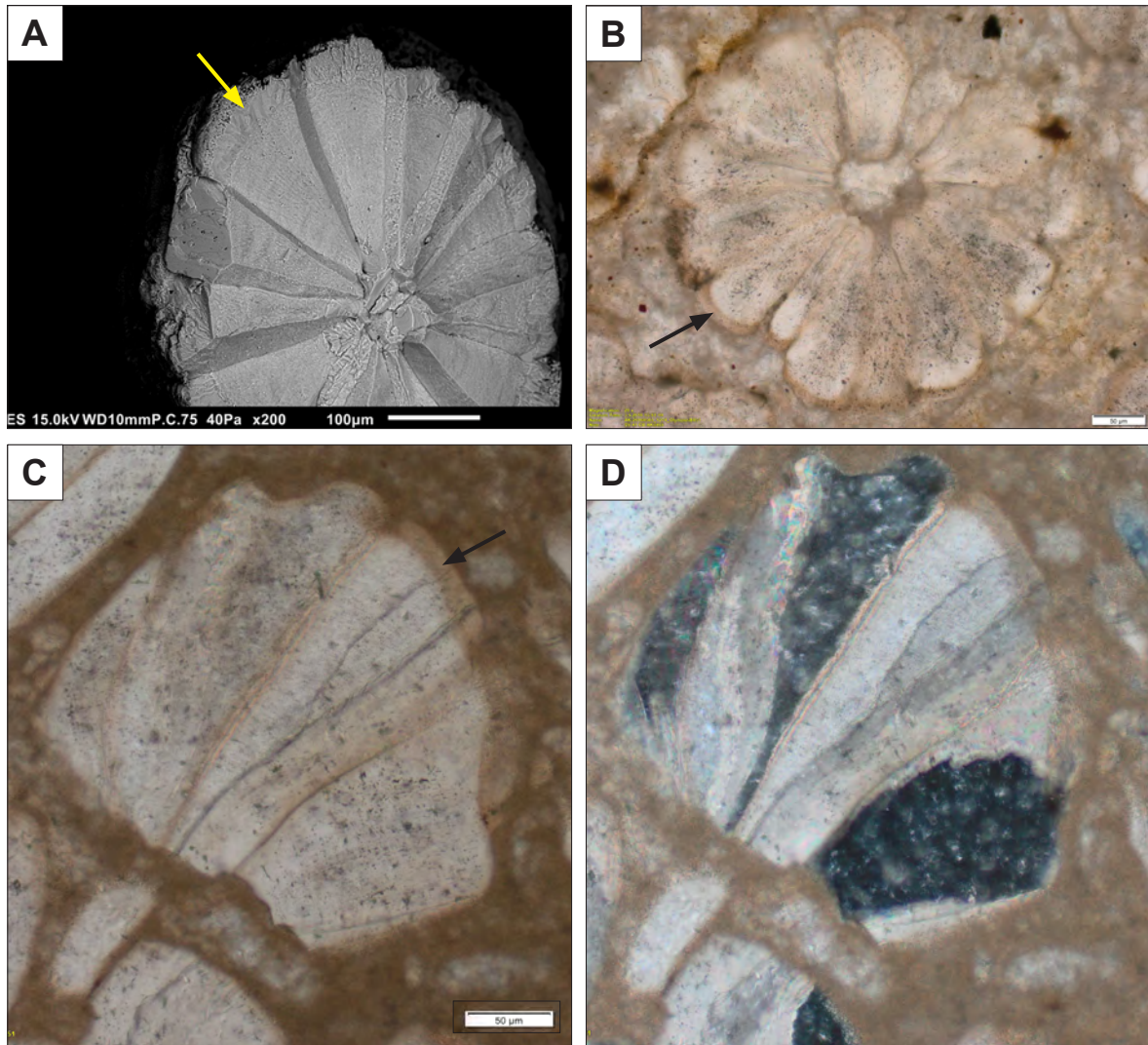


**Figure A5-4.14.** Ultrastructure and crystal morphology of *Microcodium* grains. Rare external (radial) overgrowths of pyramidal grains distinguished by their microstructure (arrow in SEM image in figure A) and (brownish) colour in PPL images (figures B and C). D) XPL pair of C showing apparent optical continuity of the overgrowth. Sample in A: Esplugafreda section; C-D) Čebulovica section.

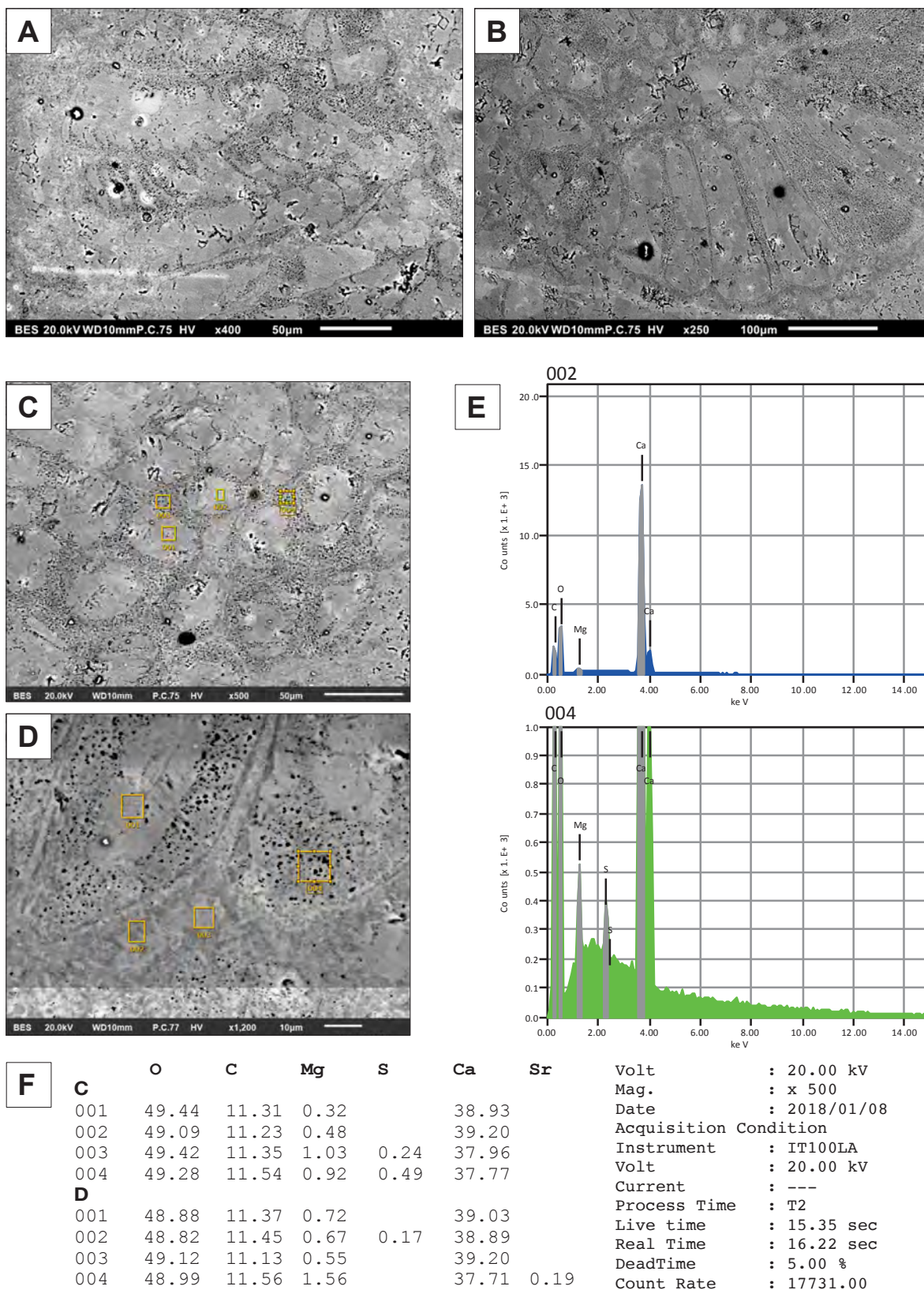
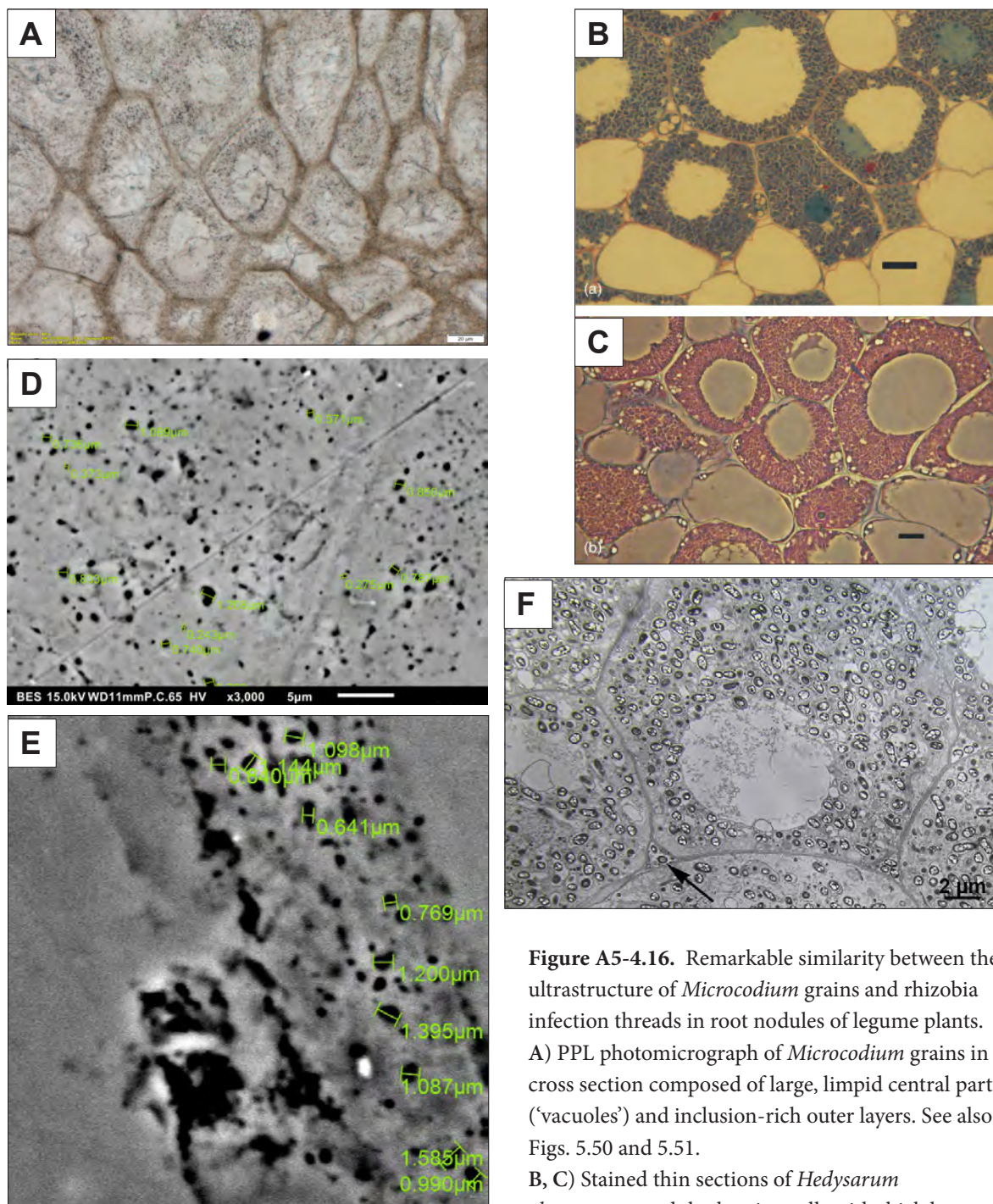


Figure A5-4.15. BES SEM photomicrographs and EDS elemental analysis of vacuolar *Microcodium*.





**Figure A5-4.16.** Remarkable similarity between the ultrastructure of *Microcodium* grains and rhizobia infection threads in root nodules of legume plants. A) PPL photomicrograph of *Microcodium* grains in cross section composed of large, limpid central parts ('vacuoles') and inclusion-rich outer layers. See also Figs. 5.50 and 5.51. B, C) Stained thin sections of *Hedysarum glomeratum* nodule showing cells with thick layers

of rhizobia (stained blue in B and red in C) between cell walls and vacuoles (large unstained central cell lumina); scale bars 10  $\mu\text{m}$ . Images copied from Muresu et al. (2008).

D, E) Close up BES SEM images of the outer layer of a *Microcodium* grain showing spherical voids/organic inclusions with diameter from 0.2 to 1.5  $\mu\text{m}$ , equivalent in size to bacterioid vesicles in fig. F. Sample (thin section) TS A-01\_UCM.

F) Cells of a root nodule, massively invaded by bacteria (bacteroids); few bacteria were found in intercellular spaces (arrow). Bacteroids are surrounded by a peribacteroid membranes; vesicles often contain osmophile material. TEM photomicrograph, taken from Marchetti et al. (2010). Scale bar 2  $\mu\text{m}$ .



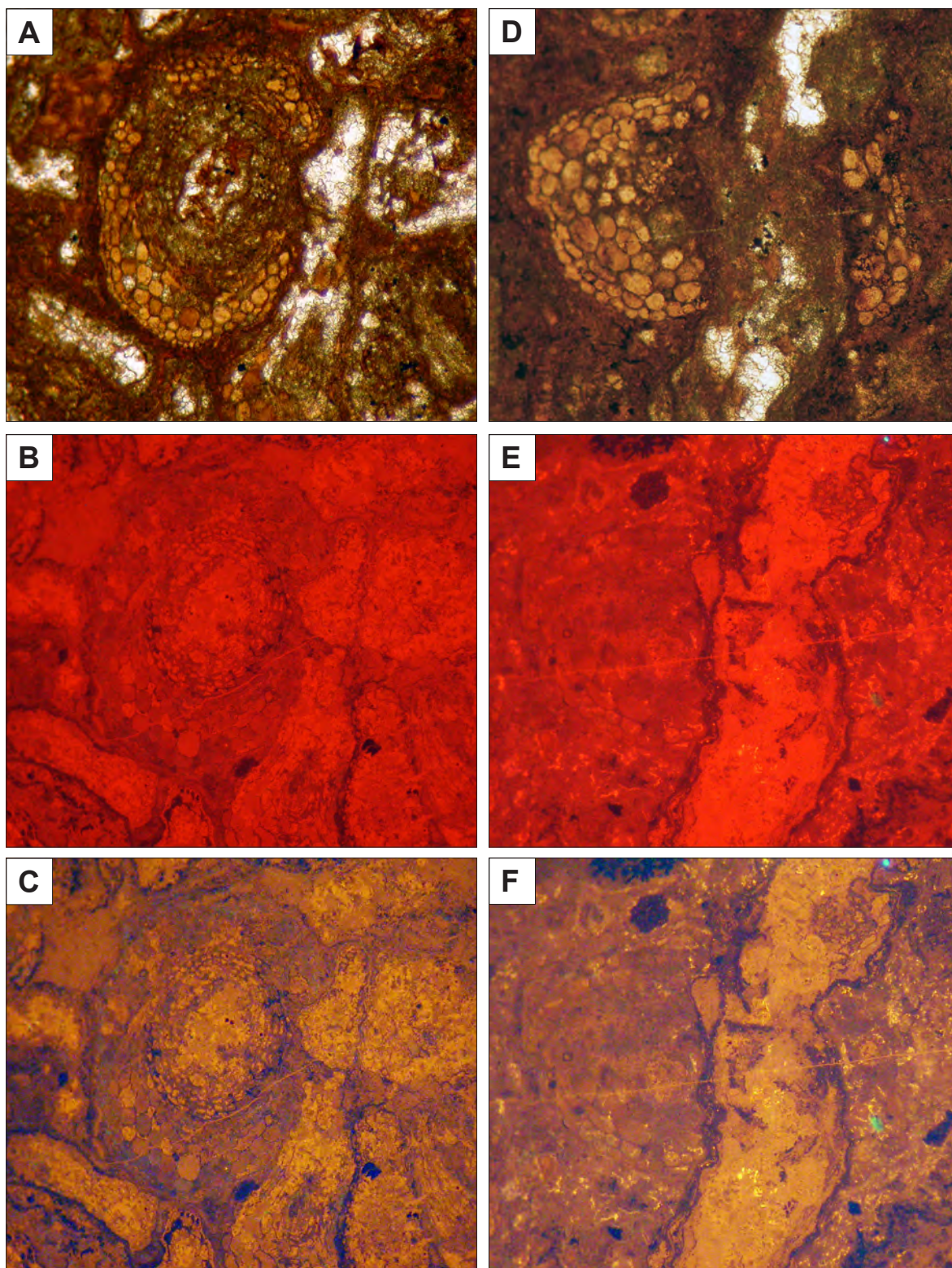


**Figure A5-4.17.** Permineralised (noncalcified) fine roots. A, D) PPL, B, E) original CL, and C, F) false-colour enhanced CL photomicrographs. See captions in Figs. 5.18 and 5.19.



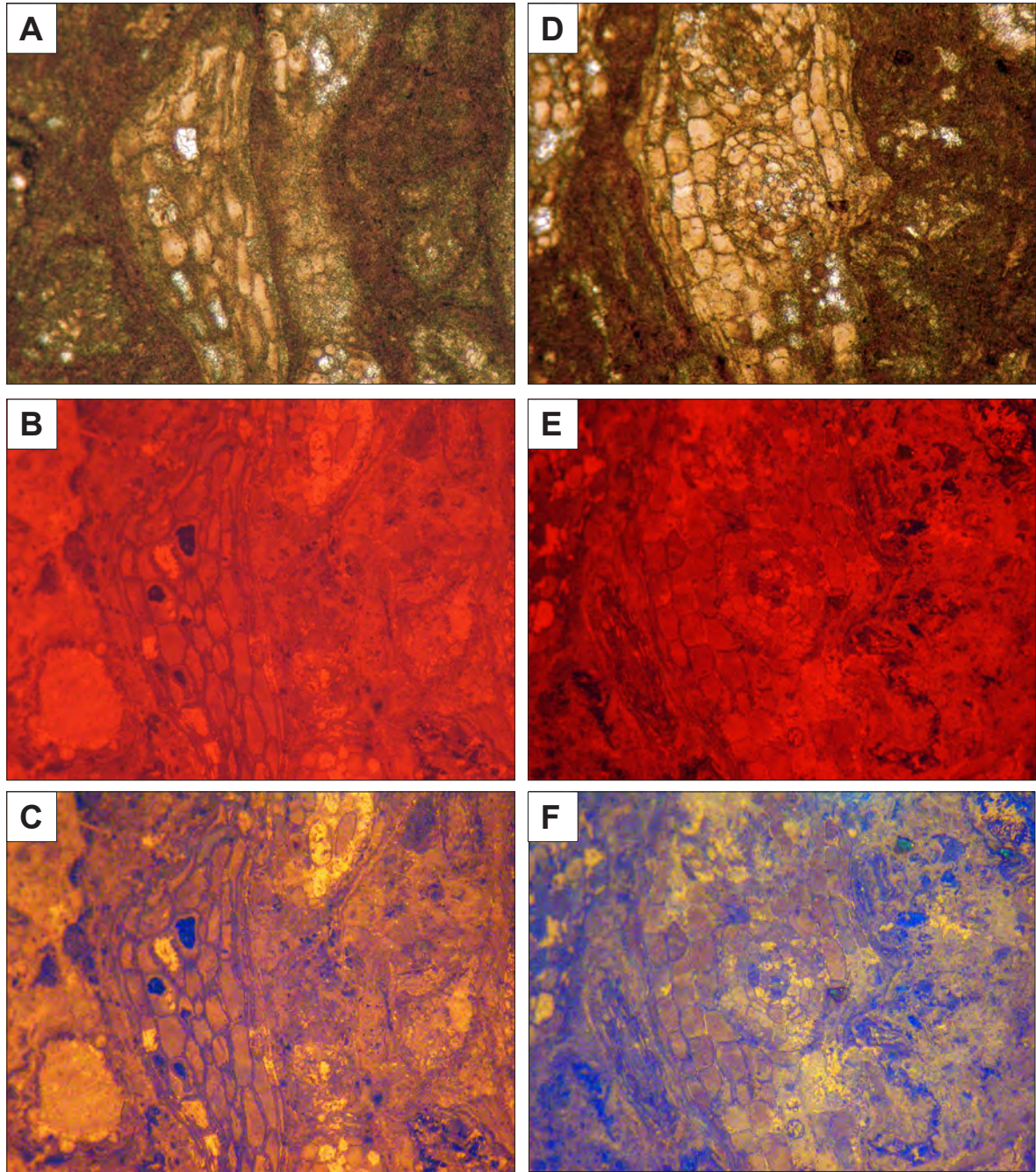


**Figure A5-4.18.** Permineralised (noncalcified) fine roots. A, D) PPL, B, E) original CL, and C, F) false-colour enhanced CL photomicrographs. See captions in Figs. 5.18 and 5.19.



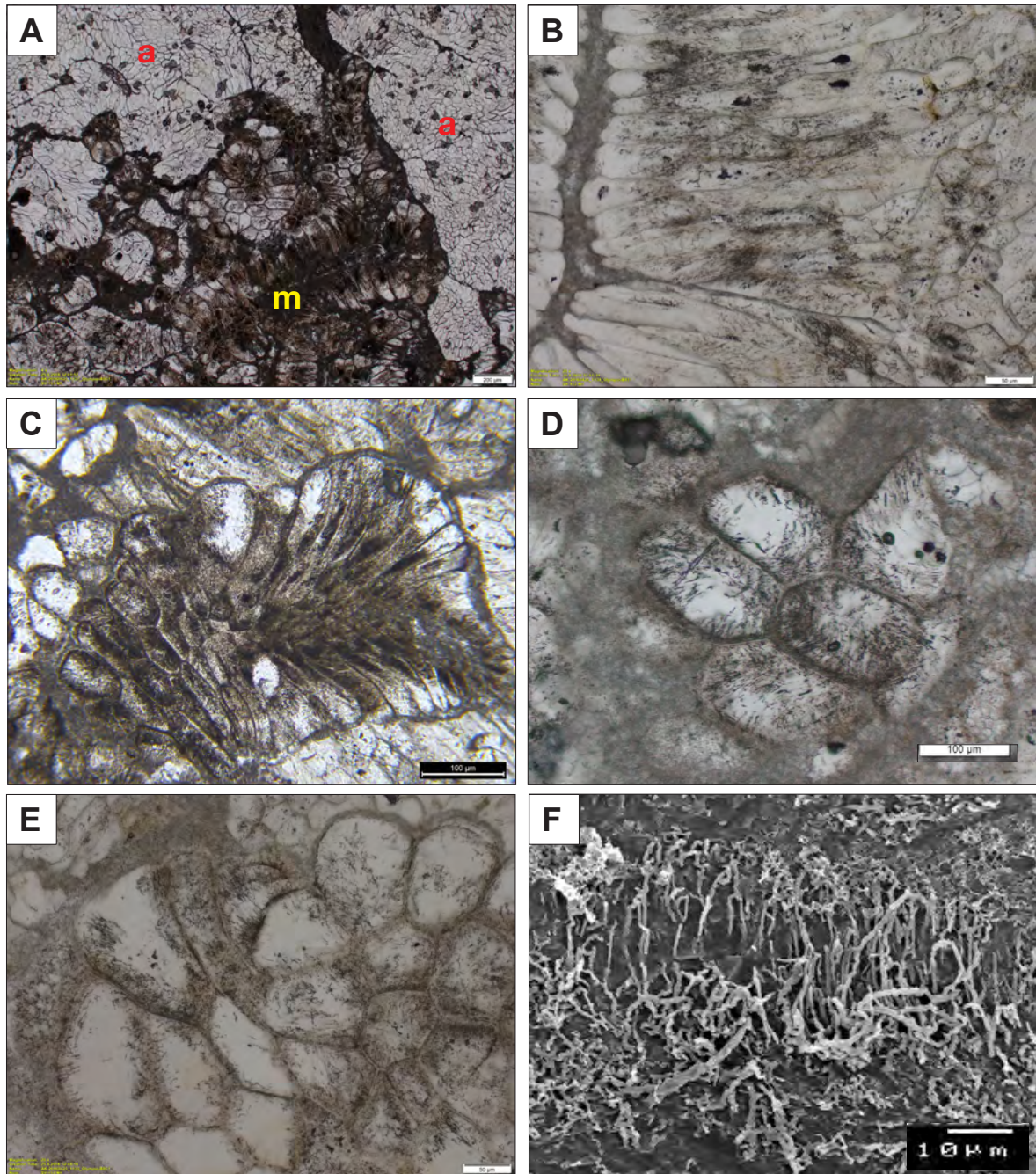


**Figure A5-4.19.** Filamentous fabric (endolithic microborings) in *Microcodium*, Paleocene breccia, Montpellier. A-E) PPL thin section photomicrographs. Longitudinal section of a lamellar form showing unaltered aggregates (a) and intensively micritised part (m) altered by microendoliths. F) SEM photomicrograph of a resin-impregnated cast of endolithic microborings in a *Microcodium* grain. Also see captions in Figs. 5.20 and 5.21.



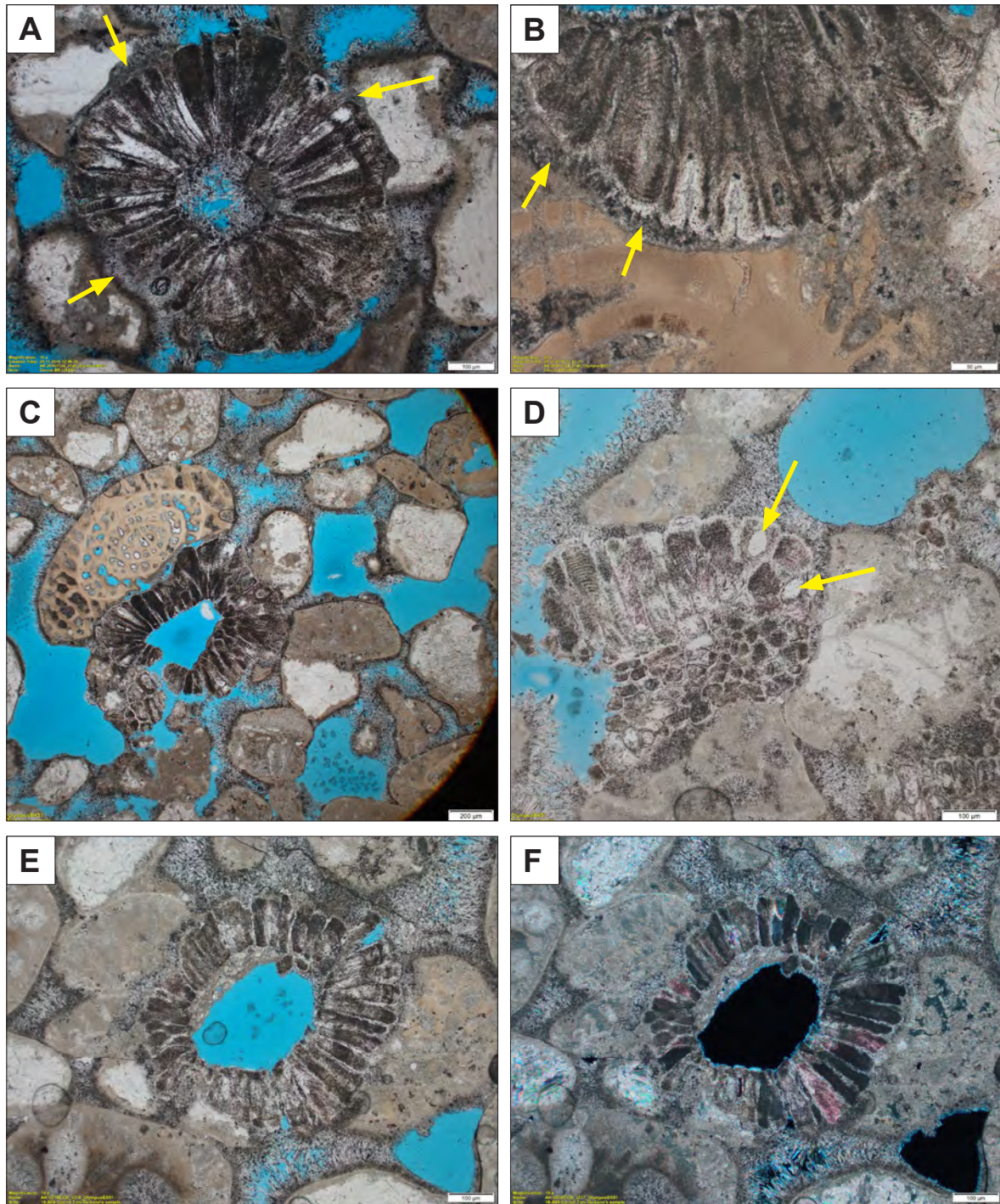


**Figure A5-4.20.** *Microcodium* from a Holocene beachrock of Providenciales, Turks an Caicos Islands. Blue resin-embedded ultrathin section. A) A rosette aggregate in corrosive contact with grains. Arrows indicate voids between *Microcodium* and grains, filled by cement. Note aragonite cement in the axial canal. B) Corrosive contact of *Microcodium* with porcellaneous foram, arrows indicate a void, filled by cement. Concentric striate features in some grains are emphasised by intensive endolithic infestation. C) Oblique section through an aggregate, corroding porcellaneous (miliolid) foram and other clasts. *Microcodium* grains appear strongly micritised (affected by endolithic borings). D) Altered *Microcodium* aggregate, arrows indicate unaltered central parts of some grains. E, F) PPL and XPL photomicrographs of a strongly micritised (microbored) *Microcodium* rosette.



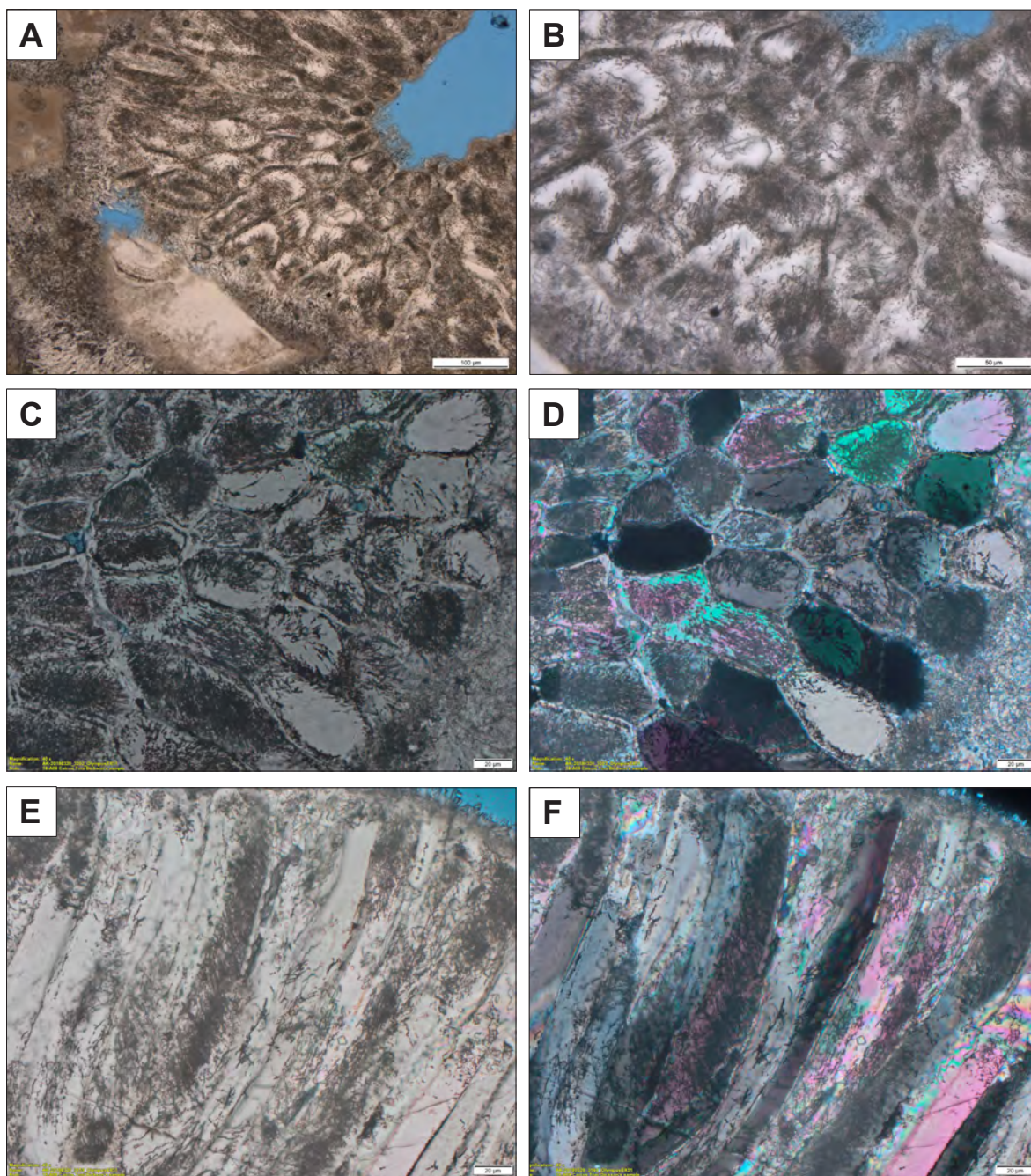


**Figure A5-4.21.** *Microcodium* from a Holocene beachrock of Providenciales, Turks an Caicos Islands. Blue resin-embedded ultrathin section. Patterns of microendolithic borings. See captions in Figs. 5.21 and 5.22.



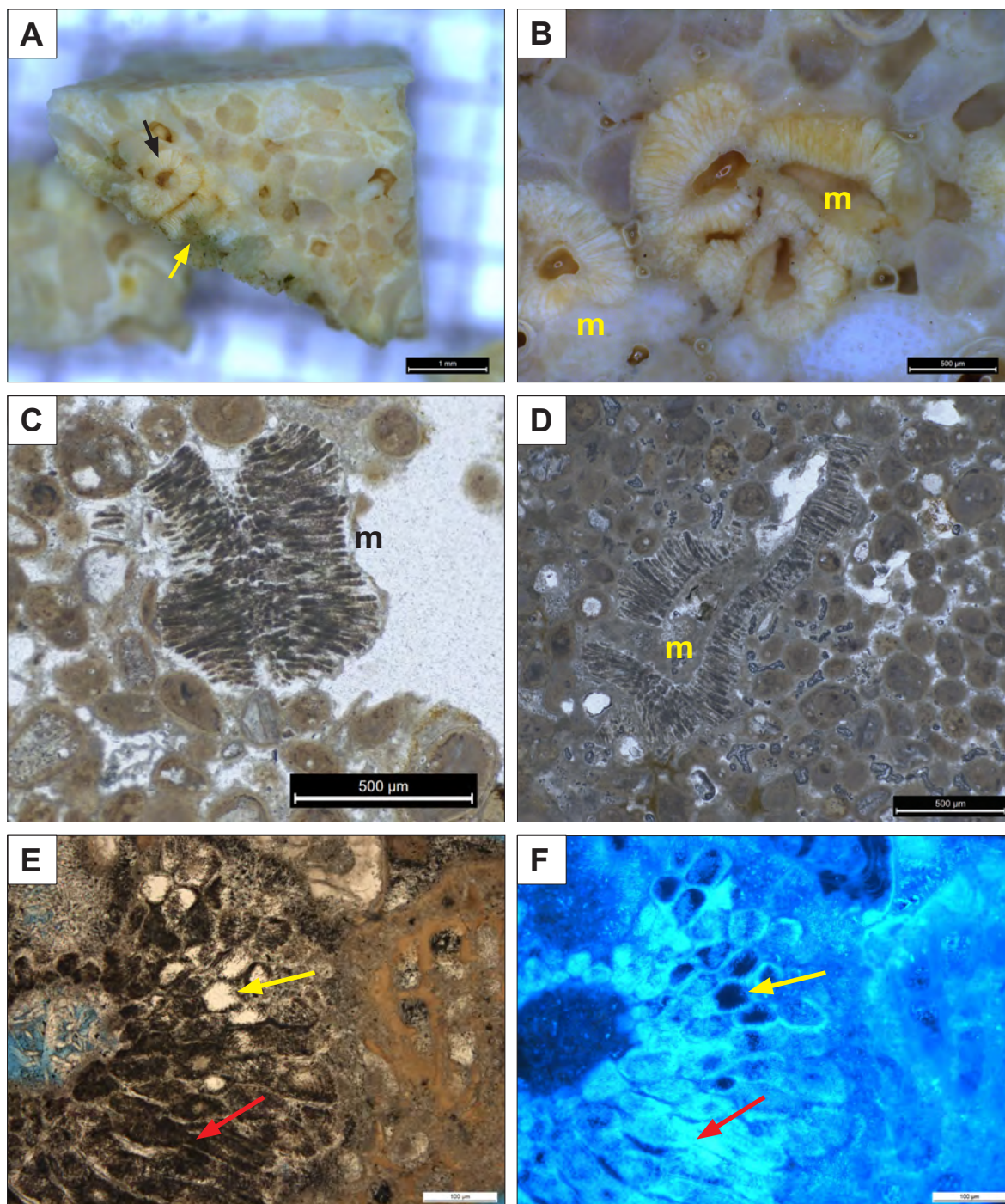


**Figure A5-4.22.** Quaternary (Holocene) *Microcodium* material. A) Fragment of a beachrock with *Microcodium* aggregates before embedding in resin. Green spots (yellow arrow) are cyanobacterial remains on a weathered surface. B) Surface of a resin-embedded slab. Reflected light photos. C, D) PPL thin section photomicrographs of strongly micritised (endolithised) *Microcodium* aggregates (m) from calcretised aeolianite. E, F) PPL and fluorescence (blue-light filter) photomicrographs of intensively microendolithised *Microcodium*. Stongest fluorescence corresponds to the most porous (resin-embedded) areas (red arrows), whereas original, mostly unaltered calcite is dark, nonluminescent (yellow arrows). A, B, E, F) Holocene beachrock, Providenciales, Turks an Caicos Islands. C, D) Holocene aeolianite, San Salvador, the Bahamas.

## Appendix A5.5 EPMA elemental analysis of *Microcodium* and permineralised fine roots/rhizoliths

Elemental analyses were performed on polished thin sections on a JEOL JXA-8900 M WD/ED Electron Microprobe (CNME, University Complutense Madrid) operating at 15 kV and 20 nA and employing an electron beam diameter of 5  $\mu\text{m}$ . The limits of detection for the analysed elements/oxides were: Ca 145 ppm, Mg 125 ppm, Fe 295 ppm, Mn 240 ppm, Sr 175 ppm, P, S 330 ppm, SiO<sub>2</sub> 400 ppm, Al<sub>2</sub>O<sub>3</sub> 170 ppm.

**Table A5-5.1** Raw data (wt% oxides). Material: mcod - *Microcodium*, PFR - permineralised fine roots/rhizoliths

thin section	material	pt #	CaO	MgO	FeO	MnO	SrO	P2O5	SO3	SiO2	Al2O3
A02	mcod	1	54.972	0.788	0.038	0	0.129	0.035	0.155	0	0.029
A02	mcod	2	51.668	0.883	0	0	0.167	0	0.32	0.021	0.025
A02	mcod	3	53.507	0.639	0	0	0.162	0.041	0.191	0	0.007
A02	mcod	4	51.099	1.802	0	0.061	0.271	0.037	0.429	0.029	0
A02	mcod	5	49.721	2.884	0	0	0.361	0.012	0.491	0	0.132
A02	mcod	6	52.301	1.079	0.056	0.006	0.479	0.038	0.45	0	0
A05	PFR	7	52.321	0.614	0.019	0.033	0.282	0	0.249	0.013	0.032
A05	PFR	8	49.151	0.83	0.239	0.006	0.295	0.046	0.23	0.034	0.016
A05	PFR	9	51.404	0.952	0.234	0.039	0.345	0.051	0.332	0	0.054
A05	PFR	10	51.217	0.816	0.279	0	0.28	0.054	0.337	0.025	0
A05	PFR	11	51.551	0.686	0.056	0	0.31	0.031	0.173	0.012	0.031
A05	PFR	12	52.358	0.716	0.154	0	0.346	0.043	0.422	0.017	0.019
A05	PFR	13	50.563	0.736	0.298	0	0.346	0.07	0.53	0.013	0
A05	PFR	14	50.2	0.724	0.116	0.033	0.331	0.062	0.477	0	0.061
A01	mcod	7	52.38	0.889	0.032	0	0.2	0.047	0.071	0.012	0.009
A01	mcod	8	52.969	1	0.01	0	0.245	0.037	0.119	0.007	0
A01	mcod	9	53.473	0.604	0	0	0.8	0.014	0	0	0
A01	mcod	10	49.762	2.533	0	0	0.383	0.017	0.341	0	0
A02	mcod	11	53.678	1.351	0.061	0	0.402	0.027	0.394	0	0
A02	mcod	12	54.689	0.732	0.022	0.03	0.308	0.065	0.146	0	0.02
A02	mcod	13	51.081	1.897	0	0.026	0.45	0.025	0.396	0.026	0.038
A02	mcod	14	52.774	0.996	0	0.015	0.211	0.038	0.253	0.004	0
A02	mcod	15	52.119	1.255	0	0	0.302	0.07	0.271	0.017	0.025
A02	mcod	16	52.357	1.059	0.035	0.068	0.293	0.032	0.236	0.018	0.004
A02	mcod	17	51.867	1.372	0	0	0.424	0.019	1.066	0.011	0.009
A02	mcod	18	51.021	1.923	0	0	0.425	0.034	0.448	0	0.008
A02	mcod	19	50.808	2.58	0	0	0.398	0.045	0.58	0	0.066



**Table A5-5.2** Selected microprobe data of *Microcodium* from table A5-5.1 expressed in element wt %. Thin section A02 (Šumka section, see Appendix A5-2). Below: BSE EPMA images show positions of measurement points, and a histogram showing Mg, Sr and S concentrations.

thin section - point #	material	Ca	Mg	Fe	Mn	Sr	P	S
A02 - 1	mcod - inner part	39.288	0.475	0.030	0.000	0.109	0.015	0.062
A02 - 2	mcod - inner part	36.927	0.533	0.000	0.000	0.141	0.000	0.128
A02 - 3	mcod - inner part	38.241	0.385	0.000	0.000	0.137	0.018	0.077
A02 - 4	mcod - outer layer	36.520	1.087	0.000	0.047	0.229	0.016	0.172
A02 - 5	mcod - outer layer	35.535	1.739	0.000	0.000	0.305	0.005	0.197

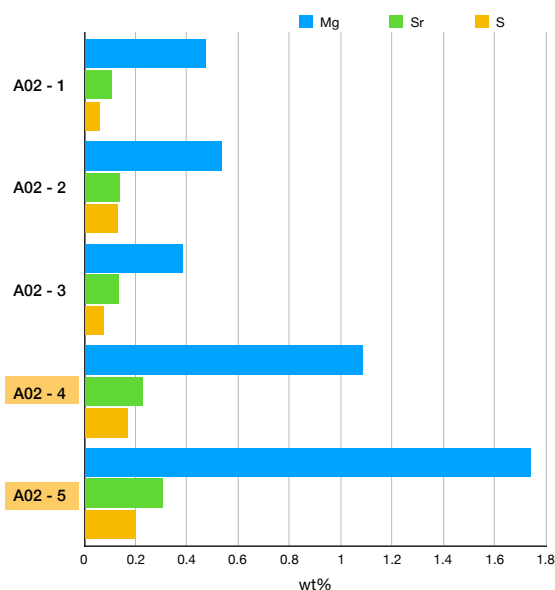
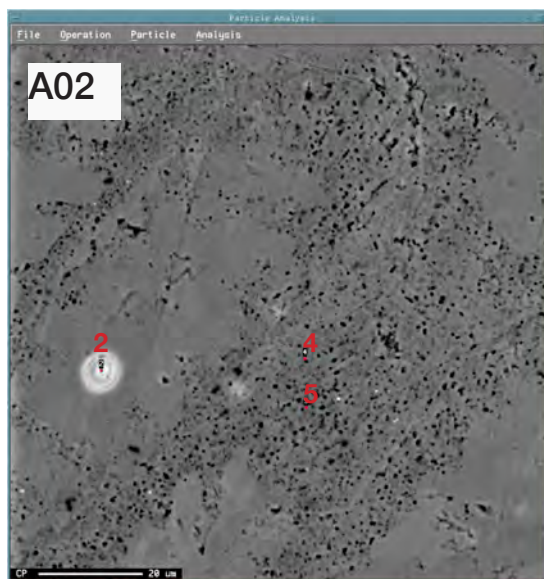
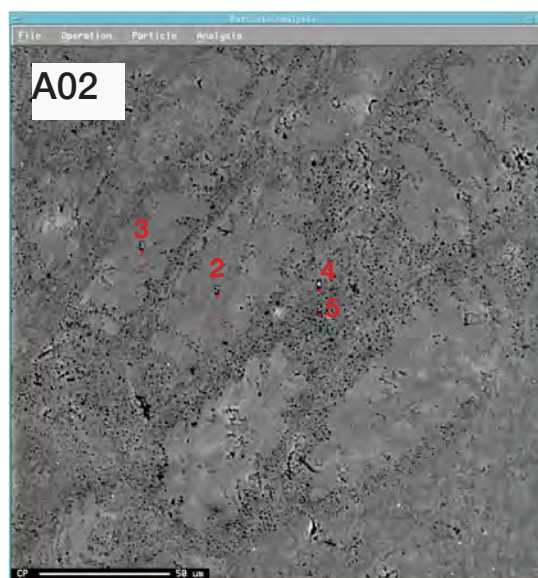
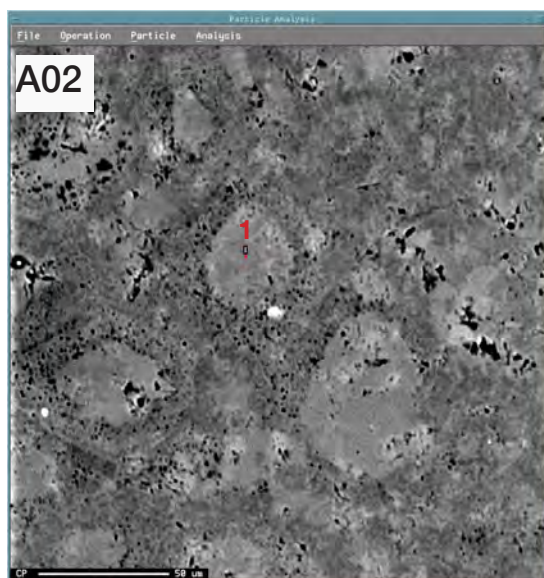




**Table A5-5.3** Selected microprobe data of *Microcodium* from table A5-5.1 expressed in element wt %. Thin sections A01 and A02. Below: BSE EPMA images show positions of measurement points, and a histogram showing Mg, Sr and S concentrations.

thin section - point #	material	Ca	Mg	Fe	Mn	Sr	P	S
A01 - 7	mcod - inner part	37.436	0.536	0.025	0.000	0.169	0.021	0.028
A01 - 8	mcod - inner part	37.857	0.603	0.008	0.000	0.207	0.016	0.048
A01 - 9	matrix	38.217	0.364	0.000	0.000	0.676	0.006	0.000
A01 - 10	mcod - outer layer	35.565	1.528	0.000	0.000	0.324	0.007	0.137
A02 - 11	matrix	38.363	0.814	0.047	0.000	0.340	0.012	0.158
A02 - 12	mcod - inner part	39.086	0.441	0.017	0.023	0.260	0.028	0.058
A02 - 13	mcod - outer layer	36.507	1.144	0.000	0.020	0.381	0.011	0.159
A02 - 14	mcod - inner part	37.717	0.601	0.000	0.012	0.178	0.017	0.101
A02 - 15	mcod - inner part	37.249	0.757	0.000	0.000	0.255	0.031	0.109
A02 - 16	mcod - inner part	37.419	0.639	0.027	0.053	0.248	0.014	0.095
A02 - 17	mcod - outer layer	37.069	0.827	0.000	0.000	0.359	0.008	0.427
A02 - 18	mcod - outer layer	36.464	1.160	0.000	0.000	0.359	0.015	0.179
A02 - 19	mcod - outer layer	36.312	1.556	0.000	0.000	0.337	0.020	0.232

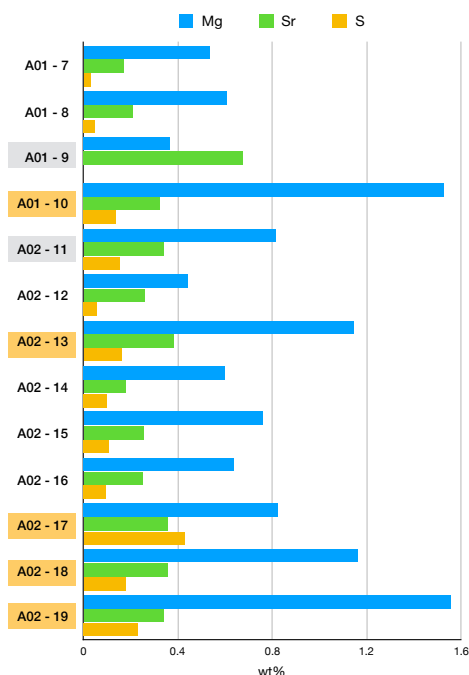
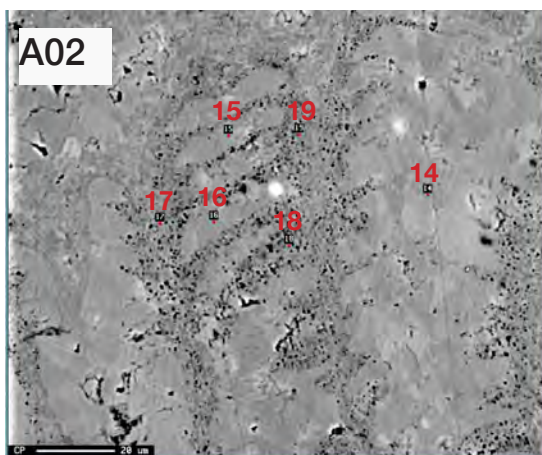
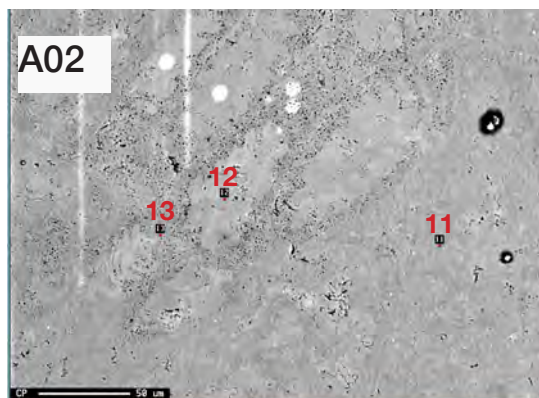
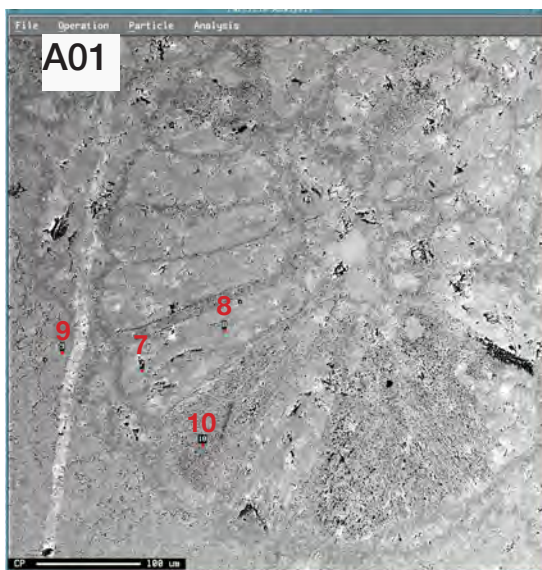
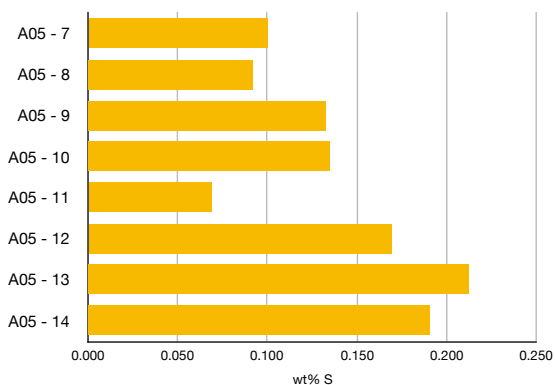
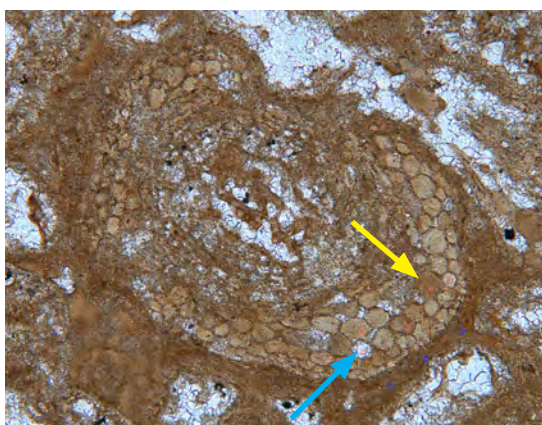
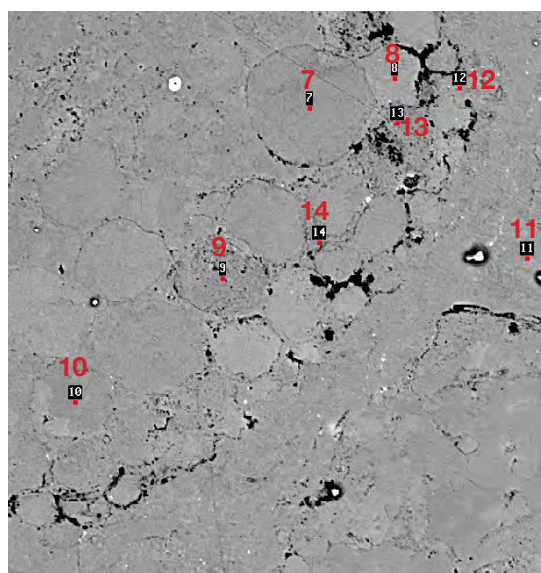
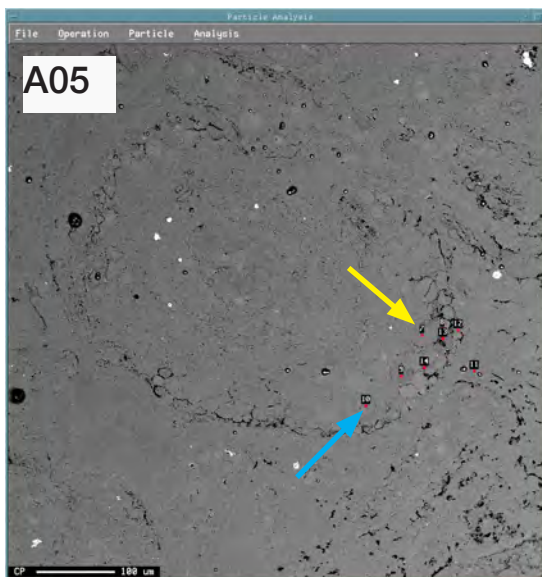


**Table A5-5.4** Selected microprobe data for permearlaised fine rhizolith from table A5-5.1 expressed in element wt %. Thin section A05 (Sv. Martin calcrete; see Appendix A5-2). Below: BSE EPMA images show positions of measurement points and a corresponding thin section microphotograph in transmitted light;; histogram shows S concentrations.

thin section - point #	material	Ca	Mg	Fe	Mn	Sr	P	S
A05 - 7	brown - intracell.	37.393	0.370	0.015	0.026	0.238	0.000	0.100
A05 - 8	brown - intracell.	35.128	0.501	0.186	0.005	0.249	0.020	0.092
A05 - 9	brown - intracell.	36.738	0.574	0.182	0.030	0.292	0.022	0.133
A05 - 10	spar - intracell.	36.604	0.492	0.217	0.000	0.237	0.024	0.135
A05 - 11	matrix	36.843	0.414	0.044	0.000	0.262	0.014	0.069
A05 - 12	brown - intracell	37.420	0.432	0.120	0.000	0.293	0.019	0.169
A05 - 13	cell wall	36.137	0.444	0.232	0.000	0.293	0.031	0.212
A05 - 14	cell wall	35.878	0.437	0.090	0.026	0.280	0.027	0.191



## Appendix A5.6 Stable isotope analysis of *Microcodium*

**Table A5-6.1** Results of C and O stable isotope analyses of *Microcodium*. See Table A1.1 (Appendix A1) for details about material, analytic procedures and laboratories.

sample #	material	$\delta^{13}\text{C}$ (VPDB)	$\delta^{18}\text{O}$ (VPDB)
AK-03-006	Fontjoncouse 01	-8.3	-6.9
AK-03-008	SV-81 Vrabče	-9.4	-5.2
AK-03-009	SV-81 Vrabče	-9.2	-5.4
AK-03-010	SV-81 Vrabče D	-9.6	-5.6
AK-03-010R	SV-81 Vrabče D	-9.2	-4.2
AK-03-011	SV-82 Vrabče	-8.5	-4.6
AK-03-012	SV-82 Vrabče	-8.9	-4.7
AK-03-012R	SV-82 Vrabče	-9.0	-3.5
AK-03-013	SV-84 Div-X-1	-11.9	-5.2
AK-03-014	SV-84 Div-X-1	-12.1	-5.4
AK-03-014R	SV-84 Div-X-1	-11.9	-4.2
AK-03-015	SV-84 Div-X-1	-12.1	-5.4
AK-03-016	Fontjoncouse 01	-8.5	-6.0
AK-03-017	Fontjoncouse 01	-8.3	-7.1
AK-07-300	SV-81 bulk mcod	-13.8	-5.9
AK-07-301	SV-82 bulk mcod	-8.7	-4.6
AK-14-436	T14-449; Claret Fm	-14.1	-7.0
AK-14-436-2	T14-449; Claret Fm	-14.0	-6.8
AK-14-436-3	T14-449; Claret Fm	-14.2	-7.2
AK-14-436-4	T14-449; Claret Fm	-13.6	-6.7
AK-14-436-5	T14-449; Claret Fm	-14.2	-6.9
AK-14-437	T14-449; Claret Fm	-12.6	-6.6
AK-14-437-2	T14-449; Claret Fm	-12.6	-6.7
AK-14-437-3	T14-449; Claret Fm	-12.9	-6.8
AK-14-438	T14-441 Esplugafreda	-9.7	-6.2



Table A5-6.1 (continued)

sample #	material		
AK-14-439	T14-441 Esplugafreda	-8.5	-5.8
AK-14-440	T14-441 Esplugafreda	-10.4	-6.2
AK-14-440-2	T14-441 Esplugafreda	-10.0	-5.8
AK-14-441	T14-436 Esplugafreda	-8.4	-4.7
AK-14-441-2	T14-436 Esplugafreda	-8.2	-4.6
AK-14-441-3	T14-436 Esplugafreda	-8.2	-4.9
AK-14-442	T14-422 (!) Fontllonga	-7.7	-4.4
AK-14-443	T14-430 Espulgafreda, Talarn Fm	-18.5	-7.6
AK-14-443-2	T14-430 Espulgafreda, Talarn Fm	-18.9	-8.0
AK-14-444	T14-430 Espulgafreda, Talarn Fm	-13.0	-4.9
AK-14-444-2	T14-430 Espulgafreda, Talarn Fm	-13.0	-5.4
AK-14-444-3	T14-430 Espulgafreda, Talarn Fm	-12.3	-5.1
AK-14-444-4	T14-430 Espulgafreda, Talarn Fm	-12.4	-5.4
AK-15-502	Caicos Beachrock, mcod	-5.0	-3.1
AK-15-502-2	Caicos Beachrock, mcod	-4.7	-3.5
AK-15-507	Caicos Beachrock, mcod ~90%	-4.9	-3.5
AK-14-434	M-7 M.Cond./lam. mcod	-12.2	-7.8
AK-14-435	M-7 M.Cond./lam. mcod	-12.5	-7.2
AK-14-435-2	M-7 M.Cond./lam. mcod	-12.4	-7.3
AK-14-435-3	M-7 M.Cond./lam. mcod	-11.9	-7.1
AK-14-435-4	M-7 M.Cond./lam. mcod	-12.6	-6.9
AK-14-435-5	M-7 M.Cond./lam. mcod	-12.2	-7.2
AK-14-435-6	M-7 M.Cond./lam. mcod	-11.3	-6.7

## Appendix A5-7 Published C and O stable isotope data of *Microcodium* and calcified roots

**Table A5-7.1** C and O stable isotope composition of *Microcodium* and corresponding host rock carbonates from Tertiary localities of France, and comparative data of modern calcified roots (Morin 1993, p. 131-131). *Microcodium* data include selected analyses of Bodergat (1974) and Casanova & Nury (1989). Key: *Microcodium* morphotypes: 1 - rosette; 2 - intermediate; 3 - laminar/lamellar; 0 - calcified roots (Recent). Stratigraphic units:

No.	Locality	<i>microcodium</i>					host rock					
		Age [My]	Strat. Unit	morpho-type	d13C mood	d18O mood	Strat. Unit	Age [My]	Material	d13C matrix	d18O matrix	
1	AumRou1	52	Vit	1	-16.20	-7.10						
2	AumRou1	52	Vit	1	-16.79	-7.10						
3	AumRou1	52	Vit	1	-13.40	-7.10	Vit	52	CPsol	-10.90	-6.10	
4	StBauz1	52	Vit	1	-12.10	-6.70						
5	StBauz1	52	Vit	1	-11.49	-6.80	Cr>	65	CPsol	-7.80	-6.58	
6	Rousse.						vit	52	CPsol	-9.68	-6.00	
7	Roussel	52	Vit	1	-6.77	-5.02	vit	52	CPsol	-7.77	-4.64	
8	Roussel	52	Vit	1	-6.78	-5.00	Vit	52	CPsol	-7.83	-5.16	
9	Roussel	52	Vit	1	-7.65	-5.87	vit	52	CPsol	-7.82	-5.32	
10	Roussel	52	Vit	1	-10.44	-5.74	vit	52	CPsol	-8.61	-5.67	
11	Roussel	52	Vit	1	-9.95	-5.83	vit	52	CPsol	-9.03	-4.69	
12	Aix1	52	Vit	1	-6.31	-4.29	Vit	52	CPsol	-7.23	-4.98	
13	Aix1	52	Vit	1	-6.66	-5.13	vit	52	CPsol	-7.21	-5.89	
14	Aix1	52	Vit	1	-9.96	-5.81	Vit	52	CPsol	-9.58	-5.11	
15	Aix1	52	Vit	1	-10.33	-6.07	vit	52	CPsol	-9.53	-5.01	
16	Ax15221	52	Vit	1	-8.25	-6.39						
17	Ax15471	52	Vit	1	-7.53	-6.46						
18	AixCar1	52	Vit	1	-6.59	-4.99						
19	Floren1	52	Vit	1	-8.94	-6.92	Vit	52	CPsol	-8.54	-6.61	
20	F10ren1	52	Vit	1	-9.86	-7.27	Vit	52	CPsol	-8.81	-6.34	
21	Arce	52	Vit	1	-8.81	-6.53	vit	52	CPsol	-8.88	-6.73	
22	Arce	52	Vit	1	-12.63	-6.26	Vit	52	CPsol	-10.00	-7.30	
23	Arce	52	Vit	1	-9.22	-6.39	Vit	52	CPsol	-8.84	-6.44	
24	Arce	52	Vit	1	-12.46	-6.33	Vit	52	CPsol	-9.53	-6.93	
25	Arce	52	Vit	1	-11.48	-6.69	Vit	52	CPsol	-8.45	-5.32	
26	Arce	52	Vit	1	-10.56	-6.38	Vit	52	CPsol	-8.68	-6.88	
27	Arce	52	Vit	1	-10.92	-6.90						
28	Arce	52	Vit	1	-10.04	-6.63	Vit	52	CPsol	-10.02	-6.61	
29	Arce	52	Vit	1	-10.56	-7.08	Vit	52	CPsol	-10.32	-7.22	
30	Arce								CTurc	-10.24	-7.15	
31	Arce	52	Vit	1	-10.44	-6.28	Vit	52	CPsol	-10.60	-6.74	
32	Vi11ev.						Vit	52	CCBlc	-8.75	-5.53	
33	Vi11ev1	62	Dan	1	-9.72	-6.47						
34	Vi11ev1	62	Dan	1	-9.81	-6.50	Dan	62	CCBgRg	-10.63	-6.11	
35	Vi11ev1	62	Dan	1	-8.64	-5.95	Dan	62	CCBgRg	-8.71	-5.68	
36	Vi11ev1	62	Dan	1	-10.32	-6.92	Dan	62	CMCRg	-10.65	-6.73	
37	Ville.								CCalci	-10.60	-5.63	
38	Vi11ev1	52	Tha	1	-8.36	-6.09	Tha	52	CCRosé	-7.66	-5.69	
39	Vi11ev.						Tha	52	CCGris	-7.68	-6.84	
40	Ville1	55	Mon	1	-11.38	-6.85						
41	Vi11ev1	55	Mon	1	-10.67	-6.20	Mon	55	CCRg	-10.42	-6.04	
42	MursBu1	39	Lut	1	-11.14	-6.80	Lut	39		-10.86	-5.94	
43	Boderg.	52	Vit		-10.30	-5.80	Més	65	MC	-1.40	-3.70	
44	Boderg.	52	Vit		-11.00	-5.30	Més	65	MC	-1.10	-3.60	
45	Boderg3	52	Vit	3	-19.51	-9.58						
46	Boderg3	52	Vit	3	-16.81	-8.75						
47	Phobos.	52	Vit		-13.70	-7.40	Més	65	MCNoir	1.20	-3.30	
48	Phobos.	52	Vit		-12.30	-6.20	Més	65	MCNoir	0.00	-4.30	
49	Phobos3	52	Vit	3	-12.55	-6.35						
50	Phobos3	52	Vit	3	-16.90	-7.11						
51	Phobos.								Cca1ci	-11.49	-5.97	
52	Phobos3	52	Vit	3	-14.63	-7.09	Més	65	MCRg	-1.64	-4.26	
53	Phobos3	52	Vit	3	-12.88	-6.35	Més	65	MCGris	-1.48	-3.88	
54	Phobos3	52	Vit	3	-14.32	-6.93	Més	65	MCGris	-1.48	-3.88	
55	Phoboa3	52	Vit	3	-20.50	-9.77	Méa	65		-4.81	-6.48	
56	Phobos.	52	Vit		-14.07	-7.23	Méa	65	MCRg	-1.33	-4.56	
57	Phoboa3	52	Vit	3	-15.45	-8.95	Méa	65	MCBg	0.78	-3.54	
58	Phoboa3	52	Vit	3	-17.92	-9.29	Més	65	MCGr	0.23	-3.00	
59	Phobos3"	52	Vit	3	-14.45	-8.10	Méa	65	MCRg	-0.43	-1.45	
60	Phobos.	52	Vit		-13.85	-7.89						

Table A5-7.1 (continued).

No.	Locality	microcodium					host rock				
		Age [My]	Strat. Unit	morpho-type	d13C mood	d18O mood	Strat. Unit	Age [My]	Material	d13C matrix	d18O matrix
61	Phobos2	52	Vit	2	-12.24	-7.16					
62	BelAir3	52	Vit	3	-11.83	-7.49					
63	BelAir2	52	Vit	2	-11.30	-6.69	Més	65	CCRg	-10.45	-5.62
64	BelAir2	52	Vit	2	-12.68	-6.67					
65	BelAir3	52	Vit	3	-12.31	-6.27	Méa	65	MCGris	-4.05	-5.07
66	BelAir2	52	Vit	2	-12.50	-6.34					
67	BelAir3	52	Vit	3	-18.73	-8.65					
68	BelAir3	52	Vit	3	-20.40	-9.47	Méa	65	MCGris	-7.64	-4.40
69	BelAir3	52	Vit	3	-9.84	-5.27	Més	65	MCBg	-1.09	-4.09
70	BelAir3	52	Vit	3	-9.10	-7.24					
71	BelAir3	52	Vit	3	-9.20	-7.50					
72	BelAir3	52	Vit	3	-14.19	-7.63					
73	Be1Air3	52	Vit	3	-14.90	-7.90					
74	BelAir2	52	Vit	2	-12.11	-6.72	Més	65	MCRg	2.38	-4.23
75	BelAir2	52	Vit	2	-11.25	-6.72	Més	65	MCGr	1.85	-3.36
76	BelAir2	52	Vit	2	-12.86	-6.72	Vit	52	CTurRg	-10.39	-5.56
77	BelAir2	52	Vit	2	-10.47	-6.42	Més	65	MCGr	1.30	-3.36
78	BelAir2	52	Vit	2	-13.62	-7.76					
79	BelAir3	52	Vit	3	-13.90	-7.25					
80	BelAir2	52	Vit	2	-12.11	-6.79	Més	65	MCNr	0.58	-3.80
81	BelAir3	52	Vit	3	-14.55	-7.30	Més	65	MCNr	0.58	-3.80
82	Bourgu2	39	Lut	2	-14.68	-8.92	Tur	88	MCRg	1.44	-4.13
83	Bourgu2	39	Lut	2	-13.93	-8.32	Tur	88	MCRg	0.43	-4.37
84	Bourgu2	39	Lut	2	-14.33	-8.91	Tur	88	MCRg	-0.64	-4.38
85	Bourgu.						Tur	88	MCBlc	1.20	-3.92
86	PAumGr.						Més	65	MCBg	0.80	-4.10
87	PAumGr.						Més	65	MCBg	0.70	-4.40
88	PAumGr3	52	Vit	3	-18.28	-9.09	Més	65	MCBg	0.70	-4.40
89	PAumGr3	52	Vit	3	-19.10	-9.20	Més	65	MCBg	0.70	-4.40
90	PAumGr3	52	Vit	3	-20.10	-9.50	Més	65	MCBg	0.70	-4.40
91	PAumGr3	52	Vit	3	-19.20	-9.10	Més	65	MCBg	0.70	-4.40
92	PAumGr3	52	Vit	3	-19.50	-9.10	Més	65	MCBg	0.70	-4.40
93	Aumela3	52	Vit	3	-16.90	-9.20	Més	65	MCBg	0.80	-3.40
94	Aumela3	52	Vit	3	-20.10	-9.10	Més	65	MCBg	1.20	-4.00
95	Aumela3	52	Vit	3	-21.84	-9.34	Més	65	MCBg	0.44	-4.72
96	Aumela3	52	Vit	3	-17.70	-8.70					
97	Aumela3	52	Vit	3	-17.55	-8.95	Més	65	CC	-8.72	-5.33
98	Aumela3	52	Vit	3	-16.72	-9.05					
99	Aumela3	52	Vit	3	-17.36	-9.16					
100	Aumela3	52	Vit	3	-16.39	-8.71					
101	Aumela3	52	Vit	3	-16.17	-8.63					
102	Brouze2	34	Eoc	2	-19.80	-7.90					
103	Brouze2	34	Eoc	2	-21.95	-8.75					
104	Brouze2	34	Eoc	2	-22.91	-9.29	Eoc	34	CBlc	-8.78	-5.12
105	Brouze2	34	Eoc	2	-21.98	-9.09	Eoc	34	CBlc	-8.34	-4.84
106	Gévaud2	34	PIE	2	-12.25	-8.19	San	83	CCBlc	-9.76	-6.34
107	Gévaud2	34	PIE	2	-10.26	-7.52	San	83	CCBlc	-10.21	-6.58
108	Gévaud2	34	PIE	2	-8.70	-6.60					
109	Gévaud2	34	PIE	2	-8.71	-6.62	San	83	MCBlc	0.24	-4.13
110	Senanq2	39	Lut	2	-19.30	-9.60	Urg	107	MCBlc	0.30	-4.40
111	Senanq2	39	Lut	2	-19.10	-9.20	Urg	107	MCBlc	0.40	-4.30
112	Senanq2	39	Lut	2	-20.15	-9.63					
113	Senanq2	39	Lut	2	-19.88	-9.65	Urg	107	MCBlc	-0.09	-4.51
114	Senanq2	39	Lut	2	-17.63	-9.84	Urg	107	MCBlc	-0.14	-5.29
115	Métham3	39	Lut	3	-14.80	-7.25	Urg	107	MCBlc	0.27	-3.84
116	Chambr3	52	Vit	3	-9.48	-8.12	Ber	126	MC	1.01	-4.05
117	CFont-3	39	Lut	3	-17.89	-7.88	Béd	110	MCBlc	-2.71	-2.81
118	CFont-3	39	Lut	3	-18.49	-8.28	Béd	110	MCBlc	-3.51	-2.76
119	CFont-3	39	Lut	3	-17.30	-7.42					
120	CFont-3	39	Lut	3	-12.12	-5.94	Béd	110	MCBlc	-1.24	-3.06
121	Marsel	27	St>		-0.50	-2.60	St>	27	CBhBr	0.90	-0.20
122	Marsel	27	St>		-1.30	-4.00	st>	27	CBhCl	-0.60	-3.50
123	Marsel	27	St>		-3.30	-5.40	St>	27	CBhCl	-1.40	-3.20
124	Marsel	27	st>		-1.00	-3.00	St>	27	CBhBr	-1.60	-2.50
125	Marsel	27	st>		-2.40	-5.80	St>	27	CBhBr	0.00	-2.80
126	Marsel	27	st>		-2.80	-4.80	St>	27	CBhCl	-1.20	-3.30
127	StGél-O	0	Act	0	-9.44	-6.23	Act	0	CSol	-0.19	-2.88
128	StGél-O	0	Act	0	-10.10	-5.80					
129	StGél-O	0	Act	0	-9.17	-6.30	Act	0	CSol	-0.24	-2.75
130	StGél-O	0	Act	0	-8.50	-5.90					
131	Merca		Act	0	-5.91	-7.43	Act	0	CSolNr	0.07	-5.97
132	Aix---O	0	Act	0	-12.52	-7.23	Act	0	CSolRg	-7.71	-4.52
133	Aix---O	0	Act	0	-12.79	-7.10	Act	0	CSolRg	-7.41	-5.52
134	LubéroO	0	Act	0	-10.75	-7.09	Act	0	CSolBr	0.00	-4.06
135	LubéroO	0	Act	0	-10.84	-6.70	Act	0	CSolBr	-2.45	-6.85
136	RoujanO	0	Act	0	-12.11	-4.92	Act	0	CSolgr	-1.06	-4.64



**Table A5-7.2** C and O stable isotope composition of *Microcodium* of Kabanov et al. (2008); see their Table 1 (p. 22) for details.

sample	description	$\delta^{13}\text{C}$ (PDB)	$\delta^{18}\text{O}$ (PDB)	age
KB_01	Microcodium clump, 10–15% contamination by micritic substrate	-2.69	-4.88	Moscovian
KB_02	Microcodium corn-cob aggregates from fusulinid-rich wackestone	0.04	-2.43	Moscovian
KB_03	Microcodium (small-grained non-aggregated variety) from bioclastic grain-packstone in tempestite facies	-0.99	-2.79	Moscovian
KB_04	Microcodium (corn-cob aggregates) from bioclastic packstone	-0.81	-3.62	Moscovian
KB_05	Microcodium (corn-cob aggregates) from bioclastic wackestone	1.12	-1.10	Moscovian
KB_06	Microcodium corroding Triassic limestone, basal Paleocene	-8.81	-6.86	Paleocene
KB_07	Microcodium associated to calcrete crust. Paleocene.	-8.05	-5.53	Paleocene
KB_08	Microcodium associated to calcrete crust. Paleocene.	-11.04	-6.29	Paleocene
KB_09	Microcodium associated to calcrete crust. Paleocene.	-12.84	-6.32	Paleocene
KB_10	Microcodium corroding Triassic limestone. Base of Paleocene sequence	-7.51	-6.29	Paleocene
KB_11	Microcodium corroding Triassic limestone. Base of Paleocene sequence.	-11.86	-6.33	Paleocene
KB_12	Microcodium corroding Triassic limestone. Base of Paleocene sequence.	-10.25	-6.76	Paleocene
KB_13	Microcodium associated to red calcareous paleosol. Paleocene.	-8.32	-6.02	Paleocene
KB_14	Microcodium laminar colonies	-13.3	-7.25	Paleocene
KB_15	Microcodium laminar colonies	-12.73	-7.8	Paleocene
KB_16	Microcodium laminar colonies	-18.18	-10.09	Paleocene
KB_17	Microcodium laminar colonies	-19.33	-9.54	Paleocene
KB_18	Microcodium laminar colonies	-21.27	-8.57	Paleocene
KB_19	Microcodium laminar colonies with some neomorphic features	-12.91	-6.71	Paleocene
KB_20	Microcodium laminar colonies	-20.60	-9.23	Paleocene
KB_21	Microcodium laminar colonies	-17.93	-8.07	Paleocene
KB_22	Microcodium laminar colonies	-20.70	-8.79	Paleocene